



Study of natural nanovesicles carrying olfactory receptors for the development of biosensing platforms

Marta Sanmartí Espinal

ADVERTIMENT. La consulta d'aquesta tesi queda condicionada a l'acceptació de les següents condicions d'ús: La difusió d'aquesta tesi per mitjà del servei TDX (www.tdx.cat) i a través del Dipòsit Digital de la UB (diposit.ub.edu) ha estat autoritzada pels titulars dels drets de propietat intel·lectual únicament per a usos privats emmarcats en activitats d'investigació i docència. No s'autoritza la seva reproducció amb finalitats de lucre ni la seva difusió i posada a disposició des d'un lloc aliè al servei TDX ni al Dipòsit Digital de la UB. No s'autoritza la presentació del seu contingut en una finestra o marc aliè a TDX o al Dipòsit Digital de la UB (framing). Aquesta reserva de drets afecta tant al resum de presentació de la tesi com als seus continguts. En la utilització o cita de parts de la tesi és obligat indicar el nom de la persona autora.

ADVERTENCIA. La consulta de esta tesis queda condicionada a la aceptación de las siguientes condiciones de uso: La difusión de esta tesis por medio del servicio TDR (www.tdx.cat) y a través del Repositorio Digital de la UB (diposit.ub.edu) ha sido autorizada por los titulares de los derechos de propiedad intelectual únicamente para usos privados enmarcados en actividades de investigación y docencia. No se autoriza su reproducción con finalidades de lucro ni su difusión y puesta a disposición desde un sitio ajeno al servicio TDR o al Repositorio Digital de la UB. No se autoriza la presentación de su contenido en una ventana o marco ajeno a TDR o al Repositorio Digital de la UB (framing). Esta reserva de derechos afecta tanto al resumen de presentación de la tesis como a sus contenidos. En la utilización o cita de partes de la tesis es obligado indicar el nombre de la persona autora.

WARNING. On having consulted this thesis you're accepting the following use conditions: Spreading this thesis by the TDX (www.tdx.cat) service and by the UB Digital Repository (diposit.ub.edu) has been authorized by the titular of the intellectual property rights only for private uses placed in investigation and teaching activities. Reproduction with lucrative aims is not authorized nor its spreading and availability from a site foreign to the TDX service or to the UB Digital Repository. Introducing its content in a window or frame foreign to the TDX service or to the UB Digital Repository is not authorized (framing). Those rights affect to the presentation summary of the thesis as well as to its contents. In the using or citation of parts of the thesis it's obliged to indicate the name of the author.



Tesi doctoral

Study of natural nanovesicles carrying olfactory
receptors for the development of
biosensing platforms

Memòria presentada per
Marta Sanmartí Espinal

Per a optar al grau de **doctor en Biomedicina**

Departament d'electrònica
Universitat de Barcelona

Programa de doctorat en Biomedicina

Tesi doctoral dirigida per
Prof. Josep Samitier Martí

Barcelona, 2014

*A la meva família i en especial
als orbitals de la meva vida, l'Emma i el JoanRa*

“Només s'hi veu bé amb el cor. L'essencial és invisible als ulls”
“*On ne voit bien qu'avec le coeur. L'essentiel est invisible pour les yeux.*”
(El petit príncep – Antoine de Saint-Exupéry)

Acknowledgement

Després de cinc anys, aquesta etapa sembla que ja arriba al seu final. Han estat anys plens de moltes experiències i de gran aprenentatge, però sobretot han estat cinc anys en els quals he conegut molta gent. Persones que m'han ensenyat l'essència de fer ciència i el valor de la feina que fem aquest col·lectiu. És evident que sense tots ells aquesta tesi no seria el que és i amb l'ajuda de tots ells he pogut arribar fins aquí. És per això que m'agradaria agrair a cada un tot el que m'ha aportat durant aquest temps.

Primer de tot m'agradaria agrair al Prof. Josep Samitier, el director de la meua tesi, que m'hagi donat la oportunitat de realitzar la tesi doctoral en el seu grup i poder disposar de totes les instal·lacions necessàries per poder fer bona ciència. Josep, gràcies per haver confiat en mi des del primer dia per fer ciència i per transmetre'm la passió per entendre el “perquè” de les coses. Gràcies per haver-me involucrat tan activament en un projecte europeu format per un gran col·lectiu de científics que m'ha permès no només aprendre molt científicament sinó sobretot de les relacions humanes. Moltes gràcies per valorar l'esforç i la feina feta i per animar-me en moments en que les coses no surten com un voldria. Així doncs, moltes gràcies per haver contribuït en el meu desenvolupament científic i personal.

This thesis was carried out within the context of the BOND European Project integrated in a multidisciplinary consortium at European level with expertise in different scientific areas. Thanks to all of them I have learned about biotechnology, surface chemistry, nanofabrication, electronics and theoretical modelling. Primer de tot voldria agrair al Dr. Gabriel Gomila la seva gran aportació científica per millorar el meu disseny d'experiments i les seves llargues discussions científiques. Then, I would like to specially thank Dr. Edith Pajot and Marie-Annick Persuy because without them these thesis could not be performed. They produce the main element of my thesis, the olfactory receptor-expressed membrane fractions. Also, I would like to thanks them for their interesting scientific discussions that allow me to understand better my research. Y no podía olvidarme de Juan Fran, mi Project manager preferido. La verdad es que no tengo palabras para ti. Eres un gran ejemplo de profesionalidad, de pasión por la ciencia, de buena persona, de persona trabajadora, de persona entregada a lo que hace y

de buen compañero que te convierte en un Project manager insustituible. Tampoco me olvido de mi pequeña familia BOND: Patrizia, Lorena y Annalisa a las que nombraré más adelante.

Els resultats experimentals d'aquesta tesi han estat obtinguts majoritàriament en el laboratori de Nanobioenginyeria del IBEC així doncs no em puc deixar d'agrair a cada un dels "Nanobios" i tota la gent d'administració del IBEC (les Pilars, la Judith, la Isa, el Ricard, el Fran, etc.), gent increïble, que han fet que el dia a dia d'aquests anys hagin estat molt millors. Espero no deixar-me a ningú.

Y por quien tenía que empezar si no por ti, la Dra. Patrizia Iavicoli, la primera persona que me dio la bienvenida en mi primer día en el laboratorio. Patti, no tengo palabras para agradecerte todo el apoyo recibido por ti. Gracias por compartirlo todo, ser mi post-doc preferida, ser una chica BOND, muchas horas de experimentos, muchas discusiones de resultados, muchas charlas, muchas experiencias, muchas comidas, discrepancias, ayudas, risas, viajes; en definitiva por tu grande corazón, por ser una persona tan especial, por tu amistad. Y me falta la tercera chica BOND, Lorena. Que difícil hagués sigut treballar en aquest projecte si tu no haguessis estat al laboratori abans que jo. Tot i les nostres diferències, milions de gràcies per fer-me les coses tant fàcils des del principi i per ensenyar-me com és un físic de veritat per una química ignorant com jo. I deixa'm que et digui, de tot cor, que el teu criteri científic és admirable.

Y más tarde...llegó un nuevo fichaje en Barcelona en el grupo del Dr. Gabriel Gomila que también trabajaría en el proyecto BOND, la Dra. Annalisa Calò. Annalisa te lo he dicho una y otra vez, y no me cansaré de repetirlo: eres mi referente científico. La mejor científica que he conocido: muy trabajadora, con una gran cualidad en análisis de resultados, rigurosa, perfeccionista, con ambición, humilde, realista, con ganas de siempre aprender más, con ganas de enseñar y muy exigente. Una gran compañera de viaje: profesional y personal. Espero haber sido un buen discípulo porque para mí has sido una gran maestra.

També vull mostrar el meu agraïment als sèniors i post-docs del laboratori que han passat o encara són presents al "Nanobio-lab". A la Bea, per les seves xerrades matinals, perquè amb la mirada ja ens dèiem moltes coses, per estar sempre disposada en ajudar-me en el que fos i oberta a qualsevol consulta científica. La discreció que et

caracteritza fa que hagi estat un pilar molt important per mi en aquesta etapa i que la teva marxa del laboratori fos difícil d'afrontar. Al Xavi, sempre disposat a resoldre qualsevol dubte de bioquímica, gràcies. Al Mateu, a un gran científic que m'hagués agradat conèixer molt abans. Gràcies per tots els bons consells i per portar noves idees al laboratori quan més ho necessitàvem, energia positiva en la meua fase final de la tesi; de tot cor, moltes gràcies Mateu. A l'Elena, l'Anna, el Christian, el Marc, la Mònica, el Juanjo, el Toni, la Maria, la Marga, en Bogachan i en Tommy per tots els consells i ajudes rebudes; moltes gràcies a tots, gracias a todos, thanks to all of you.

I què seria el Nanobio sense tots els becaris. Primer de tot vull agrair als veterans en el moment que vaig arribar al Nanobio, tot aquells que em demostraven que la etapa que estava començant tenia un final i seria recompensada: al David, al Santi, a la Ivón, al Mathias, etc. Després a tota la meua petita família, els becaris amb els que he compartit més temps: al Jordi, pels seus gran raonaments i la seva manera de ser; la Sabine, per la seva gran persistència a que tothom s'apuntés a fer la Carrera de la dona, la verdad es que al final lo pasamos bien, tan bien, que al año siguiente repetimos. L'Òscar, per sempre portar a sobre tant bon rotllo i al Sergio por reírnos siempre de las cosas. La Coco, un gran exemple de superació i positivisme, ha sigut un gran plaer haver-te conegut. A la Maru, una gran amiga, pocos momentos compartidos dentro del laboratorio pero grandes momentos fuera, siempre dispuesta a ver las cosas positivas y a reírse con la gente. A Marília, por otra gran amiga, por hacer que los días duros fueran mucho mejores y saber que siempre tenía con quién confiar: muchas gracias, de verdad. Y a Juan Pablo por ser, igual que yo, de los últimos miembros de la vieja escuela de Nanobios: ánimos que esto ya se acaba! I també gràcies a la Patricia, l'Ernest, la Rossella, el Willmer, el José Luís, el Luís, etc. per formar part d'aquest gran col·lectiu, els Nanobios. Finalment als *Elenos*: la Vero, l'Albert, la Maria i la Gizem per ser tan bona gent (gracias por ser cada uno de vosotros tan buena gente). Gràcies a tots per contribuir d'una manera o altra a aquests anys.

Però aquest gran laboratori no seria el mateix sense els seus tècnics, els que hi són i els que ja han marxat. A la Eva, el Sam, la Reyes, al JuanMa, la Laura, al David perquè sempre has lluitat perquè la gran família Nanobio es mantingués unida, el laboratori no seria el mateix sense algú com tu, i sobretot a la Miriam, gràcies per la teua alegria però sobretot gràcies per la teua ajuda en tot; en ensenyar-me a treballar

millor al laboratori, a realitzar experiments quan més ho necessitava, a les discussions científiques, a la teva perseverança, i deixa'm que et digui: molta sort en el que vindrà ara. També m'agradaria agrair als tècnics del *Parc Científic de Barcelona* i del *ICMAB* que m'han ensenyat tant i en certa manera també han contribuït a la feina presentada en aquesta tesi. He tingut la gran sort de treballar amb grans científics i professionals. A tot l'equip de microscopia electrònica però sobretot a la Dr. Carmen López, por tantas horas pasadas delante del microscopio y por despertar mi curiosidad por la microscopía electrónica; al Dr. Gerard Oncins, per transmetrem tranquil·litat i professionalitat, per demostrar-me que moltes hores de AFM mai podran superar la importància de la vida personal de un gran científic. A la Dra. Marta Taulés, gràcies per involucrar-te tant en la meva feina, ajudar-me a millorar-la i per ser una gran companya científica, sincerament crec que hi hauria d'haver més tècnics com tu; moltes gràcies per tot. I per acabar a la Dra. Evelyn Moreno i al José Amable por haberme enseñado tanto y estar siempre disponibles a mis preguntas y a facilitarme el trabajo.

Una altra part dels resultats experimentals d'aquesta tesi han estat obtinguts en col·laboració amb el laboratori de "Nanobiotechnology for Diagnostics" del IQAC-CSIC dirigit per la Dra. M^a Pilar Marco. Moltes gràcies Pilar per haver-me donat la oportunitat de fer dues llargues estades al teu laboratori, per les teves grans contribucions científiques i per haver-me donat la possibilitat de treballar amb un gran grup de científics molt humans. Primer de tot, no em cansaré mai de repetir que aquesta tesi no seria el que és sense la valuosa ajuda i direcció científica del Dr. Roger Galve. Roger, no tinc paraules per agrair-te tot el que m'has ensenyat i la gran quantitat de coses que he après, ets per mi un altre gran mestre. Moltes gràcies per deixar-me prendre les meves decisions i equivocar-me de tant en tant i per la teva paciència cap a una noia tan tossuda com jo. I també voldria donar les gràcies a tots els membres d'aquest fantàstic grup, cada un de vosaltres m'heu fet sentir una més del grup. M'heu acollit com un membre més i m'heu ajudat amb tot el que he necessitat, de veritat que mai m'havia sigut tant fàcil adaptar-me a un laboratori nou. Milions de gràcies al Francisco (en pau descansi), al Pablo, a les Núries, a la Ruth, a l'Anna, a les Martes, el Salva, l'Ester (ets única), al Raül, la Sònia, l'Àlex, la Carme (un plaer haver coincidit amb tu), el Dani (un crack), la Montse, l'Enrique, la Ilaria, la Lorena i per últim i la més important la meva cosina, la Glòria. Cosineta la veritat és que ha sigut una gran experiència positiva haver compartit la ciència amb tu, no podem dir que no hem passat

bons moments juntes oi? Moltes gràcies pel teu suport moral i per les nostres confidències.

D'una manera o altra molta gent ha contribuït en el treball d'aquesta tesi doctoral però voldria destacar en especial l'esforç i l'ajuda experimental obtinguda pels següents científics: a la Dra. Annalisa Calò (Nanoscale bioelectrical characterization group, IBEC), Dr. Patrizia Iavicoli (Nanobioengineering group, IBEC), Miriam Funes (Nanobioengineering group, IBEC) i a la Gizem Altay (Nanobioengineering group, IBEC) que han col·laborat de forma activa en el treball presentat en el Capítol 3 d'aquesta tesi i en el cas de la Dra. Patrizia Iavicoli que a més a més també a col·laborat activament en el treball presentat en el Capítol 4.

Però durant aquests cinc anys no tot ha sigut treballar al laboratori, vull agrair a les meves dues grans famílies, la colla de Sant Cugat i els Troupers de Barcelona per tots els sopars, dinars, Solivelles, xerrades, piscines, Festes majors, calçotades, bodes, naixements, etc. que hem compartit junts que em permeten desconnectar de la ciència i gaudir de les petites coses essencials de la vida. També vull donar les gràcies a les meves IQSs, que encara que passin els anys seguim juntes, sobretot a la Jessi, a la Miriam i a la Laia, per tots els cafès compartits.

I per acabar, aquests agraïments no tindrien cap sentit sinó donés les gràcies al suport incondicional que he rebut de la meva família i la meva família política en cada dia d'aquests últims cinc anys. Començaré amb la meva germana petita, Irene de tot cor moltes gràcies per compartir tantes coses juntes i per estar tant present en el meu dia a dia; al meu germà, allà on estiguis i allà on et porti la teva vida jo sempre pensaré amb tu i estic convençuda que tu també ens portes a nosaltres; als meus pares per ser únics i els millors, al meu pare, per confiar SEMPRE amb mi, i a la meva mare, per ser una persona admirable, gràcies per ser la millor amiga, la millor filla, la millor dona, la millor mare, la millor àvia i per ser una persona insubstituïble a la meva vida.

I ara si que acabo, vull agrair a les meves àvies que sempre s'hagin preocupat per mi i per mostrar interès en el que feia i escoltar-me quan els hi explicava les petites anècdotes d'aquest món anomenat "Ciència". A la iaia Montse, perquè encara et puguem gaudir molts anys més amb la força que et caracteritza i a la iaia Carme perquè

allà on siguis sempre cuidis de nosaltres. Diuen que quan una vida se'n va en neix una de nova, dies abans de marxar em vas dir que portava una nena, i al cap de 9 mesos va néixer l'Emma. Petita, gràcies per arrencar-me un somriure cada dia, per haver arribat a les nostres vides, per haver donat un gir al nostre dia a dia, per ser tant i tant especial i sobretot perquè des del primer dia que et vaig veure vaig notar que series única. I al JoanRa, el meu company de viatge, el meu confident, l'amic que em dóna la mà per tornar-me a aixecar, el meu amant, el millor pare de família amb el que comparteixo tots els meus projectes, inquietuds, bogeries, amb el que ho comparteixo tot. No tinc prou paraules per agrair-te tot el que has significat per mi durant aquesta etapa, podria escriure pàgines i pàgines agraint cada un dels dies d'aquests últims cinc anys però crec que no cal que ho escrigui perquè entre tu i jo, ja ho sabem. Tot i així, deixa'm que et digui: Moltes gràcies per confiar en mi, per estar SEMPRE al meu costat, per donar-me amor cada dia i per compartir cada un dels nostres somnis fent-los realitat.

Aquesta tesi s'ha pogut realitzar gràcies a la concessió d'una beca PFIS del ISCIII.

Table of Contents

ACKNOWLEDGEMENT	V
ABBREVIATIONS	XIX
LIST OF TABLES	XXI
LIST OF FIGURES	XXIII
INTRODUCTION	1
I.1 Volatiles detection for many applications	4
I.1.1 Animals' olfaction as a biological recognition element	6
I.1.1.1 Use of dog olfaction abilities for detection	7
I.2 The olfactory system: anatomy and physiology	9
I.2.1 The olfaction.....	9
I.2.1.1 The insect olfaction	11
I.2.1.2 The vertebrates olfaction.....	11
I.2.2 Volatile molecules detection. The role of the olfactory receptors.....	12
I.2.2.1 The role of Odorant-Binding Protein.....	16
I.2.3 Volatile molecules: an approach from odorants to the pheromones kingdom	19
I.3 Bioelectronics noses based on <i>in vivo</i> experiments	21
I.4 Bioelectronic noses based on olfactory receptors	24
I.4.1 The parameters detected by the sensors are related to changes in intracellular molecules resulting from signal transduction.....	25
I.4.2 The parameters detected are not the electrophysiological potentials of the cells.....	30
I.4.2.1 Detection by Quartz Crystal Microbalance (QCM).....	31
I.4.2.2 Detection by Surface Plasmon Resonance (SPR)	32
I.4.2.3 Detection by Electrochemical Impedance Spectroscopy (EIS)	33
I.4.2.4 Detection by Field-Effect Transistor (FET).....	34
I.5 Conclusions	36
I.6 References	37
OBJECTIVES	43
O.1 Thesis structure	44

CHAPTER 1: Production and characterization of natural nanovesicles containing G-protein coupled receptors.

1.1	Background	49
1.2	Materials and Experimental Procedures	60
1.2.1	Materials	60
1.2.2	Buffers and Solutions	60
1.2.3	Equipments/Software	60
1.2.4	<i>Saccharomyces cerevisiae</i> yeast cell culture characterization	61
1.2.4.1	<i>LS Particle Size Analyser</i>	61
1.2.4.2	<i>Hydrodynamic focusing</i>	62
1.2.5	Nanovesicles solution preparation	62
1.2.6	Nanovesicles solution purification	64
1.2.6.1	<i>Indirect ELISA</i>	65
1.2.7	Western Blot	66
1.2.8	Cryo-electron microscopy (Cryo-EM)	66
1.2.9	Cryo-Fracture Transmission electron microscopy (CF-TEM)	66
1.2.10	Dynamic light scattering (DLS) measurements	67
1.2.11	Nanoparticle Tracking Analysis (NTA) measurements	67
1.3	Results and Discussion	69
1.3.1	Characterization of <i>Saccharomyces cerevisiae</i> yeast cells	69
1.3.2	Characterization of yeast membrane fractions in solution	70
1.3.2.1	<i>Receptors (7 Transmembrane proteins) expression</i>	70
1.3.2.2	<i>Sample homogenization</i>	71
1.3.2.3	<i>Nanovesicles solution purification</i>	76
1.3.2.4	<i>Determination of the nanovesicles concentration in solution</i>	79
1.4	Conclusions	83
1.5	References	84

CHAPTER 2: A novel immunochemical strategy for quantification of transmembrane proteins on natural nanovesicles.

2.1	Background	91
2.2	Materials and Experimental Procedures	101
2.2.1	Materials	101
2.2.2	Buffers and Solutions	101
2.2.3	Equipments/Software	102
2.2.4	Synthesis of Peptide-Bioconjugates	103

2.2.5	Number of crosslinkers/haptens conjugated per biomolecule	105
2.2.6	Monoclonal antibody production.....	106
2.2.7	Preparation of the protein-receptor nanovesicles solutions	106
2.2.8	Western Blot analysis	108
2.2.9	Indirect ELISA development.....	108
2.2.9.1	<i>2D Experiments: Non-competitive assays</i>	108
2.2.9.2	<i>Optimization and evaluation: physicochemical parameters</i>	109
2.2.9.3	<i>Ab9E10 vs. Ab894D12₇₇₉: antibody evaluation</i>	110
2.2.9.4	<i>Immunoassay matrix effects</i>	110
2.2.9.5	<i>General protocol: nanovesicles competitive assays</i>	111
2.2.10	Quantification of olfactory receptors embedded onto natural nanovesicle through the c-myc tag	112
2.2.11	c-myc-OR protein quantification after solubilisation.....	115
2.2.11.1	<i>Proteins solubilisation</i>	115
2.2.11.2	<i>Olfactory receptors protein quantification</i>	115
2.3	Results and Discussion	116
2.3.1	Bioconjugates. Synthesis and Characterization.....	117
2.3.2	Optimization and evaluation of the indirect competitive ELISA	119
2.3.2.1	<i>Effect of the length of competitive step</i>	120
2.3.2.2	<i>Effect of the preincubation time</i>	120
2.3.2.3	<i>Effect of the detergent Tween-20</i>	121
2.3.2.4	<i>Effect of the conductivity (ionic strength)</i>	122
2.3.2.5	<i>Effect of the pH</i>	124
2.3.2.6	<i>Effect of the Organic Solvents and the Blocking solutions</i>	124
2.3.2.7	<i>Summary of the immunoassay features</i>	125
2.3.3	Antibody production and characterization.....	126
2.3.4	Development of the c-myc-ELISA to the analysis of c-myc tagged proteins	129
2.3.4.1	<i>Matrix effect</i>	133
2.3.4.2	<i>c-myc-biomolecule reference</i>	136
2.3.4.3	<i>Model validation</i>	141
2.3.5	Olfactory Receptor quantification: GPCR integrated into natural nanovesicles.....	143
2.3.6	Quantification verification and discussion	145
2.4	Conclusions	150
2.5	References	151

CHAPTER 3: Diffusion-controlled deposition of natural nanovesicles containing GPCRs for biosensing platforms.

3.1	Background	157
3.2	Materials and Experimental Procedures	163
3.2.1	Materials	163
3.2.2	Buffers and Solutions	163
3.2.3	Equipments/Software	163
3.2.4	Nanovesicles solution preparation	164
3.2.4.1	<i>Nanovesicles membrane staining</i>	165
3.2.5	Dynamic light scattering (DLS) measurements	166
3.2.6	Nanovesicles Z-potentials measurements	166
3.2.7	Experiments on Glass substrates	166
3.2.7.1	<i>Glass substrates preparation</i>	166
3.2.7.2	<i>Samples preparation for AFM characterization</i>	167
3.2.7.3	<i>Determination of nanovesicles aspect ratio and diameter by AFM</i>	167
3.2.8	Experiments on Gold substrates	168
3.2.8.1	<i>Thiol self-assembled monolayer preparation</i>	168
3.2.8.2	<i>Ion strength-samples preparation for AFM characterization</i>	169
3.2.8.3	<i>Determination of nanovesicles aspect ratio and diameter by AFM on ion strength-dependent studies</i>	169
3.2.8.4	<i>X-ray Photoelectron Spectroscopy (XPS)</i>	169
3.2.8.5	<i>Surface Plasmon Resonance (SPR) measurements</i>	170
3.2.9	General AFM measurements	170
3.2.9.1	<i>Determination of nanovesicles surface coverage by AFM</i>	170
3.2.9.2	<i>Thickness of the residual layer determination by AFM</i>	171
3.2.10	Contact angle measurements	171
3.2.11	Surface Z-Potential measurements	171
3.2.12	Natural vesicles pattern	172
3.2.12.1	<i>Fabrication of the stamps</i>	172
3.2.12.2	<i>Stamping process</i>	172
3.2.12.3	<i>c-myc-OR1740 nanovesicles deposition and AFM characterization</i>	173
3.2.13	Natural vesicles array	173
3.2.14	Statistics	173
3.3	Results and Discussion	174
3.3.1	Nanovesicles Z-potential	174
3.3.2	Morphology of individual adsorbed nanovesicles	174
3.3.3	Concentration-dependent surface coverage	177

3.3.4	Dynamics of nanovesicles deposition.....	180
3.3.5	Ionic strength-dependent nanovesicles deposition	183
3.3.6	Concentration-dependent surface coverage by SPR.....	192
3.3.7	Dynamics of nanovesicles deposition by SPR	193
3.3.8	Role of surface chemistry	194
3.3.9	Pattern of OR1740-carrying nanovesicles onto self-assembled monolayers (SAM).....	196
3.3.10	Array of OR-carrying nanovesicles	198
3.4	Conclusions	202
3.5	References	203
CHAPTER 4: Functionality assessment of olfactory receptors in natural nanovesicles.		
4.1	Background	209
4.2	Materials and Experimental Procedures	220
4.2.1	Materials	220
4.2.2	Buffers and Solutions	220
4.2.3	Equipments/Software.....	221
4.2.4	Nanovesicles solution preparation.....	221
4.2.5	Odorant-Olfactory Receptor Binding	222
4.2.5.1	<i>First strategy: indirect competitive ELISA</i>	222
4.2.5.2	<i>Second strategy: sandwich ELISA</i>	222
4.2.6	Olfactory receptor functionality	224
4.2.6.1	<i>Odorant solubilisation</i>	224
4.2.6.2	<i>Nanovesicles capture</i>	225
4.2.6.3	<i>Odorant analysis</i>	225
4.2.6.4	<i>Data processing and analysis</i>	225
4.3	Results and Discussion	227
4.3.1	Study of helional/OR1740-nanovesicles binding by ELISA.....	227
4.3.2	Assessment of OR1740 and OR7D4 functionality by Surface Plasmon Resonance (SPR)	233
4.4	Conclusions	240
4.5	References	241
GENERAL DISCUSSION		
G.1	References	251

GENERAL CONCLUSIONS	253
EPILOGUE: Bioelectronic Olfactory Neuron Device European Project (228685-2).	
E.1 Introduction	257
E.2 The consortium	260
E.3 Results	261
E.4 My contribution	283
E.5 References	284
APPENDIX 1: HPLC chromatograms.	
A1.1 c-myc peptide characterization	287
APPENDIX 2: Characterization of c-myc/anti-c-myc interactions using Biacore T100.	
A2.1 Background	293
A2.2 Materials and Experimental Procedures	299
A2.2.1 Materials	299
A2.2.2 Buffers and Solutions	299
A2.2.3 Equipments/Software	299
A2.2.4 Thiol self-assembled monolayer (SAM) preparation	300
A2.2.5 Ligand immobilization	300
A2.2.5.1 <i>Pre-concentration analysis: determining the ligand (antibody) concentration for optimal immobilization</i>	300
A2.2.5.2 <i>Antibody immobilization</i>	301
A2.2.6 Binding measurements	301
A2.2.7 Experiments on C1 sensor chip	302
A2.2.7.1 <i>Effect of the ionic strength</i>	302
A2.2.7.2 <i>Temperature analysis</i>	302
A2.2.8 Processing antigen binding data	302
A2.2.9 Kinetic analysis from antigen binding data	303
A2.2.10 Thermodynamic analysis from antigen binding data	303
A2.3 Results and Discussion	305
A2.3.1 pH determination for optimal antibody immobilization	305
A2.3.2 Random covalent antibody immobilization	307
A2.3.3 Evaluation of the c-myc binding on the immobilized antibody	308

A2.3.4 Interpretation of binding kinetics.....	309
A2.3.5 Temperature and buffer studies	312
A2.4 Conclusions	317
A2.5 References	318
PUBLICATIONS	321
RESUM EN CATALÀ	327

Abbreviations

Abs	Absorbance
AD	Aminodextrane
AFM	Atomic Force Microscopy
ATP	Adenosine Triphosphate
BSA	Bovine Serum Albumin
cAMP	cyclic Adenosine Monophosphate
CA	Coating Antigen
CMC	Critical Micelle Concentration
CONA	Conalbumin
DLS	Dynamic Light Scattering
DMF	Dimethylformamide
DMSO	Dimethyl Sulfoxide
EAG	Electroanennography
EDC	Ethylcarbodiimide hydrochloride
ELISA	Enzyme-Linked ImmunoSorbent Assay
EIS	Electrochemical Impedance Spectroscopy
EOG	Electro-olfactogram
FET	Field-Effect Transistor
GDP	Guanosine Diphosphate
GTP	Guanosine-5'-Triphosphate
GPCR	G-Protein Coupled Receptor
HRP	Horseradish Peroxidase
KLH	Keyhole Limpet Hemocyanin
LAPS	Light-Addressable Potentiometric Sensor
mAb	Monoclonal Antibody
MALDI-TOF-MS	Matrix Assisted Laser Desorption Ionization Time-of-Flight Mass Spectrometer
MEA	Microelectrode Array
MOB	Main Olfactory Bulb
MOE	Main Olfactory Epithelium
MOS	Metal Oxide Sensors

NHS	N-hydroxysuccinimide
NS	Nanovesicle
NTA	Nanoparticle Tracking Analysis
NV	Nanovesicle
OBP	Odourant Binding Protein
OR	Olfactory Receptor
ORN	Olfactory Receptor Neuron
OSN	Olfactory Sensory Neuron
OVA	Ovalbumin
PDMS	Poly(dimethylsiloxane)
PEG	Polyethylene Glycol
PB	Phosphate Buffer
PBS	Phosphate Buffered Saline
PBST	Phosphate Buffered Saline with Tween
PBT	Phosphate Buffer with Tween
PZ	Piezoelectric
QCM	Quartz Crystal Microbalance
RI	Refractive Index
RT	Room Temperature
RU	Resonance Units
SAM	Self-Assembled Monolayer
SPR	Surface Plasmon Resonance
SSTR2	Somatostatin Receptor Subtype 2
TMB	Tetramethylbenzidine
TPC	Total Protein Concentration
UV	Ultra-Violet light
VNO	Vomeronasal Organ
VOC	Volatile Organic Compound
WB	Western Blot
XPS	X-ray Photoelectron Spectroscopy

List of Tables

Table I.1 Schematic comparison between human and electronic noses (Adapted from ref. 33).	7
Table 1.1 Expression systems for G-protein coupled receptors (GPCRs).	53
Table 1.2 Summary of the nanovesicles characteristics used in the present thesis).....	81
Table 2.1 Measurements of c-myc-tagged SF9-14 in crude host cell lysate by fluorescence polarization (FP) assay ³¹	96
Table 2.2 Hapten densities achieved for the peptide-macrobimolecule bioconjugates used in this study, in relation to the cross-linker used for the bioconjugation reaction.....	117
Table 2.3 Crosslinker/bioconjugate. Characterization by MALDI-TOF-MS	118
Table 2.4 Haptens/bioconjugate. Characterization by MALDI-TOF-MS	119
Table 2.5 Optimum conditions of the c-myc competitive immunoassay.	125
Table 2.6 First Screening.	127
Table 2.7 Second Screening.....	128
Table 2.8 Immunoassay features achieved for c-myc and the protein bioconjugates.	132
Table 2.9 Immunoassay features achieved for ³ C ₁ -M(CH ₂) ₂ CO-BSA bioconjugate of the Figure 2.25A.	135
Table 2.10 Shows the features of the competitive ELISA assay of the Figure 2.25B	136
Table 2.11 Shows the features of the competitive ELISAs.....	140
Table 2.12 Hapten/Protein density (δ)	142
Table 2.13 Quantification of ORs NV ⁻¹ using the different protein bioconjugates as standard references ^a	144
Table 4.1 Crosslinker/bioconjugate and Haptens/Bioconjugate. Characterization by MALDI-TOF-MS	231
Table 4.2 Functionality SPR based assay features.....	238
Table E.1 Members of the BOND consortium	260
Table A2.1 Observed SPR immobilization levels (RU) of the antibodies on the different SAMs.	308
Table A2.2 Affinity and Kinetic constants for antigen-antibody interactions determined on different SAM surfaces.....	311
Table A2.3 Affinity and Kinetic constants for antigen-antibody interactions determined at different assay temperatures.	313
Table A2.4 Thermodynamic parameters for the interaction between c-myc and monoclonal anti-c-myc	314
Table A2.5 Affinity and Kinetic constants for antigen-antibody interactions determined at different assay temperatures	315

List of Figures

- Figure I.1** The electronic devices simulate the different stages of the human olfactory system, resulting in volatile odour recognition, which can now be used, for example, to discriminate between different bacterial infections⁴. 2
- Figure I.2** Odorant receptors and the organization of the olfactory system. (Picture from "Press Release: The 2004 Nobel Prize in Physiology or Medicine to Richard Axel and Linda B. Buck". Nobelprize.org. Nobel Media AB 2013. Web. 7 Apr 2014) 10
- Figure I.3** Adapted from Malnic *et al.*³⁴. Combinatorial receptor codes for odorants. In this model, the receptors shown in color are those that recognize the odorant in the left. The identities of different odorants are encoded by different combinations of receptors. However, each OR can serve as one component of the combinatorial receptor codes for many odorants. Given the immense number of possible combinations of ORs, this scheme could allow for the discrimination of an almost unlimited number and variety of different odorants. 13
- Figure I.4** Schematic representation of a typical member of the serpentine (they pass through the plasma membrane seven times) class of G-protein coupled receptor. White, red, blue, and green spheres represent amino acids. Structural characteristics include the three extracellular loops (EL-1, EL-2, EL-3) and three intracellular loops (IL-1, IL-2, IL-3). Most GPCRs are modified by carbohydrate attachment to the extracellular portion of the protein. Shown is typical N-linked carbohydrate attachment. The different colored spheres are involved in ligand-binding and associated G-protein binding as indicated in the legend (Adapted from The Medical Biochemistry webpage: <http://themedicalbiochemistrypage.org>). 14
- Figure I.5** Adapted from *Nature Reviews*⁵⁵. (A) Odorant detection in vertebrates. When the odorant binds the olfactory receptor (OR) activates the trimeric transmembrane protein, olfaction-specific G protein (G_{olf}), adenylyl cyclase type III (ACIII), the olfactory cyclic nucleotide-gated channel and a Ca^{2+} activated Cl^- channel (CaCC). (B) Insect olfactory model suggests that the odorant receptor forms an ion channel that is opened directly in response to the binding of odorants. (C) On the other hand this complex insect model suggests that there are two pathways by which odor-induced depolarization can be generated. Upon odorant binding, activity is transferred to the Or83b subunit either by a direct (fast and short) or indirect (slow and prolonged) pathway. 16
- Figure I.6** Effect of OBPs on the signal intensity of Ca^{2+} influx. The signal intensity in HEK-293 cells stably expressing rat olfactory receptor I7 was measured using a spectofotometric Ca^{2+} assay, 10 mM octanal (specific odorant for ORI7) was used as stimulant. Circle: octanal only, triangle: OBP3 + octanal, square: OBP2 + octanal.⁶⁶ 17
- Figure I.7** Schematic representation of an odorant-binding protein⁵⁶ 19
- Figure I.8** Glomerulus organization in the main olfactory and vomeronasal systems. (A) Each glomerulus in the main olfactory bulb (MOB) receives axons only from cells expressing the same OR type, indicated by a different color, and connects to a dedicated mitral cell. (B) Sensory neurons in the epithelium of the VNO have their cell bodies segregated into separate zones (all have microvilli reaching the surface of the organ's lumen as illustrated). Neurons with cell bodies located in the apical zone (shown in red) express members of the V1R family of receptors and project to multiple glomeruli in the anterior half of the accessory bulb (AOB). Neurons with cell bodies in the basal zone (shown in green) express V2R receptors and project to multiple glomeruli in the posterior half of the AOB⁷⁷. 21
- Figure I.9** (A) Schematic representation of the sensor equipment consisting of the intact chemoreceptor and the FET device. (B) Typical sensor response: variation of I_D of the isolated-antenna-BioFET by changing the Z-3-hexen-1-ol gas concentration.⁸² 23

Figure I.10 Schematic diagram of a bioelectronic nose. There are two types of bioelectronic noses: cell-based and protein-based ⁹	24
Figure I.11 <i>In vivo</i> biosensor based on the olfactory-LAPS technique ⁸⁸ . (A) Scheme of the cell-based biosensor using LAPS. (B) Simplified cell-semiconductor interface. (C) Schematic circuit of the cell-LAPS hybrid system.....	26
Figure I.12 (A) LAPS system with the olfactory epithelium on the sensor surface. (B) Sheet conductor model on extracellular potentials recording of the tissue layer between electron conductor and electrolyte bath on LAPS. ⁸⁹	27
Figure I.13 (A) Typical extracellular recordings from OSNs to the odours and inhibited by MDL12330A. (B) The statistical results of the number of the recorded firing spikes from the responses presented in (A). ⁹⁰	28
Figure I.14 Photos of a microelectrode array chip (MEA) (A) and device (B) used to record extracellular potentials in intact olfactory epithelium for the development of a bioelectronic nose. ⁹¹	28
Figure I.15 (A) Kinetics of yeast OR1740 biosensor response upon 10^{-11} M helional or control addition. ⁹³ (B) Field potential profile of HEK-293 cells expressing I7 receptor in a Ca^{2+} standard solution. Cells were exposed to 10 mM octanal in the Ca^{2+} standard. ⁹⁴	29
Figure I.16 <i>In vitro</i> biosensors not base on the electrophysiological potentials of the cell. (A) QMC-based bioelectronic nose. (B) SPR-based bioelectronic nose. (C) EIS-based bioelectronic nose. (D) Possible mechanism for the specific detection of odorants using nanotube-FET sensor. <i>Picture adapted from ref. 9, 95</i>	31
Figure 1.1 GPCRs classification (A) Three families (1, 2 and 3) can be recognized when comparing their amino-acid sequences. Receptors from different families share no sequence similarity, suggesting that we are in the presence of a remarkable example of molecular convergence. <i>Family 1</i> contains most GPCRs including receptors for odorants. <i>Group 1a</i> contains GPCRs for small ligands including rhodopsin and β -adrenergic receptors. The binding site is localized within the seven transmembrane segments (TMs). <i>Group 1b</i> contains receptors for peptides whose binding site includes the N-terminal, the extracellular loops and the superior parts of TMs. <i>Group 1c</i> contains GPCRs for glycoprotein hormones. It is characterized by a large extracellular domain and a binding site which is mostly extracellular but at least with contact with extracellular loops e1 and e3. <i>Family 2</i> GPCRs have a similar morphology to group 1c GPCRs, but they do not share any sequence homology. Their ligands include high molecular weight hormones such as glucagon, secretine, VIP-PACAP and the Black widow spider toxin, α -latrotoxin. <i>Family 3</i> contains mGluRs and the Ca^{2+} sensing receptors. In 1997, however, GABA-B receptors and a group of putative pheromone receptors coupled to the G protein G_o (termed VRs and G_o -VN) became new members of this family. (B) <i>Family 4</i> comprises pheromone receptors (VNs) associated with G_i . <i>Family 5</i> includes the 'frizzled' and the 'smoothened' (Smo) receptors involved in embryonic development and in particular in cell polarity and segmentation. Finally, the <i>cAMP receptors</i> (cAR) have only been found in <i>D.discoideum</i> but its possible expression in vertebrate has not yet been reported ⁵	49
Figure 1.2 Scheme of an olfactory receptor (7 TMs protein) integrated into a lipid membrane.....	50
Figure 1.3 Recombinant protein production. ¹³	51
Figure 1.4 Cell-free protein expression system. (<i>Bioneer, Molecular biology company webpage: http://eng.bioneer.com</i>).....	52
Figure 1.5 Differential bioluminescence dose-response upon odorant stimulation of yeast-expressed olfactory receptors ²² . (A) Measurements performed on yeast transformed to coexpress the ORI7, G_{olf} and the luciferase reporter. Specific odorant-receptor interaction was observed for heptanal molecule. (B) Measurements performed on yeast coexpressing the human OR1740, G_{olf} and the luciferase reporter. Specific odorant-receptor interaction was observed for helional molecule.	55

- Figure 1.6** A cryo-fracture picture from *Saccharomyces cerevisiae* yeast cell performed by myself (Scale bar: 7 μm) and the different model membrane systems¹². A collection of model lipid membrane systems and array-based approaches towards membrane protein biosensing: liposome array (artificial or native membranes) (i), supported lipid bilayer (SLB) array (ii), and free-standing lipid bilayers spanning over a nanoporous array (iii) with incorporated membrane proteins..... 56
- Figure 1.7 (A)** Microscope picture of *Saccharomyces cerevisiae* yeast cell culture. **(B)** Yeast cell diameter size obtained by the LS Particle Size Analyser technique. **(C.1)** Microscope picture of two yeast cells (black arrows) flowing through a microchannel. **(C.2)** Graph representing the diameter size of the yeast cells is obtained after analysing 24 cells through the hydrodynamic focusing technique. 69
- Figure 1.8** Picture showing the Western Blot results performed to assess the capability of anti-c-myc antibody (Ab894D12_{r7f9}) to detect specifically different c-myc-ORs expressed in the yeast cell membrane allowing us to check that the receptor expression has been performed without any problem. Nanovesicles carrying SSTR2 receptors were used as control (-). Nanovesicles carrying c-myc-OR1740 and c-myc-OR7D4 were used as evaluation sample models (+). The monomer olfactory receptor molecular weight is around 26 kDa for the OR7D4 (red arrow) and around 35 kDa for the OR1740 (blue arrow). The expression of ORI7 and SSTR2 is reported in the literature by our collaborators²²..... 70
- Figure 1.9 (A), (B), (C)** 2D Cryo-EM image of a solution of membrane fractions carrying OR1740 olfactory receptor at TPC = 5000 $\mu\text{g mL}^{-1}$ after sonication, proteoliposomes. **(D)** Diameter of a population of 40 vesicles calculated directly from the electron micrographs..... 71
- Figure 1.10** Cryo Fracture-Transmission electron microscopy (CF-TEM) images of proteoliposomes carrying the olfactory receptor OR1740. **(A)** Scale bar: 100 nm. **(B)** Scale bar: 250 nm..... 72
- Figure 1.11** Nanovesicles diameter size calculated by DLS for each different technique at the optimal working condition (considering the smaller diameter size and less polydispersity for each technique). 73
- Figure 1.12** Results of DLS **(A)** and NTA **(B)** measurements of membrane fractions carrying OR1740 olfactory receptor at room temperature. The size distributions in cyan refer to sonicated samples (TPC = 60 $\mu\text{g mL}^{-1}$) while the ones in purple refer to samples, at the same concentration, which were first sonicated and then filtered (see Experimental Section). Data in **(B)** are fitted with the sum of 3 (sonicated sample) and 2 (sonicated + filtered sample) gaussian functions in order to extract the contribution of each population to the size distribution. 74
- Figure 1.13** Results of NTA measurements of membrane fractions carrying OR17 olfactory receptor at room temperature: ORI7-HA **(A)** and c-myc-ORI7 **(B)**. The size distributions in cyan refer to sonicated samples (TPC = 60 $\mu\text{g mL}^{-1}$) while the ones in purple refer to samples, at the same concentration, which were first sonicated and then filtered (see Experimental Section). Data are fitted with the sum of 3 (sonicated sample) and 2 (sonicated + filtered sample) gaussian functions. 75
- Figure 1.14** DLS size distributions of sonicated (proteoliposomes) and filtered (nanovesicles) control sample. The size distributions in blue refer to control proteoliposomes while the ones in orange refer to control nanovesicles. 76
- Figure 1.15.** Overview of the biological components present in the solution after the production of the nanovesicles. 2D Cryo-EM image of a solution of membrane fractions carrying OR1740 olfactory receptor at TPC = 5000 $\mu\text{g mL}^{-1}$ after sonication. It was possible to observe the proteoliposomes (black arrows) and biomolecules, i.e. proteins and/or lipid aggregates (white arrows). Scale bar: 200 nm. 77
- Figure 1.16** Results of DLS **(A)** measurements of membrane fractions carrying OR1740 olfactory receptor (TPC = 60 $\mu\text{g mL}^{-1}$) at room temperature after centrifugation-purification technique. The size distributions in purple refers to the resulting solution from sonicated and filtered samples after the Amicon Ultra-4 concentration step. While the ones in orange refer to the supernatant solution coming after the ultracentrifugation process. Finally, size distribution in blue refers to the resuspended pellet in 1 mL of PBS (see Experimental Section). **(B)** Absorbances evaluation from the aliquots obtained after

affinity chromatography (with Protein A column) purification procedure of the proteoliposome sample. Similar results were obtained for Protein G and Protein A/G columns. 78

Figure 1.17 Calibration curve of OR1740-nanovesicles concentration (C), obtained from the total area of NTA size distributions at different TPC concentrations. 80

Figure 1.18. Calibration curves of nanovesicles concentration (C), obtained from the total area of NTA size distributions at different TPC concentrations. Linear dependence of the total protein concentration (TPC, expressed as $\mu\text{g/mL}$) on the nanovesicles concentration (C, expressed as NS/mL)⁶⁷. We found that the experimental data are correctly fitted by each corresponding equation presented in Table 1.2 (A) SSTR2 (F, #41) carrying nanovesicles. (B) SSTR2 (G, #43) carrying nanovesicles. (C) OR1740 (A, #26.1) carrying nanovesicles. (D) OR1740 (B, #44) carrying nanovesicles. (E) ORI7 (D, #new) carrying nanovesicles. (F) ORI7 (C, #old) carrying nanovesicles. (G) OR7D4 (E, #58) carrying nanovesicles. 82

Figure 2.1 Different ligands use G-protein-coupled receptors (GPCRs) to stimulate membrane, cytoplasmic and nuclear targets. GPCRs interact with heterotrimeric G-proteins composed of α , β and γ subunits that in the resting state are GDP bound. Agonist binding triggers a conformational change in the receptor, which catalyses the dissociation of GDP from α subunit followed by GTP-binding to G_α and the dissociation of G_α from $G^{\beta,\gamma}$ subunits. The α subunits of G proteins are divided into four subfamilies and a single GPCR can couple to either one or more families of G_α proteins. Each G protein activates several downstream effectors. The G^β subunits and G^γ subunits function as a dimer to activate many signaling molecules, including phospholipases, ion channels and lipid kinases⁶. 91

Figure 2.2 (A) Schematic illustration of nanovesicles deposited onto a microarray substrate¹⁰. (B) Zoom of one of the nanovesicles (green) from Figure 2.2A: scheme of the natural lipidic nanovesicles carrying GPCRs expressed by genetic engineering. 92

Figure 2.3 (A) Scheme of the selective covalent labeling of a tag-fused GPCR protein on the surface of living cells. (B) Covalent labeling of GPCR expression on the surface of HEK-293 cells. Fluorescence imaging of CAD6D4x2 tag-fused bradykinin receptor type 2 (B2R, target GPCR). The fluorescence images were obtained using two different channels corresponding to the probe (i) and a protein expression marker (ii) such as Cy5-appended antagonist peptide or EGFP. The transmission image is shown in (iii) and the overlay image of (i) and (ii) is shown in (iv). Scale bar: 10 μm .²⁴ 93

Figure 2.4 (A) Scheme of the two-color labeling in which synaptic vesicles were labeled with antibodies directed against two different synaptic vesicle protein, each of which was detected with a different colored fluorescent secondary antibody. (B) Vesicle labeling. (1,2) Sample image of synaptic vesicles labeled with anti-SV2 and goat-anti-mouse Alexa-488 (green, 1) and anti-synaptotagmin1, goat-anti-rabbit Alexa-635 (red, 2). (3) Two-color overlay in which colocalization of the two probes appears yellow. (4) Sample in which primary antibodies were excluded from the labeling method. (5) Sample in which vesicles were excluded from the labeling method. Scale bar: 1 μm .²⁷ 94

Figure 2.5 Scheme of the production of monoclonal antibodies by the hybridoma method²⁸. In yellow are highlighted the two main issues to control in order to obtain high affinity antibodies: the antigen design used in the immunization and the hybridoma screening. 95

Figure 2.6 Scheme of competitive ELISA immunoassays for the detection of low molecular weight analytes. (A) Indirect competitive ELISA. (B) Direct competitive ELISA. 98

Figure 2.7 Scheme of sandwich ELISA immunoassays for the detection of high molecular weight analytes. (A) Indirect sandwich ELISA. (B) Direct sandwich ELISA. 99

Figure 2.8 Scheme of the components used for the bioconjugate synthesis. Two c-myc peptides were conjugated through two different crosslinkers. In purple (C_1 and C_2) is highlighted the cysteine position which has the reactive thiol group. 103

Figure 2.9 Synthesis of the c-myc-Bioconjugates through the crosslinker N-succinimidyl 3-maleimidopropionate ($\text{M}(\text{CH}_2)_2\text{CO}$). 104

- Figure 2.10** Synthesis of the c-myc-Bioconjugates through the crosslinker N-succinimidyl iodoacetate (CH_2CO)..... 105
- Figure 2.11** Sigmoidal curve obtained from a competitive immunoassay. The working range (lineal range of the curve) is defined between IC_{20} and IC_{80} , limit of quantification (LOQ). On the right is presented the optical response obtained from 3 of the 12 columns in the 96-well plate. It is observed how the presence of analyte inhibits the colorimetric response. 112
- Figure 2.12** Scheme of the competitive ELISA assay. (A) Calibration curve generation using the c-myc-Bioconjugate 1 in an SSTR2-carrying NS solution. (B) c-myc-OR-carrying NS signal is compared with the calibration curve performed in (A). 114
- Figure 2.13** Scheme of the natural lipidic nanovesicles carrying the c-myc-OR expressed by genetic engineering. Zoom of the quantified complex: OR1740 or OR7D4 as seven-transmembrane protein with the c-myc peptide (10 amino acids) fused to its N-terminus. 116
- Figure 2.14** Effect of the length of competitive step. The data from the left graph correspond to the average of two replicates. The right graph represents the variation of the immunoassay parameters (IC_{50} and A_{max}) as a function of the length of the competitive step. The analyte, c-myc and the Ab9E10 were incubated for different periods of time (between 30 and 150 min) in the antigen-coated plates ($^1\text{C}_2\text{-CH}_2\text{CO-OVA}$). The results reported are extracted from the four-parameter equation used to fit the standard curves. Each standard curve was run in duplicate. 120
- Figure 2.15** Effect of the preincubation of the anti-c-myc and the c-myc analyte before the competitive step. The preincubation took place overnight at 4°C and between 0 and 120 min at RT. The data correspond to the average of two replicates. 121
- Figure 2.16** Effect of the concentration of Tween-20 on the indirect competitive ELISA. Standard curves (analyte c-myc peptide) and the antibody Ab9E10 were prepared in PBS with different concentrations of Tween. The results reported are extracted from the four-parameter equation used to fit the standard curves. Each standard curve was run in duplicate in the antigen-coated plates $^x\text{C}_2\text{-CH}_2\text{CO-CONA}$ 121
- Figure 2.17** Effect of the concentration of NaCl on the indirect competitive ELISA. Standard curves (analyte c-myc peptide) and the antibody Ab 9E10 were prepared in PBS with different concentrations of Tween. The results reported are extracted from the four-parameter equation used to fit the standard curves. Each standard curve was run in duplicate in the antigen-coated plates $^x\text{C}_2\text{-CH}_2\text{CO-CONA}$. For 3.2% NaCl concentration the Abs results could not fit the sigmoidal four-parameter equation..... 122
- Figure 2.18** Effect of the concentration of NaCl on the indirect competitive ELISA. Standard curves were prepared with the antibody Ab9E10 concentration 1/32000. The results reported are extracted from the four-parameter equation used to fit the standard curves. Each standard curve was run in duplicate in the antigen-coated plates $^x\text{C}_2\text{-CH}_2\text{CO-CONA}$ 123
- Figure 2.19** Effect of the concentration of 0% NaCl on the indirect competitive ELISA. Standard curves were prepared with the antibody Ab9E10 ranging concentrations from 1/32000 to 1/128000. The results reported are extracted from the four-parameter equation used to fit the standard curves. Each standard curve was run in duplicate in the antigen-coated plates $^x\text{C}_2\text{-CH}_2\text{CO-CONA}$ 123
- Figure 2.20** Effect of the pH on the competitive immunoassay. Several standard curves were prepared using PB at different pH values and added to the antigen-coated plates ($^x\text{C}_2\text{-CH}_2\text{CO-CONA}$). The Ab9E10 (1/128000) dilutions were also prepared with the same buffers and Tween 20 was added to each of them at 0.05%. Each standard curve was run in duplicate. 124
- Figure 2.21** Effect of the concentration of Organic Solvents (left graph) and blocking solutions (right graph) on the indirect competitive ELISA. Standard curves were prepared with the antibody Ab9E10 concentration 1/32000 and a synthesized c-myc peptide as analyte. The results reported are extracted from the four-parameter equation used to fit the standard curves. Each standard curve was run in duplicate in the antigen-coated plates $^x\text{C}_2\text{-CH}_2\text{CO-CONA}$ 125

- Figure 2.22** (A) Scheme of the indirect competitive ELISA. Immunoassay scheme using the c-myc peptide as analyte to evaluate two different anti-c-myc monoclonal antibodies (mAb) (Ab9E10 and Ab894D12_{17F9}) and the absence of salts in the buffer. (B) Immunoassay scheme using c-myc bioconjugates to perform the standard calibration curves. (C). Immunoassay scheme of our model for GPCRs (c-myc-ORs) quantification in our nanovesicles (NV) sample..... 129
- Figure 2.23** Calibration curves of the competitive immunoassays using the c-myc peptide as analyte and two different anti-c-myc monoclonal antibodies, Ab9E10 and Ab894D12_{17F9}. The graph also shows that the absence of salts in the buffer (phosphate buffer with 0.05% Tween-20, PBT instead of phosphate buffer saline with 0.05% Tween-20, PBST) allowed an increase in the maximum signal of the assay. Each curve was built using three-well replicates. The parameters shown in Table 2.8 were extracted from the four-parameter equation used to fit the standard curves..... 130
- Figure 2.24** Picture showing the Western Blot results performed to assess the capability of anti-c-myc antibodies Ab9E10 and Ab894D12_{17F9} at a range of concentrations (C) to detect the c-myc-OR1740. Nanovesicles carrying SSTR2 receptors were used as control (-). Nanovesicles carrying c-myc-OR1740 were used as evaluation sample (+). The monomer olfactory receptor molecular weight is around 35 kDa⁴⁷ 131
- Figure 2.25** Matrix effect produced by a solution of natural yeast nanovesicles. (A) Standard curves using ³C₁-M(CH₂)₂CO-BSA as analyte in PBT and in blank matrix buffer (SSTR2) at a range of concentrations (3-60 µg mL⁻¹ TPC or 4.40·10⁹-8.80·10¹⁰ NS mL⁻¹). (B). Standard curves using ⁴C₁-M(CH₂)₂CO-CONA as analyte in PBT and in validation buffer (SSTR2) at a range of concentrations (3-60 µg mL⁻¹ TPC or 4.40·10⁹-8.80·10¹⁰ NV mL⁻¹). The parameters showing the effect of the matrix were extracted from the four-parameter equation used to fit the standard curves and are presented in Table 2.9 and 2.10 respectively. Each curve was built using three-well replicates..... 134
- Figure 2.26** Calibration curves resulting from the evaluation of different analytes, free c-myc peptide (the commercial one and the C₂) and the ¹C₁-M(CH₂)₂CO-HRP bioconjugate in order to choose the candidates for the quantification model. Each curve was built using three-well replicates. The assay parameters are shown in Table 2.8. 137
- Figure 2.27** Calibration curves of the c-myc-bioconjugates chosen as candidates for the quantification model in blank matrix buffer (SSTR2-NV, TPC = 35 µg mL⁻¹). Arrows in blue and purple mark the two concentration points of ⁴C₁-M(CH₂)₂CO-CONA and ³C₁-M(CH₂)₂CO-BSA to be interpolated in the ¹C₁-M(CH₂)₂CO-HRP standard curve. Immunoassay features are represented in Table 2.8. 138
- Figure 2.28** Evaluation of the unspecific adsorption of the immunoassay using the anti-c-myc (Ab894D12_{17F9}) and the M(CH₂)₂CO-biomolecule (maleimido-biomolecule) in the working conditions (PBT buffer). Not interaction existed. The antibody only recognized the C₂ peptide coming from the coating antigen. Each curve was built using three-well replicates. 139
- Figure 2.29** Inhibition curves of the three c-myc-Bioconjugates at the concentration of SSTR2 carrying nanovesicles 7.03·10¹⁰ NV mL⁻¹ (SSTR2-NV, TPC = 35 µg mL⁻¹). The horizontal lines interpolated in the calibration curve mark the absorbance of the c-myc-OR1740 carrying nanovesicles (black) and c-myc-OR7D4 carrying nanovesicles (light grey) at the corresponding concentration. Calibration curves are built using three-well replicated and fitted with a four-parameter equation. 144
- Figure 2.30** Number of receptors per NV (ORs NV⁻¹) at each concentration. The black dots correspond to the quantification of the c-myc-OR1740-NV and the grey dots correspond to the quantification of the c-myc-OR7D4-NV. Dark grey area shows (3 ± 1) c-myc-OR1740/NV and light grey area shows (6 ± 2) c-myc-OR7D4/NV. The quantification reproducibility between two different days (*) is as well presented. 145
- Figure 2.31** Western Blot of elutes of purified c-myc-OR1740 (A) and c-myc-OR7D4 (B) after solubilization of the membrane fraction of *Saccharomyces Cerevisiae* expressing these receptors. 450µg of c-myc-OR membrane fractions were solubilized using FC14 at 50 or 350 CMC..... 146

- Figure 3.1** (A) Single vesicle array interrogated by fluorescence microscopy². The sensor surface was chemically modified by BSA and biotin-streptavidin pair in order to specifically bind those nanovesicles carrying the biotin linker. (B) Fluorescence micrograph of a single vesicle array functionalised with two populations of vesicles (red and green dyes, respectively)³. 157
- Figure 3.2** (A) Schematic representation of the array assembly process. Vesicles are deposited on the substrate and after using a squeegee, the top surface of the substrate is devoid of vesicles, while the recessed well are filled. (B) Multicomponent arrays formed by microfluidic delivery of myelin and neuronal raft membranes. Fluorescence images before (1) and after (2) incubation with IgM O4 (specific for myelin). (C) Representative transmission spectra for SPR sensing of IgM O4 binding to myelin particles in a gold nanowell array (blue curve). Red curve is the negative control (SAPE does not bind myelin). Comparison of mean spectra shifts after incubation with SAPE or IgM O4¹⁰. 159
- Figure 3.3** (A) Lipidic vesicles stability explained by DLVO theory. (B) Schematic representation of the hydration forces effect. An ion adsorbed onto the outer layer of the lipid bilayer of a liposome is presented¹³. 160
- Figure 3.4** Schematic representation of zeta-potential. (www.malvern.com)..... 161
- Figure 3.5** Snapshots of a vesicle for three cases, indicated by (1), (2) and (3). For case 1, the vesicle ruptures at the left side, for case 2 the vesicle stays intact on the surface and for case 3, the vesicle does not adsorb on the surface. Red, yellow and blue beads indicate positive, neutral and negative-type beads respectively. Blue surface beads indicate negative surface charges, while white surface beads indicate neutral surface sites.¹⁵ 162
- Figure 3.6** (A) 3D tapping mode AFM image in PBS buffer of a glass substrate showing individual NS from a solution at $C = 3.22 \cdot 10^8$ NV mL⁻¹ (incubation time = 900 s) (z scale = 22 nm). (B) Detail of Figure 6A showing an individual nanovesicle and its corresponding topographical profile (D). The green line is a Gaussian fit from which we extracted the nanovesicles height and width (see Experimental Section). (C) Width vs. height extracted from the topographic profile of a population of 95 nanovesicles. (C, inset) The line in grey indicates an aspect ratio of 0.097. Histogram of the aspect ratio as obtained from data in (C). 175
- Figure 3.7** Kinetic Phase diagram of the fate of an adsorbing vesicle. X-axis indicates the extent to which the surface is charged (%) and y-axis indicates the bead mixture in the vesicle (%). Red data points (red area) mean that the vesicle ruptured, blue data points (blue area) mean that the vesicle stayed intact on the surface, green data points (green area) mean that the vesicle adsorbed and then desorbed from the surface, and black data points (grey area) mean that the vesicle did not adsorb to the surface¹⁵. 176
- Figure 3.8** Sequence of AFM images taken after incubating for 900 s on glass solutions of nanovesicles carrying ORI7 olfactory receptor at: $C = 3.22 \cdot 10^8$ NS mL⁻¹ (z scale = 5 nm) (A); $C = 6.45 \cdot 10^8$ NV mL⁻¹ (z scale = 7 nm) (B); $C = 12.83 \cdot 10^8$ NV mL⁻¹ (z scale = 20 nm) (C); $C = 25.73 \cdot 10^8$ NV mL⁻¹ (z scale = 40 nm) (D); $C = 51.40 \cdot 10^8$ NV mL⁻¹ (z scale = 35 nm) (E); $C = 411.31 \cdot 10^8$ NV mL⁻¹ (z scale = 30 nm) (F). 177
- Figure 3.9** Surface coverage vs. nanovesicles concentration. The line in grey is a linear fit with Coverage $\times 100 = (9.39 \pm 1.66) \cdot 10^{-3} C$ (10^8 NV mL⁻¹), according to the model in ref. 27, 34 and 35. Thickness of the adsorbed residual layer vs. C (inset). 179
- Figure 3.10** Surface coverage (A) and thickness of the adsorbed layer (B) vs. incubation time for nanovesicles concentration of $3.22 \cdot 10^8$ NV mL⁻¹ (data in dark cyan), $12.83 \cdot 10^8$ NV mL⁻¹ (data in violet), $51.40 \cdot 10^8$ NV mL⁻¹ (data in orange) and $205.66 \cdot 10^8$ NV mL⁻¹ (data in blue). The straight lines in (A) correspond to the predictions of a purely diffusive adsorption process with no adjustable parameters according to Equation 3. The straight lines in (B) are corresponding fits with $y = A \cdot t^b$ (Equation 4). Trend of the prefactor A, extracted from the fit of the time-evolution of the thickness of the adsorbed residual layer, vs. nanovesicles concentration (B, inset). The experiments are performed on nanovesicles carrying ORI7 olfactory receptors. 181

- Figure 3.11** Conductivity measurements of the 10 solutions used to study the effect of Na^+ ions on the size of natural OR-nanovesicles. Two different instruments Malvern-DLS (grey dots, mean value of solutions prepared in three different days) and a bench conductimeter (black dots, mean value of solutions prepared in two different days) were used. 184
- Figure 3.12 (A)** Nanovesicles size (diameter, nm) by DLS vs. NaCl concentration ($[\text{Na}^+]$). The error bars are obtained due to measurements performed onto three different days. Each day the measurement was performed as well three times. One-way ANOVA statistical analysis was performed and not significant differences between group means was obtained. **(B)** Sizes and polydispersity of EYPC synthetic liposomes as a function of Na^+ concentration¹³. 185
- Figure 3.13 (A)** Nanovesicles ζ -Potential in solution vs. NaCl concentration ($[\text{Na}^+]$). Two important regions can be differentiate: from 0 to 0.01 M $[\text{Na}^+]$ (dark yellow) and from 0.03 to 1 M (light yellow). **(B)** ζ -Potential of EYPC liposomes as a function of Na^+ (black square) and K^+ (white dots)¹³. 187
- Figure 3.14** Nanovesicles aspect ratio presented as a result of extracting the thickness (h) and the width by analyzing the topographic profiles on top of 30 nanovesicles at each different NaCl concentration ($[\text{Na}^+]$). The grey line indicate the aspect ratio mean value considering all the salts concentration: ~ 0.27 . ** $p < 0.05$ by one-way ANOVA followed by Bonferroni Test pot-hoc comparison. 189
- Figure 3.15 (A)** Nanovesicles size (diameter, nm) by DLS vs. NaCl concentration ($[\text{Na}^+]$). The error bars are obtained due to measurements performed onto three different days. Each day the measurement was performed as well three times. **(B)** Nanovesicles size (diameter, nm) by AFM vs. NaCl concentration ($[\text{Na}^+]$). The error bar is the one obtained after analyzing 30 different nanovesicles at each salt concentration. 190
- Figure 3.16** Sequence of AFM images taken after incubating for 3600 s a solution of OR1740 carrying nanovesicles at $C = 1.67 \cdot 10^{11} \text{ NV mL}^{-1}$ onto a $\text{SAM}_2\text{-COOH}$ at different NaCl concentrations: $C = 0 \text{ mM}$ (A); $C = 1.02 \text{ mM}$ (B); $C = 3.42 \text{ mM}$ (C); $C = 10.26 \text{ mM}$ (D); $C = 34.22 \text{ mM}$ (E); $C = 68.44 \text{ mM}$ (F); $C = 0.102 \text{ M}$ (G); $C = 0.146 \text{ M}$ (H); $C = 0.547 \text{ M}$ (I); $C = 1.095 \text{ M}$ (J). Z scale = 55 nm and Scale bar = 2 μm 190
- Figure 3.17** Surface coverage vs. NaCl concentration ($[\text{Na}^+]$). Thickness of the adsorbed residual layer vs. $[\text{Na}^+]$ (inset). 191
- Figure 3.18** SPR sensorgrams of three solutions of nanovesicles carrying OR1740 olfactory receptors at $C = 6.581 \cdot 10^8 \text{ NV mL}^{-1}$ (data in orange), $C = 65.81 \cdot 10^8 \text{ NV mL}^{-1}$ (data in purple) and $C = 658.10 \cdot 10^8 \text{ NV mL}^{-1}$ (data in cyan) immobilized onto SAM-COOH functionalized gold substrate (A). SPR % Reflectivity (B) and corresponding surface coverage (C) vs. nanovesicles concentration. C-evolution of the thickness of the adsorbed layer extracted from AFM images collected at the end of the SPR experiment (C, inset). 192
- Figure 3.19** Normalized SPR reflectivity of three solutions of nanovesicles carrying OR1740 olfactory receptors incubated on SAM-COOH functionalized gold substrate for increasing incubation times. The measured surface coverage determined by AFM for these samples was 1.3 % ($t = 3600 \text{ s}$), 3.8% ($t = 10800 \text{ s}$) and 7.4% ($t = 50400 \text{ s}$). Time-evolution of the thickness of the adsorbed residual layer for the three samples (inset). 193
- Figure 3.20** XPS spectra of bare Au, SAM-COOH, SAM-NH₂ and SAM-OH functionalized gold chips. 194
- Figure 3.21** AFM images taken after incubating a solution of OR1740 carrying nanovesicles at $C = 394.86 \cdot 10^8 \text{ NV mL}^{-1}$ onto a SAM-OH ($t = 3600 \text{ s}$) (A), SAM-NH₂ ($t = 3000 \text{ s}$) (B) and SAM-COOH ($t = 4500 \text{ s}$) (C) functionalized gold chip. The nanovesicles surface coverage is around 0.03 % for SAM-OH functionalized gold and around 10 % for SAM-NH₂ and SAM-COOH functionalized gold. Corresponding SPR sensorgrams (D-F). 195

Figure 3.22 Tapping-mode AFM phase image of the disk-like pattern of SAM-COOH and SAM-OH before (A) and after (B) the incubation of a solution of nanovesicles carrying OR1740 olfactory receptor at: $C = 3.29 \cdot 10^{10}$ NS/mL for 4200 s. (C), (D) Corresponding topographic profiles. 197

Figure 3.23 Staining of receptor-nanovesicles with dialkylcarbocyanines. (A), (B) Control solutions of buffer alone incubated with the dyes were observed by epifluorescence microscopy. The images were taken at 3000ms exposure time and at 60x magnification. Bars, 10 μ m. (C), (D) Vesicles after staining with DiO or DiI observed by epifluorescence microscopy. The images were taken at 3000ms exposure time and at 100x magnification. Bars, 5 μ m. (E), (F) Vesicles after staining with DiO or DiI observed by confocal microscopy, showing small brightly fluorescent spots. Arrows indicate vesicles that are magnified in the insets. The images were taken at 3000ms exposure time and at 60x magnification to enhance clarity. Bars, 5 μ m (main parts of the images) and 500 nm (insets). 199

Figure 3.24 OR1740-nanovesicles ($C = 1.67 \cdot 10^{11}$ NV mL⁻¹) previously stained with DiI (red) or DiO (green) dyes immobilized on clean glass substrates for 1 hour. Corresponding negative controls (dyes in PBS) were also printed. Array obtained before washing the glass substrate was observed by fluorescence microscopy. The images were taken at 4000ms and 6000ms exposure time for DiI and DiO stainings respectively and at 4x magnification. Scale bar 250 μ m. 200

Figure 3.25 Nanovesicles ($C = 1.67 \cdot 10^{11}$ NV mL⁻¹) carrying different receptors, previously stained with DiI (OR1740-nanovesicles, red) or DiO (SSTR2-nanovesicles, green) dyes, immobilized on clean glass substrates for 1 hour. Corresponding negative controls (dyes in PBS) were also printed. Array obtained before washing the glass substrate was observed by confocal microscopy. Confocal images were taken with 488 nm (for DiO excitation) and 532 nm (for DiI excitation) lasers with 70% laser power. A constant gain and offset values were used during visualization of different arrays for each laser. Scale bar 200 μ m. 201

Figure 4.1 Schematic illustration of a Field Effect Transistor (FET). The device is based on three electrodes: the source, the drain and the gate as a control electrode. A change in gate voltage causes a variation in the current from the source to the drain. Thus, if in the channel are immobilized olfactory receptors, their interaction with their specific odorant causes electrical changes. These electrical changes are monitored in a sensorgram [$\Delta I/I_0$]_{SD} % vs. time. 210

Figure 4.2 (A.I) A neuron (N) is attached to oxidized Si. A thin layer of gate oxide (O_G) covers n-type Si between the source (S) and drain (D) of p-type Si insulated by a thick field oxide (O_F). The electrolyte E is maintained at ground potential (Ag/AgCl electrode). Bulk silicon (B), source, and drain are held at positive bias voltages (p-channel FET). The source-drain current is measured by a current-voltage converter. The neuron is impaled by a microelectrode (ME) (Ag/AgCl). Current (I_{ST}) is injected to stimulate the cell. The membrane potential is measured by a voltage follower. **(A.II)** Single action potential. The source-drain current I_D of the FET and the membrane potential V_M , as measured by an impaled microelectrode (ME) are shown.¹² **(B.I)** Schematic illustration of the human olfactory receptor conjugated carbon polypyrrole nanotubes FET platform. Only one nanotube is shown for clarity. Covalent attachments were used to bind the nanotubes on the electrode substrate and to immobilize the receptors. **(B.II)** Real-time responses of olfactory receptor-carbon nanotubes FET sensors measured at $V_{SD} = 50$ mV. Normalized I_{SD} changes upon addition of target odorant.⁶ 211

Figure 4.3 Schematic illustration of Electrochemical Impedance Spectroscopy (EIS). The EIS cell is based on three electrodes: working electrode (WE), reference electrode (RE) and counter electrode (CE). The sensor surface is functionalized gold (SAM) with target proteins immobilized on it. As the query biomolecule binds to the target protein (i.e. odorant) changes of EIS are reflected. These electrical changes are monitored in a Nyquist plot sensorgram ($-Z''$ vs. Z'). 213

Figure 4.4 (A) Dose-response of rat OR17 in its membrane fraction to octanal (1), heptanal (2) (both specific) and helional (3) (non-specific odorant). R_{Ab-17} represents the polarization resistance before injection of odorants. R_{od} represents the polarization resistance after injection of specific or non-specific odorant at different concentrations. **(B)** Response to odorant at 10^{-11} M under different conditions. In that

case, R_{od} corresponds to the polarization resistance upon injection of odorants at a concentration of 10^{-11} M⁻¹. (C) and (D) are sensor responses to 10^{-11} M of helional on OR-based biosensor where the OR1740 co-expressed with a-subunit of G_{olf} protein in yeast were immobilized onto the surface. Measurements were conducted at 4°C in the absence (C) or presence (D) of 10 μ M GTP γ S in PBS pH 7.0¹³.....214

Figure 4.5 Schematic illustration of Surface Plasmon Resonance (SPR). The sensor surface is gold with target proteins immobilized on it. As the query biomolecule binds to the target protein, the refractive index shifts and the SPR-dip moves to larger angles. The movement of the SPR-dip is the actual monitored signal, and the movement over time forms the sensorgram.216

Figure 4.6 Functionality of human OR1740 olfactory receptors in natural membrane fractions obtained from yeast cells co-expressed with the heterotrimeric G-protein complex (G_{α} subunit, β and γ) and immobilized them on a Biacore 3000 sensor chips L1. (A) No shift of the SPR signal is observed when nanovesicles are stimulated either with odorant alone, or GTP alone (B), as compared to the control stimulated with water. (C) The signal modification is only observed when odorant and GTP are injected at the same time (compared to the control stimulated with water and GTP). (D) The signal modification, due to the release of the G_{α} subunit can be enhanced 4-fold by replacing GTP by GTP γ S (compared to the corresponding control stimulated with water).²⁰217

Figure 4.7 (A) HEK-293 cells expressing ORI7 were seeded on the sterilized SPR chip. Dose-dependent curve of the SPR response to different concentrations of octanal (specific odorant). **Inset:** SPR response after injection of 100 μ M octanal²⁵. (B) Testing the binding activity of detergent-solubilized hOR17-4 using SPR. The hOR17-4 was captured on the SPR chip surface via a covalently immobilized rho1D4 monoclonal antibody. The receptor bound the specific odorant lilial in a concentration-dependent manner. Odorant binding curves shown are: blank control (black), 5 μ M (red), 10 μ M (light blue), 20 μ M (dark blue), and 40 μ M (green). **Inset:** No response was seen for the non-binding control odorant sulfuryl acetate²¹.218

Figure 4.8 (A) Scheme of an Indirect ELISA to evaluate the solvent effect (DMSO, helional) compared to PBT. (B) Absorbance signal (matrix effect) obtained from the anti-c-myc and the coating antigen interaction produced in the presence of solvent (DMSO, helional) in the medium.228

Figure 4.9 (A) Scheme of an Indirect competitive ELISA to evaluate the solvent effect (DMSO, helional) in a control nanovesicles solution (SSTR2-nanovesicles). (B) Absorbance signal (matrix effect) obtained from the anti-c-myc and the coating antigen interaction produced in the presence of solvent: DMSO (lighter colors) or helional (darker colors) at different concentration of SSTR2-nanovesicles solutions (TPC = 0-45 μ g mL⁻¹).228

Figure 4.10 (A) Scheme of an Indirect competitive ELISA to study the specific binding between odorant and olfactory receptor (helional-OR1740-NS) through the c-myc tag. (B) Absorbance signal obtained in the presence of solvent: DMSO (control, lighter colors) or helional (specific odorant, darker colors) at different concentration of c-myc-OR1740-nanovesicles solutions (TPC = 0-30 μ g mL⁻¹).229

Figure 4.11 Scheme of a Sandwich ELISA to study the specific binding between odorant and olfactory receptor (helional-OR1740-NV) through a direct (A) and indirect (B) configuration.230

Figure 4.12 Absorbance signal obtained at different anti-c-myc coating antibody concentration (1/10000-1/640000) and different helional-HRP bioconjugate analyte (1-0.05 μ g mL⁻¹) with and without the presence of c-myc-OR1740-nanovesicles solutions (TPC = 0-40 μ g mL⁻¹).232

Figure 4.13 Absorbance signal obtained at different helional-BSA coating antigen concentration (1-0 μ g mL⁻¹) and different anti-c-myc concentrations (1/10000-1/80000) with and without the presence of c-myc-OR1740-nanovesicles solutions (TPC = 0-40 μ g mL⁻¹).233

Figure 4.14 Typical Biacore sensorgram profile for NV carrying in this case OR1740 receptor (concentration = 15 μ g mL⁻¹, t = 1800 s) and BSA (t = 300 s) immobilization onto a L1 chip. Analogous profiles were obtained for NV carrying SSTR2 receptor and NV carrying OR7D4 receptor.234

Figure 4.15 Scheme representing the SPR signal obtained by the SPR based assay presented that uses double-reference analysis.	234
Figure 4.16 (A) Optical images of the Biacore T100 flow cell. In the SPR assay a solution of nanovesicles and control nanovesicles is flown in two different channels. (B) Then three helional solutions at different concentrations are sequentially flown across the cell. Again a solution of nanovesicles and control nanovesicles is flown in the two remaining channels (C) and control heptanal solutions sequentially flown through the cell (D).....	235
Figure 4.17 Schematic drawing of the SPR setup showing the L1 sensor chip with the immobilized nanovesicles (also called nanosomes).	235
Figure 4.18 (A) Double-subtracted SPR sensorgrams obtained flowing solutions of helional at 2 μM (data in violet), 3 μM (data in green) and 5 μM (data in orange) onto a L1 chip (flow rate: $60\mu\text{L min}^{-1}$). The association phase was followed for 180 s and the dissociation phase was followed for 800 s. Inset: Corresponding sensorgrams obtained flowing on the same chip heptanal solutions at the same concentrations. (B) Double-subtracted SPR sensorgrams obtained flowing solutions of androstenone at 1 μM (data in violet), 5 μM (data in green) and 10 μM (data in orange) onto a L1 chip (flow rate: $60\mu\text{L/min}$).	236
Figure 4.19 SPR response of OR1740-NV vs. helional concentration (data in blue) and of OR7D4-NV vs. androstenone concentration (data in red). The corresponding linear fits give: $y = 1.82 \cdot x$ (blue line) and $y = 0.55 \cdot x$ (red line).....	237
Figure 4.20 (A) Double-subtracted SPR sensorgrams obtained flowing solutions of helional at 1 μM (data in violet), 5 μM (data in green) and 10 μM (data in orange) onto a L1 chip (flow rate: $60\mu\text{L min}^{-1}$). (B) SPR response of OR1740-NV vs. helional concentration (data in blue). The corresponding linear fits give: $y = 1.21 \cdot x$ (blue line).	238
Figure E.1 (A) Concept model of a bioelectronic device with user friendly interface and odorant identification algorithm that will detect and discriminate the odorants within a mixture (<i>from BOND European Project</i>). (B) Inside of the new generation of bioelectronic devices presented in picture (A). Representation of array of nanoelectrodes integrated in an electronic chip that will detect the current from the olfactory receptors when bind its specific odorant. The electronic signal will be digitally converted and acquired by the final bioelectronic device. Different arrays will immobilize different types of ORs to provide the possibility of a complex pattern detection. Red arrow indicate immobilized vesicles onto the array surface that is magnified in the inset.	257
Figure E.2 Target applications for the BOND platform.	259
Figure E.3 EOG recordings from turbinates stimulated with PCO1 from various dilutions, showing optimum response from turbinate IV (best response at lowest PCO1 concentration). Lower right: Scheme of a rat olfactory mucosa and the turbinates position.	261
Figure E.4 Representative Immunoblots revealing an appropriate expression of PCOR2 in yeast (membrane fractions FM78 and FM79).	262
Figure E.5 Functional evaluation of OR7D4 by EIS. (A) Nyquist diagrams obtained for the impedance measurements on the biosensors under various concentrations of androstenone (specific odorant). (B) Nyquist diagrams obtained for the impedance measurements on the biosensors under various concentrations of the helional (unspecific odorant). (C) Relative variation of the charge transfer resistance as a function of concentrations of helional (red) and androstenone (blue). R_0 corresponds to the polarization resistance when the OR7D4 is immobilized on the functionalized electrode.	263
Figure E.6 Representative results for BRET with hOR1740, using helional (red) as odorant ligand, and octanal (green) as negative control odorant. This experiment was reproduced in 5 repeats. Here we present just two of them, (A) and (B).	264
Figure E.7 Layout for the disc (A) and band (B) working electrodes.	266

Figure E.8 The final version of the BOND nanotransducer with an integrated working (WE), counter (CE) and reference (RE) electrode.	266
Figure E.9 SEM analysis (A) and EDX (B) of the AgCl layer.....	267
Figure E.10 SEM analysis (A) and EDX (B) of the Au working electrode array.	267
Figure E.11 (A) SEM image of recessed microdiscs prior to modification tilted to 60°. (B) Zoom from image (A). Scale bar: 3 μm . (C) SEM image of gold microdisc array modified with 190 nm nanoporous gold. Scale bar: 50 μm . (D) Zoom from image (C). Scale bar: 5 μm	268
Figure E.12 Photograph of the BOND device electronic front-end board.	268
Figure E.13 (A) Experimental setup for testing the final version of BOND nanotransducers. (B), (C) Comparison of device with disk geometry as working electrodes with a commercial electrode setup: cyclic voltammetry measurements (B) and electrochemical impedance spectroscopy measurements (C).	269
Figure E.14 (A) Impedance spectroscopy of a known impedance obtained by using a standard potentiostat alone (red curve) and by using our electronic front-end in between the impedance network and the potentiostat (blue curve). (B) Measurement of the resolution obtained by the system when using our electronic front-end (blue bars) compared with the potentiostat alone (red bars).	270
Figure E.15 Scheme of the immobilization strategies evaluated: using 6xHis tag (A) or c-myc tag (B).	271
Figure E.16 Nyquist diagram corresponding to 2 electrodes of disk design (A.1, A.2) and band design (B.1, B.2) prepared in each case in the same conditions.	271
Figure E.17 Transfer charge resistance variation as a function of different concentrations of nanovesicles (also called nanosomes): comparison between c-myc (black) and 6xHis (red) tag immobilisation strategies. Disk WE were used for the analysis.	272
Figure E.18 c-myc-OR7D4 relative variation of the charge transfer resistance as a function of concentrations of different odorants: helional (red points) used as control, testosterone (blue points) and androstenone (black points) the specific odorant.	273
Figure E.19 SEM micrograph of a full chip for the AC non-contact nanotools.	273
Figure E.20 Topographic AFM image of a functionalized microelectrode with nanovesicles adsorbed (A.1) and a bare microelectrode (A.2). Topographic AFM image of a functionalized microelectrode with nanovesicles adsorbed at three different nanovesicle solution concentration at the Total Protein Content of 20 $\mu\text{g mL}^{-1}$ (B.1), 40 $\mu\text{g mL}^{-1}$ (B.2) and 60 $\mu\text{g mL}^{-1}$ (B.3).	274
Figure E.21 (A) Optical image of the AFM probe located on a band type microelectrode. (B) Large scale AFM topographic image of a single band (10 μm wide). (C) Small scale AFM image of the functionalized microelectrode showing the presence of individual nanovesicles (larger white spots). The small spots correspond to the granular structure of the gold used in the microfabrication. (D) Nanoscale dielectric image of individual nanovesicles revealing its dielectric response. Sample was prepared following the c-myc immobilization procedure presented before.	275
Figure E.22 (A) Preliminary EIS data on chimpanzee OR7D4 confirming the sensitivity of the device to the presence of androstenone odorant. Nyquist plot with Zi (imaginari) and Zr (real) part of the small signal impedance. (B) Relative resistance variation as a function of androstenone (specific odorant) and helional (non-specific odorant) concentration obtained from EIS data and Z-plot fitting. R is the resistance at the given odorant concentration and Ro is the resistance in the absence of the odorant.	276
Figure E.23 Theoretical Nyquist plots for native and active state of the selected 3D structures of OR7D4 chimpanzee. The interaction radius, $R_c=62 \text{ \AA}$ gave the maximal resolution.	276
Figure E.24 Linear fit of experimental data.	277
Figure E.25 Instrument 3D CAD design (A) and assembled prototype (B).	278

Figure E.26 (A) Connector 3D CAD top view. (B) Connector 3D CAD section view.	279
Figure E.27 (A) Simulated network. (B), (C), Nyquist plot of the simulated response (B) and the overlaid response (C).....	279
Figure E.28 (A) Software interaction. (B) Complex numerical entry.....	280
Figure E.29 Representation of the integration of the main components of the BOND analytical platform.	282
Figure E.30 Cyclic voltammetry (current vs potential) tests of the final prototypes of the nanotransducers. Disk array (A) and band array (B) variants of the transducers were tested.	282
Figure A1.1 Auto-Scaled Chromatogram from c-myc peptide (C ₁). The % area at the real time 3.719 min was 100% (peptide).	287
Figure A1.2 HPLC-MS chromatogram from C ₁ peptide. In blue are highlighted the characteristics peaks of the peptide. Considering the molecular weight of the C ₁ peptide as 1306.44 Da we can observed the peaks corresponding to $M^+ + 1 = 1306.84$ and $M^+ + 2/2 = 654.21$	288
Figure A1.3 Auto-Scaled Chromatogram from c-myc peptide (C ₂). The % área at the real time 3.544 min was 94.84% (peptide) and at real time 3.739 the area was 5.16% (impurities).	288
Figure A1.4 HPLC-MS chromatogram from C ₂ peptide. In blue are highlighted the characteristics peaks of the peptide. Considering the molecular weight of the C ₂ peptide as 1306.44 Da we can observed the peaks corresponding to $M^+ + 1 = 1306.91$ and $M^+ + 2/2 = 654.14$	289
Figure A2.1 Biacore T100 flow cell. Four flow cells (dark blue arrows) are connected in pairs creating two U-shaped flow paths.	293
Figure A2.2 Representation of an SPR measurement (sensorgram) showing the steps of an analysis cycle. First, the buffer is in contact with the sensor surface (baseline); then the sample solution is injected (association); after, the buffer is injected (dissociation) and finally, the bounded antigen is remove from the surface during injection of regeneration solutions (regeneration) followed by a new analysis cycle. ⁸	294
Figure A2.3 An antibody or immunoglobulin (Ig) is a Y-shaped molecule. The antigen-binding site is the area of the antibody that recognizes and binds to the antigen. <i>Image adapted from: Darryl Leja, NHGRI.</i>	295
Figure A2.4 Amine coupling of ligands to the sensor chip surface ¹⁸	305
Figure A2.5 Pre-concentration experiments of anti-c-myc antibodies and anti-CEA using SPR. The relative adsorption signals (expressed RU, Reflectivity) for the different antibody are plotted versus the buffer pHs used during electrostatic concentration of the antibody.	306
Figure A2.6 SPR sensorgram of a random covalent antibody immobilization on a thiol SAM: (1) activation of the surface using EDC/NHS mixture, (2) injection of the antibody, (3) deactivation of the surface using ethanolamine.	307
Figure A2.7 Random (via the -NH ₂ groups) covalent antibody coupling procedure on an EDC/NHS activated mixed thiol layer (5% 16-MHA and 95% 11-MUOH) ²⁰	308
Figure A2.8 c-myc peptide response (RU) test. Antigen binding responses were done at a wide range of c-myc concentrations (in this example: (1) 798 pM, (2) 7.98 nM, (3) 79.8 nM, (4) 798 nM, (5) 3.99 μM, (6) 7.98 μM, (7) 39.9 μM, (8) 79.8 μM, (9) 399 μM). Green line refers to the injection point and the blue line determines the end of the injection point. (A) c-myc peptide was injected over the home-made anti-c-myc antibody (Ab894D12 ₁₇₁₉). (B) c-myc peptide was injected over the commercial anti-c-myc antibody (Ab9E10).....	309
Figure A2.9 Example of biacore data of c-myc antigen binding to mAb amine coupled to a 16-MHDA functionalized gold sensor chip. Straight red lines correspond to a Langmuir 1:1 fitting. (A) Double-	

referenced sensorgram from a serie of four antigen concentrations (79.8 nM – 3.99 μ M) injected for 10 min with a dissociation followed for 10 min flown onto home-made anti-c-myc (Ab894D12_{f7f9}). **(B)** Double-referenced sensorgram from a serie of four antigen concentrations (79.8 nM – 7.98 μ M) injected for 10 min with a dissociation followed for 10 min flown onto a commercial anti-c-myc (Ab9E10)..... 310

Figure A2.10 Kinetic distribution plot for antibody/antigen interactions with dashed isoaffinity lines. The blue dots correspond to the c-myc/Ab894D12_{f7f9} complex while the yellow dots correspond to the c-myc/Ab9E10 complex. Graph obtained with the Biacore T200 software. 313

Introduction

In 1914, the scientist Alexander Graham Bell noted:

“Can you measure the difference between one kind of smell and another? It is very obvious that we have very many different kinds of smells, all the way from the odour of violets and roses up to asafetida. But until you can measure their likeness and differences you can have no science of odour.” (Alexander Graham Bell, 1914)¹

And he continued saying:

If your ambition is to discover a new science, measure a smell.

In many decades since Bell made his observation, no such science of odour has materialized, and it was not until the 50s that any real progress was made.

Nowadays, we can say that we have reached this point. The introduction of electronic noses on the market has been revolutionary due to the recent developments that have brought new capabilities and possibilities. An **electronic nose** is known as a sensing device capable of producing a digital fingerprint, also known as pattern, of a group of chemical volatiles which characterize a specific **odour**. Comparing the detected profiles with the standard patterns in database allows for the identification and quantification of the odorants presents in a mixture. Such devices consist of two main components: a chemical sensing system and a pattern recognition system² (Figure I.1).

The first reported developments about sensor noses are dated to the 1970s. The possibility of using redox reactions of volatile compounds and detecting the conductivity change was studied. But, the first complete electronic nose system was reported by Persaud and Dodd in 1982³. It was based on the idea of mimicking the human olfactory system to detect different volatile compounds by using biochemical sensors. The sensor signal responses treatment was done using neural networks to recognize the key components presents in the odour.

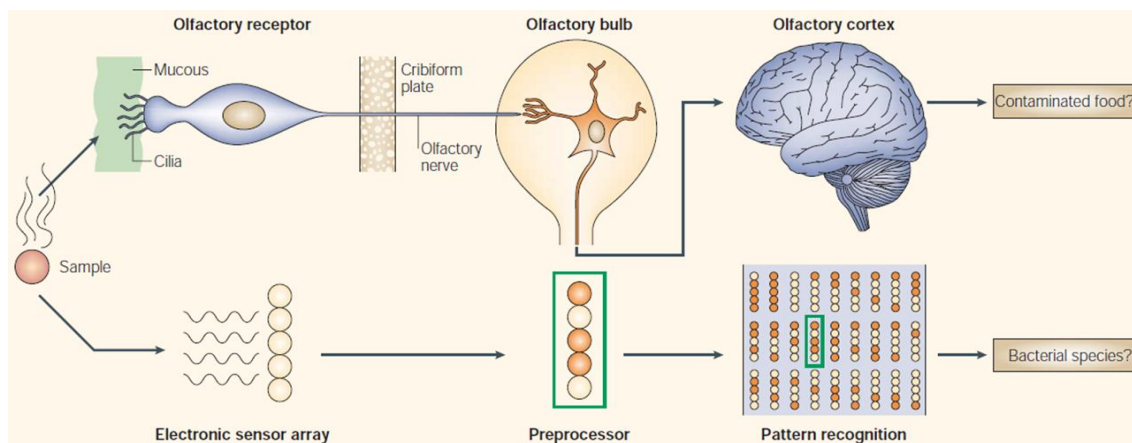


Figure I.1 The electronic devices simulate the different stages of the human olfactory system, resulting in volatile odour recognition, which can now be used, for example, to discriminate between different bacterial infections⁴.

Further, sensor technology has developed rapidly over the last three decades and this has resulted in a range of different sensor formats and in the development of complex microarray sensor devices. In the specific area of electronic-nose systems, several different physicochemical techniques have been used to produce sensor arrays for odour characterization. Since 2000 more than 1800 papers have been published with the label electronic nose (*ISI web of knowledge*) with annual production between 180 and 200 in the last 5 years.

Technologies used for electronic nose sensors include the main transducer mechanisms used to obtain general chemical sensors⁵. Depending of the transducer mechanism we can distinguish between:

Conductivity sensors based on polymers or metal oxides. In this case the interaction between the chemical volatile and the material produce a modification of the conductivity. The selectivity depends on the material, which can be doped, and on the temperature conditions. Some drawbacks to be considered in the design are the dependence on humidity and the drift over time.

Field-effect sensors. These sensors are related to metal oxide sensors, the oxide materials in these sensors contain chemically adsorbed oxygen species, which can interact with the volatile molecules. Thus, the output signal is obtained from a change in potential when the volatile molecules react at the catalytic surface.

Piezoelectric sensors. They use the radio frequency resonance of quartz materials coated with acetyl cellulose or lecithin membranes. The adsorption of volatile molecules onto the membrane produces a change in the magnitude of the resonance frequency that is related to the mass of the volatile analyte. The selectivity of these sensors depends on the thickness of the coatings.

Surface acoustic-wave sensors. These devices are an alternative to the piezoelectric sensors and are based on waves that are emitted along the surface of a crystal by the electric field of surface-deposited aluminium electrodes.

Optical sensors. These sensors are based on a light source that excites the volatile analyte, and the signal can be measured in the resulting absorbance, reflectance, fluorescence or chemiluminescence. In the case of surface plasmon resonance devices, changes in the optical properties of the polymer materials can be also used for volatile detection.

Electrochemical sensors. These sensors contain electrodes and an electrolyte. The responses generated are dependent on the electrochemical characteristics of the volatile molecules that are oxidized or reduced at the working electrode, with the opposite occurring at the counter electrode. The voltage or current generated by the reactions between the electrodes is measured.

There are a large number of papers treating all these sensor technologies based on chemical sensors⁶⁻⁹, but the main drawback is the general poor selectivity, which requires a complex signal processing post-treatment. In many reported papers the devices obtained can be used only in specific environments where the number of volatiles and the ambient conditions can be limited and controlled.

Thus, researches have been trying to develop artificial sensing devices based on the olfactory system with higher sensitivity and selectivity. They proposed to use olfactory receptors (ORs) as the biological sensing elements (primary transducer) and the non-biological devices described above as a sensor platform part (secondary transducer), they call them **bioelectronics noses**. The developments of a general purpose bioelectronic nose system which mimic the physiological olfaction system of

insects or mammals constitute a promising scientific and technological research field¹⁰. The mammalian nose is the gold standard of odour detection, displaying both an unmatched chemical space (estimates vary from tens of thousands up to one million of compounds) and the highest sensitivity. These sensing devices have the potential to be used as effective tools to detect and discriminate lots of odorants with high sensitivity and selectivity. Thus, there are potential targeted approaches and applications of these devices in the food and drink industry, diagnosis, security, environment, etc.

I.1 Volatiles detection for many applications

Diagnostic of different diseases

Odours emitted by the human body and present in body fluids characterize an individual, and depend both on its genetic signature and on its physiopathological status. Some medical practices have used, or are still using, i.e. sensorial diagnosis (mainly olfactory), to check good health or to determine various pathologies (phenylketonuria, typhoid, scurvy, etc.). The patient samples used include human pus, urine, blood plasma and alveolar air.

As an example, studies *in vitro* have shown that it is possible to discriminate between different aerobic bacteria, such as *Helicobacter pylori*, *Escherichia coli* and *Enterococcus species* that are present in samples, both alone and as a mixture of the three species using electronic noses devices¹¹. Also, *Mycobacterium tuberculosis*, the causative agent of tuberculosis, has been detected in cultured sputum samples either directly or following treatment with enzymes to enhance volatile production. Samples from patients with urinary tract infections (UTIs) and tuberculosis were identified correctly in 90–99% of cases compared with traditional culture techniques¹².

It is reported, that electronic-nose devices can be also used to detect diseases other than infectious diseases. For instance; it has been shown that patients with kidney disorders produce characteristic volatile compounds, which can be a useful tool in the diagnosis and control of renal dialysis¹³. Additionally, other studies have shown that lung cancer can be detected by breath analysis of the volatile organic compounds

(VOC) using non-selective gas sensors¹⁴ or more recently, using an array of nanosensors¹⁵.

A major challenge of these diagnostic tools lies in the establishment of a precise odorant disease signature, understood as the ensemble of volatile compounds whose concentration in a body fluid (i.e. urine, blood, pus, etc.) or in the breath varies in patients with the malignancy with respect to healthy individuals. For example, for bladder and prostate cancers formaldehyde has already been shown to be one member of the odorant disease signature of the patients' urine¹⁶.

Nowadays, other techniques such as Gas Chromatography and Gas Chromatography-Mass Spectroscopy have already been used to monitor patterns of volatile compounds as an aid to the clinical diagnosis for example of aerobic and anaerobic bacterial infections and cardiopulmonary disease¹⁷. However, the uses of these techniques require expensive analytical equipment and are time consuming. Perhaps in the future, it might be possible to have electronic nose devices as point-of-care systems that could be used as a rapid screen for specific diseases or disorders⁴.

Food industry

Very encouraging results of volatile detection have been reported in the past for multiple other applications. For example, electronic noses have been applied in various food contexts: process monitoring¹⁸, freshness evaluation¹⁹, shelf-life investigation¹⁸, authenticity determination²⁰, contamination and spoilage²¹ and product traceability²². As well, they have been employed for the classification and characterization of foodstuffs such as beverage²³, wine^{24,25}, coffee²⁶, and milk²⁷. In addition, electronic nose could be very valuable tools to evaluate microbiological food quality and safety.

In all these applications the complexity of most food aromas make them difficult to be characterized with conventional flavour analysis techniques such as gas chromatography or gas chromatography olfactometry. Hence, the need of an instrument such as the electronic nose has been revolutionary in this research field. The most common electronic noses used in the food industry are the ones that use metal oxide gas sensor²⁸. The sensing systems based on metal oxide sensors (MOS) reached the food industry more than a decade ago and it was presented as a non-critical technique.

Explosives detection

Furthermore, another challenging application of electronic noses in the last few years is the detection of explosives. The number of terrorist attacks, and suicide bombings has risen dramatically in the last few years. Thus, the early detection of unseen explosive devices therefore has the potential to save many lives. Recently, Patil and co-worker²⁹ present a novel compact, nonoptical and inexpensive polymer nano-composite microcantilever sensor platform for the detection of explosive vapours at room temperature such as TNT, RDX and PETN. The electronic nose platform provides detection sensitivities in the below parts-per-trillion level within few seconds of exposure under ambient conditions.

Environmental monitoring

More recently, during the past two decades, another important area of application of e-noses is the environmental monitoring due to the increasing conscience of the effects of pollution on human health and the quality of the environment. Before, e-noses have been used for environmental monitoring in applications such as detection of smoke compounds, the determination of the quality of indoor air and odour emission rate of a compost hall. Now, the monitoring of a large number of pollutant gases and particles in the air is an emerging application and the introduction of the electronic nose for this task is very challenging³⁰. While many sensors are currently available, there is still a need for a detection system that is highly sensitive and selective, robust, accurate, fast, adaptable to mass production, and capable of monitoring many different chemical gases. In 2013, Kim and his team³¹ have addressed some of these issues by developing an “electronic nose” (high performance gas sensors) based on an array of TiO₂ nanohelices fabricated by the method of rotating oblique angle deposition (OAD).

I.1.1 Animals’ olfaction as a biological recognition element

As compared to traditional (or even up-to-date) electronic noses, animal olfaction is repeatedly reported to display much lower detection limits (below 0.1 ppb down to 10⁻⁶ ppb, or even less in some insects)³² (Table I.1).

Table I.1 Schematic comparison between human and electronic noses (Adapted from ref. 33).

MAMMALIAN OLFACTION	ELECTRONIC NOSE based on Chemical Sensors
Around 10–40 millions	5–100 chemical receptors
Around 100 to 1000 selectivity classes	5–100 selectivity patterns
Initial reduction of number of signals from 1000 to 1	Smart signal processing
Cannot detect very small molecules	Can detect simple molecules (H ₂ ; CO ₂ ; CO)
Limit detection 0.1 ppb (Insects 10 ⁻⁶ ppb)	Limit detection around 0.1 ppb
Size Olfactory neuron cell 40–50 microns	Size of chemical sensors 100–800 microns
Size olfactory receptor 5 nanometers	Size of nanosensors around 100 nm

In association with this unchallenged sensitivity, animal olfaction offers a second outstanding analytical property, that is, the capability of detecting a wealth of odorant chemicals, provided that they are of rather small molecular size (molecular weight below 300 Dalton). This is made possible thanks to the so-called ‘combinatorial code of odours’, through which the repertoire of olfactory receptors (about 1500 genes in rodents), combined with the possibility for each given receptor to detect (and likely discriminate, at least partially) 10s of odorants³⁴ yields an amazing number of different possibilities to identify chemical compounds (Figure I.3). Most of these characteristics of animal olfaction arise directly from the **olfactory receptors** themselves (described below).

I.1.1.1 Use of dog olfaction abilities for detection

The use of dogs for diagnostic purposes of skin cancers was published for the first time as anecdotal reports by Williams and Pembroke (1989)³⁵, Church and Williams (2001)³⁶. Later on, in 2004, Willis et al.³⁷ reported that dogs can distinguish urine from patients with bladder cancer with a mean success rate of 41% and Elliker et al.³⁸ show the capability of dogs to detect prostate cancer. Confirmed three years ago (2011) by Cornu et al.³⁹ obtaining a sensitivity of 91% and a specificity of 91%.

In 2006, McCulloch et al.⁴⁰, show that ordinary household dogs can be trained to distinguish breath samples of patients with lung and breast cancer with high accuracy (sensitivity and specificity of 99% and 99% in lung cancer and 88% and 98% in breast cancer respectively). Furthermore, Horvath and coauthors⁴¹ reported that between ovarian cancer tissues samples and control tissues, the sensitivity obtained was 100% and the specificity 97.5%.

More recently, Sonoda et al.⁴², report an exhaustive analysis of colorectal cancer screening performed by dogs using breath samples of patients and compared with colonoscopy showing a good sensitivity and specificity (91% and 99% respectively). Most interesting is that accuracy of canine scent detection was even higher for early stage cancers and canine scent detection was not confounded by current smoking, benign colorectal disease, inflammatory disease or the presence of human haemoglobin or transferrin. The authors conclude that the results indicate that a specific cancer scent indeed exists. The volatile organic compounds detected during canine scent presumably occur early in the pathogenesis of colorectal cancer.

But dogs, not only have been used for diagnostic purposes, their level of olfactory sensitivity play a key role in the dog's ability to use concentration gradient information to locate an odour source for multiple applications.

In 1998, William et al.⁴³ presented that dogs were capable of detecting and discriminating a number of compounds constituting a complex odour. It was performed by training dogs under behavioural laboratory conditions to respond differentially on separate levels. First, to blank air; then, to a target odour, such as an explosive, and finally to all other odours (non-target odours). This study was conducted using TNT, C-4, and commercial dynamite as explosives.

More recently, the academics from the University of Lincoln⁴⁴, present a new study based on whether dogs can be trained to recognize the significance of a group of odours, rather than having to learn each scent individually. This study is on going. Furthermore, the role of canine cognition in processing complex odours is an important and exciting new research area and the work done by the scientists at the University of

Lincoln will potentially support long-term improvements to the ways we train dogs for detection.

I.2 The olfactory system: anatomy and physiology

I.2.1 The olfaction

The odours detection allows the animals to locate food, danger, to avoid predators, to identify mates, to communicate between themselves and to reproduce. The animals in their natural environments are immersed in odours, the detection of which is necessary for their survival. The odorants, these chemical substances, are rich in information, for that reason the animals have evolved to detect and interpret them. Depending on the biological information that they give are known as odorants or pheromones.

When we talk about the sense of smell, this may involve a large number of distinct receptors capable of associating with one or a small number of odorants⁴⁵. In general, olfactory systems have evolved great sensitivity and discriminatory power. It is reported in the literature that the mammalian olfactory system can recognize and discriminate a large number of different odorant molecules. The detection of the odorants results from the interaction between odorant ligands and specific receptors in the cilia or dendrites of the olfactory sensory neurons (OSNs)⁴⁶, also called olfactory receptor neurons, ORNs (Figure I.2).

The olfactory receptor neurons (ORNs) are one of the main classes of the chemoreceptors (also called chemosensors). They are sensory receptors that transduce a chemical signal (stimuli in the environment) into an action potential. In comparison with the ear and eye, the mammalian nose is much more complicated, at least regarding the mechanisms responsible for the primary reaction to an external stimulus. In olfaction hundreds of different classes of biological receptors are involved, whereas in vision in principle only three different classes are found.

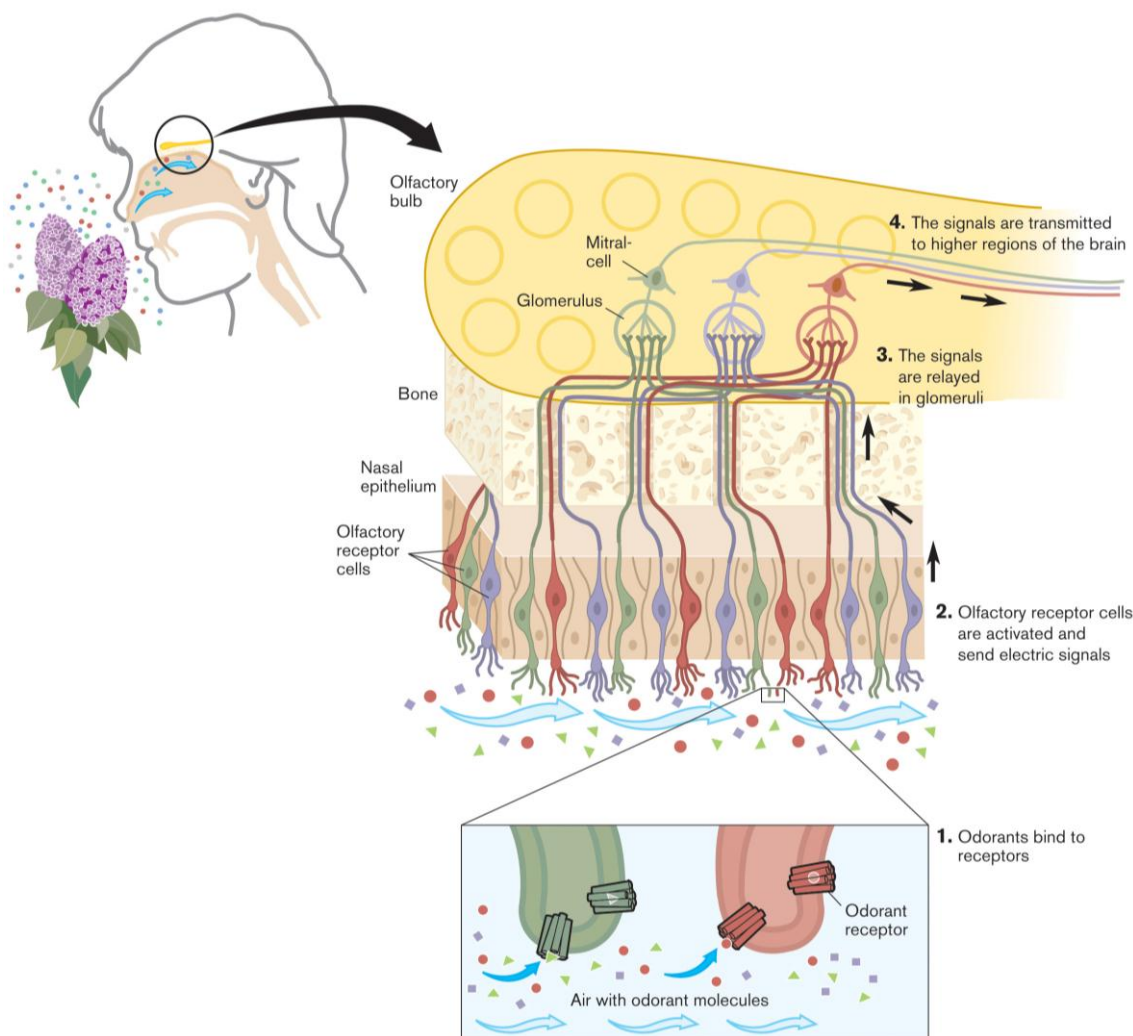


Figure I.2 Odorant receptors and the organization of the olfactory system. (Picture from "Press Release: The 2004 Nobel Prize in Physiology or Medicine to Richard Axel and Linda B. Buck". Nobelprize.org. Nobel Media AB 2013. Web. 7 Apr 2014)

The human olfactory system is very complex, and is not yet fully understood. However, it is known that olfaction is less developed in humans than in other mammals, such as rodents or dogs (named microsmatic animals). Dogs are up to 100 times more sensitive to certain odour compounds than humans. These differences are due to the anatomy of the olfactory apparatus (i.e. size of the olfactory epithelium and the olfactory bulb, a brain region involved in odour detection), and in the genome. However, is reported, that in all the cases the identification of a large family of G-protein-coupled receptors (GPCRs) in the nose manages the olfactory system discriminatory task⁴⁷.

I.2.1.1 The insect olfaction

Not all the animals detect odours in the same way. Before 1999 it was reported that insects, as well as mammals, detect odours through GPCRs. Three laboratories identified a family of these seven-transmembrane receptors whose expression in the antennae of the fruit fly *Drosophila melanogaster* turned out to control the responses of individual olfactory neurons to chemical odorants⁴⁸. The first experiments prove that insects detect odours differently from mammals came from the analysis of the receptors' amino-acid sequences.

As well as mammals' olfaction system, the insects' one is divided in olfactory subsystems. In flies, the number of chemosensory systems is lower than in mammals. In the *D. melanogaster* three chemosensory subsystems have been identified: olfactory receptors (that are not related with the vertebrates ORs) localized in the basiconic and trichoid sensilla, gustatory receptors (GRs) expressed in taste organs through the body and ionotropic glutamate receptors (IRs) expressed in coeloconic sensilla. The flies, with a difference of the vertebrate olfactory system, have two bilaterally symmetrical pairs of olfactory organs, the third segment of the antennae and the maxillary palps (located in the head).

The observation of Sato et al.⁴⁹ gives evidence that for odour detection, insects use an unusual strategy and unusual receptor (they focus their studies on the fact that the receptor is an ion channel). But there are other groups, such as Wicher et al.⁵⁰ that have different views to understand the sequence of events that occur from ligand binding to channel opening.

I.2.1.2 The vertebrates olfaction

It is reported that the olfaction takes place in several olfactory subsystems of the nose. During the last 20 years the following five types of chemosensory GPCRs in the mammalian nose have been identified:

- odorant receptors (ORs)⁴⁵,
- trace amine-associated receptors (TAARs)⁵¹,
- two distinct vomeronasal receptors (V1R and V2R)^{52,53} and
- formyl peptide receptors (FPRs)⁵⁴.

Until now, the **ORs** are the largest family, with up to 2130 genes discovered involved in the expression of the olfactory receptors. The ORs are expressed in the main olfactory epithelium of mammals and bind small, volatile molecules as it has been mentioned before⁵⁵. So, the ORs are responsible for the sense of smell. Vertebrates ORs are known to be expressed in different olfactory sensory neurons in the nasal neuroepithelium^{45,56}.

The olfactory sensory neuron has the characteristic to be bipolar: each OSN extends a dendrite to the mucosal surface and an axon to the olfactory bulb of the brain which is involved in neural processing. When the axons reach the olfactory bulb, they make synapses with the dendrites of projection neurons, within discrete structures known as glomeruli. The characteristic of the dendrites is that they include the cilia which contain the ORs and their main goal is to increase the surface area of their exposure to volatiles (Figure I.2).

In vertebrates, as it has proved in 2000s^{57,58} each OSN express mainly a single type of OR, only one receptor gene. But in the nasal mucosa there are other proteins that have an important role. These proteins allow the OR-odorant interaction process, such as the water-soluble odorant-binding proteins (OBPs). It is difficult to prove the specific function of these proteins but there is some hypothesis that seems to focus that they act to solubilize and transport specific odorants, making them available to the ligand-binding site of ORs in order to enable the ORs in the aqueous phase, to access volatile compounds⁵⁹.

I.2.2 Volatile molecules detection. The role of the olfactory receptors.

By studying odorant receptors we can understand the events of olfaction providing crucial knowledge for the development of a novel odorant receptor-based biosensor for chemical screening. Each odorant receptor seems to recognize multiple odorants, as well as each odorant seems to be recognized by more than one odorant receptor (Figure I.3).

This combinational odorant receptor coding scheme allows the differentiation of a great number of several odours with relatively few odorant receptors.

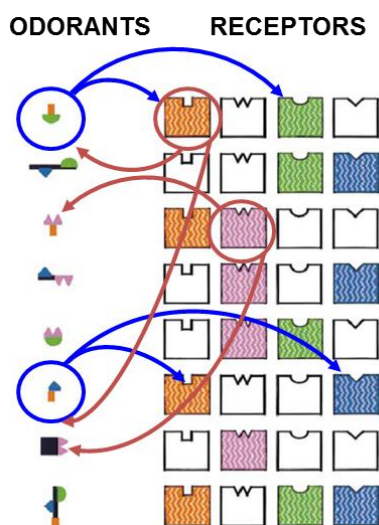


Figure I.3 Adapted from Malnic *et al.*³⁴. Combinatorial receptor codes for odorants. In this model, the receptors shown in color are those that recognize the odorant in the left. The identities of different odorants are encoded by different combinations of receptors. However, each OR can serve as one component of the combinatorial receptor codes for many odorants. Given the immense number of possible combinations of ORs, this scheme could allow for the discrimination of an almost unlimited number and variety of different odorants.

Several studies conducted in **odour detection of vertebrates** supported a G-protein-coupled, cAMP-mediated transduction in the main olfactory system⁶⁰. These types of proteins, the GPCRs, are very well-known. The vertebrates OR genes encode a large family of GPCRs to recognize the odorant molecules in the olfactory epithelium. In particular, the mammalian OR gene family encodes around 400 and 1200 different olfactory receptor proteins in humans and mice respectively, indeed they are the largest family of genes reported in the literature⁶¹.

The sequence of the **GPCRs proteins** contains seven segments with mostly hydrophobic amino acid residues that form a α -helix structure through the lipid bilayer membrane, alternated with hydrophilic segments that form loops, which are stable in water, connecting each helices^{56,62,63}. The GPCRs are a group of proteins that exhibit a seven-transmembrane domain topology. They are very well-known proteins and have two important binding sites. One, the odorant binding site on the mucosal layer, in the extracellular side and the other, the binding site made up of three subunits on the

cytoplasmatic domain that couples a heterotrimeric G-protein (guanine nucleotide binding protein) (Figure I.4).

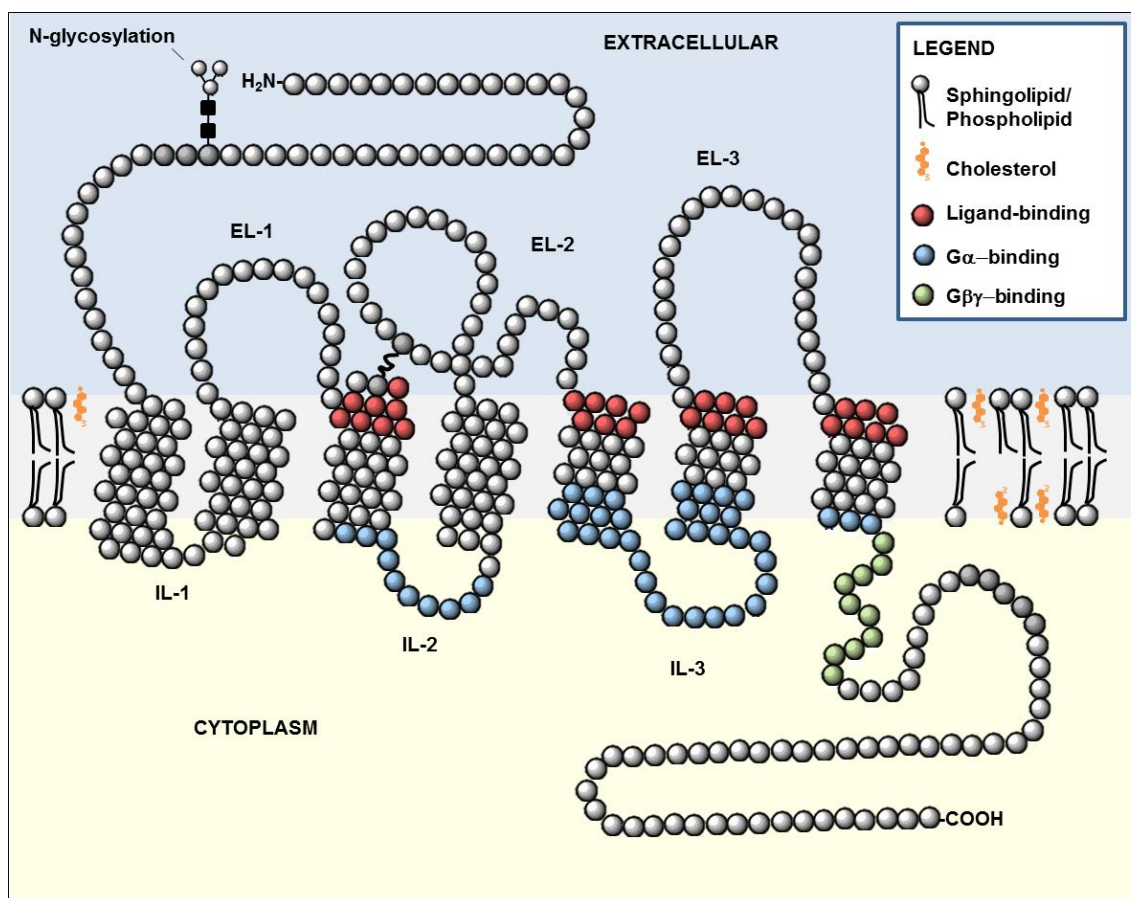


Figure I.4 Schematic representation of a typical member of the serpentine (they pass through the plasma membrane seven times) class of G-protein coupled receptor. White, red, blue, and green spheres represent amino acids. Structural characteristics include the three extracellular loops (EL-1, EL-2, EL-3) and three intracellular loops (IL-1, IL-2, IL-3). Most GPCRs are modified by carbohydrate attachment to the extracellular portion of the protein. Shown is typical N-linked carbohydrate attachment. The different colored spheres are involved in ligand-binding and associated G-protein binding as indicated in the legend (Adapted from The Medical Biochemistry webpage: <http://themedicalbiochemistrypage.org>).

When the odorant attaches to the binding site of the GPCR, the olfactory signal transduction is initiated. The binding gives a conformational change that activates an olfactory-specific subtype of G-protein, the G_{olf} . This subunit is responsible for activating the adenylyl cyclase enzyme. The role of this enzyme in the olfactory system is to convert intracellular adenosine triphosphate (ATP) into cyclic adenosine monophosphate (cAMP), following with a cascade of events that lead to the nerve cell signal⁴⁷. This is the first step of the transduction cascade that is organized in two stages. After that, the cyclic AMP levels increase the opening nucleotide-gated channel, giving an influx of Na^+ and Ca^{2+} ions⁶⁴ that will generate a potential done by Ca^{2+} -dependent

Cl⁻ channels (the depolarization of the cell is amplified through the activation of these ions). After this process, the ORNs accumulate chloride through the Na⁺/K⁺/2Cl⁻ cotransporter NKCC1 and maintain an elevated intracellular Cl⁻ concentration to support amplification⁶⁵ (Figure I.5A).

On the other hand, recent studies^{49,50} about **olfactory receptors in insects** show that the mechanism of signal transduction when the odorant binds the OR is not the same for all the animals.

In the case of the insects, they proved that the co-receptor OR83b (expressed in all OSNs) together with the OR forms a heteromeric ligand-gated cation channel in the *Drosophila*. What is not clear at present is the exact mechanism of fly signal transduction. The receptors in insects recognize olfactory stimuli by ion channels, not only GPCRs⁵⁵. One of the authors reported that evidence does not exist for the involvement of G-proteins or intracellular messengers such as cAMP, cGMP or inositol-1,4,5-trisphosphate for a fast ionotropic response⁴⁹. They suggest that an ion channel opened when an odorant binds the odorant receptor directly. In that case, the receptor consists of a common receptor (a GPCR) and a co-receptor (OR83b) (Figure I.5B). This hypothesis doesn't specify the location of the channel pore and would be the simplest model. On the other hand, another group proved that common insect ORs activate the synthesis of cAMP through the G-protein, and thus this in turn activates OR83b co-receptor, which serves as a cAMP-gated ion channel⁵⁰. They suggest two different pathways by which odour induced-depolarization can be generated. When an odorant binds the OR, the signal is transferred to the OR83b co-receptor. This transfer can be direct or indirect. The direct transfer consists of opening a channel formed by the OR83b subunit directly after the odorant binding, giving a fast and short depolarization. However, the authors also consider an alternative, the indirect pathway. The activation of a G-protein and adenylyl cyclase allows the production of the cAMP. When the cyclic AMP binds the co-receptor OR83b, the channel opens and generates slow and prolonged depolarizing currents (Figure I.5C). This controversy between the different studies done on invertebrates olfactory receptors is very well-documented in the literature⁵⁵.

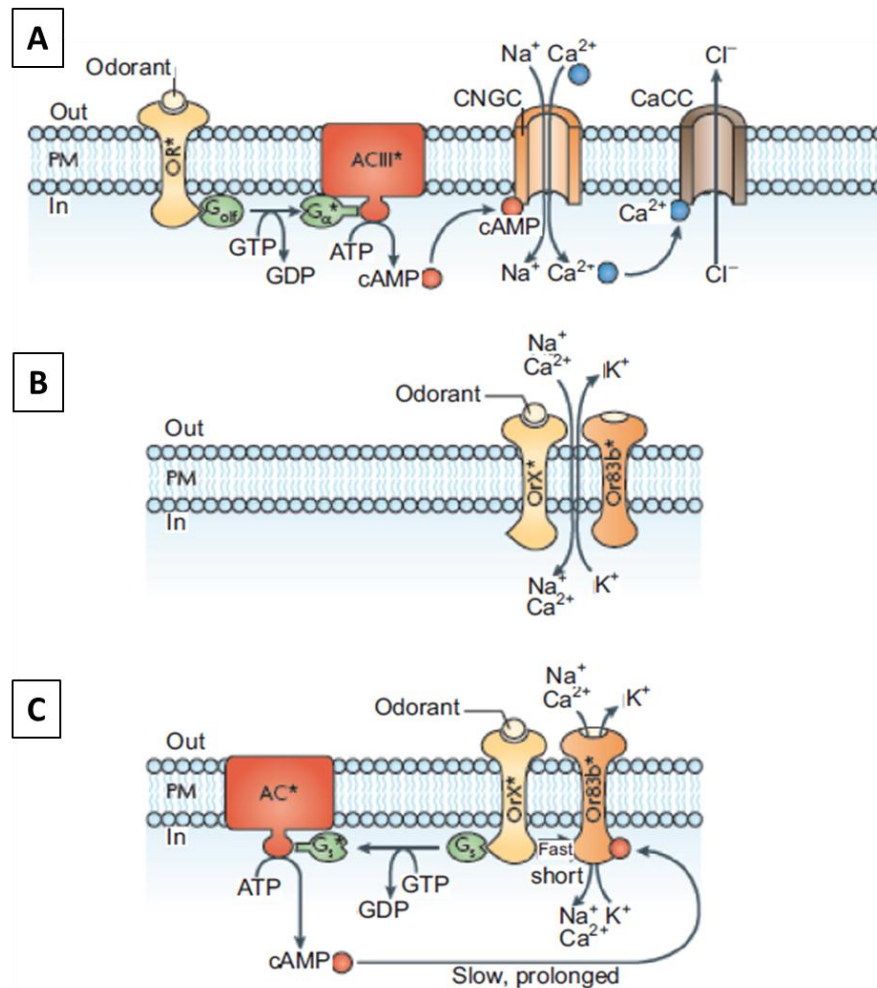


Figure I.5 Adapted from *Nature Reviews*⁵⁵. (A) Odorant detection in vertebrates. When the odorant binds the olfactory receptor (OR) activates the trimeric transmembrane protein, olfaction-specific G protein (G_{olf}), adenylyl cyclase type III (ACIII), the olfactory cyclic nucleotide-gated channel and a Ca^{2+} activated Cl^{-} channel (CaCC). (B) Insect olfactory model suggests that the odorant receptor forms an ion channel that is opened directly in response to the binding of odorants. (C) On the other hand this complex insect model suggests that there are two pathways by which odor-induced depolarization can be generated. Upon odorant binding, activity is transferred to the Or83b subunit either by a direct (fast and short) or indirect (slow and prolonged) pathway.

Despite their differences, invertebrates and vertebrates, in a wide range of habitats, are similar to each other in the way that they use chemical communication.

1.2.2.1 The role of Odorant-Binding Protein

When odorants enter the nasal cavity two types of processes occur. The important one is the specific interaction with receptor proteins on the membrane of the olfactory cilia as it has been presented until now. But, it should not be forgotten that before reaching the neuronal membrane, the odorant molecules have to cross a layer of

mucus containing high concentration of several classes of proteins that will interact with the odorants, one of these proteins are the odorant-binding proteins that are extracellular proteins located in the fluid surrounding the sensory dendrite. Like other similar systems, the olfactory mucus is very complex in its composition and several aspects are under investigation.

However it is known that odorant-binding proteins (OBPs) play a crucial role in the interaction between the OR and the volatile compound. Till now, the complete role of OBPs in olfactory biosensors of their physiological function remains unresolved. For this reason some OR signalling *in vitro* studies include the OBP and in others do not⁵⁹.

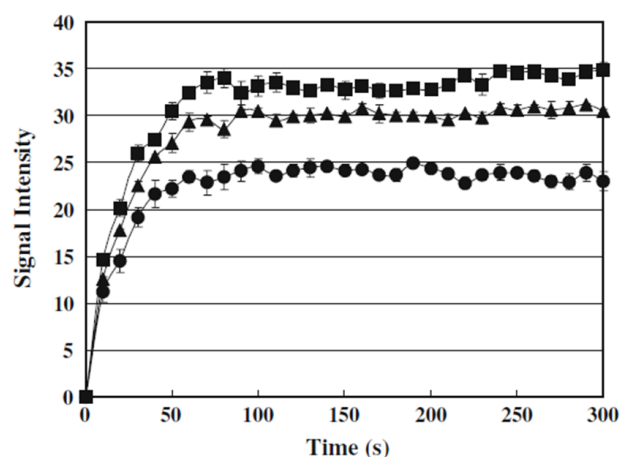


Figure I.6 Effect of OBPs on the signal intensity of Ca^{2+} influx. The signal intensity in HEK-293 cells stably expressing rat olfactory receptor I7 was measured using a spectofotometric Ca^{2+} assay, 10 mM octanal (specific odorant for ORI7) was used as stimulant. Circle: octanal only, triangle: OBP3 + octanal, square: OBP2 + octanal.⁶⁶

However, odour solubilisation is still required in these researches. In the last years, some groups have focused their studies on the role of these proteins and how to improve their previous results. For example, Vidic et al.⁶⁷ investigated the role of OBP-1F in regulating binding kinetics of the ligand helional on yeast-derived nanovesicles, nanovesicles, containing OR1740. They showed that the presence of OBP-1F increased sensitivity at lower odorant concentrations. Assuming that the sensitivity is a highly important issue in the development of an effective biosensor, Ko et al.⁶⁶ also proved that OBPs can be used to increase the sensitivity of olfactory receptor-based biosensors (Figure I.6).

Their results suggest that OBPs can bind to different olfactory receptors with different specificity and have the highest affinity to olfactory receptors that originate from the same species⁶⁸. Thus, they can bind to various different odorants.

It is well-known that odorant-binding proteins are low-molecular-weight proteins highly concentrated in the nasal mucus of vertebrates and in the sensillar lymph of insects with affinity towards odours and pheromones. They were discovered by Pelosi et al.⁶⁹ during the 80s in the search for olfactory receptors using radioactively labelled odorants in ligand-binding experiments, and were detected in the nasal olfactory mucosa of bovines and other mammals as a soluble protein able to fix pyrazine (2-isobutyl-3-metoxypyrazine) with low detection thresholds. They hypothesized that this protein could serve as an odorant-carrier⁷⁰. However if the different species are compared, literature shows no homology between vertebrate OBPs and insect OBPs in aminoacid sequence and three-dimensional structure^{71,72}.

If we focus on the vertebrates OBPs, these proteins are small lipocalin-like proteins defined by their property of reversibly binding volatile chemicals, but insect OBPs do not have this structural morphology^{59,71,73}. As reported in the literature, insects OBPs are better characterized than mammalian ones. The first study of the OBPs in insects was in the 80s that were discovered as small, secreted molecules present in fluid that bathed pheromone-sensitive OSNs and originally called pheromone-binding-proteins. In addition, the first OBP of insects (called pheromone-binding protein, PBP) was identified in the moth *Antheraea polyphemus* using its sex-specific pheromone⁷⁴.

Till now, a lot of OBPs have been discovered and classified in three groups: pheromone-binding-protein, general odorant-binding proteins groups 1 and 2⁷⁵.

Some structure analysis reported in the literature revealed that generally the vertebrates OBPs consist of a polypeptide chain of about 150 amino acids. This globular protein is folded into eight antiparallel β -sheets with α -helical domain located near the carboxy terminal. The β -sheets form a continuously hydrogen-bonded β -barrel, with the internal cavity accommodating the hydrophobic small ligands⁵⁶ (Figure I.7). The binding pocket located inside the barrel can accommodate ligands of 10–20 carbon atoms of hydrophobic nature.

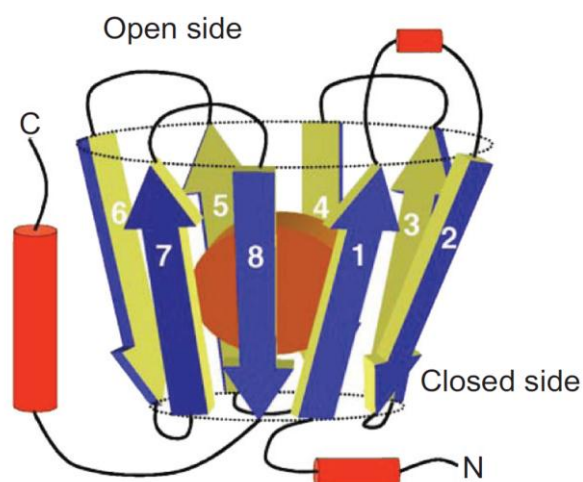


Figure I.7 Schematic representation of an odorant-binding protein⁵⁶.

Also, seems that each OBP has a unique ligand-binding profile. According to this hypothesis, some authors present the role of the OBPs as key proteins involved in preselecting those volatile compounds that finally interact with the olfactory sensory cells. In other words, the OBPs could play a role as a specific filter rather than a passive carrier protein for odorants in the mucus layer.

I.2.3 Volatile molecules: an approach from odorants to the pheromones kingdom

As it was mentioned previously, odour detection is crucial for animal survival. These small molecules, called **odorants**, are defined as a volatile chemical compound with a molecular weight lower than 300 Da that humans or other animals can perceive. It is important not to confuse odorants with pheromones. Taking this into account we can define an odorant as any molecule capable of stimulating the olfactory neurons.

The exact number of odorant molecules on earth is unknown. However, literature has reported that humans can distinguish and detect approximately 10000 different odours. However, the exact number of known smells or the number that we can perceive is unknown⁵⁸.

How we can classify the volatile substances? A substance is volatile depending on the strength of intermolecular forces. For example, charged compounds are odourless

because volatility is minimal when strong ionic or polar interaction is present⁷¹. However, these characteristics are not common between all animals. For example, the best odorants for aquatic animals are amino acids. These days it seems that irrespective of the structure or chemical properties, an odorant is volatile enough to reach the nose.

On the other hand, pheromones, defined as specific substances that are secreted by an individual and received by a second individual from the same species, or induce a specific reaction such as stereotype behaviour or endocrinological change⁵⁸. It is reported that the same pheromone can have a variety of effects, depending on the context or the receiver⁷⁶.

Sometimes, the difference between a general odorant and a pheromone is not clear. For this reason it is easier to define a **pheromone** as a substance that is utilized for intraspecies communication. Pheromones themselves can send information about sex, strain, and be meaningful or informative for the species, mediate an amazing diversity of animal behaviour. The first result describing the pheromone kingdom was about pheromone moths, how these animals were capable of detecting a single molecule of female pheromone over an enormous distance.

During these years a lot of work has been done trying to understand the functional properties of these neurons (capable of detecting the pheromones) and the chemistry of these chemicals, but until now no evidence can clearly explain the biochemical mechanisms by which pheromones selectively activate sensory neurons⁷³. The vomeronasal organ (VNO) is the one that detects the pheromones. This is located in the nasal cavity and is a chemosensory system different from the olfactory sensory organ. Two families of VN receptor genes that encode proteins with seven transmembrane domains, V1R and V2R have been identified in the VNO.

Most of the mammal olfactory system has two olfactory organs: the main olfactory epithelium (MOE) and the vomeronasal organ (VNO), then the information is preceded in separate neural pathways (Figure I.8).

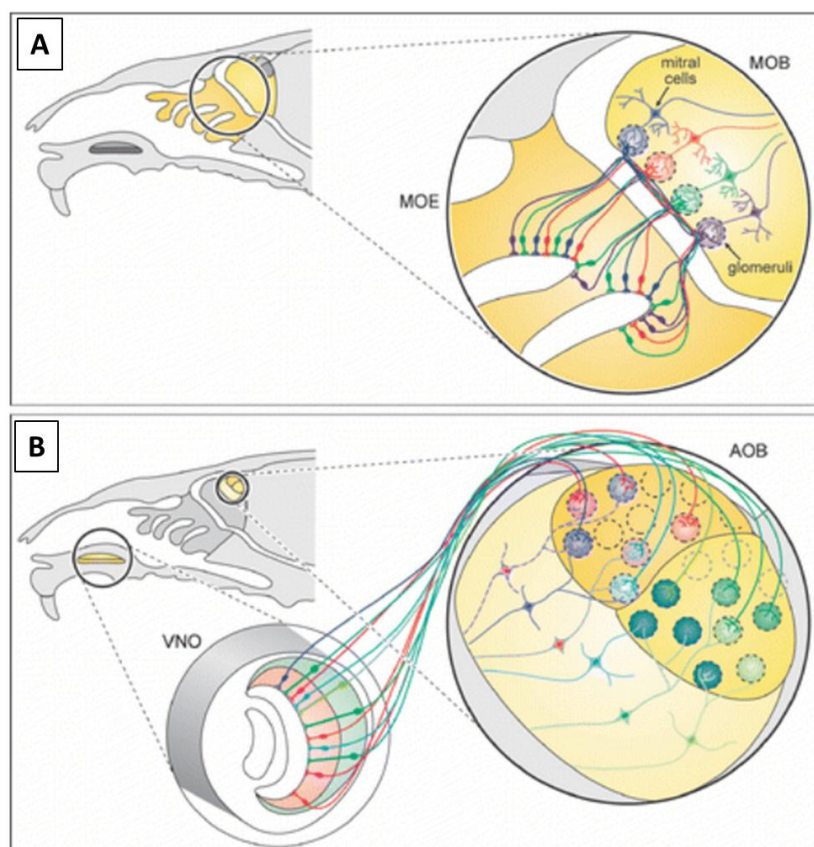


Figure I.8 Glomerulus organization in the main olfactory and vomeronasal systems. **(A)** Each glomerulus in the main olfactory bulb (MOB) receives axons only from cells expressing the same OR type, indicated by a different color, and connects to a dedicated mitral cell. **(B)** Sensory neurons in the epithelium of the VNO have their cell bodies segregated into separate zones (all have microvilli reaching the surface of the organ's lumen as illustrated). Neurons with cell bodies located in the apical zone (shown in red) express members of the V1R family of receptors and project to multiple glomeruli in the anterior half of the accessory bulb (AOB). Neurons with cell bodies in the basal zone (shown in green) express V2R receptors and project to multiple glomeruli in the posterior half of the AOB⁷⁷.

I.3 Bioelectronics noses based on *in vivo* experiments

More than one million species of insects with sometimes extraordinary sensory abilities present a tremendous potential of highly optimized chemoreceptors. In order to make these abilities usable for mankind in terms of analytical tools, some interface between chemoreceptive organs of insects and microelectronic components of analytical instruments has to be established.

One promising strategy is the design of biosensors on the basis of intact chemoreceptors utilizing electrophysiological techniques like electroantennography (EAG), which records the 'slow' changes of potential that are caused by the

superposition of simultaneous membrane depolarizations of numerous receptor cells. Another one is the electro-olfactogram (EOG) technique, based on the recording of an extracellular field potential produced by the odour induced generator currents in the olfactory receptor neurons, on the whole animal and tissue, to using methods such as voltage clamping on single cells or patch clamping to monitor single channels⁷⁸, the electrophysiological approach to these techniques forms the basis for a range of biosensor transduction mechanisms.

Considering that detection limits of analytes are typically in the ppb range or even lower, a biosensor on the basis of intact chemoreceptors could serve as an analytical device with unrivalled data acquisition time. Therefore, the number of applications of this biosensor type is increasing. Most of them are developed for agricultural problems in integrated pest management as detection of insect pheromones, e.g., in greenhouses, in cotton fields^{79,80} or for the detection of plant damage in potato fields for the timing of pesticide application⁸¹.

In order to circumvent major drawbacks of conventional EAG methods, such as electrical and mechanical instability, the need for preamplification and the limited ability for miniaturization, new methods were designed. A biosensor device based on a field-effect transistor (FET)–insect antenna junction was presented for the first time by Shoning et al.⁸².

The antennae of insects are covered with sensillae, among them the olfactory sensillae, which contain within them the olfactory receptor neurons (ORN). Many of the ORNs of insect species are interesting and challenging objects of investigation, because of their very low thresholds to ambient odorous chemicals.

As an example, an antenna of the Colorado potato beetle (*Leptinotarsa decemlineata* Say) was directly connected by means of an electrolyte solution with the gate of a FET device which acted as a measuring electrode. When an air current loaded with a component of host plant odour (Z-3-hexen-1-ol) was flushed over the antenna, the induced depolarization response would modify the conductance of the FET channel between source and drain. This resulted in a corresponding change of the drain current as the sensor output signal. The gas concentration of Z-3-hexen-1-ol was determined in

the concentration range from 0.01 to 100 ppm with short response time of less than 1 s and a high reversibility of the sensor signal in ambient air (Figure I.9).

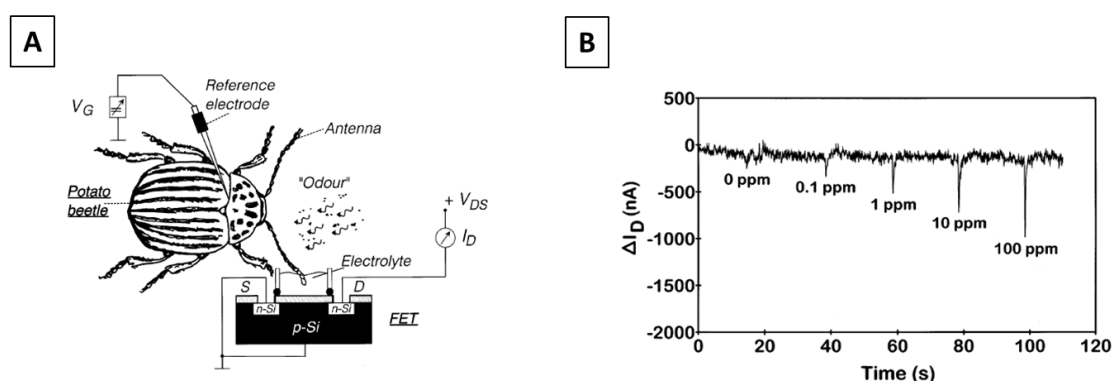


Figure I.9 (A) Schematic representation of the sensor equipment consisting of the intact chemoreceptor and the FET device. (B) Typical sensor response: variation of I_D of the isolated-antenna-BioFET by changing the Z-3-hexen-1-ol gas concentration.⁸²

Further, insect ORNs used for sensing odours were also reported and the odour response of individual ORN was recorded by microelectrodes⁸³. Action potentials of insect olfactory receptor neurons (ORN) were picked up with microelectrodes and amplified by a high-impedance amplifier connected to an oscilloscope, an audio amplifier, and an instrumentation amplifier. The amplified action potentials and odour exposure times were recorded on a DAT (digital audio tape) recorder for later analysis. This measurement of the stimulated action potential rates of the ORN of a blowfly (*Calliphora vicina*) made it possible to estimate odour concentrations to which the ORNs of the antenna were exposed. Odours of 1,4-diaminobutane (14DAB), 1-hexanol (HX), and butanoic acid (BA) were used in the experiments to stimulate various ORNs, which discharged action potentials. Spontaneous and stimulated action potential rates were analysed by means of a time-to-voltage converter connected to a signal analyser. The ORNs of the *Calliphora* antenna were sensitive and specific for 14DAB, BA and HX, but not sensitive to the other odour chemicals tested. The lowest concentrations (about 1 ppb for 14DAB, 20 ppm for BA and 8 ppm for HX) caused the action potential rates to increase from the spontaneous level to distinct levels that were very suitable for both signal analysis and concentration measurement purposes.

I.4 Bioelectronic noses based on olfactory receptors

Although the *in vivo* techniques, used to distinguish different odours, have greatly contributed to the studies of olfactory mechanism and ORN biosensors, they are merely elementary at present. The olfactory biosensors have evolved successfully for the last few years. If we compare the biosensors that work with ORNs or cells transfected with ORs with those that work with intact olfactory epithelium we notice that several advantages exist such as the level of miniaturization that the device can reach, the simplicity, controllability, non-invasive detection and dispensing with sophisticated surgical operation⁸⁴.

Because of their natural characteristics, ORs can be used to design a bioelectronic nose that mimics the olfactory system for the detection of odorants. ORs used as biological detectors are more sensitive in detecting their respective ligands than the most advanced physical approaches such as chemical noses or gas chromatography/mass spectrometry. Since ORs are G-protein-coupled-receptors, olfactory receptors need to stay in their membrane environment to be functional.

There are two types of bioelectronic noses based on olfactory receptors: the cell-based and protein-based bioelectronic noses (Figure I.10).

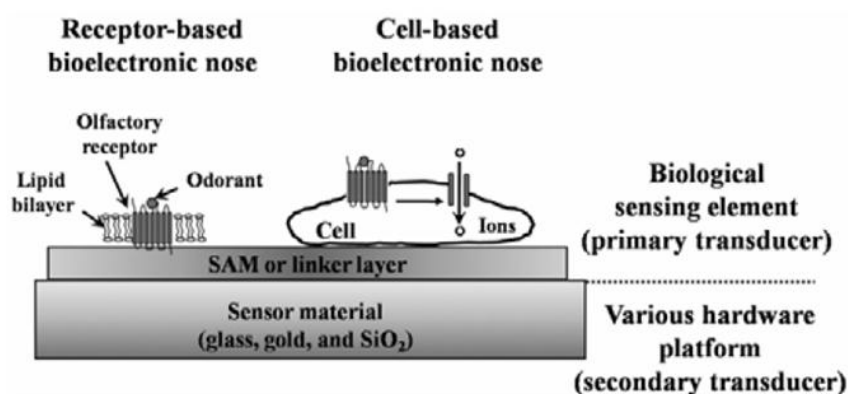


Figure I.10 Schematic diagram of a bioelectronic nose. There are two types of bioelectronic noses: cell-based and protein-based⁹.

The type of bioelectronics nose depends on whether the sensor uses living cells that express olfactory receptors or just the olfactory receptor protein itself as a sensing element.

The first type involves the use of ORs expressed in their native olfactory sensory neurons (OSNs), such as those of rats and mice, or in heterologous systems such as yeast, amphibian, insect and mammalian cell lines. These cell-based biosensors offer non-invasive, easy operating, low cost, and long-term methods to measure the intrinsic signals of the cell. But, the use of a living cell in a biosensor device has the inconvenience of requiring specific conditions to maintain their health and function. Also, further reactions occurring in a cell and other elements might interfere with the signal being monitored.

As alternative, ORs can be partially purified and used as recognition element in electronic noses. This type of bioelectronics nose has an individual secondary transducer where the ORs are anchored to it. As secondary transducer (to monitor the functional response of ORs to odorants) different sensing devices (QCM, SPR and nanotube-FET) were used. All these methods have the potential to detect the odorant binding in a more stable manner than the methods used for the cell-based biosensors (such as the cAMP assay, Ca²⁺ imaging, microelectrode and SPR). This is important because the stability of the odorant binding detection is a prerequisite for high throughput screening.

Thus, the use cell extract or purified ORs as recognition element has a range of advantages over the use of the ORN biosensor *in vivo*.

I.4.1 The parameters detected by the sensors are related to changes in intracellular molecules resulting from signal transduction

Cell-based biosensors, which use living cells or tissues as their sensitive elements, can produce signals that are related to biological sensation directly. In order to record the extracellular potentials of neurons, researchers developed microelectrode array (MEA) and light-addressable potentiometric sensor (LAPS) based on cell-based biosensors using microelectromechanical systems.

LAPS measure photocurrents generated when a site directed light source is applied⁸⁵. Changes in extracellular potential due to cell activity can generate modifications in the photocurrent signal that can be measured (Figure I.11).

Studies have found that it was possible to detect the extracellular potential of receptor cells in intact epithelium surgically obtained from the rat, by keeping neuronal membrane in almost the same environment condition as *in vivo*^{86,87}. The first example of an olfactory biosensor based on LAPS was from Liu et al. in 2006⁸⁸. They investigated the extracellular potentials of primary cultured olfactory cells under odorant stimulation. This device was sensitive to environmental odour changes.

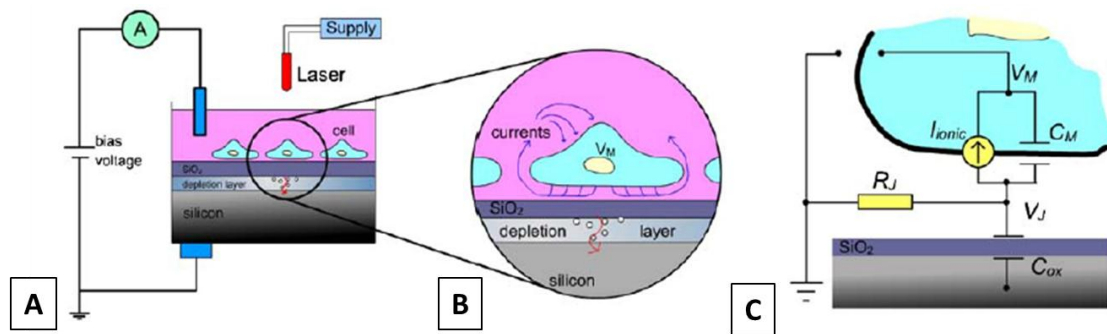


Figure I.11 *In vivo* biosensor based on the olfactory-LAPS technique⁸⁸. (A) Scheme of the cell-based biosensor using LAPS. (B) Simplified cell-semiconductor interface. (C) Schematic circuit of the cell-LAPS hybrid system.

Years later, the same group developed an olfactory neuronchip by combining the olfactory epithelium with LAPS⁸⁹ (Figure I.12). The recording of the extracellular potentials of the olfactory receptor neurons in the epithelium was analysed in response to odour stimulation. After stimulation by two different odorants, acetic acid and butanedione, olfactory epithelium activities were analysed on the basis of local field potentials and presented different firing modes. The signals fired in different odorants could be distinguished into different clusters by principal component analysis (PCA).

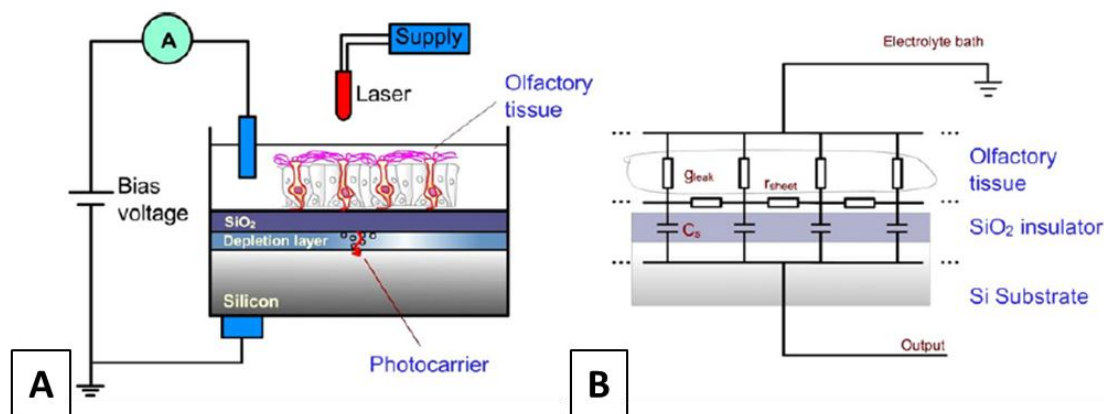


Figure I.12 (A) LAPS system with the olfactory epithelium on the sensor surface. (B) Sheet conductor model on extracellular potentials recording of the tissue layer between electron conductor and electrolyte bath on LAPS.⁸⁹

Furthermore, in 2009, Wu et al.⁹⁰ cultured rat olfactory sensory neurons (OSNs) on the surface of LAPS chip and used them as sensing elements. As well, OSNs could respond to the stimulation of odours and convert chemical signals of odour molecules into electrical signals. In that case, to validate the response capacity of OSNs cultured on the LAPS chip to odours, an odour mixture was first used to stimulate OSNs. The response of OSNs to the mixture was recorded by the LAPS measurement system (as firing spikes signal). The number of recorded firing spikes increased significantly. In order to confirm that the recorded firing spikes have originated from the olfactory signals of OSNs, MDL12330A, which is the specific inhibitor of adenylyl cyclase (see Figure I.5A, was used to inhibit the olfactory transduction pathway in OSNs and subsequently inhibits the responses of OSNs to the stimulations. The number of firing spikes decreased dramatically, which implies the responses of OSN to the mixture are inhibited by MDL12330A (Figure I.13).

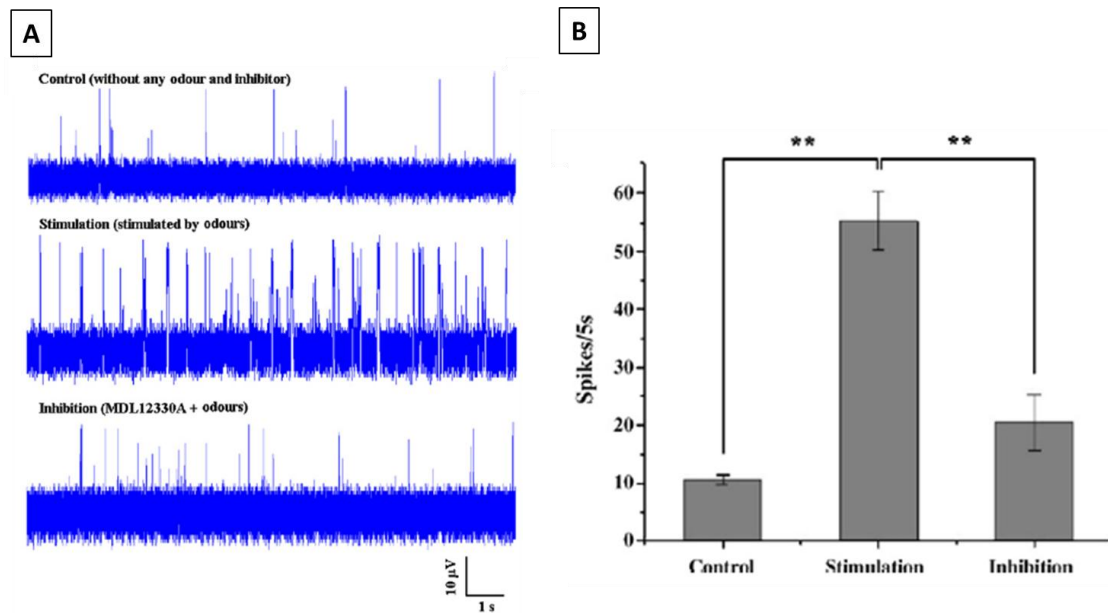


Figure I.13 (A) Typical extracellular recordings from OSNs to the odours and inhibited by MDL12330A. (B) The statistical results of the number of the recorded firing spikes from the responses presented in (A).⁹⁰

In contrast to LAPS, which is a single channel recording system, microelectrodes arrays (MEA) can record the multisite potentials simultaneously. That means that MEA can detect signals of many cells synchronously, which is convenient to comparatively analyse recorded information in parallel (Figure I.14).

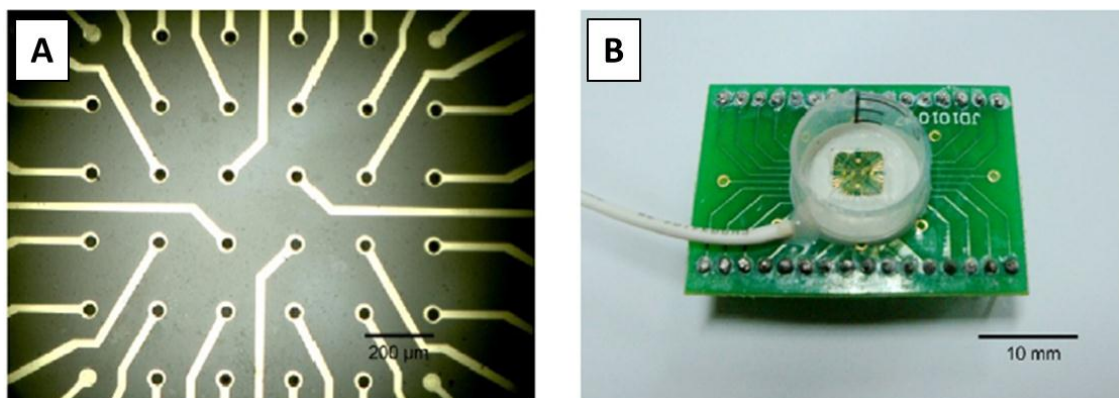


Figure I.14 Photos of a microelectrode array chip (MEA) (A) and device (B) used to record extracellular potentials in intact olfactory epithelium for the development of a bioelectronic nose.⁹¹

Due to the technical expertise required for some of techniques (i.e. electro-olfactogram, EOG and electro-antenography, EAG⁹²), in addition to the need for miniaturization, stability and portability in a biosensor device, transducer systems utilizing planar microelectrodes (microelectrodes arrays, MEA) to monitor

electrophysiological changes in the active cells are becoming more popular. Microfabricated planar electrodes can be used to measure the change in the membrane potential of the OSNs generated after the interaction between odorant and receptor (Figure I.15).

For example, in 2009 was presented for the first time how whole yeast cells expressing human receptor OR-1740 were immobilized onto an interdigitated thin film microelectrode and odour specific changes in conductance were measured⁹³. In that specific case, when yeast cells attached to the gold microelectrode surface, pre-treated with poly-lysine solution, were stimulated with the receptor ligand helional, it was possible to detect conductometric changes due to the ionic exchanges resulting from the recognition of the ligand molecules by the olfactory receptor. They justified the use of *S. cerevisiae* yeasts cells instead than mammalian cells for olfactory receptor expression since they are much cheaper and easier to cultivate.

In parallel, other works presented how a microfabricated planar electrode connected to an oscilloscope was also used to measure the electrical responses generated after the interaction of octanal and ORI7 expressed in HEK-293 cells⁹⁴. As a way of amplifying the signal for the biosensor, the HEK cells were produced coexpressing ORI7 with a cyclic nucleotide gated (CNG) channel, providing the opportunity for increased calcium influx from outside the cell upon octanal binding (specific for the ORI7), therefore resulting in a larger change in membrane potential.

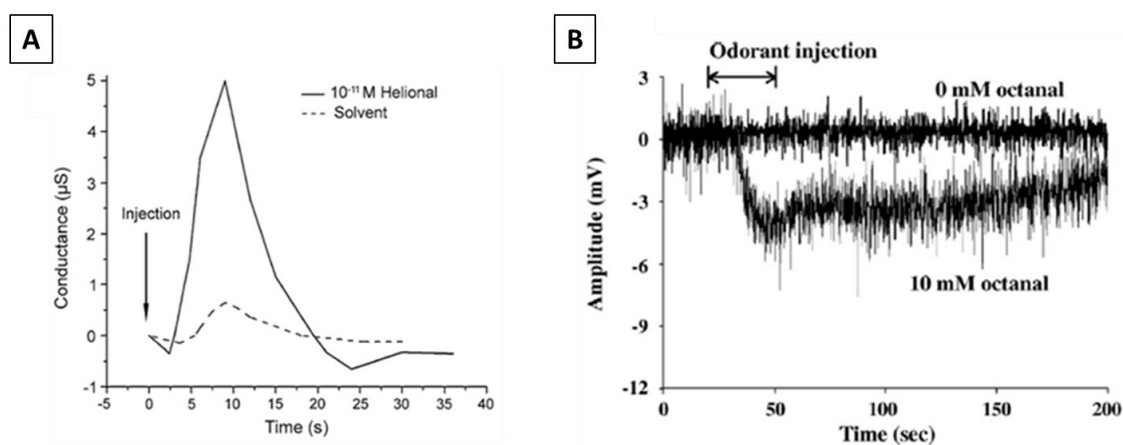


Figure I.15 (A) Kinetics of yeast OR1740 biosensor response upon 10^{-11} M helional or control addition.⁹³ (B) Field potential profile of HEK-293 cells expressing I7 receptor in a Ca^{2+} standard solution. Cells were exposed to 10 mM octanal in the Ca^{2+} standard.⁹⁴

Not only whole cells were immobilized on the surface of MEAs to measure the specific odour changes. In an experiment conducted by Liu et al.⁹¹ 36-channel MEAs were fabricated on a glass substrate and olfactory epithelium was stripped from rats and fixed on the surface of MEAs. Electrophysiological activities of olfactory receptor neurons in intact epithelium were measured through the multi-channel recording system. The extracellular potentials of cell networks could be effectively analysed by correlation analysis between different channels. After being stimulated by odorants, such as acetic acid and butanedione, the olfactory cells generate different firing modes. These firing characteristics can be derived by time-domain and frequency-domain analysis, and they were different from spontaneous potentials.

In a different work rat ORNs were cultivated on the surface of a 60-channel MEA device and in order to study the odour-response characteristics of ORNs, two types of odorants at different concentrations were quantitatively pumped into the neurochip by a customized gas intake system⁸⁴. The odour-response features of ORNs such as firing amplitude, firing threshold, firing rate as well as firing channels were analysed quantitatively and qualitatively in terms of ORN spike trains. After introducing the classification algorithm based on the spike threshold, the odour-response maps from the multitude sites could be used to identify DL-limonene and isoamyle acetate odorants.

I.4.2 The parameters detected are not the electrophysiological potentials of the cells

Odorant detection can be measured recording the interaction between the OR and the odorant molecules as a change in weight, light, sound, heat, chemical composition or electrochemical signal. These measurements can be made using a variety of techniques including surface plasmon resonance (SPR), quartz crystal microbalance (QCM) electrochemical impedance spectroscopy (EIS) and field-effect transistor (FET).

1.4.2.1 Detection by Quartz Crystal Microbalance (QCM)

QCM is a bulk acoustic wave sensor which by applying an alternating electric field induces a resonance in a quartz crystal. The crystal oscillates at a tuned frequency, which changes in accordance with the mass on the crystal. When a material is adsorbed on the crystal surface, the frequency of oscillation changes and this change can be measured. QCM can detect the interaction between various odorants and chemicals coated on the crystal surface (Figure I.16A).

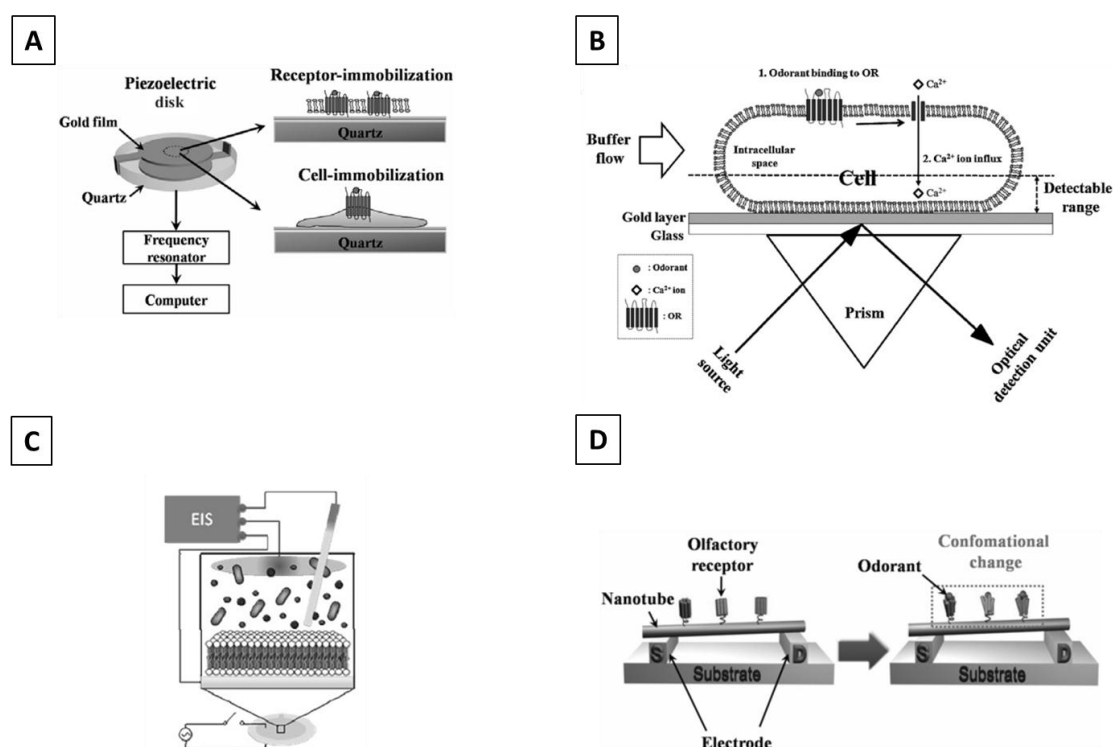


Figure I.16 *In vitro* biosensors not based on the electrophysiological potentials of the cell. (A) QCM-based bioelectronic nose. (B) SPR-based bioelectronic nose. (C) EIS-based bioelectronic nose. (D) Possible mechanism for the specific detection of odorants using nanotube-FET sensor. *Picture adapted from ref. 9, 95.*

The first bioelectronic nose was based on the direct immobilization of olfactory cilia onto a sensor solid surface. In 1999 Wu et al.⁹⁶ immobilized a crude bullfrog cilia preparation onto a piezoelectric (PZ) electrode which served as a signal transducer. Using this biosensor he was able to detect trace levels of various odorants with concentrations fully correlated with olfactory threshold values of human noses. The results indicate rapid (about 400s), reversible and long-term (up to 3 min) stable response to different volatile compounds. They also fractionated olfactory receptors from the cilia preparation and coated them separately onto the PZ crystal surface. A

quartz crystal microbalance was used for detecting the binding of odorant molecules to the ORs.

Later on, an array made of six sensors consisting of five different cilia fractions was able to rapidly and stably detect responses to different volatile compounds. A study was conducted that demonstrated the high specificity and sensitivity of QCM to detect odorants⁹⁷. In this case ORI7 was expressed in HEK-293 cells which were then adsorbed on the gold surface of QCM. The ORs were exposed to various odorant vapours but only octanal, the specific odorant of ORI7, gave a high signal. This signal increased with the concentration of the odorant. Furthermore, Sung et al.⁹⁸ coated QCM crystal surface with crude membrane extracts of *E.coli* expressing the receptor protein ODR-10 and examined its interactions with various odorant molecules. They showed linear dose-dependent responses upon stimulation of the membrane extracts with the natural receptor ligand diacetyl. This work demonstrated how membrane extracts, containing ORs, can retain full activity and can discriminate its specific odorant.

I.4.2.2 Detection by Surface Plasmon Resonance (SPR)

SPR spectroscopy is a technique based on the measurement of small changes of the resonance angle (θ_{SPR}) between incident light and the plasmon present on a thin metal layer. This value depends on the refractive index (RI) at the solid-liquid interface. Hence the SPR angle shifts are dependent upon the amount of material adsorbed on the gold surface, generating the corresponding analytical signal (Figure I.16B). SPR technique has been used to characterize biomolecular interactions without labelling. SPR is a label-free and high sensitive optical sensing method. However, despite its advantages, SPR selectivity is rather low and it does not provide a cheap and portable transducer solution.

The binding between ORs and odorants has been examined by SPR by many research groups. In 2006, Vidic and co-workers⁹⁹ co-expressed ORI7 and OR1740 with $G_{\alpha olf}$ subunit in *S. cerevisiae* yeast cells producing nanometre size vesicles, called nanovesicles, and immobilized them on a Biacore sensor chips L1. Nanovesicles were grafted thanks to the presence of lipophilic alkyl chains in the dextran polymer that covers the L1 chip. The binding of OR-odorants, in that specific case, was followed by

SPR by measuring the activation of the trimeric G protein and the consequent mobilization of the G_{olf} subunit in presence of GTP. They detected a significant SPR signal when the specific odorant together with GTP was injected onto the nanovesicles. On the other hand, when the odorant and GTP were alone and a non-specific odorant together with GTP were used, no SPR signal was observed as a consequence of a missed activation of the ORs. Moreover, the sensitivity of the experiment was enhanced by replacing the GTP with its non-hydrolysable analogue, $GTP\gamma S$. With this study they showed that ORs can be expressed in yeast cells and retain their full activity in isolated nanovesicles immobilized on sensor chips. The specific odorant was discriminated among odorants with a similar structure and different concentrations of the odorant could be measured.

The SPR technique was also used in the measurement of odorant molecules in a cell-based biosensing technique⁹⁵. ORI7 was fused with a rho-tag import sequence at the N-terminus of ORI7 and expressed on the surface of human embryonic kidney (HEK)-293 cells. The cells were then immobilized on a SPR sensor chip treated previously with poly-D-lysine. Octanal, the specific ORI7 odorant, was then injected. The SPR signal was linearly dependent on the amount of injected odorant. Since the distance between the OR expressed on the cell surface and the gold surface is longer than the SPR detectable range, the response cannot be associated to the simple binding between the odorant and the OR. The binding event must trigger intracellular signal transduction, which causes changes in intracellular components. These intracellular changes may generate a change in SPR signal. In fact, only when the odorant was used together with a Ca^{2+} solution the SPR response was observed. This means that the binding of odorant with OR induces Ca^{2+} influx through intrinsic transmembrane ion channels and this influx of Ca^{2+} ions into cells generated the SPR signal change.

I.4.2.3 Detection by Electrochemical Impedance Spectroscopy (EIS)

Electrochemical impedance spectroscopy is a technique that measures the electrical resistance of a system and changes which occur in this resistance due to changes at a transducer surface¹⁰⁰ (Figure I.16C).

In the framework of the SPOT-NOSED European Project (Single PrOTEIn Nanobiosensor Grid Array, 2003-2006), where our group was involved, the EIS technique was used for the first time to detect the modifications of the electrical properties of the bilayer including the receptor in its lipidic environment due to the odorant recognition. Specifically, in a study by Hou et al.¹⁰¹ ORI7 were expressed in yeast and its membrane fractions were immobilized on a gold electrode. The immobilization technique made use of a mixed self-assembled monolayer and of a biotinylated ORI7-specific antibody. The odorant detection was electronically measured in a quantitative manner by electrochemical impedance spectroscopy measurements on samples (octanal and heptanal) and controls (helional). The responses for the specific detection of odorants were higher than those obtained in the negative control tests, giving a higher variation in impedance. The corresponding biosensor was stable during 7 days. This study demonstrated that the electrical properties of the receptor in its lipidic environment can be modified by the process of odorant recognition and these modifications can be detected by EIS measurements.

Another example of electrochemical study of ORs stimulation by odorants, is represented by a study from Benilova et al.¹⁰² also in the framework of the SPOT-NOSED project. OR1740 was expressed in yeast and the membrane fractions were anchored to a gold substrate modified with thiol-based multilayer. The ORs were specifically immobilized via a biotinylated antibody specific for the c-myc tag carried by the ORs. Under injections of helional (specific odorant of OR1740) activation of the OR was electrochemically revealed. Applying GTP- γ -S at 4°C as a specific enhancer of biochemical signal, it became possible to detect 10^{-11} M helional. The low temperature improved the lifetime of the biosensor by 2 days of continuous work. The selectivity was also tested by using the non-specific odorant heptanal which did not give any shift of the impedance spectrum.

1.4.2.4 Detection by Field-Effect Transistor (FET)

FETs have the ability of measuring ion concentrations and cell potential changes. Single walled nanotubes represent attractive components for use in FET devices due to their size and electrical properties. They provide great potential to

produce low-cost, large-area, lightweight and flexible devices. Carbon nanotubes can be used to immobilize ORs onto a device (Figure I.16D).

When the odorant binds the OR, a charge transfer occurs in the OR and the response is monitored by the change in the current of nanotubes. The first example of FET-type bioelectronics nose based on human olfactory receptors and nanotubes (hOR-conjugated conducting polymer) is represented by a study from Yoon et al.¹⁰³ in which they express hOR2AG1 in *E. coli* with a glutathione-S-transferase (GST) tag at its N-terminus. The *E. coli* cells were sonicated to obtain membrane fractions. Carboxylated polypyrrole nanotubes (CPNT) were synthesized and immobilized on an interdigitated microelectrode array (IDA) of gold microelectrodes generating a FET device. The IDA substrate was treated with an aminosilane and the carboxy functional groups of the CPNTs were then coupled with the surface amino group of the IDA. hOR2AG1 were conjugated to the CPNTs through the covalent interaction between the terminal amine groups on cysteine residues of OR and the carboxy groups of CPNTs. hOR2AG1 specifically responds to amyl butyrate, a common reagent for fruit flavour. The FET showed a concentration-dependent increase in current change (ISD) when exposed to amyl butyrate.

It is believed that the current increase is due to a change in the charge-transport behaviour of the CPNTs. Specifically, the cysteine residues of hORs adopt an uncharged (RSH) state or negative charged (RS⁻) state, associated with the acid-to-base transition of the sulfhydryl group¹⁰⁴. The specific binding of odorants initiates the structural rearrangement of hORs finally leading to an increase in negatively charged base state (RS⁻). The increased negative charge density at the OR-CPNT interface can induce the increase in the ISD. When other odorants different from amyl butyrate were used, no significant changes in ISD were observed showing the specificity of this FET-type bioelectronic nose. The detection limit of the FET was found to be 10 fM, which is two orders of magnitude lower than those of other bioelectronics noses⁹⁸. Single-walled carbon nanotubes (swCNT) were also used to develop a FET-olfactory sensor system¹⁰⁵. hOR2AG1 was expressed in *E. coli* and coated on swCNT-FET and the deformation of the hOR2AG1 protein upon binding specific odorant molecules was detected by the swCNT-FET. The detection limit was 100fM and the high selectivity was tested by molecules with a chemical structure very similar to that of amyl butyrate.

I.5 Conclusions

The use of smell in different fields has been rediscovered due to major advances in odour sensing technology and artificial intelligence. However, current electronic noses, based on electronic sensors, have significant limitations concerning sensitivity, reliability and selectivity, amongst others. These limitations are the basis of recurrent problems of this technology to reach essential applications in multiple areas. Mass spectroscopy analysis and the use of dogs to distinguish between samples of patients and samples control confirm that this approach can be useful for medical diagnostic purposes if the electronic nose development allows distinguishing the odorant patterns with high accuracy and short measurement time. New bioelectronic noses based on olfactory receptors in order to mimic the animal nose could be an interesting approach combining nano, bio and information technologies.

I.6 References

- (1) Wise, P.M., Olsson, M. J., Cain, W. S. *Chem. Senses*, **2000**, *25*, 429-443.
- (2) Ortega, A., Marco, S., Sundic, T. et al. *Sensor actuat B-Chem.*, **2000**, *69*, 302–307.
- (3) Persaud, K., Dodd, G. *Nature*, **1982**, *299*, 352–355.
- (4) Turner, A.P.F., Magan, N. *Nature Reviews/Microbiology*, **2004**, *2*, 161–166.
- (5) Gardner, J.W., Bartlett, P.N. *Electronic Noses: Principles and Application*, Oxford Univ Press, UK. **1999**.
- (6) Pearce, T.C., Schiffman, S.S., Nagle, H.T., Gardner, J.W. *Handbook of Machine Olfaction: Electronic Nose Technology*. Wiley. (eds.). **2002**.
- (7) Wilson, A.D., Baietto, M. *Sensors*, **2011**, *11*, *1*: 1105–1176.
- (8) Wilson, A.D., Baietto, M. *Sensors*, **2009**, *9*, 5099–5148.
- (9) Lee, S.H., Park, T.H. *Biotechnol. and Bioprocess Engin.*, **2010**. *15*, 22–29.
- (10) Turner, A.P.F. *Science*, **2000**, *290*, 1315–1317.
- (11) Pavlou, A. et al. *Biosens. Bioelectron.*, **2000**, *15*, 333–342.
- (12) Pavlou, A. et al. *Biosens. Bioelectron.*, **2002**, *17*, 893–899.
- (13) Di Natale, C. et al. *Physiol Measurement*, **1999**, *20*, 377–384.
- (14) Di Natale, C. et al. *Biosens. Bioelectron.* **2003**, *18*, 1209–1218.
- (15) Peng, G., Hakim, M., Broza, Y.Y. et al. *Br J Cancer*, **2010**, *103*, 542–551.
- (16) Spänzel, P. et al. *Rapid Commun Mass Spectrom*, **1999**, *13*, 1354.
- (17) Filipiak, W., Sponring, A., Filipiak, A. et al. *Cancer Epidemiol Biomarkers Prev*, **2010**, *19*, 182–195.
- (18) Peris, M., Escuder-Gilabert, L. *Anal Chim Acta*, **2009**, *638*, 1–15.
- (19) Dutta, R., Hines, E.L., Gardner, J.W., Udrea, D.D., Boilot, P. *Meas. Sci. Technol.* **2003**, *14*, 190-198.
- (20) Reid, L. M., O'Donnell, C. P., Downey, G. *Trends Food Sci Tech* **2006**, *17*, 344-353.
- (21) Magan, N., Evans. P. *J Stored Prod Res* **2000**, *36*, 319-340.
- (22) Falasconi, M., Concina, I., Gobbi, E., Sberveglieri, V., Pulvirenti, A., Sberveglieri, G. *Int. J. Electrochem.* **2012**, doi: 10.1155/2012/715763.
- (23) Ciosek, P., Brzozka, Z., Wroblewski, W. *Sens. Actuators B*, **2004**, *103*, 76–83.
- (24) Lozano, J., Santos, J. P., Aleixandre, M., Sayago, I., Gutierrez, J., Horrillo, M. C. *IEEE Sensors J.*, **2006**, *6*, 173–178.

- (25) Aleixandre, M., Lozano, J., Guitierrez, J., Sayago, I., Fernandez, M.J., Horrillo, M.C. *Sens. Actuators*, **2008**, *131*, 71–76.
- (26) Pardo, M., Niederjaufnes, G., Benussi, G., Comini, E., Faglia, G., Sberveglieri, G., Holmberg, M., Lundstorm, I. *Sens. Actuators B*, **2000**, *69*, 397–403.
- (27) Brudzewska, K., Osowiki, S., Markiewicz, T. *Sens. Actuators B*, **2004**, *98*, 291–298.
- (28) Zohora, S.E., Khan, A.M., Srivastava, A.K., Hundewale, N. *IJSCE*, **2013**, *3*, 5, 199-205.
- (29) Patil, S.J., Duragkar, N., Rao, V.R. *Sensor Actuat B-Chem* **2014**, *192*, 444-451.
- (30) Kim, H., Konnanath, B., Sattigeri, P., Wang, J., Mulchandani, A., Myung, N., Deshusses, M.A., Spanias, A., Bakkaloglu, B. *Analog Integr Circ Sig Process* **2012**, *70*, 15–32.
- (31) Hwang, S., Kwon, H., Chhajed, S., Byon, J. W., Baik, J. M., Im, J., Oh, S. H., Jang, H. W., Yoon, S. J., Kim, S.J. *Analyst*, **2013**, *138*, 443-450.
- (32) Angioy, A.M. et al. *Chem Senses*, **2003**, *284*, 279.
- (33) Davide, F., Holmberg, M., Lindström, I. *Communications Through Virtual Technology*. p. 194. In: G. Riva and F. Davide. (eds). **2001**. Identity Community and Technology in the Internet Age. IOS Press: Amsterdam, The Netherlands.
- (34) Malnic, B. et al. *Cell*, **1999**, *965*, 713.
- (35) Williams, H., Pembroke, A. *Lancet*, **1989**, 1734.
- (36) Church, J., Williams, H. *Lancet*, **2001**, *358*, 930.
- (37) Willis, C.M., Church, S.M., Guest, C.M. et al. *BMJ*, **2004**, *329*, 712.
- (38) Elliker, K.R., Sommerville, B.A., Broom, D.M. *Paper presented at the Chemical Signals in Vertebrates Workshop XII*, **2004**, Withersdane Hall, Wye, England.
- (39) Cornu, J.N., Cancel-Tassin, G. et al. *Eur Urol*, **2011**, *59*, 2, 197-201.
- (40) McCulloch, M., Jezierski, T., Broffman et al. *Integr Cancer Ther*, **2006**, *5*, 30–39.
- (41) Horvath, et al. *Integr. Cancer Ther*, **2008**, *7*, 76–80.
- (42) Sonoda, H., Kohnoe, V., Yamazato, T. et al. *Gut*, **2011**, *60*, 814-819.
- (43) Williams, M., Johnston, J. M., Cicoria, M., Paletz, E., Waggoner, P. Edge, C., Hallowell, S. F. *Canine detection odor signatures for explosives*. Presented at the Association for Behavior Analysis, Chicago, May, **1999**.
- (44) Zulch, H., Wilkinson, A., Croxton, R. *Improving dogs' ability to detect explosives*. University of Lincoln. (**2013**, July 30). ScienceDaily. Retrieved July 21, 2014 from www.sciencedaily.com/releases/2013/07/130730091148.htm.

-
- (45) Buck, L., Axel, R. *Cell*, **1991**, *65*, 175–187.
- (46) Su, C.Y. et al. *Cell*, **2009**, *139*, 45–59.
- (47) Firestein, S. *Nature*, **2001**, *413*, 211–217.
- (48) Chesler, A., Firestein, S. *Nature*, **2008**, *452*, 944.
- (49) Sato, K. et al. *Nature*, **2008**, *452*, 1002–1006.
- (50) Wicher, D. et al. *Nature*, **2008**, *452*, 1007–1011.
- (51) Liberles, S.D., Buck, L. *Nature*, **2006**, *442*, 645–650.
- (52) Dulac, C., Axel, R. *Cell*, **1995**, *83*, 195–206.
- (53) Matsunami, H., Buck, A. *Cell*, **1997**, *90*, 775–784.
- (54) Riviere, S. et al. *Nature*, **2009**, *459*, 574–577.
- (55) Kaupp, U.B. *Nature*, **2010**, *11*, 188–200.
- (56) Breer, H. *Anal Bioanal Chem*, **2003**, *377*, 427–433.
- (57) Mombaerts, P., Nei, M. *Nature Rev Neurosci*, **2004**, *5*, 263–278.
- (58) Touhara, K., Vosshall, L.B. *Annu Rev Physiol*, **2009**, *71*, 307–332.
- (59) Glatz, R., Bailey-Hill, K. *Progress in Neurobiology*, **2011**, *93*, 270–296.
- (60) Spehr, M., Munger, D. *Journal of Neurochemistry*, **2009**, *109*, 1570–1583.
- (61) Zhuang, H., Matsunami, H. *Nature Protocols*, **2008**, *3*, 9, 1402–1413.
- (62) Zarzo, M. *Biological Reviews*, **2007**, *82*, 455–479.
- (63) DeMaria, S., Ngai, J. *The Journal of Cell Biology*, **2010**, *191*, 3, 443–452.
- (64) Song, H.G. et al. *Sensors*, **2008**, *8*, 6303–6320.
- (65) Hengl, T. et al. *PNAS*, **2010**, *107*, 13, 6052–6057.
- (66) Ko, H.J., Park, T.H. *Biosens Bioelectron*, **2008**, *23*, 1017–1023.
- (67) Vidic, J. et al. *Lab Chip*, **2008**, *8*, 5, 678–688.
- (68) Ko, H.J. et al. *Bioprocess Biosyst Eng*, **2010**, *33*, 55–62.
- (69) Pelosi, P. et al. *Chem Senses*, **2005**, *30*, 291–292.
- (70) Tegoni, M. et al. *Biochimica et Biophysica Acta*, **2000**, *1482*, 229–240.
- (71) Pelosi, P. *Critical Reviews in Biochemistry and Molecular Biology*, **1994**, *29*, 3, 199–228.
- (72) Zhou, J.J. *Chapter ten: Odorant-Binding Proteins in insects. Vitamins and Hormones*, **2010**, *83*, 241–272.
- (73) Vosshall, L.B., Stensmyr, M.C. *Neuron*, **2005**, *45*, 179–187.
- (74) Vogt, R., Riddiford, L. *Nature*, **1981**, *293*, 161–163.
- (75) Wang, G.R. et al. *Insect Biochem Mol Biol*, **2003**, *33*, 115–124.
- (76) Wyatt, T.D. *J Comp Physiol A*, **2010**, *196*, 685–700.

- (77) Dulac, C., Wagner, S. *Annu Rev Genet*, **2006**, 40, 449-467.
- (78) Sakmann, B., Neher, E. *Annu Rev Physiol*, **1984**, 46, 455-472.
- (79) Baker, T.C., Haynes, K.F. *Physiol Entomol*, **1989**, 14, 1-12.
- (80) Sauer, A.E., Karg, G., Koch, U.T., De Kramer, J.J., Milli, R. *Chem Sens*, **1992**, 17, 543-553.
- (81) Schütz, S., Weißbecker, B., Hummel, H.E. *Biosens Bioelectron*, **1996**, 11, 427-433.
- (82) Schöning, M.J., Schütz, S., Schroth, P., Weißbecker, B., Steffen, A., Kordo, P., Hummel, H.E., Lüth, H. *Sens. Actuators B: Chem*, **1998**, 5, 47, 235.
- (83) Huotari, M.J. *Sens. Actuators B: Chem*, **2000**, 71, 212.
- (84) Ling, S. et al. *Biosensors and Bioelectronics*, **2010**, 26, 1124-1128.
- (85) Owicki, J.C., Bousse, L.J., Hafeman, D.G., Kirk, G.L., Olson, J.D., Wada, H.G., Parce, J.W. *Ann Rev Biophys Biomol Struct*, **1994**, 23, 87-113.
- (86) Ma, M., Chen, W.R., Shepherd, G.M. *J Neurosci Methods*, **1999**, 92, 31-40.
- (87) Kleene, S.J. *Chem Senses*, **2008**, 3, 839-859.
- (88) Liu, Q., Cai, H., Xu, Y., Li, Y., Li, R., Wang, P. *Biosens Bioelectron*, **2006**, 22, 318.
- (89) Liu, Q., Ye, W., Hu, N., Cai, H., Yu, H., Wang, P. *Biosens Bioelectron*, **2010**, 26, 1672-1678.
- (90) Wu, C., Chen, P., Yu, H., Liu, Q., Zong, X., Cai, H., Wang, P. *Biosens Bioelectron*, **2009**, 24, 1498.
- (91) Liu, Q., Ye, W., Xiao, L., Du, L., Hu, N., Wang, P. *Biosens Bioelectron*, **2010**, 25, 2212.
- (92) Ziesmann, J., Valterova, I., Haberkorn, K., De Brito Sanchez, M.G., Kaissling, L-E. *Chem Senses*, **2000**, 25, 31-37.
- (93) Marrakchi, M., Vidic, J., Jaffrezic-Renault, N., Martelet, C., Pajot-Augy, E. *Eur Biophys J*, **2007**, 36, 1015.
- (94) Lee, S.H., Jun, S.B., Ko, H.J., Kim, S.J., Park, T.H. *Biosens Bioelectron*, **2009**, 24, 2659.
- (95) Lee, S.H., Ko, H.J., Park, T.H. *Biosens Bioelectron*, **2009**, 25, 55.
- (96) Wu, T. *Biosens Bioelectron*, **1999**, 1, 14, 9-18.
- (97) Ko, H.J., Park, T.H. *Biosens Bioelectron*, **2005**, 20, 1327.
- (98) Sung, J.H., Ko, H.J., Park, T.H. *Biosens Bioelectron*, **2006**, 21, 1981-1986.
- (99) Vidic, J. et al. *Lab on a Chip*, **2006**, 6, 1026-1032.

- (100) Lisdat, F., Schäfer, D. *Anal Bioanal Chem*, **2008**, *391*, 1555–1567.
- (101) Hou, Y. et al. *Biosens Bioelectron*, **2007**, *22*, 1550.
- (102) Benilova, I., Vidic, V., Pajot-Augy, J., Soldatkin, E., Martelet, A.P., Jaffrezic-Rneaults, C., Mater, N. *Sci Eng C*, **2008**, *28*, 633.
- (103) Yoon, H. et al. *Angewante Chemie Int*, **2009**, *48*, 2755.
- (104) Neuhaus, E.M., Mashukova, A., Zhang, W., Barbour, J., Hatt, H. *Chem Senses*, **2006**, *31*, 445–452.
- (105) Kin, T.H. et al. *Adv Mater*, **2009**, *21*, 91.

Objectives

This thesis, entitled “**Study of natural nanovesicles carrying olfactory receptors for the development of biosensing platforms**” aims to contribute into the G-protein coupled receptors-based biosensors research field. For this purpose, this research work deals with a systematic and controlled study based on a previous proof-of-concept bioelectronic sensor developed in the framework of the SPOT-NOSED European project where our group was involved. We have focused the main objective of this thesis to understand and control all the essential process and parameters in order to develop an olfactory receptor (OR) well-characterized platform making possible the ORs immobilization onto a specific surface. The achievement of this objective constitutes an important step in the practical realization of biosensor devices based on natural nanovesicles integrating G-protein coupled membrane receptors.

This general objective will be approached through the following specific scientific and technological objectives:

1. Controlled production of natural nanovesicles carrying olfactory receptors heterologously expressed onto the membrane.
2. Characterization of the olfactory receptor-nanovesicles in solution (i) their size, (ii) morphology, (iii) electrical charge, (iv) concentration and (v) determination of the number of olfactory receptors expressed per nanovesicle.
3. Study and quantification of nanovesicles deposition onto different biosensor supports, (i) glass and (ii) functionalized gold surfaces.
4. Study the capability of the olfactory receptor embedded in natural nanovesicles for capturing specific odorant molecules.

O.1 Thesis structure

This thesis is structured in four experimental chapters, which are described in what follows.

In **Chapter 1**, we present that various olfactory receptors are heterologously expressed onto membrane nanovesicles from *Saccharomyces Cerevisiae* yeast cells. Around 100 nm-diameter vesicles in solution are controlled-produced and extensively characterized: their morphology by cryo-Transmission Electron Microscopy (cryo-EM) and the nanovesicles density and size distribution in solution by Nanoparticle Tracking analysis (NTA).

In **Chapter 2**, the ORs expression level in the individual nanovesicles studied in Chapter 1 is determinate since it is an outstanding challenge in the road map to realize practical biomolecular devices based on GPCRs. A novel immunochemical strategy for quantification of transmembrane proteins embedded on natural nanovesicles was developed. The immunochemical method developed is an innovative approach to determine the expression of membrane protein receptors in their natural environment without the need to isolate and purify them. In addition, the proposed approach uses monoclonal antibodies addressed against the c-myc tag on a microplate-based ELISA format. Due to the lack of highly sensitive commercial antibodies, we had the obligation to produce our own monoclonal antibody. A very sensitive and specific monoclonal anti-c-myc antibody was produced achieving the assay detectability in the picomolar range. *This work it was carried out partially at the Laboratory of “The Nanobiotechnology for Diagnostics Group, Nb4D”, iQAC-CSIC (Barcelona, Spain).*

In **Chapter 3**, the reproducible and accurate deposition of non-ruptured nanovesicles carrying the olfactory receptors on glass and functionalized gold substrates was studied at different nanovesicles concentrations, time scales and solution ion strengths. As well, different surface chemistry modification (i.e. acid, amino, alcohol modified surfaces) of gold substrates was presented as biosensor surface. We present that the evolution of the nanovesicles surface coverage on glass is found to follow a diffusive law. We obtained surface coverages by nanovesicles larger than 20-25% on the glass substrate and around 10-15% on functionalized gold substrate. As well, we

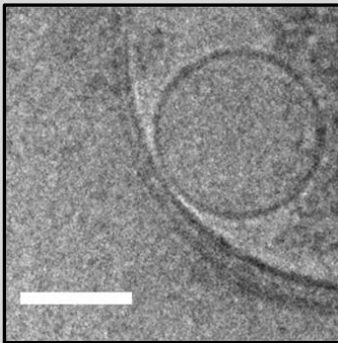
presented a proof-of-concept of a multiple nanovesicle arrays on glass substrate, substrate used as biosensor support.

In **Chapter 4**, we verify systematically the capability of the olfactory receptor embedded in natural nanovesicles for capturing specific odorant molecules. This issue has been addressed by SPR technique. The results obtained definitely open the perspective to use the surface plasmon resonance technique for the detection of small odorants at concentration in the micromolar range.

All the four chapters are divided as follows: an introductory section that will present the state-of-the art of the research subject, the experimental section used to obtain the results presented, the results obtained and discussed and finally the main contributions of each chapter are summarized in the conclusions section. The thesis ends with a section of general conclusions including all the achievements obtained.

Finally, an **Epilogue** presenting an overview of the main results achieved in the BOND European project and two **Appendix** sections describing the HPLC characterization of the c-myc peptide synthesized and the c-myc/anti-c-myc interaction characterization can be found.

Chapter 1. Production and characterization of natural nanovesicles containing G-protein coupled receptors.



*Natural vesicles produced from genetically engineered cells with tailored membrane receptor composition are promising building blocks for sensing biodevices. This is particularly true for the case of G-protein coupled receptors (GPCRs) present in many sensing processes in cells, whose functionality crucially depends on their lipid environment. However, the controlled production of natural vesicles containing GPCRs, their characterization and their reproducible deposition on surfaces are among the outstanding challenges in the road map to realize practical biomolecular devices based on GPCRs. In this **Chapter** we present the production and characterization of membrane nanovesicles from *Saccharomyces Cerevisiae* containing heterologously expressed olfactory receptors - a member of the family of GPCRs.*

1.1 Background

G-protein-coupled receptors (GPCRs), largely expressed in the human body because they are encoded by about 5% of human genes, are implicated in a wide range of disease pathways¹⁻³, due to their implication in most of the sensory functions in cells. They are as well one of the largest protein families towards which drug target investigations are focused and actually around 30% of the present drugs on the market directly target GPCR⁴. Among the GPCRs, olfactory receptors (OR), an important subfamily of the superfamily of G-Protein coupled receptors (GPCRs) (Figure 1.1), have gained a progressively increasing interest for their high potentiality in biomedical diagnosis.

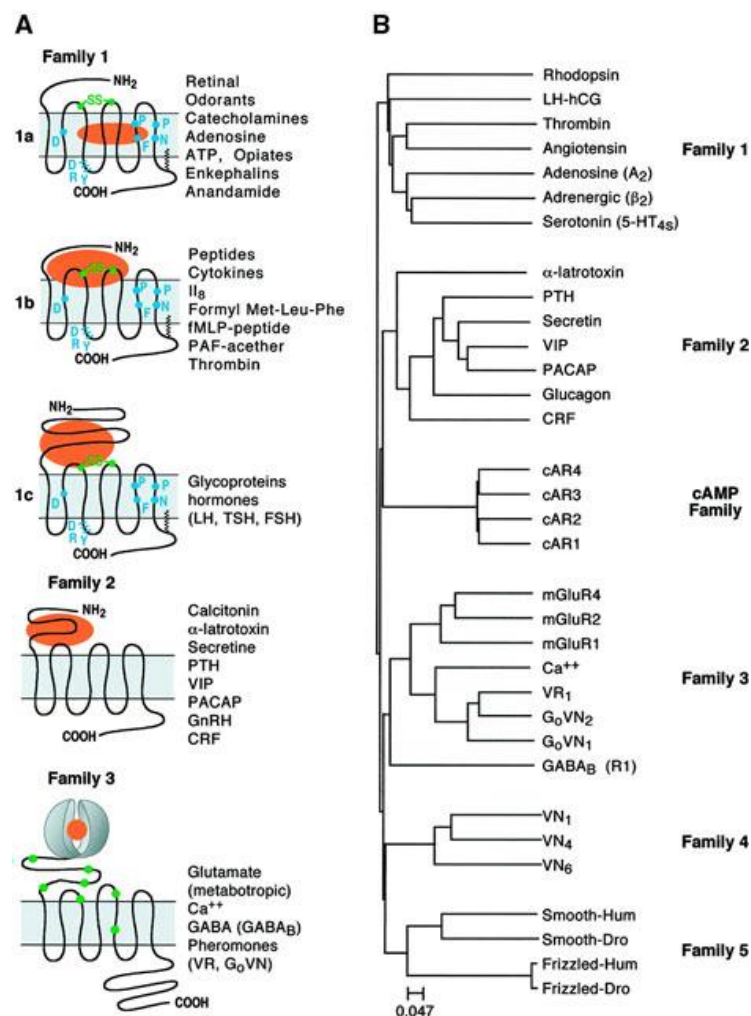


Figure 1.1 GPCRs classification (A) Three families (1, 2 and 3) can be recognized when comparing their amino-acid sequences. Receptors from different families share no sequence similarity, suggesting that we

are in the presence of a remarkable example of molecular convergence. *Family 1* contains most GPCRs including receptors for odorants. *Group 1a* contains GPCRs for small ligands including rhodopsin and β -adrenergic receptors. The binding site is localized within the seven transmembrane segments (TMs). *Group 1b* contains receptors for peptides whose binding site includes the N-terminal, the extracellular loops and the superior parts of TMs. *Group 1c* contains GPCRs for glycoprotein hormones. It is characterized by a large extracellular domain and a binding site which is mostly extracellular but at least with contact with extracellular loops e1 and e3. *Family 2* GPCRs have a similar morphology to group 1c GPCRs, but they do not share any sequence homology. Their ligands include high molecular weight hormones such as glucagon, secretine, VIP-PACAP and the Black widow spider toxin, α -latrotoxin. *Family 3* contains mGluRs and the Ca^{2+} sensing receptors. In 1997, however, GABA-B receptors and a group of putative pheromone receptors coupled to the G protein G_o (termed VRs and G_o -VN) became new members of this family. **(B)** *Family 4* comprises pheromone receptors (VNs) associated with G_i . *Family 5* includes the 'frizzled' and the 'smoothened' (Smo) receptors involved in embryonic development and in particular in cell polarity and segmentation. Finally, the *cAMP receptors* (cAR) have only been found in *D.discoideum* but its possible expression in vertebrate has not yet been reported⁵.

Based on the fact that animal noses are able to discriminate with high selectivity combinations of odours at very low concentrations^{6,7}, mammalian OR-based sensing devices and bioelectronic noses have been demonstrated to be sensitive to a variety of odorant molecules. These devices may find applications for the early detection of human cancer^{8,9,10}. Basically, the biologically active part of these devices is made up of olfactory receptors variously immobilized¹¹ on functionalized surfaces. As olfactory receptors are integral membrane proteins, their integration into a lipid envelope is considered necessary to guarantee their tertiary structure and functionality to be retained¹² (Figure 1.2).

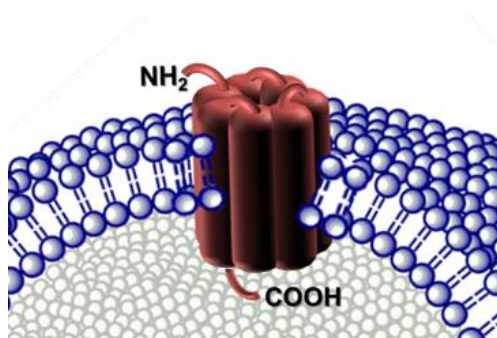


Figure 1.2 Scheme of an olfactory receptor (7 TMs protein) integrated into a lipid membrane.

In particular, the isolation of natural vesicles from a cell source where mammalian olfactory receptors have been heterologously expressed provides an as native as possible environment for the receptor proteins and has already proven to be successful in the design of the active part of the device¹⁰.

The expression of the olfactory receptors in heterologous systems such as *E. coli*, *S. cerevisiae* or mammalian cells has overcome thanks to the recombinant fusion protein technology where the protein is generated from recombinant DNA by biomolecular engineering (Figure 1.3). This is done by isolating a target DNA sequence and then transferring it to a cloning vector that has the ability to self-reproduce. The DNA of the cloning vector interacts with the target DNA and produces a new blueprint of gene information called recombinant DNA. The recombinant DNA is transferred to RNA into a host cell, which in turn produces the recombinant protein.

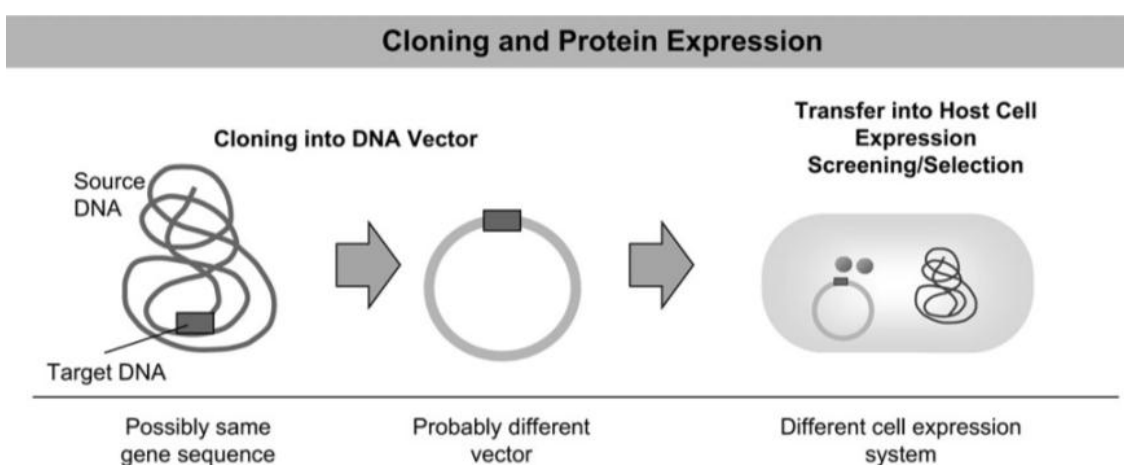


Figure 1.3 Recombinant protein production.¹³

Only a few examples have found in the literature presenting the extreme difficulty of the heterologous expression of the olfactory receptors¹⁴⁻¹⁶. The reason is that there are several important and difficult steps to obtain these membrane proteins: production of large quantities, purification of stable and functional membrane proteins and long-term stabilization of non-aggregated membrane proteins.

More recently, Zhang¹⁷ and co-workers demonstrate an efficient cell-free production of these receptors directly from plasmid DNA. This is performed without the use of living cells. All components needed to transcribe DNA to RNA and translate the RNA to protein (ribosomes, enzymes, etc.) are provided in solution for use *in vitro* (Figure 1.4). Normally, these solutions are obtained from cell lysate. Cell-free technology is well established for producing soluble proteins. In the case of transmembrane proteins, such as the ORs, the technology needs to be adapted by

including an appropriate detergent in the reaction mixture due to the necessity to guarantee their tertiary structure and functionality retained.

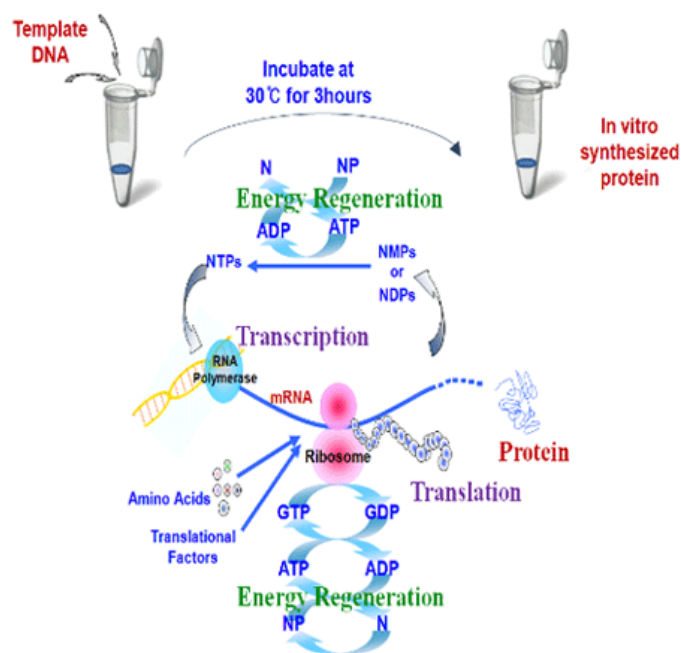


Figure 1.4 Cell-free protein expression system. (Bioneer, Molecular biology company webpage: <http://eng.bioneer.com>)

Cell-based expression systems for protein production have been extensively used but they have as well limitations in terms of the quality and quantity of the proteins produced and for high-throughput production. Some of these limitations can be avoid by the use of cell-free expression systems. However, the drawback of this revolutionary technology is due to the lack of suitable detergents, requiring laborious detergents screens, high costs of production and also low yields.

Each expression system has its advantages and drawbacks. Table 1.1 summarized different cell-based, animal-based and cell-free expression systems for GPCRs¹⁸⁻²⁰.

Table 1.1 Expression systems for G-protein coupled receptors (GPCRs).

Expression system	Subsystems	Advantages	Disadvantages
Cell-based	<i>Escherichia coli</i>	<ul style="list-style-type: none"> • Low cost • Homogeneity of the recombinant proteins • Fast • Ease of use • Scalable 	<ul style="list-style-type: none"> • Lack of post-translational modifications (not the best for functional studies in vivo) • Low yields • High yields in inclusion bodies • Membrane toxicity • Fusion protein required • Refolding required
	Yeast	<ul style="list-style-type: none"> • Low cost • Capacity to perform posttranslational modifications • Fast • Easy manipulation • Grow on simple media • Scalable • High yields 	<ul style="list-style-type: none"> • Composition and quantity of N-glycans • Different membrane lipid composition than mammalian cells • Thick cell wall (may impede purification)
	Baculovirus/Insect	<ul style="list-style-type: none"> • Mammalian-like 	<ul style="list-style-type: none"> • Complex culture media • Slow virus stock production • Not optimum for large-scale productions.
	Mammalian > Transient expression (performed under non-selective conditions) > Stable (performed under selective-conditions)	<ul style="list-style-type: none"> • Environment close to the native tissue in which the GPCR naturally occurs • Able to perform complex posttranslational modifications • Membrane lipid composition close to that of the native receptor 	<ul style="list-style-type: none"> • Transfection methods to be established for each cell line. • Cells die after several days (problems of high amount of material for repetitive experiments)
Animal-based	<i>Xenopus oocytes</i>		<ul style="list-style-type: none"> • Low yields • Time-consuming productions • High costs • Stability problems.
	<i>Drosophila melanogaster</i>	<ul style="list-style-type: none"> • Good yields for glutamate receptor (transmembrane protein) expression 	<ul style="list-style-type: none"> • Requires mRNA injection into each oocyte • Not large-scale production. • GPCRs expression in this system is still a challenge
Cell-free		<ul style="list-style-type: none"> • Simple • Fast • Only the protein of interest is produced 	<ul style="list-style-type: none"> • Very low yields • Laborious detergent screens • High costs

Focusing in cell-based expression systems, until now, it was known that *S. cerevisiae* yeasts^{21,22} are better than mammalian cells for olfactory receptor expression since they are much cheaper, easier to cultivate and the expression yield in yeast cells is higher than in mammalian cells. In addition, expression in mammalian cell lines is time consuming and expensive. Furthermore, the yeast strain has been successfully used for functional expression of many G-protein coupled receptors including the olfactory receptors²¹. *Saccharomyces cerevisiae* was first used to functionally express many different GPCRs²³⁻²⁶ before being optimized as a host system for expressing ORs and for efficient coupling to a signalling pathway able to produce a measurable response to odorant stimulation²¹. In addition, in the literature are also presented other systems different than yeast where the ORs were heterologously expressed such as *C. elegans* olfactory receptor ODR-10 in HEK cells (mammalian) which molecular interactions characterization is presented by Surface Plasmon Resonance technique²⁷.

One of the most important advantages of yeast cells, as systems for ORs expression, is that they are eukaryotic organisms. Thus, they have all the machinery necessary to allow the protein folding and trafficking. In addition, it is reported that the tolerance of yeast cells to pH variations and temperature allows higher receptor functional expression. Thus, yeast constitutes an attractive system to study mammalian GPCRs.

In 2003, our group was involved in a framework of a European project called SPOT-NOSED. The aim was the development of a nanobiosensor based on single olfactory receptor, in order to mimic the natural olfactory system. We successfully worked together with the team "Biology of Olfaction and Biosensors" (BOB) of the "Neurobiology of Olfaction and Modelization in Imaging" (NOeMI) research unit in the Institute National de la Recherche Agronomique (INRA-NOeMI-BOB, France), among other collaborators, to produce a proof-of-concept of the bioelectronic sensor. They have a wide expertise in the expression of olfactory receptors in heterologous systems such as yeast and other mammalian cells. Also, they have a good experience in G-protein-coupled-receptors (GPCRs) in general. Thus, for that project, they expressed two different receptors, ORI7 from a rat and OR1740 from a human in *Saccharomyces cerevisiae* yeast. The first problem they faced was how to improve and achieve the proper plasma membrane expression of the receptor because normally the ORs remain

in the membrane of the endoplasmatic reticulum or were directed to the vacuoles to undergo proteolytic degradation. For that reason they made various adaptations of the classical way of GPCR expression on yeast cells²².

The ORs expression procedure that they suggested improved the system using modified yeast strain, MC18 of *S. cerevisiae* with the luciferase gene. This gene was used as luminescence reporter gene due to its high sensitivity. With this modification they could control the odorant stimulation by a sensitive bioassay, the functionality of this one and control where the olfactory receptor was mainly expressed by immuno analysis. Minic et al.^{21,22}, also proved that working at 15°C during the yeast growth of a strain that was induced in galactose-containing medium allows an improvement of the functional response of the receptor (Figure 1.5).

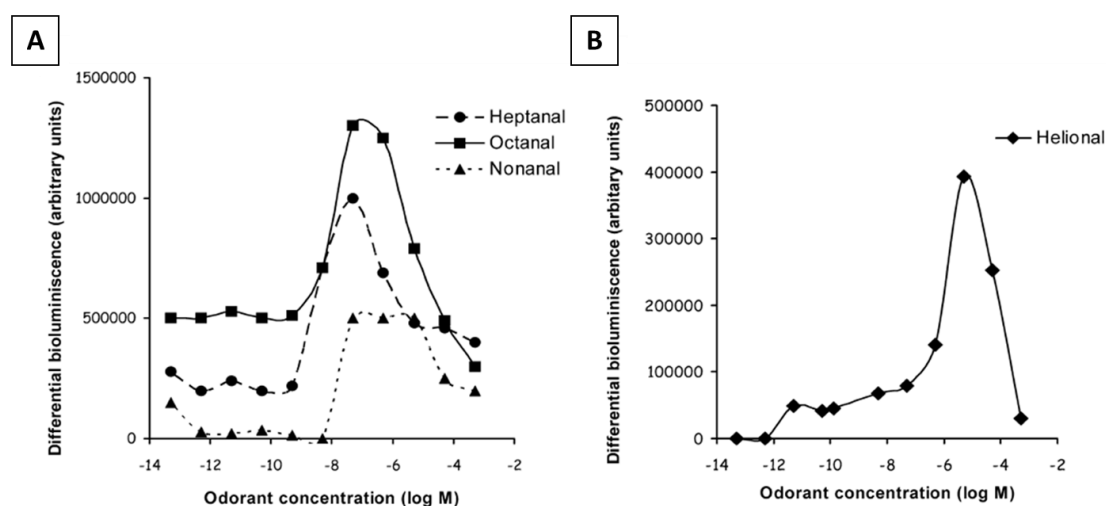


Figure 1.5 Differential bioluminescence dose-response upon odorant stimulation of yeast-expressed olfactory receptors²². (A) Measurements performed on yeast transformed to coexpress the ORI7, G_{olf} and the luciferase reporter. Specific odorant-receptor interaction was observed for heptanal molecule. (B) Measurements performed on yeast coexpressing the human OR1740, G_{olf} and the luciferase reporter. Specific odorant-receptor interaction was observed for helional molecule.

In recent years, much attention has been directed towards the integration of membrane receptor proteins into biosensor devices, due to their key role as targets in many disease developments^{28,29}, as well as in the sensory functions of cells. Dealing with membrane receptors is challenging due to the fact that they are difficult to produce, in comparison with other biomolecules, such as, for instance, soluble proteins or oligonucleotides.¹² Besides, their activity on a substrate depends crucially on their

orientation and functional conformation³⁰, which is largely determined by the lipid membrane environment fundamental to retain their tertiary structure and functional integrity³¹.

Current strategies developed for biosensing applications³² with membrane receptors include immobilization into supported lipid bilayers or into lipid vesicles (liposomes), made from artificial³³⁻³⁷ or native membranes^{38,39}, as well as their inclusion into free-standing lipid bilayers lying on nanoporous substrates⁴⁰⁻⁴². Isolation of native membrane fractions from a cell source, which integrate membrane receptors heterologously expressed in the cell line, constitutes one of the preferred approaches as it provides the same lipidic environment found in the native cell, thus preventing the protein denaturation during the insertion into an artificial membrane³⁸ (Figure 1.6).

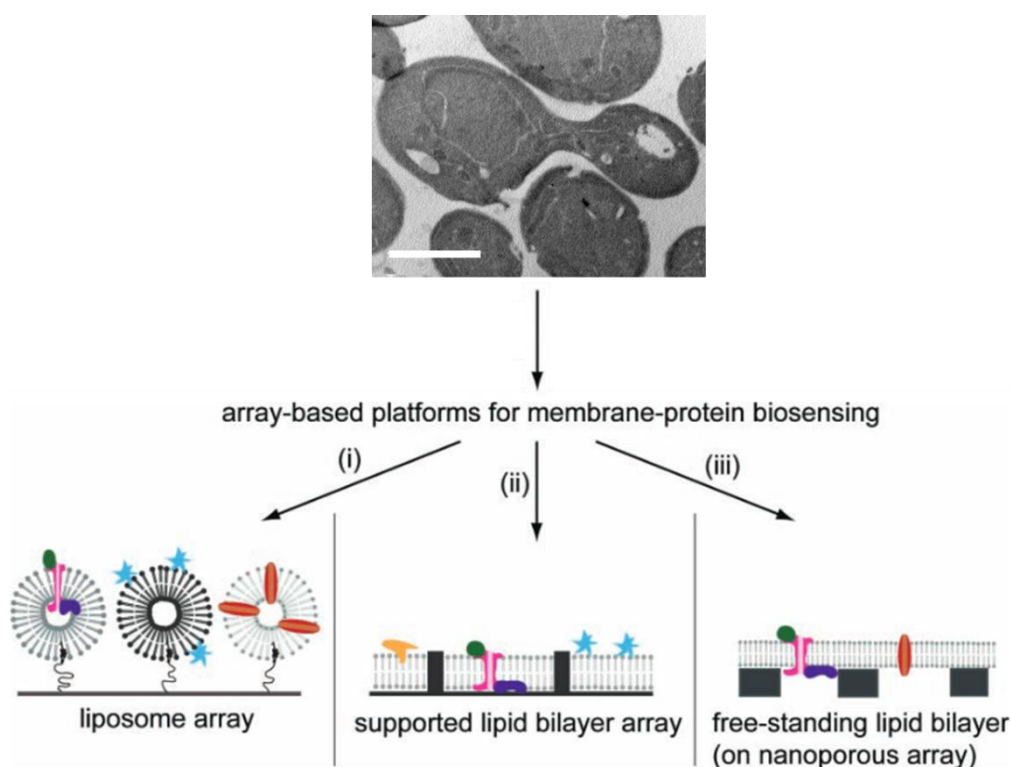


Figure 1.6 A cryo-fracture picture from *Saccharomyces cerevisiae* yeast cell performed by myself (Scale bar: 7 μm) and the different model membrane systems¹². A collection of model lipid membrane systems and array-based approaches towards membrane protein biosensing: liposome array (artificial or native membranes) (i), supported lipid bilayer (SLB) array (ii), and free-standing lipid bilayers spanning over a nanoporous array (iii) with incorporated membrane proteins.

These days, the development of specific analytical devices for fast routine measurements using receptor proteins becomes a hot research topic. Their

characteristics rely on their easy of use, portability, fast measurement, small size, relatively inexpensive cost, and improved sensitivity. In addition, the emerging technologies (i.e. advances functional nanomaterials and microfluidics) are improving the sensitivity of such devices, miniaturizing the platforms and reducing assay costs for high-throughput multiplex detection⁴³.

The multiplex detection is carry on thanks to the protein microarray technology. A protein microarray (also commonly referred to as a protein biochip) is a collection of miniaturized test sites, or spots, arranged on a solid substrate where a molecular affinity probe, specific for a particular analyte, is immobilized at a defined test position in a two-dimensional array. The main advantage of protein microarrays configuration is that enable massively parallel tracking of proteins, i.e. biomarker candidates, from large numbers of clinical samples in a very short time⁴⁴. The protein microarray technology was introduced for the first time in 1983 as an antibody matrix⁴⁵ and was relatively easy to develop since it was based on the DNA microarray technology, which have become the most widely used microarrays. DNA microarrays have been very important in genomic research (i.e. study gene expression patterns, locate transcription factor binding sites, and to detect sequence mutations on a grand scale). However, they give us only information about the genes and provide just few information regarding the function of the proteins they encode. Thus, the necessity of protein microarrays platforms was emerged⁴⁶.

In addition, the use of micro- and nano-technologies has an important role in medicine. For this reason, the use of isolated olfactory receptors instead of whole-cells enables the researchers to develop an olfactory biosensor using the nano-technologies⁴⁷. According to this proposal Vidic et al.¹⁶ in the framework of the SPOT-NOSED project (2003-2006) found a way to work with nano-objects carrying olfactory receptors with the aim to develop a bioelectronics nose.

In order to develop biomimetic noses based on olfactory receptors one strategy consists in expressing the receptor proteins at the surface of natural cells that constitute the source for nanovesicles production. This strategy keeps the receptors surrounded by a natural membrane made up of a lipid bilayer, the natural environment for keeping these proteins functional and structurally stable. This together with recent studies

showing the capture of GPCRs onto biosensor surfaces⁴⁸ and demonstrating a maintained receptor activity into natural membranes,⁴⁹ opens definitively the possibility for the development of practical biosensor devices based on GPCRs membrane receptors.

This thesis is involved in the framework of the BOND (Bioelectronic Olfactory Neuron Device) European project. Due to the successful work obtained in the SPOT-NOSED European project, and following the new concept of electronic noses using the olfactory receptors, most of the partners were involved in a second European project called BOND (2009-2012). The aim of that project was to develop an array of smart nanobiosensors based on ORs for the detection of odorant molecules and improve the bioelectronics nose proposed in the previous project. BOND project was based on a multidisciplinary network from biotechnology, surface chemistry, nanofabrication, electronics and simulations fields.

The development of practical biomolecular devices based on membrane receptors integrated in native membrane fractions requires, among other aspects, a strict control of the relevant parameters determining the membrane fraction characteristics, their integrity and morphology of the membrane receptors containers. Part of this information is almost absent in the current literature. Thus, the aim of this *Chapter* is to address these issues in a systematic way for the case of natural membrane fractions isolated directly from yeast cells expressing either of different olfactory receptors (ORs), i.e. the human OR1740 (ORL520 in OrDB), rat ORI7 (ORL11 in OrDB) and chimpanzee OR7D4 and the seven transmembrane receptor the human somatostatin receptor subtype 2 (SSTR2).

All these receptors have been used as model GPCRs; however, all of them have their specific characteristics and application.

OR1740 olfactory receptor is selectively activated by the molecule helional⁵⁰. Helional, an odorant reminiscent of the ocean breeze is well-use in the fragrance soap industry.

Then, ORI7 receptor is selectively activated by the molecules heptanal⁵¹ and octanal⁵². Heptanal has been identified as a volatile in fruits and vegetables, microbial processes and animal wastes, freshwater diatoms and chrysophytes, and autoxidation of unsaturated fatty acids. For example, in the food industry, the odours of alkylamines liberated by bacterial actions and aliphatic acids aldehydes (i.e. heptanal and octanal) generated by lipid oxidation contain a fatty, fishy note, and they are major components of the fatty, tallowy, fishy off-flavour associated with oxidative degradation of lipids in meats and seafoods⁵³. Thus, their detection is an important issue in the food quality control.

However, OR7D4 odorant receptor is selectively activated by the molecule androstenone⁵⁴. Androstenone is a testicular steroid with a strong urine odour. This odorant is characteristic of boar taint (a penetrating unpleasant odour and taste) in pork. In addition, boar taint is dependent on the concentration and combination of certain substances in the pork fat⁵⁵. With castrated and female pigs, the probability of boar taint is very low. A person can only smell the odour when the meat is heated. Thus, to prevent that pork that contains boar taint is sold to consumers and to avoid the pork castration many methods to detect them have been developed or are in development, i.e. several analytical and biosensing methods (such as bioelectronics noses). Bioelectronic noses with OR7D4 could be used in the food industry as food quality control.

Finally, SSTR2 receptor is activated by the somatostatin peptide hormone⁵⁶, that regulates the endocrine system (may play a role in regulation of intestinal peristalsis) and affects neurotransmission and cell proliferation. SSTR2 is not a GPCR, is a member of the superfamily of receptors having seven transmembrane segments and is expressed in highest levels in cerebrum and kidney. In the present thesis has been used as control transmembrane protein.

1.2 Materials and Experimental Procedures

1.2.1 Materials

Reagents such as PBS (phosphate buffer saline), glycine, azide, bovine serum albumin (BSA), anti-c-myc-biotin 9E10, anti-mouse IgG peroxidase (anti-IgG-HRP for ELISA assays), tetramethylbenzidine (TMB) were purchased from Sigma-Aldrich Chemie GmbH (Germany). Tris (hydroxymethyl) aminomethane was from Merck (Darmstadt, Germany). Bis[sulfosuccinimidyl]suberate (BS³) was purchased from Thermo Fisher Scientific, Pierce (Rockford, IL, USA). Low binding protein filters (diameter = 13 mm; pores size = 0.22 μm) and the anti-mouse IgG peroxidase (anti-IgG-HRP for Western Blot assays) were from Millipore (Temecula, CA). The home-made monoclonal anti-c-myc (Ab894D12_{f7f9}, 1.44 mg mL⁻¹, *Chapter 2*) was produced and purified by Abyntek Biopharma (Bizcaia, Spain). Nitrocellulose membranes (HybondTM-C extra) were from Amersham (GE Healthcare Europe).

1.2.2 Buffers and Solutions

Buffers used were as follows: phosphate-buffered saline (PBS) 10mM at pH 7.5 (always filtered) and PBST buffer was PBS with 0.05% Tween 20. The blocking buffer was 4.5% skim milk powder in PBST. Coating buffer was 50 mM carbonate/bicarbonate at pH 9.6. Citrate buffer was sodium citrate 40 mM solution at pH 5.5. The substrate solution was 0.01% TMB and 0.004% H₂O₂ in citrate buffer.

1.2.3 Equipments/Software

To determine the yeast cell size the Beckman Coulter LS 13 320 (USA) laser-diffraction particle dimension analyser and the Centrifuge 5415 D (Eppendorf, USA) were used. Proteins from the different yeast membrane fractions batches were quantified with the Pierce BCA Protein Assay kit (Thermo Scientific, USA) to obtain the Total Protein Concentration (TPC). For the sample preparation (proteoliposomes and nanovesicles) an Ultrasons bath was used (50 kHz Ultrasons, Selecta). DLS

measurements were performed with a Malvern Zetasizer-Nano ZS90 (Malvern Instrument Ltd., UK) and the system was equipped with a red (633 nm) laser, 4 mW He-Ne (size measurement range ~ 0.3 nm-6µm, www.malvern.com).

For sample purification a centrifuge (Beckman Coulter TJ-25; rotor: TS-5.1-500 or 90.i) and Amicon Ultra-4 tubes (Millipore) were used. The two-dimensional (2D) imaging of vitrified samples were performed on a FEI Tecnai microscope (FEI Company, Eindhoven, Netherlands) operating at 200 kV, at a temperature between – 170 °C and – 175 °C and using low-dose imaging conditions. The samples were vitrified using a Vitrobot (FEI Company, Eindhoven, Netherlands) and transferred to the microscope into a Gatan cryoholder (Gatan, Pleasanton, CA). The CF-TEM samples were observed at Tecnai SPIRIT electron microscope (FEI, Netherlands) at 120 kV. First, the samples were frozen in a Leica EM CPC cryopreparation system (Leica, Vienna, Austria) and fractured at in a Bal-Tec BAF 060 freezeetching system (BAL-TEC, Liechtenstein).

NTA measurements were performed with a NanoSight LM20 (NanoSight, Amesbury, UK), equipped with a sample chamber with a 640 nm laser that interacts with the liquid containing a diluted solution of nanovesicles ($\sim 10^8$ nanoparticles mL⁻¹) through a glass prism.

Concerning the software used: Cryo-EM images and snapshots of the video recorded using the hydrodynamic focusing technique were evaluated using the software Image J (<http://rsbweb.nih.gov/ij/>). To analyse the DLS data DTS applications 5.10 software was used. The NTA software used for capturing and analysing the data recorded (light scattered from nanovesicles, moving under Brownian motion, in the field of view) was the NTA 2.0 Build 127.

1.2.4 *Saccharomyces cerevisiae* yeast cell culture characterization

A culture of *Saccharomyces cerevisiae* yeast cell was grown at $D_{600} = 1.8$ (log phase).

1.2.4.1 LS Particle Size Analyser

Beckman Coulter LS 13 320 laser-diffraction particle dimension analyser measures the size distribution of particles suspended in a liquid (10 mL) by using the

principles of light scattering, as well considering the yeast refractive index as $(1.3471 + 0.01i)$ calculated by Optical Waveguide Lightmode Spectroscopy (OWLS)⁵⁷. The measurements were performed at the Scientific and Technological Center from the Universitat de Barcelona (CCiT-UB).

1.2.4.2 Hydrodynamic focusing

10 mL of yeast cell suspension was centrifuged 5 min at 1000 rpm at RT. The supernatant was removed and 1 mL of the pellet was centrifuged again 2 min at 1000 rpm (Centrifuge 5415 D eppendorf) at RT. Finally, the pellet obtained was resuspended onto 5 mL of PBS. Onto a three microchannel chip (laminar flow: dye/sample/dye) the sample was flown and thanks to the hydrodynamic focusing technique used more accurate results for determining the size of cells were obtained. Cells flowing onto the centre channel were recorded and snapshots of them were used to analyse the cells size. The diameter of 24 individual yeast cells was extracted.

1.2.5 Nanovesicles solution preparation

Before to determine the final standard protocol for nanovesicles preparation described below some techniques were evaluated to obtain them, corresponding results were presented in Results and Discussion Section after calculating the remaining nanovesicles size by DLS:

- i) Sonication: 1 mL solutions of membrane fractions in PBS were sonicated at different times (0, 2, 20 and 60 min) in ice-cold water to homogenize their size.
- ii) Centrifugation: 1.5 mL solution of membrane fractions in PBS was ultracentrifuge 48 min and 60 min at $50000\times g$ ⁵⁸ (Avanti J-30 I). The supernatant was collected and analysed by DLS.
- iii) Gel filtration: 1 mL solution of membrane fractions in PBS was eluted through a preconditioned NAPTM-10 SephadexTM G-25 DNA Grade (GE Healthcare) with PBS. The eluted subfractions solutions were analysed by DLS.

- iv) **Sonication Probe:** 1 mL solution of membrane fractions in PBS were ultrasonicated at different times (5, 10, 30 and 60 seconds) with a *Digital Sonifier Cell Disruptor S-250 (Branson)* (Amplitude = 20%, f =20 kHz) in ice bath. After each pulse, the temperature in the ice bath was calculated. As well, at 30 and 60 seconds cycle, the evaluation of pulse sequence (ON: 5 seconds; OFF: 15 seconds) and the corresponding ice-bath temperature calculation was performed.
- v) **Extrusion:** 1 mL solution of heterogeneous nanovesicles (in PBS) were homogenized and downsized to form uni-vesicles by extrusion through 400-nm and 100-nm (sequentially) polycarbonate membranes (PC) (Poretics, Livermore, CA, USA) in an extruder device (Avanti polar lipids, Inc. Extruder 250 μ L syringe) after 20 minutes of sonication in an ice-bath.
- vi) **Filtration:** 1 mL of sample solution of membrane fractions was diluted in PBS and sonicated for 20 min in ice-cold water to homogenize their size. This solution was then filtered using a sterile low binding protein filter (diameter = 13 mm; pores size = 0.22 μ m).

Standard protocol: Human olfactory receptors c-myc-OR1740 (ORL520 in OrDB), rat ORI7-HA (ORL11 in OrDB), chimpanzee c-myc-OR7D4 and somatostatin receptor subtype 2 (SSTR2) were expressed heterologously in different yeast *Saccharomyces cerevisiae* cultures following a procedure well described in the literature^{22,48}. After, the yeast cells were mechanically disrupted⁴⁸, the cell content was separated and the membrane fractions obtained were divided in aliquots and frozen at -80°C. This previous process was performed at the French National Institute for Agricultural Research (INRA, France), in collaboration within the BOND project framework. After, at the Institute of Bioengineering of Catalonia (IBEC, Spain) immediately before use, the stock suspension of membrane fractions was diluted to a concentration (expressed as total protein concentration, TPC) of 125 μ g mL⁻¹ solution in Phosphate Buffered Saline (PBS 1x) 10 mM (pH = 7.4) and sonicated for 20 min in ice-cold water to homogenize their size. The solution was further diluted in PBS to obtain the **proteoliposomes** solution described in the text, normally at a total protein concentration (TPC) of 60 μ g mL⁻¹. This solution was then filtered using a sterile low binding protein filter (diameter = 13 mm; pores size = 0.22 μ m) and we obtained the

nanovesicles that in the text are called NV or NS. The nanovesicles solutions described in the text were obtained by further dilution to the working concentration. Control vesicles solution was done following the same procedure described above using the *Saccharomyces cerevisiae* yeast cell culture explained before (without any receptor expressed genetically) and was performed at the IBEC.

For the *Western Blot* assays: 1 μL of the stock membrane suspension was loaded per gel and well (5 $\mu\text{g}/\text{well}$) and the assays performed following the procedure described by Minic et al (see below).²²

1.2.6 Nanovesicles solution purification

Two different techniques were used in order to purify the nanovesicles from the rest of cell extracts (i.e. lipids/proteins) coming from the plasma membrane solution.

- i) Centrifugation: 1 mL (TPC of 60 $\mu\text{g mL}^{-1}$) of nanovesicles solution (in PBS) was concentrated using the Amicon Ultra-4 Centrifugal Filter Devices (10000 NMWL) 45 min at 4000xg (swinging bucket). The resulting solution was discarded and the pellet was resuspended in 1 mL of PBS. An ultracentrifugation was performed 1h at 4 °C 33400 rpm (100000xg). The supernatant was removed again and the pellet was resuspended in PBS. The containing particles in the supernatants as well as in the final pellet solution were analysed by DLS.
- ii) Affinity Chromatography: In that case, we wanted to separate those nanovesicles carrying the olfactory receptor (through the c-myc tag, see Results and Discussion Section) from the rest of the solution in order to have a more selective biological sample. First, a NabTM Protein A Spin Column (1 mL, binding capacity: ≥ 34 mg of human IgG per column) was preconditioned with PBS, (it was studied three different columns, Protein A, Protein G and Protein A/G at the same conditions). The mAb anti-c-myc-biotin 9E10 (1 mg of antibody) was immobilized on the Protein A column 1h at RT. The excess of antibody was removed with PBS. Then, the antibody was crosslinked to the column with the BS³ crosslinker (5 mM in PBS) incubated 30 min at RT. The column was

rinsed with 10 mL of PBS. After, the proteoliposomes solution (2 mL at TPC $30 \mu\text{g mL}^{-1}$) was incubated 1h at RT in the column. After that time, the excess of sample solution was removed and the vesicles attached specifically to the anti-c-myc-biotin antibody were eluted with an acidic solution (1 mL of glycine 100 mM pH 2.5). The step was repeated three times. The remaining solution was neutralize with Tris buffer (pH 9) and concentrate with an Amicon Ultra-4 (10000 MWCO) centrifuged 20 min at 4000xg (Allegra centrifuge, Beckman Coulter, USA). Finally, the column was equilibrated with PBS and store at 4°C with 0.02% azide-PBS solution. In each step, an aliquot was separated in order to study if the purification process worked correctly. The evaluation was performed by and Indirect ELISA (enzyme-linked immunosorbent assay).

1.2.6.1 Indirect ELISA

Microtiter plates were coated with the aliquots to study (vesicles carrying OR immobilized in the column and the rest of the proteoliposomes sample, in coating buffer, 100 μL per well) covered with adhesive plate sealers overnight at 4 °C. Next, the coated plates were washed and the remaining uncovered well surface was blocked with BSA (2%) 1 h at room temperature. Then, the wells were washed again and the monoclonal antibody anti-c-myc-biotin (1/200 in PBST and the blanks that were just PBST without the antibody, 100 μL per well) was added. The mixture was incubated for 2 h at room temperature; the plates were washed again with PBST. Subsequently, a solution of anti-IgG-HRP (1/20000 in PBST, 100 μL per well) was added and the plates were incubated for 1 h more and washed before adding the substrate solution (100 μL per well). After 15 min at room temperature the absorbances were measured at 620 nm.

All the washing steps consisted on filling-up the wells with PBST (200 μL) and immediately removing the solutions. The solutions or washes are removed by flicking the plate over a sink manually; this was repeated on four cycles.

1.2.7 Western Blot

Briefly²², the proteins of the membrane fractions were separated on a 12% SDS-polyacrylamide gel (5 $\mu\text{g}/\text{well}$) and then transferred electrophoretically onto a PVDF Hybond-P (Amersham, GE Healthcare) membrane. Then, the membrane was treated with the blocking buffer 1 hour at room temperature under agitation. Next, the membrane was incubated overnight with the primary antibody (anti-c-myc, Abyntek) in blocking buffer at 4°C under agitation. The next day the gel was rinsed with PBST every 15 min four times. Next, the membrane was incubated 1 hour at room temperature under agitation with a mix of the secondary antibody anti-IgG-HRP (1/3000) and streptavidin-HRP conjugate (Amersham, dilution 1/1333) in blocking buffer. Finally, the membrane was rinsed again every 15 min four times with PBST and one time with H₂O milliQ and blots were revealed using the enhanced chemiluminescence (ECL) detection kit from Amersham (GE Healthcare).

1.2.8 Cryo-electron microscopy (Cryo-EM)

The two-dimensional (2D) imaging of vitrified samples was performed on a FEI Tecnai electron microscope (cryo-EM). A membrane fraction solution (TPC = 5 mg mL⁻¹) was sonicated for 20 min in ice bath. Drops of approximately 2 μL were mounted onto 4 glow-discharged holey carbon grids and blotted with filter paper to make thin aqueous films under controlled temperature and humidity. The grids were then plunged into liquid ethane at the temperature of liquid nitrogen using a Vitrobot. The samples were transferred to the microscope into a Gatan cryoholder cooled by liquid nitrogen. Cryo-EM images of proteoliposomes on the different grids were collected and the diameter of 40 individual vesicles was extracted.

1.2.9 Cryo-Fracture Transmission electron microscopy (CF-TEM)

CF-TEM was done following the protocol reported in the literature⁵⁹. The suspension of the cell membrane fractions after sonication was sandwiched between two

copper platelets using a 400-mesh gold grid as a spacer. The samples were frozen in a Leica EM CPC cryopreparation system using propane immersion, at $-189\text{ }^{\circ}\text{C}$, and fractured at $-150\text{ }^{\circ}\text{C}$ and 10^{-8} mbar in a Bal-Tec BAF 060 freezeetching. The replicas were obtained by unidirectional shadowing with 2 nm of Pt/C and 20 nm of C, and they were floated on distilled water during 5 min. The replicas were observed at Tecnai SPIRIT electron microscope at 120 kV. CF-TEM was carried out on different samples.

1.2.10 Dynamic light scattering (DLS) measurements

DLS measurements were performed with a Malvern Zetasizer-Nano ZS90. A detection angle of 90° was chosen for the size measurements. Vesicles solutions were introduced into plastic cuvettes of 1 cm optical length and measured at a controlled temperature of $25\text{ }^{\circ}\text{C}$. Proteoliposomes solutions were sonicated and then diluted at $\text{TPC} = 60\text{ }\mu\text{g mL}^{-1}$. Nanovesicles solutions were sonicated, diluted at $\text{TPC} = 60\text{ }\mu\text{g mL}^{-1}$ and filtered. For each solution, three DLS measurements were conducted with a fixed 5 runs, each run lasting 5 s in order to extract an average size distribution. We verified that the relative error between them is in the order of 10%, as expected for DLS measurements.⁶⁰ The measurements were performed in PBS solution 10 mM, at the following conditions: $\text{pH} = 7.4$, viscosity = 1.05 cP and refractive index = 1.3377, and for the sample the refractive index = 1.4, absorption = 0. The plot reported in Figure 1.12A is the result of an average of two OR1740 carrying proteoliposomes solutions for the sonicated sample and two OR1740 nanovesicles solutions for the filtered sample. The size distributions were expressed in % particles number and fitted to a Gaussian adjustment in order to extract the particles size.

1.2.11 Nanoparticle Tracking Analysis (NTA) measurements

NTA measurements were performed with a NanoSight LM20. Proteoliposomes solutions were sonicated and then diluted at $\text{TPC} = 60\text{ }\mu\text{g mL}^{-1}$. Nanovesicles solutions were sonicated, diluted at $\text{TPC} = 60\text{ }\mu\text{g mL}^{-1}$ and filtered. All the solutions were then diluted with PBS at the working concentration (C) and injected in the sample chamber with sterile syringes until the liquid reached the tip of the nozzle. The measurements

were performed at room temperature, immediately after the sample loading. The nanovesicles interacting with the laser beam are visualized using an optical microscope with a video camera. Samples were recorded during 60 seconds with manual shutter and gain adjustments. Three repeated measurements were performed for all the nanovesicle solutions. We verified that the relative error between them is in the order of 50% which is an expected value for NTA measurements⁶⁰. The plots reported in Figure 1.12B are the result of an average of two OR1740 carrying proteoliposomes solutions for the sonicated sample and two OR1740 nanovesicles solutions for the filtered sample. The particles size distribution is obtained directly from their diffusion coefficient by applying the Stokes-Einstein equation. The nanovesicles diffusion coefficient reported in Results and Discussion ($(4.51 \pm 0.98) \mu\text{m}^2 \text{s}^{-1}$) was calculated by tracking the movement of each particle in the range $(94 \pm 20) \text{nm}$.

Finally, each point in the calibration curve NS mL^{-1} vs. TPC reported in the Figure 1.17 and Figure 1.18 refer to at least one nanovesicles solution at a defined concentration. The data is fitted by a weighted linear fit. Each calibration curve is performed at least with 3 different TPC.

1.3 Results and Discussion

1.3.1 Characterization of *Saccharomyces cerevisiae* yeast cells

Saccharomyces cerevisiae yeast cells (Figure 1.7A), where the olfactory receptors were expressed, were characterized by different techniques. Their diameter size was calculated by LS Particle Size Analyser considering the yeast refractive index ($1.3471 + 0.01i$) as mean size $6.18 \mu\text{m}$, Figure 1.7B. The result was confirmed by a second technique, hydrodynamic focusing, Figure 1.7C.1. After analysing the diameter size of 24 cells the mean size obtained was $4.9 \mu\text{m}$, Figure 1.7C.2. Both results are coherent with ones reported in the literature where yeast cells are generally ellipsoidal in shape ranging from 5 to $10 \mu\text{m}$ at the large diameter and 1 to $7 \mu\text{m}$ at the small diameter⁶¹.

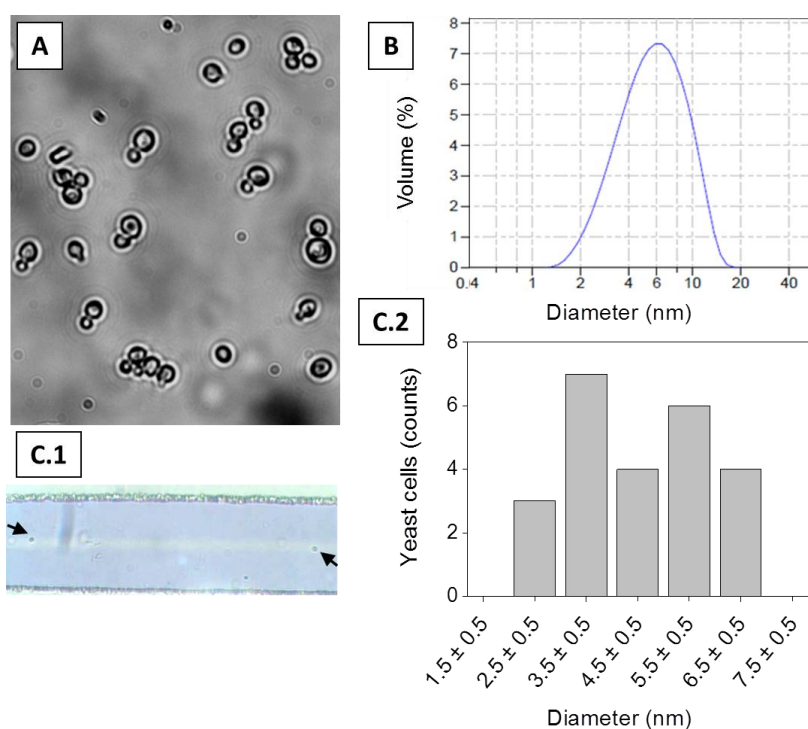


Figure 1.7 (A) Microscope picture of *Saccharomyces cerevisiae* yeast cell culture. (B) Yeast cell diameter size obtained by the LS Particle Size Analyser technique. (C.1) Microscope picture of two yeast cells (black arrows) flowing through a microchannel. (C.2) Graph representing the diameter size of the yeast cells is obtained after analysing 24 cells through the hydrodynamic focusing technique.

1.3.2 Characterization of yeast membrane fractions in solution

1.3.2.1 Receptors (7 Transmembrane proteins) expression

Some of the receptors (OR1740, ORI7, OR7D4 and SSTR2) that we present in this *Thesis* have covalently attached (by genetic engineering) either in the N-terminus (c-myc-receptors) as in the C-terminus (HA-receptors) of the receptor a peptide tag. It is known that many recombinant proteins (i.e. GPCRs) have been engineered to express some specific tags (c-myc, HA, His, etc.), which does not appear to interfere with the bioactivity or the biodistribution of the recombinant protein⁶². These tags can facilitate the detection, isolation, and purification of this kind of proteins as well as to check that the receptor expression has been performed without any problem (Figure 1.8). In our case, we will see the particular utility of these tags in the development of the present thesis (see also the following *Chapters*).

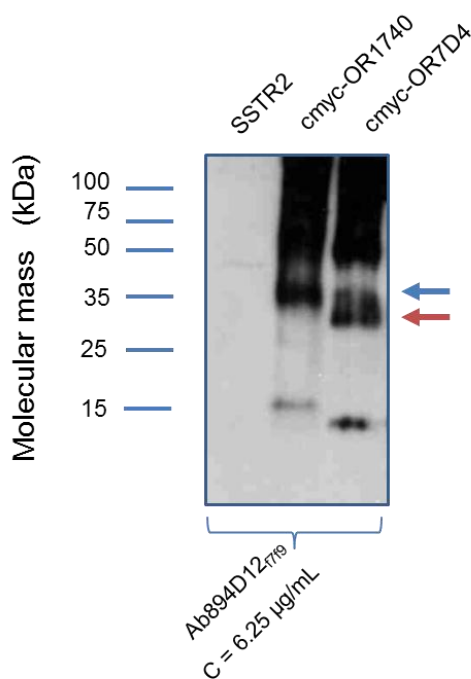


Figure 1.8 Picture showing the Western Blot results performed to assess the capability of anti-c-myc antibody (Ab894D12_{T119}) to detect specifically different c-myc-ORs expressed in the yeast cell membrane allowing us to check that the receptor expression has been performed without any problem. Nanovesicles carrying SSTR2 receptors were used as control (-). Nanovesicles carrying c-myc-OR1740 and c-myc-OR7D4 were used as evaluation sample models (+). The monomer olfactory receptor molecular weight is around 26 kDa for the OR7D4 (red arrow) and around 35 kDa for the OR1740 (blue arrow). The expression of ORI7 and SSTR2 is reported in the literature by our collaborators²².

1.3.2.2 Sample homogenization

Yeast membrane fractions carrying the human OR1740 and the rat ORI7 olfactory receptors were produced as detailed in Ref. 22 from a *Saccharomyces cerevisiae* yeast culture through a process of cell disruption. We observed the spontaneous formation of proteoliposomes of size in the range of few hundreds of nm in sonicated membrane fractions. The cryo-EM image in Figure 1.9 shows round-shaped polydispersed vesicles, with sizes ranging from 50 to 200 nm. By measuring the diameter of a population of 40 vesicles directly from the electron micrographs we obtained a relatively large polydispersity in sonicated samples with an average size of (138 ± 68) nm.

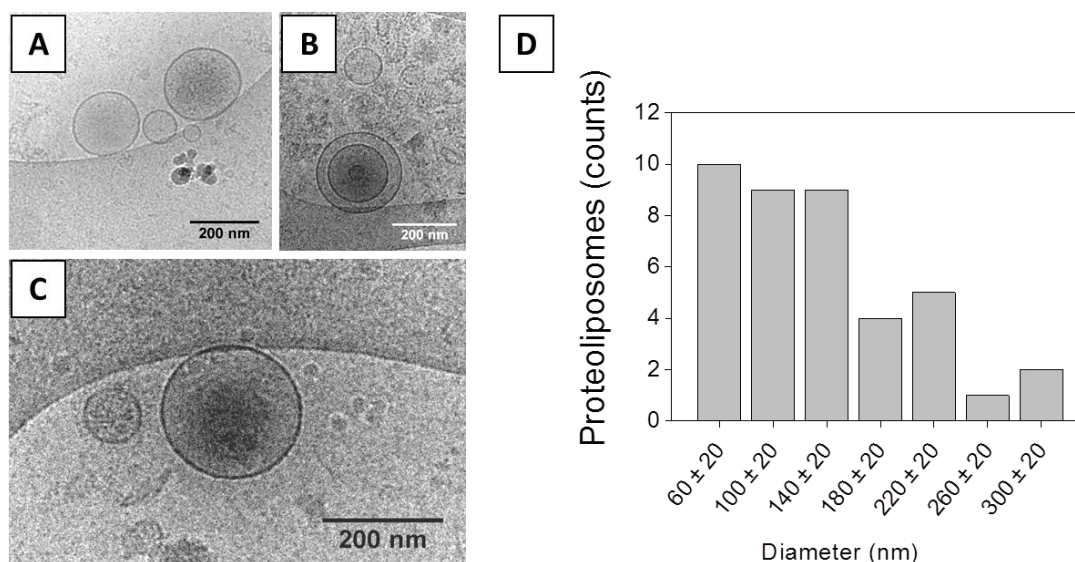


Figure 1.9 (A), (B), (C) 2D Cryo-EM image of a solution of membrane fractions carrying OR1740 olfactory receptor at TPC = $5000 \mu\text{g mL}^{-1}$ after sonication, proteoliposomes. (D) Diameter of a population of 40 vesicles calculated directly from the electron micrographs.

As well, by CF-TEM the proteoliposomes morphology was analysed (Figure 1.10A-B). Round shaped proteoliposomes were observed with a diameter value going from 50 nm (Figure 1.10A) to 500 nm (Figure 1.10B). The presence of proteins on the cell membrane surface is also clear in Figure 1.9B.

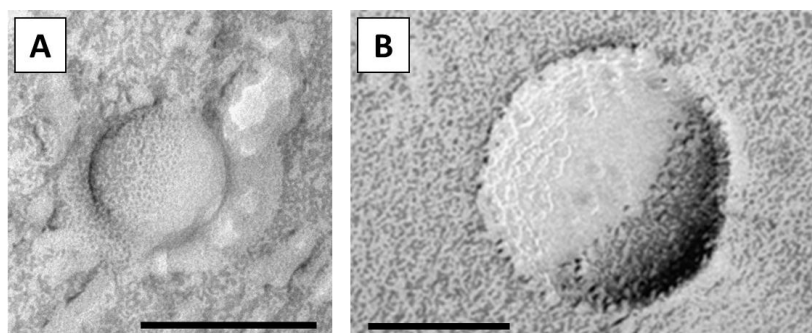


Figure 1.10 Cryo Fracture-Transmission electron microscopy (CF-TEM) images of proteoliposomes carrying the olfactory receptor OR1740. (A) Scale bar: 100 nm. (B) Scale bar: 250 nm.

In order to homogenize the proteoliposomes size distribution and to control the sample polydispersity we used different techniques: (i) sonication, (ii) extrusion, (iii) gel filtration, (iv) sonication probe, (v) centrifugation and (vi) filtration. The evaluation was done at different conditions of time, temperature, etc. and we calculated the resulting nanovesicles diameter size by DLS (Figure 1.11).

By DLS results we observed that:

- i) Sonication: Comparing the different sonication times an important decrease in the nanovesicle size was observed when the sonication reached the 20 minutes. After this time, the diameter size was maintained almost constant.
- ii) Centrifugation: It seems that increasing a little bit the centrifugation time (up to 60 min) the separation between the pellet and the supernatant (where the nanovesicles should be) was better.
- iii) Gel filtration: It did not seem that the nanovesicles separation was done correctly. The diameter size obtained was too high. More parameters optimization would be required in order to have better results.
- iv) Sonication Probe: Comparing the different ultrasonication times and the temperature reached after each ultrasonication pulse an important decrease in the nanovesicle size, as well as in the sample polydispersity was observed when the ultrasonication reached the 30 seconds. After this time, the diameter size was maintained almost constant. After 5 and 10 seconds of ultrasonication the temperature was maintained constant around 8 °C. On the other hand, after 30 seconds of ultrasonication the

temperature started to increase to 28 °C and 38 °C after 60 seconds. This issue was solved performing pulse sequences (ON/OFF) where the maximum temperature reached was 14°C.

- v) Extrusion: An important amount of sample volume was lost during the extrusion process due to the experimental set-up to obtain an homogenous population of nanovesicles.
- vi) Filtration: We observed not much notable differences with DLS results obtained with the sonication plus extrusion protocol than with the sonication plus filtration protocol.

Considering that the use of extreme conditions onto the homogenization process (such as high temperature) could denaturalize the olfactory receptors and taking into account the diameter results reported onto Figure 1.11, the combination of two of the above techniques (sonication + filtration), at controlled conditions, were finally used to obtain the desirable nanovesicles.

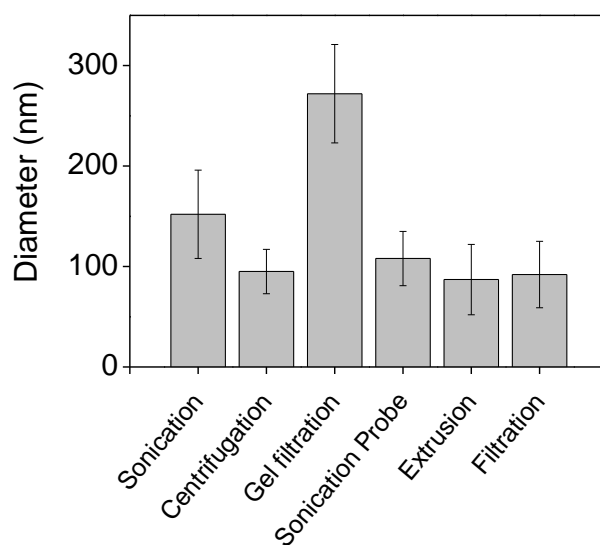


Figure 1.11 Nanovesicles diameter size calculated by DLS for each different technique at the optimal working condition (considering the smaller diameter size and less polydispersity for each technique).

Dynamic Light Scattering (DLS) experiments (with membrane fractions carrying the OR1740) show the presence of a single population of particles (after 20 minutes sonication) with size of (146 ± 34) nm in agreement with cryo-EM analysis; their relative size distribution is represented in Figure 1.12A (data in cyan). We

analysed in detail the vesicle size by NTA, which accurately enables a thorough size distribution analysis of monodisperse and polydisperse samples with a substantially improved peak resolution, compared to DLS.^{60,63} Moreover, NTA provides an improved detection of smaller vesicles, as the measured size distribution is not dramatically influenced by the presence of a small number of large, highly scattering particles.⁶⁴ The NTA results (Figure 1.12B, data in cyan) show that the membrane fractions after sonication are composed by three main populations of particles whose size are (90 ± 21) nm, (132 ± 33) nm and (216 ± 59) nm. These populations contribute respectively to the 55%, the 30% and the 15% of the sample. We performed the same measurement on one ORI7 carrying proteoliposomes and nanovesicles samples, obtaining a profile which is similar to the one reported in Figure 1.12B, after sonication, three populations can be identified in the NTA size distribution at (99 ± 23) nm, (151 ± 20) nm and (208 ± 38) nm (see Figure 1.13A).

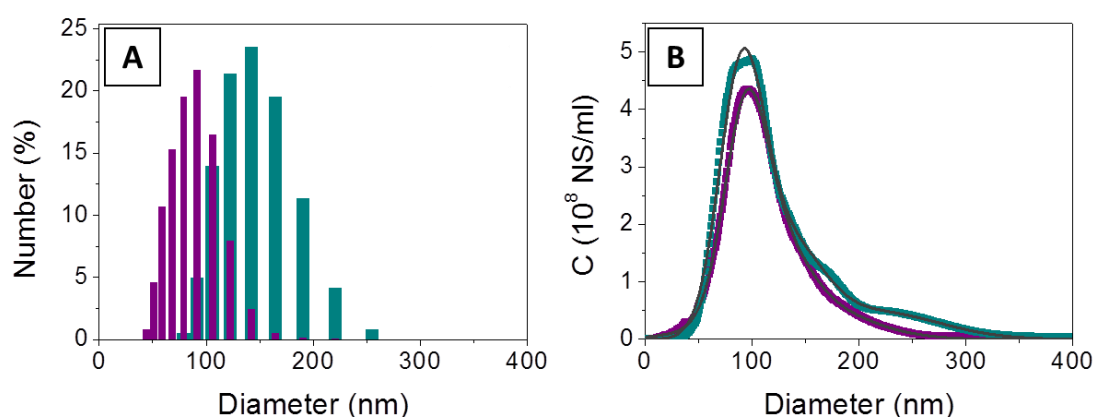


Figure 1.12 Results of DLS (A) and NTA (B) measurements of membrane fractions carrying OR1740 olfactory receptor at room temperature. The size distributions in cyan refer to sonicated samples ($\text{TPC} = 60 \mu\text{g mL}^{-1}$) while the ones in purple refer to samples, at the same concentration, which were first sonicated and then filtered (see Experimental Section). Data in (B) are fitted with the sum of 3 (sonicated sample) and 2 (sonicated + filtered sample) gaussian functions in order to extract the contribution of each population to the size distribution.

Thus, we performed after the 20 minutes sonication a filtration step by using a low-binding protein filter with pores size of $0.22 \mu\text{m}$ after sonicating the sample. We observed a shift of the size distribution measured by DLS at a lower value of (89 ± 23) nm (Figure 1.12A, data in purple); furthermore, we observed a diminished contribution of the two peaks at the higher diameters to the particles concentration in NTA

measurements (Figure 1.12B, data in purple). The overall effect of filtering is to homogenize the sample to a quasi-individual proteoliposomes population by eliminating the larger nanovesicles, more than to reduce the polydispersity of the smallest vesicles. The NTA measurements in fact show a peak at (94 ± 20) nm, with an elongated tail starting at about 130 nm that includes the biggest particles and decays to zero in correspondence of particles size = 250 nm, corresponding to the pore size of the filter. Results shown in Figure 1.12B are reproduced similarly for ORI7 carrying nanovesicles (see the Experimental Section and Figure 1.13). After the filtration step the NTA size distributions contain typically one main peak around 90 nm and an elongated tail at the high particles size contributing 40-50 % of the sample.

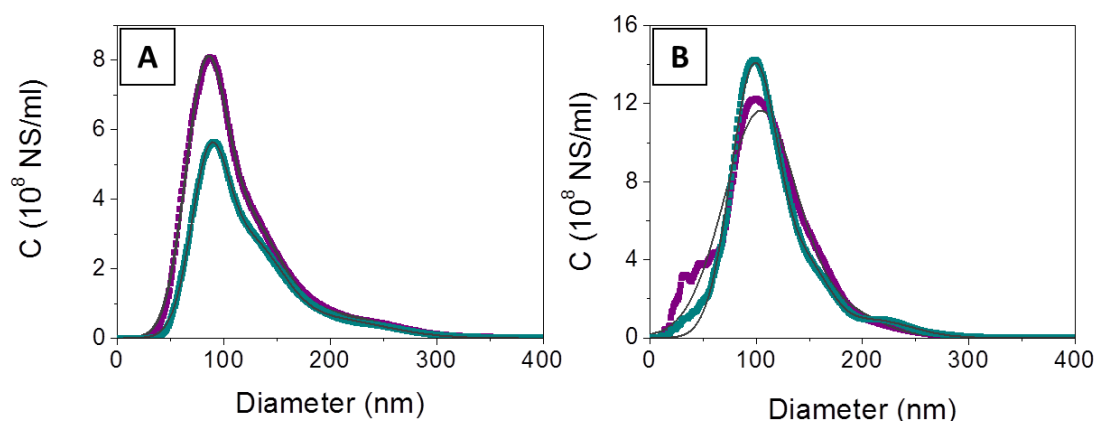


Figure 1.13 Results of NTA measurements of membrane fractions carrying OR17 olfactory receptor at room temperature: ORI7-HA (A) and c-myc-ORI7 (B). The size distributions in cyan refer to sonicated samples ($\text{TPC} = 60 \mu\text{g mL}^{-1}$) while the ones in purple refer to samples, at the same concentration, which were first sonicated and then filtered (see Experimental Section). Data are fitted with the sum of 3 (sonicated sample) and 2 (sonicated + filtered sample) gaussian functions.

It is remarkable that the preparation protocol followed improves the vesicles homogeneity. For instance, without sonication, the membrane fractions solution contains broadly distributed particles with sizes ranging from hundreds of nm to a few micrometres. After sonication and filtration vesicles of a controlled size in the range of one hundred nm are obtained with a relatively small polydispersity. Due to their size, we will refer to them as nanovesicles (NV or NS).

Finally, DLS and NTA results, combined with the TEM observation, suggest that at room temperature nanovesicles do not aggregate⁶⁵, thus indicating that thermal

agitation is sufficient to overcome eventual short range (i.e. electrostatic, Van der Waals and hydration) forces acting between individual NV.

Furthermore, the olfactory receptor genetic expression procedure does not affect the nanovesicles preparation. Figure 1.14 shows the DLS results of control proteoliposomes and control nanovesicles (vesicles from *Saccharomyces cerevisiae* yeast cell culture without any genetic modification). We can observe that the fact of olfactory receptor expression does not have any impact on the vesicles size distribution.

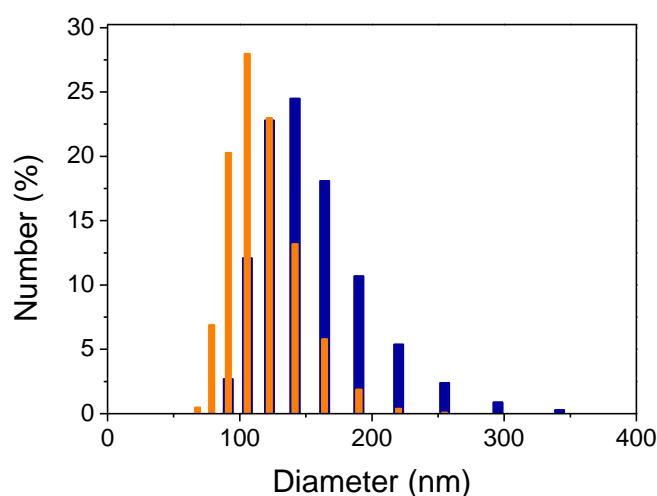


Figure 1.14 DLS size distributions of sonicated (proteoliposomes) and filtered (nanovesicles) control sample. The size distributions in blue refer to control proteoliposomes while the ones in orange refer to control nanovesicles.

1.3.2.3 Nanovesicles solution purification

In the nanovesicles solutions the presence of residuals has been recognized in the Cryo-EM images of proteoliposomes solutions were a weak background is clearly visible (see Figure 1.9B). These residuals can be clearly observed as well in Figure 1.15.

With the results obtained, we relate the observed phenomenon (the residuals present in the nanovesicles solution) to an uncontrolled presence of biomolecules, i.e. proteins and/or lipid aggregates, which are not organized in vesicles and might be still present in the resulting solution after the sonication and the filtration of the membrane fractions solution.

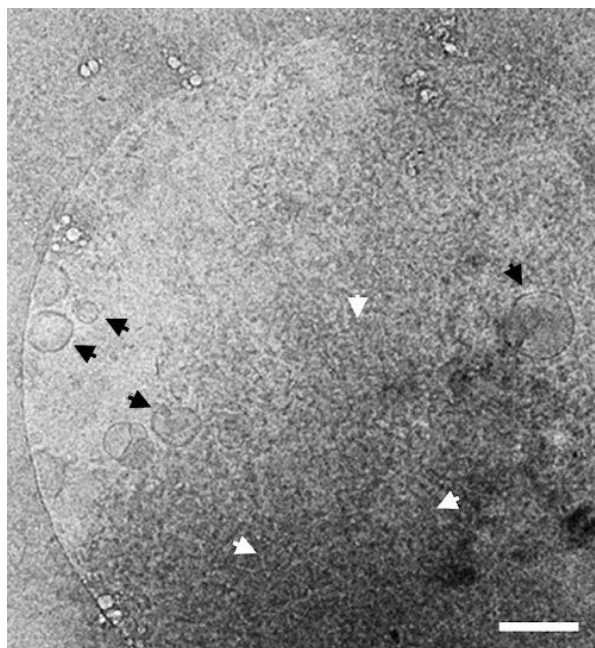


Figure 1.15. Overview of the biological components present in the solution after the production of the nanovesicles. 2D Cryo-EM image of a solution of membrane fractions carrying OR1740 olfactory receptor at TPC = 5000 $\mu\text{g mL}^{-1}$ after sonication. It was possible to observe the proteoliposomes (black arrows) and biomolecules, i.e. proteins and/or lipid aggregates (white arrows). Scale bar: 200 nm.

Several purification strategies, including further sonications, additional centrifugation steps, affinity chromatography, sucrose gradient centrifugations (with collaboration of INRA, France), did not succeed in eliminating these residuals (Figure 1.16).

In the case from using the concentration and ultracentrifugation process to purify the nanovesicles from the rest of the biological sample it can be notice (Figure 1.16A), that in the first step (after concentration) the resulting solution contained only particles smaller than 10 kDa (purple profile). We expected this result because we used a centrifugal filter with a NMWL of 10kDa to concentrate the sample. Otherwise, after the ultracentrifugation process, no significantly differences were observed in the size distribution of the particles present in each subfraction (supernatant or pellet, orange or blue profile respectively).

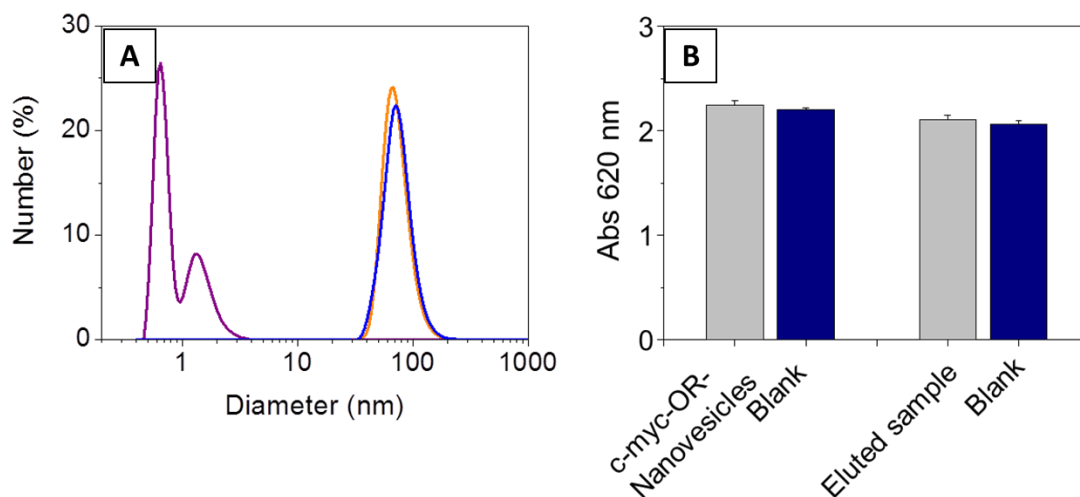


Figure 1.16 Results of DLS (A) measurements of membrane fractions carrying OR1740 olfactory receptor ($\text{TPC} = 60 \mu\text{g mL}^{-1}$) at room temperature after centrifugation-purification technique. The size distributions in purple refers to the resulting solution from sonicated and filtered samples after the Amicon Ultra-4 concentration step. While the ones in orange refer to the supernatant solution coming after the ultracentrifugation process. Finally, size distribution in blue refers to the resuspended pellet in 1 mL of PBS (see Experimental Section). (B) Absorbances evaluation from the aliquots obtained after affinity chromatography (with Protein A column) purification procedure of the proteoliposome sample. Similar results were obtained for Protein G and Protein A/G columns.

Other techniques, such as affinity chromatography was used in order to obtain a solution with pure, single nanovesicles carrying the olfactory receptors of interest. Figure 1.16B shows the absorbances obtained from the OR-nanovesicles solution (immobilized onto the column) and the rest of the sample (elute obtained after the proteoliposomes incubation, sample not attached to the column after the incubation time) by a Non-Quantitative Indirect ELISA. We expected high absorbance signal from the OR-nanovesicle solution and absorbances similar to the blank from the elute solution where nanovesicles without any olfactory receptor would be present. It is possible to observe that no significantly differences were obtained between both results. This, suggests us three main hypothesis: it would be possible that the commercial antibody was not able to select those nanovesicles carrying the c-myc-OR through the rest of the sample due to their low affinity for the c-myc tag and to their non-specific interaction for the nanovesicles, or the column did not have enough capacity to immobilized all the c-myc-nanovesicles, due to the fact that all of them carry at least one olfactory receptor, or due to the fact that the antibody immobilization in the Protein Column (A, G or A/G, the results were repeated in the three cases) was inefficient. Thus, the absorbance from the immobilized and eluted sample by affinity

chromatography is almost the same. In addition, if we observed the blank signal an important unspecific adsorption of the secondary antibody on the sample solutions is also present in both cases.

1.3.2.4 Determination of the nanovesicles concentration in solution

Once homogenized, the subsequent step is to quantify the concentration of nanovesicles in the solution. NTA was used to estimate the nanovesicles concentration in the solution⁶⁶. Such estimation is not possible by DLS, which is a technique that provides relative population values, instead of quantifications of concentration.

Using NTA it is possible to determine the nanovesicles concentration and correlate it with the total protein concentration (TPC) of nanovesicles solutions, obtained by means of a BCA Protein Assay (colorimetric assay using the BCA reagent with bovine serum albumin as standard).

The results of the calibration are shown in Figure 1.17. We find a linear dependence of the total protein concentration (TPC, expressed as $\mu\text{g mL}^{-1}$) on the nanovesicles concentration (C, expressed as NS mL^{-1} or NV mL^{-1}). For nanovesicles carrying OR1740 we found that the experimental data adapt quite well to the following Equation 1:

$$C(\text{NV} \cdot \text{mL}^{-1}) = (6.581 \pm 0.065) \cdot 10^8 \cdot \text{TPC}(\mu\text{g} \cdot \text{mL}^{-1}) \quad (\text{Eq. 1})$$

across two order of magnitudes, from 0.2 to 60 $\mu\text{g mL}^{-1}$.

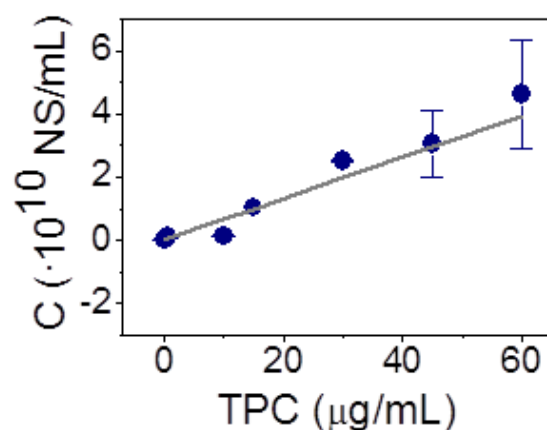


Figure 1.17 Calibration curve of OR1740-nanovesicles concentration (C), obtained from the total area of NTA size distributions at different TPC concentrations.

For nanovesicles carrying the ORI7 olfactory receptor we found a similar trend. The extracted slope was twice higher than that obtained for OR1740 carrying nanovesicles, and within the same order of magnitude (see Figure 1.18).⁶³

But we noticed that each production of yeast membrane fraction (batch) with the receptor of interest expressed by genetic engineering could have its specific calibration curve (correlation between the TPC and the nanovesicles concentration in solution). Thus, all the nanovesicles used in the present thesis (each different batch) were characterized using the BCA Protein Assay: to know the total protein concentration of the yeast membrane fraction stock, and as well characterized by the NTA technique: to correlate the total protein concentration of nanovesicles solutions with the nanovesicles concentration. The nanovesicles used and their resulting calibration curves are shown in Table 1.2 and Figure 1.18.

Table 1.2 Summary of the nanovesicles characteristics used in the present thesis).

Nanovesicles carrying	Batch (#)	Stock, TPC (mg mL ⁻¹)	C (NV mL ⁻¹) vs. TPC (μg mL ⁻¹)
c-myc-OR1740	A (26.1)	5	$C(NV mL^{-1}) = (6.581 \pm 0.065) \cdot 10^8 \cdot TPC(\mu g mL^{-1})$
	B (44)	7	$C(NV mL^{-1}) = (27.877 \pm 0.967) \cdot 10^8 \cdot TPC(\mu g mL^{-1})$
ORI7-HA	C (old)	4	$C(NV mL^{-1}) = (11.281 \pm 1.531) \cdot 10^8 \cdot TPC(\mu g mL^{-1})$
c-myc-ORI7	D (new)	5	$C(NV mL^{-1}) = (18.138 \pm 0.406) \cdot 10^8 \cdot TPC(\mu g mL^{-1})$
c-myc-OR7D4	E (58)	9	$C(NV mL^{-1}) = (16.743 \pm 0.103) \cdot 10^8 \cdot TPC(\mu g mL^{-1})$
SSTR2	F (41)	6	$C(NV mL^{-1}) = (14.668 \pm 0.703) \cdot 10^8 \cdot TPC(\mu g mL^{-1})$
	G (43)	5.7	$C(NV mL^{-1}) = (20.089 \pm 0.094) \cdot 10^8 \cdot TPC(\mu g mL^{-1})$

All the calibration curves obtained (Figure 1.18) adapt quite well to a linear fit. This suggests us that the uncontrolled presence of biomolecules observed (the residuals present in the nanovesicles solution), which are not organized in vesicles, might be mostly lipids instead of proteins. If this background was proteins, the NTA results obtained (nanovesicles concentration) would be lower than the experimental ones obtained when we would increase the TPC of the solution. Thus, we would lose the linear fit at high TPC range. This suggests us that the total protein of the sample, particularly the olfactory receptors, is embedded onto the nanovesicles and is not untied from the lipid bilayer. These results are important for the development of a biosensing platform based on the immobilization of lipid vesicles where the membrane receptors are expressed.

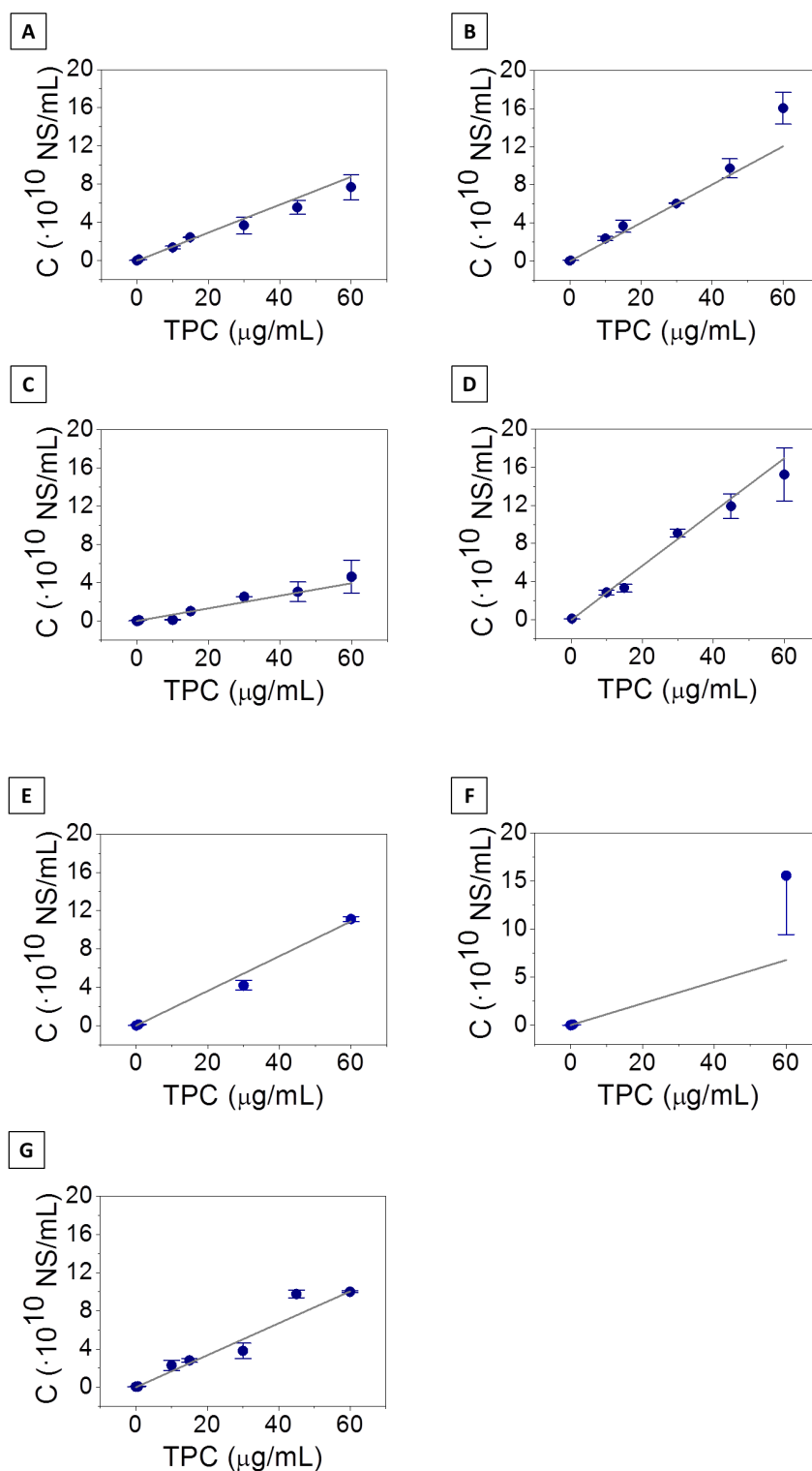


Figure 1.18. Calibration curves of nanovesicles concentration (C), obtained from the total area of NTA size distributions at different TPC concentrations. Linear dependence of the total protein concentration (TPC, expressed as $\mu\text{g/mL}$) on the nanovesicles concentration (C, expressed as NS/mL)⁶⁷. We found that the experimental data are correctly fitted by each corresponding equation presented in Table 1.2 (A) SSTR2 (F, #41) carrying nanovesicles. (B) SSTR2 (G, #43) carrying nanovesicles. (C) OR1740 (A, #26.1) carrying nanovesicles. (D) OR1740 (B, #44) carrying nanovesicles. (E) ORI7 (D, #new) carrying nanovesicles. (F) ORI7 (C, #old) carrying nanovesicles. (G) OR7D4 (E, #58) carrying nanovesicles.

1.4 Conclusions

In this **Chapter** we have demonstrated that membrane fractions from yeast cells spontaneously form closed spherical nanovesicles in solution as determined at the level of single nanovesicles from cryo-Transmission Electron Microscopy (cryo-EM). Moreover, nanovesicles density and size distribution are determined quantitatively with Nanoparticle Tracking analysis (NTA). A simple method to homogenize the size of the nanovesicles to a diameter of ~ 100 nm at a concentration of more than 10^{10} nanovesicles mL^{-1} is also presented. It is also showed that after a genetic engineering process the olfactory receptors of interest were well expressed in the yeast membrane as has been shown by Western Blot.

1.5 References

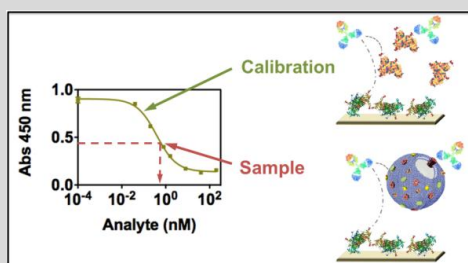
- (1) Dorsam, R.T., Gutkind, J.S. *Nat. Rev. Cancer*, **2007**, *7*, 79-94.
- (2) Maggiolini, M., Lappano, R. *Nat. Rev. Drug Discovery*, **2011**, *10*, 47-60.
- (3) Insel, P.A., Tang, C.M., Hahntow, I., Michel, M. *C. Biochim. Biophys. Acta – Biomembranes*, **2007**, *1768*, *4*, 994-1005.
- (4) Jacoby, E., Bouhelal, R., Gerspacher, M., Seuwen, K. *Chem. Med. Chem.*, **2006**, *1*, *8*, 761-782.
- (5) Bockaert, J.; Pin, J. P. *EMBO J.* **1999**, *18*, 1723 – 1729.
- (6) Cornu, J.-N., Cancel-Tassin, G., Ondet, V., Girardet, C., Cussenot, O. *Eur. Urol.*, **2011**, *197* – *201*.
- (7) Willis, C.M., Church, S.M., Guest, C.M., Cook, W.A., McCarthy, N., Bransbury, A. J., Church, M.R.T., Church, J.C.T. *BMJ.* **2004**, *329*, 712.
- (8) Kim, T.H., Lee, S.H., Lee, J., Song, H.S., Oh, E.H., Park, T.H. Hong, S. *Adv. Mater.*, **2009**, *21*, 91–94.
- (9) Vidic, J., Pla-Roca, M., Grosclaude, J., Persuy, M.-A., Monnerie, R., Caballero, D., Errachid, A., Hou, Y., Jaffrezic-Renault, N., Salesse, R., Pajot-Augy, E., Samitier, J. *Anal. Chem.*, **2007**, *79*, 3280-3290.
- (10) Jin, H.J., Lee, S.H., Kim, T.H., Park, J., Song, H.S., Park, T.H., Hong, S. *Biosens. Bioelectron.* **2012**, *35*, 335– 341.
- (11) Yoon, H., Lee, S.H., Kwon, O.S., Song, H.S., Oh, E.H., Park, T.H., Jang, J. *Angew. Chem.* **2010**, Int. Ed. *48*, 2755 –2758.
- (12) Bally, M., Bailey, K., Sugihara, K., Grieshaber, D., Vörös, J., Städler, B. *Small.* **2010**, *6*, *22*, 2481-2497.
- (13) Mellstedt, H., Niederwieser, D., Ludwig, H. *Annals of Oncology*, **2008**, *19*, 411-419.
- (14) Breer, H., Krieger, J., Meinken, C., Kiefer, H., Strotmann, J. *Ann NY Acad Sci*, **1998**, *855*, 175–181.
- (15) Kiefer H, et al. *Biochemistry*, **1996**, *35*, 16077–16084.
- (16) Minic Vidic, J., Grosclaude, J., Persuy, M.-A., Aioun, J., Salesse, R., Pajot-Augy, E. *Lab Chip*, **2006**, *6*, 1026.
- (17) Kaiser, L., Graveland-Bikker, J., Steuerwald, D., Vanberghem, M., Herlihy, K., Zhang, S. *PNAS*, **2008**, *105*, *41*, 15726-15731.

- (18) Lundstrom, K., Wagner, R., Reinhart, C., Desmyter, A., Cherouti, N., Magnin, T. et al. *J Struct Funct Genomics*, **2006**, *7*, 77-91.
- (19) Lundstrom, K. *TRENDS in Biotechnology*, **2005**, *23*, 2, 103-108
- (20) Sarramegna, V., Talmont, F., Demange, P., Milon, A. *Cell. Mol. Life Sci.*, **2003**, 1529-1546.
- (21) Minic, J. et al. *Current Medical Chemistry*, **2005**, *12*, 8, 961–969.
- (22) Minic, J., Persuy, M.-A., Godel, E., Aioun, J., Connerton, I., Salesse, R., Pajot-Augy, E. *FEBS Journal*, **2005**, *272*, 524.
- (23) King, K., Dohlman, H.G., Thorner, J., Caron, M.G., Lefkowitz, R.J. *Science*, **1990**, *250*, 121-123.
- (24) Sander, P., Grunewald, S., Bach, M., Haase, W., Reilander, H. et al. *Eur J Biochem*, **1994**, *226*, 697-705.
- (25) David, N.E., Gee, M., Andersen, B., Naider, F., Thorner, J. et al. *J Biol Chem*, **1997**, *272*, 15553-15561.
- (26) Erlenbach, I., Kostenis, E., Schmidt, C., Hamdan, F.F., Pausch, M.H. et al. *J Neurochem*, **2001**, *77*, 1327-1337.
- (27) Lee, J.Y. et al. *Enzyme and Microbial Technology*, **2006**, *39*, 3, 375–380.
- (28) Lindsay, M. A. *Nat. Rev. Drug Discov.*, **2003**, *2*, 831.
- (29) Lundstrom, K.J. *Cell. Mol. Med.*, **2007**, *11*, 224.
- (30) Fruh, V., Ijzerman, A.P., Siegal, G. *Chem. Rev.*, **2011**, *111*, 640.
- (31) Salafsky, J., Grove, J.T., Boxer, S.G. *Biochemistry*, **1996**, *35*, 14773.
- (32) Chan, Y.H., Boxer, S.G. *Curr. Opin. Chem. Biol.*, **2007**, *11*, 581.
- (33) Tanaka, M., Sackman, E. *Nature*, **2005**, *437*, 656.
- (34) Neumann-Spallart, C., Pittner, F., Schalkhammer, T. *Appl. Biochem. Biotech.*, **1997**, *68*, 153.
- (35) Bieri, C., Ernst, O.P., Heyse, S., Hofmann, K.P., Vogel, H. *Nat. Biotechnol.*, **1999**, *17*, 1105.
- (36) Ludtke, S.J., He, K., Wu, Y., Huang, H.W. *Biochim. Biophys. Acta*, **1994**, *1190*, 181.
- (37) Fang, Y., Lahiri, J., Picard, L. *Drug Discov. Today*, **2003**, *8*, 755.
- (38) Wittenberg, N.J., Im, H., Johnson, T.W., Xu, X., Warrington, A.E., Rodriguez, M., Oh, S.-H. *ACSNano*, **2011**, *5*, 7555.
- (39) Pollard, H.B., Lee Burns, A., Rojas, E. *J. Membr. Biol.*, **1990**, *117*, 101.
- (40) Bayley, H., Cremer, P.S. *Nature*, **2001**, *413*, 226.

- (41) Reimhult, E., Kumar, K. *Trends in Biotechnol.*, **2008**, 26, 82.
- (42) Cruciani, R.A., Barker, J.L., Durell, S.R., Raghunathan, G., Guy, H.R., Zasloff, M., Stanley, E.F. *Eur. J. Pharmacol., Mol. Pharmacol. Sect.*, **1992**, 226, 287.
- (43) Chan, C.P.Y., Mak, W.C., Cheung, K.Y., Sin, K.K., Yu, C.M., Rainer, T.H., Renneberg, R. *Annu. Rev. Anal. Chem.* **2013**, 6, 191-211.
- (44) Yang, L., Guo, S., Li, Y., Zhou, S., Tao, S. *Acta Biochim Biophys Sin* **2011**, 43, 3, 161-171.
- (45) Chang, T.W. *J. Immunol. Methods* **1983**, 65, 217–223.
- (46) Hall, D.A., Ptacek, J., Snyder, M. *Mech Ageing Dev.* **2007**, 128, 1, 161-167.
- (47) Gomila, G. et al. *Sensors and Actuators B. Chemical.* **2006**, 116, 1–2, 66–71.
- (48) Minic, J., Grosclaude, J., Aïoun, J., Persuy, M.-A., Gorojankina, T., Salesse, R., Pajot-Augy, E., Hou, Y., Helali, S., Jaffrezic-Renault, N., Bessueille, F., Errachid, A., Gomila, G., Ruiz, O., Samitier, J. *Biochim. Biophys. Acta*, **2005**, 1724, 324.
- (49) Rao, N.M., Silin, V., Ridge, K.D., Woodward, J.T., Plant, A.L. *Anal. Biochem.*, **2002**, 307, 117.
- (50) Mombaerts, P. *Nat. Rev. Neurosci.* **2004**, 5, 263-278.
- (51) Von Dannecker, L.E.C., Mercadante, A.F., Malnic, B. *PNAS*, **2006**, 103, 9310 – 9314.
- (52) Zhao, H., Ivic, L., Otaki, J.M., Hashimoto, M., Mikoshiba, K., Firestein, S. *Science*, **1998**, 279, 237–242.
- (53) Takahashi, Y.K., Nagayama, S., Mori, K. *J. Neurosci.*, **2004**, 24, 40, 8690 – 8694.
- (54) Keller, A., Zhuang, H., Chi, Q., Vossball, L. B., Matsunami, H. *Nature*. **2007**, 449, 468-472.
- (55) Xue, J., Dial, G. D., *Swine Health and Production*, **1997**, 5, 4, 151–158.
- (56) Patel, Y.C. *Frontiers in Neuroendocrinology*, **1999**, 20, 3, 157–198.
- (57) Diéguez, L. *Thesis: Optical Grating Coupler Biosensor and Biomedical Applications.* **2012**. Universitat de Barcelona (UB-IBEC).
- (58) Torchillin, V.P., Weissing, V. *Book: Liposomes: a practical approach.* **2003**. ISBN-10: 0199636540.
- (59) López, O., López-Iglesias, C., Cócera, M., Walther, P., Parra, J.L., de la Maza, A. *J. Struct. Biol.* **2004**, 146, 302-309.
- (60) Filipe, V., Hawe, A., Jiskoot, W. *Pharmaceutical Research*, **2010**, 27, 796.
- (61) Walker, G.M. *Book: Yeast Physiology and Biotechnology*, John Wiley & Sons, Chichester, **1998**, 12.

- (62) Li, S., Song, K.S., Lisanti, M.P. *J. Biol. Chem.* **1996**, *271*, 1, 568-573.
- (63) Dragovic, R.A., Gardiner, C., Brooks, A.S., Tannetta, D.S., Ferguson, D.J.P., Hole, P., Carr, B., Redman, C.W.G., Harris, A. L., Dobson, P.J., Harrison, P., Sargent, I.L. *Nanomed. Nanotechnol. Biol. Med.*, **2011**, *7*, 780.
- (64) Van Der Pol, E., Hoekstra, A.G., Sturk, A., Otto, C., Van Leeuwen, T.G., Nieuwland, R. *J. Thromb. Haemost.*, **2010**, *8*, 2596.
- (65) Sabín, J., Prieto, G., Ruso, J.M., Hidalgo-Álvarez, R., Sarmiento, F. *Eur. Phys. J. E.* **2006**, *20*, 401-408.
- (66) Sokolovaa, V., Ludwigb, A.-K., Hornungb, S., Rotana, O., Hornb, P.A., Epplea, M., Giebelb, B. *Colloids Surf. B*, **2011**, *87*, 146.
- (67) Calò, A., Sanmartí-Espinal, M., Iavicoli, P., Persuy, M.-A., Pajot-Augy, E., Gomila, G., Samitier, J. *Soft Matter*, **2012**, *8*, 46, 11632 – 11643.

Chapter 2. A novel immunochemical strategy for quantification of transmembrane proteins on natural nanovesicles.



Membrane receptors are involved in a variety of biochemical pathways and therefore constitute important targets for therapy and development of new drugs. Bioanalytical platforms and binding assays, using these transmembrane

*receptors, for drug screening or diagnostic require building well-characterized lipid membrane arrays, acting as supports to prevent protein denaturation during biochip processing. Quantification of the protein receptors in such lipid membrane arrays is a key issue in order to produce reproducible and well-characterized chips. We report in this **Chapter** for the first time a novel immunochemical analytical approach for the quantification of transmembrane proteins (i.e. G-protein-coupled receptor, GPCR) in their natural lipid environment. The procedure allows direct determination of tagged receptors (i.e. c-myc tag) without any previous protein purification or extraction steps. The proposed approach uses monoclonal antibodies addressed against the c-myc tag, frequently used in protein expression, on a microplate-based ELISA format. The immunochemical method quantifies this tag on proteins or bioreceptors embedded in nanovesicles with detectability in the picomolar range, using protein bioconjugates as reference standards. The applicability of the method is demonstrated through the quantification of the c-myc-olfactory receptors (ORs, c-myc-OR1740 and c-myc-OR7D4) in plasma membrane nanovesicles (NVs). The method reported opens up the possibility to develop well-characterized drug-screening platforms based on this important group of receptors, embedded on membranes.*

2.1 Background

GPCRs (G-protein-coupled receptors) are a large family of seven-transmembrane domain proteins involved in cell-response pathways to a variety of external signals and important ligands, such as hormones, neurotransmitters and inflammatory mediators^{1,2,3,4} (Figure 2.1). In fact, GPCRs are targeted by approximately 60% of all therapeutic drugs⁵.

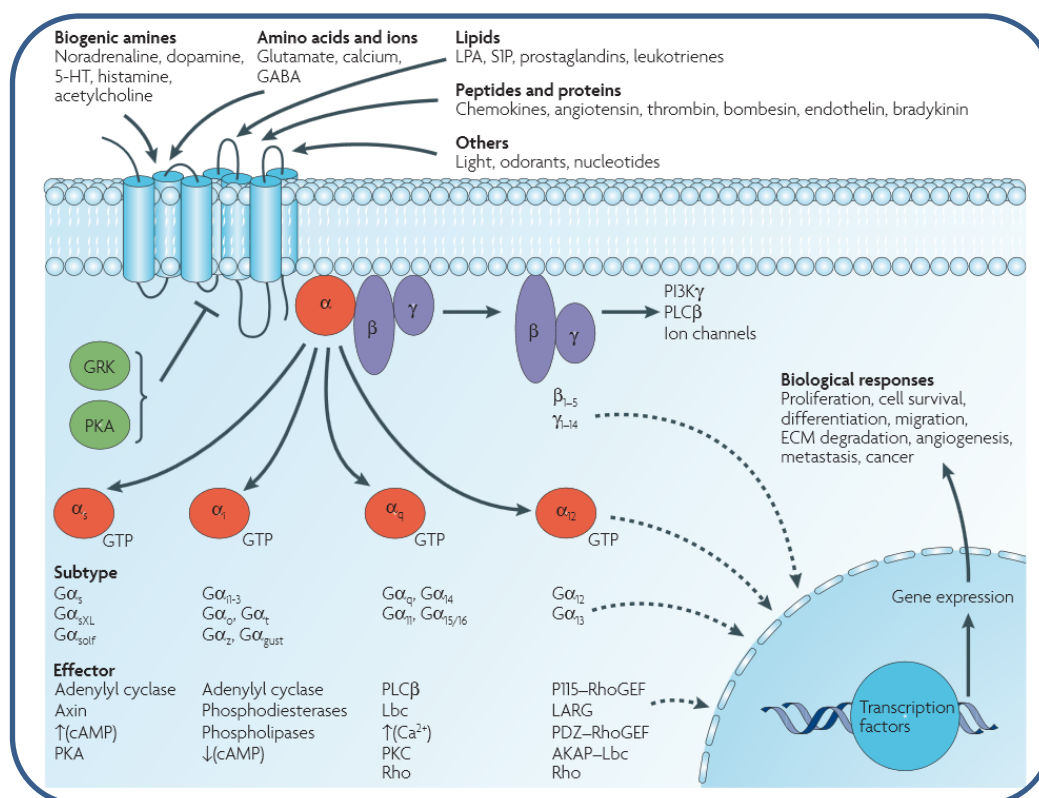


Figure 2.1 Different ligands use G-protein-coupled receptors (GPCRs) to stimulate membrane, cytoplasmic and nuclear targets. GPCRs interact with heterotrimeric G-proteins composed of α , β and γ subunits that in the resting state are GDP bound. Agonist binding triggers a conformational change in the receptor, which catalyses the dissociation of GDP from α subunit followed by GTP-binding to G_α and the dissociation of G_α from $G^{\beta,\gamma}$ subunits. The α subunits of G proteins are divided into four subfamilies and a single GPCR can couple to either one or more families of G_α proteins. Each G protein activates several downstream effectors. The G^β subunits and G^γ subunits function as a dimer to activate many signaling molecules, including phospholipases, ion channels and lipid kinases⁶.

Therefore, technology platforms (i.e. bioassay and biosensor microarrays) for drug screening based on the use of such receptors would improve the efficiency of the drug development pipeline at pre-clinical stages. Receptor binding assays developed for

this purpose require building lipid membrane arrays, acting as supports of these transmembrane proteins, to prevent denaturation during biochip processing and ensure their biofunctionality⁷⁻¹⁰ (Figure 2.2). Native liposomes, isolated directly from cell sources containing recombinant membrane proteins, retain the fluidity and lipid order of the original cell membrane, parameters that are relevant to maintain the functionality of the receptor^{11,12}. Natural nanovesicles (NVs) produced from genetically engineered cells have been reported to be promising building blocks for sensing biodevices,¹³⁻¹⁸ though, their production remains challenging¹⁹⁻²¹ in part because of the low protein expression level achieved²².

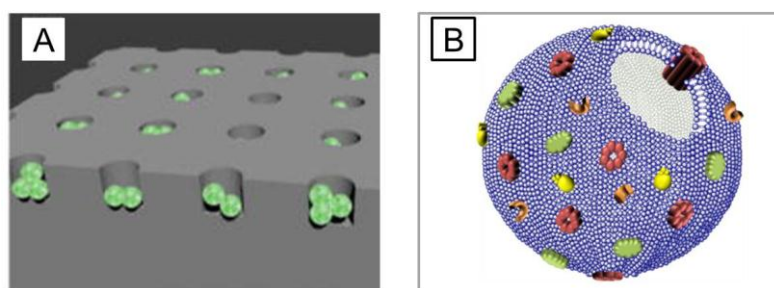


Figure 2.2 (A) Schematic illustration of nanovesicles deposited onto a microarray substrate¹⁰. (B) Zoom of one of the nanovesicles (green) from Figure 2.2A: scheme of the natural lipidic nanovesicles carrying GPCRs expressed by genetic engineering.

Several years ago, Minic and co-workers reported the preparation of the human olfactory receptor (OR) c-myc-OR1740 (ORL520 in OrDB) and pJH2-somatostatin receptor subtype 2 (SSTR2) expressed in yeast *Saccharomyces cerevisiae* cultures⁸, as well as the preparation and characterization of NVs containing such receptors^{18,23}. However, their characterization regarding direct quantification of the number of GPCR molecules (the olfactory receptors) expressed and embedded in the NVs, as well as in the sensor array, once the NVs were immobilized, was not possible. Knowing the number of functional receptor molecules on a biochip or sensor array is a key issue in order to accomplish reliable and reproducible results.

In addition to peptide tags combined with covalent labeling²⁴ or mutagenesis assays²⁵, GPCRs can be determined by methods, such as single-molecule²⁶ or TIRF microscopy²⁷. However, these approaches are not suitable for the development of well-characterized membrane-based protein biosensor arrays.

In 2010, Nonaka and co-workers²⁴ demonstrated for the first time a novel labelling method that allow to elucidate functional modification of cell surface proteins, such as GPCR proteins, by a nonenzymatic reaction between a short peptide tag (14-amino acid at their outer membrane N-termini) and a small molecular probe. This methodology allows the GPCR fluorescence visualization in living cells but not their quantification (Figure 2.3).

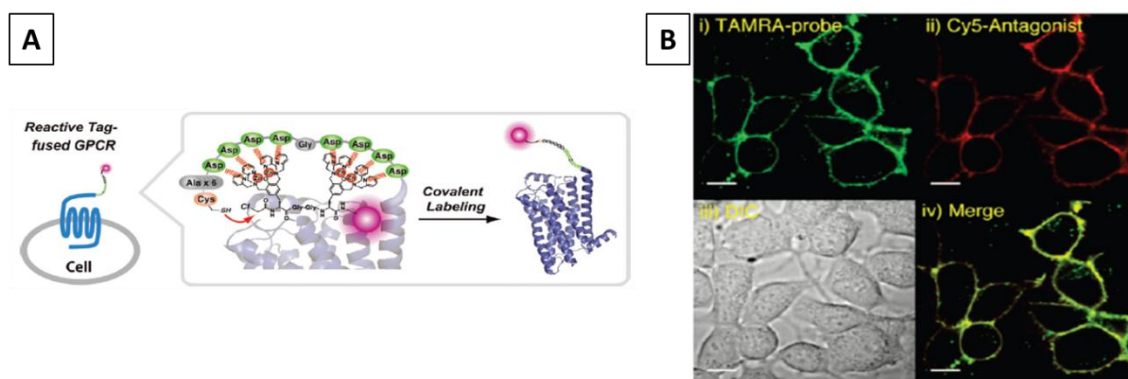


Figure 2.3 (A) Scheme of the selective covalent labeling of a tag-fused GPCR protein on the surface of living cells. (B) Covalent labeling of GPCR expression on the surface of HEK-293 cells. Fluorescence imaging of CAD6D4x2 tag-fused bradykinin receptor type 2 (B2R, target GPCR). The fluorescence images were obtained using two different channels corresponding to the probe (i) and a protein expression marker (ii) such as Cy5-appended antagonist peptide or EGFP. The transmission image is shown in (iii) and the overlay image of (i) and (ii) is shown in (iv). Scale bar: 10 μm .²⁴

Later on, in 2011, Serge²⁶ present the first GPCR quantitative detection of internalization of the cAR1, as GPCR model, in live *D. discoideum* cells. It was allowed thanks to the sensitivity of single-molecule microscopy used for the bioimaging. It was then, in 2011, when finally, the visualization and quantification of integral membrane proteins was carried on nanovesicles instead in the whole live cell. Specifically, Mutch²⁷, developed an approach to quantify native proteins in isolated, single synaptic vesicles, he used it to quantify seven major membrane proteins of rat brain synaptic vesicles by labelling them with fluorescence antibodies and imaging them using TIRF microscopy (Figure 2.4).

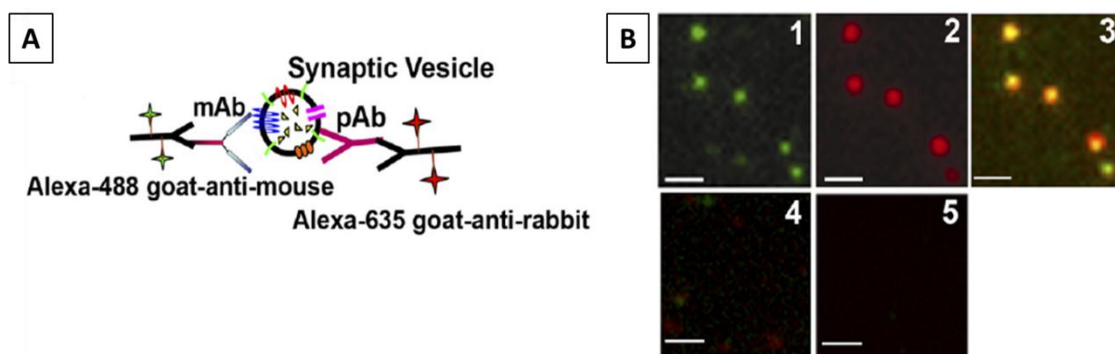


Figure 2.4 (A) Scheme of the two-color labeling in which synaptic vesicles were labeled with antibodies directed against two different synaptic vesicle protein, each of which was detected with a different colored fluorescent secondary antibody. (B) Vesicle labeling. (1,2) Sample image of synaptic vesicles labeled with anti-SV2 and goat-anti-mouse Alexa-488 (green, 1) and anti-synaptotagmin1, goat-anti-rabbit Alexa-635 (red, 2). (3) Two-color overlay in which colocalization of the two probes appears yellow. (4) Sample in which primary antibodies were excluded from the labeling method. (5) Sample in which vesicles were excluded from the labeling method. Scale bar: $1\mu\text{m}$.²⁷

Until then, any protein from the GPCR family had been quantified in nanovesicles. For this reason, we have focused on developing a straightforward method for detecting and quantifying c-myc-tagged-membrane proteins or receptors, such as c-myc-GPCRs, in the form of lipidic NVs. The strategy has consisted on developing high affinity specific antibodies against the c-myc tag, one of the most important peptide tag used in protein expression.

The importance to work with specific antibodies with high affinity is that using them in immunoassays allows us to detect low amount of antigen. It is known that the affinity is the antibody property that measures the strength of interaction between an epitope and an antibody's antigen binding site. High-affinity antibodies will bind a greater amount of antigen in a shorter period of time than low-affinity antibodies. The key issues to control in order to obtained high-affinity antibodies are the good design of the immunized antigen and the screening of the hybridomas to select the desired antibody.

Briefly, the monoclonal antibody production is based on immunization of mice with antigen to stimulates immune cells, which produce antibodies that recognize the antigen. At this point, serum can be collected to obtain a polyclonal antibody mixture, or alternatively antibody-producing cells can be fused with tumour cells to generate immortalized hybridoma cells. The hybridoma cells are screened to identify individuals

that secrete antibodies with desired specificities, and cells of interest can be amplified by clonal expansion and maintained indefinitely as cell lines that produce a unique monoclonal antibody²⁸ (Figure 2.5).

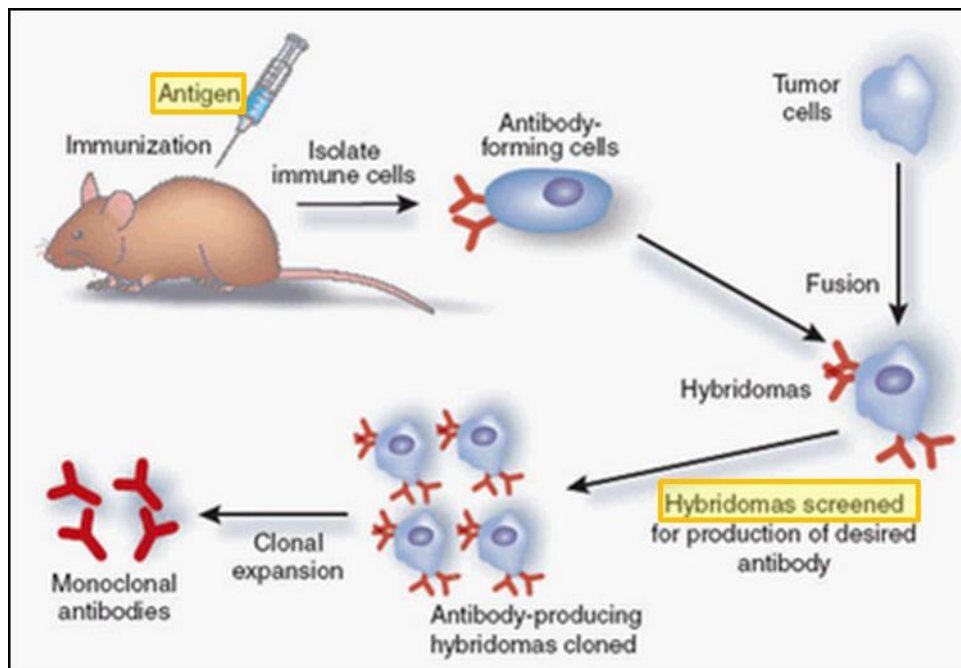


Figure 2.5 Scheme of the production of monoclonal antibodies by the hybridoma method²⁸. In yellow are highlighted the two main issues to control in order to obtain high affinity antibodies: the antigen design used in the immunization and the hybridoma screening.

In our case, the c-myc tag peptide to detect and quantify can be fused to either the N- or the C-terminus of the protein of interest without changing the tertiary structure²⁹ or biological activity of the protein³⁰. Although other techniques, such as fluorescence polarization³¹, have been used to quantify c-myc fused proteins, such approaches allow the quantification of only c-myc-protein concentration on a cell extract and not the number of c-myc-protein molecules per NV (Table 2.1).

Table 2.1 Measurements of c-myc-tagged SF9-14 in crude host cell lysate by fluorescence polarization (FP) assay³¹.

<i>Spike medium</i>	<i>Spiked SF9-14 (nM)</i>	<i>Measured SF9-14 (nM)</i>	<i>Deviation^a (%)</i>
PBS	0	0	0
	285	271	5
	570	572	0.3
<i>E. coli</i>	0	0	0
	285	228	20
	570	456	20
<i>Pichia^b</i>	0	85	NA
	285	397	9 ^b
	570	706	9 ^b
<i>T. ni</i>	0	0	0
	285	256	10
	570	441	23
SF+	0	0	0
	285	241	15
	570	441	23
HEK-293	0	0	0
	285	338	18
	570	669	17

Samples were prepared by spiking SF9-14 in the host cell lysate. The assay solution contained 100nM c-myc-peptide-fl, 100 nM anti-c-myc Fab, 0.2 mg/mL BSA, 5 mM CHAPS, and host cell lysate in PBS buffer. The total assay volume was 100 μ L. The FP signal was stable for 2h incubation time. The concentration was calculated based on an average of FP readings between 5 and 120 min after mixing.

^a The deviation was calculated as the percentage of the difference between the spiked and the measured concentrations over the spiked concentration.

^b Addition of *Pichia* cell lysate containing no c-myc-tagged protein slightly suppressed the FP signal, which resulted in a background reading. This background (85nM) was subtracted from the subsequent measurements of the spiked samples.

The quantification of small molecules, such as the peptide tags, at very low concentrations can be also performed by immunoassays methods under competitive conditions.

Immunoassays methods are simple, fast, low cost, sensitive, selective, multistep analysis and easy learned. Their use for the analysis of many compounds on different research fields have been increase in the last years. Normally, these assays are performed on microplates that allow the high throughput screening analysis working

with large number of samples in parallel with small volume (50 μ L). However, their main drawback is the tendency towards a false positive due to matrix effects in real sample measurements. Thus, an accurate control of it needs to be performed.

ELISA, also called *Enzyme-linked Immunosorbent assay*, is a very sensitive test that it is used to detect antibodies or specific antigens. As all the enzyme immunoassays it uses the enzyme substrate reaction to produce a chromogen that often absorbs in the visible region. Thanks to the amplification effect of the enzyme label it is possible to develop very sensitive assays using absorbances measurements at the end point. There are different formats of ELISA: indirect, direct, sandwich and competitive. We focused our studies working with the combination of indirect competitive assay (Figure 1.6A). The general strategy for competitive assays is based on the competition of the antibody between the free analyte (Ag or antigen) in solution and a fixed amount of labelled antigen (coating antigen, immobilized onto the 96-well microplate) for a limited number of antibody (Ab) binding sites, low concentration of antibody when we work under an indirect format. Then, the antibody complex was measured indirectly by the quantification of bound Ab with a second labelled Ab (labelled anti-IgG). At the end, the amount of labelled antigen, hence, the free analyte is determined. A decrease in the absorbance signal is directly proportional to the amount of analyte present in the sample.

On the other hand, the competitive immunoassay can be performed also directly, when the antibody, instead the antigen, is fixed on the substrate (Figure 2.6B). There are different labels used to quantify the immunoreaction. Nowadays, the most common used labels are the enzymes. Then, the enzyme immunoassays use the enzyme substrate reaction to produce a chromogen often absorbing in the visible region.

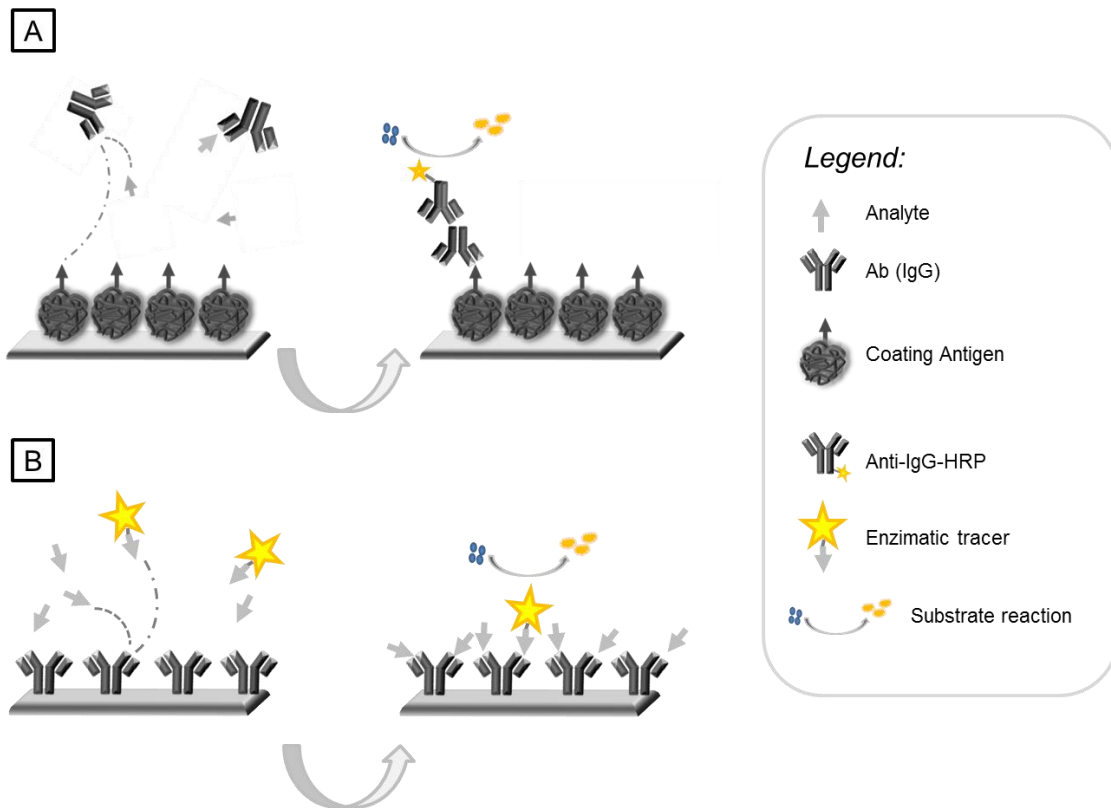


Figure 2.6 Scheme of competitive ELISA immunoassays for the detection of low molecular weight analytes. **(A)** Indirect competitive ELISA. **(B)** Direct competitive ELISA.

The second type of solid phase immunoassay, and the most familiar to most researchers, is the sandwich assay. This assay involves two antibodies which “sandwich” the analyte between them. To perform these assays the analyte needs to be large enough to allow simultaneous binding of two antibodies, i.e. proteins and peptides greater than 20 amino acids in length. The plates are coated with a capture antibody that is specific to the analyte. The antibody will bind the analyte present in a sample. A second antibody, called the detection antibody, which recognizes a different epitope on the analyte is also added to the well, resulting in the analyte being “sandwiched” between the two antibodies. The excess of unbound reagents are then washed away. The presence of the detection antibody, which is directly proportional to the amount of analyte present, can be quantified by a few different methods. The two most common methods for tagging are biotinylation or direct conjugation of an enzyme to the detection antibody (direct format). If the detection antibody is unlabelled, then a second detection antibody will be needed resulting in an indirect sandwich ELISA (Figure 2.7).

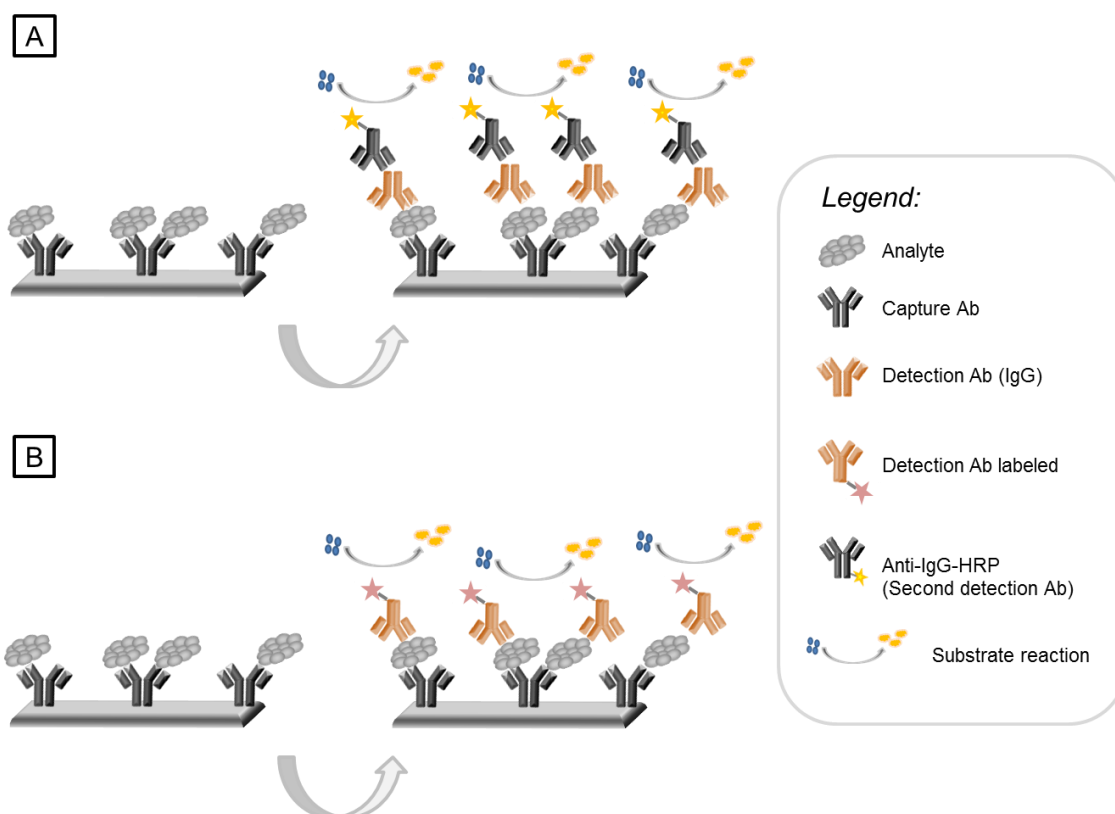


Figure 2.7 Scheme of sandwich ELISA immunoassays for the detection of high molecular weight analytes. (A) Indirect sandwich ELISA. (B) Direct sandwich ELISA.

Sometimes, the production of a proper hapten is necessary in order to obtain a successful ELISA. A hapten is a small organic molecule (MW < 2000 Da) that is not able to elicit an immune response (production of antibody molecules) in an animal. As well, it is a molecule analogous to the target analyte and properly functionalized to allow covalent attachment to a carrier compound. To be immunogenic, the analyte may be transformed to an immunogenic molecule conjugating it to a large carrier (molecule), i.e. a protein. It is important that the carrier may be one that does not elicit an immune response by itself. The ideal hapten is the one that preserves most of the steric and electronic characteristics of the analyte and mimics the target analyte in chemical structure as closely as possible, consequently increases the sites for potential molecular recognition.

As well, the attachment point to the carrier protein is another issue to be considered. It should be placed far enough from the important sites of the target analyte and separated by a spacer arm. It is reported in the literature that a spacer length between 3-6 atoms has been considered as the optimum size^{32,33}. On the other hand, in

the last 10 years other authors suggest that the spacer arm length of the immunizing hapten is not important for assay sensitivity³⁴. Otherwise, is a factor that has to be into account in the immunogen design. The spacer arm should preferably replace a carbon hydrogen bond instead of a functional group. Ideally, a spacer arm should be a chain of methylenes terminated by a functional group (-COOH, -OH, -SH, -NH₂) through which the carrier protein will be attached.

In this *Chapter* we demonstrate that competitive enzyme-linked immunosorbent assay (ELISA) can be used to quantitatively determine the expression level of two different olfactory receptors (the human OR1740 and the chimpanzee OR7D4 receptors) tagged with the c-myc epitope at their N-terminus in vesicles from *Saccharomyces Cerevisiae* (nanovesicles, NV). To the best of our knowledge, the present work is the first that reports the possibility to perform accurate quantification of c-myc-tagged-GPCRs, directly in the form of lipidic nanovesicles (NVs).

The decision to use a competitive ELISA format instead a sandwich one is due to the fact of the number of olfactory receptors per nanovesicle. In the case that this number was 1 OR/NV their quantification could not be performed by this format. In that hypothetic case, because the c-myc peptide attached to the OR would be detect for the capture antibody, any other c-myc tag would be free to be detected by the detection antibody and their quantification would not be performed. Thus, and due to the low molecular weight of the c-myc peptide (10 amino acids) the best strategy to carry on the olfactory receptor quantification is by a competitive ELISA format.

However, and it has been mentioned above, the main drawback of the competitive ELISA format are the matrix effects. Thus, nanovesicles carrying the SSTR2 receptor without the c-myc tag have been used as model sample to study and control this effect on our real sample.

2.2 Materials and Experimental Procedures

2.2.1 Materials

Biochemical reagents such as c-myc peptide (*EQKLISEEDL*), bovine serum albumin (BSA), albumin from white chicken egg (OVA), conalbumin from white chicken egg (CONA), horseradish peroxidase (HRP), anti-mouse IgG peroxidase (anti-IgG-HRP for ELISA assays) and tetramethylbenzidine (TMB) were purchased from Sigma Chemical Co. (St. Louis, MO). The amino-dextran (MW 70000) was purchased from Invitrogen, Molecular Probes (Paisley, UK). The commercial monoclonal anti-c-myc IgG₁ 9E10 antibody and the antiproteases inhibitors cocktail were supplied by Roche Diagnostics (Mannheim, Germany). The anti-mouse IgG peroxidase (anti-IgG-HRP for Western Blot) was from Millipore (Temecula, CA). Tris (hydroxymethyl) aminomethane were from Merck (Darmstadt, Germany). The FC14 detergent was acquired from Affymetrix Anatrace products (Santa Clara, USA). Nitrocellulose membranes (HybondTM-C extra) were from Amersham (GE Healthcare Europe). ProfoundTMC-Myc Tag IP/Co-IP kit was supplied by Thermo Scientific (Rockford, IL, USA). N-succinimidyl 3-maleimidopropionate ($M(CH_2)_2CO$) and N-succinimidyl iodoacetate (CH_2CO) crosslinkers were synthesized in the lab following protocols described in previous studies^{35,36}. Two modified c-myc peptides (Peptide EQKLISEEDL-Cys, named C₁, and peptide Cys-EQKLISEEDL, named C₂) were synthesized as C-terminal amides of using standard Fmoc solid-phase protocols by the Platform of Peptide Synthesis the CIBER BBN Biomedicine Scientific Services (<http://www.ciber-bbn.es>). The two peptides were characterized by mass spectrometry. Purities were >94% as assessed by HPLC (*Appendix 1*). These peptides were used as haptens for the preparation of bioconjugates and as analytes for the competitive assays. The corresponding bioconjugates were characterized by MALDI-TOF-MS. MaxiSorp polystyrene 96-well plates were purchased from Nunc (Roskilde, Denmark).

2.2.2 Buffers and Solutions

The PBS phosphate buffer used (10 mM) was a 0.8% saline solution at pH 7.5. The PBST buffer contained PBS with 0.05% Tween 20 and the PBT buffer 10 mM of

potassium dihydrogen phosphate/disodium hydrogen phosphate at pH 7.5 with 0.05% Tween 20. Borate buffer was 0.2 M boric acid/sodium borate at pH 8.7. Coating buffer was 50 mM carbonate/bicarbonate at pH 9.6. Citrate buffer was sodium citrate 40 mM solution at pH 5.5. The substrate solution was 0.01% TMB (3,3',5,5'-tetramethylbenzidine) and 0.004% H₂O₂ in citrate buffer. TMB acts as a hydrogen donor for the reduction of hydrogen peroxide to water by horseradish peroxidase (HRP), producing a diimine with a blue colour (λ , 650 nm), the addition of acid, such as H₂SO₄, turns the colour yellow (λ , 450 nm). The blocking buffer was 4.5% skim milk powder in PBST. The Tris buffer was at 1M pH 8 and TBST was 25mM tris-buffered saline (pH 7.2) and 0.15M NaCl with 0.05% Tween 20.

2.2.3 Equipments/Software

Proteins from the different yeast membrane fractions batches were quantified with the Pierce BCA Protein Assay kit (Thermo Scientific, USA) to obtain the Total Protein Concentration (TPC), and eluted c-myc-tagged OR, on a Nanodrop instrument (Labtech, UK). The bioconjugates were purified by Hi-Trap desalting columns (Sephadex G-25, 5 mL) purchased from Amersham Bioscience (Uppsala, Sweden) and ÄKTAprime from GE Healthcare Life Sciences. The protein bioconjugates were characterized by MALDI-TOF-MS (matrix assisted laser desorption ionization time-of-flight mass spectrometer from Bruker Biflex III (Bruker, Kalsruhe, Germany) equipped with a laser unit (working conditions were wavelength of 337 nm and the maximum output of 6 mW). The washing steps in the ELISA assays were carried out using an ELx405 HT microplate washer (BioTek, Winooski, VT). For the sample preparation an Ultrasons bath was used (50 kHz Ultrasons, Selecta). The SpectramaxPlus software (Molecular Devices, Sunnyvale, CA) at a single wavelength mode of 450 nm was used to read the absorbance. The data obtained was analysed with GraphPad Prism v4.00 (GraphPad Software Inc., San Diego, CA).

2.2.4 Synthesis of Peptide-Bioconjugates

The two peptide haptens (C_1 , C_2) were covalently linked to keyhole limpet hemocyanin (KLH), bovine serum albumin (BSA), conalbumin (CONA), ovalbumin (OVA), horseradish peroxidase (HRP) and aminodextrane (AD) by means of N-succinimidyl 3-maleimidopropionate ($M(CH_2)_2CO$) or N-succinimidyl iodoacetate ($(CH_2)CO$) cross-linkers at different peptide:Lys (protein) molar ratios (Figure 2.8 and Table 2.2) using procedures previously reported^{35,37}. Table 2.3 and Table 2.4 provide additional information regarding the bioconjugates synthesized and the corresponding MALDI-TOF-MS recorded to achieve information on the number of peptide molecules attached. The bioconjugates were named aC_b -Y-X, where a is the true hapten density (δ) calculated by MALDI-TOF-MS, C_b is the peptide (C_1 , C_2), Y the crosslinker ($M(CH_2)_2CO$ or $(CH_2)CO$) and X the macrobiomolecule used.

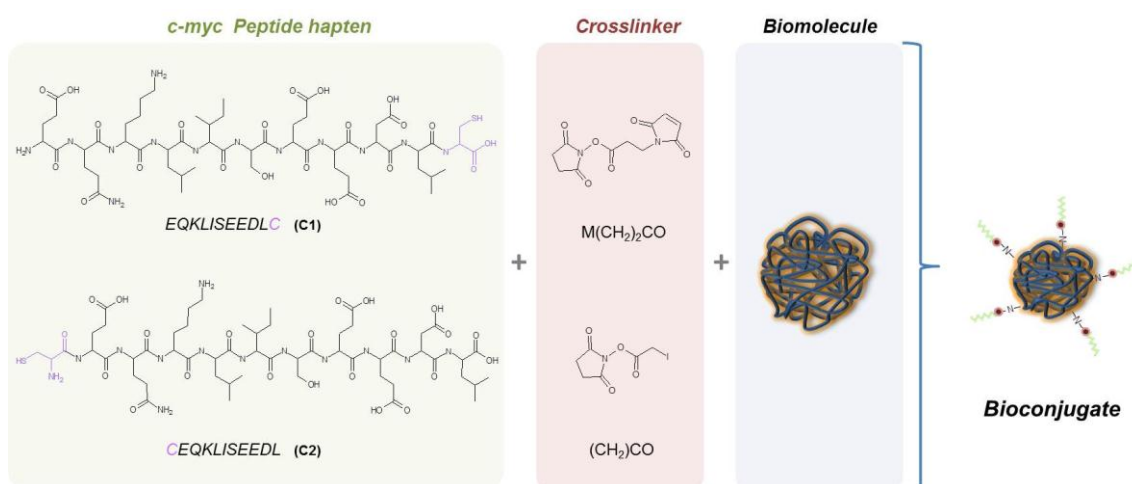


Figure 2.8 Scheme of the components used for the bioconjugate synthesis. Two c-myc peptides were conjugated through two different crosslinkers. In purple (C_1 and C_2) is highlighted the cysteine position which has the reactive thiol group.

With further detail:

- i. **Through the crosslinker N-succinimidyl 3-maleimidopropionate ($M(CH_2)_2CO$).** The c-myc C_1 peptide, with a Cys aminoacid at the C-terminus, was covalently coupled to BSA, CONA, OVA, HRP and Amino-Dextran (AD) using the N-succinimidyl 3-maleimidopropionate ($M(CH_2)_2CO$) crosslinker. The biomolecules (10 mg for BSA, CONA, OVA and AD; and 2 mg for HRP) were dissolved in PBS (1.2 mL). A solution of the crosslinker (0.63 mg, 2.36 μ mol, for BSA, CONA, OVA and AD; and 106.4 μ g, 0.40 μ mol for HRP) in

anhydrous DMF (100 μL for BSA, CONA, OVA and AD; and 50 μL for HRP) was added slowly to each solution of the biomolecules. The reaction mixture was stirred for 1 hour at room temperature and overnight at 4°C. Next, the bioconjugates were purified by size-exclusion gel filtration chromatography with degassed PBS and characterized by MALDI-TOF-MS (see Table 2.3). Subsequently, solutions of the peptide (4.48 mg mL^{-1} for BSA, CONA, OVA and AD; 0.65 mg mL^{-1} for HRP) in degassed PBS were added over the activated biomolecules (different volumes for each bioconjugate according the bioconjugate:peptide molar ratio) and the reaction mixture stirred for 2-3 hours at room temperature. Finally, the antigens were purified by size-exclusion gel filtration chromatography with H₂O MilliQ, lyophilized and characterized by MALDI-TOF-MS (Figure 2.9 and Table 2.4).

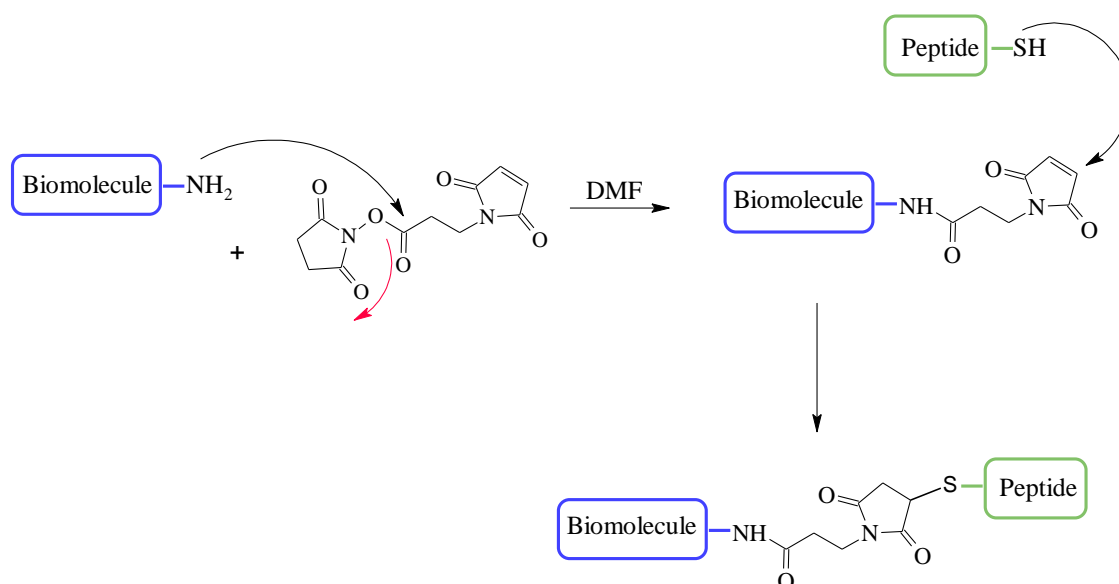


Figure 2.9 Synthesis of the c-myc-Bioconjugates through the crosslinker N-succinimidyl 3-maleimidopropionate ($\text{M}(\text{CH}_2)_2\text{CO}$).

- ii. **Through the crosslinker N-succinimidyl iodoacetate (CH_2CO).** The two c-myc haptens (C_1 and C_2) were conjugated to proteins using N-succinimidyl iodoacetate (CH_2CO) as crosslinker. The biomolecules (10 mg for BSA, CONA, OVA and AD; 2.96 mg of HRP for $^1\text{C}_2\text{-CH}_2\text{CO-HRP}$ bioconjugate) were dissolved in coating buffer (1.2 mL). A solution of the crosslinker (2.21 mg, 7.81 μmol , for BSA, CONA, OVA and AD; 0.86 mg, 3.03 μmol , for $^1\text{C}_2\text{-CH}_2\text{CO-HRP}$ bioconjugate) in anhydrous DMF (100 μL) was added slowly to

the biomolecule solution. The conjugation was performed stirring for 1 hour at room temperature and overnight at 4°C. The crosslinker-biomolecule conjugates were purified by size-exclusion gel filtration chromatography with borate buffer as a mobile phase and characterized by MALDI-TOF-MS (see Table 2.3). Next, different volumes of the solutions (1.62 mg mL⁻¹ for C₁, 1.35-11.347 mg mL⁻¹ for C₂) of the peptide in buffer (C₂ in PBS (75-85%):borate (25-15%) v/v and C₁ in PBS) were added over the activated biomolecules and mixed overnight at room temperature. The conjugated biomolecules were treated with the capping solution (~ 50 mM cysteine-hydrochlorohydrate in milliQ water, 100-500 μL) and stirred for 30 minutes at room temperature. Finally, the bioconjugates were purified as described above, lyophilized and characterized by MALDI-TOF-MS (see Figure 2.10 and Table 2.4).

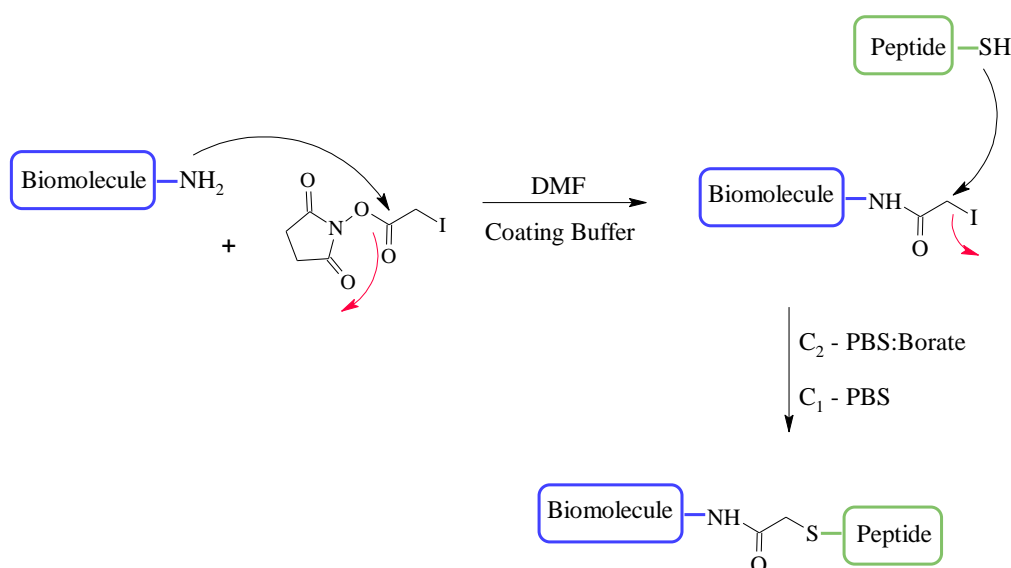


Figure 2.10 Synthesis of the c-myc-Bioconjugates through the crosslinker N-succinimidyl iodoacetate (CH₂CO).

2.2.5 Number of crosslinkers/haptens conjugated per biomolecule

The crosslinker and the hapten densities of the different bioconjugates were calculated by MALDI-TOF-MS by comparing the molecular weight of the crosslinker-biomolecule conjugate with the molecular weight of the biomolecule (Table 2.3) or the complete bioconjugate (Table 2.4). The procedure used for the analysis was exactly the same as described previously in the literature³⁸. MALDI spectra were obtained by mixing 2 μL of the matrix (trans-3,5-dimethoxy-4-hydroxycinnamic acid, 10 mg/mL in

CH₃CN/H₂O 50:50, 0.1% HCOOH) with 2 μL of a solution of the conjugates or proteins (5 mg/mL in CH₃CN /H₂O 50:50, 0.1% HCOOH).

Hapten density (δ) is calculated according to Equation 1:

$$\delta = \frac{\text{MW(Conjugate)} - \text{MW(Biomolecule)}}{\text{MW(Hapten)}} \quad (\text{Eq. 1})$$

where MW(Conjugate) is the molecular weight of the conjugate, MW(Biomolecule) is the molecular weight of the biomolecule used for the conjugation, and MW (hapten) is the molecular weight of the hapten.

2.2.6 Monoclonal antibody production

The anti-c-myc monoclonal antibody (stock solution: 1.44 mg mL⁻¹, IgG mAb) was produced by Abyntek Biopharma (Bizcaia, Spain) in Balb/c mice, using the C₂ peptide conjugated to KLH with a maleimido derivative cross-linker as immunogen. The fused cells (spleen B cells from the selected mice with SP2\0 mouse myeloma cell line) were screened by competitive ELISA (see procedure below). For this purpose, we measured the binding of the supernatants to ^xC₂-CH₂CO-CONA (where *x* corresponds to the bioconjugate synthesized at a ratio of 2:1:1, see Table 2.4) and ⁵C₁-M(CH₂)₂CO-CONA (0.2 μg mL⁻¹ each) immobilized on the microtiter plates in the absence (zero concentration) or presence of the c-myc commercial peptide (20 nM to 25 μM). The clones selected were subcloned again, and subsequent screenings were performed in the same conditions. Because of this process, three cell clones were selected, producing the antibodies named Ab894D12_{d9d10}, Ab894D12_{f7d12} and Ab894D12_{f7f9} (Table 2.5 and Table 2.6).

2.2.7 Preparation of the protein-receptor nanovesicles solutions

Human olfactory receptor c-myc-OR1740 (ORL520 in OrDB), chimpanzee c-myc-OR7D4 and pJH2-somatostatin receptor subtype 2 (SSTR2), used as negative

control, were expressed heterologously in various *Saccharomyces cerevisiae* yeast cultures, following a procedure described in literature⁸. The yeast cells were mechanically disrupted¹⁸ and the cell content separated. The membrane fractions were then obtained, divided in aliquots, and frozen at -80°C (~5 mg mL⁻¹, stock suspension). As a GPCR membrane receptor model, the fractions containing SSTR2 were used to evaluate the matrix effect of the immunochemical assay established for the quantification of c-myc-OR1740 and c-myc-OR7D4 receptors integrated in the nanovesicles (NVs). These NVs were produced and characterized in a recent publication by our group²³ and is presented as well in the *Chapter 1*: i.e. *i*) total protein content (TPC), using the BCA Protein Assay, *ii*) the average size of NVs, by means of Dynamic Light Scattering and Cryo-EM, *iii*) the concentration of NVs in the solutions (NV mL⁻¹), using Nanoparticle Tracking Analysis; *iv*) the zeta-potential of NVs in solution, by using the Malvern Zetasizer.

For the *ELISA*, the stock suspensions of the membrane fractions were diluted to a TPC of 300 µg mL⁻¹ in PBT and sonicated for 20 min in ice-cold water to homogenize the NV size. The solution was further diluted in PBT to a TPC of 60 µg mL⁻¹. This solution was then passed through a sterile low protein-binding filter (Millipore, 13 mm diameter and 0.22 µm pore size). Finally, the working solutions were obtained by adding PBT buffer until the desired concentration of NVs was reached. The ***SSTR2 blank matrix solution*** refers to PBT solutions of the nanovesicle carrying the SSTR2 receptor without the c-myc peptide. This blank matrix was used at different concentrations (10-50 µg mL⁻¹ of TPC, or 1.47·10¹⁰-7.33·10¹⁰ NV mL⁻¹)²³ in the distinct experiments. The c-myc-ORs NVs solutions were consistently at the same TPC concentrations as the reference SSTR2 blank matrix.

For the *Western Blot* assays: 1 µL of the stock membrane suspension was loaded on each well of the gel (5 µg/well), and the assays were performed following the procedure described by Minic et al.⁸

2.2.8 Western Blot analysis

Briefly⁸, the proteins of the membrane fractions were separated on a 12% SDS-polyacrylamide gel (5 µg/well) and then transferred electrophoretically onto a PVDF Hybond-P (Amersham, GE Healthcare) membrane. Then, the membrane was treated with the blocking buffer 1 hour at room temperature under agitation. Next, the membrane was incubated overnight with the primary antibody (anti-c-myc) in blocking buffer at 4°C under agitation. The next day the gel was rinsed with PBST every 15 min four times. Next, the membrane was incubated 1 hour at room temperature under agitation with a mix of the secondary antibody anti-IgG-HRP (1/3000) and streptavidin-HRP conjugate (Amersham, dilution 1/1333) in blocking buffer. Finally, the membrane was rinsed again every 15 min four times with PBST and one time with H₂O milliQ and blots were revealed using the enhanced chemiluminescence (ECL) detection kit from Amersham (GE Healthcare).

2.2.9 Indirect ELISA development

2.2.9.1 2D Experiments: Non-competitive assays

First, appropriate concentrations of the immunoreagents were determined through checkerboard titration experiments. For this purpose, we measure the binding of serial dilutions of the antibodies ($10 - 9.76 \cdot 10^{-3} \mu\text{g mL}^{-1}$ and zero in PBST, 100 µL per well) to the microtiter plate coated with different concentrations of the bioconjugates ($1 - 7.81 \cdot 10^{-3} \mu\text{g mL}^{-1}$ and zero in coating buffer, 100 µL per well), as described in in Ref. 39 (but in this case no analyte was added). One row of the plate was reserved to test non-specific binding of the anti-c-myc to the microplate. One column of the plate was used to test non-specific binding of the anti-IgG-HRP to the coating antigen (CA).

All the washing steps consisted on filling the wells with PBST (300 µL) and immediately aspirating the solutions by vacuum with an automated microplate washer, in four cycles.

2.2.9.2 Optimization and evaluation: physicochemical parameters

- Length of competitive step: The mixture of antibody and analyte were incubated during different periods of time (30, 45, 60, 90, 120 and 150 min) at RT on the same antigen coated plate. The plates were processed as described below with a general competitive ELISA protocol. The working immunoreagents conditions were: Ab9E10 anti-c-myc antibody (1/4000, in PBST), the coating antigen $^1\text{C}_1\text{-CH}_2\text{CO-OVA}$ ($0.062 \mu\text{g mL}^{-1}$) and the analyte used was the commercial c-myc peptide (Sigma), with a working range of $50\mu\text{M} - 2\text{nM}$.
- Preincubation time: The anti-c-myc and the c-myc analyte solutions were incubated under two different conditions (overnight at 4°C and 0, 30, 60, 90, 120 min at RT) and, subsequently, added to the antigen coated plates. The plates were processed as described below with a general competitive ELISA protocol. The working immunoreagents conditions were: Ab9E10 anti-c-myc antibody (1/4000, in PBST), the coating antigen $^1\text{C}_1\text{-CH}_2\text{CO-OVA}$ ($0.062 \mu\text{g mL}^{-1}$) and the analyte used was the commercial c-myc peptide (Sigma), with a working range of $50\mu\text{M} - 2\text{nM}$.
- Effect of Tween 20: PBST solutions containing different concentrations of Tween 20 (0.2; 0.1; 0.05; 0.025; 0.0125%) were used to dilute the anti-c-myc antibody and prepare different c-myc peptide solutions as analyte that were run simultaneously in the competitive ELISA. The working immunoreagents conditions were: Ab9E10 anti-c-myc antibody (1/16000, in PBST), the coating antigen $^x\text{C}_2\text{-CH}_2\text{CO-CONA}$ ($0.062 \mu\text{g mL}^{-1}$) and the analyte used was the commercial c-myc peptide (Sigma), with a working range of $50\mu\text{M} - 2\text{nM}$.
- Effect of ionic strength (conductivity): PBS solutions at different NaCl concentrations (0; 0.2; 0.4; 0.8; 1.6 and 3.2% corresponding to conductivities of 1.7; 5.5; 9.0; 16; 28.7; 52.8 mS/cm respectively) were prepared from PB, their conductivity was measured and the solutions were used to dilute the antibody. The solutions were employed in the below described ELISA. The calibration curves obtained with each PBS solution were compared after adjusting them to a four-parameter equation. The working immunoreagents conditions were: Ab9E10 anti-c-myc antibody (from 1/128000 to 1/16000, in PBST), the coating antigen $^x\text{C}_2\text{-CH}_2\text{CO-CONA}$ ($0.062 \mu\text{g mL}^{-1}$) and the analyte used was the commercial c-myc peptide (Sigma), with a working range of $50\mu\text{M} - 2\text{nM}$.

- Effect of pH: PB solutions were prepared with pH values ranging from 4.5 to 9.5 units. These solutions were used to prepare c-myc analyte curves and the anti-c-myc solution and employed for the competitive immunoassay. The absorbances were adjusted to a four-parameter equation and the features of the resulting ELISAs were compared. The working immunoreagents conditions were: Ab9E10 anti-c-myc antibody (1/128000), the coating antigen $^x\text{C}_2\text{-CH}_2\text{CO-CONA}$ ($0.062 \mu\text{g mL}^{-1}$) and the analyte used was the commercial c-myc peptide (Sigma), with a working range of $50\mu\text{M} - 2\text{nM}$.
- Effect of Organic solvents (DMSO, MeOH, EtOH, acetonitrile) and blocking solutions (PVP, PEG₆₀₀₀): PBT 0.05% solutions (pH 7.5) containing different concentrations of DMSO, MeOH, EtOH, acetonitrile (v/v) (20%; 10%; 5%; 2.5%; 1.25%; 0%) and PVP, PEG₆₀₀₀ (v/v) (4%; 2%; 1%; 0.5%; 0.25%; 0%) were used to prepare standard curves and were run simply with a competitive immunoassay. The working immunoreagents conditions were: Ab9E10 anti-c-myc antibody (1/128000), the coating antigen $^x\text{C}_2\text{-CH}_2\text{CO-CONA}$ ($0.062 \mu\text{g mL}^{-1}$) and the analyte a synthesized c-myc peptide.

2.2.9.3 Ab9E10 vs. Ab894D12_{f7f9}: antibody evaluation

The sensitivities of different anti-c-myc antibodies were studied by a competitive ELISA (procedure described below), and different physicochemical parameters were evaluated. At the end, three different combinations were studied with the same coating antigen: Ab9E10 anti-c-myc antibody (1/4000, in PBST) and the coating antigen $^5\text{C}_1\text{-M(CH}_2)_2\text{CO-CONA}$ ($0.062 \mu\text{g mL}^{-1}$), Ab894D12_{f7f9} (dilution 1/4000, in PBST) and the coating antigen $^5\text{C}_1\text{-M(CH}_2)_2\text{CO-CONA}$ ($0.031\mu\text{g mL}^{-1}$), and Ab894D12_{f7f9} (dilution 1/4000, in PBT) and the coating antigen $^5\text{C}_1\text{-M(CH}_2)_2\text{CO-CONA}$ ($0.016\mu\text{g mL}^{-1}$). In the competitive step, the analyte used was the commercial c-myc peptide (Sigma), with a working range of $50\mu\text{M} - 0.005\text{nM}$.

2.2.9.4 Immunoassay matrix effects

The application of this technique to measure the amount of c-myc-olfactory receptors expressed in a real biological sample was preliminarily studied regarding potential interferences caused by the nanovesicles environment matrix. For this purpose

nanovesicles carrying another transmembrane receptor (SSTR2) without the c-myc tag were produced and used in solution at different concentrations. Concentrations of (3-60 $\mu\text{g mL}^{-1}$ TPC or $4.40 \cdot 10^9$ - $8.80 \cdot 10^{10}$ NV mL^{-1}) were studied to assess the interference of this matrix in the ELISA. As it can be observed in Figure 2.25 (i.e. $^4\text{C}_1$ -M(CH₂)₂CO-CONA), the matrix produced a significant decrease in the maximum signal of the assay accompanied by a slight decrease of the assay detectability (Table 2.9 and Table 2.10), but still is possible to quantify under these conditions. Therefore, quantification of the c-myc-nanovesicles was addressed using the SSTR2 sample as “Blank matrix buffer” to prepare the calibration curves. For this purpose, the SSTR2 matrix buffer has to contain more or less the same concentration of vesicles than the c-myc-OR1740 and c-myc-OR7D4 sample. It was fixed the amount of TPC. Moreover, and due to the heterologous nature of these type of samples it was found that agitation (600 rpm) during the competition step allowed to minimize the matrix effect.

2.2.9.5 General protocol: nanovesicles competitive assays

Microtiter plates were coated with the antigen ($^3\text{C}_2$ -CH₂CO-OVA, 0.01 $\mu\text{g mL}^{-1}$ in coating buffer, 100 μL per well) for four hours at room temperature covered with adhesive plate sealers. Next, the plates were washed and solutions of the c-myc-ORs NV samples and/or the bioconjugate standards ($^4\text{C}_1$ -M(CH₂)₂CO-CONA, $^3\text{C}_1$ -M(CH₂)₂CO-BSA and $^1\text{C}_1$ -M(CH₂)₂CO-HRP, 1000-0.008 nM in PBT or in the SSTR2 NV matrix) were added (50 μL per well), followed by the monoclonal antibody (Ab894D12_{17f9}, 1/250000 in PBT or in the SSTR2 NV matrix, 50 μL per well). The mixture was incubated for 30 min at room temperature and the plates were then washed again with PBST. Whenever nanovesicles samples or standards were measured, the microplates were agitated at 600 rpm during the competition step. Subsequently, a solution of anti-IgG-HRP (1/6000 in PBST, 100 μL per well) was added, and the plates were incubated for 30 min more and washed before addition of the substrate solution (0.01% TMB and 0.004% H₂O₂ in citrate buffer, 100 μL per well). After 30 min at room temperature, the enzymatic reaction was stopped by adding 4N H₂SO₄ (50 μL per well), and the absorbance was measured at 450 nm.

The standard curves were fitted to a four-parameter logistic equation³⁵ according to the following formula: $Y=(A - B)/[1 - (x/C)^D]+ B$ (Figure 2.11), where A is the maximal absorbance, B is the minimum absorbance, C is the concentration producing 50% of the difference between the maximal and the minimal absorbance (also IC_{50}) and D is the slope at the inflection point of the sigmoid curve. Unless otherwise indicated, the data presented correspond to the average of three well replicates.

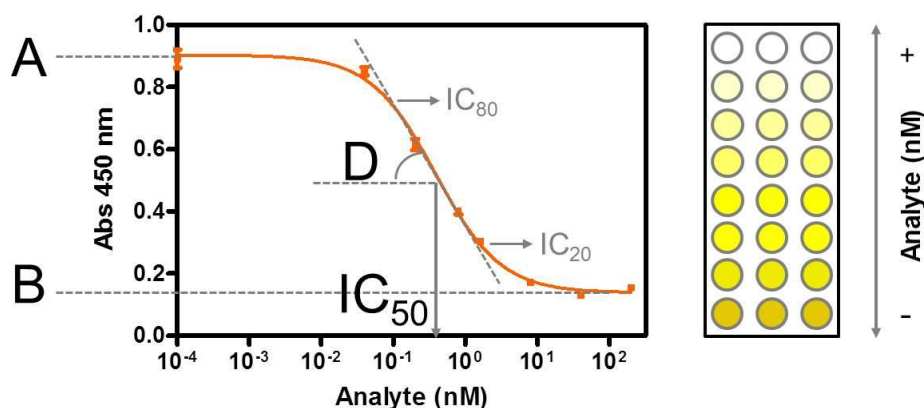


Figure 2.11 Sigmoidal curve obtained from a competitive immunoassay. The working range (linear range of the curve) is defined between IC_{20} and IC_{80} , limit of quantification (LOQ). On the right is presented the optical response obtained from 3 of the 12 columns in the 96-well plate. It is observed how the presence of analyte inhibits the colorimetric response.

2.2.10 Quantification of olfactory receptors embedded onto natural nanovesicle through the c-myc tag

The samples containing NVs carrying an unknown number of c-myc-tagged OR1740 or c-myc-tagged OR7D4 were diluted at several TPC concentrations in PBT and measured using the ELISA procedure described above. In these experiments, the standard curves were built in SSTR2 blank matrices containing the same TPC as in the samples. The three bioconjugates (4C_1 -M(CH₂)₂CO-CONA, 3C_1 -M(CH₂)₂CO-BSA and 1C_1 -M(CH₂)₂CO-HRP) were used as standard references taking into consideration the number of peptides linked to the macrobiomolecule, as calculated by MALDI-TOF-MS. Interpolation of the immunochemical response of the NV solutions on the calibration curves build with these standards allowed calculating the number of c-myc molecules in the solutions, and therefore the number of c-myc-ORs receptors using the Avogadro number. Knowing that each OR has only one c-myc tag and the concentration of NVs in

such solution, it was thus possible to obtain an estimative value of the average number of c-myc-ORs of our NVs. Notice that only those c-myc tags externally oriented in the NV will be quantified.

The c-myc-OR1740 and c-myc-OR7D4 quantification per nanovesicle done with competitive assays were carried out at different nanovesicles concentrations, for c-myc-OR1740 at ($6.9 \cdot 10^{10}$ - $12.5 \cdot 10^{10}$ NV mL⁻¹, 25-45 µg mL⁻¹ of TPC) and for c-myc-OR7D4 at ($4.2 \cdot 10^{10}$ - $7.5 \cdot 10^{10}$ NV mL⁻¹, 25-45 µg mL⁻¹ of TPC). The data presented correspond to the average of three well replicates and the assay reproducibility was also evaluated, for c-myc-OR1740 (n = 6) and for c-myc-OR7D4 (n=4).

Figure 2.12 shows a scheme of the Indirect Competitive ELISA developed for the quantification of c-myc tagged OR embedded onto natural nanovesicles.

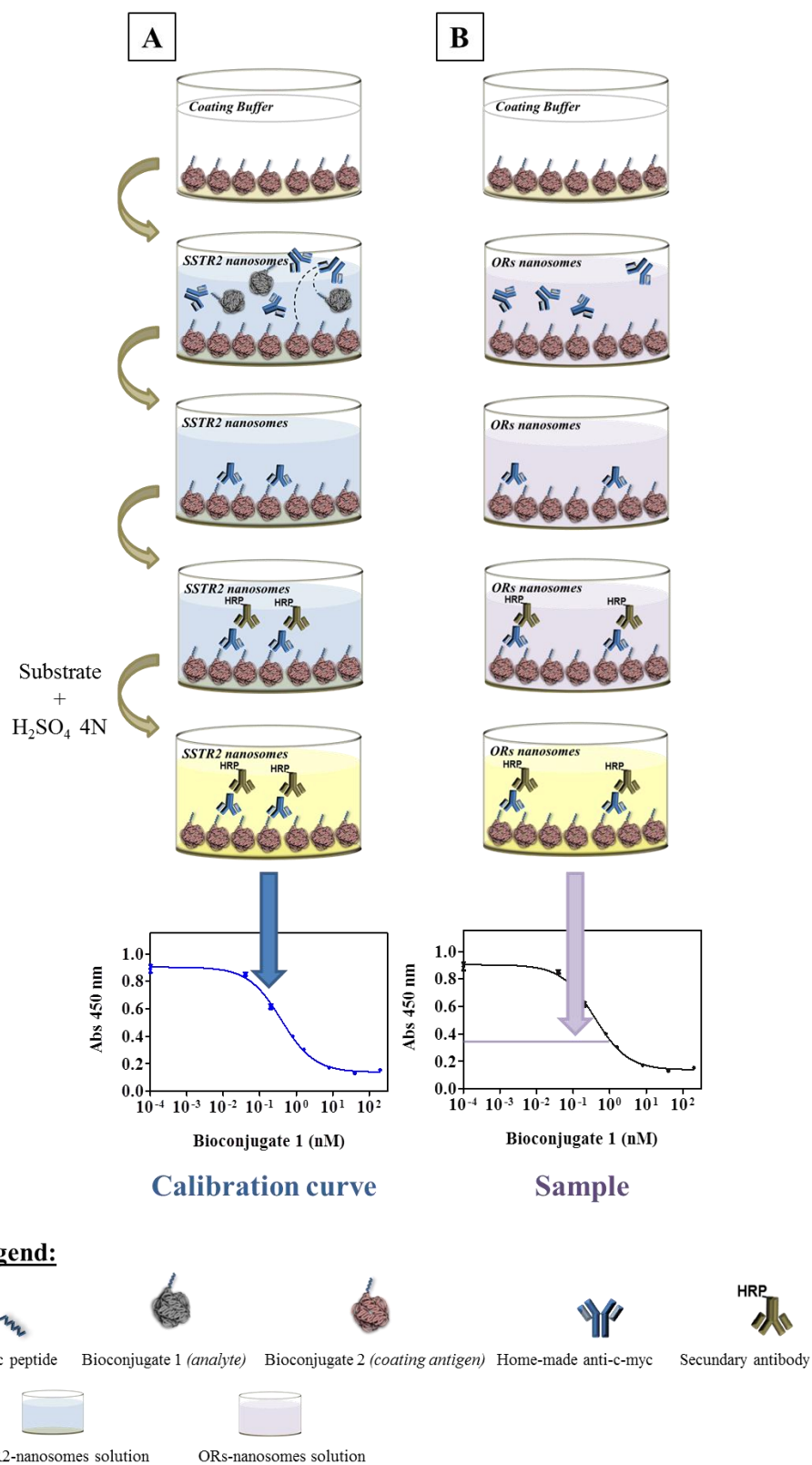


Figure 2.12 Scheme of the competitive ELISA assay. (A) Calibration curve generation using the c-myc-Bioconjugate 1 in an SSTR2-carrying NS solution. (B) c-myc-OR-carrying NS signal is compared with the calibration curve performed in (A).

2.2.11 c-myc-OR protein quantification after solubilisation

2.2.11.1 Proteins solubilisation

For efficient ORs solubilisation fos-choline-14 (FC14) detergent was used as in Cook⁴⁰. To investigate the critical step of solubilisation, a range of detergent concentrations relative to its critical micelle concentration, CMC (10 to 350 CMC) were tested with a same amount of membrane fraction. Then, the samples were dot blotted onto a nitrocellulose membrane and hybridized with a commercial anti-c-myc mAb. The minimal efficient FC14 concentration (50 CMC) was determined by assessing a correlation between the diameter of the dot and the level of solubilisation. In addition, a concentration of 350 CMC of FC14 was used as described in Cook et al.⁴⁰. Solubilisation of c-myc-OR1740 and c-myc-OR7D4 from 450 µg of membrane fractions was performed using FC14 detergent (50 or 350 CMC) together with antiproteases inhibitors cocktail at 4°C during 3 hours with gentle end-over-end mixing.

2.2.11.2 Olfactory receptors protein quantification

The quantification of solubilized c-myc-ORs was performed using the ProfoundTMC-Myc Tag IP/Co-IP kit. 10 µL anti c-myc-agarose were dispensed to the solubilized c-myc-ORs in spin columns. The incubation was done with gentle end-over-end mixing at 4°C overnight. To be sure that contaminating proteins were discarded, the number of washes was determined by measuring protein concentration after each wash. After eight washes with 0.5 mL TBST, the c-myc-tagged proteins were eluted with 4 x 10 µL elution buffer. The elutes were neutralized with 2 µL of Tris buffer pH 9. Proteins were quantified on a Nanodrop at 280nm, 10 measures were performed on each elute. Each elute was analysed by western blotting with anti-c-myc antibody (20 µL of elute, commercial anti-c-myc antibody 1:8000).

2.3 Results and Discussion

The c-myc peptide sequence (Glu-Gln-Lys-Leu-Ile-Ser-Glu-Glu-Asp-Leu) is one of the most important peptide tags used in protein expression. It can be fused to either the N- or C- terminus of the protein of interest without changing its tertiary structure²⁹ or the biological activity of the protein³⁰. In the case of the c-myc-ORs, used as model of the GPCR family in this study, the c-myc was attached through its -COOH terminal amino acid to the -NH₂ terminal amino acid of the protein. Therefore, on the OR-NVs prepared, the NH₂ terminus of the c-myc tag is exposed to the external media (see Figure 2.13).

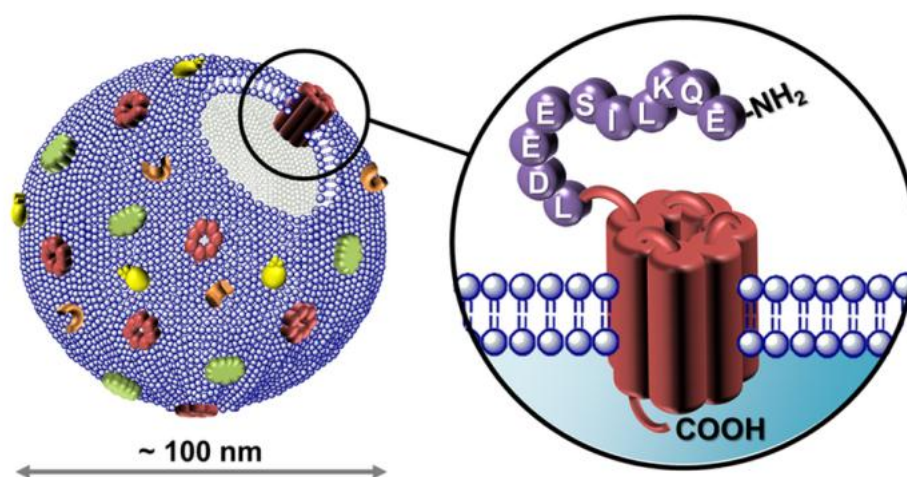


Figure 2.13 Scheme of the natural lipidic nanovesicles carrying the c-myc-OR expressed by genetic engineering. Zoom of the quantified complex: OR1740 or OR7D4 as seven-transmembrane protein with the c-myc peptide (10 amino acids) fused to its N-terminus.

Determination of the average number of protein receptors per NV has always been challenging. Hence, with the aim to ensure reproducibility and potential biofunctionality of each NV batch, usually the total protein concentration (TPC), rather than just the receptor, is used to estimate the amount of receptor in these preparations. Moreover, the expression of tagged recombinant proteins is a common strategy for surface immobilization (i.e. biosensing platforms^{13,14}). However, the lack of information on the number of c-myc-ORs molecules embedded in the NVs is an important drawback.

2.3.1 Bioconjugates. Synthesis and Characterization.

Antibodies against c-myc were produced by synthesizing two c-myc- related hapten peptides (C₁ and C₂, see Table 2.2 for peptide sequences), bearing an additional Cys residue for conjugation at the carboxy and the amino terminus, respectively. These peptides were then coupled to macrobiomolecules (KLH, BSA, CONA, OVA, HRP and AD)⁴¹ at different molar ratios using two different cross-linkers (see Table 2.3 and 2.4).

Table 2.2 Hapten densities achieved for the peptide-macrobiomolecule bioconjugates used in this study, in relation to the cross-linker used for the bioconjugation reaction.

Heterobifunctional Cross-linkers ▶ Peptide ▼	M(CH ₂) ₂ CO ^a		CH ₂ CO ^a	
	Bioconjugate	δ ^b	Bioconjugate	δ ^b
C ₁ : EQKLISEEDLC _{ys}	C ₁ -M(CH ₂) ₂ CO-BSA	1/3*	C ₁ -CH ₂ CO-BSA	1
	C ₁ -M(CH ₂) ₂ CO-OVA	--	C ₁ -CH ₂ CO-OVA	1
	C ₁ -M(CH ₂) ₂ CO-CONA	4/5/6*		
	C ₁ -M(CH ₂) ₂ CO-HRP	1		
	C ₁ -M(CH ₂) ₂ CO-AD	--		
C ₂ : CysEQKLISEEDL			C ₂ -CH ₂ CO-BSA	6/8*
			C ₂ -CH ₂ CO-OVA	3/5*
			C ₂ -CH ₂ CO-CONA	--
			C ₂ -CH ₂ CO-HRP	1
			C ₂ -CH ₂ CO-AD	--

^a, M(CH₂)₂CO or CH₂CO refers to the spacers resulting from the bioconjugation reaction using respectively N-succinimidyl 3-maleimidopropionate or N-succinimidyl iodoacetate, as cross-linkers.

^b, number of peptide residues bound to the protein according to MALDI-TOF-MS analysis.

*, bioconjugate synthesized at different molecular concentration (Peptide:Crosslinker:Lys)

--, bioconjugate that was not possible characterized with the MALDI-TOF-MS conditions used.

The KLH conjugates were used for antibody production while the rest were used as secondary immunoreagents or reference standards. BSA, CONA and OVA are proteins widely used to prepare bioconjugates. HRP was selected because it has a low number of Lys residues available for bioconjugation, thus allowing to obtain bioconjugates with an ideal c-myc-HRP 1:1 ratio, suitable for quantification (see below). Finally, AD was selected, because of its hydrophilic character, to minimize potential non-specific adsorptions of the lipidic NV. The bioconjugates were

characterized by MALDI-TOF-MS to determine the c-myc:protein ratio (Table 2.3 and Table 2.4).

The bioconjugates were used for antibody production and monoclonal screening, in addition to as standards, as it will be explained below.

Table 2.3 Crosslinker/bioconjugate. Characterization by MALDI-TOF-MS

	N-succinimidyl 3-maleimidopropanoate (M(CH ₂) ₂ CO)		N-succinimidyl iodoacetate (CH ₂ CO)	
	(0.5 : 1) (Y:X)	(4 : 1) (Y:X)	(1 : 1) (Y:X)	(14 : 1) (Y:X)
BSA	27	--	20 ± 4	--
CONA	14	--	17 ± 4	--
OVA	*	--	*	--
HRP	--	*	--	--
Amino Dextran	*	--	*	2

The bioconjugates were synthesized at different molecular ratios (Y:X) where X is the number of equivalents of Lysines (accessible lysines of the biomolecule) and Y is the number of equivalents of crosslinker used.

All the bioconjugates synthesized were characterized except those with (), which were not possible with the MALDI-TOF-MS conditions used.*

(--) Bioconjugates were not synthesized.

Table 2.4 Haptens/bioconjugate. Characterization by MALDI-TOF-MS

		N-succinimidyl 3-maleimidopropanoate (M(CH ₂) ₂ CO)			N-succinimidyl iodoacetate (CH ₂ CO)			
		(0.25:0.5:1) (Z:Y:X)	(0.5:0.5:1) (Z:Y:X)	(4:4:1) (Z:Y:X)	(0.19:1:1) (Z:Y:X)	(1:1:1) (Z:Y:X)	(2:1:1) (Z:Y:X)	(5:14:1) (Z:Y:X)
BSA	EQKLISEEDLC (C1)	1	3	--	1	--	--	--
	CEQKLISEEDL (C2)	--	--	--	--	8	6	--
CONA	EQKLISEEDLC (C1)	6	4/5 ^a	--	--	--	--	--
	CEQKLISEEDL (C2)	--	--	--	--	*	x*	--
OVA	EQKLISEEDLC (C1)	*	*	--	1	--	--	--
	CEQKLISEEDL (C2)	--	--	--	--	5	3	--
HRP	EQKLISEEDLC (C1)	--	--	1	--	--	--	--
	CEQKLISEEDL (C2)	--	--	--	--	--	--	1
Amino Dextran	EQKLISEEDLC (C1)	*	*	--	--	--	--	--
	CEQKLISEEDL (C2)	--	--	--	--	*	*	--

The bioconjugates were synthesized at different molecular concentrations (Z:Y:X) where X is the number of equivalents of Lysines (accessible lysines of the biomolecule), Y is the number of equivalents of crosslinker used and Z is the number of equivalents of the peptide.

All the bioconjugates synthesized were characterized except those with (*), which were not possible with the MALDI-TOF-MS conditions used.

(--) Bioconjugates were not synthesized.

^a The bioconjugate was synthesized twice and characterized respectively.

2.3.2 Optimization and evaluation of the indirect competitive ELISA

It is well known that immunoassay performance may be affected by a variety of experimental conditions. As well, to improve the detectability of the assay it is well reported that immunoassay performance may be affected by many different physicochemical factors of the media. Here we evaluated the immunoassay (analyte: c-myc peptide, coating antigens: ¹C₂-CH₂CO-OVA or ^xC₂-CH₂CO-CONA, antibody: commercial anti-c-myc Ab9E10) behaviour under several conditions, such as pH,

conductivity (concentration of NaCl), content of detergent (Tween 20), incubation time and competition time (immunoreaction times).

2.3.2.1 Effect of the length of competitive step

The detectability of the competitive immunoassay can be improved by the different lengths of the competition step. As shown in Figure 2.14 the best detectability (the lowest IC_{50}) was obtained with the shortest incubation time (30 min), IC_{50} 1820 nM. Therefore, a competitive incubation period of 30 min was chosen because of the greater A_{max}/IC_{50} ratio encountered (see Figure 2.14B) that it is more or less the same than the ratio encountered for 45 min.

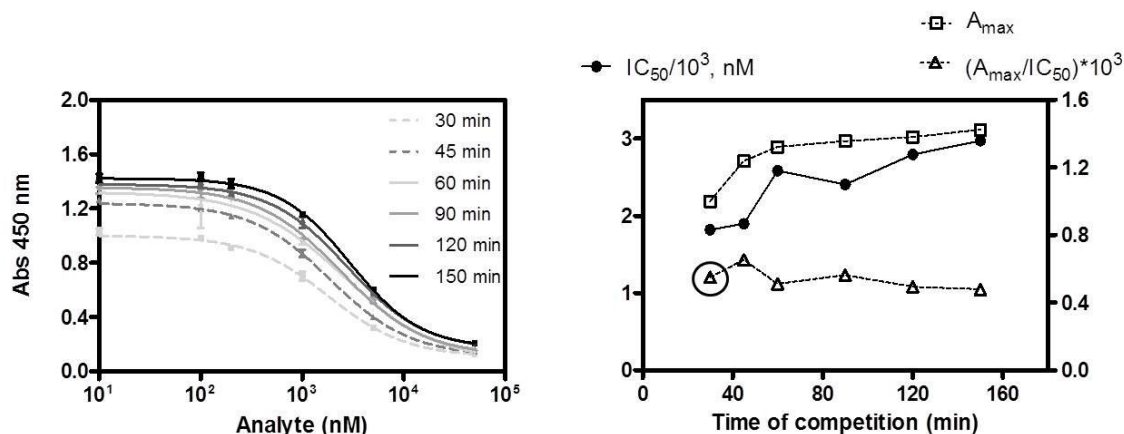


Figure 2.14 Effect of the length of competitive step. The data from the left graph correspond to the average of two replicates. The right graph represents the variation of the immunoassay parameters (IC_{50} and A_{max}) as a function of the length of the competitive step. The analyte, c-myc and the Ab9E10 were incubated for different periods of time (between 30 and 150 min) in the antigen-coated plates ($^{12}C_2$ -CH₂CO-OVA). The results reported are extracted from the four-parameter equation used to fit the standard curves. Each standard curve was run in duplicate.

2.3.2.2 Effect of the preincubation time

The influence of the preincubation time through the detectability of an immunoassay it is reported⁴². The detectability can be improved by preincubation of the analyte with the antibody prior to the competition step. In our case no significant effect on the immunoassay detectability was observed after an overnight incubation of the antibody with the analyte at 4°C (IC_{50} at 4°C = 1340 nM versus IC_{50} at RT_{120 min} = 1188 nM), Figure 2.15.

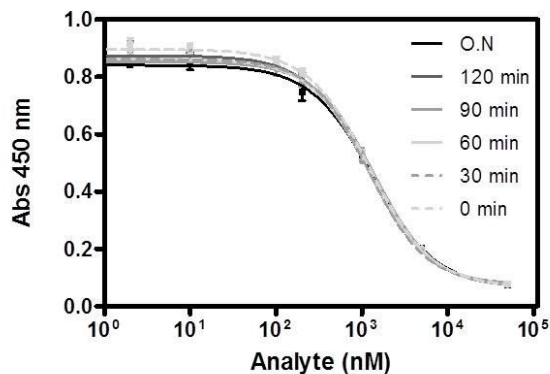


Figure 2.15 Effect of the preincubation of the anti-c-myc and the c-myc analyte before the competitive step. The preincubation took place overnight at 4°C and between 0 and 120 min at RT. The data correspond to the average of two replicates.

2.3.2.3 Effect of the detergent Tween-20

Tween-20 is a non-ionic surfactant commonly used in immunoassay protocols to reduce non-specific interactions. This effect sometimes has an important role on the immunoassay detectability. Figure 2.16 shows that in our case Tween-20 concentrations do not have an important effect on the immunoassay detectability. Concentration of 0.05% significantly decreased the detectability reaching IC_{50} values close to 1500 nM without affecting A_{max} significantly. Thus, subsequent experiments were performed at 0.05% Tween 20 final concentration because of the greater A_{max}/IC_{50} ratio encountered.

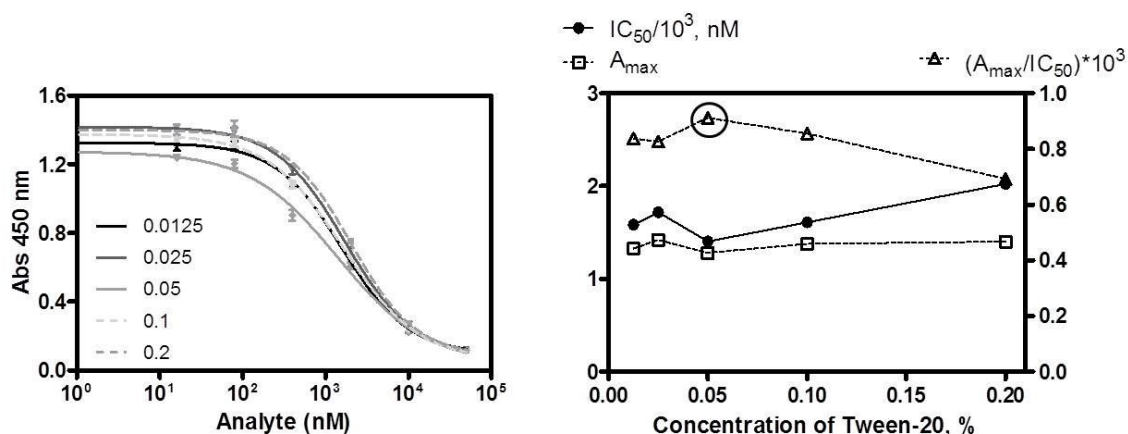


Figure 2.16 Effect of the concentration of Tween-20 on the indirect competitive ELISA. Standard curves (analyte c-myc peptide) and the antibody Ab9E10 were prepared in PBS with different concentrations of Tween. The results reported are extracted from the four-parameter equation used to fit the standard curves. Each standard curve was run in duplicate in the antigen-coated plates $^x C_2-CH_2CO-CONA$.

2.3.2.4 Effect of the conductivity (ionic strength)

The effect of the ionic strength on the immunoassay performance was evaluated in media with conductivity values ranging from 1.7 to 52.8 mS/cm (0 to 3.2% NaCl). It was observed that in the absence of salts or at lower concentrations the assay detectability was improved (decrease in IC_{50}). The A_{max} increases significantly from 0.8 to 2.0 units within the range of 0.8% (PBS 10mM) and 0% (PB).

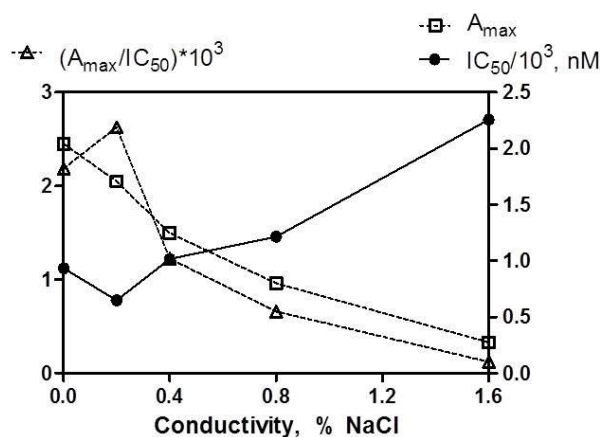


Figure 2.17 Effect of the concentration of NaCl on the indirect competitive ELISA. Standard curves (analyte c-myc peptide) and the antibody Ab 9E10 were prepared in PBS with different concentrations of Tween. The results reported are extracted from the four-parameter equation used to fit the standard curves. Each standard curve was run in duplicate in the antigen-coated plates $^x C_2$ -CH₂CO-CONA. For 3.2% NaCl concentration the Abs results could not fit the sigmoidal four-parameter equation.

In order to decrease the A_{max} in the interested working range (0-0.2% NaCl, PBS solutions) without losing detectability the immunoassay was performed at different antibody concentrations diminishing the one used in Figure 2.17 (Ab9E10 1/16000). In Figure 2.18 are reported the immunoassay results obtained working at the anti-c-myc Ab9E10 concentration of 1/32000. It was observed that at this working conditions the A_{max} decreases to 1-1.5 units keeping the IC_{50} around 450 nM. However, subsequent experiments were performed at 0% NaCl final concentration because of the greater A_{max}/IC_{50} ratio encountered (Figure 2.18).

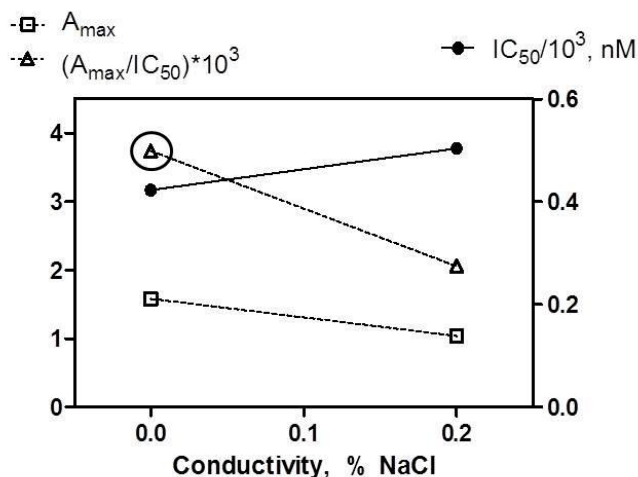


Figure 2.18 Effect of the concentration of NaCl on the indirect competitive ELISA. Standard curves were prepared with the antibody Ab9E10 concentration 1/32000. The results reported are extracted from the four-parameter equation used to fit the standard curves. Each standard curve was run in duplicate in the antigen-coated plates $^x C_2-CH_2CO-CONA$.

The initial 10 mM PBS assay buffer (conductivity near 16 mS/cm, 0.8% NaCl) was not the most appropriate. In contrast a PB buffer with conductivity value 1.7 mS/cm placed the assay under conditions with greater detectability (IC_{50} 235 nM). In Figure 2.19 are reported the immunoassay results obtained working at the anti-c-myc Ab9E10 concentration working range between 1/32000-1/128000 in order to improve the detectability achieved before.

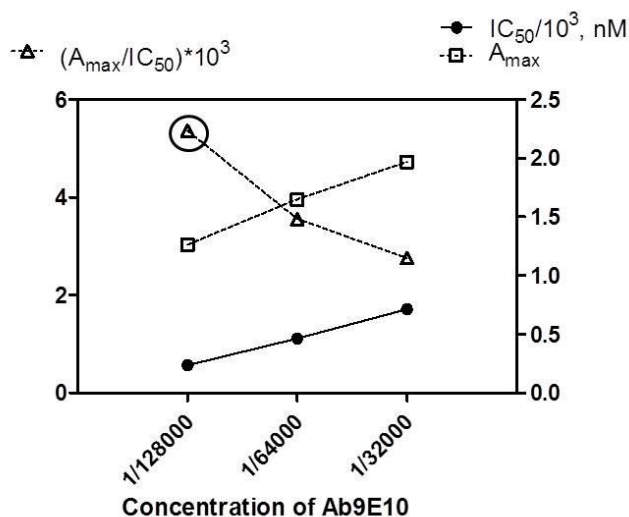


Figure 2.19 Effect of the concentration of 0% NaCl on the indirect competitive ELISA. Standard curves were prepared with the antibody Ab9E10 ranging concentrations from 1/32000 to 1/128000. The results reported are extracted from the four-parameter equation used to fit the standard curves. Each standard curve was run in duplicate in the antigen-coated plates $^x C_2-CH_2CO-CONA$.

2.3.2.5 Effect of the pH

The effect of the pH on the immunoassay performance is also evaluated. In the Figure 2.20 is represented the sigmoidal behaviour obtained at each pH condition. It was observed that the assay was only stable in media with pH value 7.5 (IC_{50} 298 nM). At pH lower than 5.5 or pH higher than 8.5 the assay was totally inhibited.

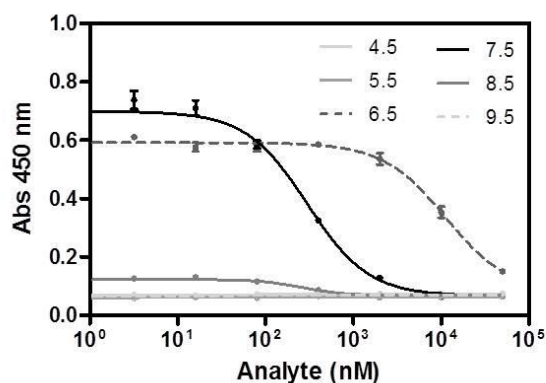


Figure 2.20 Effect of the pH on the competitive immunoassay. Several standard curves were prepared using PB at different pH values and added to the antigen-coated plates (x C₂-CH₂CO-CONA). The Ab9E10 (1/128000) dilutions were also prepared with the same buffers and Tween 20 was added to each of them at 0.05%. Each standard curve was run in duplicate.

2.3.2.6 Effect of the Organic Solvents and the Blocking solutions

Organic Solvents and Blocking solutions are commonly used in immunoassay protocols to reduce non-specific interactions increasing the assay detectability. In our case any of the solutions proposed (DMSO, MeOH, EtOH, acetonitrile, PVP and PEG₆₀₀₀) in the working range established do not improved dramatically the detectability obtained until now, IC_{50} around 100-300 nM. Because the transmembrane protein expression in heterologous systems is often low⁴³, a sensitive ELISA (detectability around 10 nM) assay was required in order to quantify the olfactory receptor (OR) expression. Thus, it was proposed an alternative experiment in order to decrease the immunoassay detectability, i.e. the production of a home-made monoclonal anti-c-myc antibody.

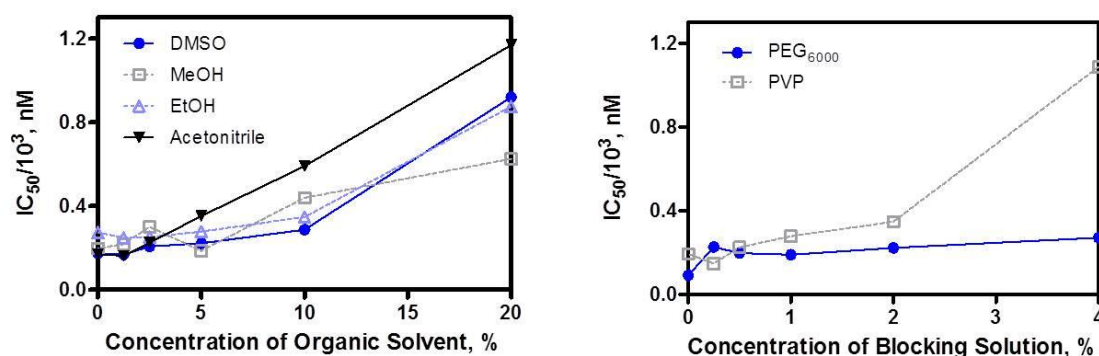


Figure 2.21 Effect of the concentration of Organic Solvents (left graph) and blocking solutions (right graph) on the indirect competitive ELISA. Standard curves were prepared with the antibody Ab9E10 concentration 1/32000 and a synthesized c-myc peptide as analyte. The results reported are extracted from the four-parameter equation used to fit the standard curves. Each standard curve was run in duplicate in the antigen-coated plates $^x C_2-CH_2CO-CONA$.

2.3.2.7 Summary of the immunoassay features

After the evaluation and optimization of the competitive immunoassay we can conclude that some parameters could allowed the improvement of the ELISA detectability. While the time of preincubation, competition, Tween-20 concentration does not affect significantly the immunoassay, we have established the conditions of best immunoassay performance regarding conductivity (ionic strength) and pH. In Table 2.5 are presented the parameters determining the best immunoassay performance.

Table 2.5 Optimum conditions of the c-myc competitive immunoassay.

Conditions	Values
Competition Time	30 min
Preincubation Time	0 min
Tween-20	0.05%
Ionic strength (conductivity)	1.7 mS/cm (PB)
pH	7.5

Nevertheless, with the detectability achieved until now (IC_{50} around 200 nM) the minimum number of olfactory receptor per nanovesicle to quantify would be around 1000 OR NV^{-1} (see below the quantification methodology proposed). It is impossible to have this amount of OR NV^{-1} in a 100 nm diameter nanovesicle for three reasons: because the distance between olfactory receptors would be less than 1 nm (see ORs

distance discussion below), there are other membrane proteins besides the ORs in the lipidic membrane and the GPCRs (i.e. ORs) are ~ 3 nm large⁴⁴. Due to those facts, a decrease in the immunoassay detectability was necessary to have a more sensitive assay. In order to achieve that, the production of a home-made monoclonal anti-c-myc antibody with high affinity was performed.

2.3.3 Antibody production and characterization

Balb/c mice were immunized with the KLH bioconjugates and the spleen cells fused to generate hybridomas. Screening assays, to select the best B cell clones producing high affinity monoclonal antibodies, were performed by measuring the binding of the antibody fraction, present in the supernatants, to the C₁ and C₂ bioconjugates immobilized on the microtiter plates. The objective was to select clones able to recognize most of the c-myc peptide structure, to ensure satisfactory performance in the immunochemical assay to be developed (Table 2.6 and 2.7). Thus, while C₁ bioconjugate perfectly mimics the orientation of c-myc on the c-myc-OR1740 receptor, C₂ bioconjugates could also assist on selection of clones showing also high affinity against amino acids in the centre of the c-myc tag sequence or the area close to the OR.

The screening assays were run in the presence (competitive conditions) and absence (non-competitive conditions) of the target analyte (c-myc), to mimic the conditions envisaged for the immunochemical assay addressed to measure this tag in the NV (see Figure 2.13). Table 2.6 shows the absorbance values obtained with the c-myc analyte at two different concentrations (0 and 1 µM) for each positive hybridoma after the first cloning. These two values allow us to study the affinity and the inhibition of each hybridoma against the c-myc-bioconjugate competitor coating antigen, respectively. It is represented in a colour table where the darkest orange corresponds to the highest absorbance value and the lightest orange corresponds to the lowest absorbance value. The three clones selected to subclone again (highlighted) were those with high affinity (high absorbance value at 0 µM c-myc concentration) for the two different coating antigens and high inhibition (low absorbance value at 1 µM c-myc

concentration compared with the absorbance value at 0 μM). In conclusion, a good competition profile.

Table 2.6 First Screening.

Coating Antigen (CA) ^a	⁵ C ₁ -M(CH ₂) ₂ CO-CONA		¹³ C ₂ -CH ₂ CO-CONA	
	c-myc		c-myc	
Target analyte (μM) \blacktriangleright	1	0	1	0
Hybridomas ^b \blacktriangledown	Abs ^c		Abs ^c	
893E7 _{a10}	0.051	0.106	0.436	1.335
896D11 _{d11}	0.049	0.110	0.235	1.627
898C9 _{e10}	0.049	0.086	0.391	1.823
892H7 _{f8}	0.048	0.107	0.354	1.829
893E7 _{e7}	0.151	0.999	0.326	1.143
900H9 _{c12}	0.643	1.837	1.099	1.892
899B10 _{e9}	0.048	0.099	0.134	1.106
895H2 _{e9}	0.070	0.159	0.077	0.156
893E7 _{d10}	0.049	0.093	0.368	1.061
894D12 _{d9}	0.312	1.584	0.567	1.649
896D11 _{h6}	0.048	0.050	0.046	0.050
898C9 _{c11}	0.050	0.080	0.479	1.946
892H7 _{b12}	0.050	0.116	0.468	1.563
894D12 _{f7}	0.167	1.384	0.273	1.317
899B10 _{e7}	0.049	0.103	0.140	0.652
891D3 _{f8}	0.049	0.109	0.178	1.068
893E7 _{e9}	0.051	0.070	0.170	0.317
893E7 _{c8}	0.049	0.095	0.442	1.079
900H9 _{c10}	0.376	1.503	1.020	1.610
898C9 _{f8}	0.051	0.075	0.239	1.185
899B10 _{b11}	0.051	0.093	0.119	0.527
892H7 _{f7}	0.052	0.110	0.355	1.402
898C9 _{g9}	0.053	0.071	0.276	1.301

^a CA 0.2 ($\mu\text{g mL}^{-1}$)

^b mAb dilution used was 1/4000

^c Average absorbance using two-well replicates



Table 2.7 shows the absorbances values obtained for each hybridoma after the second cloning in the competitive immunoassay with the c-myc peptide as analyte at two different concentrations (0 and 1 μM). It is represented in a colour table with the same interpretation than the Table 2.6.

Table 2.7 Second Screening.

Coating Antigen (CA) ^a	⁵ C ₁ -M(CH ₂) ₂ CO-CONA		¹ C ₂ -CH ₂ CO-CONA	
Target analyte (μM) \blacktriangleright	c-myc		c-myc	
	1	0	1	0
Hybridomas ^b \blacktriangledown	Abs ^c		Abs ^c	
894D12 _{d9d10}	0.163	1.293	0.466	1.562
894D12 _{d9f9}	0.078	0.272	0.107	0.368
894D12 _{d9h6}	0.123	0.939	0.339	1.181
894D12 _{d9h7}	0.090	0.457	0.154	0.633
894D12 _{f7d12}	0.154	1.439	0.358	1.674
894D12 _{f7f9}	0.135	1.431	0.339	1.588
894D12 _{f7g9}	0.152	1.396	0.332	1.573
894D12 _{f7h8}	0.112	1.029	0.206	1.096
894D12 _{f7h9}	0.131	1.218	0.259	1.363
898C9 _{c11h6}	0.060	0.063	0.064	0.151

^a CA 0.2 ($\mu\text{g mL}^{-1}$)

^b mAb dilution used was 1/4000

^c Average absorbance using two-well replicates



High antibody titers were obtained from mice immunized with the C₂-KLH bioconjugate. Three antibody clones (named Ab894D12_{d9d10}, Ab894D12_{f7d12} and Ab894D12_{f7f9}) with acceptable features in terms of signal and detectability were isolated. From these three hybridomas we decided to work with Ab894D12_{f7f9}, producing the purified antibody for the development of a competitive immunoassay for its higher affinity and good inhibition.

2.3.4 Development of the c-myc-ELISA to the analysis of c-myc tagged proteins

Particularly, from all antibody clones selected (highlighted in Table 2.7), in PBST, Ab894D12_{f7f9} provided the best immunoassay features using $^5\text{C}_1\text{-M}(\text{CH}_2)_2\text{CO-CONA}$ as competitor (coating antigen) in an indirect ELISA format (Table 2.8, Figure 2.22A). Figure 2.23 shows the calibration curves obtained in this immunochemical system using two antibody sources (Ab894D12_{f7f9} and Ab9E10). Calibration curves for ligand binding assays⁴⁵, such as a competitive ELISA (Figure 2.23), are generally characterized by a non-linear relationship between the mean response and the analyte concentration, giving an absorbance response that decreases as the concentration of competitor analyte increases. The assay features obtained after fitting the curve to a four-parameter equation are shown in Table 2.8.

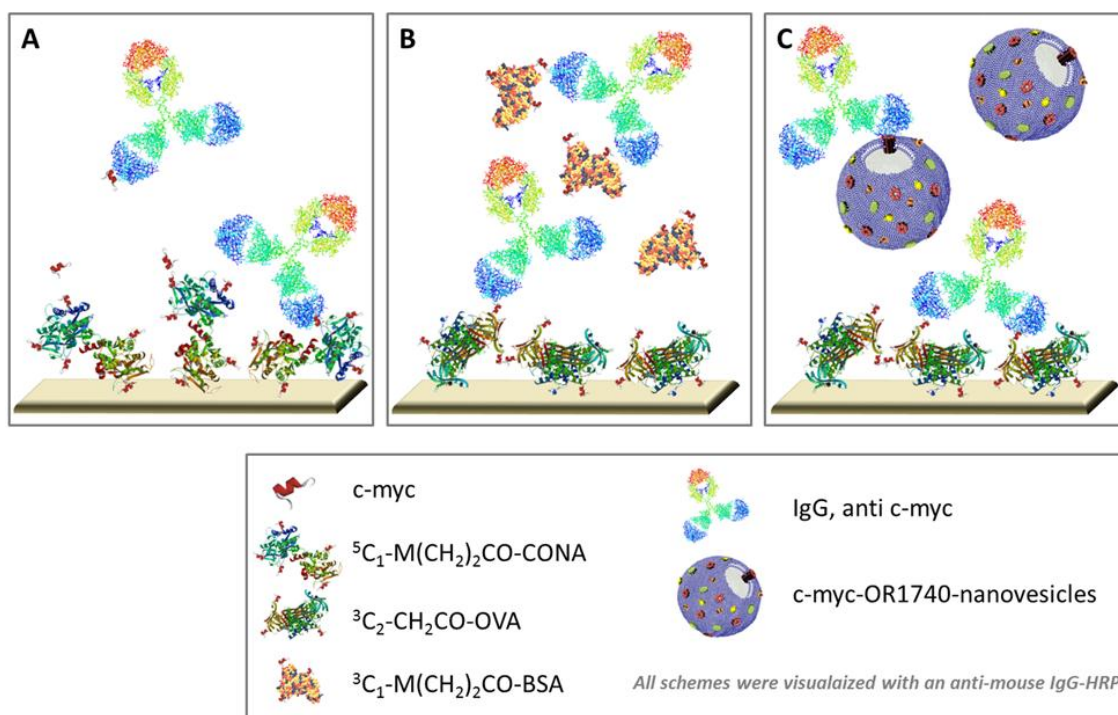


Figure 2.22 (A) Scheme of the indirect competitive ELISA. Immunoassay scheme using the c-myc peptide as analyte to evaluate two different anti-c-myc monoclonal antibodies (mAb) (Ab9E10 and Ab894D12_{f7f9}) and the absence of salts in the buffer. (B) Immunoassay scheme using c-myc bioconjugates to perform the standard calibration curves. (C). Immunoassay scheme of our model for GPCRs (c-myc-ORs) quantification in our nanovesicles (NV) sample.

As observed, in Figure 2.23 and in Table 2.8, the detectability was two orders of magnitude greater than that reached with Ab9E10 antibody, obtained from commercial

sources (IC_{50} values varied from ~ 1000 nM to ~ 10 nM in PBST buffer using Ab9E10 or Ab894D12_{f7f9}, respectively).

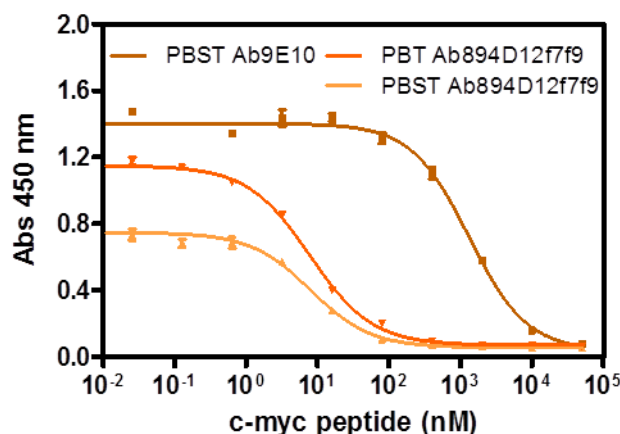


Figure 2.23 Calibration curves of the competitive immunoassays using the c-myc peptide as analyte and two different anti-c-myc monoclonal antibodies, Ab9E10 and Ab894D12_{f7f9}. The graph also shows that the absence of salts in the buffer (phosphate buffer with 0.05% Tween-20, PBT instead of phosphate buffer saline with 0.05% Tween-20, PBST) allowed an increase in the maximum signal of the assay. Each curve was built using three-well replicates. The parameters shown in Table 2.8 were extracted from the four-parameter equation used to fit the standard curves.

This difference was attributed to the immunizing hapten used. While Ab894D12_{f7f9} antibody was produced against the c-myc sequence (CysEQKLISEEDL), the commercial antibody 9E10 used a longer peptide sequence (AEEQKLISEEDLLRKRREQLKHKLEQLRNSCA) conjugated through the Cys residue (C) to KLH as immunizing hapten. Although Ab9E10 recognizes the EQKLISEEDL sequence from the human c-myc protein⁴⁶, in solution or when linked to the protein used as carrier, this peptide could have folded into the tertiary structure of the protein used as carrier, thus diminishing the capacity of these antibodies to strongly bind the c-myc peptide.

Thus, at this stage we could already presume that a high sensitive and selective monoclonal antibody was successfully produced able to detect the c-myc tag in the nanomolar range.

Because transmembrane protein expression in heterologous systems is often low⁴³, a high sensitive ELISA assay was required to quantify OR expression. Thus, the effect of several physicochemical factors (pH, ionic strength, content of Tween 20, and

incubation and competition times) on the immunochemical assay were evaluated with the aim to improve detectability. Only ionic strength produced a remarkable effect, by low values increased significantly the maximum signal while maintaining the detectability. Figure 2.23 demonstrates how the standard curves built in PBT show higher signal. Thus, at this stage we presumed that we had produced a highly sensitive and selective monoclonal antibody able to detect the c-myc tag in the nanomolar range.

This was confirmed by the Western blot assays performed to assess the capacity of Ab894D12_{17f9} to recognize the c-myc-OR1740 embedded in the NVs (Figure 2.24). As can be observed, this antibody detected the c-myc peptide fused to the OR at two orders of magnitude lower than Ab9E10. Similarly, the specificity of the binding reaction was also confirmed by the lack of signal on the trails where the SSTR2 protein receptor-NVs were run.

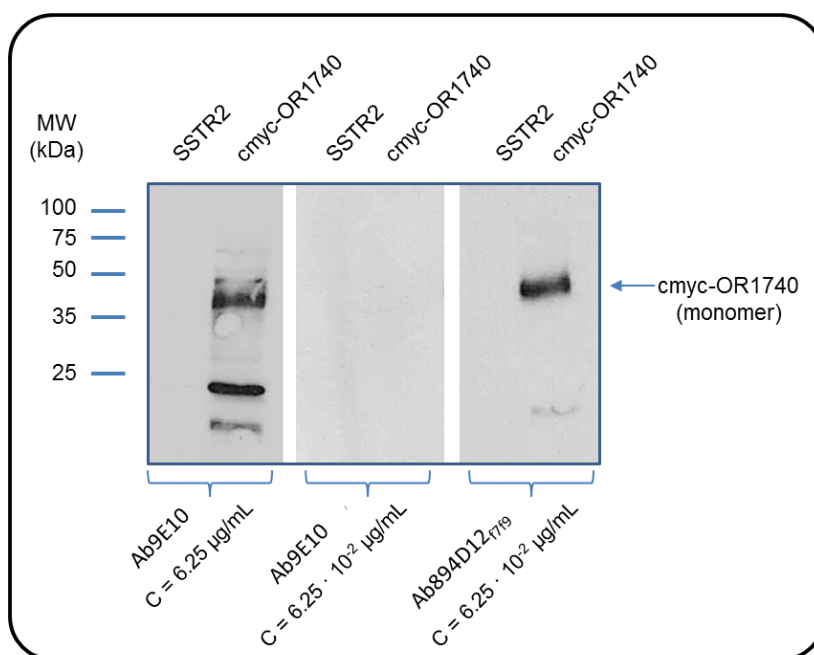


Figure 2.24 Picture showing the Western Blot results performed to assess the capability of anti-c-myc antibodies Ab9E10 and Ab894D12_{17f9} at a range of concentrations (C) to detect the c-myc-OR1740. Nanovesicles carrying SSTR2 receptors were used as control (-). Nanovesicles carrying c-myc-OR1740 were used as evaluation sample (+). The monomer olfactory receptor molecular weight is around 35 kDa⁴⁷.

Table 2.8 Immunoassay features achieved for c-myc and the protein bioconjugates.

Ab		Ab894D12 ₁₇₁₉													
Buffer		PBST		PBT				Blank Matrix ^a							
Coating Antigen (CA)		⁵ C ₁ -CONA ^c		³ C ₂ -CH ₂ CO-OVA ^e				³ C ₂ -CH ₂ CO-OVA ^e							
Target analyte		c-myc ^f		c-myc ^g		C ₂ ^g		¹ C-HRP ^g		³ C-BSA ^g		⁴ C ₁ -CONA ^g		¹ C ₁ -HRP ^g	
A_{max}	1.40 ± 0.02	0.75 ± 0.01	1.15 ± 0.01	0.89 ± 0.01	0.87 ± 0.01	0.87 ± 0.01	0.87 ± 0.01	0.87 ± 0.01	0.87 ± 0.01	0.90 ± 0.01	0.90 ± 0.01	0.86 ± 0.01	0.90 ± 0.01	0.90 ± 0.01	
A_{min}	0.04 ± 0.04	0.05 ± 0.01	0.07 ± 0.01	0.11 ± 0.02	0.08 ± 0.02	0.08 ± 0.02	0.08 ± 0.02	0.11 ± 0.01	0.11 ± 0.01	0.10 ± 0.01	0.10 ± 0.01	0.12 ± 0.01	0.14 ± 0.01	0.14 ± 0.01	
IC₅₀, nM	1318 ± 0.05	8.02 ± 0.05	7.84 ± 0.03	19.0 ± 0.05	2.72 ± 0.06	2.72 ± 0.06	2.72 ± 0.06	0.99 ± 0.04	0.99 ± 0.04	0.08 ± 0.02	0.08 ± 0.02	0.07 ± 0.03	0.39 ± 0.04	0.39 ± 0.04	
Slope	-1.07 ± 0.12	-1.03 ± 0.11	-0.99 ± 0.07	-1.01 ± 0.09	-0.80 ± 0.07	-0.80 ± 0.07	-0.80 ± 0.07	-0.85 ± 0.06	-0.85 ± 0.06	-0.90 ± 0.03	-0.90 ± 0.03	-1.15 ± 0.03	-0.96 ± 0.07	-0.96 ± 0.07	
R²	0.99 ± 0.05	0.99 ± 0.03	1.00 ± 0.03	0.99 ± 0.03	0.99 ± 0.03	0.99 ± 0.03	0.99 ± 0.03	1.00 ± 0.02	1.00 ± 0.02	1.00 ± 0.01	1.00 ± 0.01	1.00 ± 0.02	0.99 ± 0.03	0.99 ± 0.03	

^a, SSTR2-NV solution (TPC = 35 μg mL⁻¹)
^b, CA 0.062 (μg mL⁻¹)
^c, CA 0.031 (μg mL⁻¹)
^d, CA 0.016 (μg mL⁻¹)
^e, CA 0.01 (μg mL⁻¹)
^f, mAb dilution used was 1/4000
^g, mAb dilution used was 1/2500

unless otherwise indicated the cross-linker of the bioconjugates is M(CH₂)₂CO.

2.3.4.1 Matrix effect

As mentioned above, within this study we have focused on the OR1740 and OR7D4, members of the important GPCRs family. These receptors were expressed in yeast plasma membrane⁸, a system considered suitable to achieve high protein expression^{22,43}. From these cells, NVs were prepared as described in the experimental section and characterized in respect to their average size, concentration (NV mL⁻¹), charge and TPC. In this respect, previously²³, we demonstrated that there is a correlation between the TPC and the NV concentration (*Chapter 1*). In our case, we could estimate that the batch of NVs used in this study had a protein content of 3.6×10^{-4} pg protein NV⁻¹ and 5.97×10^{-4} pg protein NV⁻¹ for OR1740-NVs and OR7D4-NVs solutions respectively.

The NVs (diameter ~ 100 nm) containing the c-myc-OR1740 were formed from natural membranes, thus containing a high content of phospholipids, which comprise the core structure of cell membranes. Due to this fact, our main concern was the potential non-specific interactions of these lipophilic NVs with the immunoreagents or the labware used in the assays. In order to assess these potential undesirable effects, we built calibration curves on solutions of blank matrices and compared the immunochemical response to the curve prepared in buffer. These blank matrices were just solutions of different concentrations of NVs (different TPC), prepared under the same conditions, but carrying another transmembrane receptor (SSTR2) without the c-myc tag. As it can be observed in Figure 2.25 the response of the calibration curves built on these blank matrices ($3\text{-}60 \mu\text{g mL}^{-1}$ TPC or $4.40 \cdot 10^9\text{-}8.80 \cdot 10^{10}$ NV mL⁻¹) did not differ significantly from the curve prepared in buffer. Only solutions with a high TPC concentration ($60 \mu\text{g mL}^{-1}$) produced a slight decrease of the maximum absorbance that did not affect the detectability. Moreover, this effect was eliminated by just diluting the solution one-half ($20 \mu\text{g mL}^{-1}$) with PBT.

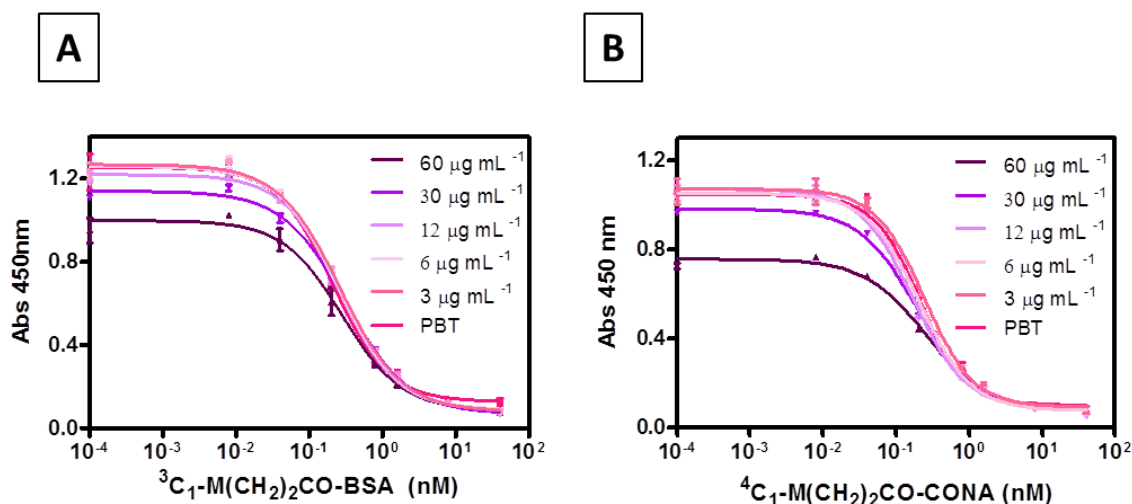


Figure 2.25 Matrix effect produced by a solution of natural yeast nanovesicles. **(A)** Standard curves using ³C₁-M(CH₂)₂CO-BSA as analyte in PBT and in blank matrix buffer (SSTR2) at a range of concentrations (3-60 µg mL⁻¹ TPC or 4.40·10⁹-8.80·10¹⁰ NS mL⁻¹). **(B)**. Standard curves using ⁴C₁-M(CH₂)₂CO-CONA as analyte in PBT and in validation buffer (SSTR2) at a range of concentrations (3-60 µg mL⁻¹ TPC or 4.40·10⁹-8.80·10¹⁰ NV mL⁻¹). The parameters showing the effect of the matrix were extracted from the four-parameter equation used to fit the standard curves and are presented in Table 2.9 and 2.10 respectively. Each curve was built using three-well replicates.

Therefore, the microplate-ELISA developed performed well on such media, despite the lipidic nature of the membrane components. In these experiments, the analyte used was ³C₁-M(CH₂)₂CO-BSA and ⁴C₁-M(CH₂)₂CO-CONA (Figure 2.25) to mimic better c-myc-tagged ORs.

Table 2.9 Immunoassay features achieved for $^3\text{C}_1\text{-M}(\text{CH}_2)_2\text{CO-BSA}$ bioconjugate of the Figure 2.25A.

Ab	Ab894D12 _{T719} ^a						
Coating Antigen (CA)	$^3\text{C}_2\text{-CH}_2\text{CO-OVA}$ ^b						
Target analyte	$^3\text{C}_1\text{-M}(\text{CH}_2)_2\text{CO-BSA}$ ^c						
Buffer	Blank Matrix ^c						
	0 $\mu\text{g mL}^{-1}$ (PBT)	60 $\mu\text{g mL}^{-1}$	30 $\mu\text{g mL}^{-1}$	12 $\mu\text{g mL}^{-1}$	6 $\mu\text{g mL}^{-1}$	3 $\mu\text{g mL}^{-1}$	
A_{max}	1.254 ± 0.027	0.997 ± 0.028	1.139 ± 0.016	1.218 ± 0.018	1.258 ± 0.020	1.269 ± 0.018	
A_{min}	0.128 ± 0.026	0.087 ± 0.031	0.070 ± 0.018	0.090 ± 0.019	0.088 ± 0.021	0.081 ± 0.019	
IC₅₀, nM	0.209 ± 0.050	0.283 ± 0.070	0.315 ± 0.035	0.216 ± 0.035	0.251 ± 0.038	0.263 ± 0.033	
Slope	-1.135 ± 0.127	-1.070 ± 0.159	-1.004 ± 0.070	-1.112 ± 0.085	-1.062 ± 0.085	-1.036 ± 0.071	
R²	0.992 ± 0.048	0.985 ± 0.053	0.996 ± 0.029	0.996 ± 0.034	0.995 ± 0.036	0.997 ± 0.032	

^a mAb dilution used was 1/100000^b CA 0.0125 ($\mu\text{g mL}^{-1}$)^c SSTR2-NV solution

Table 2.10 Shows the features of the competitive ELISA assay of the Figure 2.25B

Ab	Ab894D12 _{F719} ^a						
Coating Antigen (CA)	³ C ₂ -CH ₂ CO-OVA ^b						
Target analyte	⁴ C ₁ -M(CH ₂) ₂ CO-CONA ^c						
Buffer	Blank Matrix ^c						
	0 µg mL ⁻¹ (PBT)	60 µg mL ⁻¹	30 µg mL ⁻¹	12 µg mL ⁻¹	6 µg mL ⁻¹	3 µg mL ⁻¹	
A_{max}	1.046 ± 0.032	0.757 ± 0.012	0.983 ± 0.013	1.072 ± 0.021	1.053 ± 0.018	1.072 ± 0.021	
A_{min}	0.101 ± 0.028	0.074 ± 0.013	0.076 ± 0.012	0.084 ± 0.019	0.076 ± 0.018	0.093 ± 0.021	
IC₅₀, nM	0.211 ± 0.058	0.261 ± 0.040	0.199 ± 0.030	0.171 ± 0.042	0.208 ± 0.048	0.243 ± 0.042	
Slope	-1.383 ± 0.235	-1.021 ± 0.084	-1.091 ± 0.070	-1.194 ± 0.120	-1.219 ± 0.129	-1.291 ± 0.142	
R²	0.985 ± 0.056	0.995 ± 0.022	0.997 ± 0.022	0.994 ± 0.037	0.995 ± 0.034	0.993 ± 0.040	

^a mAb dilution used was 1/100000
^b CA 0.0125 (µg mL⁻¹)
^c SSTR2-NV solution

2.3.4.2 c-myc-biomolecule reference

An important challenge was to identify a suitable reference for the quantification of the c-myc-ORs on the NVs. Since this tagged receptor is stable only when incorporated on membranes, a well-characterized NV with a defined number of OR molecules would have been the ideal standard. However, up to now, the lack of analytical tools to characterize the NV from this point of view made this approach

unfeasible. In this regard, we proposed using well-characterized c-myc-bioconjugates as standards rather than the c-myc peptide alone, since the former mimics better the c-myc-ORs. Figure 2.26 shows the calibration curves of the c-myc-bioconjugates and free c-myc peptides as analytes, where it can be observed a significant increase in the detectability for c-myc-bioconjugates ($IC_{50}=0.083-0.386$ nM, see Table 2.8). Thus, by using 3C_1 -Y-X bioconjugates, in which the c-myc was coupled through the N-terminal amino acid of the protein, the c-myc epitopes will be exposed for antibody recognition on a similar manner to the c-myc-OR in the NVs (Figure 2.13).

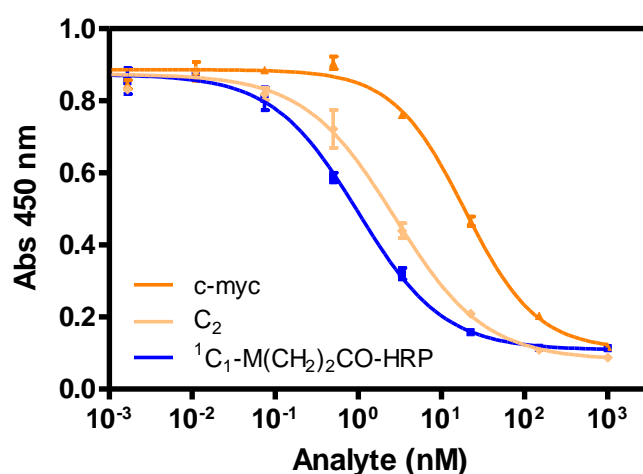


Figure 2.26 Calibration curves resulting from the evaluation of different analytes, free c-myc peptide (the commercial one and the C₂) and the ¹C₁-M(CH₂)₂CO-HRP bioconjugate in order to choose the candidates for the quantification model. Each curve was built using three-well replicates. The assay parameters are shown in Table 2.8.

Therefore, the immunochemical response of three well-characterized bioconjugates (⁴C₁-M(CH₂)₂CO-CONA, ³C₁-M(CH₂)₂CO-BSA and ¹C₁-M(CH₂)₂CO-HRP, see Table 2.8) and that of the c-myc-OR in the NVs (Figures 2.22B and 2.22C) was assessed. For this purpose calibration curves of these bioconjugates were prepared in the blank matrix and run them in the microplate-ELISA developed.

In these experiments, ³C₂-CH₂CO-bioconjugates were used as coating antigens since they provided greater detectability (Table 2.11), due to the greatest heterology in respect to the immunogen (different cross-linker). As it can be observed in Figure 2.26 and Figure 2.27 (see also Table 2.8) the detectability achieved for the c-myc-bioconjugates was in all cases in the low nM range ($IC_{50}=0.083-0.386$ nM).

Table 2.11 shows the features of the competitive ELISAs to evaluate the best combination of coating antigen-analyte (in PBT) to be used as standards in our quantification model. Only those bioconjugates well characterized by MALDI-TOF-MS were studied. C₂-bioconjugates as competitor coating antigen were evaluated after showing better affinity and inhibition characteristics compared to C₁-bioconjugates (see Table 2.6 and Table 2.7) particularly if prepared from the iodoacetate derivatized molecules, probably due to the different crosslinker in respect to the immunogen one. In green are highlighted those combinations that reach the most sensitive competitive assay considering that we studied: *a*) three biomolecules (BSA, CONA, HRP) used to synthesized the c-myc-bioconjugate analyte, *b*) two biomolecules (BSA, OVA) used to synthesized the c-myc-bioconjugate competitor coating antigen, and *c*) their molecular ratios c-myc:biomolecule. Finally the coating antigen selected for our model was the ³C₂-CH₂CO-OVA and the three different bioconjugates as competitors analytes were the ⁴C₁-M(CH₂)₂CO-CONA, ³C₁-M(CH₂)₂CO-BSA and ¹C₁-M(CH₂)₂CO-HRP. Figure 2.27 reported the calibration curves of the three c-myc-bioconjugates chosen as candidates for the quantification model.

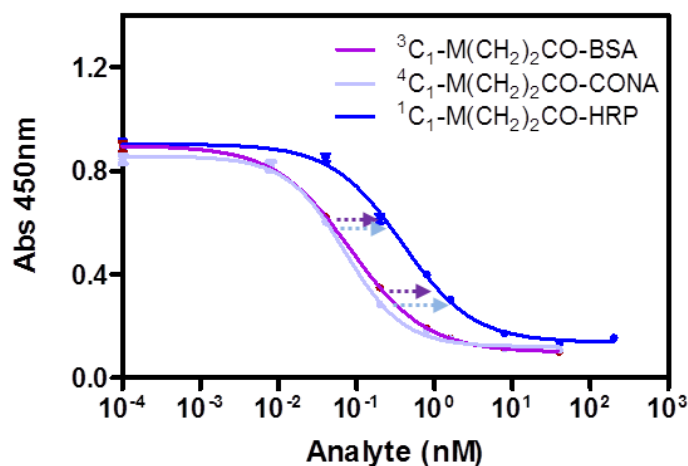


Figure 2.27 Calibration curves of the c-myc-bioconjugates chosen as candidates for the quantification model in blank matrix buffer (SSTR2-NV, TPC = 35 $\mu\text{g mL}^{-1}$). Arrows in blue and purple mark the two concentration points of ⁴C₁-M(CH₂)₂CO-CONA and ³C₁-M(CH₂)₂CO-BSA to be interpolated in the ¹C₁-M(CH₂)₂CO-HRP standard curve. Immunoassay features are represented in Table 2.8.

As expected, the immunochemical response was different depending on the protein used and on the hapten density of each bioconjugate (Table 2.8). Thus, the HRP

bioconjugate, with only one hapten attached, provided the lower detectability, while no significant differences were observed between the BSA and CONA bioconjugates.

Controls using the maleimido-derivatized proteins as analytes demonstrated that the response was only due to the c-myc peptide and that there was no interference from the cross-linker which was also used for the preparation of the immunogen (Figure 2.28) since no inhibition curves were obtained.

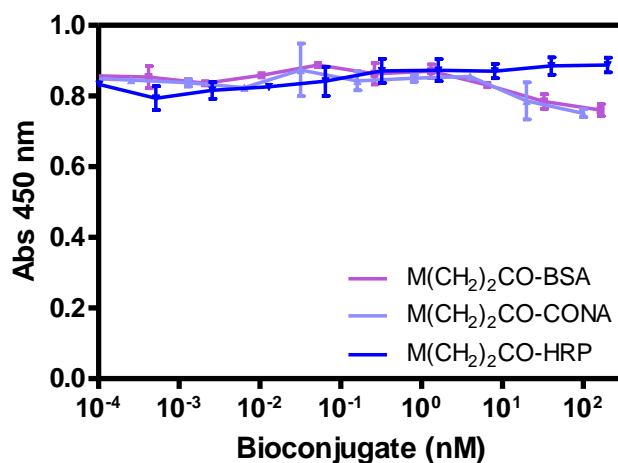


Figure 2.28 Evaluation of the unspecific adsorption of the immunoassay using the anti-c-myc (Ab894D12₁₇₇₉) and the M(CH₂)₂CO-biomolecule (maleimido-biomolecule) in the working conditions (PBT buffer). Not interaction existed. The antibody only recognized the C₂ peptide coming from the coating antigen. Each curve was built using three-well replicates.

Table 2.11 Shows the features of the competitive ELISAs.

Ab	Ab894DI2 _{r719} ^a																			
	⁸ C ₂ -CH ₂ CO-BSA ^a					⁶ C ₂ -CH ₂ CO-BSA ^b					⁵ C ₂ -CH ₂ CO-OVA ^c					³ C ₂ -CH ₂ CO-OVA ^d				
Coating Antigen (CA)	A	B	C	D	E	A	B	C	D	E	A	B	C	D	E	A	B	C	D	E
Target analyte	0.83	0.82	0.82	0.77	0.99	0.74	0.72	0.74	0.70	0.88	0.94	0.91	0.90	0.70	1.12	0.83	0.80	0.80	0.75	0.87
A _{max}	± 0.01	± 0.01	± 0.01	± 0.02	± 0.01	± 0.01	± 0.01	± 0.01	± 0.01	± 0.01	± 0.01	± 0.01	± 0.01	± 0.01	± 0.02	± 0.01	± 0.01	± 0.01	± 0.01	± 0.01
A _{min}	0.11	0.10	0.10	0.10	0.11	0.10	0.10	0.10	0.08	0.12	0.10	0.10	0.10	0.09	0.07	0.10	0.11	0.10	0.09	0.11
	± 0.01	± 0.01	± 0.01	± 0.01	± 0.01	± 0.01	± 0.01	± 0.01	± 0.01	± 0.01	± 0.01	± 0.01	± 0.01	± 0.01	± 0.03	± 0.01	± 0.01	± 0.01	± 0.01	± 0.01
IC ₅₀ , nM	0.08	0.12	0.10	0.08	0.92	0.07	0.11	0.08	0.10	1.27	0.08	0.16	0.12	0.11	1.23	0.07	0.11	0.09	0.09	0.99
	± 0.05	± 0.05	± 0.05	± 0.06	± 0.05	± 0.06	± 0.04	± 0.05	± 0.06	± 0.03	± 0.05	± 0.04	± 0.04	± 0.07	± 0.08	± 0.03	± 0.03	± 0.04	± 0.07	± 0.04
Slope	-0.8	-0.8	-0.8	-0.8	-0.7	-0.8	-0.8	-0.8	-0.7	-0.8	-0.6	-0.7	-0.8	-0.7	-0.6	-0.7	-0.9	-0.9	-0.8	-0.8
	± 0.07	± 0.07	± 0.07	± 0.08	± 0.04	± 0.08	± 0.05	± 0.07	± 0.06	± 0.04	± 0.04	± 0.05	± 0.06	± 0.07	± 0.07	± 0.04	± 0.05	± 0.07	± 0.09	± 0.06
R ²	0.99	0.99	0.99	0.99	1.00	0.99	1.00	0.99	1.00	1.00	0.99	1.00	1.00	0.99	0.99	1.00	1.00	1.00	0.99	1.00
	± 0.03	± 0.03	± 0.03	± 0.03	± 0.02	± 0.03	± 0.02	± 0.02	± 0.02	± 0.02	± 0.02	± 0.02	± 0.03	± 0.03	± 0.05	± 0.02	± 0.02	± 0.02	± 0.03	± 0.02

^a mAb dilution used was 1/320000 and CA 0.006 (µg mL⁻¹)
^b mAb dilution used was 1/250000 and CA 0.006 (µg mL⁻¹)
^c mAb dilution used was 1/160000 and CA 0.006 (µg mL⁻¹)
^d mAb dilution used was 1/250000 and CA 0.01 (µg mL⁻¹)

A = ³C₁-M(CH₂)₂CO-BSA
B = ¹C₁-M(CH₂)₂CO-BSA
C = ⁵C₁-M(CH₂)₂CO-CONA
D = ⁶C₁-M(CH₂)₂CO-CONA
E = ¹C₁-M(CH₂)₂CO-HRP

2.3.4.3 Model validation

First, as proof-of-concept, we probed the viability of the approach by quantifying the c-myc hapten load of c-myc protein bioconjugates. For this purpose, we measured the immunochemical response of two solutions of $^4\text{C}_1\text{-M}(\text{CH}_2)_2\text{CO-CONA}$ and $^3\text{C}_1\text{-M}(\text{CH}_2)_2\text{CO-BSA}$ in respect to the $^1\text{C}_1\text{-M}(\text{CH}_2)_2\text{CO-HRP}$ reference standard curve (Figure 2.27). As mentioned above, HRP has few lys residues available for conjugate, for which reason the chances to obtain a bioconjugate with just one hapten per protein^{48,49} are high, as corroborated by MALDI-TOF-MS. By interpolating the signal of the BSA and CONA bioconjugates we could estimate the hapten density of $^4\text{C}_1\text{-M}(\text{CH}_2)_2\text{CO-CONA}$ and $^3\text{C}_1\text{-M}(\text{CH}_2)_2\text{CO-BSA}$ by ELISA. Hence, as it can be observed in Table 2.12 (see below), the difference between the calculated hapten densities using MALDI-TOF-MS and the immunochemical approach was close.

Table 2.12 Hapten/Protein density (δ)

Bioconjugate	[SSTR2 matrix] ^b		[Bioconjugate] _{measured}		Hapten Density, δ	
	nM	TPC, $\mu\text{g mL}^{-1}$	IR equiv (nM) ^c	ELISA ^d	ELISA ^e , \bar{x}	MALDI-TOF-MS
³ C ₁ -M(CH ₂) ₂ CO-BSA	0.80	35	2.626	3.39 ± 0.16	3.97 ± 0.81	2.6
	0.20		0.703			
	0.80	45	3.117	4.54 ± 0.91		
	0.20		1.037			
⁴ C ₁ -M(CH ₂) ₂ CO-CONA	0.80	35	3.026	3.04 ± 0.01	3.47 ± 0.62	3.9
	0.20		0.609			
	0.80	45	2.855	3.91 ± 0.48		
	0.20		0.849			

^a, Solutions of the bioconjugates, at two different concentrations (0.8 and 0.2 nM), were prepared in the blank matrix (SSTR2 solution)^b also at two different TPC values. The solutions were measured by ELISA using ¹C₁-M(CH₂)₂CO-HRP (ratio c-myc:HRP, 1:1) as reference on the calibration curve. Interpolation of the normalized absorbance values on the standard curve allowed to calculate bioconjugate concentration as immunoreactivity equivalents (IR equiv)^c of the HRP bioconjugate.

^d, Knowing that the hapten density of the ¹C₁-M(CH₂)₂CO-HRP is 1, as calculated by MALDI-TOF-MS, and taking into consideration the Avogadro number, it was possible to estimate the number of c-myc residues on the protein bioconjugates used as models. The value is the average and standard deviation obtained for two bioconjugates concentrations at each concentration of the blank matrix.

^e, The value is the average and standard deviation of the estimation obtained at two distinct concentrations of the blank matrix (SSTR2).

^f, Hapten densities of the bioconjugates calculated by MALDI-TOF-MS

2.3.5 Olfactory Receptor quantification: GPCR integrated into natural nanovesicles

The major benefit of indirect competitive ELISA immunoassay developed is that the quantification of the olfactory receptor expression can be performed directly without the necessity of a previous solubilisation and purification step of the olfactory receptors from their natural lipid environment. With the promising results obtained in the paragraph above we approached the quantification of the number of ORs of our nanovesicles.

For this purpose, solutions with different concentrations of c-myc-ORs-NVs (in PBT) were measured using standard curves prepared with the three peptide-protein bioconjugates in blank matrix mentioned above. Only those NV solutions providing an immunochemical response within the lineal range of the assay (between 20-80% of the maximum absorbance) could be used for quantization ($TPC = 25-45 \mu\text{g mL}^{-1}$) of the assay.

Figure 2.29 shows the calibration curves of the absorbance signal of the three c-myc-Bioconjugates (analytes) diluted into a solution of control nanovesicles carrying the SSTR2 receptor at the total protein concentration of $35 \mu\text{g/mL}$ ($7.03 \cdot 10^{10} \text{ NV mL}^{-1}$). The absorbances obtained at this total protein concentration of samples containing NS carrying c-myc-OR7D4 ($5.9 \cdot 10^{10} \text{ NS/mL}$) and c-myc-OR1740 ($9.8 \cdot 10^{10} \text{ NV mL}^{-1}$) were interpolated to each of the corresponding calibration. As it has been mentioned above the intention to use three different bioconjugates was to minimize the error obtained when comparing the c-myc sample with just a single bioconjugate.

The assay features are repeated at each different NV concentration (Table 2.13) and each curve was built using three-well replicates.

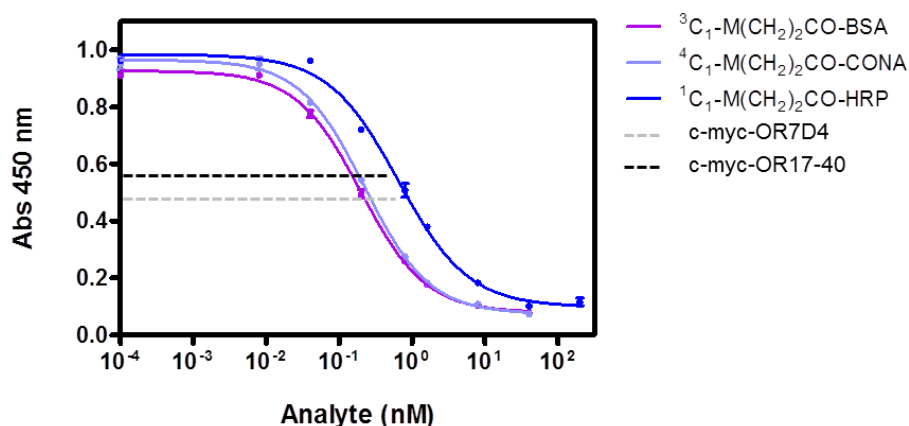


Figure 2.29 Inhibition curves of the three c-myc-Bioconjugates at the concentration of SSTR2 carrying nanovesicles $7.03 \cdot 10^{10}$ NV mL⁻¹ (SSTR2-NV, TPC = 35 μ g mL⁻¹). The horizontal lines interpolated in the calibration curve mark the absorbance of the c-myc-OR1740 carrying nanovesicles (black) and c-myc-OR7D4 carrying nanovesicles (light grey) at the corresponding concentration. Calibration curves are built using three-well replicated and fitted with a four-parameter equation.

Table 2.13 Quantification of ORs NV⁻¹ using the different protein bioconjugates as standard references^a

	[TPC] (μ g/mL)	[Vesicles] (NV/mL)	OR NV ^{-1, b}			ORs NV ^{-1, c} \bar{x}	
			³ C ₁ -BSA	⁴ C ₁ -CONA	¹ C ₁ -HRP	x_0	x_f
c-myc-OR1740	25	$7.0 \cdot 10^{10}$	1.04 ± 0.17	1.80 ± 0.34	--	1.42 ± 0.54	2.81 \pm 1.08
	30	$8.4 \cdot 10^{10}$	2.04 ± 0.10	4.69 ± 0.22	--	3.37 ± 1.88	
	35	$9.8 \cdot 10^{10}$	1.32 ± 0.01	2.86 ± 0.02	--	2.09 ± 1.08	
			3.79 ± 0.37	4.52 ± 0.37	5.53 ± 0.56	4.61 ± 0.87	
	45	$12.6 \cdot 10^{10}$	2.04 ± 0.02	3.81 ± 0.04	--	2.92 ± 1.25	
c-myc-OR7D4	25	$4.2 \cdot 10^{10}$	4.08 ± 0.41	7.48 ± 0.77	--	5.78 ± 2.41	5.56 \pm 2.35
	30	$5.0 \cdot 10^{10}$	4.35 ± 0.05	9.92 ± 0.12	--	7.14 ± 3.93	
	35	$5.9 \cdot 10^{10}$	2.74 ± 0.33	5.57 ± 0.60	4.04 ± 0.64	4.11 ± 1.41	
	45	$7.5 \cdot 10^{10}$	3.64 ± 0.19	6.77 ± 0.32	--	5.21 ± 2.21	

^a According to the linear correlation between the Total Protein Concentration (TPC, μ g mL⁻¹) and the nanovesicle concentration (NV mL⁻¹) a ratio of 3.6×10^{-4} pg protein/ NV for OR1740-NVs and a ratio of 5.9×10^{-4} pg protein/NV for OR7D4-NVs are estimated. Results were obtained in different days.

^b Concentration of OR per nanovesicle resulting from interpolating the immunochemical response of each solution on the corresponding standard curve of each bioconjugate. Calculations have been made, as described before (see experimental section and Table 2.12) considering the δ of each bioconjugate.

^c Concentration ORs per nanovesicle calculated as average of the measurements using the different bioconjugates as standards for each TPC (x_0) and taking into consideration all measurements made at different TPC (x_f),

unless otherwise indicated the cross-linker of the bioconjugates is $M(CH_2)_2CO$.

Deconvolution of the concentration values found on the three calibration curves, taking into consideration the NV concentration, as described in the experimental section, indicated that our preparations contained approximately (3 ± 1) c-myc-OR1740 NV^{-1} , weighted mean of six samples at four different concentrations, and (6 ± 2) c-myc-OR7D4 NV^{-1} , weighted mean of four samples at four different concentrations (Figure 2.30).

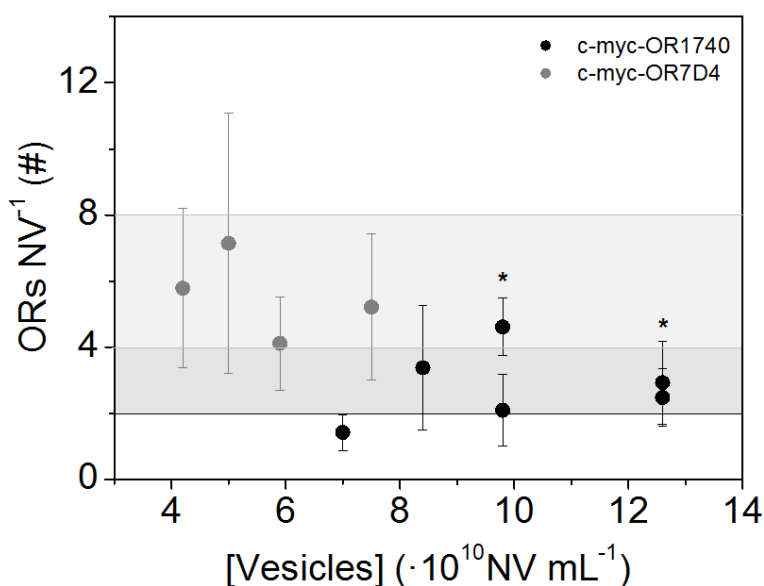


Figure 2.30 Number of receptors per NV (ORs NV^{-1}) at each concentration. The black dots correspond to the quantification of the c-myc-OR1740-NV and the grey dots correspond to the quantification of the c-myc-OR7D4-NV. Dark grey area shows (3 ± 1) c-myc-OR1740/NV and light grey area shows (6 ± 2) c-myc-OR7D4/NV. The quantification reproducibility between two different days (*) is as well presented.

2.3.6 Quantification verification and discussion

The quantification presented above is compared with that obtained with a standard procedure based on the yeast membrane fraction disruption, the solubilisation and the subsequent purification of the c-myc-tagged expressed proteins.

Total membrane fraction of *Saccharomyces Cerevisiae* yeast cells carrying heterogeneously expressed human c-myc-OR1740 olfactory receptors or chimpanzee c-myc-OR7D4 olfactory receptors were prepared by cell disruption⁸. The olfactory receptors content in the membrane fraction was determined after solubilizing all the proteins from the yeast lipid membrane in fos-choline 14 (FC14) detergent and purifying the c-myc-ORs onto an affinity column with an anti-c-myc antibody. Subsequent absorbance quantification of the eluted purified receptors gives (0.0030 ± 0.0005) g c-myc-OR1740/g total proteins and (0.008 ± 0.002) g c-myc-OR7D4/g total proteins. Western blotting (WB) was also performed to check the quality of the proteins in these elutes.

Figure 2.31 shows the WB of a c-myc-OR1740 purified sample (2.31-A) and a c-myc-OR7D4 purified sample (2.31-B). An immunoreactive band is observed around 30 kDa for c-myc-OR1740 and around 26 kDa for c-myc-OR7D4 that can be associated to the monomeric form of the receptors (see the blue arrows in Figure 2.31). Bands corresponding to oligomeric forms of the receptors are also observed. The higher intensity of the monomeric OR band with 50 CMC (critical micelle concentration) compared to 350 CMC for the c-myc-OR1740 elute may be due to a modification of the receptor conformation that reduces the accessibility of the c-myc epitope or its affinity, or induces the masking of the c-myc epitope by the detergent. For the c-myc-OR7D4 eluate, 50 CMC and 350 CMC conditions did not induce such differences.

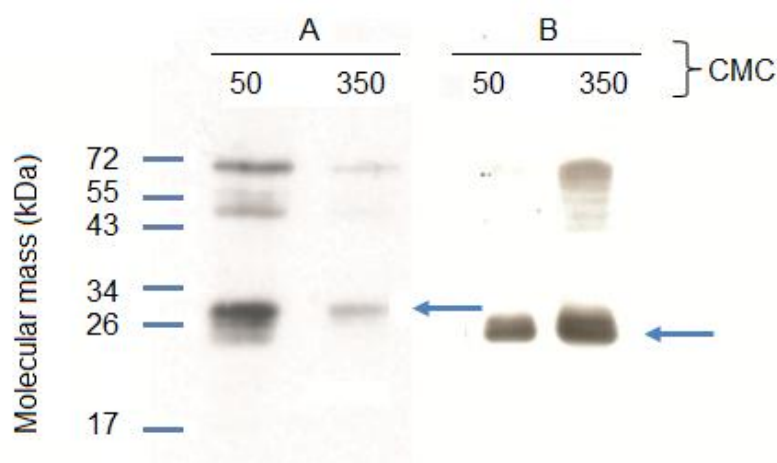


Figure 2.31 Western Blot of elutes of purified c-myc-OR1740 (**A**) and c-myc-OR7D4 (**B**) after solubilization of the membrane fraction of *Saccharomyces Cerevisiae* expressing these receptors. 450 μ g of c-myc-OR membrane fractions were solubilized using FC14 at 50 or 350 CMC.

It is interesting to compare the quantification results obtained with both methods. The quantification of solubilized ORs and of the ORs NV⁻¹ by ELISA globally seem to be correlated since OR7D4 NV⁻¹ appear to carry about twice as many receptors as OR1740 NV⁻¹, whereas the weight ratio of solubilized OR7D4 receptors relative to the total protein concentration (TPC) is ~ 2.7 times larger than that of OR1740.

It is worthwhile to mention that ORs in the total membrane fraction may take any orientation during NV production (i. e. upon sonication and closing in the form of nanovesicles). Thus, the ELISA assay can only quantify those receptors oriented with their N-terminus towards the outside of the nanovesicles, and thus the reported value obtained by ELISA could be an underestimation of the total number of ORs NV⁻¹. But the results obtained by these two very different procedures anyway remain within the same order of magnitude, which strengthens their validity.

Besides, we tried to confirm the underestimation quantification by ELISA comparing both methods. For c-myc-OR1740-nanovesicles 3 ORs were quantify as well as 0.003 g OR/g Total Protein. Considering the molecular weight of the receptor (30 kDa) and the membrane composition of the *Saccharomyces cerevisiae* yeast cell (total protein composition)⁵⁰, without taking into account the lipids density, the weight of the nanovesicles membrane was calculated, Equation 2:

$$\begin{aligned} & 3 \frac{OR}{NV} \cdot \frac{30 \text{ kDa}}{1 OR} \cdot \frac{1.66 \cdot 10^{-21}}{1 \text{ kDa}} \cdot \frac{1 \text{ g Total Protein}}{0.003 \text{ g}} \cdot \frac{100 \text{ g membrane}}{49.3 \text{ g TP}} \\ & = 1.01 \cdot 10^{-16} \text{ g membrane/NV} \end{aligned}$$

(Eq. 2)

Subsequently, if the double membrane width was around 7.5 nm⁵¹, then the volume of a 100 nm diameter nanovesicle was 202043 nm³. Thus, the membrane nanovesicle density was calculated, Equation 3:

$$\text{Membrane Density} = \frac{1.01 \cdot 10^{-16} \text{ g/NV}}{202043 \text{ nm}^3/\text{NV}} \cdot \frac{1 \cdot 10^{21} \text{ nm}^3}{1 \text{ cm}^3} = 0.50 \text{ g/cm}^3$$

(Eq. 3)

For c-myc-OR7D4-nanovesicles 6 ORs were quantified as well as 0.008 g OR/g Total Protein. Considering the molecular weight of the receptor (26 kDa) the membrane density was as well calculated, Eq. (4) and Eq. (5):

$$\begin{aligned} & 6 \frac{\text{OR}}{\text{NV}} \cdot \frac{26 \text{ kDa}}{1 \text{ OR}} \cdot \frac{1.66 \cdot 10^{-21}}{1 \text{ kDa}} \cdot \frac{1 \text{ g Total Protein}}{0.008 \text{ g}} \cdot \frac{100 \text{ g membrane}}{49.3 \text{ g TP}} \\ & = 0.656 \cdot 10^{-16} \text{ g membrane/NV} \end{aligned}$$

(Eq. 4)

$$\text{Density} = \frac{0.656 \cdot 10^{-16} \text{ g/NV}}{202043 \text{ nm}^3/\text{NV}} \cdot \frac{1 \cdot 10^{21} \text{ nm}^3}{1 \text{ cm}^3} = 0.324 \text{ g/cm}^3$$

(Eq. 5)

If we compare the membrane density obtained 0.324-0.50 g/cm³ with the one reported in the literature⁵², 1.15-1.17 g/cm³, the one obtained was 2-3 times lower. We can explain this factor of ~ 2 assuming that the 50% of the ORs expressed on the nanovesicles are oriented with its N-terminus (the c-myc tag) outside the membrane. Thus, with the ELISA we can only quantify just half of the total ORs.

Furthermore, taking into account the surface area of a 100 nm diameter nanovesicle, the number of OR/NV obtained can be converted into a density of ~ 150 ORs/μm². That means that a typical distance between receptors in the order of approximately 100 nm is expected in OR1740 and OR7D4 carrying nanovesicles. The obtained density (ORs/μm²) is in the order of the one that can be estimated at the whole cell level (diameter: 10 μm) in yeast cells expressing the ORI7 olfactory receptor, assuming that all the receptor proteins lie on the plasma membrane (~400 ORs/μm²)⁸.

However, proteins and/or lipid-protein aggregates < 50 nm in the sample solution were below the limit of detection of the technique used to determine the nanovesicle concentration (Nanoparticle Tracking Analysis)⁵³, and these small aggregates could also contain ORs. AFM measurements and Cryo-EM analysis of the nanovesicle solutions show that small aggregates are readily present and cannot be removed²³, in spite of efforts to optimize the NV sample preparation protocol as it was presented in *Chapter 1*. This effect could produce an increase of the number of receptors per nanovesicle quantified. Despite this, from the results obtained that agree with the literature⁸ seems that the olfactory receptors that could be in the small aggregates are not relevant.

2.4 Conclusions

The novel immunochemical method described here has the capacity to quantify the number of receptors per NV in preparations of c-myc-transmembrane proteins embedded in such vesicles. Using c-myc peptide-protein bioconjugates prepared by chemical means, we have first demonstrated the feasibility of the approach. Thus, the estimated hapten density value calculated from the immunochemical response of these bioconjugates in the ELISA was very close to that obtained by MALDI-TOF-MS. Finally NVs prepared from yeast expressing the human c-myc-OR1740 and chimpanzee c-myc-OR7D4 (c-myc-GPCR) have been measured by ELISA and this has allowed to estimate that number of olfactory receptors embedded in the nanovesicles (3 ± 1) OR molecules NV^{-1} and (6 ± 2) respectively in the preparation used. The possibility to obtain this parameter will allow to characterize much better these preparations and to know the biofunctionality expected. This finding is relevant in order to pursue the development of drug-screening platforms that use these bioreceptors as target biomolecules. The immunochemical method developed is an innovative approach to determine the expression of membrane protein receptors in their natural environment without the need to isolate and purify them. In order to develop the assay, we produced a new monoclonal anti-c-myc antibody and a microplate-based ELISA with high detectability. The capacity of this antibody to bind c-myc bioconjugates, and therefore c-myc-GPCRs, was also verified by Western blot. The method has proven effective for the study of GPCR proteins. We propose that it could also be useful in multiple fields because the analysis of c-myc-tagged molecules, especially membrane proteins, continues to be a challenge in biology and biomedicine.

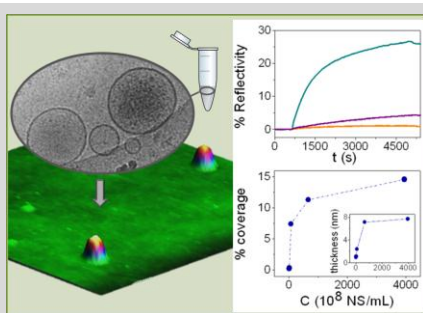
2.5 References

- (1) Brady, A.E., Limbird, L., E. *Cell Signal.* **2002**, *14*, 4, 297-309.
- (2) Schöneberg, T., Schulz, A., Biebermann, H., Hermsdorf, T., Römpler, H., Sangkhul, K. *Pharmacol Ther.* **2004**, *104*, 3, 173–206.
- (3) Wurm, F.-M. *Nat. Biotechnol.* **2004**, *22*, 11, 1393-1398.
- (4) Insel, P.A., Tang, C.-M., Hahntow, I., Michel, M.C. *Biochim. Biophys. Acta – Biomembranes.* **2007**, *1768*, 4, 994-1005.
- (5) González-Maeso, J. *Nat Neurosci.* **2010**, *13*, 5, 524-526.
- (6) Dorsam, R.T., Gutkind, J. S. *Nat. Rev. Cancer.* **2007**, *7*, 79-94.
- (7) Bally, M., Bailey, K., Sugihara, K., Gieshaber, D., Vörös, J., Städler, B. *Small.* **2010**, *6*, 22, 2481-2497.
- (8) Minic, J., Persuy, M.-A., Godel, E., Aioun, J., Connerton, I., Salesse, R., Pajot-Augy, E. *FEBS Journal.* **2005**, *272*, 2, 524-537.
- (9) Bieri, C., Ernst, O. P., Heyse, S., Hofmann, K. P., Vogel, H. *Nat. Biotechnol.* **1999**, *17*, 11, 1105-1108.
- (10) Wittenberg, N. J., Im, H., Johnson, T. W., Xu, X., Warrington, A. E., Rodriguez, M., Oh, S. H. *ACS Nano*, **2011**, *5*, 9, 7555-7564.
- (11) Mukherjee, S., Maxfield, F. R. *Annu. Rev. Cell Dev. Biol.* **2004**, *20*, 839-866.
- (12) Simons, K., Vaz, W. L. C. *Annu. Rev. Biophys. Biomol. Struct.* **2004**, *33*, 269-295.
- (13) Vidic, J., Pla-Roca, M., Grosclaude, J., Persuy, M.-A., Monnerie, R., Caballero, D., Errachid, A., Hou, Y., Jaffrezic-Renault, N., Salesse, R., Pajot-Augy, E., Samitier, J. *Anal. Chem.* **2007**, *79*, 3280-3290.
- (14) Minic-Vidic, J., Grosclaude, J., Persuy, M.-A., Aioun, J., Salesse, R., Pajot-Augy, E. *Lab Chip.* **2006**, *6*, 1026-1032.
- (15) Casuso, I., Pla-Roca, M., Gomila, G., Samitier, J., Minic, J., Persuy, M.A., Salesse, R., Pajot-Augy, E. *Mat Sci Eng C.* **2008**, *28*, 686-691.
- (16) Hou, Y., Jaffrezic-Renault, N., Martelet, C., Zhang, A., Minic-Vidic, J., Gorojankina, T., Persuy, M.-A., Pajot-Augy, E., Salesse, R., Akimov, V., Reggiani, L., Pennetta, C., Alfinito, E., Ruiz, O., Gomila, G., Samitier, J., Errachid, A. *Biosens Bioelectron.* **2007**, *22*, 1550-1555.
- (17) Park, J., Lim, J.H., Jin, H.J., Namgung, S., Lee, S.H., Park, T.H., Hong, S. *Analyst.* **2012**, DOI: 10.1039/c2an16274a.

- (18) Minic, J., Grosclaude, J., Aioun, J., Persuy, M.-A., Gorojankina, T., Salesse, R., Pajot-Augy, E., Hou, Y., Helali, S., Jaffrezic-Renault, N., Bessueille, F., Errachid, A., Gomila, G., Ruiz, O., Samitier, J. *Biochim. Biophys. Acta*, **2005**, 1724, 324.
- (19) Rosenbaum, D.M., Rasmussen, S.G.F., Kobilka, B.K. *Nature*. **2009**, 459, 356-363.
- (20) Daulat, A. M., Maurice, P., Froment, C., Guillaume, J.-L., Broussard, C., Monsarrat, B., Delagrangé, P., Jockers, R. *Mol. Cel. Proteomics*. **2007**, 6, 5, 835-844.
- (21) Ren, H., Yu, D., Ge, B., Cook, B., Xu, Z., Zhang, S. *PLoS ONE*. **2009**, 4, 2, e4509, 1-15.
- (22) Sarramegna, V., Talmont, F., Demange, P., Milon, A. *CMLS, Cell. Mol. Life Sci*. **2003**, 60, 1529–1546.
- (23) Calò, A., Sanmartí-Espinal, M., Iavicoli, P., Persuy, M.-A., Pajot-Augy, E., Gomila, G., Samitier, J. *Soft Matter*. **2012**, 8, 46, 11632 – 11643.
- (24) Nonaka, H., Fujishima, S., Uchinomiya, S., Ojida, A., Hamachi, I. *J. Am. Chem. Soc.* **2010**, 132, 27, 9301–9309.
- (25) Dodevski, I., Plückthun, A. *J. Mol. Biol.* **2011**, 408, 599–615.
- (26) Sergé, A., de Keijzer, S., Van Hemert, F., Hickman, M. R., Hereld, D., Spaink, H. P., Schmidt, T., Snaar-Jagalska, B. E. *Integr Biol*. **2011**, 3, 6, 675-683.
- (27) Mutch, S.A., Kensel-Hammes, P., Gadd, J. C., Fujimoto, B.S., Allen, R.W., Schiro, P.G., Lorenz, R.M., Kuyper, C.L., Kuo, J.S., Bajjalieh, S.M., Chiu, D.T. *J. Neurosci*. **2011**, 31, 4, 1461-470.
- (28) Michnick, S.W., Sidhu, S.S. *Nature Chem. Biol.* **2008**, 4, 6, 326-329.
- (29) Manstein, D.-J., Schuster, H.-P., Morandini, P., Hunt, D.-M. *Gene*. **1995**, 162, 129–134.
- (30) Terpe, K. *Appl Microbiol Biotechnol*. **2003**, 60, 623-633.
- (31) Sun, S., Nguyen, L.-H., Ross, O.-H., Hollis, G.-F., Wynn, R. *Anal. Biochem*. **2002**, 307, 287-296.
- (32) Marco, M.P., Gee, S.J., Hammock, B.D. *Trends Anal. Chem.* **1995**, 14, 415.
- (33) Szurdoki, F., Bekheit, H.K.M., Marco, M.P., Goodrow, M.H., Hammock, B.D. In, D.A. Kurtz, J.H. Skerritt, L. Stanker, *New Frontiers in Agricultural Immunoassays*, AOAC, Arlington, VA, **1995**, p. 39
- (34) Kim, Y.J., Cho, Y.A., Lee, H.-S., Lee, Y.T., Gee, S.J, Hammock, B.D. *Anal. Chim. Acta* **2003**, 475, 85-96.
- (35) Estévez, M.-C., Galve, R., Sánchez-Baeza, F., Marco, M.-P. *Chem. Eur. J.* **2008**, 14, 1906-1917.

- (36) Nielsen, O., and Buchardt, O. *Synthesis*. **1991**, *10*, 819-821.
- (37) Pinacho, D.G., Sánchez-Baeza, F., Marco, M.-P. *Anal Chem*. **2012**, *84*, 4527-4534.
- (38) Estévez, M.-C., Galve, R., Sánchez-Baeza, F., Marco, M.-P. *Anal. Chem*. **2005**, *77*, 5283-5293.
- (39) Estévez, M.C., Kreuzer, M., Sánchez-Baeza, F., Marco, M.-P. *Environ Sci Technol*. **2006**, *40*, 2, 559-568.
- (40) Cook, B.L., Steuerwald, D., Kaiser, L., Graveland-Bikker, J., Vanberghem, M., Berke, A. P., Herlihy, K., Pick, H., Vogel, H., Zhang, S. *PNAS*. **2009**, *106*, 29, 11925–11930.
- (41) Galve, R., Sanchez-Baeza, F., Camps, F., Marco, M.-P. *Anal. Chim. Acta*. **2002**, *452*, 191–206.
- (42) Weller, M.G., Weil, L., Niessner, R. *Mikrochim. Acta*. **1992**, *108*, 29-40.
- (43) McCusker, E.C., Bane, S.E., O'Malley, M.A., Robinson, A. S. *Biotechnol. Prog*. **2007**, *23*, 540-547.
- (44) Serebryany, E., Zhu, G.A., Yan, E.C.Y. *Biochim. Biophys. Acta* **2012**, *1818*, 225-233.
- (45) Findlay, J.W.A., Dillard, R.F. *The AAPS Journal*. **2007**, *9*, E269-E267.
- (46) Evan, G.I., Lewis, J.K., Ramsay, G., Bishop, J.M. *Mol. Cell. Biol*. **1985**, *5*, 3610-3616.
- (47) Wade, F., Espagne, A., Persuy, M.-A., Vidic, J., Monnerie, R., Merola, F., Pajot-Augy, E., Sanz, G. *J. Biol. Chem*. **2011**, *286*, *17*, 15252-15259.
- (48) Hassani, L., Ranjbar, B., Khajeh, K., Naderi-Manesh, H., Naderi-Manesh, M., Sadeghi, M. *Enzyme Microbial Technol*. **2006**, *38*, 118-125.
- (49) O'Brien, A.M., Ó'Fágain, C., Nielsen, P.F., Welinder, K.G. *Biotechnol. Bioeng*. **2001**, *76*, *4*, 277-284.
- (50) Longley, R.P., Rose, A.H., Knights, B.A. *Biochem. J*. **1968**, *108*, 401-412.
- (51) Van der Rest, M.E., Kamminga, A.H., Nakano, A., Anraku, Y., Poolman, B., Konings, W. N. *Microbiol. Rev*. **1995**, *59*, *2*, 304-322.
- (52) Tschopp, J., Schekman, R. *J. Bacteriol*. **1983**, *156*, *1*, 222-229.
- (53) Van Der Pol, E., Hoekstra, A. G., Sturk, A., Otto, C., Van Leeuwen, T. G., Nieuwland, R. *J. Thromb. Haemost*. **2010**, *8*, 2596-2607.

Chapter 3. Diffusion-controlled deposition of natural nanovesicles containing GPCRs for biosensing platforms



In this **Chapter** we present the deposition study of membrane nanovesicles (containing heterologously expressed olfactory receptors) onto substrates used as biosensor supports. We show by direct observation with Atomic Force Microscopy that nanovesicles deposit and flatten without rupturing

on glass substrates following approximately a diffusive law. We show that surface coverages larger than 20-25% of the substrate can be reproducibly achieved under practical nanovesicle concentrations and reasonable time scales, while keeping to the minimum the presence of background residuals coming from the nanovesicles production process. Surface chemistry modification of gold substrates indicates a higher affinity of natural nanovesicles for acid modified surfaces as compared to amino or alcohol modified surfaces. Nanovesicles deposition in acid modified gold surfaces and glass have been exploited for the generation of an array of multiple nanovesicles. Present results constitute an important step in the practical realization of biosensor devices based on natural nanovesicles integrating G-protein coupled membrane receptors.

3.1 Background

Until now, the two main strategies used to immobilize GPCRs, and in general membrane proteins, embedded in a lipidic environment in order to maintain their structure and functionality, are in the form of immobilized vesicles arrays or supported lipid bilayers arrays¹. In the last decade, the majority of GPCR-vesicles array publications were based on their immobilization using chemical modification of the substrate².

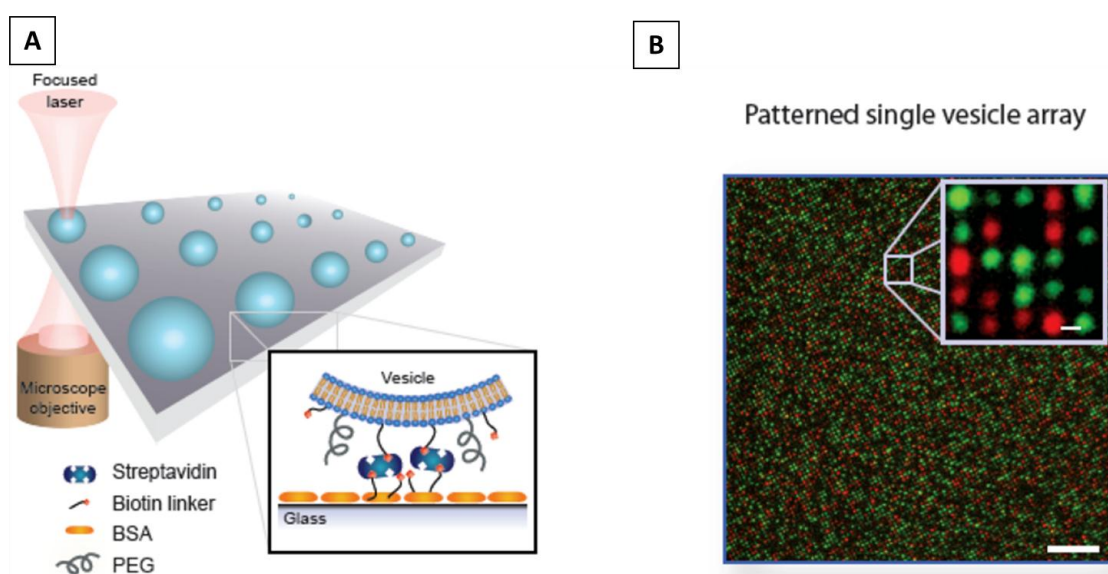


Figure 3.1 (A) Single vesicle array interrogated by fluorescence microscopy². The sensor surface was chemically modified by BSA and biotin-streptavidin pair in order to specifically bind those nanovesicles carrying the biotin linker. (B) Fluorescence micrograph of a single vesicle array functionalised with two populations of vesicles (red and green dyes, respectively)³.

The aim to modify the sensor surface is for two reasons, to be inert against nonspecific vesicle adsorption and nonspecific protein binding to guarantee the specificity of the biosensing platform, and for the GPCR-vesicles to immobilize in an array format. The proposed passivation surface approaches include protein layers (i.e. BSA)³, self-assembled monolayers (SAM)⁴, poly(ethylene glycol) (PEG)-based polymeric layers⁵ or supported lipid bilayers⁶. Furthermore, the need for multiplexing sensor capability is presented with the interaction of a modified surface with the GPCR-nanovesicles with their tethering linker. The interactions within the biotin-streptavidin

systems³, and antibody-antigen pair⁷, and the chemical linkage between histidines (HIS)⁸ or disulphide bridging⁹ are the most common used.

A specific GPCR-nanovesicles immobilization onto a sensor surface through on of the interactions presented above in addition to allow us to immobilize them in an array format has as well other advantages, i.e. to select and increase the amount of desires GPCR-nanovesicles onto the surface to achieve higher sensor signal from the binding of the specific ligand to the GPCR protein. For example, using the antibody-antigen pair, normally, a specific tag, which is genetically expressed in the N-terminus of the GPCRs, is detected by the antibody that was previously immobilized onto the sensor surface. These immobilization strategies are also really important when the GPCR/nanovesicle expression is very low, i.e. less than 1 receptor per nanovesicles. Conversely, when the protein expression is more than 1 GPCR/nanovesicle, their specific immobilization is not necessary. Thus, nonspecific immobilization of the nanovesicles onto the surface can be considered optimal to obtain a good signal/noise ratio from the sensor platform.

Recently, Wittenberg and co-workers¹⁰ in 2011 demonstrated for the first time a unique assembly method for forming micro- to nanoscale biomembrane arrays, with the advantage that no chemical modification of the substrate was required beyond microfabrication. In addition, the resulting arrays were also used for sensing (Figure 3.2).

Not only is the chemical modification of the substrate important to performed such array, there are other parameters that allow successful non-specific GPCRs immobilization.

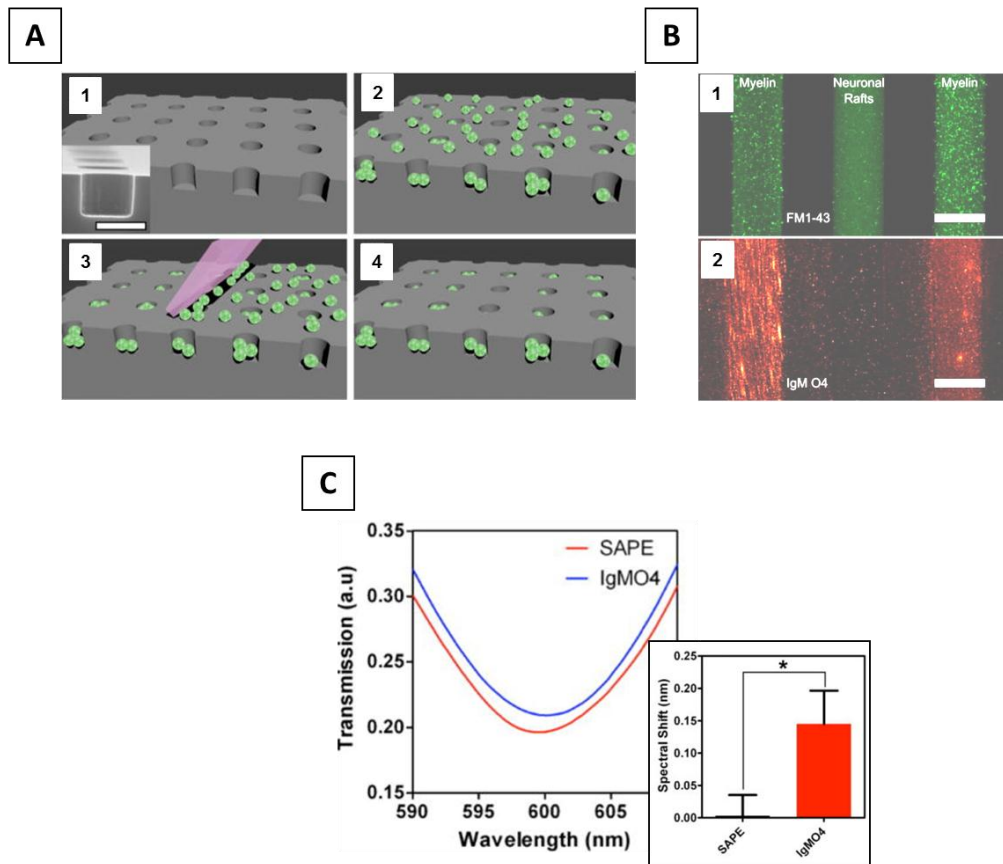


Figure 3.2 (A) Schematic representation of the array assembly process. Vesicles are deposited on the substrate and after using a squeegee, the top surface of the substrate is devoid of vesicles, while the recessed well are filled. (B) Multicomponent arrays formed by microfluidic delivery of myelin and neuronal raft membranes. Fluorescence images before (1) and after (2) incubation with IgM O4 (specific for myelin). (C) Representative transmission spectra for SPR sensing of IgM O4 binding to myelin particles in a gold nanowell array (blue curve). Red curve is the negative control (SAPE does not bind myelin). Comparison of mean spectra shifts after incubation with SAPE or IgM O4¹⁰.

The development of practical biomolecular devices based on membrane receptors (such as GPCRs) integrated in native membrane fractions requires, among other aspects, a strict control of the relevant parameters determining the membrane fraction characteristics and the surface coverage achievable under practical conditions, as well as, of the integrity and morphology of the deposited membrane receptors containers. Such information is almost absent in the current literature. From our point of view, the most important parameters to control in order to achieve high surface coverages are the sensor substrate (as has been mention below), the ionic strength of the solution, the nanovesicles concentration and their deposition time.

Concerning the solution ionic strength, has known that some ions in solution have an important effect on the stability of synthetic liposomes in solution.

Accordingly, this stability will affect their deposition onto a surface. This stability can be theoretically explained by the classical colloidal Derjaguin-Landau-Verwey-Overbeek (DLVO) theory^{11,12} and by considering the hydrated radius of the adsorbed ions onto the liposome surfaces (hydration force)¹³. According DLVO theory, stability is predicted by two independent types of forces that govern the interaction between similar colloidal particles immersed in polar solutions: attractive van der Waals forces and repulsive electrostatic forces. These interactions were due to the electric charge of the particles. (Figure 3.3A). Concerning the hydration force we understand a force associated with the molecular nature of the solvent (water)¹⁴. The basic idea is that we refer to a strong short-range repulsive force that acts between polar surfaces separated by a thin layer (< 3 nm) of water (or some other polar solvents). In the case of biological membranes, the bilayer surface orients the water molecules in direct contrast with the surface and a repulsive force is generated when a second bilayer approaches. Hence, surface charges are induced by the ionic groups (Figure 3.3B). The repulsion between the polar lipids head group and their own dielectric images is due to the surface polarization induced at the dielectric boundaries. Since now, any results have been published applying this theory on natural lipidic nanovesicles.

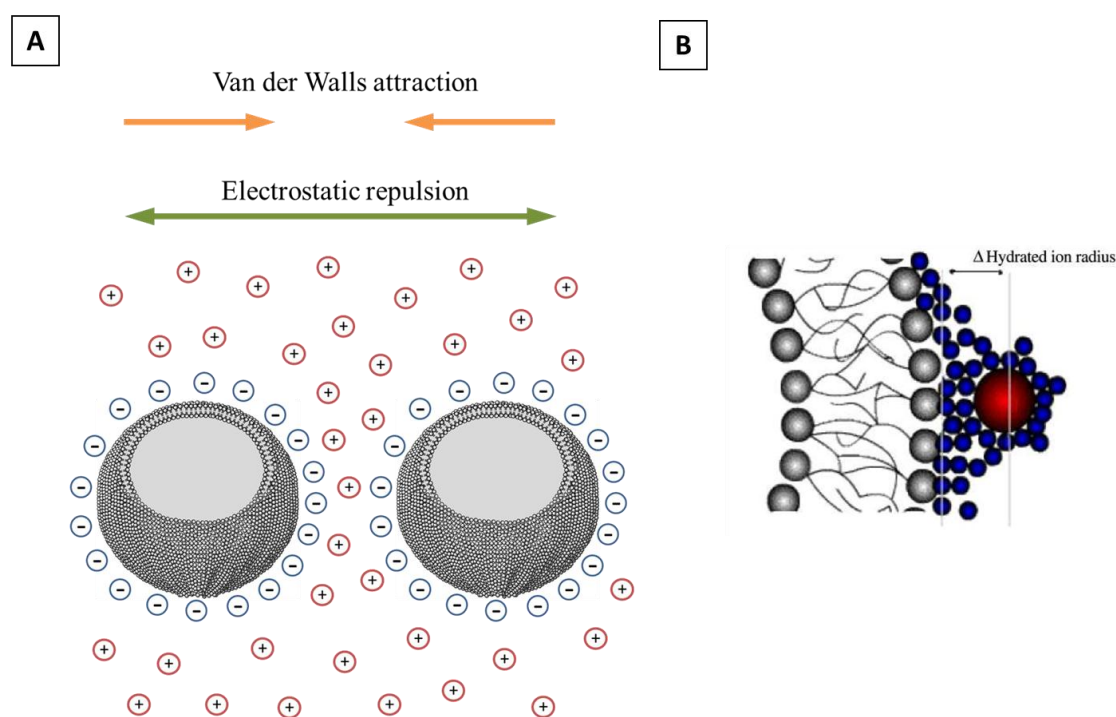


Figure 3.3 (A) Lipidic vesicles stability explained by DLVO theory. (B) Schematic representation of the hydration forces effect. An ion adsorbed onto the outer layer of the lipid bilayer of a liposome is presented¹³.

It is known that the electrolyte concentration has also an important influence on the vesicles stability as well as in their surface charge¹³. The overall charge that a particle acquires in a particular medium is also called zeta-potential (ζ -potential). In other words, zeta-potential is the potential difference between the dispersion medium and the stationary layer of fluid attached to the dispersed particle (Figure 3.4). It is a measure of the magnitude of the electrostatic or charge repulsion or attraction between particles.

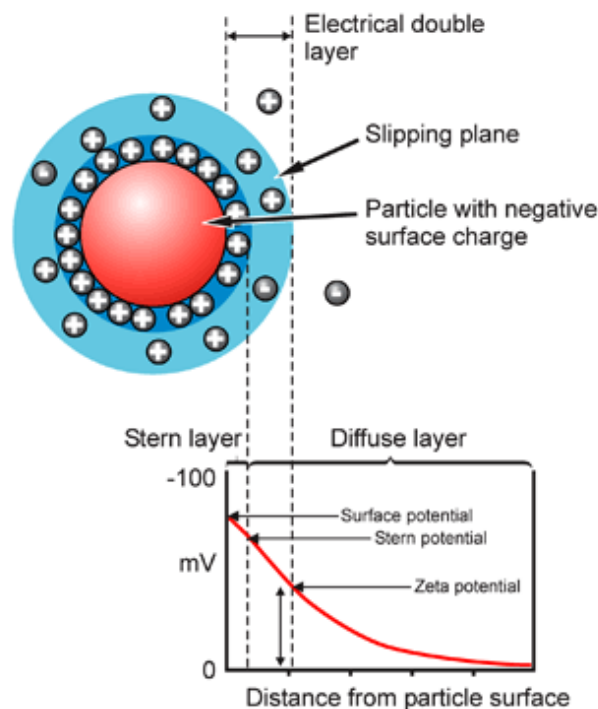


Figure 3.4 Schematic representation of zeta-potential. (www.malvern.com)

In 2008, Dimistrievsky and co-workers demonstrated that electrostatic interactions constitute one of the major factors governing the vesicles-surface interaction, determining at the end the phase behaviour of artificial lipid vesicles¹⁵ (Figure 3.5).

Thus, knowing the vesicle charge as well the surface charge it is possible to predict high surface coverage with immobilized GPCR-nanovesicles for the development of a sensor surface platform.

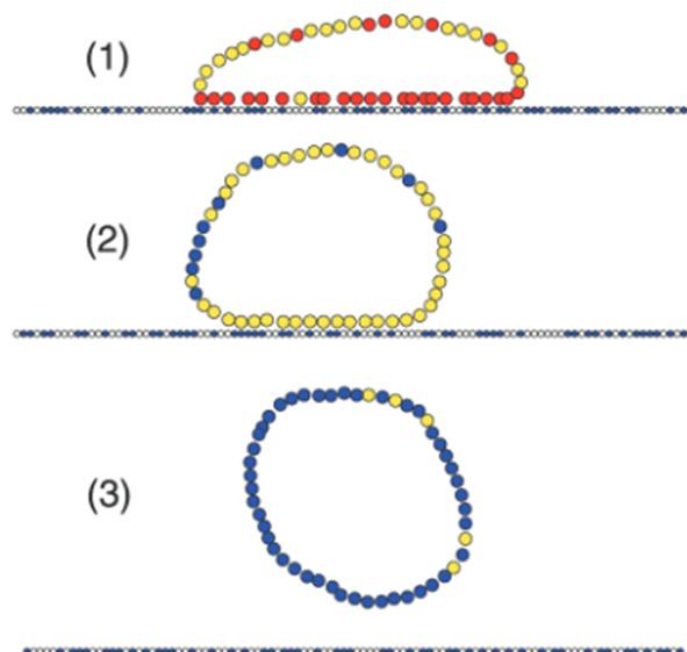


Figure 3.5 Snapshots of a vesicle for three cases, indicated by (1), (2) and (3). For case 1, the vesicle ruptures at the left side, for case 2 the vesicle stays intact on the surface and for case 3, the vesicle does not adsorb on the surface. Red, yellow and blue beads indicate positive, neutral and negative-type beads respectively. Blue surface beads indicate negative surface charges, while white surface beads indicate neutral surface sites.¹⁵

The aim of this *Chapter* is to study all these issues in a systematic way for the case of natural membrane fractions isolated directly from yeast cells expressing either of two commonly used olfactory receptors (ORs), i.e. the human OR1740 (ORL520 in OrDB) and the rat ORI7 (ORL11 in OrDB). We characterize the shape and size of the nanovesicles deposited on glass at the single particle level through a statistical analysis done by Atomic Force Microscopy. The role of the surface chemistry was also analysed at the whole substrate level with combined Surface Plasmon Resonance (SPR) and Atomic Force Microscopy measurements on gold functionalized substrates. Moreover, the nanovesicle distribution on glass surface and its surface coverage was studied at the nanoscale by AFM as a function of nanovesicle concentration and deposition time. A methodology to maximize the nanovesicle deposition with minimum residual background was as well studied. Ion-strength studies have been carried out to study their effect in surface coverages. Finally, nanovesicles deposition in acid modified gold surfaces and glass have been exploited for the generation of an array of multiple nanovesicles.

3.2 Materials and Experimental Procedures

3.2.1 Materials

PBS (phosphate buffer saline), thiol solution of SHC₁₁PEG₆OCH₂COOH (SAM-COOH), SHC₁₅COOH (SAM₂-COOH), SHC₁₁PEG₆OCH₂NH₂ (SAM-NH₂) and SHC₁₁PEG₆OH (SAM-OH) were purchased from Sigma-Aldrich Chemie GmbH (Germany). Glass slides (diameter = 25 mm, thickness = 0.13-0.16 mm) were from Menzel-Gläser. Gold SPR sensor chips were purchased from GWC Technologies Inc. The silicon master was obtained from Centre Nacional de Microelectrònica – CNM (Bellaterra, Spain) and the gold chips for the microcontact printing experiments and for the ion strength-dependent studies were obtained from NTB (Buchs, Switzerland). The poly(dimethylsiloxane) (PDMS) pre-polymer and the curing agent were from Sylgard 184 (Dow Corning, MI, USA). Cell-labelling solution (Vybrant™ Cell-Labelling Solution, DiI, DiO) were purchased from Molecular Probes. Filtration column Amicon Ultra 100K was from Millipore.

3.2.2 Buffers and Solutions

Buffers used were as follows: phosphate-buffered saline (PBS) 10mM at pH 7.5 (always filtered). PB buffer (10x) was 100 mM potassium dihydrogen phosphate/disodium hydrogen phosphate, at pH 7.5. Stock NaCl solution (10x) was prepared with 8 g of NaCl in 100 mL milliQ water. The ion strength-dependent studies were performed with phosphate-buffer (PB 10x) adding the corresponding amount of NaCl (10x) and milliQ water to the total desire volume. NaCl solutions (0-0.068 mM) were adjusted to pH 7.5 with phosphate ions. Otherwise, NaCl solutions (0.102-1.095 mM) were not adjusted to pH 7.5 due to the fact that their initial value was lower.

3.2.3 Equipments/Software

DLS measurements were performed with a Malvern Zetasizer-Nano ZS90. A detection angle of 90° was chosen for the size measurements. To analyse the data DTS

applications 5.10 software was used. To estimate the nanovesicles surface charge, Z-potential measurements were performed with a Malvern Zetasizer Nano ZS instrument equilibrated at 25 °C. Glass slides were treated with an UV/Ozone cleaner (Bioforce Nanosciences). The images of nanovesicles deposited on glass and on SAM₂-COOH functionalized gold were acquired with a MFP-3D AFM (Asylum Research) in tapping mode in liquid, using Si₃N₄ tips coated with Au/Cr with spring constant = 0.08 N m⁻¹ (Olympus cantilevers) at the scan rate of 1 Hz. Each AFM image was analysed after the trend correction by line-by-line removal of the best-fit curve using the WSxM software (Nanotech, <http://www.nanotec.es/>). Wettability of the glass and the SAM functionalized gold substrates was determined with an OCA 15+ (Dataphysics, Germany) contact angle goniometer and data treatment and angle determination were carried out with the software SCA20 (Dataphysics, Germany). Streaming potential measurements of the glass and the SAM functionalized gold substrates were performed using a SurPASS analyser for solid surface analysis (Anton Paar, Austria). The SPR measurements were performed with a RT2005 instrument (Resonant Technologies GmbH, Germany). Stained nanovesicles were prepared onto protein LoBind eppendorf tubes (Eppendorf, Germany) and imaged by an epifluorescence microscope (Nikon E1000) and an inverted confocal microscope (Leica, SP2) using 63x or 100x objectives. Nanovesicles array was performed with the SpotBot 2 Personal Microarrayer (Arrayit Corp. ARYC, USA) with 946MP4 stainless steel printing pins (Arrayit Corp. ARYC, USA) and visualized with Nikon E800 Fluorescence Microscope (Japan) and upright Confocal Laser Scanning Microscope (Leica SPE, Germany). Statistical differences were analysed with GraphPad Prism 5 and OriginPro 7.0.

3.2.4 Nanovesicles solution preparation

Standard protocol (Chapter 1): Human olfactory receptors c-myc-OR1740 (ORL520 in OrDB) and rat ORI7-HA (ORL11 in OrDB) were expressed heterologously in different yeast *Saccharomyces cerevisiae* cultures following a procedure well described in the literature^{16,17}. After, the yeast cells were mechanically disrupted¹⁷, the cell content was separated and the membrane fractions obtained were divided in aliquots and frozen at – 80 °C. This previous process was performed at the French National Institute for Agricultural Research (INRA, France), in collaboration within the BOND

project framework. After, at the Institute of Bioengineering of Catalonia (IBEC, Spain) immediately before use, the stock suspension of membrane fractions was diluted to a concentration (expressed as total protein concentration, TPC, see *Chapter 1*) of $125 \mu\text{g mL}^{-1}$ solution in Phosphate Buffered Saline (PBS 1x) 10 mM (pH = 7.4) or Phosphate Buffer (PB 10mM) at different Na^+ concentrations and sonicated for 20 min in ice-cold water to homogenize their size. The solution was further diluted in PBS or PB (at different NaCl concentration) to obtain the **proteoliposomes** solution described in the text, normally at a total protein concentration (TPC) of $60 \mu\text{g mL}^{-1}$. This solution was then filtered using a sterile low binding protein filter (diameter = 13 mm; pores size = $0.22 \mu\text{m}$) and we obtained the **nanovesicles** (in the text called NS or NV). The nanovesicles solutions described in the text were obtained by further dilution to the working concentration.

3.2.4.1 Nanovesicles membrane staining

1 mL of nanovesicle solution ($C = 1.67 \cdot 10^{11} \text{ NV mL}^{-1}$) in PBS (10mM) was prepared as described above. Then, 1 or 5 μL of the cell-labelling solution (DiI or DiO respectively) was added in the nanovesicle solution and the mixture was gently mix by pipetting onto protein LoBind eppendorf tubes. The mixture was incubated for 1 hour at room temperature protected from the light. 500 μL of the mixture was added to the filtration column (MWCO 100K) and centrifuge at $14000 \times g$ for 15 minutes at 4°C in a microcentrifuge. Then, the elution solution was discarded and the others 500 μL of the nanovesicles mixture were added in the same column and centrifuged. The elution solution was discarded again and the nanovesicles were washed by adding 500 μL of PBS (10mM) filtered and centrifuged again with the same conditions. The washing procedure was repeated two more times. Finally, to recover the stained nanovesicles, the column was placed upside-down un a clean tube and centrifuged at $1000 \times g$ for 2 minutes at 4°C (this time was adapted depending on the desired final volume collected). Control solutions were prepared adding the dyes directly onto PBS and following the same procedure described above.

3.2.5 Dynamic light scattering (DLS) measurements

Vesicles solutions were introduced into plastic cuvettes of 1 cm optical length and measured at a controlled temperature of 25 °C. Nanovesicles solutions were sonicated, diluted at $1.67 \cdot 10^{11}$ NV mL⁻¹ and filtered. For each solution, three DLS measurements were conducted with a fixed 10 runs, each run lasting 10 s in order to extract an average size distribution. We verified that the relative error between them is in the order of 10%, as expected for DLS measurements.¹⁸ The measurements were performed in PB (10mM) at different NaCl concentrations (0-1.095M), at the following conditions: pH ~ 7.4, viscosity = 1.05 cP and refractive index = 1.3377, and for the sample the refractive index = 1.4, absorption = 0.

3.2.6 Nanovesicles Z-potentials measurements

1 mL of nanovesicles solution in a DTS1061 Z-Potential cuvette was inserted into the measurement chamber. Z-Potential was determined by measuring the direction and velocity that the nanovesicles moved in the applied electric field. The measurement was performed in PBS (10mM) or PB (10mM) at different NaCl concentrations (0-1.095M), at the following conditions: pH = 7.4, viscosity = 1.05 cP and refractive index = 1.3377. The software uses Smoluchowsky equation to convert the particles electrophoretic mobility into Z-Potential values. We verified that the field strength does not affect the measurements for V ranging between 10 and 40 V. The value reported in the text in PBS is the weighted mean on 7 different nanovesicles solutions at TPC = 2.5 µg mL⁻¹. In addition, the values reported in the text in PB at different NaCl concentration are the weighted mean of 3 different measurements of each nanovesicles solution ($1.67 \cdot 10^{11}$ NV mL⁻¹).

3.2.7 Experiments on Glass substrates

3.2.7.1 Glass substrates preparation

Glass slides were sonicated in ethanol/water 50/50 (v/v) for 10 min and dried with pure nitrogen. They were then treated with an UV/Ozone cleaner for 10 min, in

order to remove the organic contamination, before incubating the nanovesicles solutions. The glass RMS roughness, as measured by AFM, was (0.29 ± 0.02) nm.

3.2.7.2 Samples preparation for AFM characterization

40 μL of nanovesicle solutions at fixed concentrations were deposited on an area of $1 \times 1 \text{ cm}^2$ of cleaned glass slides for a fixed time. This area was delimited by using a water repellent ink (Dako Pen). After incubation, the surface was rinsed 3 times with PBS and stored in PBS solution. For each sample characterized by a certain nanovesicles concentration (incubation time = 900 s), at least 3 AFM images of $10 \times 10 \mu\text{m}^2$ (256×256 pixels) and 3 AFM images of $2 \times 2 \mu\text{m}^2$ (256×256 pixels) were collected in randomly distributed places of the glass slides. For each sample characterized by a certain incubation time, at least 3 AFM images of $10 \times 10 \mu\text{m}^2$ (256×256 pixels) were collected in randomly distributed places of the glass slides at four selected concentrations of $3.22 \cdot 10^8 \text{ NV mL}^{-1}$, $12.83 \cdot 10^8 \text{ NV mL}^{-1}$, $51.40 \cdot 10^8 \text{ NV mL}^{-1}$ and $205.66 \cdot 10^8 \text{ NV mL}^{-1}$.

3.2.7.3 Determination of nanovesicles aspect ratio and diameter by AFM

The topographic profile on top of 95 individual nanovesicles from $2 \times 2 \mu\text{m}^2$ AFM images at different C ($t = 900$ s) was fitted with a Gaussian function, and the nanovesicles thickness (h) and width extracted. In order to account for possible tip convolution effects affecting the width determination, the radius of AFM tips was characterized with the tip reconstruction procedure implemented in SPIP 4.6.1 software (Image Metrology, Denmark). A calibration grid (NiO probe tip check, Aurora Nanodevices, Canada) was scanned with the AFM tip in air at the rate of 1 Hz. Scanned area was $2.5 \times 2.5 \mu\text{m}^2$ and image resolution was 512×512 pixels. The images were obtained in a Multimode 8 AFM attached to a Nanoscope V electronics (Bruker), using the Peak Force imaging mode in order to ensure a minimum tip wear during the measurement. Calibration grid images were flattened with SPIP software; in order to eliminate the effect of faulty scan lines, the option “reduce spikes” was selected. Then the tip reconstruction routine was applied. After the reconstruction, the $2 \times 2 \mu\text{m}^2$ images of nanovesicles obtained with the software-characterized tip were loaded on SPIP and deconvoluted; that is, the effect of the tip shape was subtracted from the

nanovesicles image so as to get closer to their real dimensions. As expected, the height of the nanovesicles did not change between the original and the deconvoluted images. We found that the width of deconvoluted nanovesicles was $\sim 3\%$ smaller when the reconstruction procedure was applied to new AFM tips and $\sim 7\%$ smaller, when the reconstruction procedure was applied to AFM tips after some scans on glass surfaces covered by nanovesicles. The width reported in the paper is obtained by subtracting the 7% to the nanovesicles width in the real images. We estimated the nanovesicles aspect ratio by fitting the width vs. h data with a line passing through the zero and disregarding the data points at width > 350 nm and $h > 40$ nm (see Figure 3.6C).

To estimate the equivalent diameter of the adsorbed nanovesicles we considered the nanovesicles as spherical caps lying on glass and we extracted their volume from their height and deconvoluted width as (Equation 1):

$$V = \pi \cdot h^2 \cdot \left(\left(\frac{1}{2 \cdot h} \cdot \left(\left(\frac{width}{2} \right)^2 + h^2 \right) \right) - \left(\frac{h}{3} \right) \right)$$

(Eq.1)

By knowing the nanovesicles volume, we extracted the diameter of the equivalent sphere originating the spherical cap as $2 \cdot (V \cdot 3/4 \cdot \pi)^{1/3}$.

3.2.8 Experiments on Gold substrates

3.2.8.1 Thiol self-assembled monolayer preparation

Before use, the chips were sonicated for 10 min in UHQ water, then for 10 min in absolute ethanol, then for 10 minutes in piranha solution (H_2SO_4/H_2O_2 , 5/1) and finally for 10 min in UHQ water. SAMs were prepared by immersion of the SPR sensor chip in the appropriate 2 mM thiol solution (SHC₁₁PEG₆OCH₂COOH (SAM-COOH), SHC₁₅COOH (SAM₂-COOH), SHC₁₁PEG₆OCH₂NH₂ (SAM-NH₂) and SHC₁₁PEG₆OH (SAM-OH)) for 16-20 hours to obtain a uniform SAM surface coverage. Then the

substrates were rinsed with absolute ethanol in order to remove physisorbed molecules, dried under a nitrogen stream and immediately used.

The RMS roughness of SAM-COOH, SAM-NH₂ and SAM-OH functionalized gold surfaces, as measured by AFM, was respectively (1.17 ± 0.06) nm, (1.57 ± 0.01) nm, (1.49 ± 0.11) nm, the RMS of bare gold being (1.29 ± 0.14) nm).

3.2.8.2 Ion strength-samples preparation for AFM characterization

40 µL of nanovesicle solutions (at different NaCl concentration) at fixed concentration ($C = 1.67 \cdot 10^{11}$ NV mL⁻¹) were deposited on an area of 1 x 1 cm² of SAM₂-COOH functionalized gold surface for a fixed time ($t = 3600$ s). This area was delimited by using a water repellent ink (Dako Pen). After incubation, the surface was rinsed 3 times with the corresponding Na⁺ solution and stored in this solution. For each nanovesicle sample characterized by a certain Na⁺ concentration, at least 3 AFM images of 10 x 10 µm² (512 x 512 pixels) and 3 AFM images of 3 x 3 µm² (512 x 512 pixels) were collected in randomly distributed places of the functionalized gold surface.

3.2.8.3 Determination of nanovesicles aspect ratio and diameter by AFM on ion strength-dependent studies

The topographic profile on top of 30 individual nanovesicles from 3 x 3 µm² AFM images prepared at different Na⁺ concentration ($t = 3600$ s) was fitted with a Gaussian function, and the nanovesicles thickness (h) and width were extracted. We estimated the nanovesicles aspect ratio disregarding the data points at width > 350 nm and $h > 40$ nm (see Figure 3.6C). To estimate the equivalent diameter of the adsorbed nanovesicles on the functionalized gold surface we used Equation 1 (see above).

3.2.8.4 X-ray Photoelectron Spectroscopy (XPS)

XPS experiments to characterize the SAM formation on gold were performed in a PHI 5500 Multitechnique System (Physical Electronics) with a monochromatic X-ray source (Al Kα line of 1486.6 eV and 350 W), placed perpendicular to the analyser axis and calibrated using the 3d_{5/2} Ag line with a full width at half maximum (FWHM) of 0.8 eV. The analysed area was a circle of 0.8 mm diameter, and the selected resolution for the spectra was 187.5 eV of Pass Energy and 0.1 eV/step for the spectra of the

different elements. All measurements were made at a pressure between 5×10^{-9} and 2×10^{-8} torr inside an ultra-high vacuum chamber. All spectra were referenced to Au 4f at 84 eV.

XPS was used to obtain the elemental composition of SAM-COOH, SAM-NH₂ and SAM-OH functionalized gold chips. The XPS spectra shows a decrease of the surface peaks of Au with respect to bare Au, and a growth of the peaks related to the organic monolayers containing Carbon, Sulphur and Nitrogen. A high-resolution spectrum for each significant element of the SAMs was also carried out.

3.2.8.5 Surface Plasmon Resonance (SPR) measurements

The chips were index matched to the prism and fitted with a 20 μ L flow cell connected to a peristaltic pump from Ismatec (Glattbrugg, Switzerland). The flow used in all experiments was 58 μ L min⁻¹. The interaction of nanovesicles with the functionalized gold substrates was followed by Surface Plasmon Resonance to estimate the total mass deposited onto 1 cm² delimited area of the substrate. The baseline in the SPR response was first established with PBS. At the end of the nanovesicle incubation a PBS solution was flowed to remove weakly adsorbed vesicles. Reflectivity levels were compared before and after the vesicle injection (PBS levels) to evaluate the amount of material grafted onto the gold substrate. At the end of each experiment performed with a fixed nanovesicles concentration and incubation time, an AFM image was taken to evaluate the nanovesicles surface coverage and to estimate the thickness of the adsorbed layer according to the procedure described for the glass substrates.

3.2.9 General AFM measurements

3.2.9.1 Determination of nanovesicles surface coverage by AFM

Nanovesicles density was extracted from the 10 x 10 μ m² AFM images by filtering and counting the number of particles having $h \geq 10$ nm and width ≥ 100 μ m. These two thresholds were chosen according to the width vs. height plot of Figure 3.6C. This number was then multiplied by the average nanovesicles width and divided for the image area in order to obtain the nanovesicles surface coverage.

3.2.9.2 Thickness of the residual layer determination by AFM

In order to estimate the thickness of the residual layer an area of $500 \times 500 \text{ nm}^2$ was scratched with the AFM tip in contact mode for each sample characterized by a fixed nanovesicles concentration and incubation time. A $2 \times 2 \text{ }\mu\text{m}^2$ image (glass) or $3 \times 3 \text{ }\mu\text{m}^2$ (gold) was then collected to visualize the scratched area and the thin layer around it. The thickness of the residual layer was extracted from the topographic profile across the scratched area in a region where a continuous layer was present without any particle with a typical shape and size. The thickness was determined as the average between the highest and the lowest feature of the topographic profile out of the scratch, once assigned to the scratched region the value of $h = 0$. The reported thickness on glass (inset of Figure 9 and 10B) and on gold (inset of Figure 3.17, 3.18C and 3.19) is an average of 3 different topographic profiles in regions where nanovesicles were not present for each concentration and incubation time. For diluted samples and low incubation times we found a continuous, relatively flat layer 1-2 nm higher with respect to the scratched region. By increasing nanovesicles concentration or the incubation time, the roughness of this continuous layer increases.

3.2.10 Contact angle measurements

Wettability of the glass and the SAM functionalized gold substrates was determined. A drop of water ($3 \text{ }\mu\text{L}$) was deposited over the surface, and the resultant angle between the drop and the substrate was measured. Four sets of static contact angles, at different positions on each sample, were measured. The contact angle of the cleaned glass substrates was $(7 \pm 2)^\circ$. For SAM-COOH, SAM-NH₂ and SAM-OH functionalized gold surfaces we measured contact angles of $(33.8 \pm 1)^\circ$, $(34.3 \pm 1)^\circ$ and $(33.9 \pm 1)^\circ$ respectively.¹⁹ The contact angle of the gold substrate before functionalization was $(73.5 \pm 1)^\circ$.

3.2.11 Surface Z-Potential measurements

Surface Zeta-Potential was determined using an adjusting gap cell where two equal substrates are fixed on stamps and placed oppositely. The gap was adjusted to a

size where a flow rate between 30 and 150 mL min⁻¹ at a maximum pressure of 300 mbar was reached. A flow check was performed to achieve a constant flow in both directions. A KCl solution 1 mM was used as model electrolyte, while a HCl solution 0.1 M and a NaOH solution 0.1 M were used for pH titration. Before starting the measurement, a rinsing step was performed for 6000 s adjusting the pH of the model electrolyte to a value between 6 and 7. A first automated titration program was performed from pH 7 to pH 9 using titration steps of 0.01 mL, in order to check the sample stability vs. pH. Then, an automated titration program was performed from pH 9 to pH 2 using titration steps of 0.01 mL. We measured the Zeta-Potential of two cleaned glass substrates obtaining a value of (-100 ± 34) mV at pH 7.4, the isoelectric point being at pH 2.5. The measured Z-Potential of SAM-COOH, SAM-NH₂ and SAM-OH functionalized gold surfaces at pH 7.4 was respectively -66.5 mV, -52.5 mV and -42 mV, their isoelectric point being respectively at pH = 3.2, pH = 4 and pH < 2.

3.2.12 Natural vesicles pattern

3.2.12.1 Fabrication of the stamps

PDMS stamps were fabricated by pouring a 10:1 mixture of PDMS pre-polymer and curing agent onto a silicon master. The silicon master had a regular array of cylindrical holes of 10 μ m in diameter and pitch. After curing for 1 h at 65° C, the PDMS replica was peeled from the master.

3.2.12.2 Stamping process

To produce a patterned self-assembled monolayer (SAM) on the gold chip, the PDMS stamp was inked with a 2 mM ethanolic solution of PEG₃-thiol during 15 min, rinsed thoroughly with absolute ethanol and then blown dry with nitrogen. The inked stamp was placed onto the gold surface for an average contact time of 5 min. After the PEG₃-thiol pattern was printed, the gold chip was incubated with a 5 mM ethanolic solution of SAM-COOH for 3 hours, rinsed with absolute ethanol and blown dry with nitrogen.

3.2.12.3 c-myc-OR1740 nanovesicles deposition and AFM characterization

The gold patterned surface described above was submerged onto a 1.3 mL c-myc-OR1740 nanovesicles solution at $3.29 \cdot 10^{10}$ NV mL⁻¹ and incubated for 1 hour at room temperature. After incubation, the surface was rinsed 3 times with PBS, blown dry with nitrogen and analysed by AFM. The AFM images were acquired in liquid (PBS) with the same procedure described above.

3.2.13 Natural vesicles array

The arrays with OR-nanovesicles ($C = 1.67 \cdot 10^{11}$ NV mL⁻¹) in PBS (10mM) stained with dialkylcarbocyanines dyes (DiO and DiI) with their respective negative controls were performed using the SpotBot 2 Personal Microarrayer with 946MP4 stainless steel printing pins. The spot spacing used was 0.5 mm spot in order to avoid the merging of the spots. Around 1.1 nL of nanovesicles solution were deposited on an area of ~ 0.06 mm² of cleaned glass slides (see procedure above, Glass substrates preparation). After printing, that takes 30 min, the array was incubated at room temperature. During incubation, images of the slide were performed with a fluorescence microscope (imaging the slides takes about 30 min) or a Confocal Laser Scanning Microscope (CLSM). Thus, total incubation time was 1 hour. Then, the array was washed manually three times with 1 mL of PBS (1x) each time. Finally, a cover slip was placed onto the array and it was visualized again. In order to avoid crystallization the arrays were left wet during all the process.

3.2.14 Statistics

All values were expressed as mean–standard deviation. One-way ANOVA analysis followed by Bonferroni Test pot-hoc comparison was used to test the significance level. The level of significance was set to $p < 0.05$.

3.3 Results and Discussion

3.3.1 Nanovesicles Z-potential

One important issue to consider for the development of a biosensor platform is the determination of the nanovesicle surface z-potential. Knowing that, the design of a proper surface (functionalized substrate) to deposit the nanovesicles can be achieved. For our sample, OR1740 carrying nanovesicles (as model OR-nanovesicles) onto PBS (10 mM, pH 7.5) solution, we measured a zeta-potential of (-6 ± 16) mV.

3.3.2 Morphology of individual adsorbed nanovesicles

We studied in detail the deposition of nanovesicles on glass and the morphology of individual nanovesicles as a consequence of their adsorption on this substrate. Figure 3.6A shows a 3D AFM image taken in liquid (PBS buffer), after incubating on glass 40 μL of a diluted solution of nanovesicles carrying ORI7 olfactory receptor at $C = 3.22 \cdot 10^8$ NV mL^{-1} (incubation time $t = 900$ s). Flattened integer vesicles are present on the surface, which seems to exhibit homogeneous features of few tens of nm in height and few hundreds of nm in width (tip convolution included, see the Experimental Section). Note that full collapsed vesicles would show a thickness around 10 nm, corresponding to the double of the membrane thickness, as measured on occasionally occurring planar membrane fractions. Figure 3.6B is a detail representing one of these vesicles; the corresponding topographic profile is shown in Figure 3.6D. We extracted the thickness (h) and the width by analysing the topographic profiles on top of 95 nanovesicles; the results are shown in Figure 3.6C. For our population we found an average aspect ratio $h/\text{width} = 0.097 \pm 0.003$ (see also the inset of Figure 3.6C) and an average width of (246 ± 75) nm. From the topographic profiles we also estimated the volume of the deposited nanovesicles and the equivalent sphere diameter (see the Experimental Section). The value that we obtained, (88 ± 26) nm, is in striking agreement with the results obtained in solution by DLS and NTA measurements (*Chapter 1*), thus indicating that upon adsorption nanovesicles deform keeping the same volume they have in solution. The fact that nanovesicles flatten once adsorbed on the substrate and occupy a larger substrate area than the one corresponding to a non-

deformed spherical particle is taken into account in the theoretical analysis of the measured surface coverage, as we will show later on.

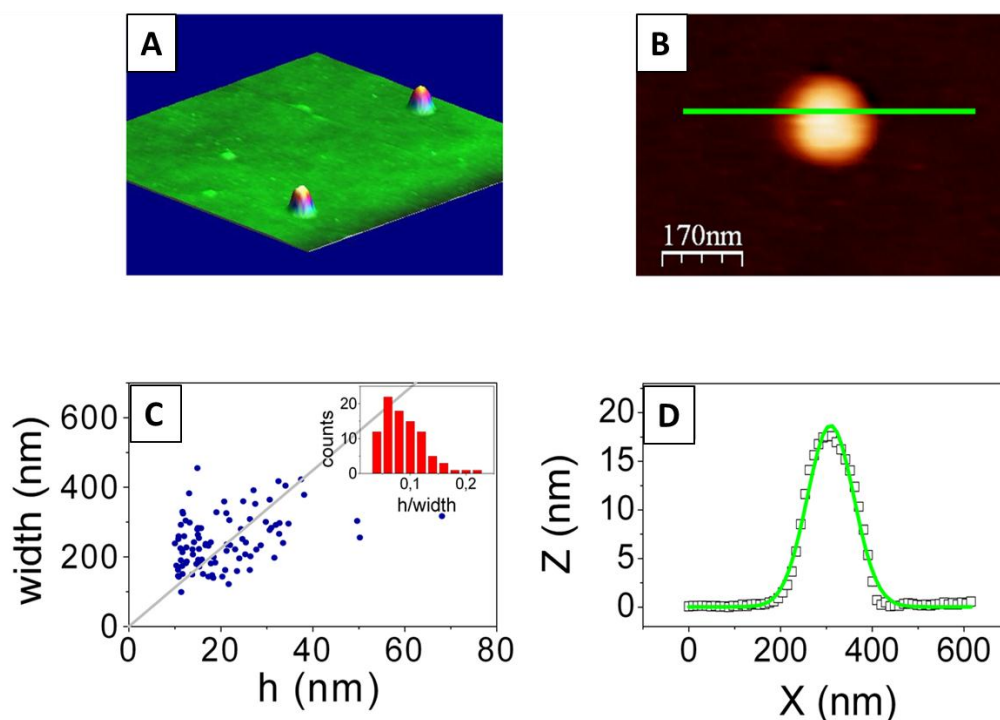


Figure 3.6 (A) 3D tapping mode AFM image in PBS buffer of a glass substrate showing individual NS from a solution at $C = 3.22 \cdot 10^8$ NV mL⁻¹ (incubation time = 900 s) (z scale = 22 nm). (B) Detail of Figure 6A showing an individual nanovesicle and its corresponding topographical profile (D). The green line is a Gaussian fit from which we extracted the nanovesicles height and width (see Experimental Section). (C) Width vs. height extracted from the topographic profile of a population of 95 nanovesicles. (C, inset) The line in grey indicates an aspect ratio of 0.097. Histogram of the aspect ratio as obtained from data in (C).

A remarkable fact is represented by the phase behaviour of the deposited nanovesicles solution. In our experimental conditions nanovesicles adsorb without rupturing on glass and we did not find any evidence of the formation of extended supported lipid bilayers immediately upon the adsorption event or after reaching a critical vesicle coverage, in contrast with the results detected in real time with quartz crystal microbalance (QCM-D) technique coupled with AFM observation²⁰ in artificial reconstructed lipid vesicles.

It has been demonstrated that, among other factors, electrostatic interactions^{21,22} constitute one of the major factors governing the vesicles-surface interaction, determining at the end the phase behaviour of artificial lipid vesicles.²³ Based on

electrostatics, Dimitrievsky and Kasemo theoretically built a kinetic phase diagram (Figure 3.7) where neutral or weakly charged vesicles lie intact onto a negatively charged surface,¹⁵ thus supporting the experimental evidence of stable neutral POPC and slightly negatively charged DOPC/DOPS vesicles adsorbed on SiO₂.²⁰

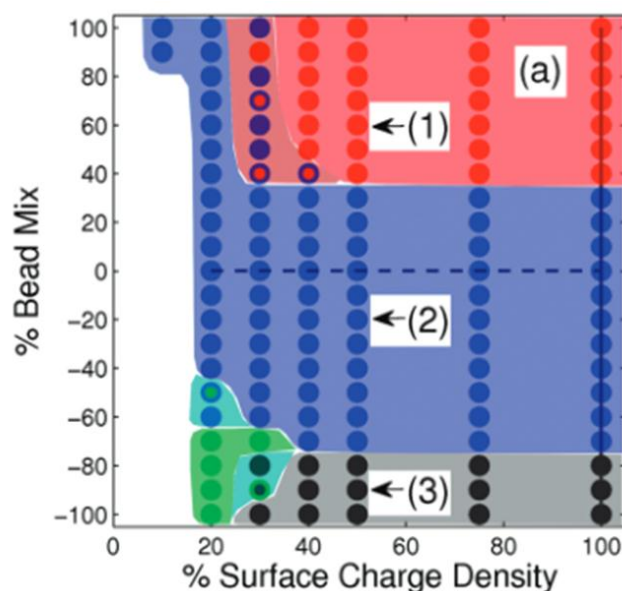


Figure 3.7 Kinetic Phase diagram of the fate of an adsorbing vesicle. X-axis indicates the extent to which the surface is charged (%) and y-axis indicates the bead mixture in the vesicle (%). Red data points (red area) mean that the vesicle ruptured, blue data points (blue area) mean that the vesicle stayed intact on the surface, green data points (green area) mean that the vesicle adsorbed and then desorbed from the surface, and black data points (grey area) mean that the vesicle did not adsorb to the surface¹⁵.

Furthermore, in the case of neutral vesicles, they predict a characteristic height-to-width ratio, which diminishes from 0.8 to 0.3 with increasing (negative) substrate charge and which is limited by a fixed critical bending angle that defines the vesicles rupture.¹⁵ This height-to-width ratio is expected to be dependent on the vesicle size, approaching a very low limiting value of 0.1 for vesicles of size in the order of a few hundreds of nm.²² Although our experiments are performed on vesicles made up of natural membranes, the results that we obtain seem coherent with these findings. Our observation is consistent with this picture if nanovesicles are neutral or weakly negatively charged vesicles and the substrate is negatively charged. Both conditions are indeed satisfied for our system as for OR1740 carrying nanovesicles we measured a zeta-potential of (-6 ± 16) mV and the measured zeta potential of glass at pH 7.4 is (-100 ± 34) mV.²⁴

3.3.3 Concentration-dependent surface coverage

The concentration of ~ 100 nm size nanovesicles in a solution in the order of 10^{10} NV mL⁻¹ achievable with the procedure described above is considered adequate to achieve large surface coverages. Indeed it has been shown that with polystyrene nanoparticles solutions of similar concentrations and dimensions, the maximum theoretical surface coverage on mica substrate (~ 54 %) under diffusion limited deposition and appropriate solution conditions^{25,26} can be obtained. This is a very relevant conclusion for the development of practical biosensor devices based on natural nanovesicles.

We studied the surface coverage as a function of the concentration of the nanovesicles solutions (C). Figure 3.8 shows a set of AFM images taken after incubating nanovesicles solutions on glass at progressively increasing concentrations for a fixed incubation time ($t = 900$ s); Figure 3.9 shows the evolution of the nanovesicles surface coverage in function of C.

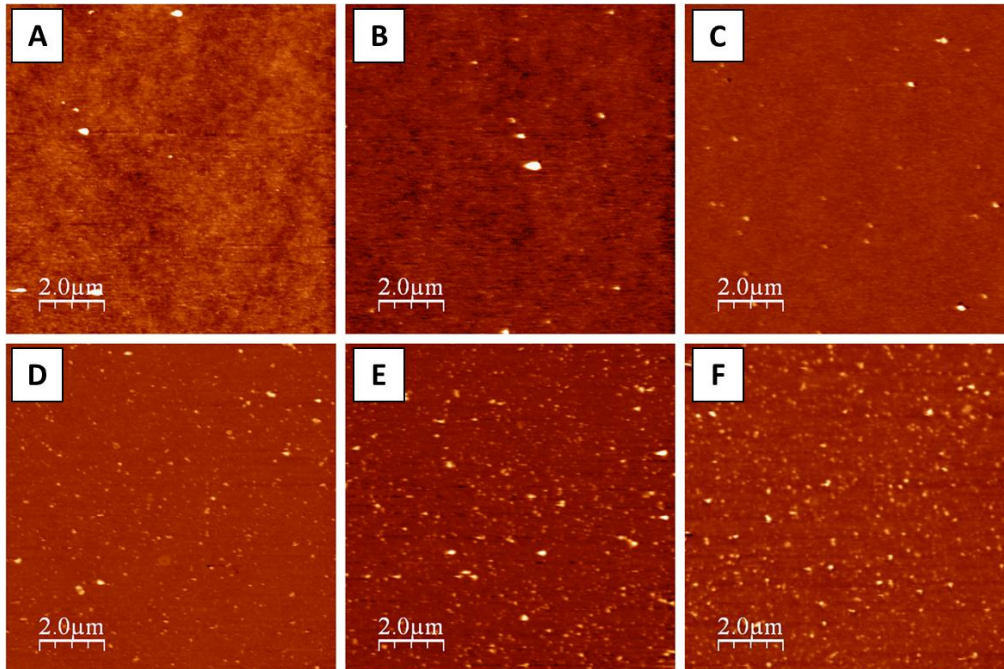


Figure 3.8 Sequence of AFM images taken after incubating for 900 s on glass solutions of nanovesicles carrying ORI7 olfactory receptor at: $C = 3.22 \cdot 10^8$ NS mL⁻¹ (z scale = 5 nm) (A); $C = 6.45 \cdot 10^8$ NV mL⁻¹ (z scale = 7 nm) (B); $C = 12.83 \cdot 10^8$ NV mL⁻¹ (z scale = 20 nm) (C); $C = 25.73 \cdot 10^8$ NV mL⁻¹ (z scale = 40 nm) (D); $C = 51.40 \cdot 10^8$ NV mL⁻¹ (z scale = 35 nm) (E); $C = 411.31 \cdot 10^8$ NV mL⁻¹ (z scale = 30 nm) (F).

In this range, which spans three orders of magnitudes of C , we observed that the glass surface is progressively covered with individual vesicles which at the highest concentrations (see Figure 3.8) seem to be isotropically distributed on the surface. The coverage expressed in Figure 3.9 derives from filtering the AFM images and counting the number of particles higher than 10 nm, according to the results in Figure 3.6C. Their contribution to the total area of the AFM images ($10 \times 10 \mu\text{m}^2$) is obtained by multiplying the number of particles by the average nanovesicles area, calculated from the mean width of adsorbed nanovesicles from data in Figure 3.6C (see the Experimental Section). In our concentration range the experimental surface coverage adapts to a linear dependence on C in the form (Equation 2):

$$\text{Coverage}100 = (9.39 \pm 1.66) \cdot 10^{-3} \cdot C \quad (\text{Eq. 2})$$

where C is expressed as 10^8 NV mL^{-1} .

This is consistent with a diffusion-limited deposition process governing the transfer of nanovesicles from the solution onto the substrate (see below). Such behaviour has been proved to describe the adsorption of a variety of biomolecules (DNA, proteins),²⁷⁻²⁹ intact lipidic vesicles³⁰ and nanoparticles^{25,26} onto solid supports.

According to the results in Figure 3.9, for nanovesicles concentrations of $10^{11} \text{ NV mL}^{-1}$ a coverage above 20% is obtained with an incubation time of just 15 min.

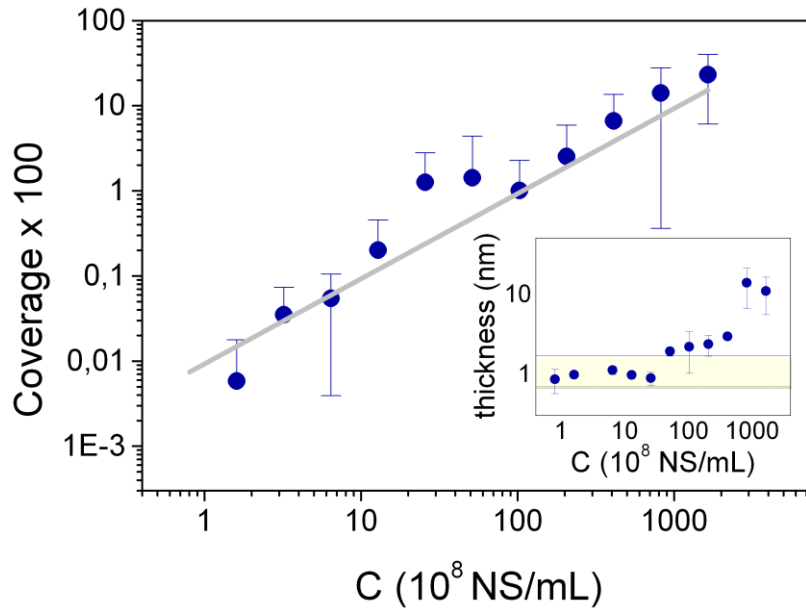


Figure 3.9 Surface coverage vs. nanovesicles concentration. The line in grey is a linear fit with Coverage $\times 100 = (9.39 \pm 1.66) \cdot 10^{-3} C$ (10^8 NV mL^{-1}), according to the model in ref. 27, 34 and 35. Thickness of the adsorbed residual layer vs. C (inset).

In principle, the surface coverage could be increased by either increasing the incubation time (see below) or increasing the concentration of the nanovesicles solution. However, in the latter case we found that when increasing the nanovesicles solution concentration a thin layer of residuals starts being adsorbed on the surface, whose thickness increases with concentration and whose growth cannot be easily interpreted in the framework of a diffusion-limited adsorption model. The presence of such residuals has been recognized in the Cryo-EM images of proteoliposomes solutions where a weak background is clearly visible (*Chapter 1*). Several purification strategies, including further sonications, additional centrifugation steps, sucrose gradient centrifugations, did not succeed in eliminating these residuals. The thickness of the residual layer on the substrate is reported in function of C in the inset of Figure 3.9. At $C \leq 25 \cdot 10^8$ NV mL^{-1} it is almost indistinguishable from that obtained incubating on glass $40 \mu\text{L}$ of PBS buffer for 900 s. At concentrations above $C = 25 \cdot 10^8$ NV mL^{-1} the thickness of the adsorbed layer increases, reaching the value of about 10 nm at a concentration of $\sim 10^{11}$ NV mL^{-1} . Beyond such concentration the sample surface becomes very rough and nanovesicles identification from AFM images becomes critical. By means of an

exponential fitting we extrapolated a value of the thickness of about 80 nm for a concentration of $\sim 10^{12}$ NV mL⁻¹.

As a consequence, the filtering of the AFM images for the coverage determination as reported in Figure 3.9 was done by adding the corresponding thickness of the adsorbed layer (inset of Figure 3.9) to the threshold value of 10 nm for each NV concentration.

We relate the observed phenomenon to an uncontrolled deposition of biomolecules, i.e. proteins and/or lipid aggregates, which are not organized in vesicles and might be still present in the incubating solution after the sonication and the filtration of the membrane fractions solution. The presence of this layer may have an impact in the performances of devices based on nanovesicles array and hence its effects need to be minimal and a trade-off between surface coverage maximization and thickness of adsorbed layer minimization needs to be achieved in order to not compromise the device response.

3.3.4 Dynamics of nanovesicles deposition

In order to increase the nanovesicle coverage controlling at the same time the thickness of the adsorbed residual layer, we investigated the time-dependence of the surface coverage and of the thickness of the adsorbed layer on glass at low nanovesicles concentrations ($C < 2.06 \cdot 10^{10}$ NV mL⁻¹) (Figures 3.10A and 3.10B).

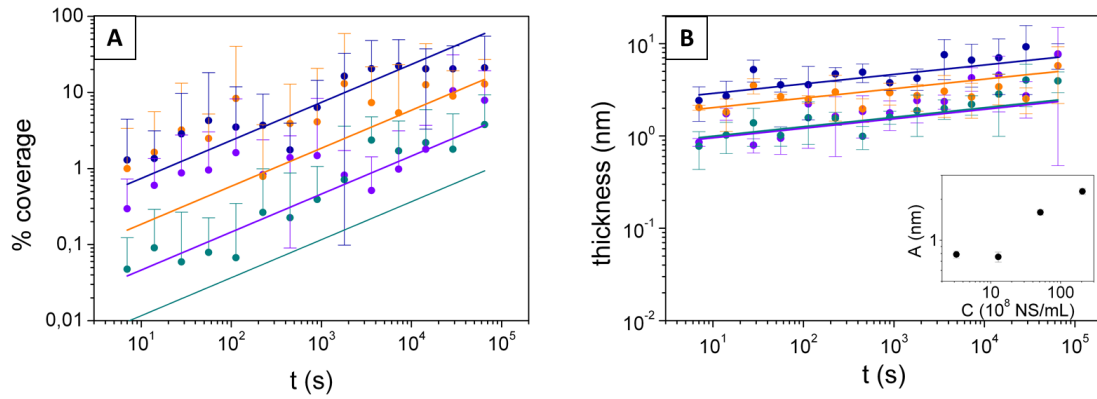


Figure 3.10 Surface coverage (A) and thickness of the adsorbed layer (B) vs. incubation time for nanovesicles concentration of $3.22 \cdot 10^8$ NV mL $^{-1}$ (data in dark cyan), $12.83 \cdot 10^8$ NV mL $^{-1}$ (data in violet), $51.40 \cdot 10^8$ NV mL $^{-1}$ (data in orange) and $205.66 \cdot 10^8$ NV mL $^{-1}$ (data in blue). The straight lines in (A) correspond to the predictions of a purely diffusive adsorption process with no adjustable parameters according to Equation 3. The straight lines in (B) are corresponding fits with $y = A \cdot t^b$ (Equation 4). Trend of the prefactor A , extracted from the fit of the time-evolution of the thickness of the adsorbed residual layer, vs. nanovesicles concentration (B, inset). The experiments are performed on nanovesicles carrying ORI7 olfactory receptors.

Figure 3.10A shows the time evolution of the surface coverage at four different nanovesicles concentrations, ranging from $3.22 \cdot 10^8$ to $2.06 \cdot 10^{10}$ NV mL $^{-1}$. Increasing the incubation time we observed a steady increase in the glass coverage with nanovesicles. Furthermore, an increase in solution concentration statistically shifts to higher values the coverage at a fixed time. Experimental results are compared with theoretical predictions for a diffusion limited irreversible adsorption process. For such process the surface coverage is given by (Equation 3):^{25,27,31,32}

$$\text{Coverage} \times 100 = 100 \cdot \pi \cdot a^2 \cdot 2 \cdot \sqrt{\frac{D \cdot t}{\pi}} \cdot C \quad (\text{Eq. 3})$$

where a is the radius of the adsorbed particles and D its diffusion coefficient in the bulk solution, t and C being respectively the incubation time and the concentration in the solution.

By using the measured value for the radius of the adsorbed particles, $\bar{a} = 123$ nm, and the measured diffusion coefficient from NTA measurements (*Chapter 1*), $D = 4.51 \mu\text{m}^2 \text{s}^{-1}$, we obtain a reasonably good agreement with experimental results without the use of any fitting parameter (Figure 3.10A). Therefore, we can conclude that the

adsorption process of natural nanovesicles onto solid supports, in spite of its intrinsic complexity, can be reasonably well explained by a simple diffusion theory. In the experiments reported here no clear evidence of surface saturation effects were observed, although for the highest concentrations some symptoms of surface saturation can be appreciated. However, at coverages higher than 20-25% the evaluation of the surface coverage from AFM images gets difficult, due to the increasing presence of the adsorbed residual layer.

The time-evolution of the thickness of the adsorbed residual layer is shown in Figure 3.10B. For all the samples we found that a layer of about 1-2 nm, compatible with PBS residuals, is present on the surface at the shortest times, whose thickness slowly increases in time as the density of adsorbed nanovesicles increases. We fitted the experimental data according to a power law (Equation 4):

$$y = A(C) \cdot t^b \quad (\text{Eq. 4})$$

The power law fitting according to Equation 4 gives a scaling exponent of (0.103 ± 0.012) , which is considerably lower compared to the expected exponent for a purely diffusive process, and a concentration-dependent prefactor shown in the inset of Figure 3.10B.

The scenario depicted in Figure 3.10 indicates that incubating nanovesicles solutions at fixed concentrations and increasing the incubation time will improve the nanovesicles/background ratio. Increasing for instance 100 times, the concentration of the nanovesicles solution will increase 100 times the nanovesicles coverage and 5-10 times the thickness of the adsorbed layer; an identical increase in the incubation time will increase 4.8 times the coverage and 1.6 times the thickness of the adsorbed layer. These two parameters need to be carefully assessed in the design of surface-sensitive devices for studying adsorption phenomena of intact vesicles³⁰ and for testing the functional response of GPCRs containing natural vesicles.³³ Our experimental data suggest that to maximize the nanovesicles coverage on glass it is convenient to work with low nanovesicles concentrations ($C < 2 \cdot 10^{10}$ NV mL⁻¹) and to incubate the nanovesicles solutions for long times (hours). By applying these conditions we obtained

a nanovesicles coverage of about 20-25%, keeping at the same time the thickness of the adsorbed layer at a few nanometres.

3.3.5 Ionic strength-dependent nanovesicles deposition

The presence of monovalent ions (Na^+ and K^+) in the solution have been study on how affects the stability (such as diameter size and membrane impermeability to these ions which generate osmotic forces) of synthetic liposomes¹³. Sabín et al. concluded that EYPC liposomes (these phospholipids are the most common components of biological membranes) kept stable in solution in a wide range of ion concentration. In addition, they observed a decrease in the liposomes diameter on low concentrations. They explained that fact, because the concentration gradient at both membrane sides generates an osmotic force and due to the membrane impermeability to some ions, the liposomes react sending off water, so decreasing their size.

From the best of our knowledge, these kinds of experiments have not been performed with natural nanovesicles. Our goal, is to carry on this study with OR-natural nanovesicles in a systematically and controlled way. Then, we will try to find a correlation with the different nanovesicle size and charge and their surface deposition. An increase on the surface coverage would have an impact in the performances of biosensors devices.

The experiments were performed with Phosphate Buffer (PB 1x) 10 mM (pH = 7.5) with different $[\text{Na}^+]$ in the range between (0 - 1.095 M) in order to work with a solution closer to physiological conditions. The importance to work with physiological solutions is to maintain the functionality of the olfactory receptors expressed on the natural nanovesicles. Figure 3.11 shows the conductivity of 10 different solutions used to perform the experiments. The conductivity of each solution was measured by two different instruments in order to check the validity of them.

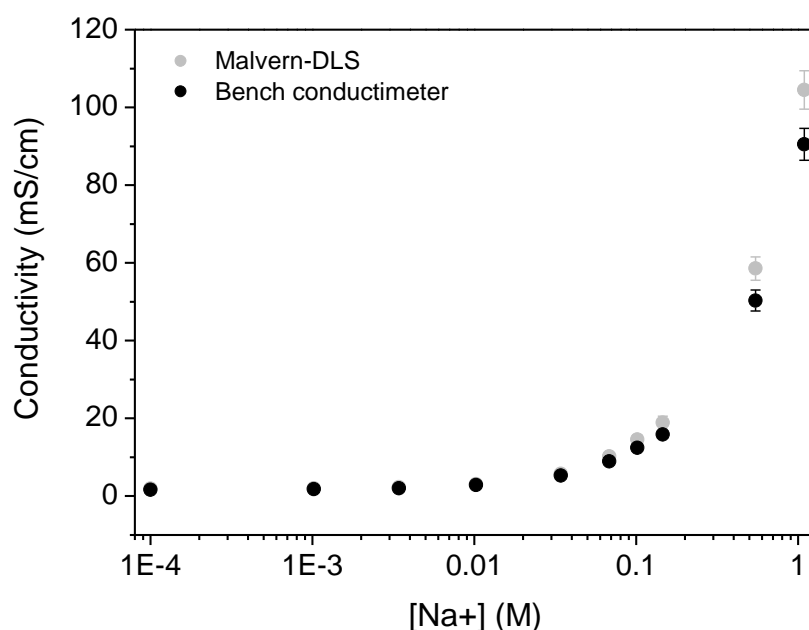


Figure 3.11 Conductivity measurements of the 10 solutions used to study the effect of Na^+ ions on the size of natural OR-nanovesicles. Two different instruments Malvern-DLS (grey dots, mean value of solutions prepared in three different days) and a bench conductimeter (black dots, mean value of solutions prepared in two different days) were used.

The first results make reference to size measurements of natural nanovesicles prepared in the presence of Na^+ salts. Figure 3.12 shows the variation of size and polydispersity of nanovesicles as a function of NaCl concentration. Not a drastic increase of the size of nanovesicles was observed. There were no statistically significant differences between group means as determined by one-way ANOVA ($F = 2.021$, $p = 0.0553$).

Polydispersity (PdI) presented in Figure 3.12 in both plots (insets) indicates the distribution of individual molecular weights in a bath of particles. Hence, the polydispersity value near zero indicates that the samples are monodispers and the value near one means that aggregation occurs³⁴. Inset of Figure 3.12A shows that the PdI, within the experimental error, is practically constant and near zero, so not aggregation is presented.

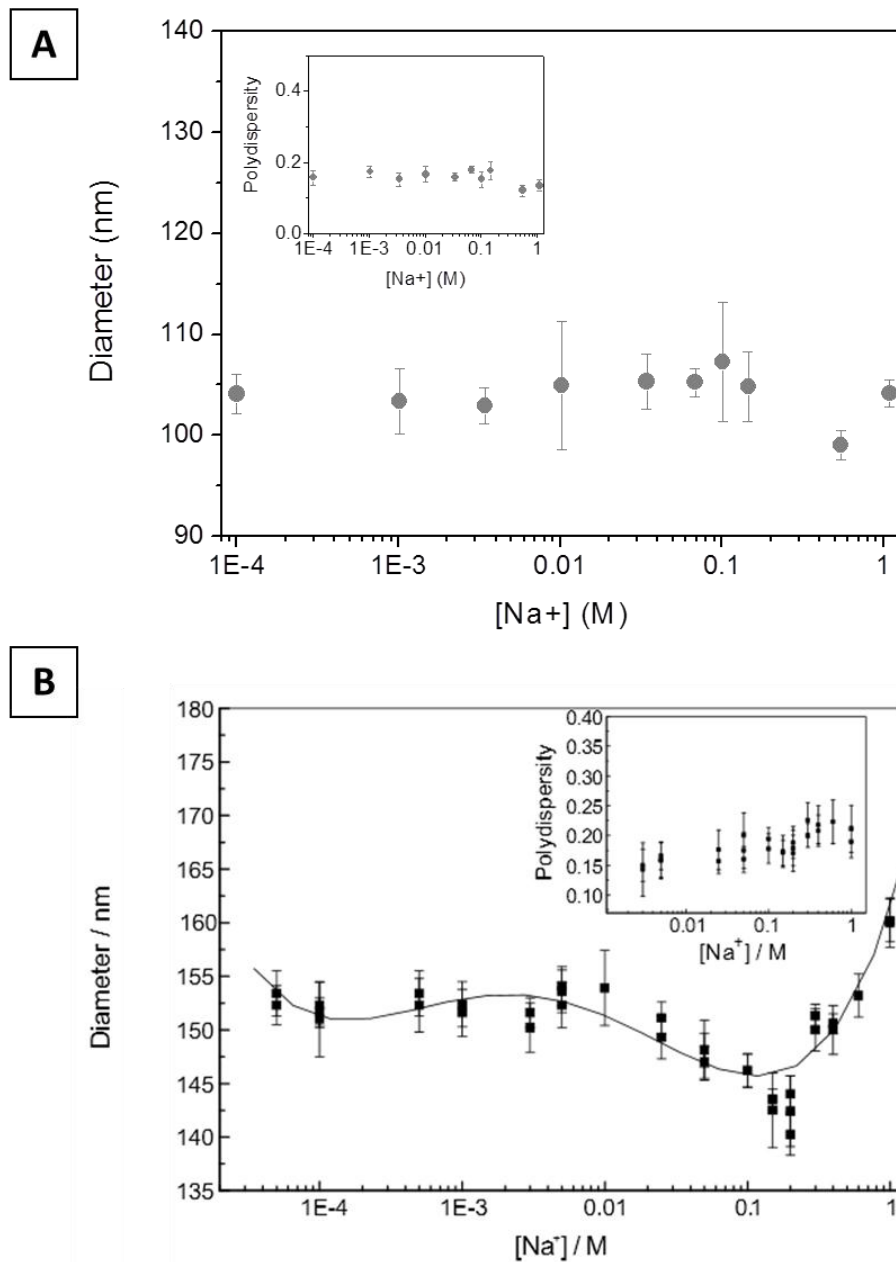


Figure 3.12 (A) Nanovesicles size (diameter, nm) by DLS vs. NaCl concentration ($[Na^+]$). The error bars are obtained due to measurements performed onto three different days. Each day the measurement was performed as well three times. One-way ANOVA statistical analysis was performed and not significant differences between group means was obtained. (B) Sizes and polydispersity of EYPC synthetic liposomes as a function of Na^+ concentration¹³.

Considering that PDI and diameter size numbers remain practically constant, we can conclude that natural nanovesicles prepared in a wide range of NaCl concentration, do not aggregate and keep stable in all working range of salt concentration. In addition, small variation of the diameter of nanovesicles is observed but is not significantly

different. These results agree with ones obtained with EYPC liposomes (Figure 3.12B)¹³.

As has been explained before, the particles charge has an important impact in their deposition onto negatively charged surface. Thus, working with a monodispers sample and knowing the charge of nanovesicles solutions at different ionic strength will allow us to predict high surface coverage.

Figure 3.13 shows the ζ -potential of lipidic nanovesicles at different concentration of salts. As can be seen, either in natural nanovesicles (Figure 3.13A) and synthetic liposomes (Figure 3.13B) vesicles have negative charge at very low salts concentrations^{13,35-37}. Then, a fast decrease of the negative ζ -potential can be observed due to the absorption of Na^+ ions to the vesicles surface. Reaching concentration values higher than 0.1 M it can be noticed that the ζ -potential is practically constant (~ -11 mV) and smaller variations are observed due to the high ionic strength of the medium.

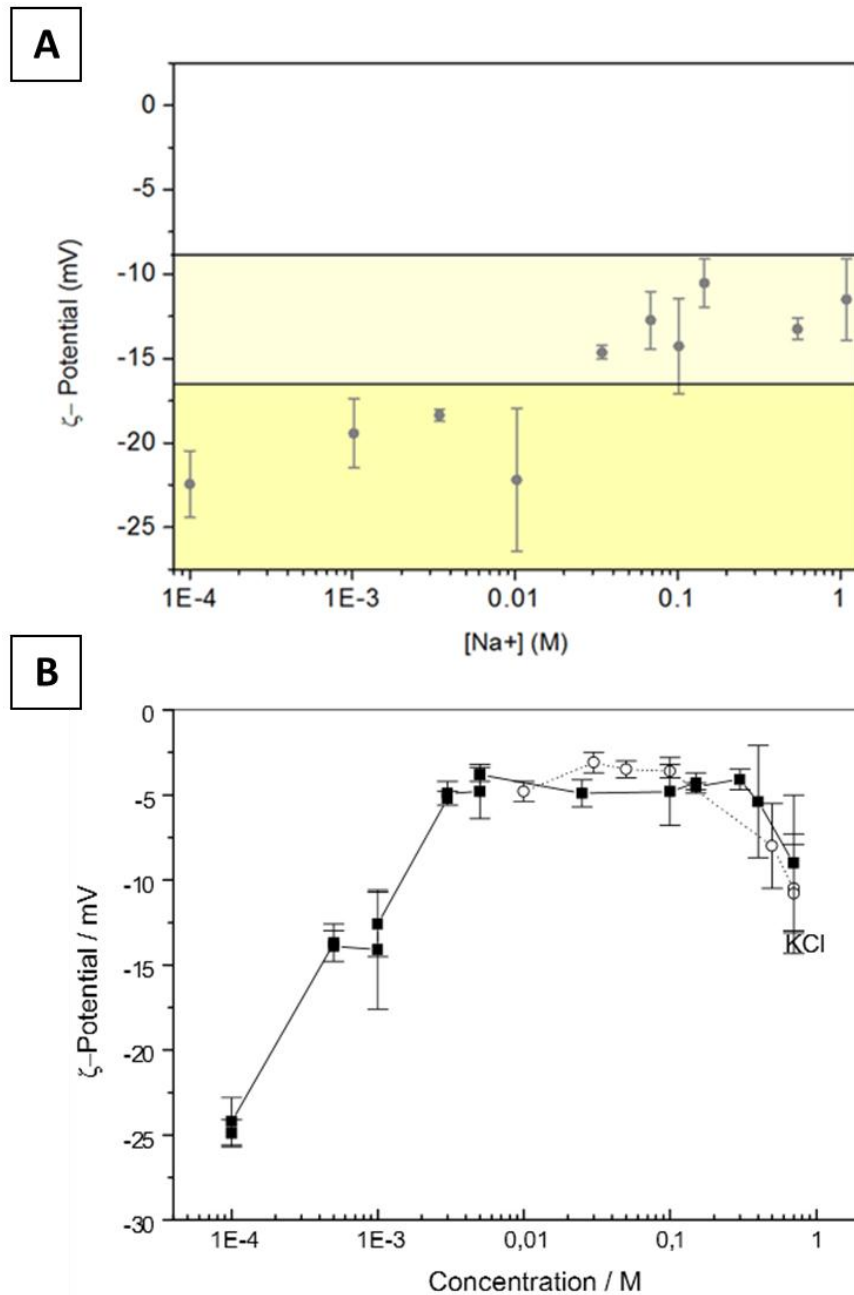


Figure 3.13 (A) Nanovesicles ζ -Potential in solution vs. NaCl concentration ($[\text{Na}^+]$). Two important regions can be differentiate: from 0 to 0.01 M $[\text{Na}^+]$ (dark yellow) and from 0.03 to 1 M (light yellow). (B) ζ -Potential of EYPC liposomes as a function of Na^+ (black square) and K^+ (white dots)¹³.

Once the nanovesicles were produced at different ion concentration solutions and their size and surface charge were calculated we studied in detail their deposition on SHC₁₅COOH SAM (hereafter called SAM₂-COOH, an hydrophilic alkanethiol self-assembled monolayer) functionalized gold surface and the morphology of individual nanovesicles as a consequence of their adsorption on this substrate. Carboxyl-

terminated SAMs have often been used in many devices for the immobilization of proteins³⁸ and cells³⁹⁻⁴¹ onto gold supports.

Figure 3.14 shows the aspect ratio obtained from AFM images taken in liquid (PB buffer at different concentration of Na⁺ ions), after incubating on SAM₂-COOH functionalized gold 40 μL of a diluted solution of nanovesicles carrying OR1740 olfactory receptor at $C = 1.67 \cdot 10^{11}$ NV mL⁻¹ (incubation time $t = 3600$ s). Flattened integer vesicles are also present on the surface at different solutions of Na⁺ concentration, exhibiting as well homogeneous features of few tens of nm in height and few hundreds of nm in width. The aspect ratios presented in the plot are the result of extracting the thickness (h) and the width by analysing the topographic profiles on top of 30 nanovesicles at each different salt concentration. All the aspect ratio values obtained were ~ 0.27 . However, for our population we found that there were statistically significant differences between group means as determined by one-way ANOVA ($F = 15.95$, $p < 0.0001$). Then, followed by Bonferroni Test pot-hoc comparison, we can distinguish that the nanovesicles aspect ratio prepared at two specific Na⁺ concentrations (0.068 M, and 0.146 M) mainly differ from the rest. This results are coherent with the nanovesicles ζ -potential in solution. Less negative vesicles ζ -potential provides higher aspect ratios when the vesicles are immobilized in a negatively charge functionalized gold surface.

For the SAM₂-COOH functionalized substrate we found a relatively higher nanovesicles aspect ratio than on SAM-COOH (it is 0.148 ± 0.029 , see below). This can be due to the fact that SAM₂-COOH, that has not PEG groups on their alkilic chain, could exhibits a slightly less negative surface zeta-potential. Furthermore, the nanovesicles batch used is a different one and small differences between them can be observed due to that fact⁴².

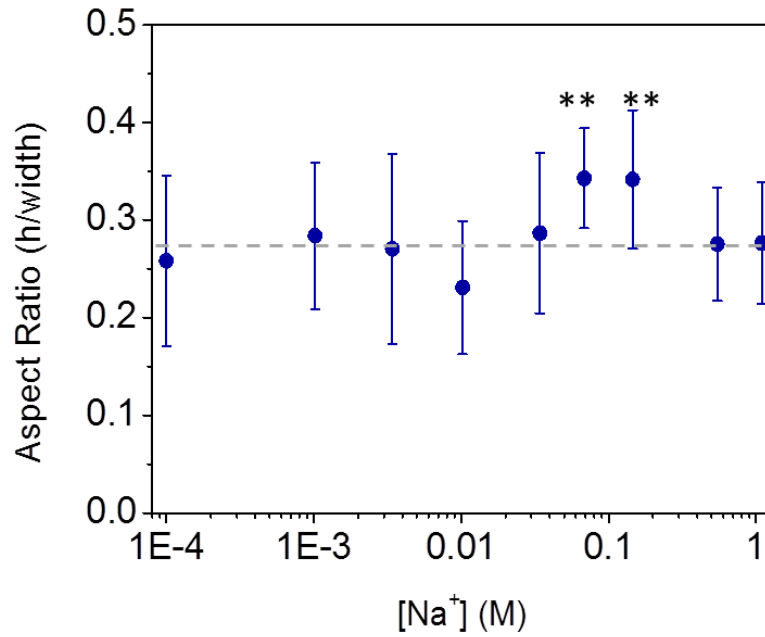


Figure 3.14 Nanovesicles aspect ratio presented as a result of extracting the thickness (h) and the width by analyzing the topographic profiles on top of 30 nanovesicles at each different NaCl concentration ([Na⁺]). The grey line indicate the aspect ratio mean value considering all the salts concentration: ~ 0.27. ** p < 0.05 by one-way ANOVA followed by Bonferroni Test pot-hoc comparison.

From the topographic profiles we also estimated the volume of the deposited nanovesicles and the equivalent sphere diameter (see the Experimental Section). The values that we obtained are presented in Figure 3.15B. The equivalent diameter size extracted by AFM analysis was significantly different after a one-way ANOVA statistical analysis ($p < 0.05$). We would expect no significant differences between different salt concentrations such as measurements obtained by DLS (Figure 3.15B). However, these differences, as well as the larger standard deviation of the AFM measurements compared to DLS measurement can be due to the complexity of the AFM measurement and analysis, as well as the nanovesicles recognition adsorbed on the surface. Considering that, we can conclude that both results are in agreement indicating that upon adsorption nanovesicles deform keeping the same volume they have in solution (~ 100 nm diameter size).

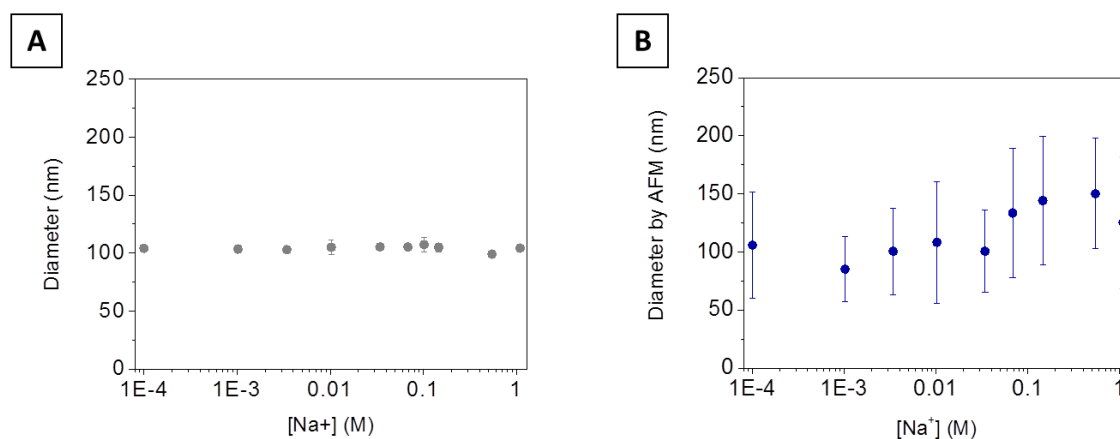


Figure 3.15 (A) Nanovesicles size (diameter, nm) by DLS vs. NaCl concentration ($[\text{Na}^+]$). The error bars are obtained due to measurements performed onto three different days. Each day the measurement was performed as well three times. (B) Nanovesicles size (diameter, nm) by AFM vs. NaCl concentration ($[\text{Na}^+]$). The error bar is the one obtained after analyzing 30 different nanovesicles at each salt concentration.

We also studied the surface coverage as a function of the concentration of the Na^+ in solutions ($[\text{Na}^+]$). Figure 3.16 shows a set of AFM images taken after incubating nanovesicles solutions on $\text{SAM}_2\text{-COOH}$ functionalized gold surface at progressively increasing Na^+ ion concentrations for a fixed incubation time ($t = 3600$ s); Figure 3.17 shows the evolution of the nanovesicles surface coverage in function of $[\text{Na}^+]$.

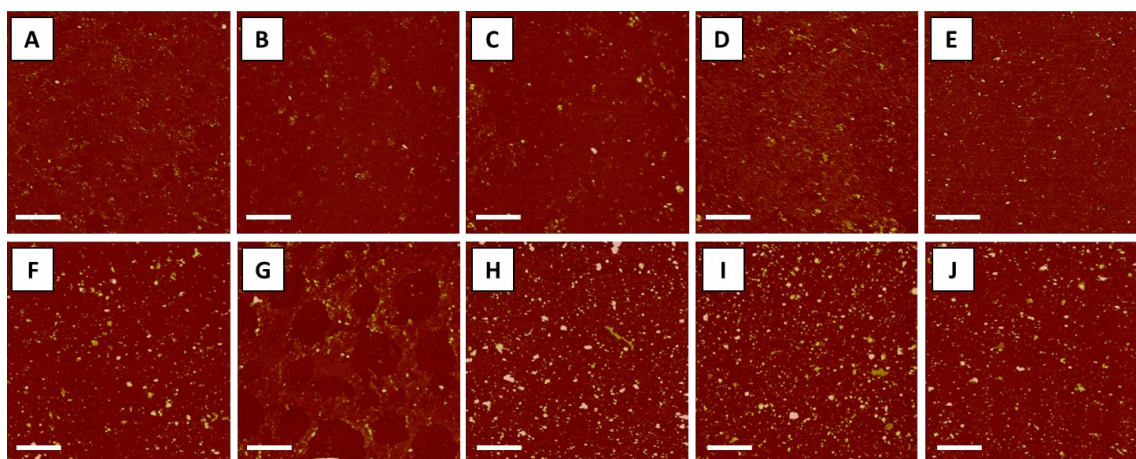


Figure 3.16 Sequence of AFM images taken after incubating for 3600 s a solution of OR1740 carrying nanovesicles at $C = 1.67 \cdot 10^{11}$ NV mL^{-1} onto a $\text{SAM}_2\text{-COOH}$ at different NaCl concentrations: $C = 0$ mM (A); $C = 1.02$ mM (B); $C = 3.42$ mM (C); $C = 10.26$ mM (D); $C = 34.22$ mM (E); $C = 68.44$ mM (F); $C = 0.102$ M (G); $C = 0.146$ M (H); $C = 0.547$ M (I); $C = 1.095$ M (J). Z scale = 55 nm and Scale bar = 2 μm .

In this range, we observed that the functionalized gold surface is progressively covered with individual vesicles (see Figure 3.16). As it can be observed in the Figure

3.16G the AFM image obtained, after the nanovesicles deposition, does not have the same sensitivity level than the rest of the images. Thus, the aspect ratio measurement, as well as the surface coverage was not possible to calculate correctly. From the rest of Na^+ concentrations, in our concentration range the experimental surface coverage adapts to the same behaviour that the vesicles ζ -potential adopted in the different $[\text{Na}^+]$ (Figure 3.17). Two main regions can be differentiate achieving at low $[\text{Na}^+]$ less than 1% surface coverages and at high $[\text{Na}^+]$ surface coverages $\sim 10\%$. As expected, less negatively charged native vesicles from yeast cells are suitable to induce a large surface coverage working with $\text{SAM}_2\text{-COOH}$ functionalized gold substrates keeping at the same time the thickness of the adsorbed layer at a few nanometres (inset Figure 3.17).

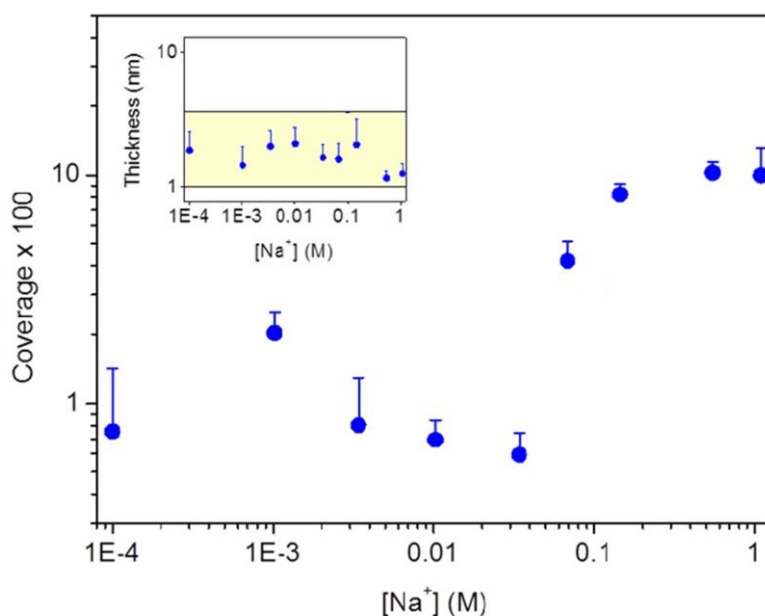


Figure 3.17 Surface coverage vs. NaCl concentration ($[\text{Na}^+]$). Thickness of the adsorbed residual layer vs. $[\text{Na}^+]$ (inset).

Our objective of the ion strength study was to measure the maximum possible nanovesicle surface coverage. Changing the $[\text{Na}^+]$ we were able to reach $\sim 10\%$ nanovesicle surface coverage on $\text{SAM}_2\text{-COOH}$ surfaces ($C = 1.67 \cdot 10^{11} \text{ NV mL}^{-1}$, time = 3600 s). Seems that for the development of practical biosensor devices based on natural nanovesicles in COOH- functionalized surfaces the maximum surface coverage achievable until now is around 10% at the working conditions studied.

However, we also note that the presence of this type of unavoidable residuals mentioned before can have direct implications when applying surface sensitive

techniques to detect the immobilization of nanovesicles from cellular extracts, as for instance by means of Surface Plasmon Resonance (SPR).

3.3.6 Concentration-dependent surface coverage by SPR

In order to investigate the effect just mention above and trying to increase the nanovesicle surface coverage on functionalized gold, we complicated the study using SPR to follow the deposition on a SHC₁₁PEG₆OCH₂COOH SAM (hereafter called SAM-COOH) modified gold surface after exposure to a continuous flow of a nanovesicle solution. The nanovesicles surface coverage was analysed by AFM imaging in liquid. Figure 3.18A shows the evolution of the SPR signal variation obtained by flowing nanovesicles solutions at three different concentrations (C) on SAM-COOH modified gold surfaces. Figure 3.18B shows the trend of the % Reflectivity vs. nanovesicles concentration in a range between $6.58 \cdot 10^8$ and $3.9 \cdot 10^{11}$ NV mL⁻¹. The reflectivity is calculated from the SPR sensorgrams, as the response after flowing the nanovesicles solution for 4500 s (see Figure 3.18A). The corresponding nanovesicles surface coverage is shown in Figure 3.18C.

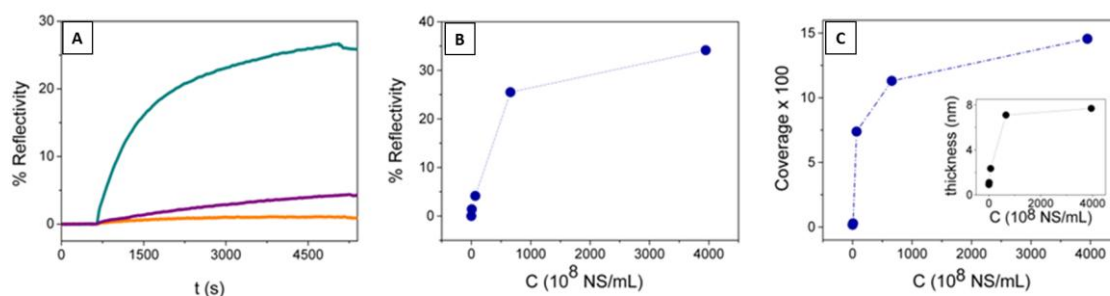


Figure 3.18 SPR sensorgrams of three solutions of nanovesicles carrying OR1740 olfactory receptors at $C = 6.581 \cdot 10^8$ NV mL⁻¹ (data in orange), $C = 65.81 \cdot 10^8$ NV mL⁻¹ (data in purple) and $C = 658.10 \cdot 10^8$ NV mL⁻¹ (data in cyan) immobilized onto SAM-COOH functionalized gold substrate (A). SPR % Reflectivity (B) and corresponding surface coverage (C) vs. nanovesicles concentration. C-evolution of the thickness of the adsorbed layer extracted from AFM images collected at the end of the SPR experiment (C, inset).

The analysis of both Figures 3.18B and 3.18C suggests that the nanovesicles surface coverage evolution can explain the increase in the SPR signal until a value around $5 \cdot 10^{10}$ NV mL⁻¹. For higher concentrations ($C > 5 \cdot 10^{10}$ NV mL⁻¹) it seems that a distinctive behaviour and/or a saturation of the response starts to occur.

Correspondingly, a full coverage of the substrate by a thick residual layer of thickness ~ 7 nm (see the inset of Figure 3.18C) is revealed by AFM. The presence of such layer can make the reflectivity to become insensitive to the further deposition of material on top of it. The measured nanovesicles surface coverage at $C = 3.9 \cdot 10^{11}$ NV mL $^{-1}$ was ~ 15 %.

3.3.7 Dynamics of nanovesicles deposition by SPR

Finally, for the SAM-COOH functionalized substrate we also studied the time-dependence of the surface coverage and of the thickness of the adsorbed layer at low nanovesicles concentrations.

Figure 3.19 shows the normalized SPR response of three diluted nanovesicles solutions at $C = 5.14 \cdot 10^9$ NV mL $^{-1}$, flowing on SAM-COOH functionalized gold substrates for different incubation times of 1 hour, 3 hours and 14 hours. In this example, the observed increase in the % reflectivity can be assigned to the increase of the nanovesicles surface coverage with more confidence. The thickness of the adsorbed layer, in fact, remains almost constant at the value of 1-3 nm during the time scale of the experiment (see the inset of Figure 3.19).

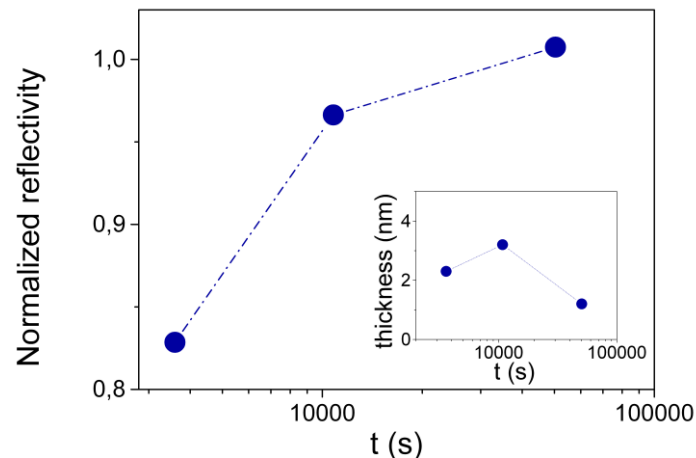


Figure 3.19 Normalized SPR reflectivity of three solutions of nanovesicles carrying OR1740 olfactory receptors incubated on SAM-COOH functionalized gold substrate for increasing incubation times. The measured surface coverage determined by AFM for these samples was 1.3 % ($t = 3600$ s), 3.8% ($t = 10800$ s) and 7.4% ($t = 50400$ s). Time-evolution of the thickness of the adsorbed residual layer for the three samples (inset).

3.3.8 Role of surface chemistry

Carboxyl- and amino-terminated alkanethiolated SAMs have been proven to favour the adsorption of a variety of biomolecules on gold through hydrogen bond formation,⁴³ compared to alcohol-terminated SAMs, which are generally used to reduce non-specific adsorption of undesired entities,⁴⁴ and bare gold.

XPS was used to obtain the elemental composition of SAM-COOH, SAM-NH₂ and SAM-OH functionalized gold chips. The XPS spectra (Figure 3.20) shows a decrease of the surface peaks of Au with respect to bare Au, and a growth of the peaks related to the organic monolayers containing Carbon, Sulphur and Nitrogen. A high-resolution spectrum for each significant element of the SAMs was also carried out. In these spectra C 1s, N 1s, S 2p orbitals show identical binding energies in all the SAMs. The C 1s spectrum reveals an ether component peaks (C-O) at 286.5 eV associated to carbon species from the PEG groups of the thiol linker and a component peak (C-C/C-H) at 285.0 eV due to the carbon species from the alkyl chains of the thiol linker.⁴⁵⁻⁴⁷ High-resolution S 2p XPS spectra reveal a peak at 161.8 eV which corresponds to the sulphur species and is usually observed for thiolate-based SAM on gold.⁴⁸ The N 1s high-resolution spectra shows a peak at 399.62 only for the SAM-NH₂, confirming the presence of the functional group at the monolayer-air interface for the SAM-NH₂ modified gold surface.

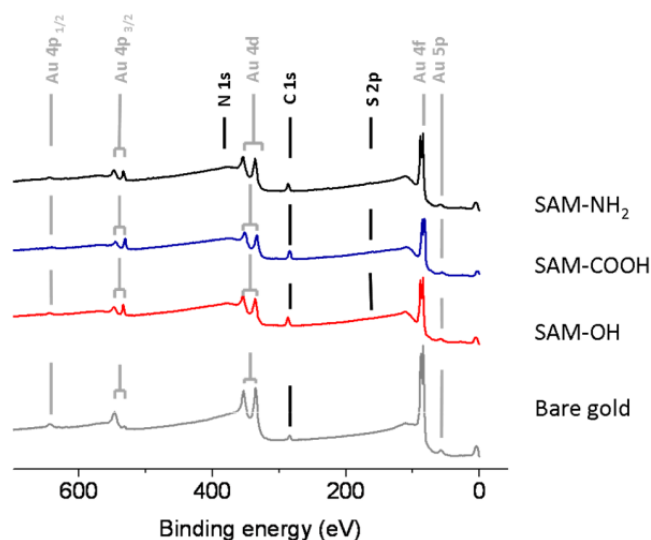


Figure 3.20 XPS spectra of bare Au, SAM-COOH, SAM-NH₂ and SAM-OH functionalized gold chips.

In Figure 3.21 the nanovesicles surface coverage on SAM-COOH functionalized gold substrate is compared with that observed on a SAM-NH₂ (SHC₁₁PEG₆OCH₂NH₂) and on a SAM-OH (SHC₁₁PEG₆OH) functionalized gold substrate. A clear dependence of the measured SPR signal on the type of surface used can be observed, where the SAM-COOH seems to induce the highest nanovesicle coverage, as confirmed by the AFM images, thus supporting the effect of surface charge in the nanovesicles deposition.

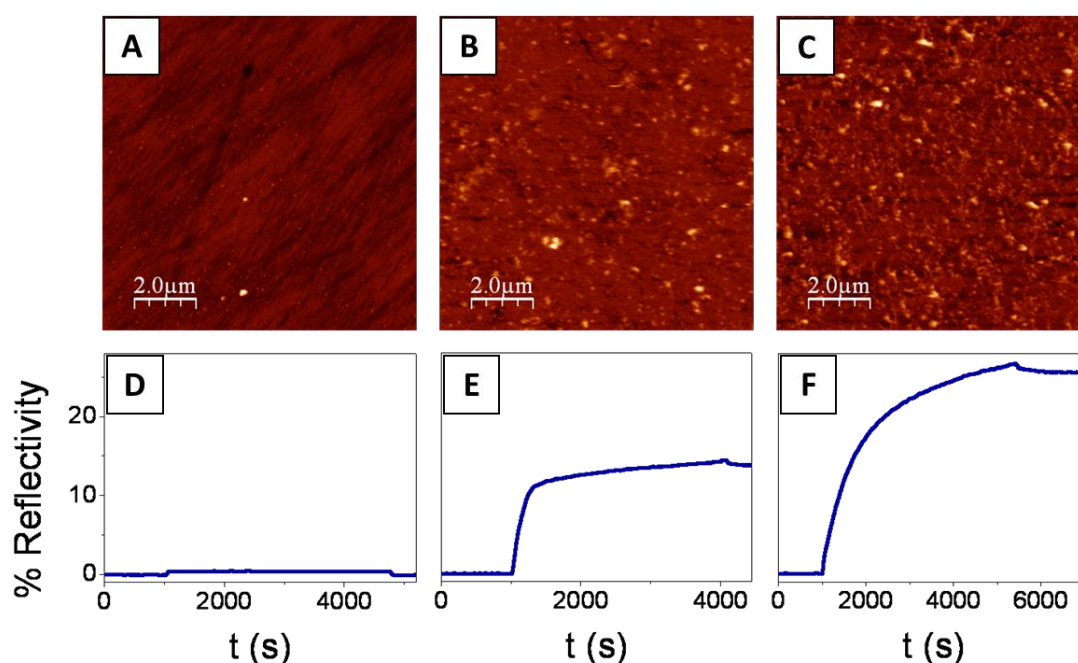


Figure 3.21 AFM images taken after incubating a solution of OR1740 carrying nanovesicles at $C = 394.86 \cdot 10^8 \text{ NV mL}^{-1}$ onto a SAM-OH ($t = 3600 \text{ s}$) (A), SAM-NH₂ ($t = 3000 \text{ s}$) (B) and SAM-COOH ($t = 4500 \text{ s}$) (C) functionalized gold chip. The nanovesicles surface coverage is around 0.03 % for SAM-OH functionalized gold and around 10 % for SAM-NH₂ and SAM-COOH functionalized gold. Corresponding SPR sensorgrams (D-F).

For the SAM-COOH functionalized substrate we found a relatively high surface coverage comparable with that observed in the experiments performed on glass. This can be due to the fact that it exhibits a negative surface zeta-potential = - 66 mV⁴⁹ relatively close to the one of glass substrates ($-100 \pm 34 \text{ mV}$). In this case the measured average nanovesicles aspect ratio of $(0.148 \pm 0.029)^{15}$ is slightly higher than on glass, which is compatible with a less negative surface.¹⁵ The lower adsorption observed on the SAM-NH₂ functionalized electrode is attributed to its still lower surface zeta-potential (- 52 mV), while the very poor adsorption on SAM-OH functionalized substrates can be more probably attributed to a limited formation of hydrogen bonds on

this type of substrate, as reported earlier,⁴⁴ than to its surface zeta-potential (- 42 mV) which is only slightly smaller compared with the corresponding zeta potentials for SAM-COOH and SAM-NH₂. Thus, negatively charged substrates allowing the formation of hydrogen bonds are suitable to induce a large surface coverage with native nanovesicles from yeast cells.

A final remark concerns the role of the substrate surface properties (wettability, RMS roughness) on nanovesicles deposition. Even if the substrate wettability and roughness are considered to be key parameters governing the adsorption of cells^{50,51} and proteins^{52,53} on solid supports, in our experimental conditions we did not find significant differences in both. The contact angle of water with SAM-COOH, SAM-NH₂ and SAM-OH functionalized gold surfaces was respectively: (33.8 ± 1)°, (34.3 ± 1)° and (33.9 ± 1)° and in the RMS roughness of these substrates was respectively: (1.17 ± 0.06) nm, (1.57 ± 0.01) nm, (1.49 ± 0.11) nm and the RMS of bare gold being (1.29 ± 0.14) nm. These results could justify the different nanovesicles coverage observed. Indeed the literature specifically points out the role of electrostatic interactions more than substrate hydrophilicity and roughness in the nanometric range on vesicles deposition and supported lipid bilayer formation.^{54,55}

3.3.9 Pattern of OR1740-carrying nanovesicles onto self-assembled monolayers (SAM)

Gold substrates are ideal surfaces for surface plasmon resonance and electrochemical measurements to probe receptors-ligand interactions. In these cases a proper functionalization of the surface is required to allow an almost full coverage with the biological matrix for sensing purposes. In this Chapter we demonstrated that gold functionalization with different amino-, alcohol- and carboxyl-terminated SAMs affects the resulting surface coverage with OR1740-carrying nanovesicles, where the carboxy-terminated SAM (here called SAM-COOH) gave the highest surface coverage, comparable with that obtained on hydrophilic glass substrates. Vice versa, alcohol-terminated SAM (SHC₁₁PEG₆OH) practically did not induce any nanovesicle adsorption in the concentration and time scale of the experiment. This behaviour is reproduced as well for other alcohol-terminated SAMs and can be exploited to design a

disk-like pattern, where disks of SAM-COOH lie in a matrix of SAM-OH functionalized gold (SH-PEG₃-OH, here called SAM-OH).

The tapping-mode AFM phase image of the pattern immediately after preparation and nanovesicles deposition is shown respectively in Figure 3.22A and Figure 3.22B. The corresponding topographic profiles are shown in Figure 3.22C and D. Spatial confinement of nanovesicles within the disks can thus be achieved through an appropriate fabrication technique which combines microcontact printing (see Experimental Section) with the selection of the terminal group of the SAM thiol⁵⁶.

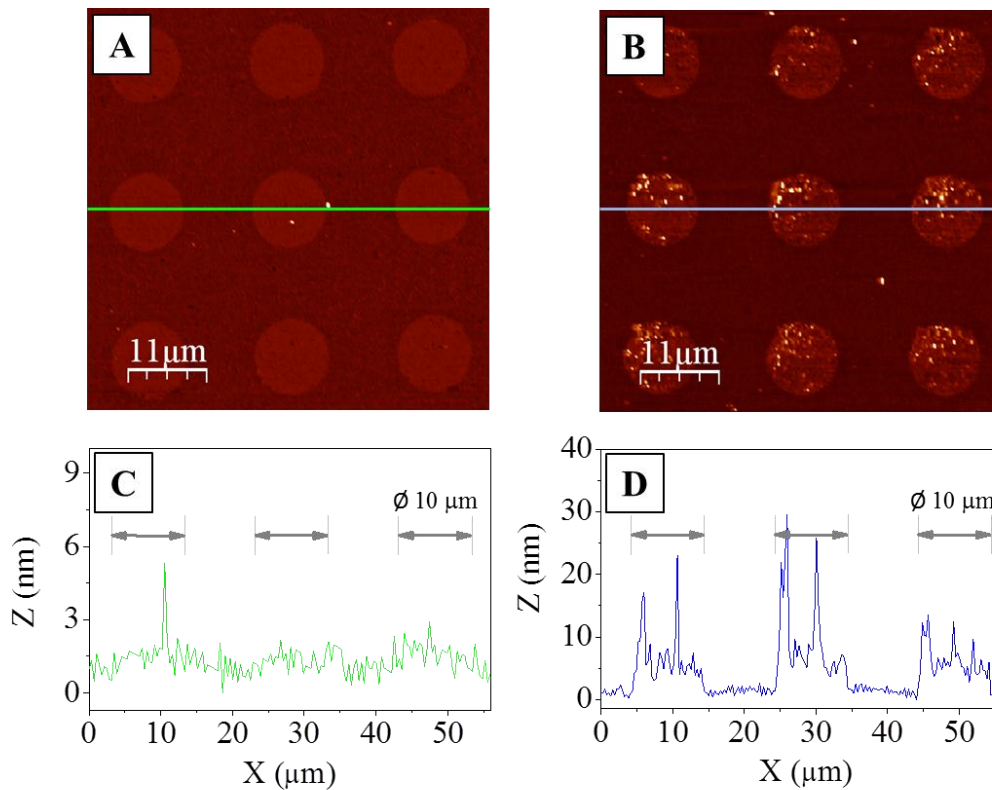


Figure 3.22 Tapping-mode AFM phase image of the disk-like pattern of SAM-COOH and SAM-OH before (A) and after (B) the incubation of a solution of nanovesicles carrying OR1740 olfactory receptor at: $C = 3.29 \cdot 10^{10}$ NS/mL for 4200 s. (C), (D) Corresponding topographic profiles.

SAM-COOH-mediated nanovesicles deposition on gold could be exploited for the generation of an array of multiple nanovesicles, each one carrying a different olfactory receptor at its surface, which could be integrated into the same chip.

3.3.10 Array of OR-carrying nanovesicles

In order to assess the issue presented in the paragraph above, a proof-of-concept of an OR-carrying nanovesicles array was performed onto a simplest biosensor surface such as glass. Glass and gold substrates, as has been explained before, are representative examples of surfaces for applications in optical and electrical biosensing, respectively.⁵⁷⁻⁵⁹ Due to the simplicity to work with glass surfaces instead of functionalized gold surface the nanovesicles proof-of-concept array was performed on it.

To visualize the array by fluorescence microscopy we stained two different nanovesicles, OR1740-nanovesicles and SSTR2-nanovesicles, as model nanovesicles to perform the array. The nanovesicles were stained with either DiI or DiO respectively. Receptor-nanovesicles in buffer suspension stained brightly enough with the probes to be readily observed by epifluorescence (Figure 3.23C and D) and confocal microscopy (Figure 3.23E and F) as bright dots on a dark background. As controls, we also incubated the dialkylcarbocyanine dyes in buffer alone. As expected, no dye precipitation was observed (Figure 3.23A and B), confirming that the probes are indeed staining the nanovesicles based on their affinity for lipidic bilayers⁶⁰.

Our results presented that both nanovesicles were efficiently labelled with the two different probes: DiI, which has the excitation at 549 nm and emission at 565 nm, and DiO, which has the excitation at 484 nm and emission at 501 nm. DiI and DiO dyes (dialkylcarbocyanines) are amphiphilic molecules composed by a polar fluorescent head linked to two hydrophobic alkyl tails. The chains insert into the phospholipid bilayer of the vesicles and the positively charged fluorophore rests close to the polar head group of it, parallel to the membrane surface. Due to that, these dyes are well-use as lipidic membrane probes⁶⁰. The fluorescence of these environment-sensitive dyes is greatly enhanced when incorporated into membranes or bound to lipophilic biomolecules such as proteins although they are weakly fluorescent in water. They have high extinction coefficients, polarity-dependent fluorescence and short excited-state lifetimes.

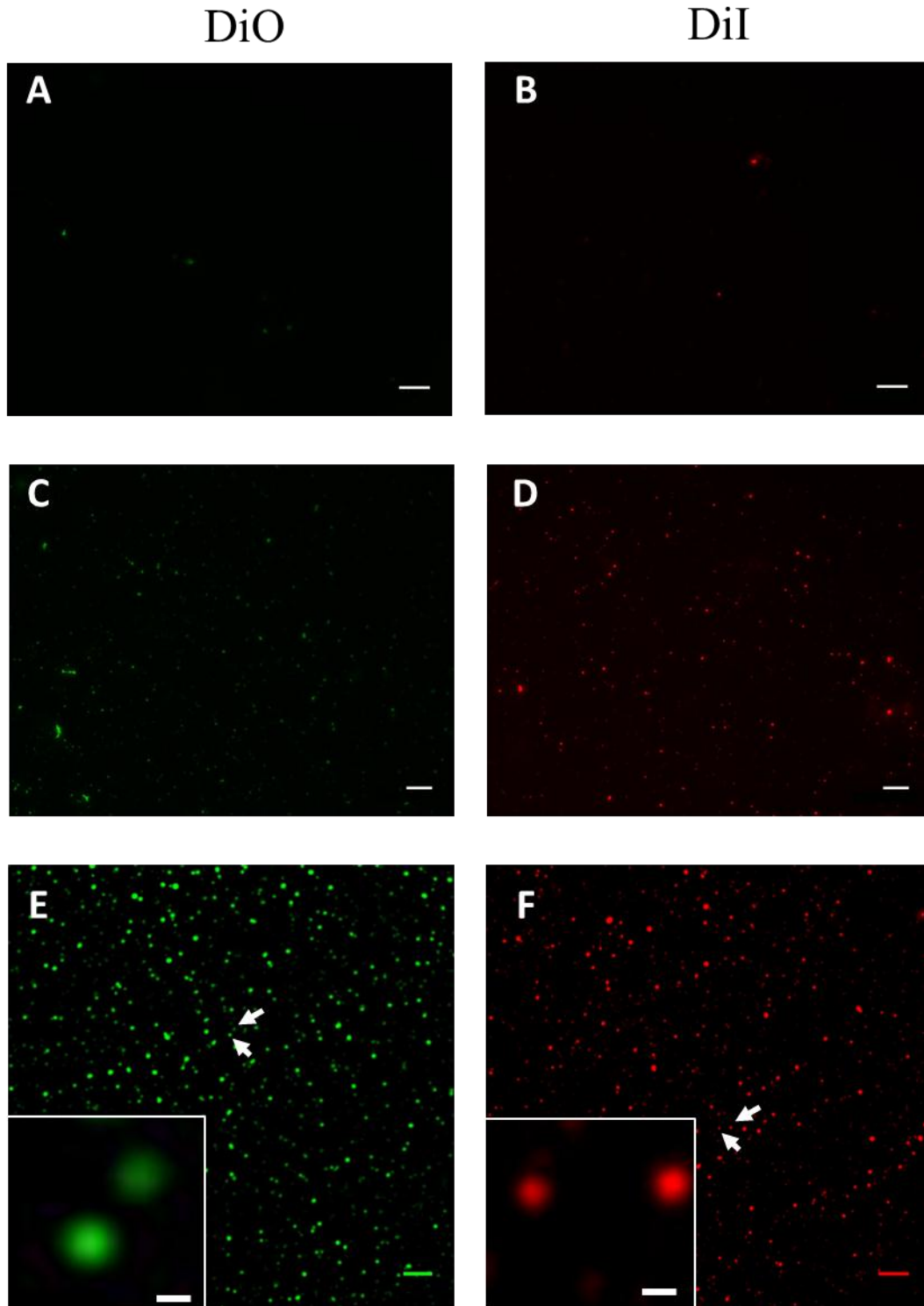


Figure 3.23 Staining of receptor-nanovesicles with dialkylcarbocyanines. (A), (B) Control solutions of buffer alone incubated with the dyes were observed by epifluorescence microscopy. The images were taken at 3000ms exposure time and at 60x magnification. Bars, 10 μ m. (C), (D) Vesicles after staining with DiO or DiI observed by epifluorescence microscopy. The images were taken at 3000ms exposure time and at 100x magnification. Bars, 5 μ m. (E), (F) Vesicles after staining with DiO or DiI observed by confocal microscopy, showing small brightly fluorescent spots. Arrows indicate vesicles that are magnified in the insets. The images were taken at 3000ms exposure time and at 60x magnification to enhance clarity. Bars, 5 μ m (main parts of the images) and 500 nm (insets).

First, an array of OR1740-nanovesicles ($C= 1.67 \cdot 10^{11}$ NV mL^{-1} , incubation time 1 hour) stained with two different dyes was successfully obtained on glass substrates. Its visualization before washing the slide is presented in Figure 3.24. As it was expected, weak fluorescence was obtained in the controls. That fact, confirm that our stained vesicles, observed by brightly spots, were efficiently immobilized in a microarrayer format.

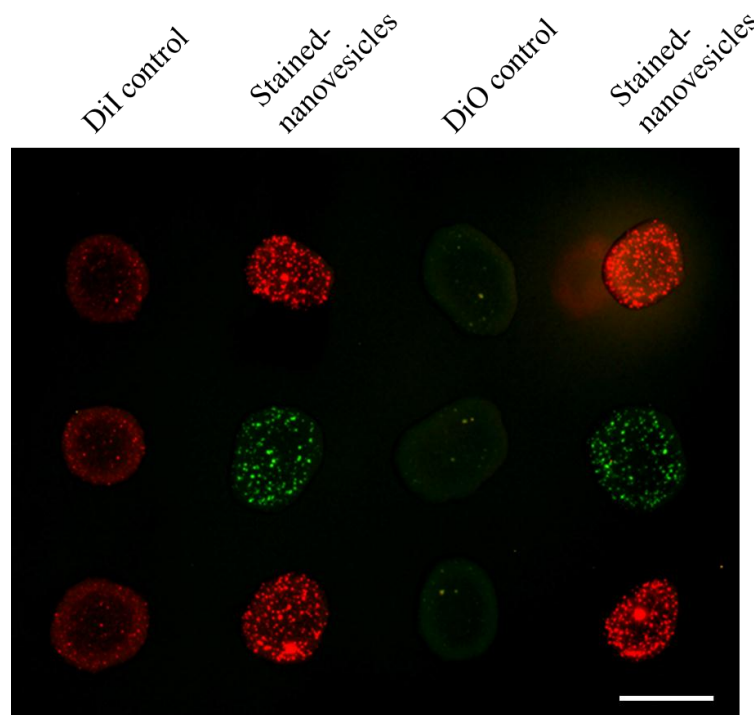


Figure 3.24 OR1740-nanovesicles ($C= 1.67 \cdot 10^{11}$ NV mL^{-1}) previously stained with DiI (red) or DiO (green) dyes immobilized on clean glass substrates for 1 hour. Corresponding negative controls (dyes in PBS) were also printed. Array obtained before washing the glass substrate was observed by fluorescence microscopy. The images were taken at 4000ms and 6000ms exposure time for DiI and DiO stainings respectively and at 4x magnification. Scale bar 250 μm .

To perform the array we used 0.5 mm spot spacing to avoid the merging of the spots as it is shown in Figure 3.24 and 3.25.

Then, we decided to use OR1740-nanovesicles and SSTR2-nanovesicles as model systems to perform the multiple nanovesicle arrays on glass substrate. In order to visualize the array by fluorescence, these nanovesicles were also stained with either DiI or DiO dyes respectively. Figure 3.25 shows the array of multiple nanovesicles ($C= 1.67 \cdot 10^{11}$ NV mL^{-1} , incubation time 1 hour), each one carrying a different receptor integrated into the same glass surface.

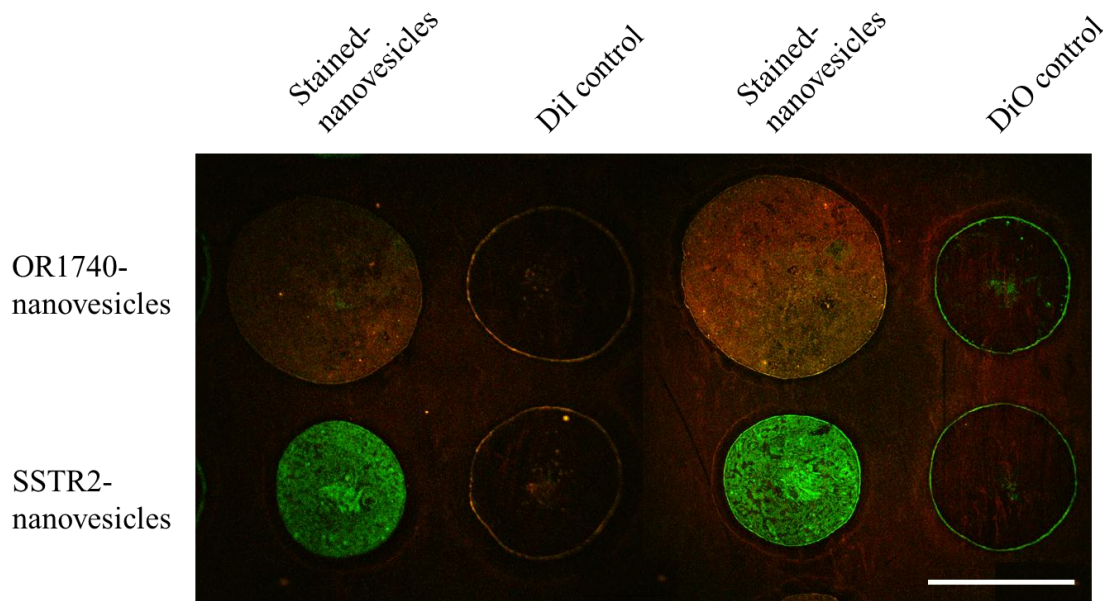


Figure 3.25 Nanovesicles ($C= 1.67 \cdot 10^{11}$ NV mL⁻¹) carrying different receptors, previously stained with DiI (OR1740-nanovesicles, red) or DiO (SSTR2-nanovesicles, green) dyes, immobilized on clean glass substrates for 1 hour. Corresponding negative controls (dyes in PBS) were also printed. Array obtained before washing the glass substrate was observed by confocal microscopy. Confocal images were taken with 488 nm (for DiO excitation) and 532 nm (for DiI excitation) lasers with 70% laser power. A constant gain and offset values were used during visualization of different arrays for each laser. Scale bar 200 μ m.

In order to detect the possible nanovesicle cross-contamination and to confirm that the microarray remained clearly identifiable after washing, repeated washing steps were performed. What we expected, either for DiI and DiO stained nanovesicles array spots was to visualize them even after wash. After wash we expected an erosion to a certain extent. Maybe, due to the loss of excess nanovesicles those were not adsorbed to the surface. Unfortunately, any spot was visualized by fluorescence after washing. The reason is that we used confocal microscopy. The first idea was to obtain images with high resolution, and confocal microscopy allow us to have it, but at the same time this technique produced an important amount of photobleaching, sample heating and more working time. Maybe, the choice to use this technique for visualization was not the correct one. Further working conditions optimization should be necessary in order to obtain the nanovesicles microarray after washing.

3.4 Conclusions

This study reveals that natural vesicles from yeast of a diameter around 100 nm (nanovesicles) and to a concentration above 10^{10} NS/mL suitable for large surface coverages. Such nanovesicles do not rupture once immobilized onto glass and gold surfaces and retain their closed nature although they flatten considerably displaying an aspect ratio of about 0.1-0.3.

The evolution of the nanovesicles surface coverage on glass is found to follow a diffusive law, being proportional to their concentration in the solution and evolving approximately with the square root of the incubation time. In our range of concentration and time we observed the formation of only a single layer of vesicles and we demonstrate that a maximum coverage of 20-25% can be achieved with reasonably workable membrane fraction concentrations and incubation times, controlling at the same time the deposition of not-desired cell fragments, unavoidable in natural samples. Such surface coverage is quite remarkable as compared to the maximum theoretical value of around 54% corresponding to ideal hard sphere models.

Surface coverage on functionalized gold substrates was as well studied. We demonstrated that the maximum coverage of 10-15% can be achieved in gold substrates functionalized with a carboxylic terminated SAM. Furthermore, substrates showing large negative zeta-potentials and allowing hydrogen bonds formation are the best candidates to give large surface coverages with nanovesicles. The present study shows that the deposition of natural vesicles carrying membrane receptor proteins can indeed be achieved in a controlled way.

In addition, nanovesicles deposition on gold or glass substrates could be exploited for the generation of an array of multiple nanovesicles, each one carrying a different olfactory receptor at its surface, which could be integrated into the same chip.

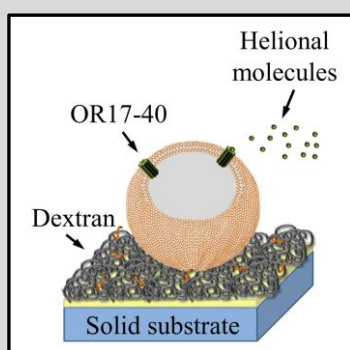
3.5 References

- (1) Bally, M., Bailey, K., Sugihara, K., Grieshaber, D., Vörös, Städler, B. *Small*, **2010**, *6*, 2481.
- (2) Christensen, S.M., Stamou, D.G. *Sensors*, **2010**, *10*, 11352-11368.
- (3) Stamou, D., Duschl, C., Delamarche, E., Vogel, H. *Angewandte Chem Int Ed*, **2003**, *42*, 45, 5580-5583.
- (4) Sott, K., Karlsson, M., Pihl, J., Hurtig, J., Lobovkina, T., Orwar, O. *Langmuir*, **2003**, *19*, 3904-3910.
- (5) Stadler, B., Bally, M., Grieshaber, D., Brisson, A., Vörös, J., Grandin, H.M., *Biointerphases*, **2006**, *1*, 142-145.
- (6) Yoshina-Ishii, C., Miller, G.P., Kraft, M.L., Kool, E.T., Boxer, S.G. *J. Am. Chem. Soc.* **2005**, *127*, 1356-1357.
- (7) Shibataseki, T., Masai, J., Tagawa, T., Sorín, S., Kondo, S. *Thin Solid Films*, **1996**, *273*, 297.
- (8) Stora, T., Dienes, Z., Vogel, H., Duschl, C. *Langmuir*, **2000**, *16*, 5471.
- (9) Stanish, I., Santos, J.P., Singh, A., *J. Am. Chem. Soc.* **2001**, *123*, 1008.
- (10) Wittenberg, N.J., Hyungsoon, I., Johnson, T.W., Xu, X., Warrington, A.E., Rodriguez, M., Oh, S.-H. *ACS Nano*, **2011**, *9*, 7555-7564.
- (11) Derjaguin, B.V., Landau, L.D., *Acta Physicochim. URSS* **1941**, *14*, 633.
- (12) Verwey, E.J.B., Overbeck, J.Th.G. *Theory of the Stability of Lyophobic Colloids* (Elsevier, Amsterdam, **1948**).
- (13) Sabín, J., Prieto, G., Ruso, J. M., Hidalgo-Álvarez, R., Sarmiento, F. *Eur. Phys. J E*. **2006**, *20*, 401-408.
- (14) Marcelja, S., Radic, N., *Chem Phys Lett.* **1972**, *42*, 129
- (15) Dimitrievski, K., Kasemo, B. *Langmuir*, **2009**, *25*, 8865.
- (16) Minic, J., Persuy, M.-A., Godel, E., Aioun, J., Connerton, I., Salesse, R., Pajot-Augy, E. *FEBS Journal*, **2005**, *272*, 524.
- (17) Minic, J., Grosclaude, J., Aioun, J., Persuy, M.-A., Gorojankina, T., Salesse, R., Pajot-Augy, E., Hou, Y., Helali, S., Jaffrezic-Renault, N., Bessueille, F., Errachid, A., Gomila, G., Ruiz, O., Samitier, J. *Biochim. Biophys. Acta*, **2005**, *1724*, 324.
- (18) Filipe, V., Hawe, A., Jiskoot, W. *Pharmaceutical Research*, **2010**, *27*, 796.
- (19) DiMilla, P.A., Folkers, J.P., Biebuyck, H.A., Härter, R., López, G.P., Whitesides, G.M. *J. Am. Chem. Soc.*, **1994**, *116*, 2225.

- (20) Richter, R., Mukhopadhyay, A., Brisson, A. *Biophys. J.*, **2003**, 85, 3035.
- (21) Dimitrievski, K. *Langmuir*, **2010**, 26, 5706.
- (22) Dimitrievski, K., Kasemo, B. *Langmuir*, **2008**, 24, 4077.
- (23) Solon, J., Streicher, P., Richter, R., Brochard-Wyart, F., Bassereau, J. *Proc. Natl. Acad. Sci. U.S.A.*, **2006**, 103, 12382.
- (24) Lee, J. S. H., Barbulovic-Nad, I., Wu, Z., Xuan, X., Li, D., *J. Appl. Phys.*, **2006**, 99, 054905.
- (25) Johnson, C.A., Lenhoff, A.M. *J. Colloid Interface Sci.*, **1996**, 179, 587.
- (26) Adamczyk, Z. *J. Colloid Interface Sci.*, **2000**, 229, 477.
- (27) Rivetti, C., Guthold, M., Bustamante, C. *J. Mol. Biol.*, **1996**, 264, 919.
- (28) Calonder, C., Van Tassel, P.R. *Langmuir*, **2001**, 17, 4392.
- (29) Green, R.J., Davies, J., Davies, M.C., Roberts, C.J., Tendler, S.J. B. *Biomaterials*, **1997**, 18, 405.
- (30) Reimhult, E., Hook, F., Kasemo, B. *Langmuir*, **2003**, 19, 1681.
- (31) Lang, D., Coates, P. *J. Mol. Biol.*, **1968**, 36, 137
- (32) Hilbert, D.B., Gooding, J.J., Erokhin, P. *Langmuir*, **2002**, 18, 1770
- (33) Minic Vidic, J., Grosclaude, J., Persuy, M.-A., Aioun, J., Salesse, R., Pajot-Augy, E. *Lab Chip*, **2006**, 6, 1026
- (34) Sabín, J., Prieto, G., Messina, P.V., Ruso, J.M., Hidalgo-Álvarez, R., Sarmiento, F. *Langmuir*, **2005**, 21, 10968
- (35) E Carrion, F.J., Maza, A.D., Parra, J.L., *J. Colloid Interface Sci.* **1994**, 164, 78.
- (36) F McLaughlin, A., Eng, W.K., Vaio, G., Wilson, T., McLaughlin, S. *J. Membr. Biol.* **1983**, 76, 183.
- (37) G Liu, D.-Z., Chen, W.-Y., Tasi, L.-M., Yang, S.-P. *Colloids Surf. A* **2000**, 172, 57.
- (38) Choi, S.H., Lee, J.W., Sim, S.J. *Biosens. Bioelectron.*, **2005**, 21, 378
- (39) Guedri, H., Durrieu, C. *Microchim. Acta*, **2008**, 163, 179
- (40) Tidwell, C.D., Ertel, S.I., Ratner, B.D., Tarasevich, B.J., Atre, S., Allara, D.L. *Langmuir*, **1997**, 13, 3404
- (41) Chen, H., Heng, C.K., Puiu, P.D., Zhou, X.D., Lee, A.C., Lim, T.M., Tan, S.N. *Anal. Chim. Acta*, **2005**, 554, 52
- (42) Calò, A., Sanmartí-Espinal, M., Iavicoli, P., Persuy, M.-A., Pajot-Augy, E., Gomila, G., Samitier, J. *Soft Matter*, **2012**, 8, 46, 11632 – 11643.
- (43) Johnson, S.R., Evans, S.D., Brydson, R. *Langmuir*, **1998**, 14, 6639

- (44) Jans, K., Bonroy, K., De Palma, R., Reekmans, G., Jans, H., Laureyn, W., Smet, M., Borghs, G., Maes, G. *Langmuir*, **2008**, *24*, 3949
- (45) Noh, J., Kato, H.S., Kawai, M., Hara, M. *J. Phys. Chem. B*, **2006**, *110*, 2793
- (46) Perdew, J.P., Burke, K., Ernzerhof, M. *Phys. Rev. Lett.*, **1996**, *77*, 3865
- (47) Cavalleri, O., Gonella, G., Terreni, S., Vignolo, M., Pelori, P., Floreano, L., Morgante, A., Canepa, M., Rolandi, R. *J. Phys.: Condens. Matter*, **2004**, *16*, S2477
- (48) Gonella, G., Terreni, S., Cvetko, D., Cossaro, A., Mattera, L., Cavalleri, O., Rolandi, R., Morgante, A., Floreano, L., Canepa, M. *J. Phys. Chem. B*, **2005**, *109*, 18003
- (49) Lin, W.-C., Lee, S.-H., Karakachian, M., Yu, B.-Y., Chen, Y.-Y., Lin, Y.-C., Kuo, C.-H., Shyue, J.-J. *Phys. Chem. Chem. Phys.*, **2009**, *11*, 6199
- (50) Arima, Y., Iwata, H. *Biomaterials*, **2007**, *28*, 3074
- (51) Tonazzini, I., Bystrenova, E., Chelli, B., Greco, P., Stoliar, P., Calò, A., Lazar, A., Borgatti, F., D'Angelo, P., Martini, C., Biscarini, F. *Biophys. J.*, **2010**, *98*, 2804
- (52) Sethuraman, A., Han, M., Kane, R.S., Belfort, G. *Langmuir*, **2004**, *20*, 7779
- (53) Dufrière, Y.F., Marchal, T.G., Rouxhet, P.G. *Langmuir*, **1999**, *15*, 2871
- (54) Richter, R.P., Bérat, R., Brisson, A.R. *Langmuir*, **2006**, *22*, 3497
- (55) Cha, T., Guo, A., Zhu, X.-Y. *Biophys. J.*, **2006**, *90*, 1270
- (56) Vidic, J., Pla-Roca, M., Grosclaude, J., Persuy, M.-A., Monnerie, R., Caballero, D., Errachid, A., Hou, Y., Jaffrezic-Renault, N., Salesse, R., Pajot-Augy, E., Samitier, J. *Anal. Chem.*, **2007**, *79*, 3280-3290
- (57) Sackmann, E. *Science*, **1996**, *271*, 43
- (58) Das, A., Zhao, J., Schatz, G.C., Sligar, S.G., Van Duyne, R.P. *Anal. Chem.*, **2009**, *81*, 3754
- (59) Jung, H., Robison, A.D., Cremer, P.S. *J. Struct. Biol.*, **2009**, *168*, 90
- (60) Moraes Nicola, A., Frases, S., Casadevall, A. *Eukaryot. Cell*. **2009**, *8*, 9, 1373-1380.

Chapter 4. Functionality assessment of olfactory receptors in natural nanovesicles.



Natural nanovesicles from *Saccharomyces Cerevisiae* (nanovesicles, NV), of ~ 100 nm diameter, carrying the human OR1740 or the chimpanzee OR7D4 olfactory receptor (OR) tagged with the c-myc epitope at their N-terminus are in this **Chapter** presented as model systems for the development of high throughput screening devices that can recognize selectively odorant molecules. Surface Plasmon Resonance (SPR) measurements on L1 Biacore chips indicate that the receptors are functional. We found that the SPR response vs. odorants is approximately linear, exhibiting a high sensitivity in the micromolar range (0.5-1.8RU/ μ M). The selectivity of OR1740 carrying NS towards helional and of OR7D4 carrying NS towards androstenone was proved in cross-check experiments with unspecific odorant molecules (i.e. respectively, heptanal and pentadecalactone) and control receptors. Our results point to improve the odorant sensing capabilities in SPR devices by expressing receptor proteins by using them embedded into membrane fractions from a cell source that means in their natural membrane environment.

4.1 Background

GPCRs, unlike the channel proteins (or ion channels), do not transmit ions following conformational changes in response to ligand binding. Thus, the sensors used for GPCR binding needs to be sensitive enough to detect another event. For example, this event could be the receptor-ligand binding induced protein changes^{1,2,3}. To follow this protein changes a number of techniques have been recently employed for OR biosensors applications. Basically, these techniques relies on label-free assays, which do not need labelling techniques to visualize the odorant-OR binding. In contrast, conventional label-based sensors require a label that could be a fluorophor, a radioisotope or an enzyme that is attached to the molecule to study directly or using a secondary or tertiary recognition element. In these sensors, when the measurement is performed the instrument detect the label and not the target molecule⁴.

In contrast, the main advantage of label-free sensors is that the presence of the target molecule is directly monitored. In consequence, assay development time and cost can be significantly reduced since no additional labelling steps are required. Another important issue to consider is that the molecular binding characteristics are not altered by the presence of any markers^{1,5,6,7}.

The olfactory biosensors utilize similar signal transduction mechanisms than the biological olfactory process to recognize and discriminate distinct odorants, converting the odorant chemical signals into detectable ones, such as electrical and optical ones⁸.

Concerning the electrical ones, when we talk about electrochemical transducers we refer on those that measure a current (amperometric), a potential or change accumulation (potentiometric) or conductive properties of a medium between electrodes (conductometric). In OR-based biosensors, many types of electrochemical sensors and techniques are used for olfactory signal transductions such as microelectrodes⁹, light addressable potentiometric sensors (LAPSs)^{10,11}, field effect transistors (FETs)⁶ and electrochemical impedance spectroscopy (EIS)¹.

Concerning the field effect transistors (FETs) is known as a commonly used semiconductor amplifier. It is a device which enables us to use one electrical signal to control another. The principle of FET is using exterior or interior electric field effect of semiconductor to control the movement of majority carriers in the apparatus. In the FET, current flows along a semiconductor path called the *channel*. At one end of the channel, there is an electrode called the *source*. At the other end of the channel, there is an electrode called the *drain*. The physical diameter of the channel is fixed, but its effective electrical diameter can be varied by the application of a voltage to a control electrode called the *gate*. The conductivity of the FET depends, at any given instant in time, on the electrical diameter of the channel. A small change in gate voltage can cause a large variation in the current from the source to the drain. This is how the FET amplifies signals (Figure 4.1).

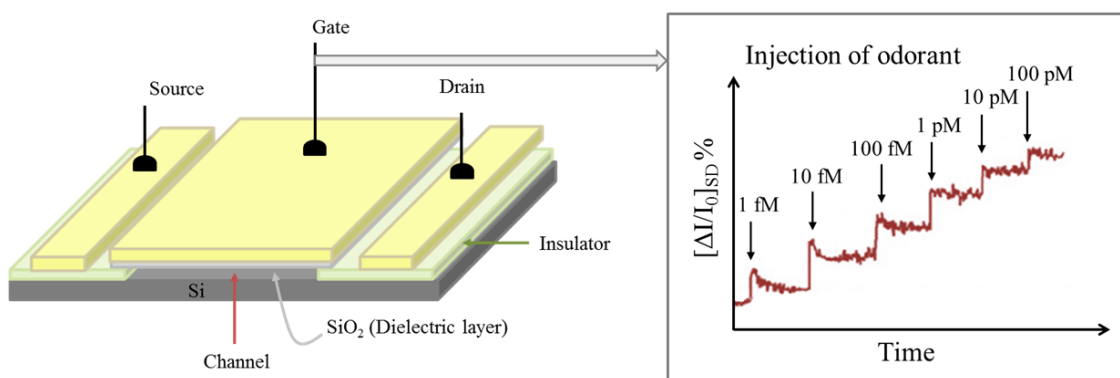


Figure 4.1 Schematic illustration of a Filed Effect Transistor (FET). The device is based on three electrodes: the source, the drain and the gate as a control electrode. A change in gate voltage cause a variation in the current from the source to the drain. Thus, if in the channel are immovilized olfactory receptors, its interaction with their specific odorant cause electrical changes. This electrical changes are monitored in a sensorgram $[\Delta I/I_0]_{SD} \%$ vs. time.

The first study applying FET to a biomimetic olfactory biosensor was in 1991 done by Fromherz et al¹². It was a cell-based biosensor where it was coupled a single neuron to the surface of bare FET (without metal bar), using a microscope and micro glass straw to adsorb cell to the transistor, with a micro glass electrode inserted into the cell in order to stimulate the cell and record the intracellular potential (Figure 4.2A).

More recently, in 2009, Yoon and co-workers⁶, presented for the first time a FET-type bioelectronic nose based on human olfactory receptors conjugated with conducting polymer nanotubes as the transistor channel and sensitive element. The

chemical immobilization that they propose enables the fabrication of the carbon polypyrrol nanotubes FET substrate with excellent electrical properties. The FETs showed the possibility of specific odorant detection down to concentrations as low as tens of femptomols (Figure 4.2B).

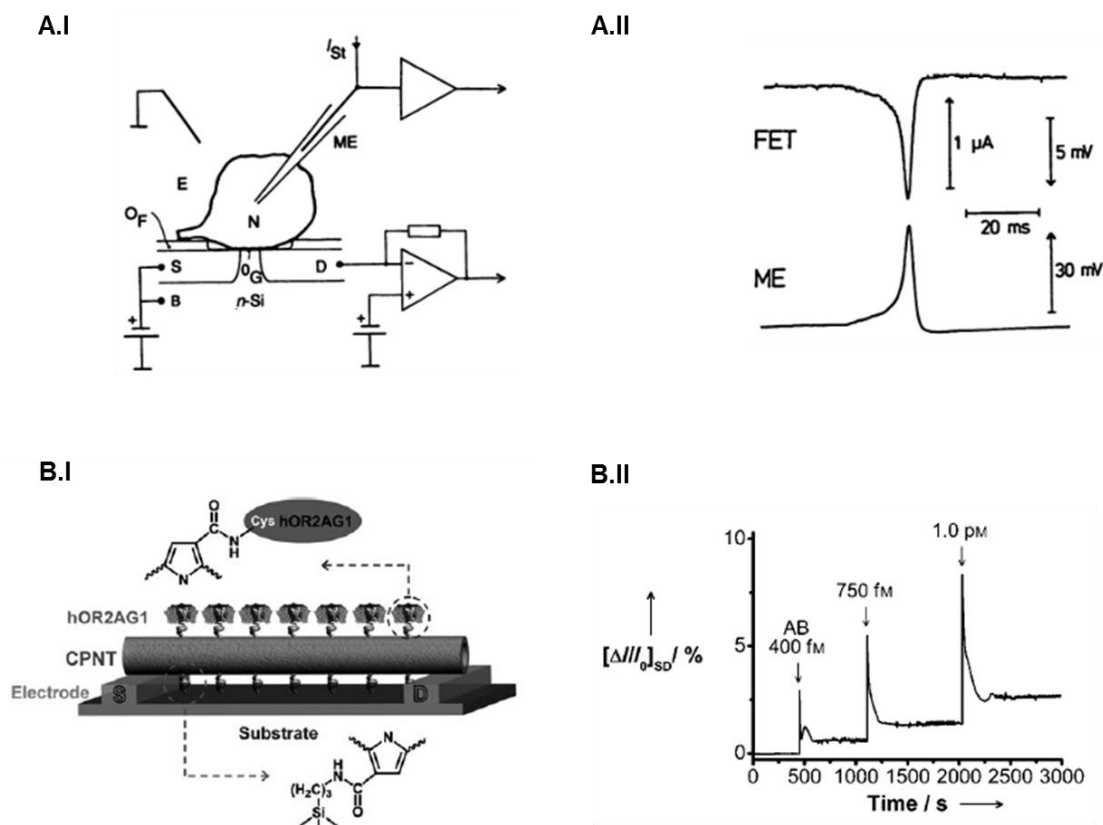


Figure 4.2 (A.I) A neuron (N) is attached to oxidized Si. A thin layer of gate oxide (O_G) covers n-type Si between the source (S) and drain (D) of p-type Si insulate by a thick field oxide (O_F). The electrolyte E is maintained at ground potential (Ag/AgCl electrode). Bulk silicon (B), source, and drain are held at positive bias voltages (p-channel FET). The source-drain current is measured by a current-voltage converter. The neuron is impaled by a microelectrode (ME) (Ag/AgCl). Current (I_{ST}) is injected to stimulate the cell. The membrane potential is measured by a voltage follower. (A.II) Single action potential. The source-drain current I_D of the FET and the membrane potential V_M , as measured by an impaled microelectrode (ME) are shown.¹² (B.I) Schematic illustration of the human olfactory receptor conjugated carbon polypyrrol nanotubes FET platform. Only one nanotube is shown for clarity. Covalent attachments were used to bind the nanotubes on the electrode substrate and to immobilize the receptors. (B.II) Real-time responses of olfactory receptor-carbon nanotubes FET sensors measured at $V_{SD} = 50$ mV. Normalized I_{SD} changes upon addition of target odorant.⁶

In recent studies, label-free electrochemical impedance spectroscopy (EIS) technique has also been used for olfactory biosensing. This technique is applied to the characterization of the electrodes processes as well to the complex interfaces. The technique is non-destructive and is particularly sensitive to small changes in the system.

The electronic properties of a system can be defined in terms of its ability to store and transfer charge (i.e. its capacitance and conductance). EIS studies the system response to the application of a small perturbation applied (periodic small amplitude AC signal). These measurements are carried out at different AC frequencies. The applied AC voltage and the resultant AC current are measured and the impedance is calculated ($Z^* = V / I$). The principle for EIS detection is due to three electrodes: working electrode (WE), reference electrode (RE) and counter electrode (CE). To detect the odorants, usually, the olfactory receptors are immobilized on the surface of the WE. To obtain a response, electrodes are placed in contact with the system of interest and a sinusoidal voltage is applied. This produces sample polarization, the resultant current having the same frequency but different phase and amplitude. Hence, the frequency is the same but the phase is shifted. This phase shift occurs due to the capacitive and the resistive effects that are observed in the electrochemical cell, wherein the electrode-electrolyte interface the electrochemical interface behaves as a capacitor and the solution resistance and electron transfer events (occurring in the electrochemical cell) that offer a resistive effect.

By measuring the complex impedance, Z^* , (i.e. the ratio of the applied voltage to the resultant current) and separating the real and imaginary terms, Z' and Z'' (i.e. conductance and capacitance) may be calculated. These parameters relate to the dielectric measurement of materials giving information on molecular structure and dipole alignment. Analysis of the system response contains information about the interface, its structure and reactions taking place there (Figure 4.3).

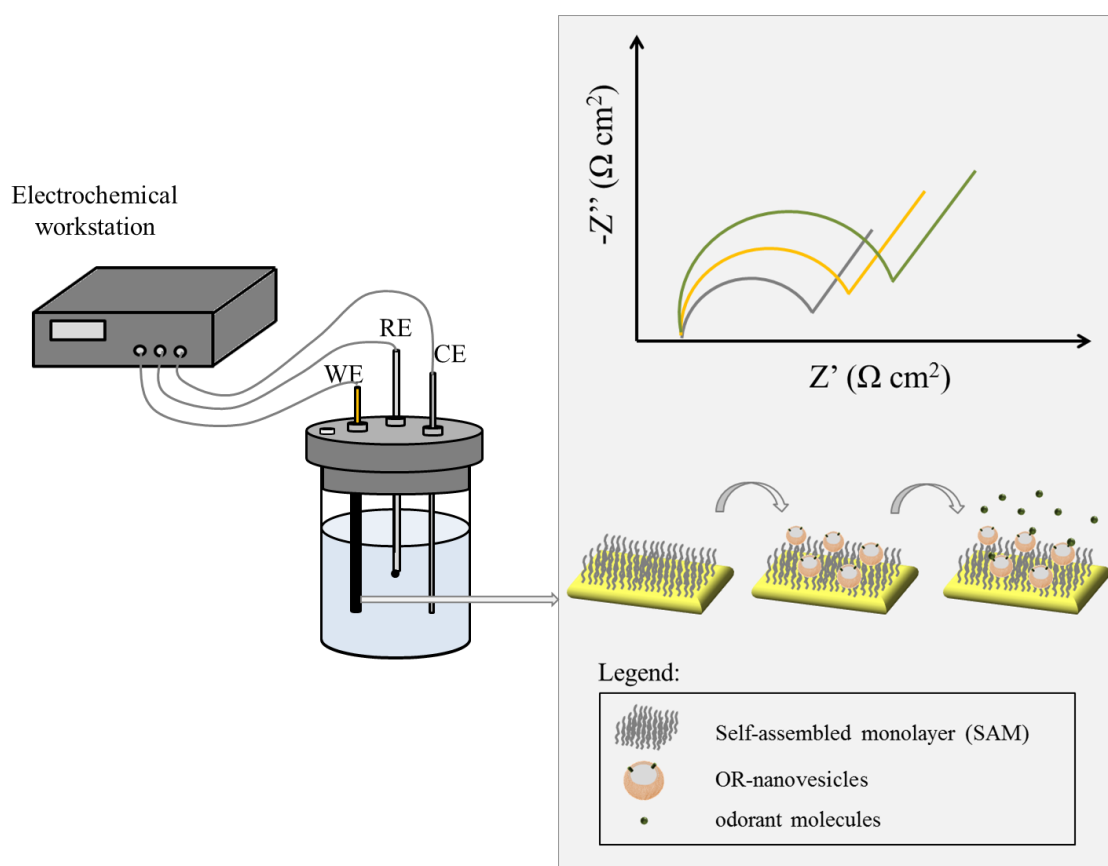


Figure 4.3 Schematic illustration of Electrochemical Impedance spectroscopy (EIS). The EIS cell is based on three electrodes: working electrode (WE), reference electrode (RE) and counter electrode (CE). The sensor surface is functionalized gold (SAM) with target proteins immobilized on it. As the query biomolecule binds to the target protein (i.e. odorant) changes of EIS are reflected. This electrical changes are monitored in a Nyquist plot sensorgram ($-Z''$ vs. Z').

In practice, a steady state in these systems sometimes can be difficult to achieve. The cell can change through adsorption of solution impurities, growth of an oxide layer, build-up of reaction products in solution, coating degradation, or temperature changes, to list just a few factors. Thus, the results achieved using this technique can be due to the odorant-OR binding or due to the changes listed above that take place in the electrical double layer that exists on the interface between the electrode and its surrounding electrolyte.

Electrochemical Impedance Spectroscopy (EIS) has been used to test affinity of a number of odorants to the rat ORI7 receptor immobilized onto the sensor surface in membrane fraction⁷ (Figure 4.4A-B). In 2010, Alfinito et al.² speculate that EIS is able to detect specific protein conformational changes following ligand binding based on their impedance characteristics. When the odorant binds the olfactory receptor differences in the structural conformation of the protein can be reflected by the changes

of EIS. In addition, OR1740 co-expressed with α -subunit of G_{olf} protein in yeast was used as a biorecognition element in the impedimetric biosensor¹³. In that case, in the presence of $GTP\gamma S$ at 4°C, the activation of OR1740 was enhanced with four times higher detection sensitivity (Figure 4.4C-D).

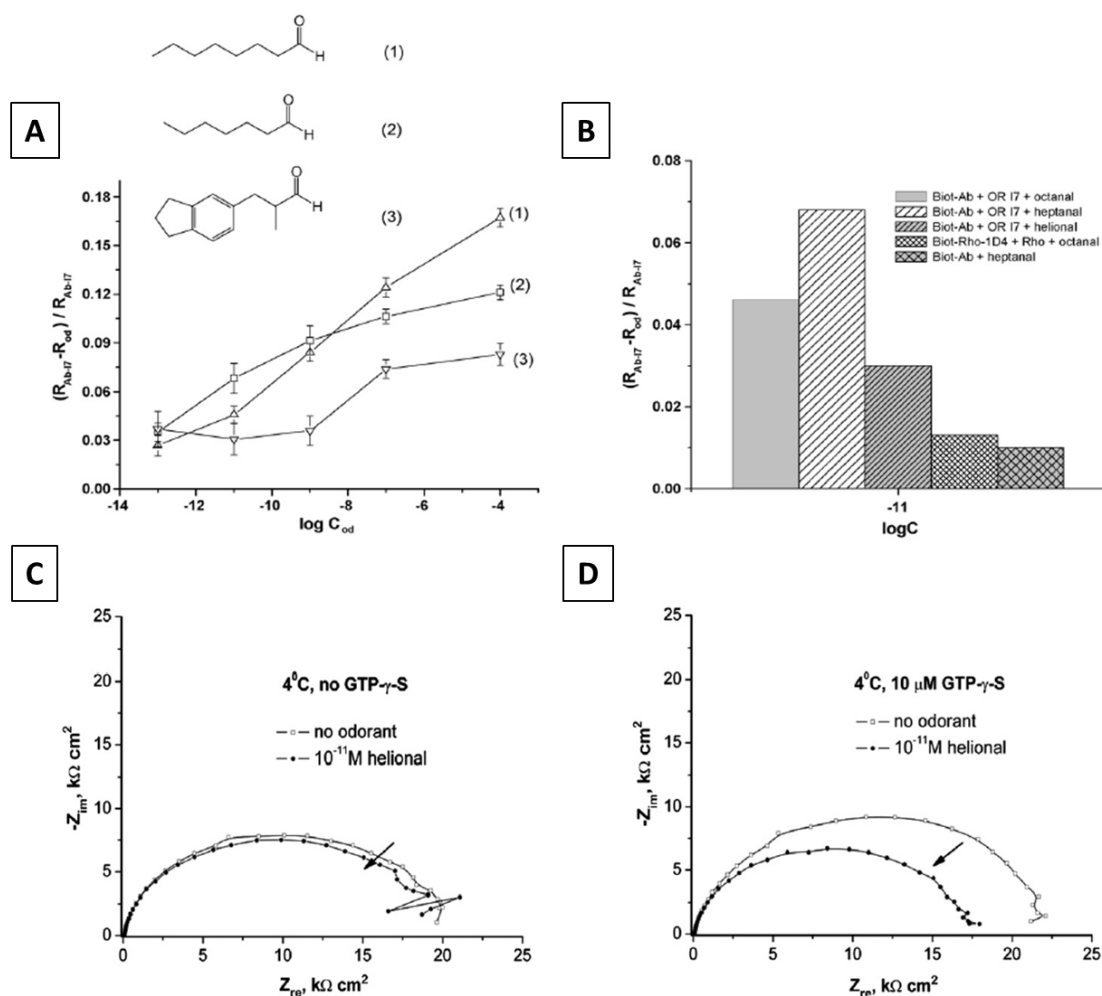


Figure 4.4 (A) Dose-response of rat ORI7 in its membrane fraction to octanal (1), heptanal (2) (both specific) and helional (3) (non-specific odorant). R_{Ab-17} represents the polarization resistance before injection of odorants. R_{od} represents the polarization resistance after injection of specific or non-specific odorant at different concentrations. (B) Response to odorant at 10^{-11} M under different conditions. In that case, R_{od} corresponds to the polarization resistance upon injection of odorants at a concentration of 10^{-11} M⁻¹. (C) and (D) are sensor responses to 10^{-11} M of helional on OR-based biosensor where the OR1740 co-expressed with α -subunit of G_{olf} protein in yeast were immobilized onto the surface. Measurements were conducted at 4°C in the absence (C) or presence (D) of $10 \mu M$ $GTP\gamma S$ in PBS pH 7.0¹³

But, as it has been mentioned above, the correlation between impedimetric changes and OR protein conformational changes due to ligand binding is in our case just a speculation. EIS is a very sensitive technique but its measurements may contain some

errors if the substrate is not blocked properly because this technique is based on a black-box experimental procedure.

As an alternative, optical techniques, label free or not label free, such as SPR or conventional ELISA (*enzyme immunosorbent assay*) respectively¹⁴, have been used to study the odorant-olfactory receptor interaction. From our knowledge, the odorant-olfactory receptor interaction studies due to structural change configuration of the protein expressed in the level of nanoobjects, such as nanovesicles from plasma membrane, is a less common research field. Thus, in this *Chapter* we have attempted to address as well this issue using the well-known conventional optical labelled technique ELISA (enzyme-linked immunosorbent assay).

In addition, optical transduction techniques such as SPR could play an important role in the research of olfaction mechanisms (i.e. intracellular signal transduction pathways and cellular activation events induced by the interaction between odorants and ORs) and the development of biosensor nose.

SPR is a label-free surface sensitive, spectroscopic method which measures change in the thickness or refractive index of biomaterials at the interface between metal surfaces, usually a thin gold film (50–100 nm) coated on a glass slide, and an ambient medium. It is based on the generation of electron charge density waves (plasmons) at the solid (gold) and liquid interface, following evanescent wave generation by polarized light. SPR is a phenomenon that occurs under conditions of total internal reflection and is observed as a decrease or dip in reflected light intensity at a specific angle. In SPR the target proteins are immobilized on a gold-surface, unlabelled query molecule is added, and change in angle of reflection of light (or changes in the wavelength of the plasmon) caused by binding or dissociation of the probe to the immobilized protein is measured to characterize biomolecular interactions in real-time. This technique provides important information about binding affinity and kinetics. The angle at which the minimum intensity of the reflected light is obtained is known as the “SPR angle”, which is directly related to the amount of biomolecules bound to the gold surface. The SPR angle is dependent on the optical characteristics of the system, i.e. on the refractive indices of the media at both sides of the metal, usually gold. While the refractive index at the prism side is not changing, the refractive index in

the immediate vicinity of the metal surface will change when accumulated mass adsorb on it (Figure 4.5). Thus, the use of the SPR technique allows us to obtain a direct measurement of the system to study.

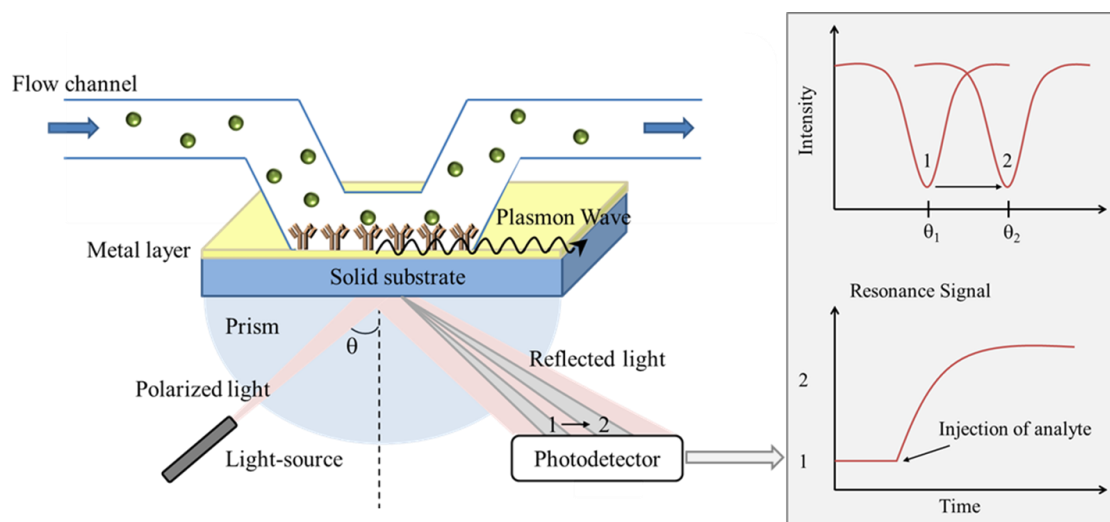


Figure 4.5 Schematic illustration of Surface Plasmon Resonance (SPR). The sensor surface is gold with target proteins immobilized on it. As the query biomolecule binds to the target protein, the refractive index shifts and the SPR-dip moves to larger angles. The movement of the SPR-dip is the actual monitored signal, and the movement over time forms the sensorgram.

Using this technique, it is possible to analyse the amount of bound ligand, the rate of association and the rate of dissociation between biomolecules. This technique has been used to characterize G-protein coupled receptors recently¹⁵⁻¹⁸.

Several well-established commercial tools that are available take advantage of SPR, such as the Biacore system (GE Health). Biacore (www.biacore.com) was the pioneer and is the world leader in monitoring protein interactions using surface plasmon resonance (SPR) technology¹⁹. Most people associate label-free detection with SPR and Biacore instruments. Biacore is an SPR-based label-free technology that is sensitive enough to enable detection to extremely small changes in mass when an odorant binds to the receptor captured on the sensor chip surface. However, while SPR has shown promise in OR biosensors applications, questions remain as to its sensitivity toward small molecules, including a number of volatile/odorant compounds^{7,20-22}.

In 1999, Biacore company launched Biacore® 3000, the most automated, sensitive and flexible research system with a sensitivity of detecting small molecules

down to 180 Da at < 1nM concentration. Later on, in 2005, was launched Biacore T100, a system that was able to do everything that the 3000 did, plus analyse the interaction of lower MW molecules (>100 Da) to high molecular weight proteins (also DNA, RNA, polysaccharides, lipids, cells and viruses), in various samples environments, e.g. in DMSO-containing buffers, plasma and serum.

In 2006, Vidic et al.²⁰ proved the functionality of human OR1740 and rat ORI7 olfactory receptors in natural membrane fractions obtained from yeast cells co-expressed with the heterotrimeric G-protein complex ($G_{\alpha\text{olf}}$ subunit, β and γ) and immobilized them on a BIacore 3000 sensor chips L1, by means of Surface Plasmon Resonance (SPR). The binding of OR-odorants, in that specific case, was followed by SPR by measuring the activation of the trimeric G protein and the consequent dissociation of the $G_{\alpha\text{olf}}$ subunit from the complex in presence of GTP, resulting in a large SPR response. The indirect binding measurement of helional (MW 192.21 Da) and heptanal/octanal (MW 114.19 Da/ 128.21 Da) odorants to OR1740 and ORI7 respectively, was due to the limit of detection of the instrument (>180 Da). They detected a significant SPR signal when the specific odorant together with GTP was injected. On the other hand, when the odorant and GTP were alone and a non-specific odorants together with GTP was used, no SPR signal was observed as a consequence of a missed activation of the ORs. Moreover the sensitivity of the experiment was enhanced by replacing the GTP with its non-hydrolysable analogue, GTP γ S (Figure 4.6). Thus, these natural membrane fractions constitute good candidates to develop a practical biosensing device²³ capable of recognizing and detecting odorant molecules²⁴.

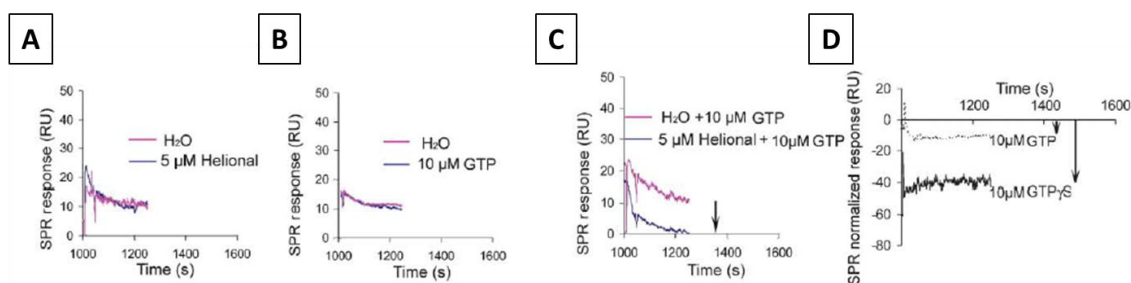


Figure 4.6 Functionality of human OR1740 olfactory receptors in natural membrane fractions obtained from yeast cells co-expressed with the heterotrimeric G-protein complex ($G_{\alpha\text{olf}}$ subunit, β and γ) and immobilized them on a BIacore 3000 sensor chips L1. **(A)** No shift of the SPR signal is observed when nanovesicles are stimulated either with odorant alone, or GTP alone **(B)**, as compared to the control stimulated with water. **(C)** The signal modification is only observed when odorant and GTP are injected at the same time (compared to the control stimulated with water and GTP). **(D)** The signal modification,

due to the release of the $G\alpha$ subunit can be enhanced 4-fold by replacing GTP by GTP γ S (compared to the corresponding control stimulated with water).²⁰

In the literature we found that SPR biosensing technique has been also used in cell-based biosensors measurements of odorants molecules, i.e. HEK-293 cells expressing ORI7²⁵ (Figure 4.7A) and in cell-free systems where SPR was used to show binding of a known ligand undecanal to hOR17-4²¹. (Figure 4.7B).

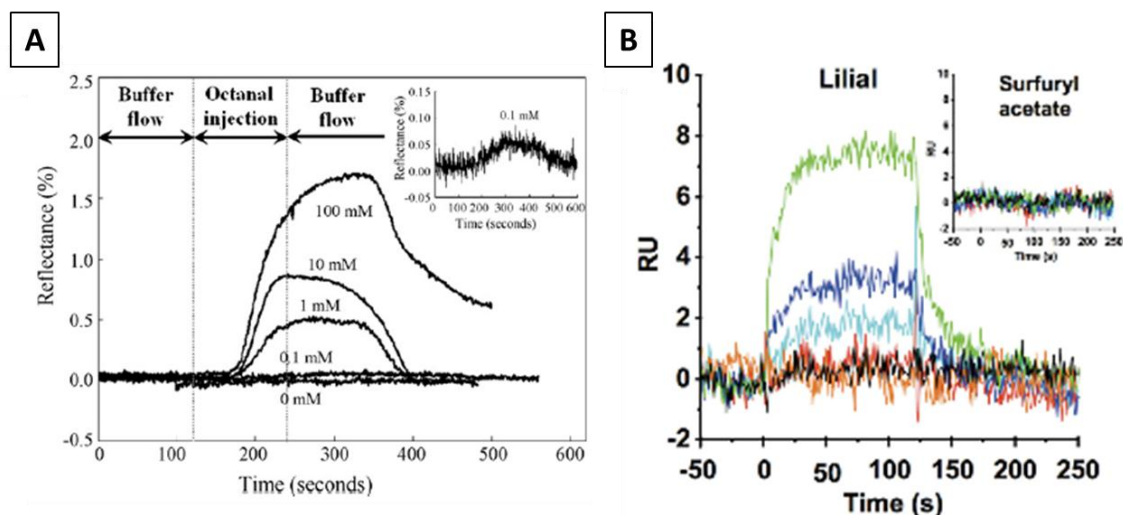


Figure 4.7 (A) HEK-293 cells expressing ORI7 were seeded on the sterilized SPR chip. Dose-dependent curve of the SPR response to different concentrations of octanal (specific odorant). **Inset:** SPR response after injection of 100 μ M octanal²⁵. (B) Testing the binding activity of detergent-solubilized hOR17-4 using SPR. The hOR17-4 was captured on the SPR chip surface via a covalently immobilized rho1D4 monoclonal antibody. The receptor bound the specific odorant lilial in a concentration-dependent manner. Odorant binding curves shown are: blank control (black), 5 μ M (red), 10 μ M (light blue), 20 μ M (dark blue), and 40 μ M (green). **Inset:** No response was seen for the non-binding control odorant sulfuryl acetate²¹.

The use of cells as sensing elements, has been used for the development of a bioelectronic nose as well to measure the interaction between OR and odorants in the cellular level resulting from the signal transduction. Also, the cell-based assays can be used to derive functional information of biologically active analytes. The most common techniques used to perform this odorant binding assays are based on labelled optical methods. These basic optical methods include Ca^{2+} imaging²⁶, cAMP-reporter assay²⁷, fluorescent resonant energy transfer (FRET)²⁸ and bio-luminescence resonant energy transfer (BRET)²⁹. All of them, as well as the SPR technique, allow a more direct measurement of the odorant-olfactory receptor binding.

In this *Chapter*, we developed in a more systematically and controlled way a proof-of-concept of the sensitivity of OR1740-carrying vesicles for helional and of the sensitivity of OR7D4-carrying vesicles for androstenone presented based on Surface Plasmon Resonance (SPR)³⁰ Biacore T100 direct measurements (sensitivity MW >100 Da).

4.2 Materials and Experimental Procedures

4.2.1 Materials

Reagents such as PBS (phosphate buffer saline), CHAPS, dimethyl sulfoxide (DMSO), 4-(2-hydroxyethyl)-1-piperazine-ethanesulfonic acid (HEPES), glycine, azide, bovine serum albumin (BSA), horseradish peroxidase (HRP), (carboxymethyl)hydroxylamine hemihydrochloride 98%, ethylcarbodiimide hydrochloride (EDC), anti-mouse IgG peroxidase (anti-IgG-HRP for ELISA assays), tetramethylbenzidine (TMB), androstenedione, pentadecalactone and heptanal were purchased from Sigma-Aldrich Chemie GmbH (Germany). Helional was a generous gift from Givaudan-Roure (Dübendorf, Switzerland), courtesy of B. Schilling. Tris (hydroxymethyl) aminomethane was from Merck (Darmstadt, Germany). NaOH pellets and sodium chloride were obtained from Panreac Química S.A.U. (Barcelona, Spain). Low binding protein filters (diameter = 13 mm; pores size = 0.22 μm) were from Millipore (Temecula, CA). The home-made monoclonal anti-c-myc (Ab894D12_{f7f9}, 1.44 mg mL⁻¹, *Chapter 2*) was produced and purified by Abyntek Biopharma (Bizcaia, Spain). The antigen ³C₂-CH₂CO-OVA (OVA protein linked with 3 c-myc peptides) was synthesized as described in *Chapter 2*. The L1 sensor chips were acquired from GE Healthcare Bio-Sciences AB (Uppsala, Sweden).

4.2.2 Buffers and Solutions

Buffers used were as follows: phosphate-buffered saline (PBS) 10mM at pH 7.5 (always filtered). PBT buffer was 10 mM potassium dihydrogen phosphate/disodium hydrogen phosphate, at pH 7.5 with 0.05% Tween 20. Coating buffer was 50 mM carbonate/bicarbonate at pH 9.6. Citrate buffer was sodium citrate 40 mM solution at pH 5.5. The substrate solution was 0.01% TMB and 0.004% H₂O₂ in citrate buffer. The running buffer used in Biacore experiments was HBSN (25 mM HEPES, 150 mM sodium chloride) with 1% dimethyl sulfoxide (DMSO) at pH 7.4. The CHAPS solution used was 20 mM at pH 7.4.

4.2.3 Equipments/Software

For the sample preparation (nanovesicles) an Ultrasons bath was used (50 kHz Ultrasons, Selecta). The olfactory receptor functionality experiments were performed on a Biacore T100 instrument, GE Healthcare Bio-Sciences AB. The bioconjugates were purified by Hi-Trap desalting columns (Sephadex G-25, 5 mL) purchased from Amersham Bioscience (Uppsala, Sweden) and ÄKTAprime from GE Healthcare Life Sciences. The protein bioconjugates were characterized by MALDI-TOF-MS (matrix assisted laser desorption ionization time-of-flight mass spectrometer from Bruker Biflex III (Bruker, Kalsruhe, Germany) equipped with a laser unit (working conditions were wavelength of 337 nm and the maximum output of 6 mW).

Concerning the software used: All biosensor data processing and analysis (from Biacore T100) was performed using the software Scrubber2 (BioLogic Software).

4.2.4 Nanovesicles solution preparation

Standard protocol (see Chapter 1): Briefly, Human olfactory receptors c-myc-OR1740 (ORL520 in OrDB), rat ORI7-HA (ORL11 in OrDB), chimpanzee c-myc-OR7D4 and somatostatin receptor subtype 2 (SSTR2) were expressed heterologously in different yeast *Saccharomyces cerevisiae* cultures. After, the yeast cells were mechanically disrupted³¹, the cell content was separated and the membrane fractions obtained were divided in aliquots and frozen at $-80\text{ }^{\circ}\text{C}$. Immediately before use, the stock suspension of membrane fractions was diluted to a concentration (expressed as total protein concentration, TPC) of $125\text{ }\mu\text{g mL}^{-1}$ solution in Phosphate Buffered Saline (PBS 1x) 10 mM (pH = 7.4) or PBT and sonicated for 20 min in ice-cold water to homogenize their size. The solution was further diluted in PBS or PBT normally at a total protein concentration (TPC) of $60\text{ }\mu\text{g mL}^{-1}$. This solution was then filtered using a sterile low binding protein filter (diameter = 13 mm; pores size = $0.22\text{ }\mu\text{m}$) and we obtained the nanovesicles. The nanovesicles solutions described in the text were obtained by further dilution to the working concentration.

Biacore T100 assays: The nanovesicle solutions were prepared in PBS following the same protocol at the total protein working concentration of $15\text{ }\mu\text{g mL}^{-1}$.

4.2.5 Odorant-Olfactory Receptor Binding

4.2.5.1 First strategy: indirect competitive ELISA

Microtiter plates were coated with the antigen ($^3\text{C}_2\text{-CH}_2\text{CO-OVA}$, $0.05 \mu\text{g mL}^{-1}$ in coating buffer, $100 \mu\text{L}$ per well) covered with adhesive plate sealers for 4 hours at room temperature. Next, the plates were washed and the nanovesicle solutions (c-myc-OR1740-NV, SSTR2 matrix nanovesicles as control, or just PBT as blank, $45.0 \mu\text{g mL}^{-1}$ in PBT) were added ($50 \mu\text{L}$ per well) followed by the monoclonal antibody Ab894D12_{f7f9} ($1/160000$) dissolved in DMSO, helional or PBT solution ($50.0 \mu\text{M}$, $50 \mu\text{L}$ per well). The mixture was incubated for 30 min at room temperature; the plates were washed again with PBST. Whenever nanovesicles samples or controls were measured, the microplates were sometimes agitated at 600 rpm during the competition step. Other times, the competition step took place 1h and 30 min at room temperature without agitation. Subsequently, a solution of anti-IgG-HRP ($1/6000$ in PBST, $100 \mu\text{L}$ per well) was added and the plates were incubated for 30 min more and washed before adding the substrate solution ($100 \mu\text{L}$ per well). After 30 min at room temperature the enzymatic reaction was stopped by adding $4\text{N H}_2\text{SO}_4$ ($50 \mu\text{L}$ per well) and the absorbances were measured at 450 nm.

The data presented correspond to the average of three well replicates. For more assay optimization details (i.e. antibody concentration, coated antigen concentration, etc.) see *Chapter 2*.

4.2.5.2 Second strategy: sandwich ELISA

i) Direct:

Microtiter plates were coated with the antibody Ab894D12_{f7f9} at serial dilutions ($1/10000 - 1/640000$ and zero in coating buffer, $100 \mu\text{L}$ per well) covered with adhesive plate sealers overnight at 4°C . Next, the plates were washed and the nanovesicle solutions (c-myc-OR1740-NV, or just PBT as blank, $40.0 \mu\text{g mL}^{-1}$ in PBT) were added ($100 \mu\text{L}$ per well). The solutions were incubated for 30 min at room temperature; the plates were washed again with PBST. Whenever nanovesicles samples were incubated, the microplates were agitated at 750 rpm during the incubation time. Then, the helional-bioconjugate synthesized (helional-HRP described below) dissolved in PBST ($1-0.05$

$\mu\text{g mL}^{-1}$, 100 μL per well) was incubated for 30 min at room temperature; the plates were washed again with PBST. Subsequently, the substrate solution was added (100 μL per well). After 30 min at room temperature the enzymatic reaction was stopped by adding 4N H_2SO_4 (50 μL per well) and the absorbances were measured at 450 nm (Figure 4.11).

The data presented correspond to one well. Further experiments should be required in order to have strong conclusions.

ii) Indirect:

Microtiter plates were coated with the helional-BSA bioconjugate (described below) at serial dilutions (1 – 0.016 $\mu\text{g mL}^{-1}$ and zero in coating buffer, 100 μL per well) covered with adhesive plate sealers overnight at 4°C. Next, the plates were washed and the nanovesicle solutions (c-myc-OR1740-NV, or just PBT as blank, 40-0 $\mu\text{g mL}^{-1}$ in PBT) were added (100 μL per well). The solutions were incubated for 30 min at room temperature; the plates were washed again with PBST. Whenever nanovesicles samples were incubated, the microplates were agitated at 750 rpm during the incubation time. Then, the anti-c-myc antibody Ab894D12_{r7f9} at serial dilutions (1/10000 – 1/80000 and zero in PBT, 100 μL per well) was incubated for 30 min at room temperature; the plates were washed again with PBST. Subsequently, a solution of anti-IgG-HRP (1/6000 in PBST, 100 μL per well) was added and the plates were incubated for 30 min more and washed before adding the substrate solution (100 μL per well). After 30 min at room temperature the enzymatic reaction was stopped by adding 4N H_2SO_4 (50 μL per well) and the absorbances were measured at 450 nm (Figure 4.11).

The data presented correspond to one well. Further experiments should be required in order to have strong conclusions.

Synthesis of Helional-Bioconjugates:

Through the crosslinker ((Carboxymethyl)hydroxylamine hemihydrochloride) ($\text{NH}_2\text{OCH}_2\text{CO}$). The helional odorant, an aldehyde, was covalently coupled to BSA and HRP using the (carboxymethyl)hydroxylamine hemihydrochloride ($\text{NH}_2\text{OCH}_2\text{CO}$) crosslinker in a *One pot* reaction. The biomolecules (10 mg for BSA and 5 mg for HRP) were dissolved in PBS (1.8 mL). A solution of the crosslinker (3.5 mg, 25 μmol , for BSA; and 1.7 mg, 12.5 μmol for HRP) in PBS (100 μL) was added slowly to each

solution of the biomolecules. Secondly, a solution of the coupling reagent ethylcarbodiimide hydrochloride (EDC) (9.8 mg, 50 μmol , for BSA; and 4.9 mg, 25 μmol for HRP) in PBS (100 μL) was also added slowly to each solution of the biomolecules. The reaction mixture was stirred overnight at room temperature. Next, the bioconjugates were purified by size-exclusion gel filtration chromatography with degassed PBS (pH 6.8) and characterized by MALDI-TOF-MS (see Table 4.1). Subsequently, solutions of the helional odorant (62.5 μmol , 10.35 μL for BSA and 31.25 μmol , 5.18 μL for HRP) in DMF anhydrous (200 μL) were added slowly over the activated biomolecules and the reaction mixture was stirred for 5 hours at room temperature. Finally, the helional-bioconjugates were purified by dialysis (regenerated cellulose tubular membranes, nominal MWCO: 12000-14000) with H₂O MilliQ, lyophilized and characterized by MALDI-TOF-MS (see Table 4.1).

4.2.6 Olfactory receptor functionality

Studies were performed at 25°C using Biacore T100 and L1 sensor chips preconditioned with three pulses of CHAPS during 1 min each at 15 $\mu\text{l min}^{-1}$ and three pulses of Isopropanol:NaOH 50mM (2:3) during 1 min each at 15 $\mu\text{l min}^{-1}$. All solutions were filtered before use.

4.2.6.1 Odorant solubilisation

The odorants solutions were prepared in a fume hood to avoid contamination by the pure odorant and the air. A stock solution of helional or heptanal at 10^{-1} M in DMSO was prepared. From the stock solution the subsequently odorant working concentrations (1, 2, 3, 5, or 10 μM) were prepared maintaining the 1% of DMSO. For androstenone and pentacalactone a stock solution at 10^{-2} M in DMSO was prepared and subsequently odorant working concentrations (1, 5, 10 μM) were prepared maintaining exactly the 1% of DMSO. The blank solutions were prepared in the exact way as the odorant solution, replacing the odorant by water.

4.2.6.2 Nanovesicles capture

Nanovesicles were injected onto L1 sensor chips at $5 \mu\text{L min}^{-1}$ for 30 minutes to achieve capture levels of about 1000 resonance units (RU). A short pulse (1-3 minutes) of 5mM NaOH was injected on the deposited nanovesicles to get rid of potential multilayers. BSA (0.1 mg mL^{-1} in PBS) was flown afterwards at $5 \mu\text{L min}^{-1}$ for 5 minutes to block the sensor chip surface from unspecific odorant adsorption, see Figure 4.14. The odorant binding assessment at different concentrations was performed on non-regenerated nanovesicles surface.

4.2.6.3 Odorant analysis

Three start-ups with running buffer solution (HBSN with 1% DMSO) were done in order to stabilize the chip and then different concentration (1, 2, 3, 5 or 10 μM) of odorants were injected (from the lowest concentration to the highest as well as randomly) during 3 minutes at a flow rate of $60 \mu\text{l/min}$. The dissociation phase was followed for 15 minutes.

4.2.6.4 Data processing and analysis

A double reference was used to analyse the responses³² (Figure 4.15): for c-myc-OR1740 a reference channel (functionalized with SSTR2 nanovesicles or c-myc-OR7D4) and the blank. Signals from both references were subtracted to the one obtained from the injection of helional (or heptanal respectively). For c-myc-OR7D4 a reference channel (functionalized with c-myc-OR1740) and the blank were used. Signals from both references were subtracted to the one obtained from the injection of androstenone (or pentadecalactone respectively). The limit of detection (LOD) was estimated as the concentration corresponding to the signal of the blank, i.e. that coming from flowing the running buffer through the captured nanovesicles, plus three times its standard deviation. The assay sensitivity was determined as the slope of the linear fitting representing all the data points as RU/odorant concentration, μM .

The total number of experiments performed for each odorant concentration was 7 (OR1740-NS vs. helional, control NV: SSTR2-NV), 4 (OR1740-NV vs. helional, control NV: OR7D4) and 20 (OR7D4-NV vs. androstenone, control NV: OR1740-NV).

The percentage of experiments that follow the trend reported in Figure 4.19 and Figure 4.20B is respectively 76%, 75% and 35%.

4.3 Results and Discussion

4.3.1 Study of helional/OR1740-nanovesicles binding by ELISA

We proposed a strategy to verify the binding activity of the olfactory receptors towards odorants once integrated in nanovesicles. We based our experimental setup using the ELISA technique. The first strategy used was an Indirect competitive ELISA studying the binding activity between helional and the OR1740 embedded in the nanovesicles. The idea was to follow the odorant-receptor binding through the c-myc tag covalently attached to the N-terminus of the receptor. Thanks to the production of a monoclonal anti-c-myc antibody with a detectability in the picomolar range (*Chapter 2*) we expected to see absorbance signal differences when the antibody recognize the c-myc-OR1740 with or without the helional attached. Our hypothesis was that this absorbance changes could be due to the olfactory receptor configuration change (with or without the odorant) that could directly affect the electronic cloud of the c-myc tag. Therefore, different interaction between the anti-c-myc antibody and the c-myc tag would take place.

First, we studied if it exist any matrix effect due to the odorant solution (DMSO and helional). As can be observed in Figure 4.8B no solvent matrix effect was obtained when we compare the absorbance signal from the interaction between anti-c-myc and c-myc tag (coating antigen) in PBT and helional or DMSO solutions, the values do not seem to be significantly different. As well, it can be notice that no absorbances differences exist between solvent concentrations at the working range.

After, it was as well evaluate the matrix effect that the odorant solution (helional or DMSO) could have on the yeast cell membrane of the nanovesicles, unspecific interactions. Thus, control nanovesicles (carrying the SSTR2 receptor) were used. Figure 4.9B shows the matrix effect due to the nanovesicles sample resulting in an absorbance decrease when the number of nanovesicles increase (as well the TPC increases). For more nanovesicles matrix effect details see *Chapter 2*. Otherwise, no significantly differences exist between the helional and DMSO solutions at the concentrations working range.

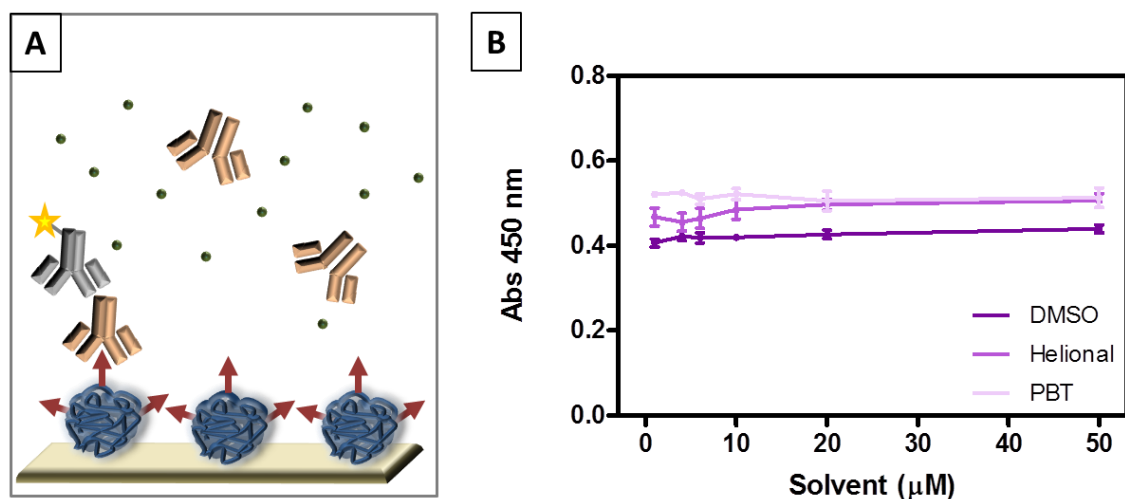


Figure 4.8 (A) Scheme of an Indirect ELISA to evaluate the solvent effect (DMSO, helional) compared to PBT. (B) Absorbance signal (matrix effect) obtained from the anti-c-myc and the coating antigen interaction produced in the presence of solvent (DMSO, helional) in the medium.

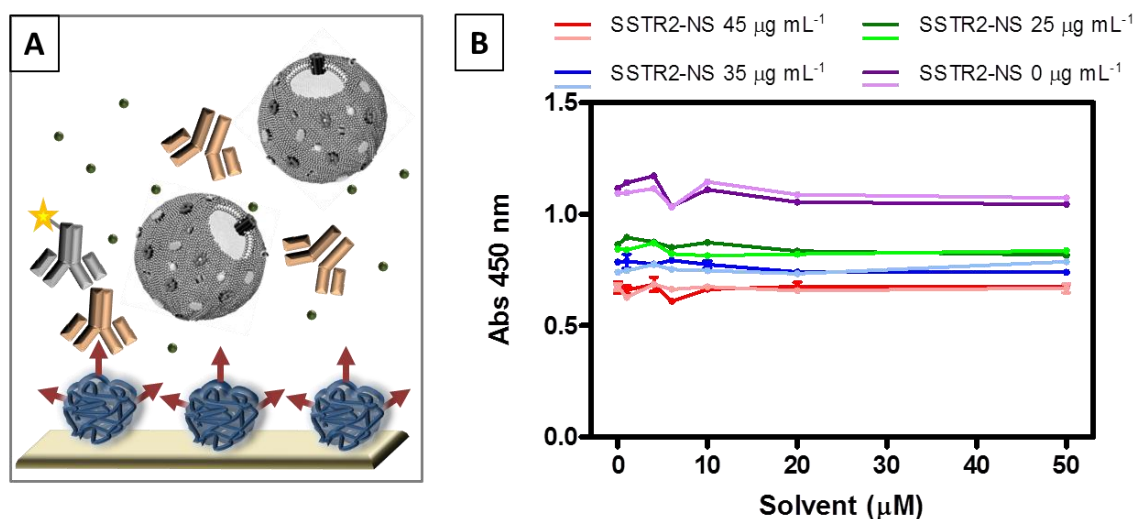


Figure 4.9 (A) Scheme of an Indirect competitive ELISA to evaluate the solvent effect (DMSO, helional) in a control nanovesicles solution (SSTR2-nanovesicles). (B) Absorbance signal (matrix effect) obtained from the anti-c-myc and the coating antigen interaction produced in the presence of solvent: DMSO (lighter colors) or helional (darker colors) at different concentration of SSTR2-nanovesicles solutions (TPC = 0-45 $\mu\text{g mL}^{-1}$).

Finally, we checked if absorbances differences in c-myc-OR1740-NS solutions exist adding helional or DMSO in the competitive step. We expected a big difference due to the specific interaction of the helional with the OR1740. Otherwise, in Figure 4.10B we show how these differences were not achieved.

Thus, we decided to apply a second strategy based on the Sandwich ELISA methodology (Figure 4.10A).

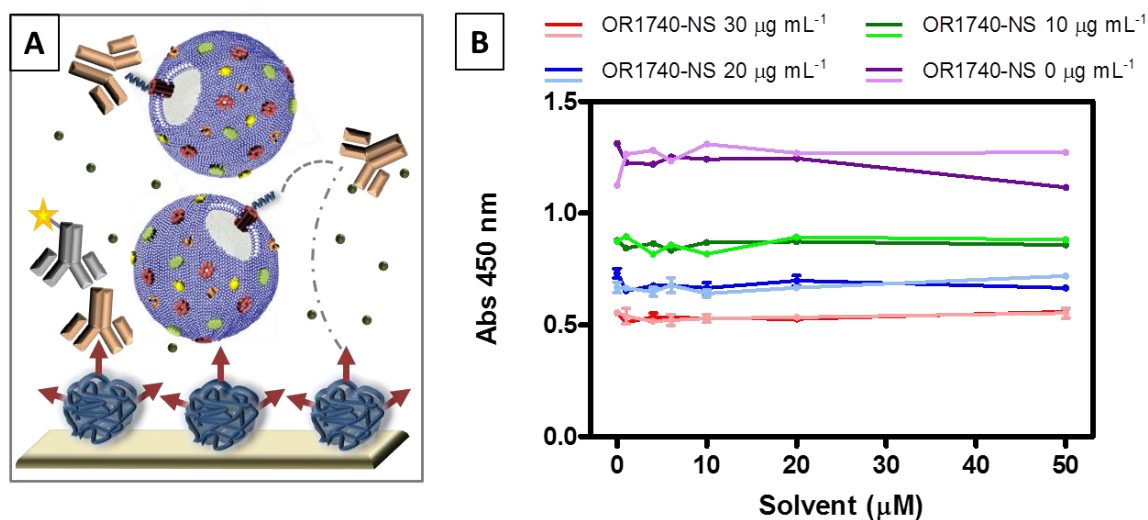


Figure 4.10 (A) Scheme of an Indirect competitive ELISA to study the specific binding between odorant and olfactory receptor (helical-OR1740-NS) through the c-myc tag. (B) Absorbance signal obtained in the presence of solvent: DMSO (control, lighter colors) or helional (specific odorant, darker colors) at different concentration of c-myc-OR1740-nanovesicles solutions (TPC = 0-30 $\mu\text{g mL}^{-1}$).

The idea was to immobilized our nanovesicles in a sandwich format using two different interaction: the specific interaction between the helical and the OR1740 and the interaction between the c-myc peptide (covalently attached to the OR1740) with the anti-c-myc antibody. In this second strategy we assumed that we had at least two OR1740 per nanovesicles. We worked with two formats, direct and indirect sandwich ELISA using the helional-HRP-bioconjugate as analyte and helional-BSA-bioconjugate as coating antigen, respectively (Figure 4.11).

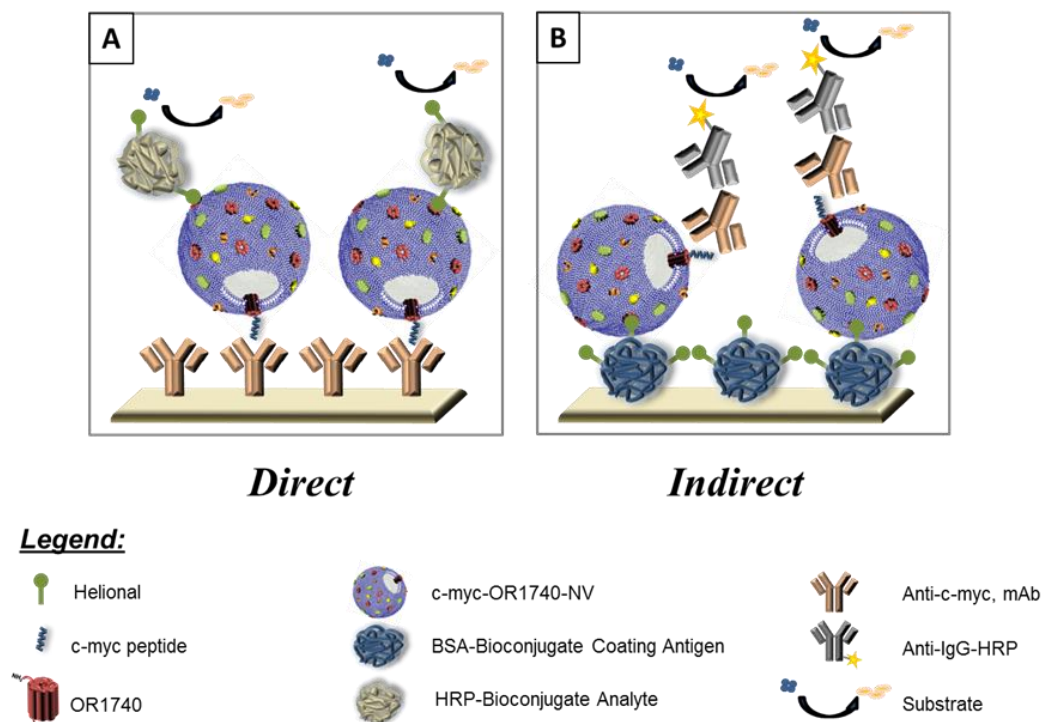


Figure 4.11 Scheme of a Sandwich ELISA to study the specific binding between odorant and olfactory receptor (helional-OR1740-NV) through a direct (**A**) and indirect (**B**) configuration.

With the aim to study the specific interaction between the helional odorant and the olfactory receptor (OR1740) two helional related haptens (helional bearing a terminal aldehyde group for conjugation) were synthesized. The odorant was coupled to macrobiomolecules (BSA and HRP)³³ at a specific molar ratio and using the cross-linker (Carboxymethyl)hydroxylamine hemihydrochloride ($\text{NH}_2\text{OCH}_2\text{CO}$) (Table 4.1).

It is reported that BSA is a protein, with the number of ~ 35 Lysines residues on the surface that could potentially be used from conjugation³⁴, usually employed to prepare bioconjugates for immunoassay. On the other hand, HRP enzyme, due to its property to produce coloured derivative of a labelled molecule when incubated with a proper substrate, was in this case selected because allowed us to study the helional-OR1740 interaction by a direct Sandwich ELISA format. The number of Lys residues available for bioconjugation in the case of HRP is ~ 1 ³⁵. MALDI-TOF-MS was used to characterize most of the bioconjugates in order to determine the helional:protein ratio (Table 4.1).

Table 4.1 Crosslinker/bioconjugate and Haptens/Bioconjugate. Characterization by MALDI-TOF-MS

	(Carboxymethyl)hydroxylamine hemihydrochloride (NH ₂ OCH ₂ CO)		Helional odorant	
	(4.8 : 1) (Y:X)	(50 : 1) (Y:X)	(2.5 : 4.8 : 1) (Z:Y:X)	(2.5: 50 : 1) (Z:Y:X)
BSA	47 ± 1*	--	3 ± 2	--
HRP	--	3 ± 1*	--	1 ± 1

The bioconjugates were synthesized at a specific molecular ratio (Z:Y:X) where X is the number of equivalents of Lysines (accessible lysines of the biomolecule), Y is the number of equivalents of crosslinker used and Z is the number of equivalents of the hapten (helional odorant).

(*),The number of crosslinker per bioconjugate cannot be well determined. It could exist a secondary reaction with the coupling agent (EDC) and the protein –COOH groups.

(--) Bioconjugates were not synthesized.

We noticed that the number of crosslinker:bioconjugate obtained after their MALDI-TOF-MS characterization exceeded the number of accessible Lys for each bioconjugate. Our explanation on that was that maybe a secondary reaction with the coupling agent (EDC) and the protein –COOH groups could take place without control. We did not control that parameter; further experiments may be required in order to have a more pure intermediate bioconjugate.

Figure 4.12 shows the results of the direct sandwich ELISA obtained with the helional-HRP-bioconjugate. No significantly absorbances signal changes were observed varying the coating antibody, the helional-HRP analyte or the c-myc-OR1740-nanovesicles concentrations. These results suggested us that the interaction between the odorant and its specific receptor cannot be observed by this ELISA format. Due to that, we decided to amplify the absorbance signal using the indirect ELISA format.

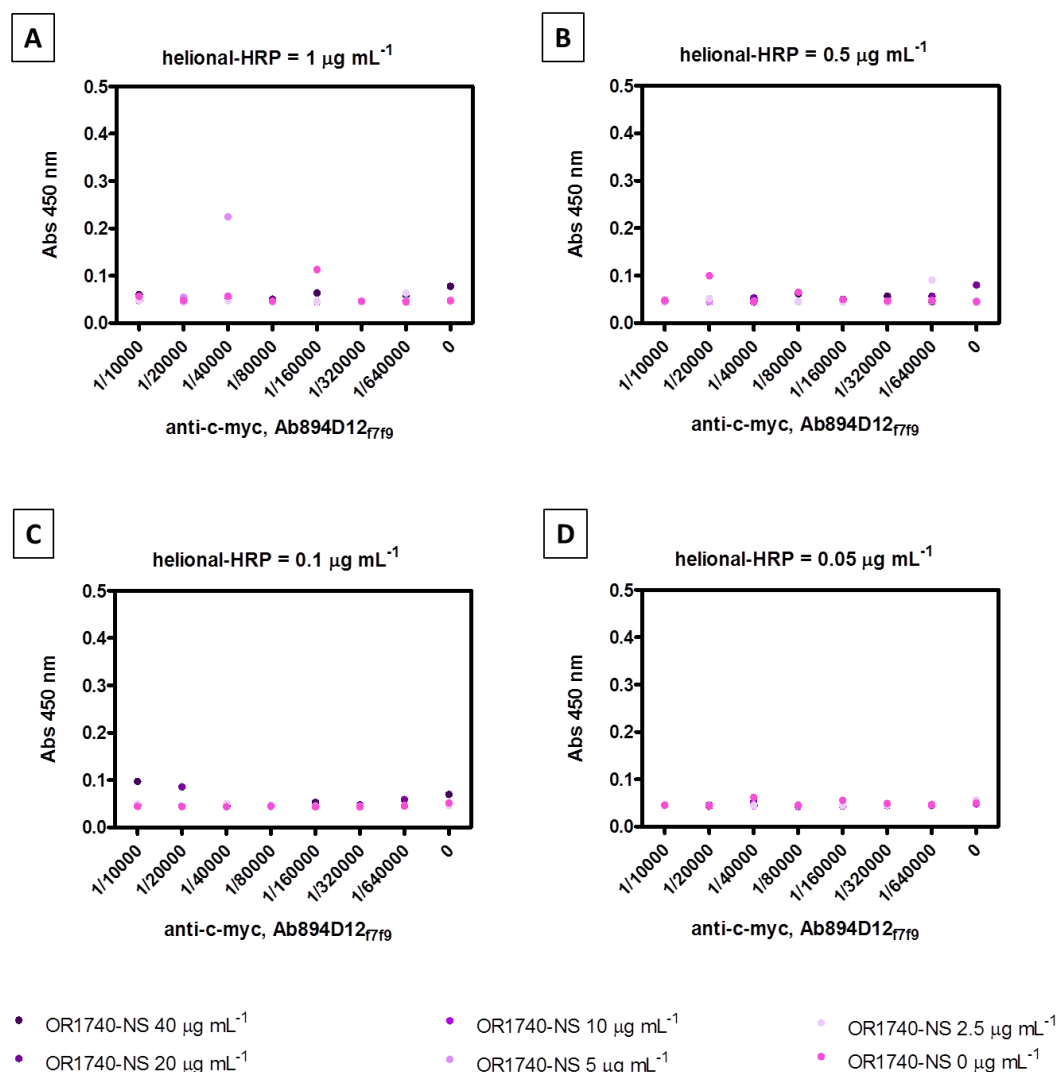


Figure 4.12 Absorbance signal obtained at different anti-c-myc coating antibody concentration (1/10000-1/640000) and different helional-HRP bioconjugate analyte (1-0.05 $\mu\text{g mL}^{-1}$) with and without the presence of c-myc-OR1740-nanovesicles solutions (TPC = 0-40 $\mu\text{g mL}^{-1}$).

The results obtained using the indirect ELISA format were reported in Figure 4.13. No significantly absorbances signal changes were observed varying the helional-BSA coating antigen, the anti-c-myc or the c-myc-OR1740-nanovesicles concentrations. These results suggested us that the interaction between the odorant and its specific receptor neither can be observed by this ELISA format at the working conditions defined. Further optimization experiments maybe required to see significantly absorbance changes due to the specific odorant-olfactory receptor interactions. In our group we are still interested to follow the research in this field.

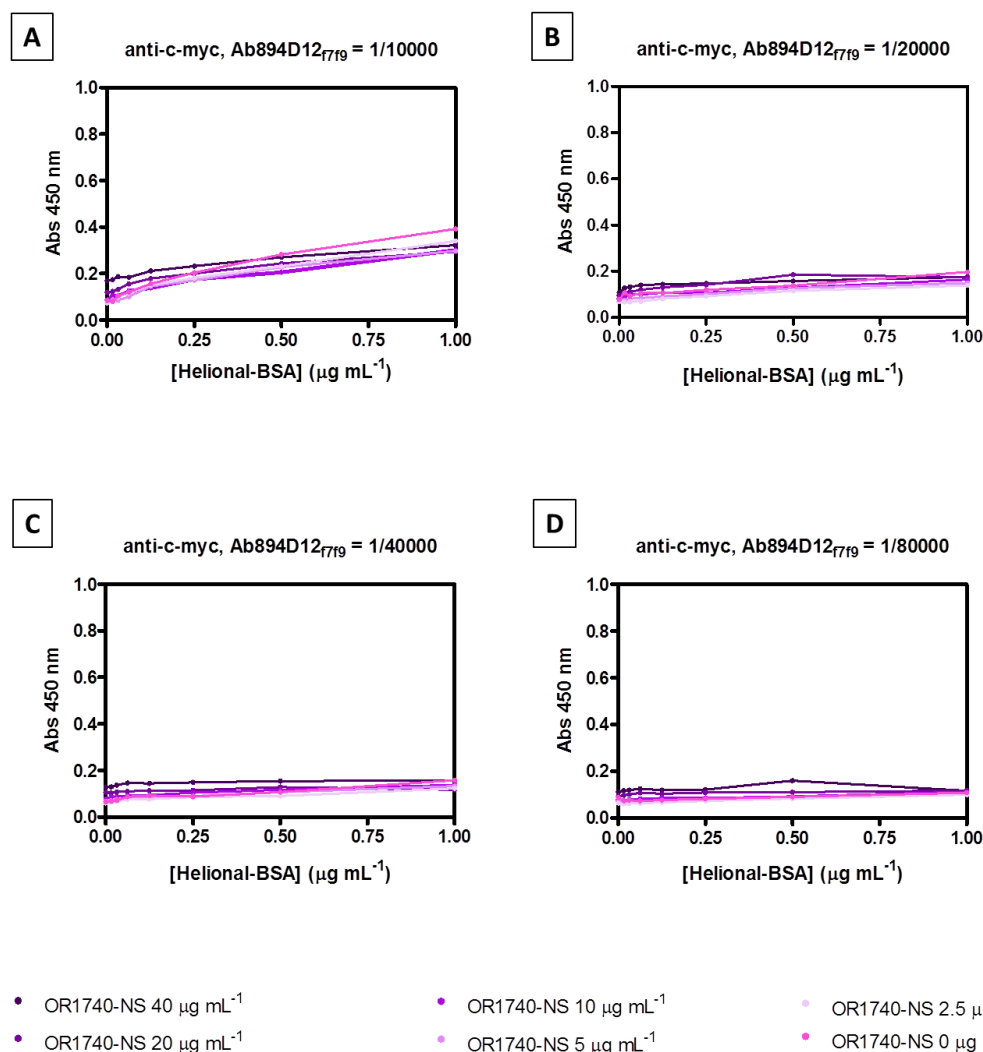


Figure 4.13 Absorbance signal obtained at different helional-BSA coating antigen concentration ($1\text{-}0\ \mu\text{g mL}^{-1}$) and different anti-c-myc concentrations ($1/10000\text{-}1/80000$) with and without the presence of c-myc-OR1740-nanovesicles solutions (TPC = $0\text{-}40\ \mu\text{g mL}^{-1}$).

4.3.2 Assessment of OR1740 and OR7D4 functionality by Surface Plasmon Resonance (SPR)

In order to verify the binding activity of the olfactory receptors towards odorants once integrated in nanovesicles, we developed a SPR based assay that uses double-reference analysis³². The experiment is described in Figure 4.16 for the case of the assessment of OR1740 response towards odorants. The double reference analysis has been applied for measuring the device response either to the specific odorant helional³⁶ (see Figure 4.16B) or for the unspecific control odorant heptanal (see Figure 4.16D). Nanovesicles (NV or NS) solutions containing the OR1740 and the SSTR2 control

receptors are captured in equivalent amount (capture level ~ 1000 RU, see Experimental Section, Figure 4.14) in two channels of the device (Figure 4.16A).

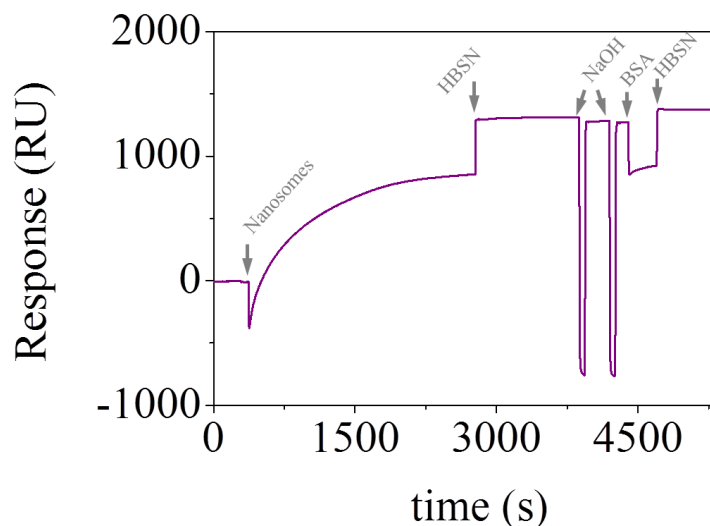


Figure 4.14 Typical Biacore sensorgram profile for NV carrying in this case OR1740 receptor (concentration = $15 \mu\text{g mL}^{-1}$, $t = 1800$ s) and BSA ($t = 300$ s) immobilization onto a L1 chip. Analogous profiles were obtained for NV carrying SSTR2 receptor and NV carrying OR7D4 receptor.

Then a solution of helional at different concentrations (2, 3, 5 μM) is flown across the SPR channels (see Figure 4.16B). The signal coming from the OR1740-NV is subtracted from that coming from SSTR2-NV (reference channel). These two signals in turn are obtained by first subtracting the signals that the two nanovesicles independently give when loaded with the running buffer that does not contain odorant molecules, i. e. when the helional concentration is zero (blank, Buffer) (see Experimental Section and Figure 4.15).

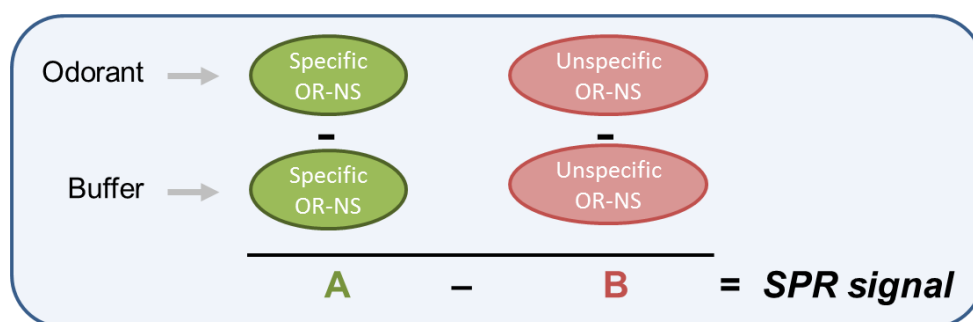


Figure 4.15 Scheme representing the SPR signal obtained by the SPR based assay presented that uses double-reference analysis.

The same procedure is repeated for the control odorant heptanal (Figure 4.16C and D). The two odorants solutions were flown sequentially on the same chip, in order to avoid measurement dispersion due to heterogeneities among different Biacore chips. The same experiment was performed with OR7D4-NV to assess its functionality against androstenone³⁷ using OR1740-NV as control NV and pentadecalactone as unspecific control odorant.

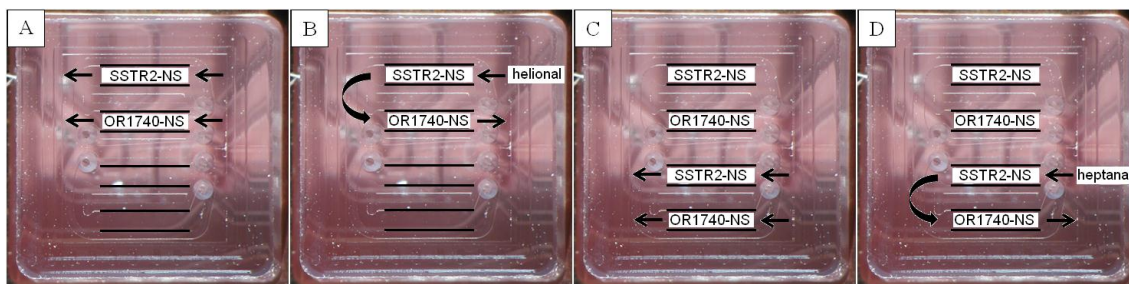


Figure 4.16 (A) Optical images of the Biacore T100 flow cell. In the SPR assay a solution of nanovesicles and control nanovesicles is flown in two different channels. (B) Then three helional solutions at different concentrations are sequentially flown across the cell. Again a solution of nanovesicles and control nanovesicles is flown in the two remaining channels (C) and control heptanal solutions sequentially flown through the cell (D).

Nanovesicles were immobilized on the surface of a L1 Biacore chip whose matrix contains lipophilic groups covalently attached to carboxymethylated dextran (Figure 4.17).

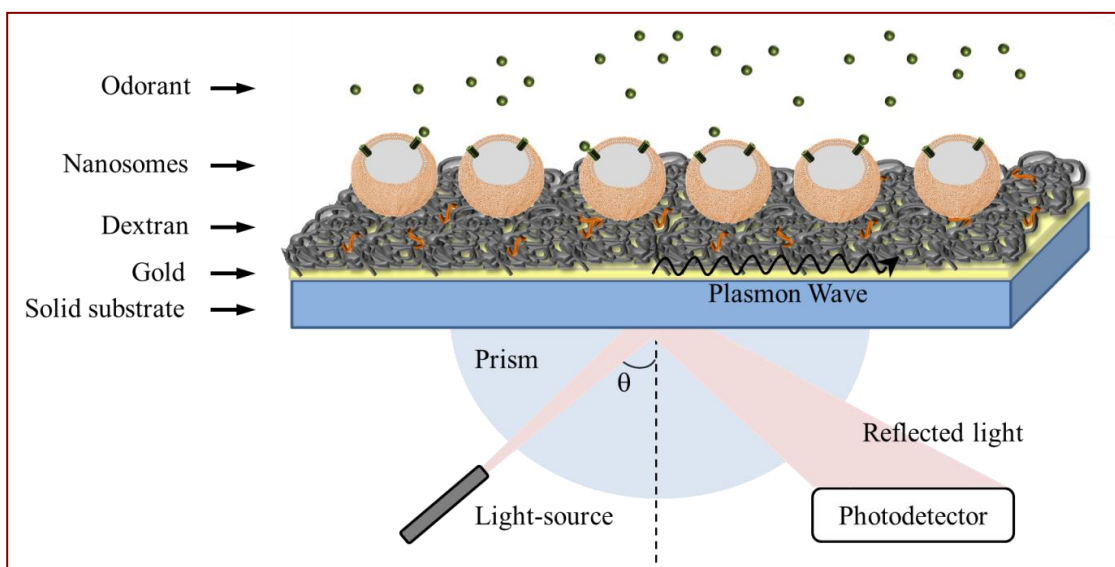


Figure 4.17 Schematic drawing of the SPR setup showing the L1 sensor chip with the immobilized nanovesicles (also called nanosomes).

This sensor chip was chosen for its high capacity for direct attachment of lipid vesicles and its stability over time. After attachment, the lipid bilayer structure is retained and this fact facilitates the study of interactions involving transmembrane receptors in a native-like environment.

In Figure 4.18 the signal coming from the OR1740-NV (4.18A) and from the OR7D4-NV (4.18B) after the double subtraction respectively vs. helional and androstenone is reported. Figure 4.18A shows the mass-based refractive index change vs. time due to the application of helional at three different concentrations (2, 3, 5 μM). No change in the RU signal is observed when applying the unspecific odorant heptanal (see the inset of Figure 4.18A). Figure 4.18B shows the mass-based refractive index change vs. time due to the application of androstenone at three different concentrations (1, 5, 10 μM). Our results show that both the ORs carrying NV responds to the corresponding specific odorant in a concentration-dependent manner exhibiting selectivity towards the different odorant molecules. For the case of OR7D4-NV we found a similar behaviour vs. the pentadecalactone control odorant (inset Figure 4.18B) as the one reported in the inset of Figure 4.18A. To assess that the choice of the control NV does not affect significantly the SPR measurement, we performed the assessment of OR1740-NV functionality vs. helional also with the OR7D4-NV control (see Figure 4.20A).

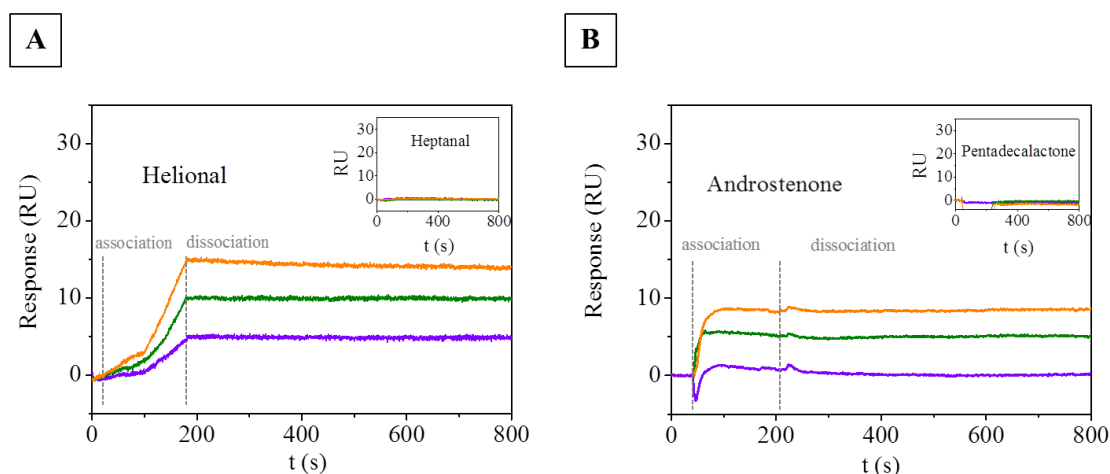


Figure 4.18 (A) Double-subtracted SPR sensorgrams obtained flowing solutions of helional at 2 μM (data in violet), 3 μM (data in green) and 5 μM (data in orange) onto a L1 chip (flow rate: $60\mu\text{L min}^{-1}$). The association phase was followed for 180 s and the dissociation phase was followed for 800 s. Inset: Corresponding sensorgrams obtained flowing on the same chip heptanal solutions at the same concentrations. (B) Double-subtracted SPR sensorgrams obtained flowing solutions of androstenone at 1

μM (data in violet), 5 μM (data in green) and 10 μM (data in orange) onto a L1 chip (flow rate: 60 $\mu\text{L}/\text{min}$).

It has to be observed that the working concentration in SPR measurements with odorant molecules is limited for very low odorant concentrations, due to the odorants low molecular weight that results in a low surface plasmon resonance, close to the detection limit of the SPR equipment. Furthermore, in the case of OR7D4-NV, the functionality assessment by SPR is also critical for high androstenone concentrations (> 20 μM) due to the limited odorant solubility in the running buffer. This fact, together with the highly non-ideal behaviour of the SPR response upon odorant injection renders critical the determination of the equilibrium dissociation constant. Indeed deviations from ideality have been found in all our measurements, that do not always reach the steady state during the association time (see the association part of Figure 1.18A) and that exhibit very slow, or no dissociation process at all, after running buffer injection (see the dissociation part of Figure 4.18A and 1.18B).

In Figure 4.19 we report the evolution of the SPR signal corresponding to the dissociation part of the SPR curves, vs. the odorant concentration. The minimum odorant concentration that we detect with this method is 0.3 μM helional and 0.9 μM androstenone (see Experimental Section). The linear fits in Figure 4.19 give a sensitivity of 1.8 $\text{RU}/\mu\text{M}$ for helional and 0.6 $\text{RU}/\mu\text{M}$ for androstenone, Table 4.2.

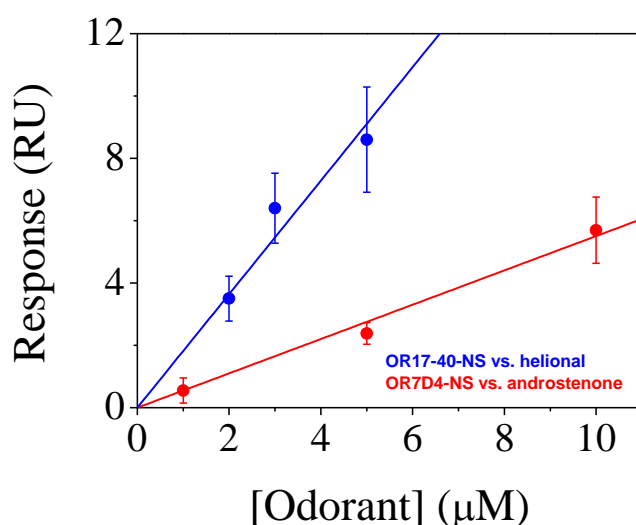


Figure 4.19 SPR response of OR1740-NV vs. helional concentration (data in blue) and of OR7D4-NV vs. androstenone concentration (data in red). The corresponding linear fits give: $y = 1.82 \cdot x$ (blue line) and $y = 0.55 \cdot x$ (red line).

Table 4.2 Functionality SPR based assay features.

	OR1740-NV vs. helional		OR7D4-NV vs. androstenone
<i>Control NV</i>	SSTR2-NV	OR7D4-NV	OR1740-NV
<i>L.O.D.</i>	0.3 μM	0.4 μM	1.1 μM
<i>Sensitivity</i>	1.8 RU/ μM	1.2 RU/ μM	0.5 RU/ μM
<i>n</i>	7	4	20
<i>Reproducibility</i>	76%	75%	35%

The corresponding linear fit for the curve SPR signal vs. odorant concentration performed with OR1740-NV using OR7D4-NV as control nanovesicles gives a limit of detection of 0.4 μM helional and a sensitivity of 1.2 RU/ μM (Figure 4.20B and Table 4.2).

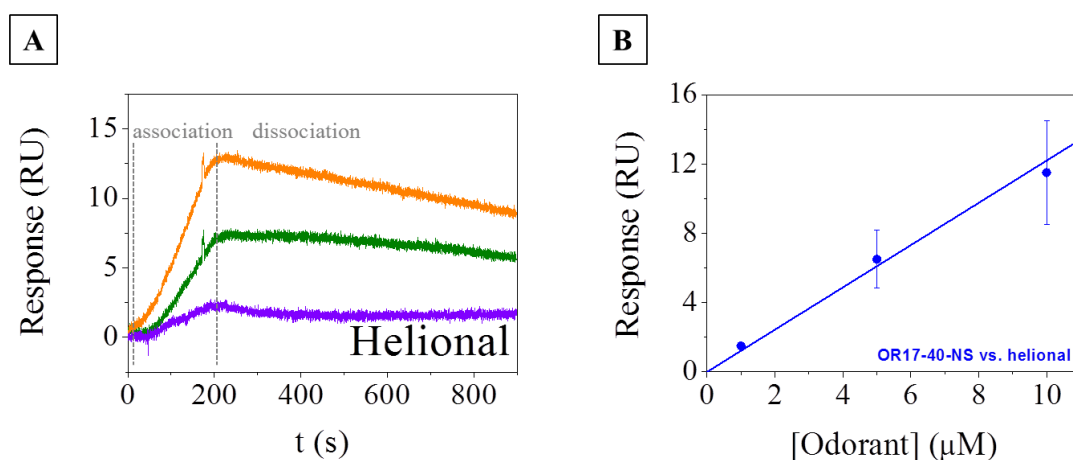


Figure 4.20 (A) Double-subtracted SPR sensorgrams obtained flowing solutions of helional at 1 μM (data in violet), 5 μM (data in green) and 10 μM (data in orange) onto a L1 chip (flow rate: $60\mu\text{L min}^{-1}$). (B) SPR response of OR1740-NV vs. helional concentration (data in blue). The corresponding linear fits give: $y = 1.21 \cdot x$ (blue line).

This suggests that effectively the choice of the control NV (also called NS) does not affect the calibration parameters of the SPR signal vs. concentration curve. The 2-3 times higher sensitivity of OR1740-NV towards helional compared to that of OR7D4-NV towards androstenone could suggest a qualitative higher affinity constant of the OR1740 receptor for its specific odorant, considering that other parameters affecting the

SPR signal evolution vs. concentration (NV deposited mass, odorant molecular weight, number of OR/NV) can be considered constant during the experiment.

Our results indicate that the ORs retain their binding capacity when embedded in nanovesicles. It has to be noticed that the curvature of the association part for OR1740 in Figure 4.20A is highly not-ideal and this fact suggests complex association kinetics³⁸. Furthermore, the association profile suggests a slow association rate constant k_a between OR1740 and helional. In the case of OR7D4-NV, the association profile suggests a faster association constant rate (k_a), because within the same association time a steady state is reached. The dissociation phase for both ORs-NV, in contrast, does not show any curvature. This unexpected behavior²¹ is not an effect of the use of the double reference method for analysing the data and seems to indicate strong stability of the protein-ligand complex *in vitro*. Indeed, Lee et al.²⁵ found a fast dissociation rate in experiments performed with human embryonic kidney (HEK)-293 cells expressing olfactory receptors, a fact that could be explained with the presence in this case of all the biological cell machinery that guarantees the reversible binding of odorants to receptors. Further experiments would be required to fully characterize the association and dissociation profiles to reach a comprehensive characterization of the binding kinetics.

4.4 Conclusions

In order to develop biomimetic noses based on olfactory receptors one strategy consists in expressing the receptor proteins at the surface of natural cells that constitute the source for nanovesicles production. This strategy keeps the receptors surrounded by a natural membrane made up of a lipid bilayer, the natural environment for keeping these proteins functional and structurally stable. This together with recent studies showing the capture of GPCRs onto biosensor surfaces and demonstrating a maintained receptor activity into natural membranes, opens definitively the possibility for the development of practical biosensor devices based on GPCRs membrane receptors.

When olfactory receptors are genetically expressed in closed vesicles from natural yeast membrane fractions (nanovesicles) the verification of their capability for capturing specific odorant molecules are critical for the design of artificial noses. In this **Chapter** we address this issue systematically. By SPR technique we proved that the expressed receptors (OR1740 and OR7D4) are functional towards the specific helional and androstenone odorants respectively. Despite the fact that the expression of olfactory receptors in nanovesicles is low, a fact that is coherent with the general expression level of GPCRs proteins in cells, the integration in nanovesicles together with a careful choice of the SPR experimental conditions and data analysis allowed us to obtain a concentration-dependent SPR response vs. odorant concentration with a sensitivity of 0.5-1.8RU/ μ M. These results constitute a proof-of-concept that ORs embedded in nanovesicles properly respond to odorants and definitely open the perspective to use the surface plasmon resonance technique for the detection of small odorants at concentration in the micromolar range.

4.5 References

- (1) Hou, Y. et al. *Biosens Bioelectron*, **2007**, *22*, 1550.
- (2) Alfinito, E., Millithaler, J.-F., Pennetta, C., Reggiani, L. *Microelectronics Journal* **2010**, *41*, 718-722.
- (3) Alfinito, E., Penneta, C., Reggiani, L. *Sensors and Actuators B* **2010**, *146*, 554-558.
- (4) Dacres, H., Wang, J., Leitch, V., Horne, I., Anderson, A.R., Trowell, S.C. *Biosens and Bioelectron* **2011**, *29*, 119-124.
- (5) Kim, T.H., Lee, S.H., Lee, J., Song, S.H., Oh, E.H., Park, T.H. *Adv. Mater.* **2009**, *21*, 91-94.
- (6) Yoon, H., Lee, S.H., Kwon, O.S., Song, H.S., Oh, E.H., Park, T.H., Jang, J. *Angew. Chem. Int. Ed.* **2009**, *48*, 2755-2758.
- (7) Vidic, J., Pla-Roca, M., Grosclaude, J., Persuy, M.-A., Monnerie, R., Caballero, D., Errachid, A., Hou, Y., Jaffrezic-Renaould, N., Salesse, R., Pajou-Augy, E., Samitier, J. *Anal. Chem.* **2007**, *79*, 3280-3290.
- (8) Du, L., Wu, C., Liu, Q., Huang, L., Wang, P. *Biosens Bioelectron*, **2013**, *42*, 570-580.
- (9) Marrakchi, M., Vidic, J., Jaffrezic-Renault, N., Martelet, C., Pajot-Augy, E. *Eur Biophys J*, **2007**, *36*, 1015.
- (10) Liu, Q., Cai, H., Xu, Y., Li, Y., Li, R., Wang, P. *Biosens Bioelectron*, **2006**, *22*, 318.
- (11) Wu, C., Chen, P., Yu, H., Liu, Q., Zong, X., Cai, H., Wang, P. *Biosens Bioelectron*, **2009**, *24*, 1498.
- (12) Fromherz, P., Offenhausser, A., Vetter, T., et al. *Science*, **1991**, *252*, 1290—1293.
- (13) Benilova, I., Vidic, V., Pajot-Augy, J., Soldatkin, E., Martelet, A.P., Jaffrezic-Reneaults, C., Mater, N. *Sci Eng C*, **2008**, *28*, 633.
- (14) Zappelli, E., Daniele, S., Abbracchio, M. P., Martini, C., Trincavelli, M. L. *Int. J. Mol. Sci.* **2014**, *15*, 4, 6252-6264.
- (15) Harding, P.J., Hadingham, T.C., McDonnell, J.M., Watts, A. *Eur. Biophys. J.* **2006**, *35*, 709-712.
- (16) Stenlund, P., Babcock, G.J., Sodroski, J., Myszka, D.G. *Anal. Biochem.* **2003**, *316*, 243-250.
- (17) Bieri, C., Ernst, O.P., Heyse, S., Hofmann, K.P., Vogel, H. *Nat. Biotech.* **1999**, *17*, 1105-1108.

- (18) Komolov, K.E., Senin, I., Philippov, P.P., Koch, K.W. *Anal. Chem.* **2006**, *78*, 1228-1234.
- (19) Rich, R.L. et al. *Anal. Biochem.* **2009**, *386*, 194–216.
- (20) Minic Vidic, J., Grosclaude, J., Persuy, M.-A., Aioun, J., Salesse, R., Pajot-Augy, E. *Lab Chip*, **2006**, *6*, 1026.
- (21) Cook, B.L., Steuerwald, D., Kaiser, L., Graveland-Bikker, J., Vanberghem, M., Berke, A.P., Herlihy, K., Pick, H., Vogel, H., Zhang, S. *PNAS*, **2009**, *106*, *29*, 11925–11930.
- (22) Kaiser, L., Graveland-Bikker, J., Steuerwald, D., Vanberghem, M., Herlihy, K., Zhang, Shuguang. *PNAS*, **2008**, *105*, *41*, 15726-15731.
- (23) Bally, M., Bailey, K., Sugihara, K., Grieshaber, D., Vörös, J., Städler, B. *Small*. **2010**, *6*, *22*, 2481-2497.
- (24) Firestein, S. *Nature*, **2001**, *413*, 211.
- (25) Lee, S.H., Ko, H.J., Park, T.H. *Biosens Bioelectron*, **2009**, *25*, 55.
- (26) Spehr, M., Gisselmann, G., Poplawski, Ai et al. *Science* **2003**, *299*, 2054-2058.
- (27) Radhika, V., Proikas-Cezanne, T., Jayaraman, M. et al. *Nat Chem Biol* **2007**, *3*, 325-330.
- (28) German, P.F., van der Poel, S., Carraher, C. et al. *Insect Biochem Mol Biol* **2013**, *43*, 138-145.
- (29) Wade, F., Espagne, A., Persuy, M.A. et al. *J Biol Chem* **2011**, *286*, 15252-15259.
- (30) Piliarik, M., Vaisocherová, H., Homola, J. *Biosens. Bioelectron.* **2005**, *20*, 2104-2110.
- (31) Minic, J., Grosclaude, J., Aioun, J., Persuy, M.-A., Gorjankina, T., Salesse, R., Pajot-Augy, E., Hou, Y., Helali, S., Jaffrezic-Renault, N., Bessueille, F., Errachid, A., Gomila, G., Ruiz, O., Samitier, J. *Biochim. Biophys. Acta*, **2005**, *1724*, 324.
- (32) Myszka, D.G. *J. Mol. Recognit.* **1999**, *12*, 279–284.
- (33) Mombaerts, P., *Nat. Rev. Neurosci.* **2004**, *5*, 263-278.
- (34) Galve, R., Sanchez-Baeza, F., Camps, F., Marco, M.-P. *Anal. Chim. Acta.* **2002**, *452*, 191–206.
- (35) Xie, H., Tkachenko, A.G., Glomm, W.R., Ryan, J.A., Brennaman, M.K., Papanikolas, J.M., Franzen, S., Feldheim, D.L. *Anal. Chem.* **2003**, *75*, 5797-5805.
- (36) McCusker, E. C., Bane, S. E., O'Malley, M. A., Robinson, A. S. *Biotechnol. Prog.* **2007**, *23*, 540-547.

(37) Keller, A., Zhuang, H., Chi, Q., Vosshall, L. B., Matsunami, H. *Nature*. **2007**, *449*, 468-472.

(38) Sigmundsson, K., Beauchemin, N., Lengqvist J., Öbrink, B. *Determination of binding kinetics between proteins with multiple non identical binding Sites by SPR flow Cell biosensor technology*, *Biosensors - Emerging Materials and Applications*, **2011**, Prof. Pier Andrea Serra (Ed.), ISBN: 978-953-307-328-6, InTech.

General Discussion

Natural vesicles with membrane receptors (i.e. G-protein coupled receptor) expressed on it produced by genetic engineering cells are promising building blocks for sensing biodevices. Membrane receptors are involved in a variety of biochemical pathways and therefore constitute important targets for therapy and development of new drugs. For example, G-protein coupled receptors (GPCRs) are present in many sensing processes in cells and their functionality crucially depends on their lipid environment. Bioanalytical platforms and binding assays, using these transmembrane receptors, for drug screening or diagnostic require building well-characterized lipid membrane arrays, acting as supports to prevent protein denaturation during biochip processing. The work presented in this thesis has as main objective the exhaustive study of natural olfactory receptors-nanovesicles properties when are in solution or deposited onto a biosensor support. With this study we contribute directly in the development of biosensing platforms. The controlled production of natural vesicles containing GPCRs, their characterization and their reproducible deposition on surfaces are among the outstanding challenges in the road map to realize practical biomolecular devices based on GPCRs. In addition, quantification of the protein receptors and validity of their functionality in such lipid membrane arrays are key issues in order to produce reproducible and well-characterized chips.

We started from *Saccharomyces Cerevisiae* yeast cell membrane fractions where olfactory receptors (a GPCR subfamily); the human OR1740, the rat ORI7, and the chimpanzee OR7D4; were heterologously expressed. The receptors had covalently attached either in the N-terminus as in the C-terminus of the receptor a peptide tag which does not appear to interfere with the bioactivity or the biodistribution of the recombinant protein¹, in our case the olfactory receptor. These tags allowed us to detect, isolate, and purify the OR as well as to check that the receptor expression had performed successfully. We demonstrated by Western Blot that olfactory receptors were successfully expressed on the yeast cell membrane. We also shown by direct observation with cryo-EM that membrane fractions in solution spontaneously form closed spherical vesicles of size in the range of nm. Furthermore, a simple method based on two steps (sonication plus filtration) to homogenize the size of the nanovesicles to a

diameter of around 100 nm at a concentration of more than 10^{10} nanovesicles mL^{-1} is also presented. It is well-reported that extrusion technique is extensively used in the production of synthetic nanovesicles such as liposomes^{2,3}. However, in our case, an important amount of sample volume was lost during the extrusion process. Thus, the combination of sample sonication and filtration allowed us to obtain nanovesicles in solution without losing large amount of material. The vesicle size was analysed by Dynamic Light Scattering (DLS) and in more detail by Nanoparticle Tracking Analysis (NTA). It is reported that this last technique (NTA) enables a thorough size distribution accurate analysis of monodisperse and polydisperse samples with an improved peak resolution, compared to DLS.^{4,5} In addition, NTA provides an improved detection of smaller vesicles, as the measured size distribution is not dramatically influenced by the presence of a small number of large, highly scattering particles⁶. Furthermore, NTA was used to estimate the nanovesicles concentration in the solution⁷. Such estimation is not possible by DLS, which is a technique that provides relative population values, instead of quantifications of concentration. All the results obtained by DLS and NTA, combined with the TEM observation, suggest that at room temperature nanovesicles do not aggregate⁸, thus indicating that thermal agitation is sufficient to overcome eventual short range (i.e. electrostatic, Van der Waals and hydration) forces acting between individual NV. In the nanovesicles solutions the presence of residuals has been recognized in the Cryo-EM images where a weak background was clearly visible. We relate the observed phenomenon to an uncontrolled presence of biomolecules, i.e. proteins and/or lipid aggregates, which are not organized in vesicles and might be still present in the resulting solution after the sonication and the filtration of the membrane fractions solution. Several techniques were used in order to eliminate this background without any success. We performed calibration curves plotting the concentration of nanovesicles in the solution (parameter obtained by NTA) versus the total protein concentration of the solution (parameter obtained by BCA Assay) and all the calibration curves obtained for each OR-nanovesicle preparation adapted quite well to a linear fit. This suggests us that the uncontrolled presence of biomolecules observed (the residuals present in the nanovesicles solution), which were not organized in vesicles, might be mostly lipids instead of proteins. If this background was proteins, the NTA results obtained (nanovesicles concentration) would be lower than the experimental ones obtained when we would increase the TPC of the solution. Thus, we would lose the linear fit at high TPC range. This suggests us that the total protein of the sample,

particularly the olfactory receptors, is embedded onto the nanovesicles and is not untied from the lipid bilayer. These results are important for the development of a biosensing platform based on the immobilization of lipid vesicles where the membrane receptors are expressed.

In 2010, Nonaka and co-workers⁹ demonstrated for the first time a novel labelling method that allow to elucidate functional modification of cell surface proteins, such as GPCR proteins, by a nonenzymatic reaction between a short peptide tag and a small molecular probe. This methodology allows the GPCR fluorescence visualization in living cells but not their quantification. Later on, in 2011, Serge¹⁰ present the first GPCR quantitative detection of internalization of the cAR1, as GPCR model, in live *D. discoideum* cells. It was then, in 2011¹¹, when finally, the visualization and quantification of integral membrane proteins was carried on nanovesicles instead in the whole live cell. Until then, any protein from the GPCR family had been quantified in nanovesicles. For this reason, in this thesis, we report for the first time a novel immunochemical analytical approach for the quantification of transmembrane proteins (i.e. GPCR) in their natural lipid environment directly in nanovesicles (NVs). The procedure allows direct determination of tagged receptors (i.e. c-myc tag) without any previous protein purification or extraction steps. The proposed approach uses monoclonal antibodies addressed against the c-myc tag, frequently used in protein expression, on a microplate-based competitive ELISA format with high detectability. The decision to use a competitive ELISA format instead a sandwich one was due to the fact of the number of olfactory receptors per nanovesicle. In the case that this number was 1 OR/NV their quantification could not be performed by this format. In that hypothetic case, because the c-myc peptide attached to the OR would be detect for the capture antibody, any other c-myc tag would not be free to be detected by the detection antibody and their quantification would not be performed. Thus, and due to the low molecular weight of the c-myc peptide (10 amino acids) the best strategy to carry on the olfactory receptor quantification was by a competitive ELISA format. However, the main drawbacks of the competitive ELISA format were the matrix effects. Thus, nanovesicles carrying the SSTR2 receptor (7 transmembrane receptor) without the c-myc tag were used as model sample to study and control this effect on our real sample. The immunochemical method quantifies this tag on proteins or bioreceptors embedded in nanovesicles with detectability in the picomolar range, using protein bioconjugates as

reference standards. The necessity to work with a very sensitive assay was because transmembrane protein expression in heterologous systems is often low¹². The high detectability of the assay was thanks to the self-production of a monoclonal anti-c-myc antibody and the ionic strength of the medium assay. The optimum NaCl concentration of the phosphate buffer (PB) medium was 0M. The applicability of the method was demonstrated through the quantitative determination of the expression level of two different c-myc-olfactory receptors (ORs, human c-myc-OR1740 and chimpanzee c-myc-OR7D4) in plasma membrane nanovesicles (NVs) and were quantified as (3 ± 1) OR molecules NV^{-1} and (6 ± 2) OR molecules NV^{-1} , respectively. The olfactory receptors quantify were those that had the c-myc peptide in the N-terminus of the protein; thus, the accessible ones. In order to validate the method, the quantification presented was compared with a standard quantification procedure based on the yeast membrane fraction disruption, the solubilisation and the subsequent purification of the c-myc-tagged expressed proteins.

In addition, we also show by direct observation with Atomic Force Microscopy that nanovesicles deposit and flatten without rupturing on glass and gold substrates following approximately a diffusive law. Such behaviour has been proved to describe the adsorption of a variety of biomolecules (DNA, proteins),¹³⁻¹⁵ intact lipidic vesicles¹⁶ and nanoparticles^{17,18} onto solid supports. We show that on glass surface coverages larger than 20-25% of the substrate can be reproducibly achieved under practical nanovesicle concentrations and reasonable time scales, while keeping to the minimum the presence of background residuals coming from the nanovesicles production process. On the other hand, on functionalized gold substrates surface coverages around 10-15% were achieved. Indeed it has been shown that with polystyrene nanoparticles solutions of similar concentrations and dimensions, the maximum theoretical surface coverage on mica substrate ($\sim 54\%$) under diffusion limited deposition and appropriate solution conditions^{17,18} can be obtained. The surface coverages obtained with natural nanovesicles are quite remarkable as compared to the maximum theoretical value of around 54% corresponding to ideal hard sphere models. Then, the role of surface chemistry was studied showing that modification of gold substrates indicates a higher affinity of natural nanovesicles for acid modified surfaces as compared to amino or alcohol modified surfaces. Thus, substrates showing large negative zeta-potentials^{19,20} and allowing hydrogen bonds²¹ formation are the best candidates to give large surface

coverages with nanovesicles. Finally, nanovesicles deposition in acid modified gold surfaces and glass have been exploited for the generation of an array of multiple nanovesicles. Glass and gold substrates, are representative examples of surfaces for applications in optical and electrical biosensing, respectively.²²⁻²⁴ Thus, present results constitute an important step in the practical realization of biosensor devices based on natural nanovesicles integrating G-protein coupled membrane receptors.

Finally, when olfactory receptors are genetically expressed in closed vesicles from natural yeast membrane fractions the verification of their capability for capturing specific odorant molecules is critical for the design of artificial noses. Thus, we demonstrated by Surface Plasmon Resonance (SPR) measurements on L1 Biacore chips that the receptors were functional. Despite the fact that the expression of olfactory receptors in nanovesicles is low, a fact that is coherent with the general expression level of GPCRs proteins in cells¹², the integration in nanovesicles together with a careful choice of the SPR experimental conditions and data analysis allowed us to obtain a concentration-dependent SPR response vs. odorant concentration with a sensitivity of 0.5-1.8RU/micromolar. The functionality of the expressed receptors (OR1740 and OR7D4) towards their specific odorants, helional and androstenone respectively, was verified in a systematic SPR assay. The selectivity of OR carrying NV towards its specific odorant was proved in cross-check experiments²⁵ with unspecific odorant molecules and control receptors. These results constitute a proof-of-concept that ORs embedded in nanovesicles properly respond to odorants and definitely open the perspective to use the surface plasmon resonance technique for the detection of small odorants at concentration in the micromolar range. Concerning the binding kinetics, it has to be noticed that results obtained with helional-OR1740 binding showed a highly not-ideal profile and this fact suggests complex association kinetics²⁶. Furthermore, the association profile suggests a slow association rate constant k_a between OR1740 and helional. In the case of OR7D4-NV, the association profile suggests a faster association constant rate (k_a), because within the same association time a steady state was reached. The dissociation phase for both ORs-NV, in contrast, does not show any curvature. This unexpected behavior²⁷ was not an effect of the use of the double reference method for analysing the data and seems to indicate strong stability of the protein-ligand complex *in vitro*. Indeed, Lee et al.²⁸ found a fast dissociation rate in experiments performed with human embryonic kidney (HEK)-293 cells expressing olfactory receptors, a fact that

could be explained with the presence in this case of all the biological cell machinery that guarantees the reversible binding of odorants to receptors.

The results presented constitute an important step in the development of biomimetic noses based on olfactory receptors. We worked with a strategy that consisted in expressing the receptor proteins at the surface of natural cells that constitute the source for nanovesicles production. This strategy keeps the receptors surrounded by a natural membrane made up of a lipid bilayer, the natural environment for keeping these proteins functional and structurally stable. These nanovesicles were characterized exhaustively. This, together with the studies showing the capture of OR-nanovesicles onto two different biosensor surfaces (i.e. glass and functionalized gold) and demonstrating a maintained receptor activity into natural membranes, opens definitively the possibility for the development of practical biosensor devices based on GPCRs membrane receptors.

G.1 References

- (1) Li, S., Song, K.S., Lisanti, M.P. *J. Biol. Chem.* **1996**, *271*, 1, 568-573.
- (2) Olson, F., Hunt, C.A., Szoka, F.C., Vail, W.J., Papahadjopoulos, D. *Biochim Biophys Acta – Biomembranes* **1979**, *557*, 1, 9-23.
- (3) Samad, A., Sultana, Y., Aqil, M. *Curr. Drug Delivery* **2007**, *4*, 4, 297-305.
- (4) Filipe, V., Hawe, A., Jiskoot, W. *Pharmaceutical Research*, **2010**, *27*, 796.
- (5) Dragovic, R.A., Gardiner, C., Brooks, A.S., Tannetta, D.S., Ferguson, D.J.P., Hole, P., Carr, B., Redman, C.W.G., Harris, A. L., Dobson, P.J., Harrison, P., Sargent, I.L. *Nanomed. Nanotechnol. Biol. Med.*, **2011**, *7*, 780.
- (6) Van Der Pol, E., Hoekstra, A.G., Sturk, A., Otto, C., Van Leeuwen, T.G., Nieuwland, R. *J. Thromb. Haemost.*, **2010**, *8*, 2596.
- (7) Sokolovaa, V., Ludwigb, A.-K., Hornungb, S., Rotana, O., Hornb, P.A., Epplea, M., Giebelb, B. *Colloids Surf. B*, **2011**, *87*, 146.
- (8) Sabín, J., Prieto, G., Ruso, J.M., Hidalgo-Álvarez, R., Sarmiento, F. *Eur. Phys. J. E*. **2006**, *20*, 401-408.
- (9) Nonaka, H., Fujishima, S., Uchinomiya, S., Ojida, A., Hamachi, I. *J. Am. Chem. Soc.* **2010**, *132*, 27, 9301–9309.
- (10) Sergé, A., de Keijzer, S., Van Hemert, F., Hickman, M. R., Hereld, D., Spaink, H. P., Schmidt, T., Snaar-Jagalska, B. E. *Integr Biol.* **2011**, *3*, 6, 675-683.
- (11) Mutch, S.A., Kensel-Hammes, P., Gadd, J. C., Fujimoto, B.S., Allen, R.W., Schiro, P.G., Lorenz, R.M., Kuyper, C.L., Kuo, J.S., Bajjalieh, S.M., Chiu, D.T. *J. Neurosci.* **2011**, *31*, 4, 1461-470.
- (12) McCusker, E.C., Bane, S.E., O'Malley, M.A., Robinson, A. S. *Biotechnol. Prog.* **2007**, *23*, 540-547.
- (13) Rivetti, C., Guthold, M., Bustamante, C. *J. Mol. Biol.*, **1996**, *264*, 919.
- (14) Calonder, C., Van Tassel, P.R. *Langmuir*, **2001**, *17*, 4392.
- (15) Green, R.J., Davies, J., Davies, M.C., Roberts, C.J., Tendler, S.J. B. *Biomaterials*, **1997**, *18*, 405.
- (16) Reimhult, E., Hook, F., Kasemo, B. *Langmuir*, **2003**, *19*, 1681.
- (17) Johnson, C.A., Lenhoff, A.M. *J. Colloid Interface Sci.*, **1996**, *179*, 587.
- (18) Adamczyk, Z. *J. Colloid Interface Sci.*, **2000**, *229*, 477.
- (19) Dimitrievski, K., Kasemo, B. *Langmuir*, **2009**, *25*, 8865.
- (20) Richter, R., Mukhopadhyay, A., Brisson, A. *Biophys. J.*, **2003**, *85*, 3035.

- (21) Calò, A., Sanmartí-Espinal, M., Iavicoli, P., Persuy, M.-A., Pajot-Augy, E., Gomila, G., Samitier, J. *Soft Matter*, **2012**, *8*, 46, 11632 – 11643.
- (22) Sackmann, E. *Science*, **1996**, *271*, 43.
- (23) Das, A., Zhao, J., Schatz, G.C., Sligar, S.G., Van Duyne, R.P. *Anal. Chem.*, **2009**, *81*, 3754
- (24) Jung, H., Robison, A.D., Cremer, P.S. *J. Struct. Biol.*, **2009**, *168*, 90.
- (25) Myszka, D.G. *J. Mol. Recognit.* **1999**, *12*, 279–284.
- (26) Sigmundsson, K., Beauchemin, N., Lengqvist J., Öbrink, B. *Determination of binding kinetics between proteins with multiple non identical binding Sites by SPR flow Cell biosensor technology, Biosensors - Emerging Materials and Applications*, **2011**, Prof. Pier Andrea Serra (Ed.), ISBN: 978-953-307-328-6, InTech.
- (27) Cook, B.L., Steuerwald, D., Kaiser, L., Graveland-Bikker, J., Vanberghem, M., Berke, A.P., Herlihy, K., Pick, H., Vogel, H., Zhang, S. *PNAS*, **2009**, *106*, 29, 11925–11930.
- (28) Lee, S.H., Ko, H.J., Park, T.H. *Biosens Bioelectron*, **2009**, *25*, 55.

General Conclusions

1. After a genetic engineering process the olfactory receptors of interest were well expressed in the yeast membrane.
2. Membrane fraction from yeast cells heterologously expressed olfactory receptors have been demonstrated that spontaneously form closed spherical nanovesicles (NV) in solution.
3. A simple method to homogenize the size of the nanovesicles to a diameter of ~ 100 nm at a concentration of $\sim 10^{10}$ nanovesicles mL^{-1} is also presented.
4. A novel immunochemical method based onto a competitive ELISA using monoclonal anti-c-myc antibodies addressed against the c-myc tag of the OR was developed in order to determine the ORs expression level in the individual nanovesicles.
5. A very sensitive and specific monoclonal anti-c-myc antibody was produced achieving a high ELISA detectability (in the picomolar range).
6. The human c-myc-OR1740 and chimpanzee c-myc-OR7D4 olfactory receptors expressed in the nanovesicles were quantified as (3 ± 1) OR molecules NV^{-1} and (6 ± 2) OR molecules NV^{-1} , respectively.
7. Substrates showing large negative zeta-potentials and allowing hydrogen bonds formation are the best candidates to give large surface coverages with nanovesicles.
8. Nanovesicles do not rupture once immobilized onto glass and functionalized gold surfaces and retain their closed nature although they flatten considerably displaying an aspect ratio of about 0.1-0.3.

9. The evolution of the nanovesicles surface coverage on glass is found to follow a diffusive law.
10. Surface coverages by only a single layer of nanovesicles larger than 20-25% on the glass substrate and around 10-15% on functionalized gold substrate were obtained.
11. Preliminary results demonstrate that nanovesicles deposition on functionalized gold or glass substrates could be exploited for the generation of an array of multiple nanovesicles, each one carrying a different olfactory receptor at its surface that could be integrated into the same chip and used as biosensor support.
12. The functionality of the expressed receptors (OR1740 and OR7D4) towards their specific odorants, helional and androstenone respectively, was verified in a systematic SPR assay.
13. The SPR assay sensitivity allowed us the detection of small odorants at concentration in the micromolar range.

Epilogue. Bioelectronic Olfactory Neuron Device

European Project (228685-2).



The general objective of the BOND project was to develop an array of smart nanobiosensors containing a large number of different ORs working simultaneously and in a complementary way for detection of odorant signature offering: extremely high sensitivity, maximum reliability and capability of detecting odorant volatile molecules of small size (< 300 Da), high specificity, real-time response, easy-to-use environment, portable equipment and affordable sensor system (low price).

E.1 Introduction

The fabrication of sensitive and selective biosensors for high-throughput screening is a key point in the development of modern medical care^{1,2} (Figure E.1) another applications such as food quality control. The assembly of large numbers of biomolecules in a spatially confined environment, or in an array, is considered to be beneficial for the development of biosensors which can identify target molecules in a fast and reliable way. Nanofabrication techniques,^{3,4} combined with microfluidic set-ups,^{5,6} are promising for the creation of a new generation of biochips, which contain a high density of information, and use at the same time a low volume of biological fluid for the screening.⁷

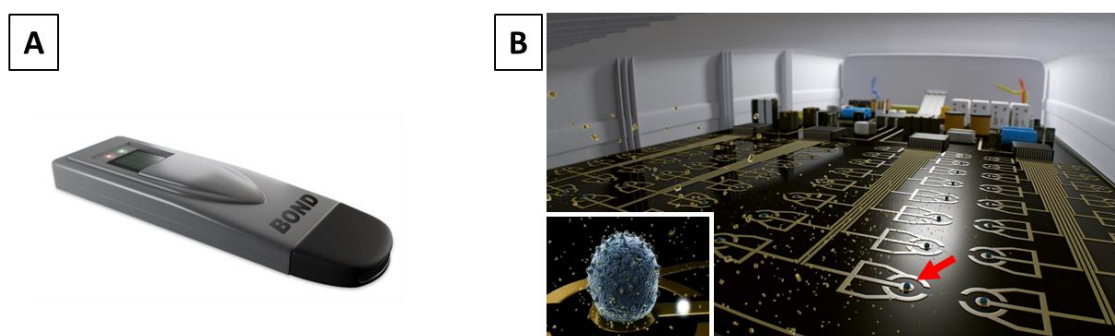


Figure E.1 (A) Concept model of a bioelectronic device with user friendly interface and odorant identification algorithm that will detect and discriminate the odorants within a mixture (from *BOND European Project*). (B) Inside of the new generation of bioelectronic devices presented in picture (A). Representation of array of nanoelectrodes integrated in an electronic chip that will detect the current from the olfactory receptors when bind its specific odorant. The electronic signal will be digitally converted and acquired by the final bioelectronic device. Different arrays will immobilize different types of ORs to provide the possibility of a complex pattern detection. Red arrow indicate immobilized vesicles onto the array surface that is magnified in the inset.

In last years, much attention has been directed towards the integration of membrane receptor proteins, such as GPCRs, into biosensor devices, due to their key role as targets in many disease developments^{8,9}. In addition, microarray-based assays allow us to evaluate multitude of different parameters at the same time. Thus, the immobilization of these GPCRs, as membrane proteins, in arrays is nowadays an interesting research field for the scientific community.

An example of a GPCR subfamily are the olfactory receptors (ORs), proteins responsible for the smell. The use of smell in different fields has been rediscovered recently due to major advances in odour sensing technology and artificial intelligence basically demanded by a large number of potential end users in different areas, such as food safety, diagnosis, security and environment.

Between (2003-2006), in the SPOT-NOSED project, an European project funded by the FP5 Future and Emerging Technologies program, a new approach was developed proving that it was possible to use olfactory receptors as sensing elements of electronic noses. Following this new concept, some years later, a new European project called BOND (2009-2012), funded by the FP7 Nanosciences, Nanotechnologies, Materials and new Production Technologies program, was approved in order to develop a new generation of bio-electronic nose devices that relies, contrary to previous approaches, on the fantastic analytical properties of the mammalian nose: specificity, sensitivity, identification of mixed signatures and real-time response. Thus, the objective of the BOND project was to obtain an integrated bioelectronic analytical platform where the currently used physical or chemical sensing elements were replaced by ORs. The device resulted from scaling down this new biotechnology and integrating it into a single artificial device using nano and information technologies. Due to the large number of potential applications which the device could be used, the BOND consortium has decided to focus on two main applications related to two important economic areas such as the Food Industry, and the Health/Medical Industry (Figure E.2).

The application of the device in the field of health and medicine would drastically diminish the cost of disease diagnosis and monitoring for early detection and prevention of diseases as highly specific, highly sensitive and non-invasive diagnostic tools. For example, the possibility to diagnose and monitor diseases such as cancers by measuring the concentration of volatile markers in body fluids (or in the breath) has gained acceptance in recent years within the medical community^{10,11}.

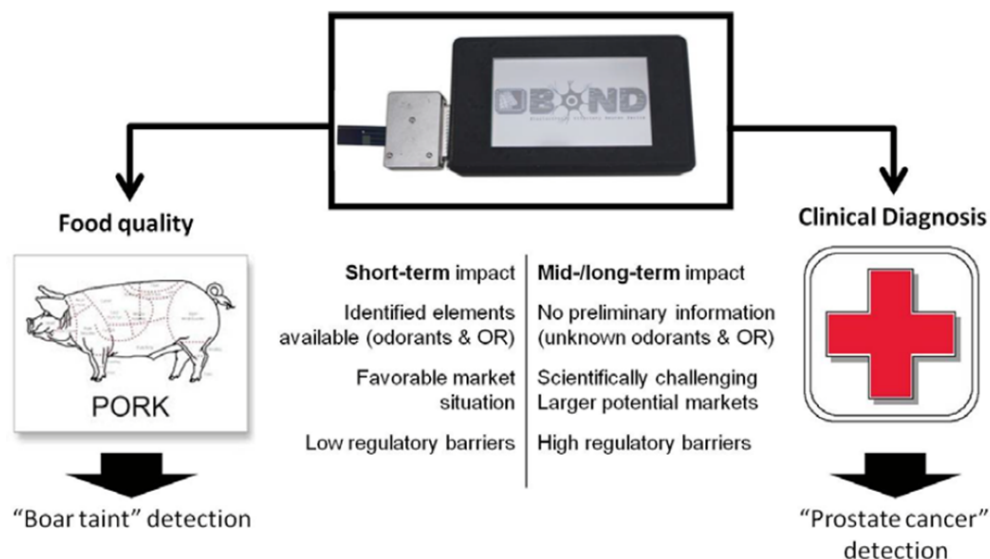










Figure E.2 Target applications for the BOND platform.

On the other hand, measurements to ensure food safety and food quality are a critical need for our society. The detection of contaminated food products in a rapid and accurate manner before consumption would benefit the buyer market¹². Thus, the second application for the bioelectronic nose device was related in the food industry. Specifically, the detection of boar taint compounds for food quality controls (pig meat quality control).

E.2 The consortium

The partners involved in the BOND project were integrated in a multidisciplinary consortium at European level with expertise in areas such as biotechnology, surface chemistry, nanofabrication, electronics and theoretical modelling. Some of them have been working together previously in the SPOT-NOSED Project. Table E.1 shows the members of the BOND consortium.

Table E.1 Members of the BOND consortium

Beneficiary Name	Beneficiary Short Name	Country
Universitat de Barcelona - IBEC (Coordinator)	UB-IBEC	Spain 
Institut National de la Recherche Agronomique	INRA	France 
Université Claude Bernard de Lyon 1	UCBL	France 
Centro Nacional de Microelectrónica (CSIC)	CNM-CSIC	Spain 
Università de Salento	UNILE	Italy 
Politecnico de Milano	POLIMI	Italy 
Tyndall National Institute	TYNDALL	Ireland 
Uniscan Instruments Ltd	UNISCAN	U.K. 

E.3 Results

For the application related in cancer diagnosis four odorant markers for prostate cancer were validated. One of them, hereafter named PCO1, was selected and the corresponding OR, PCOR2, was identified, cloned and expressed. The identification was performed with *in vitro* methods such as electroolfactograms (EOG) of a rat olfactory mucosa (Figure E.3) and confirmed by PCR using specific primers.

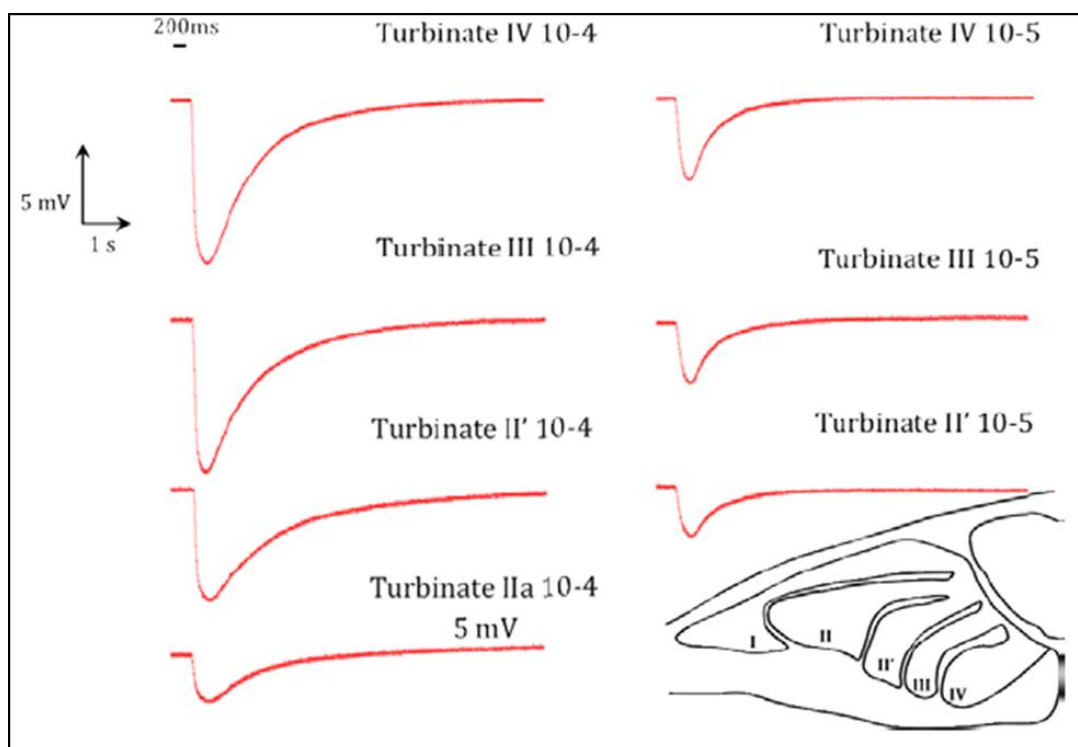


Figure E.3 EOG recordings from turbinates stimulated with PCO1 from various dilutions, showing optimum response from turbinate IV (best response at lowest PCO1 concentration). Lower right: Scheme of a rat olfactory mucosa and the turbinates position.

The validated receptors were cloned in a yeast expression vector. The successful PCOR2 expression in yeast was confirmed by Western Blot (Figure E.4).

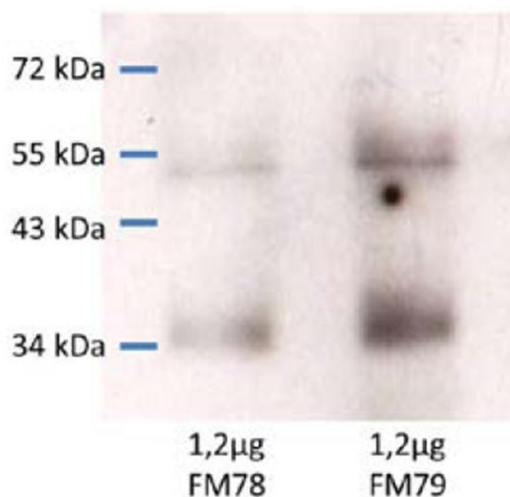


Figure E.4 Representative Immunoblots revealing an appropriate expression of PCOR2 in yeast (membrane fractions FM78 and FM79).

However, as described previously, the main application selected for the BOND platform was the detection of boar taint compounds for food quality controls. The consortium, was basically focused to one odorant, androstenone, and its corresponding olfactory receptor, OR7D4. In addition, different variants of OR7D4 were cloned and expressed in yeast. The specific response of yeast derived nanovesicles containing OR7D4 to androstenone was finally assessed by electrochemical impedance spectroscopy (EIS) providing the first evidence of the functionality of this receptor. OR1740, receptor expressed in the SPOT-NOSED Project was used as control receptor on the BOND Project and helional odorant was used as unspecific molecule for OR7D4.

The response of OR7D4 to the target odorant (androstenone) immobilized in electrodes is shown in Figure E.5.

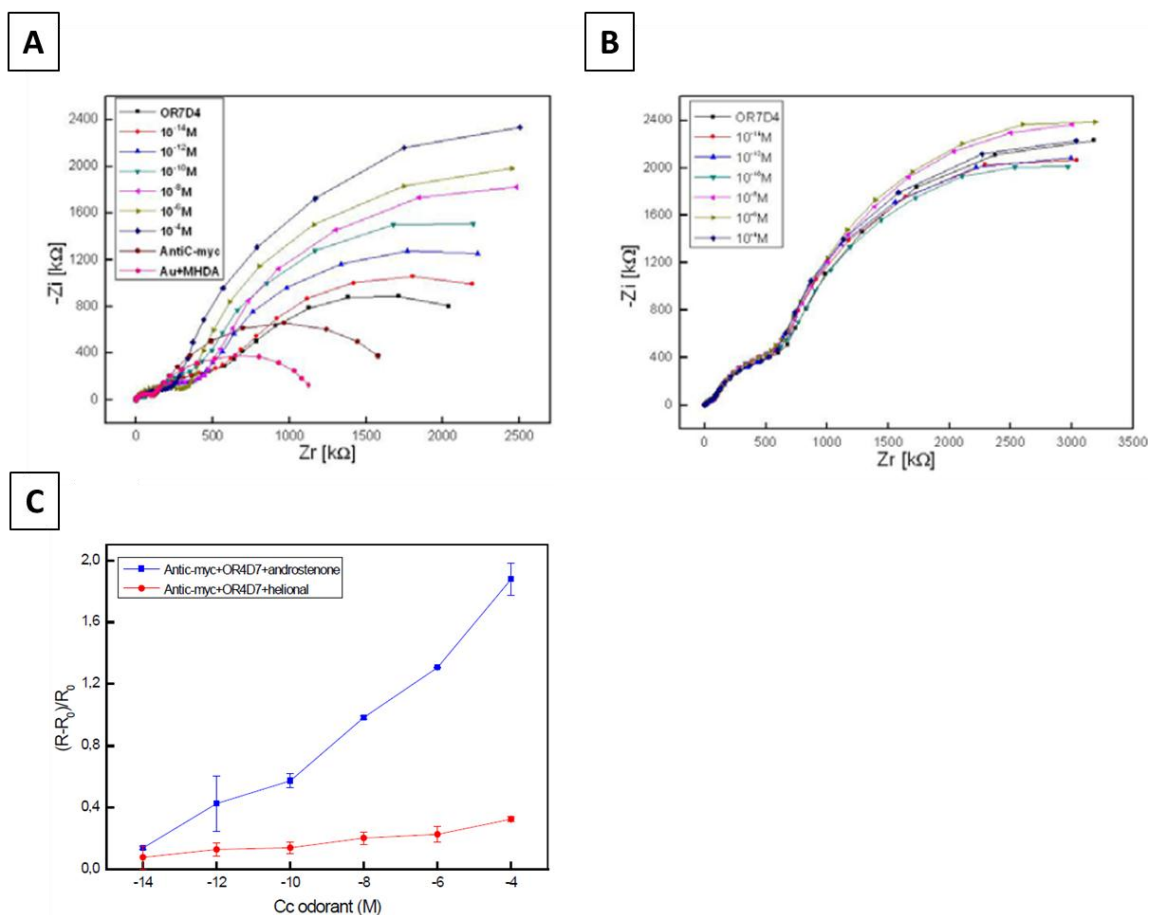


Figure E.5 Functional evaluation of OR7D4 by EIS. **(A)** Nyquist diagrams obtained for the impedance measurements on the biosensors under various concentrations of androstenone (specific odorant). **(B)** Nyquist diagrams obtained for the impedance measurements on the biosensors under various concentrations of the helional (unspecific odorant). **(C)** Relative variation of the charge transfer resistance as a function of concentrations of helional (red) and androstenone (blue). R_0 corresponds to the polarization resistance when the OR7D4 is immobilized on the functionalized electrode.

Other methods were used to monitor functional response of ORs to its specific odorant, i.e. surface plasmon resonance on a sensitive Biacore T100 (see *Chapter 4*) and Bioluminescence Resonance Energy Transfer (BRET) assays. This BRET method was tested on human OR1740, with helional as odorant ligand, and octanal as negative control odorant, which required the use of 2 yeast strains: OR1740-Rluc, and OR1740-Rluc overtransformed with $G\alpha$ -YFP. Representative results are shown below (Figure E.6). A clear BRET level change is induced, only in the presence of the odorant ligand of hOR1740. Unfortunately BRET results could not be obtained with OR7D4, due to a low expression level of $G\alpha$ protein in the selected strains.

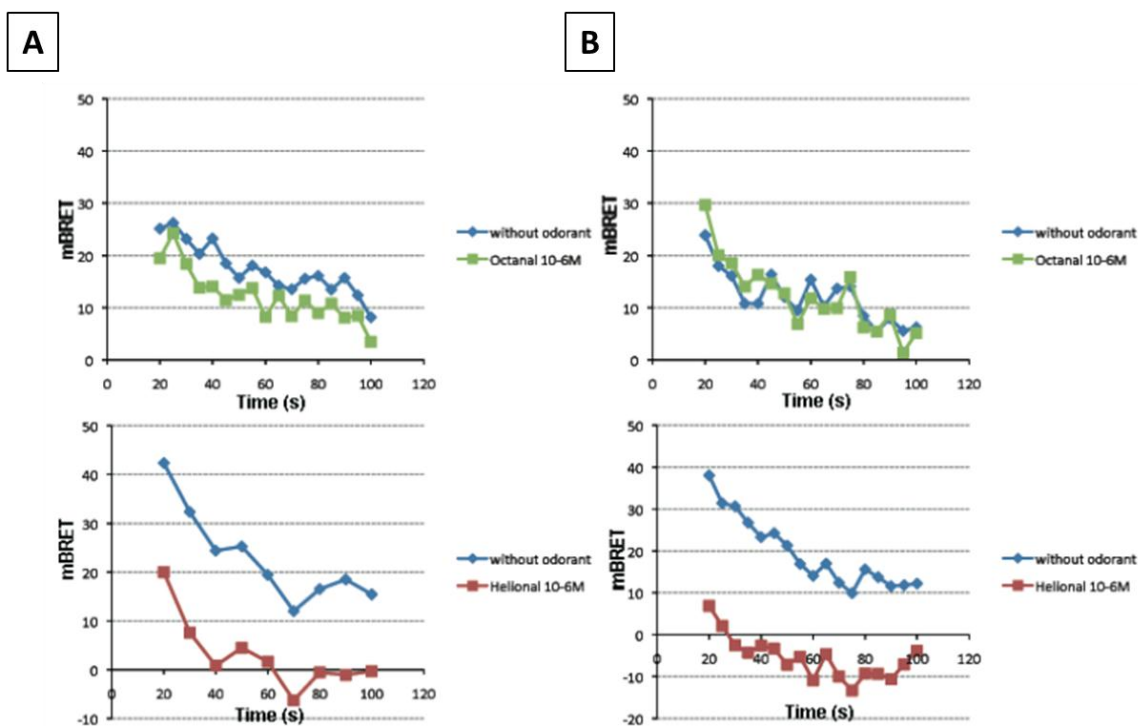


Figure E.6 Representative results for BRET with hOR1740, using helional (red) as odorant ligand, and octanal (green) as negative control odorant. This experiment was reproduced in 5 repeats. Here we present just two of them, (A) and (B).

In addition, ORs quantification in membrane fraction was performed on solubilized, centrifuged membrane fractions (see *Chapter 2*) obtaining the relative amount of c-myc-OR7D4 receptors (0.008 ± 0.002) g c-myc-OR7D4/g total proteins. For the control receptor, OR1740, the relative amount of c-myc-OR1740 receptors was (0.0030 ± 0.0005) g c-myc-OR1740/g total proteins.

In order to develop the BOND platform the ORs were carried by natural membrane nanovesicles. The origin of these nanovesicles was the total membrane fraction (MF) obtained from yeast cells (*S.Cerevisiae*). The average size of the selected lipidic nanovesicles was determined ~ 100 nm of diameter and the average number of functional olfactory receptors per nanosome was obtained by ELISA methods (see *Chapter 2*). Nanosomes from yeast cells expressing OR7D4 contained (6 ± 2) receptors per nanosome.

In addition, a c-myc tag was genetically expressed at the N-terminus of the receptor. This specific tag, allowed us to immobilize the nanovesicles on the

nanotransducer surface. The immobilization strategy of the nanovesicles containing these tagged OR on the nanotransducers is presented below.

On the other hand, focusing into the technological part of the BOND Project, smart nanotransducers were fabricated. The smart nanotransducer was composed of two components: the chip of nanoscaled electrochemical cell accommodated working nanoelectrode array and the front-end integrated electronic circuit providing pre-amplification of electrical signal generated by the electrochemical cell.

The sensing part of the smart nanotransducer, the electrochemical cell, was designed to be realized as an easy handle disposable chip. This chip was compatible with a specially designed connector, which will secure connection of this chip to the low noise highly sensitive front-end electronics incorporated in the integrated electronic circuit. The suggested approach eliminates needs of the nanoscale electrochemical cell packaging that reduces the cost of the nanotransducer device fabrication and increases the chip reliability. The chip was based on a three electrode electrochemical cell contained a working electrode, an integrated counter electrode (5.2 x 5 mm) and the reference electrode (1.1mm diameter circle).

The selection of the optimum working electrode geometry and the optimum operating conditions of the nanotransducers was based on results of immobilization and stimulation after the application of an AC sine wave over a large frequency range. In order to optimize the sensor design for signal/noise ratio improvement, simulations of the different nanotransducers were performed. The objective was to analyse the diffusion behaviour at a single electrode and electrode array with application of sine wave signal. The separate simulations were set up for AC using Comsol 4.2a Multiphysics Engineering software. The performance of the cell with integrated WE, CE, RE was within the limits of the commercial electrodes setup that confirms correctness of the final version of the nanotransducers design and fabrications.

Finally, 2 different geometries, see Figure E.7, (disc, has 3D diffusion behaviour, or band, 2D diffusion behaviour combining features of radial and plane diffusion) with a critical dimension of 10 μm as gold working electrodes, a platinum counter electrode and a Ag/AgCl reference electrode were used.

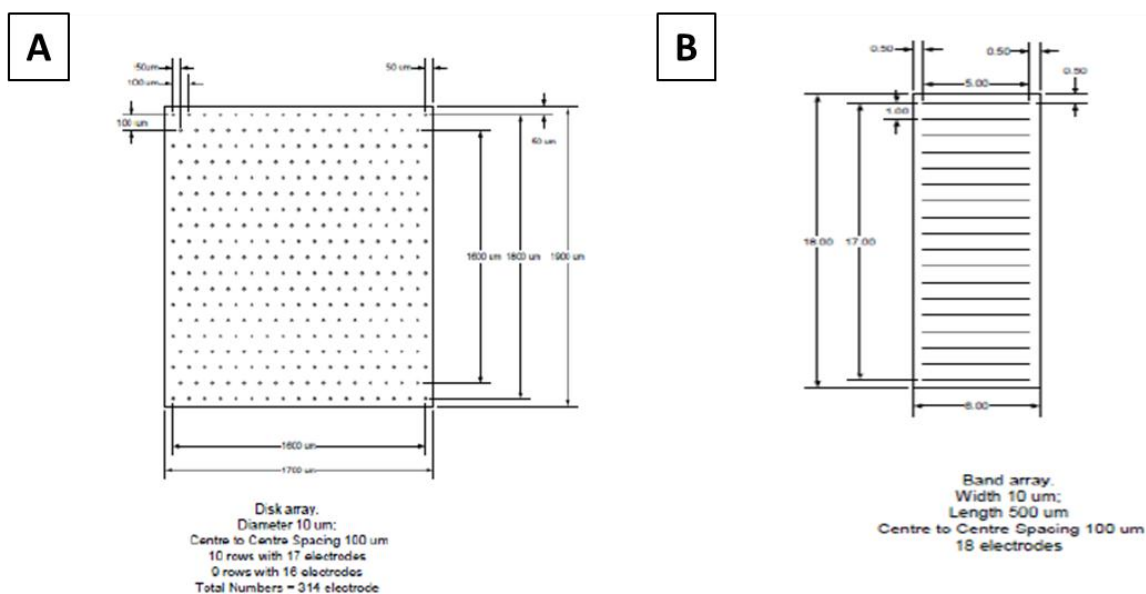


Figure E.7 Layout for the disc (A) and band (B) working electrodes.

The availability of 4 pads and correspondingly 4 contact springs in the connector was to facilitate flexibility for the nanotransducer design (Figure E.8).

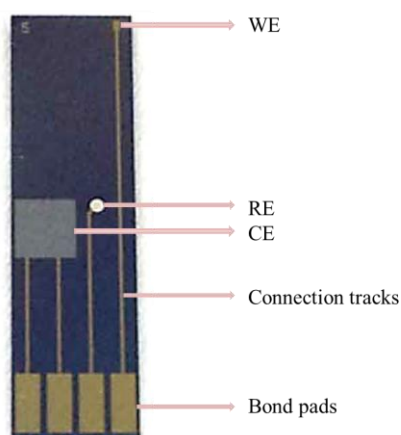


Figure E.8 The final version of the BOND nanotransducer with an integrated working (WE), counter (CE) and reference (RE) electrode.

The successful metal deposition of the fabricated electrodes was characterized by scanning electron microscopy (SEM) and energy-dispersive X-ray spectroscopy (EDX) analysis. Figure E.9 shows the analysis of the reference electrode Ag/AgCl. Figure E.9B clearly showed the present of Ag seen by the dominant peak on the right-hand side of the EDX plot. Analogous analysis was performed for gold working electrodes and results are shown in Figure E.10.

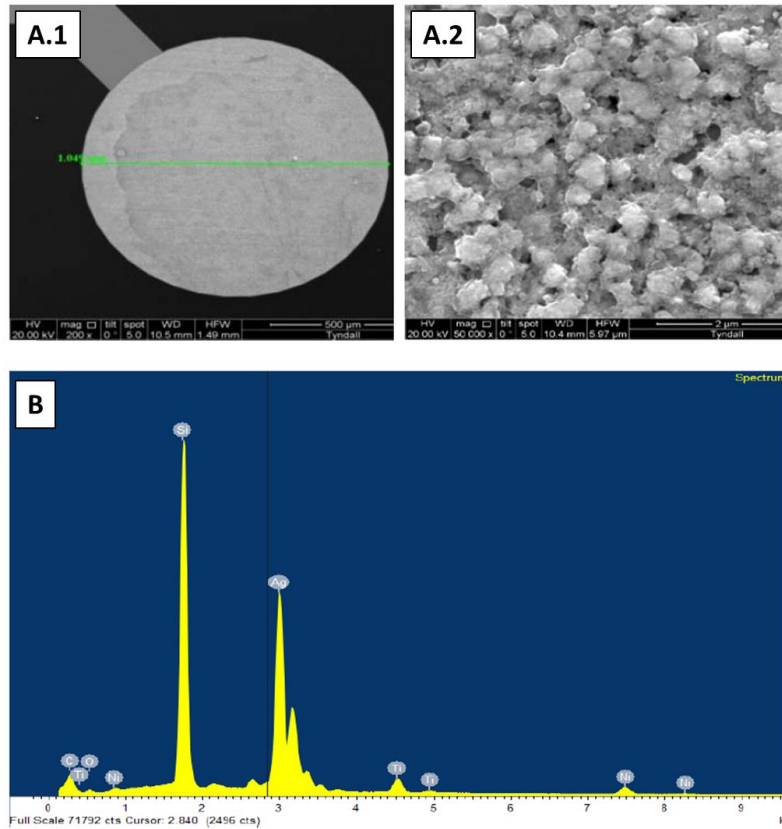


Figure E.9 SEM analysis (A) and EDX (B) of the AgCl layer.

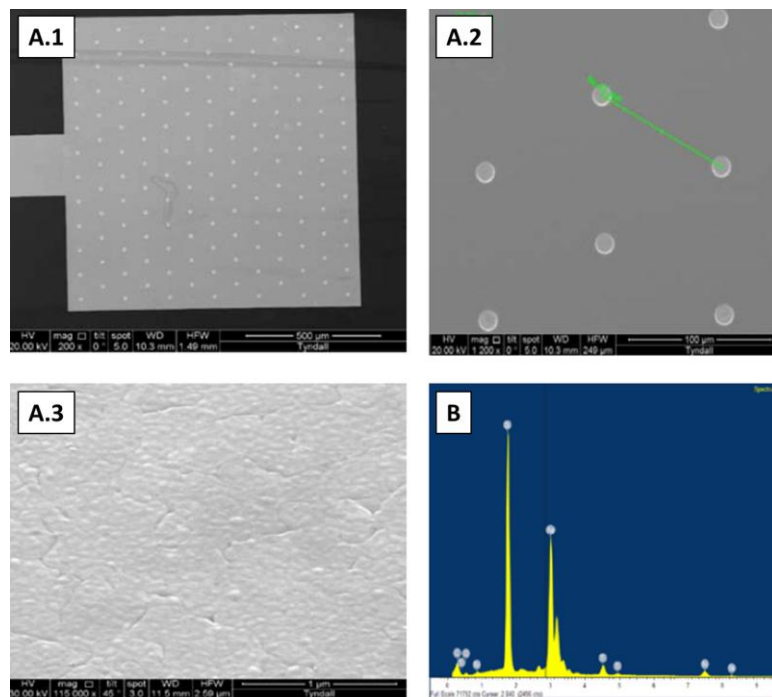


Figure E.10 SEM analysis (A) and EDX (B) of the Au working electrode array.

Then, in order to enhanced surface area (tunable pore size and density with an increase of the number of sites for immobilization), to reduce or eliminate the electrode

recess and to allow hydrophobic/hydrophilic surface functionalization additional experimental work was carried out on modification of the working electrode surface with 3D nanoporous gold (Figure E.11).

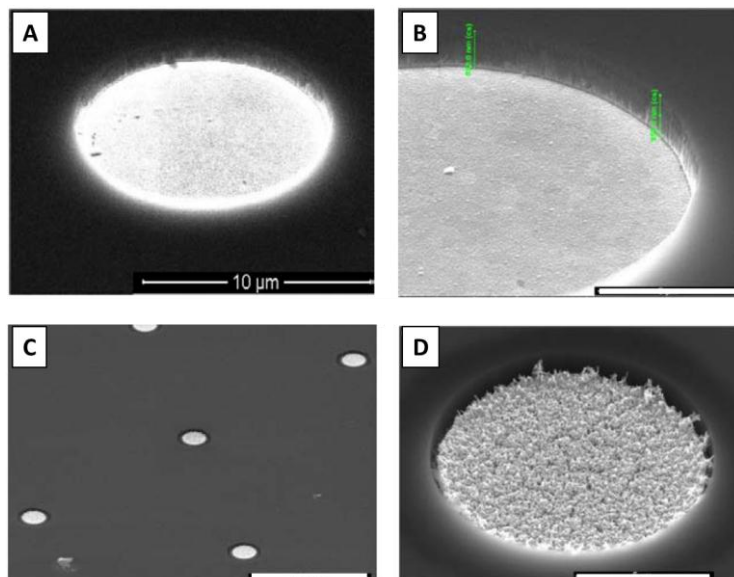


Figure E.11 (A) SEM image of recessed microdiscs prior to modification tilted to 60°. (B) Zoom from image (A). Scale bar: 3 μm . (C) SEM image of gold microdisc array modified with 190 nm nanoporous gold. Scale bar: 50 μm . (D) Zoom from image (C). Scale bar: 5 μm .

The other part of the smart nanotransducer was the fabrication of the front-end integrated electronic circuit providing pre-amplification of electrical signal generated by the electrochemical cell in order to obtain high sensitivity impedance spectroscopy measurements (Figure E.12).

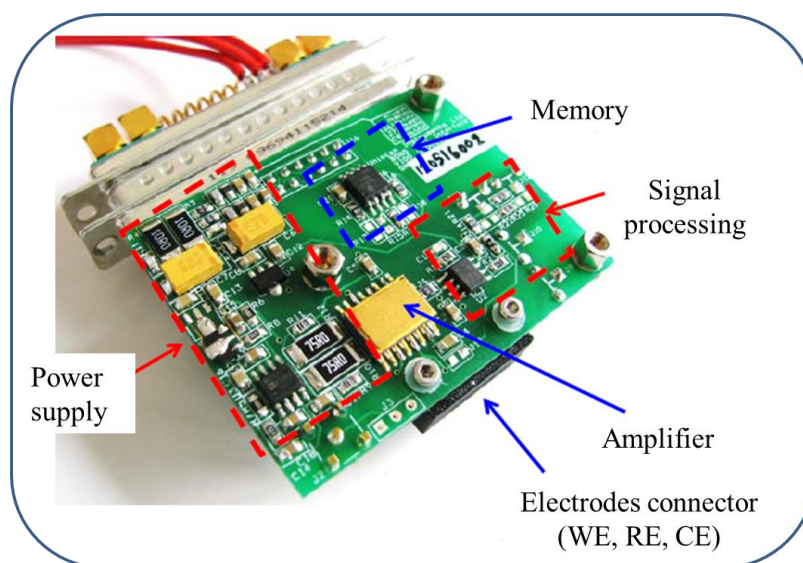


Figure E.12 Photograph of the BOND device electronic front-end board.

The smart nanotransducers were characterized using cyclic voltammetry and electrochemical impedance spectroscopy. Figure E.13 shows the experimental set up used and the measurements obtained for disk WE nanotransducers. With on-chip WE, CE and RE for band electrodes same results were obtained that confirms correctness of the two final versions of the nanotransducers designs and fabrications.

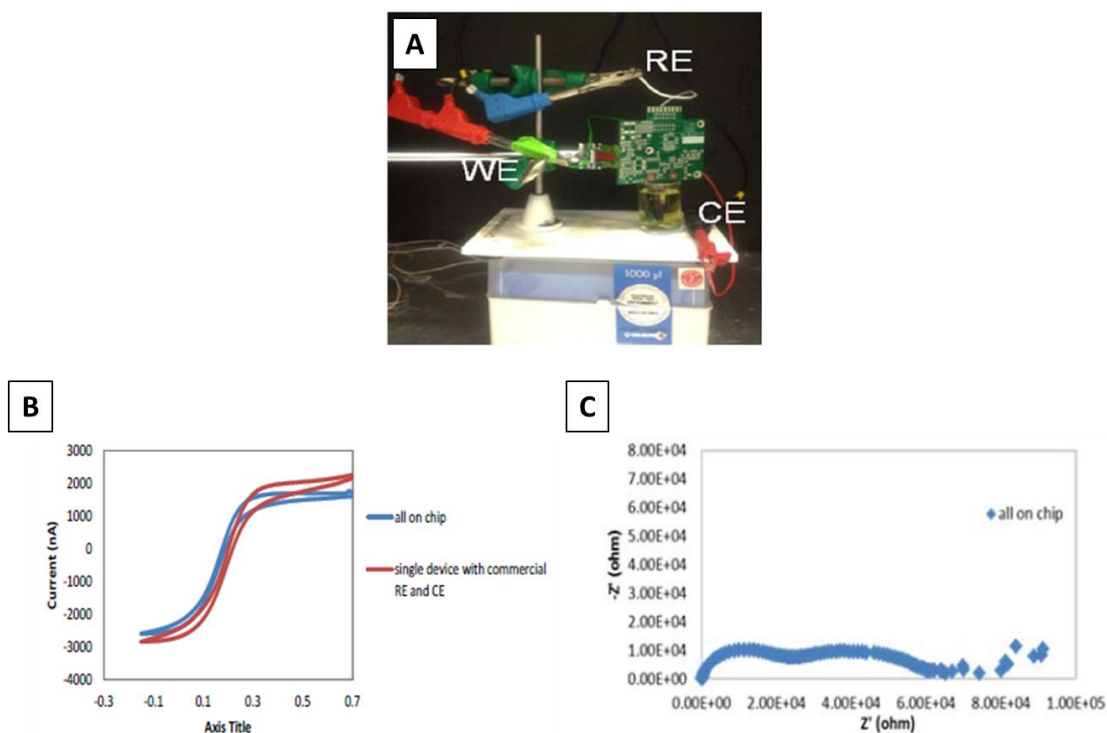


Figure E.13 (A) Experimental setup for testing the final version of BOND nanotransducers. (B), (C) Comparison of device with disk geometry as working electrodes with a commercial electrode setup: cyclic voltammetry measurements (B) and electrochemical impedance spectroscopy measurements (C).

In order to address the effectiveness of the improved module in increasing the performance in impedance spectroscopy, a comparison tests were made between a standard potentiostat (AUTOLAB instrument) alone with a dummy impedance connected to its input and the same instrument connected to the same dummy impedance through the our electronic front-end. Figure E.14 shows the improvement in measuring capability of the BOND instrumentation when the electronic front-end module was used. The improvement in performance was noticeable also when measuring directly the noise of the system, where more than an order of magnitude is gained when using our electronic front-end.

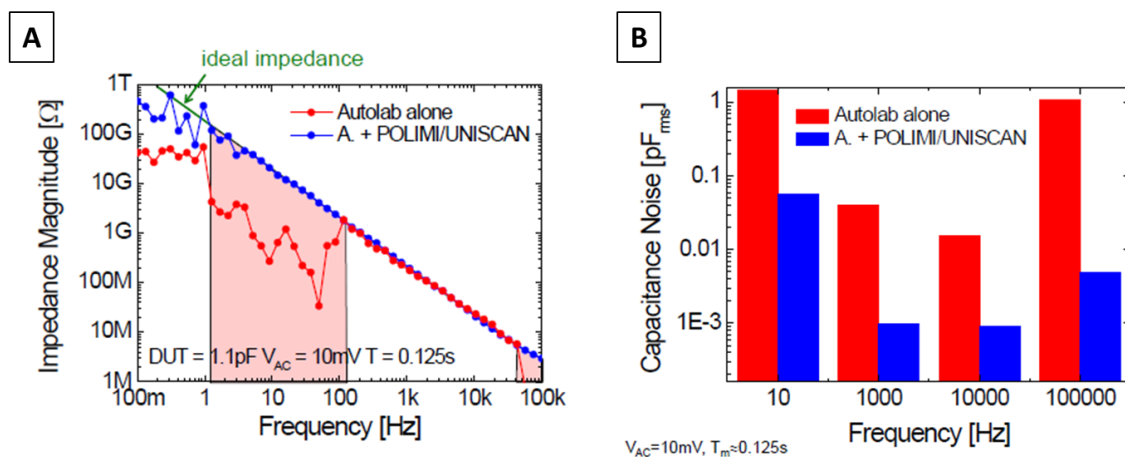


Figure E.14 (A) Impedance spectroscopy of a known impedance obtained by using a standard potentiostat alone (red curve) and by using our electronic front-end in between the impedance network and the potentiostat (blue curve). (B) Measurement of the resolution obtained by the system when using our electronic front-end (blue bars) compared with the potentiostat alone (red bars).

Thanks to the higher sensibility of the input amplifier, a precise measurement of the sensor capacitance of 1.1pF was able to be performed down to 100mHz while without our new module the measurement was precise only in a limited frequency window, completely failing below 100Hz. The electronic front-end fabricated matched to the BOND nanotransducers and the portable analyser was demonstrated that worked a frequency extension of more than 3 decades and a reduction of the equivalent noise of the system of much more than an order of magnitude.

Following, the different prototypes of the nanotransducers (disk and band WE) were functionalized and characterized by impedance measurements. The principal functionalization was based on the use of self-assembled monolayers (SAMs) with specific anti-c-myc antibodies. Another method using OR with N-terminal 6xHis tags and a functionalization strategy based on Copper-nitrilotriacetate (Cu-NTA) was also studied. Thus, two immobilization strategies were tested using either 6xHis or c-myc tagged OR (Figure E.15). The strategy using a 6xHis tag instead of a c-myc tag was selected with 2 expected advantages: direct binding of 6xHis to Ni-NTA or Cu-NTA would decrease the distance between ORs and electrode surface, and thus increase the impedance variation.

Both tagging strategies were validated and compared first on standard gold macroelectrodes and then on the BOND nanotransducers.

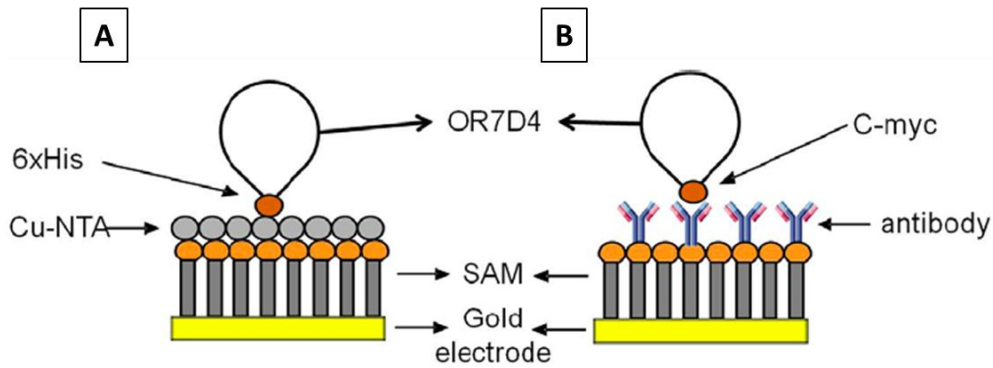


Figure E.15 Scheme of the immobilization strategies evaluated: using 6xHis tag (A) or c-myc tag (B).

First, the immobilization procedure was characterized by EIS. Figure E.16 shows the Nyquist plots obtained, in all the graphs the curves correspond to the different c-myc immobilization steps: bare gold (black), gold + thiol acid (red) and gold + thiol acid + antibody (blue). 2 electrodes were used for each design (disk or band). We present here the Nyquist diagrams of 2 electrodes prepared and processed in the same conditions.

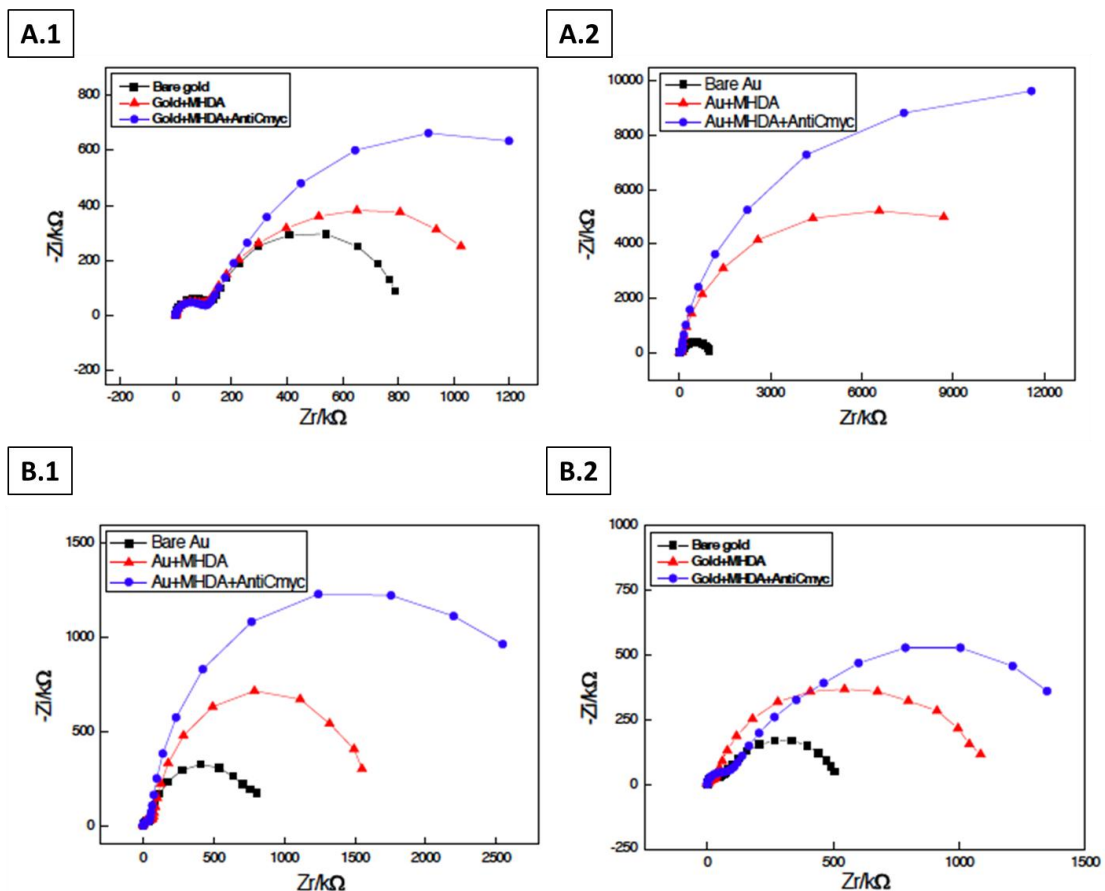


Figure E.16 Nyquist diagram corresponding to 2 electrodes of disk design (A.1, A.2) and band design (B.1, B.2) prepared in each case in the same conditions.

Preliminary characterization of the integrated reference and counter electrodes were also done. The results obtained were similar to those obtained with the non-integrated version of the nanotransducers presented above. The results confirmed the functionality of the final nanotransducers.

Figure E.17 shows the results obtained for both the 6xHis-OR7D4 and the c-myc-OR7D4 immobilization at different concentrations on the non-integrated disk nanotransducers. It is shown an increase of the impedance (charge transfer resistance) with the concentration of the nanovesicles. This increase shows the good interaction between the nanovesicles and the functionalized gold surface. However the variation of the transfer charge resistance for 6xHis-OR7D4 was lower than the one for the c-myc tag. Thus, the c-myc tag strategy was selected to develop the final BOND prototype.

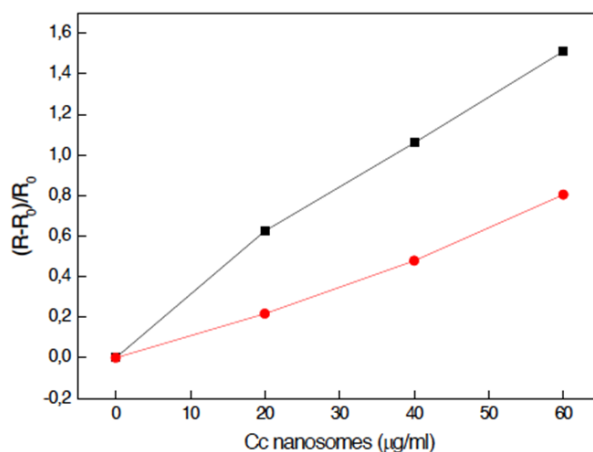


Figure E.17 Transfer charge resistance variation as a function of different concentrations of nanovesicles (also called nanosomes): comparison between c-myc (black) and 6xHis (red) tag immobilisation strategies. Disk WE were used for the analysis.

Preliminary results of validation tests showed that the fabricated BOND nanobiosensors were suitable for the detection of the key “boar taint” compound, androstenone, in laboratory samples. Figure E.18 demonstrates that when c-myc-OR7D4 interacts with its specific odorant, androstenone, an impedance measurement is obtained. Impedance increases with the increase of the androstenone concentration. The developed functionalized nanoelectrodes based on the c-myc-OR7D4 chimpanzee olfactory receptor show good response to androstenone (10^{-14} M – 10^{-4} M) odorant, non-sensitivity to helional (control) and very low sensitivity to testosterone (control).

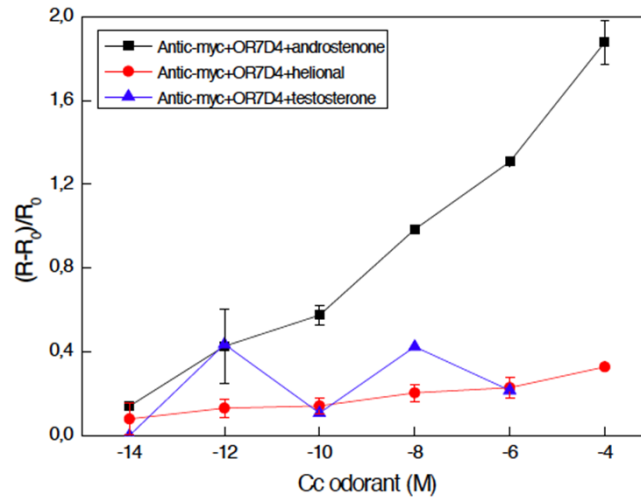


Figure E.18 c-myc-OR7D4 relative variation of the charge transfer resistance as a function of concentrations of different odorants: helional (red points) used as control, testosterone (blue points) and androstenone (black points) the specific odorant.

Furthermore, in order to perform electrical measurements by scanning probe microscopy of our sample (the nanovesicles) specific conductive Scanning Probe Microscopy (SPM) probes were fabricated (Figure E.19). Two types of probes were defined: DC contact probes, to be used for DC electrical measurements with the tip in contact with the sample, and AC-non-contact probes, to be used for AC electrical measurements with the tip not contacting the sample. The nanotools were fabricated by using silicon-based micro and nanofabrication processes to define micromachined cantilevers with tips. The AC probe characteristics (spring constant, resonance frequency, apex radius, cone geometry and electrical actuation) were determined. Remarkably, the design of the conduction path of the AC probes was made the parasitic effects of the cantilever undetectable, which was one of the main objectives.

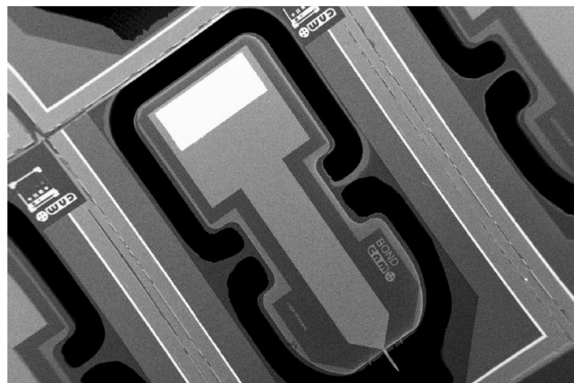


Figure E.19 SEM micrograph of a full chip for the AC non-contact nanotools.

The morphology and electrical properties of the developed functionalized microelectrodes containing immobilized nanovesicles (nanobiosensors) were analysed at the nanoscale, revealing the small scale properties of these sensing systems. The nanoscale morphological properties of the nanobiosensors were analysed by means of AFM imaging in liquid environment. To this end nanovesicles were immobilized onto functionalized BOND microelectrodes following the procedure presented above. Figure E.20 shows AFM images that have clearly evidenced the presence of the nanovesicles on the functionalized microelectrodes and the evolution of the microelectrode coverage with the variation of the nanovesicle concentration solution.

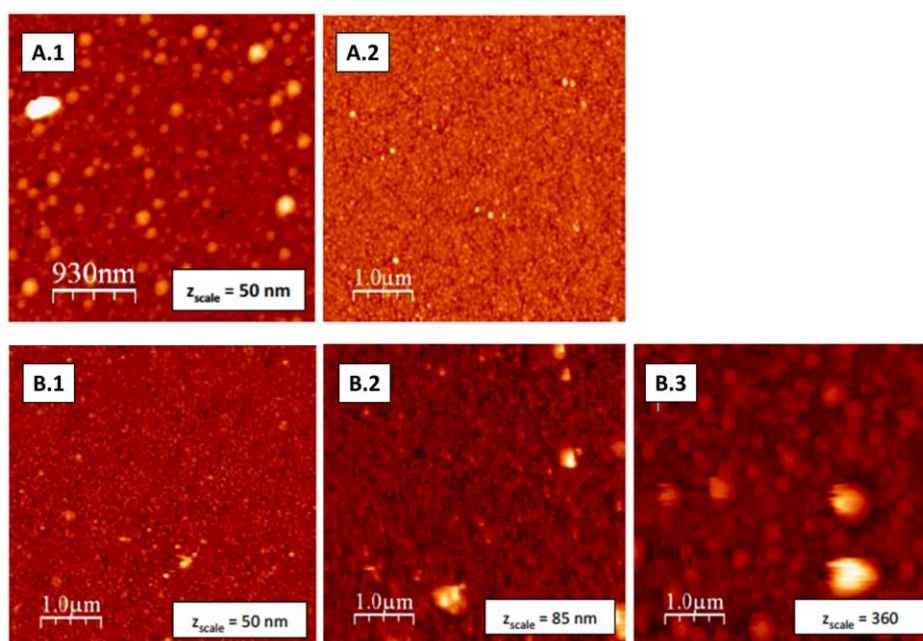


Figure E.20 Topographic AFM image of a functionalized microelectrode with nanovesicles adsorbed (A.1) and a bare microelectrode (A.2). Topographic AFM image of a functionalized microelectrode with nanovesicles adsorbed at three different nanovesicle solution concentration at the Total Protein Content of 20 $\mu\text{g mL}^{-1}$ (B.1), 40 $\mu\text{g mL}^{-1}$ (B.2) and 60 $\mu\text{g mL}^{-1}$ (B.3).

Furthermore, the electrical properties of the adsorbed nanovesicles were as well investigated by means of Electrostatic Force Microscopy measurements. This technique enables to determine the dielectric polarization properties (e.g. dielectric constant) of nanoscale objects and it offers the highest possible spatial resolution of the existing techniques for this type of measurements. Measurements were performed in air where the spatial resolution for single nanovesicle characterization could be achieved. Figure E.21 shows the optical and nanoscale topographic and dielectric images of a nanobiosensor. The dielectric images show a relatively large dielectric response of the

nanovesicles, which could be compatible with the presence of water enclosed inside them.

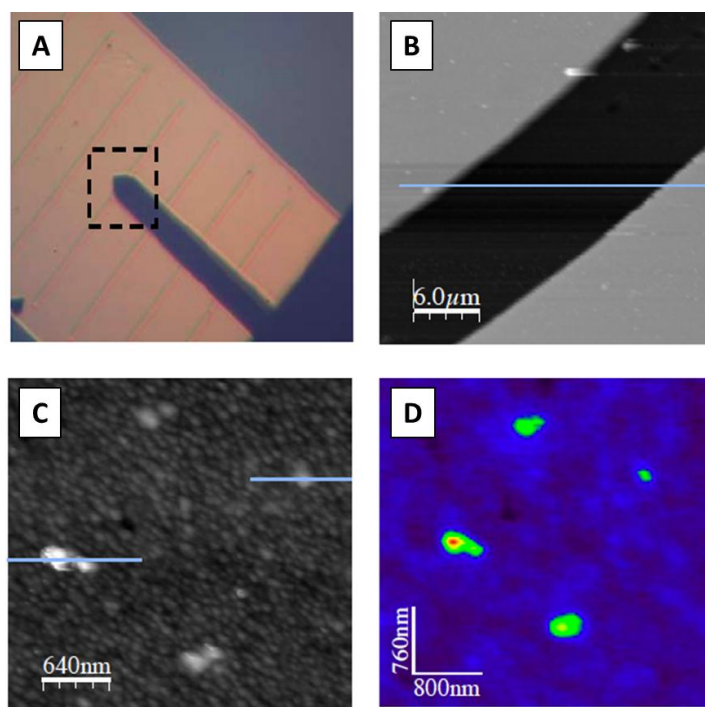


Figure E.21 (A) Optical image of the AFM probe located on a band type microelectrode. (B) Large scale AFM topographic image of a single band (10 μm wide). (C) Small scale AFM image of the functionalized microelectrode showing the presence of individual nanovesicles (larger white spots). The small spots correspond to the granular structure of the gold used in the microfabrication. (D) Nanoscale dielectric image of individual nanovesicles revealing its dielectric response. Sample was prepared following the c-myc immobilization procedure presented before.

In order to understand the charge transfer in transmembrane proteins such as olfactory receptors a theoretical model for the electron tunnelling through single proteins was as well developed (using the bacterio-rhodopsin, a light receptor, as protein model) as well as a theoretical interpretation of the nanobiosensor response. As has been presented before, preliminary set of EIS experiments were performed on chimpanzee OR7D4, in the absence and presence of the specific odorant, androstenone. In addition, the specific sensitivity was also tested with success by substituting androstenone with helional, a non-specific odorant. Figure E.22 shows the corresponding Nyquist plots at different concentration of the odorant, showing a rather ideal semicircle shape. Thus, their fitting performed by Z-plot software, provided the change of the polarization resistance at increasing odour concentration. A systematic increase of the normalized change of resistance at increasing odorant concentration was found, with a maximum variation of about 300 % at the highest concentration.

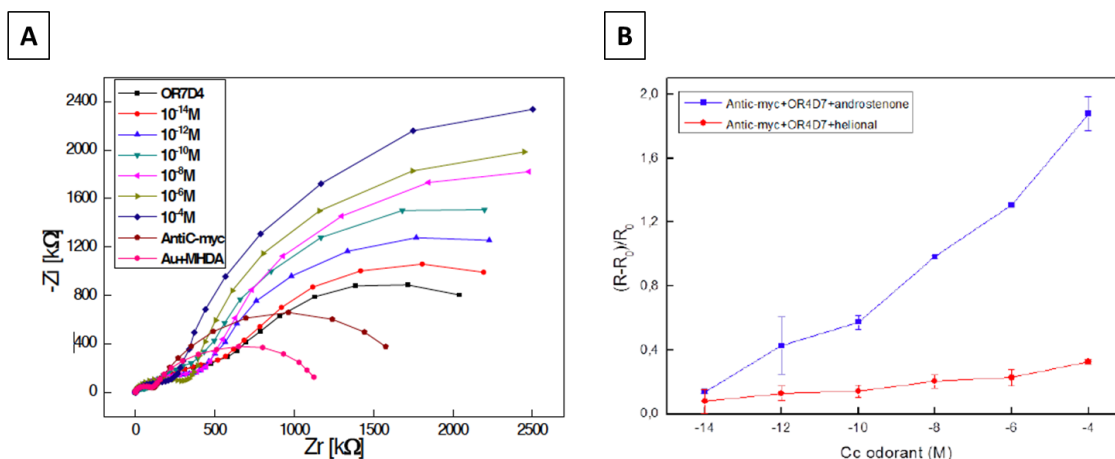


Figure E.22 (A) Preliminary EIS data on chimpanzee OR7D4 confirming the sensitivity of the device to the presence of androstenone odorant. Nyquist plot with Zi (imaginary) and Zr (real) part of the small signal impedance. (B) Relative resistance variation as a function of androstenone (specific odorant) and helional (non-specific odorant) concentration obtained from EIS data and Z-plot fitting. R is the resistance at the given odorant concentration and R₀ is the resistance in the absence of the odorant.

In order to perform a microscopic interpretation of these results the selection among the possible 3D structures of the single protein (native/activated state) those that best approximate the experimental outcomes was carried out. A set of different 3D models used to predict the change of resistance of a single protein associated with the conformational change due to the capture of the specific ligand as function of the interacting radius R_c were obtained. The corresponding theoretical Nyquist plots of the native and activated states were calculated and the results are shown in Figure E.23.

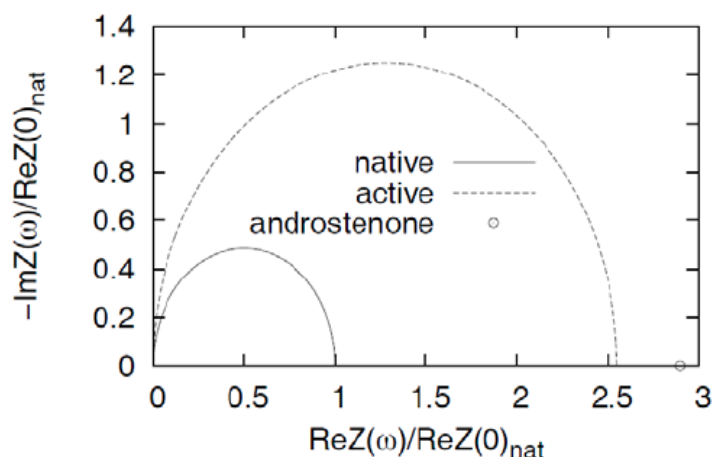


Figure E.23 Theoretical Nyquist plots for native and active state of the selected 3D structures of OR7D4 chimpanzee. The interaction radius, R_c=62 Å gave the maximal resolution.

Some different theoretical interpretations of the experimental data on the relative resistance variation were tested. However, the main results were based on a Hill linear

fit (Eq.2). In this case, the relative resistance variation, $\Delta R / R_0$ was taken proportional to the natural logarithm of the ratio between the active and native states constituting the protein sample (Eq.1):

$$\frac{\Delta R}{R_0} = \lambda \ln \left(\frac{\theta}{1-\theta} \right) \quad (\text{Eq. 1})$$

θ is the % of proteins in the active state. The right-hand side of the above equation is the left-hand side of the Hill equation (Eq.2):

$$\ln \left(\frac{\theta}{1-\theta} \right) = n \ln [Cc] - n \ln K_d \quad (\text{Eq. 2})$$

where n is the Hill parameter, describing the protein-ligand affinity, and K_d is the dissociation constant. Thus, finally (Eq. 3):

$$\frac{\Delta R}{R_0} = \lambda n \ln [Cc] - \lambda n \ln K_d \quad (\text{Eq. 3})$$

The best fit of this equation gave, assuming $n=1$, $\lambda=0.07$ and $K_d \sim 10^{-15} \text{M}$, a value corresponding to a strong binding. Figure E.24 shows the results of the fitting. The agreement between theory and experiments was found to be satisfactory both from a qualitative and quantitative point of view.

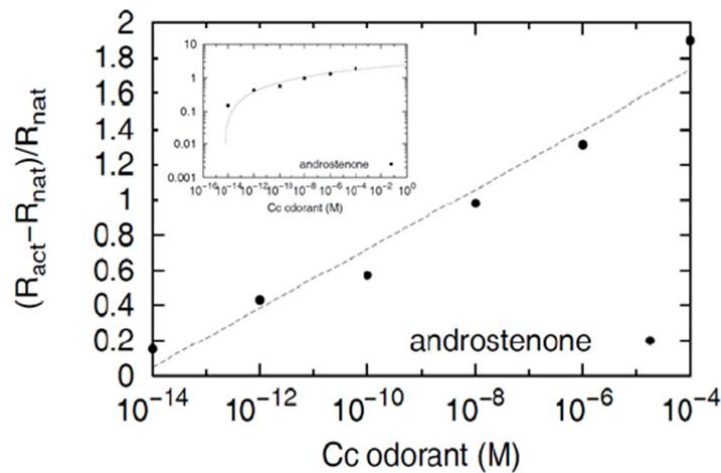


Figure E.24 Linear fit of experimental data.

Finally, electromechanical interface between the removable sensor substrate and the instrumentation was also completed and manufactured. This connector was evaluated to show that it was able to ensure reliable and repeatable measurements.

But first, the BOND data acquisition and processing instrumentation was developed as a self-contained portable analyser. The instrument implements a portable electrochemical potentiostat/galvanostat analyser. The instrument was based on a bespoke hardware design (designed in 3D CAD) which runs the Windows CE operating system and was fabricated using 3D printing technology (Figure E.25).

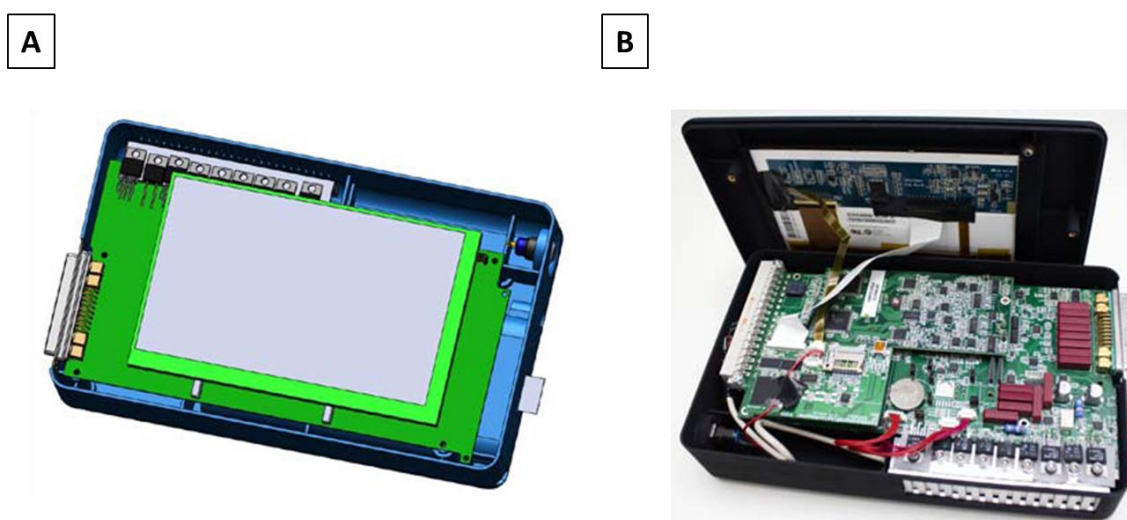


Figure E.25 Instrument 3D CAD design (A) and assembled prototype (B).

The principle electrochemical technique used was EIS (Electrochemical Impedance Spectroscopy). Data was acquired at high sampling rates in synchronisation with a sine wave used to modulate the electrochemical cell. The data measured was then processed wholly in software using signal processing algorithms. The data processing follows a software based in a sequential model.

As has been mentioned before, to obtain that, an electromechanical interface between the removable sensor substrate and the instrumentation electronics was developed. This was an important engineering task to ensure reliable and repeatable measurements. This connector was based as a plastic retainer part and a printed circuit board (PCB) designed having minimum dimensions to fit the connector retainer making it much easier to handle and clamp in a standard lab clamp or retort stand. Cap head hex

stainless steel screws were used to secure the plastic retainer part to the PCB and the retainer part had retaining features added to accommodate a standard nut. Thus, the screws can easily be loosened to insert the sensor with no damage to the substrate. The screws can then be tightened to secure the substrate and make a reliable connection to the contact areas. Short colour coded cable was provided to allow easy connection to the device (Figure E.26).

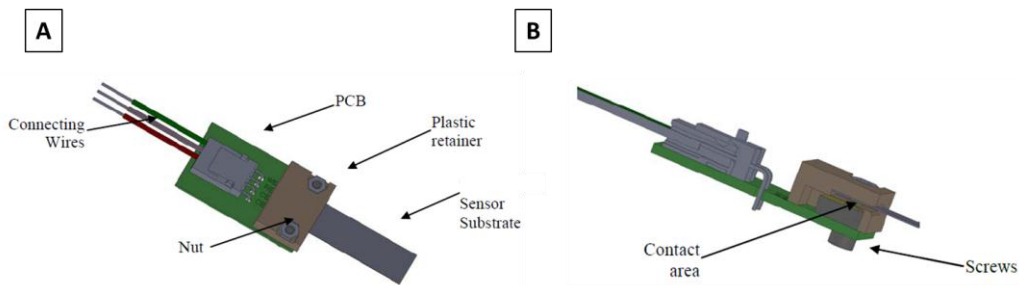


Figure E.26 (A) Connector 3D CAD top view. (B) Connector 3D CAD section view.

Finally, to verify the operation of the EIS measurement and data processing implemented in the instrument to produce the correct and expected results, a software simulation of the EIS results for an electrochemical cell assembled using a network of standard electronic components was created. For the network shown in the simulated network above (Figure E.27A) modelling an electrochemical cell we produced a complex Nyquist plot of the EIS response over several decades of frequency range.

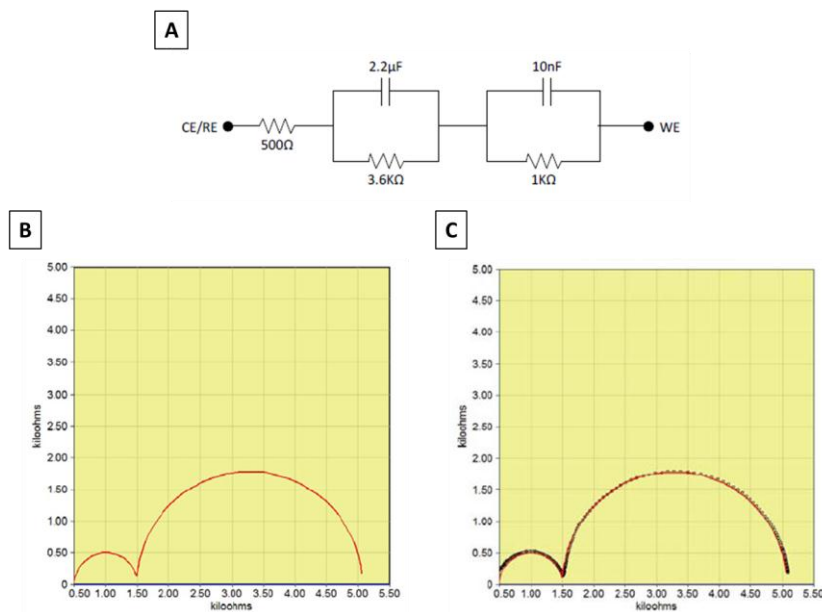


Figure E.27 (A) Simulated network. (B), (C), Nyquist plot of the simulated response (B) and the overlaid response (C).

We then construct a physical circuit using real components with the best tolerance available having the same component values. The simulated data and the real measured data are overlaid on the same plot to observe any difference as shown in Figure E.27C.

The data processing was specified and implemented on the instrument. Testing and evaluation of the instrument relative to simulated models of electrochemical cells created from a network of standard electronic components shown that the data processing performed was the one expected.

Also, the design of the interface was developed and was influenced by the now common concepts in use daily on consumer devices such as tablet computers and smart phones. These devices use a touch screen with an emphasis on finger control via a set of gestures. The current instrument hardware display design supported touch screen technology utilising a resistive method. This supported single touch only, so an interface using advanced multi-touch gestures was not possible. An interface using a reduced gesture set was developed with simple, but intuitive interaction.

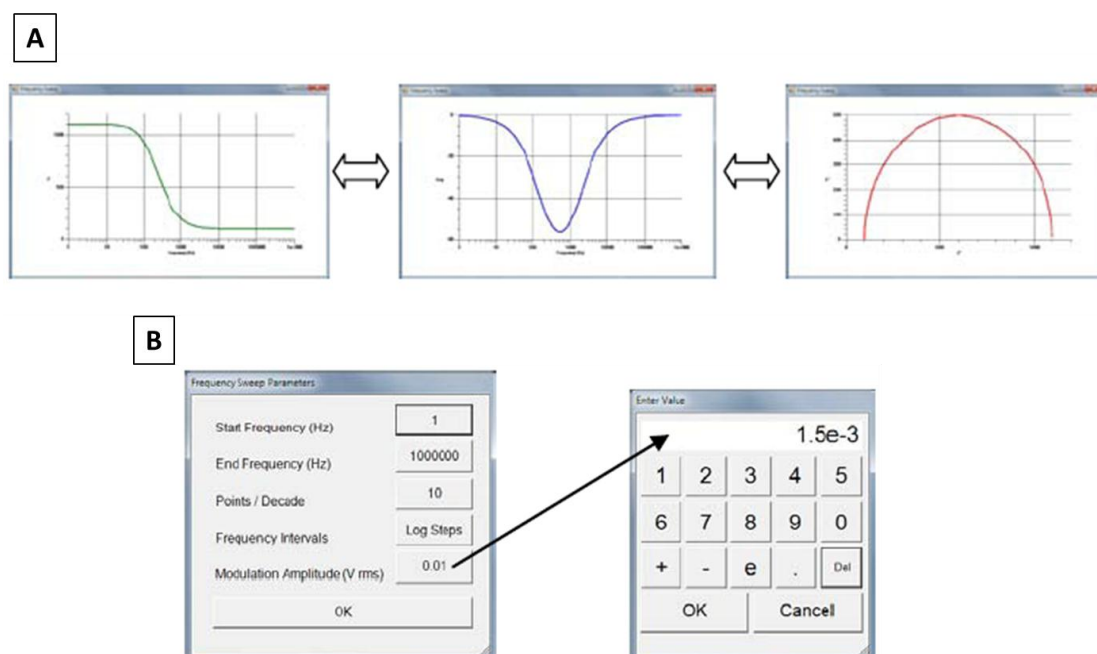


Figure E.28 (A) Software interaction. (B) Complex numerical entry.

The system displayed a typical line graph of impedance magnitude vs. frequency, the user swiped the display from left to right by placing a finger on the display, then moving it horizontally. The display scrolls to the next “page” showing a graph of impedance phase angle vs. frequency. A second swipe moves the display to the third page showing a graph of complex impedance. The interaction would loop round if the user continued swiping left to right or would operate in the reverse order if the user swiped right to left (Figure E.28A)

A second issue with this type of interface was the requirement for the user to be able to enter complex numerical values including scientific exponential formats. To address this issue a pop-up control was developed which was launched whenever the user needs to change a numerical value. The control features large buttons easily operable by a finger-tip, and controls to enter a full range of numerical values (Figure E.28B)

The BOND platform components had successfully integrated and assembled together to comprise the whole system. The major components which were integrated are represented in Figure E.29: i) data acquisition and processing hardware, (ii) electromechanical interface, (iii) amplifier, (iv) nano-transducer, (v) data processing software and user-friendly interface.

The BOND platform was validated through two different major tests. First, the nanobiosensors were validated for “boar taint” detection: the preliminary tests of androstenone showed that was specifically detected by olfactory receptors immobilized on the nanotransducers. And, secondly the performance of the nanobiosensors was assessed with the portable analyser. The instrument was tested with the nano-transducers in defined electrochemical conditions (Figure E.30). Cyclic voltammetry experiments were run for the variants disc array device (Figure E.30A) and band array device (Figure E.30B) of the transducer for verification.

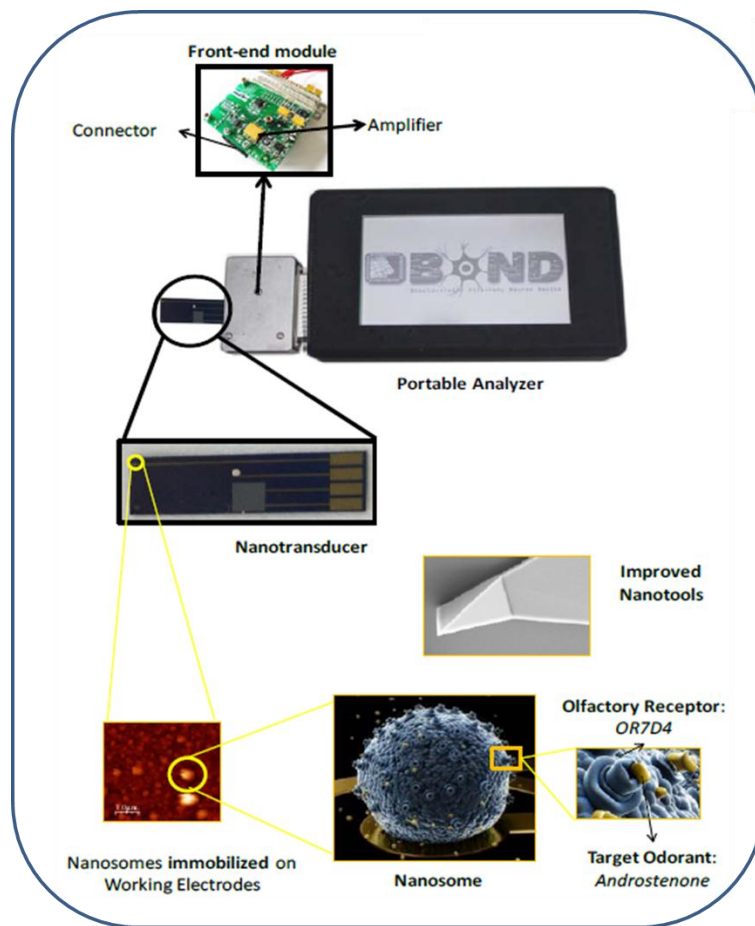


Figure E.29 Representation of the integration of the main components of the BOND analytical platform.

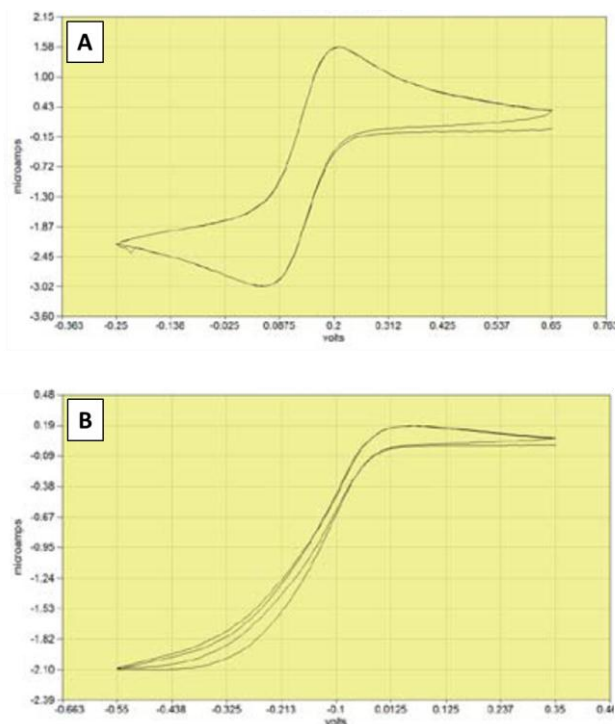


Figure E.30 Cyclic voltammetry (current vs potential) tests of the final prototypes of the nanatransducers. Disk array (A) and band array (B) variants of the transducers were tested.

E.4 My contribution

This thesis was carried out within the context of the BOND European Project coordinated by Prof. Dr. Josep Samitier. The studies done during the four year thesis were integrated into the BOND consortium, a multidisciplinary group of people with expertise in different scientific areas. This thesis was based on basic science research. Its goal was getting results and experiences in order to design and test theories and hypotheses and laws to get a basis for application-oriented knowledge. Thus, the well-study of the natural nanovesicles carrying olfactory receptors contribute directly in the development of the BOND biosensing platform.

E.5 References

- (1) Bally, M., Bailey, K., Sugihara, K., Grieshaber, D., Vörös, Städler, B. *Small*, **2010**, 6, 2481.
- (2) Ramachandran, N., Srivastava, S., LaBaer, J. *Proteomics Clin. Appl.*, **2008**, 2, 1444.
- (3) Blatter, T., Huwiler, C., Ochsner, M., Stadler, B., Solak, H., Vörös, J., Grandin, H.M. *J. Nanosci. Nanotechnol.*, **2006**, 6, 2237.
- (4) Mele, E., Pisignano, D. *Prog. Mol. Subcell. Biol.*, **2009**, 47, 341.
- (5) Delamarche, E., Juncker, D., Schmid, H. *Adv. Mater.*, **2005**, 17, 2911.
- (6) Dittrich, P. S., Manz, A. *Nat. Rev. Drug Discovery*, **2006**, 5, 210.
- (7) Stamou, D., Duschl, C., Delamarche, E., Vogel, H. *Angew. Chem., Int. Ed.*, **2003**, 42, 5580.
- (8) Lindsay, M.A. *Nat. Rev. Drug Discov.*, **2003**, 2, 831.
- (9) Lundstrom, K. *J. Cell. Mol. Med.*, **2007**, 11, 224.
- (10) Probert, C.S.J., Ahmed, I., Khalid, T., Johnson E., Smith, S., Ratcliffe, N. *Volatile Organic Compounds as Diagnostic Biomarkers in Gastrointestinal and Liver Diseases. Revs.*, 337-343.
- (11) Jantus-Lewintre, E., Usó, M., Sanmartín, E., Camps, C. *Lung Cancer: Targets and Therapy. Review*. **2012**, 3, 21-29.
- (12) Alasconi, M., Concina, I., Gobbi, E., Sberveglieri, V., Pulvirenti, A., Sberveglieri, G. *Int. J. Electrochem.* **2012**, 1-12.

Appendix 1. HPLC chromatograms

A1.1 c-myc peptide characterization

Two different modified c-myc peptides (Peptide EQKLISEEDL-Cys was called C₁, and peptide Cys-EQKLISEEDL was called C₂) were presented in *Chapter 2* and were synthesized as C-terminal amides of using standard Fmoc solid phase protocols by the Platform of Peptide Synthesis CIBER BBN Biomedicine Scientific Services (<http://www.ciber-bbn.es>). The two peptides were characterized by mass spectrometry by the same platform, and purities were >94% as assessed by HPLC. In the following graphs are presented the HPLC chromatograms for the purity analysis.

- For EQKLISEEDL-Cys (c-myc peptide C₁):

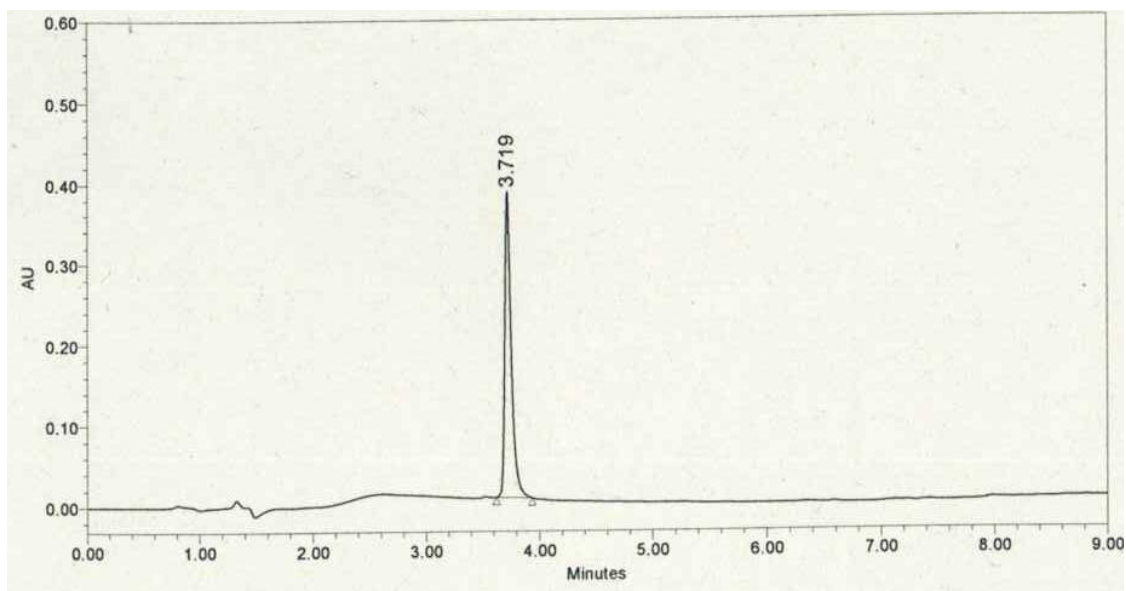


Figure A1.1 Auto-Scaled Chromatogram from c-myc peptide (C₁). The % area at the real time 3.719 min was 100% (peptide).

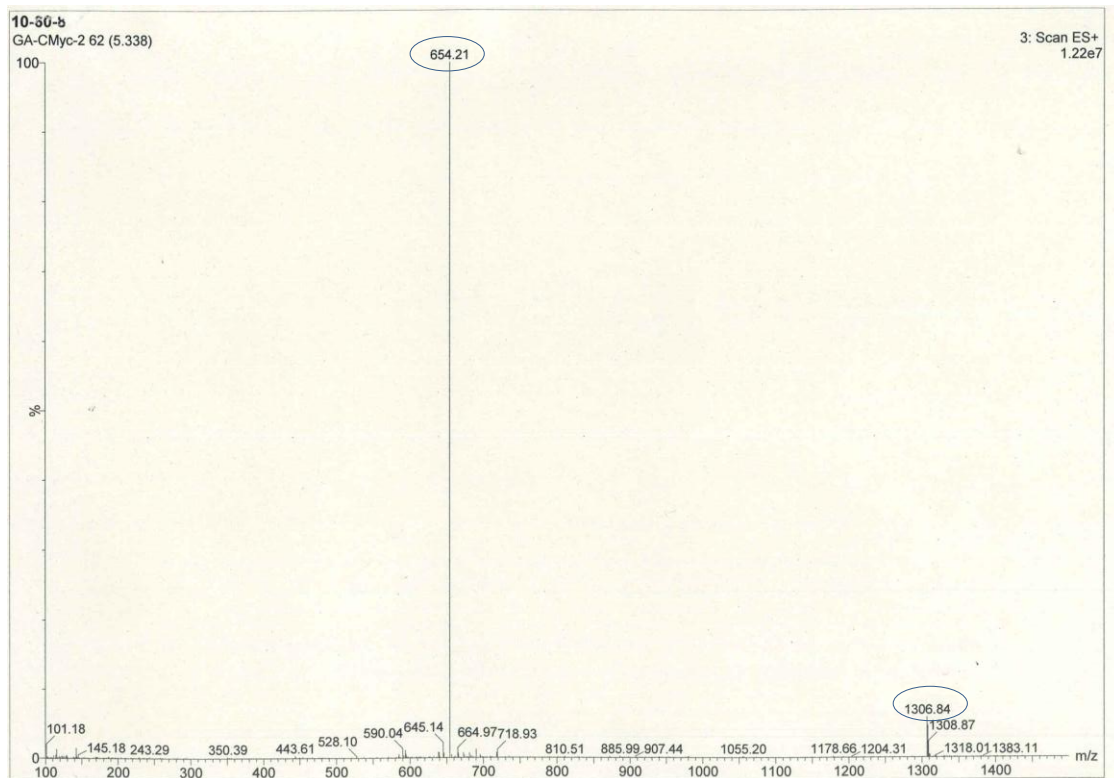


Figure A1.2 HPLC-MS chromatogram from C_1 peptide. In blue are highlighted the characteristics peaks of the peptide. Considering the molecular weight of the C_1 peptide as 1306.44 Da we can observe the peaks corresponding to $M^+ + 1 = 1306.84$ and $M^+ + 2/2 = 654.21$.

- For Cys-EQKLISEEDL (c-myc peptide C_2):

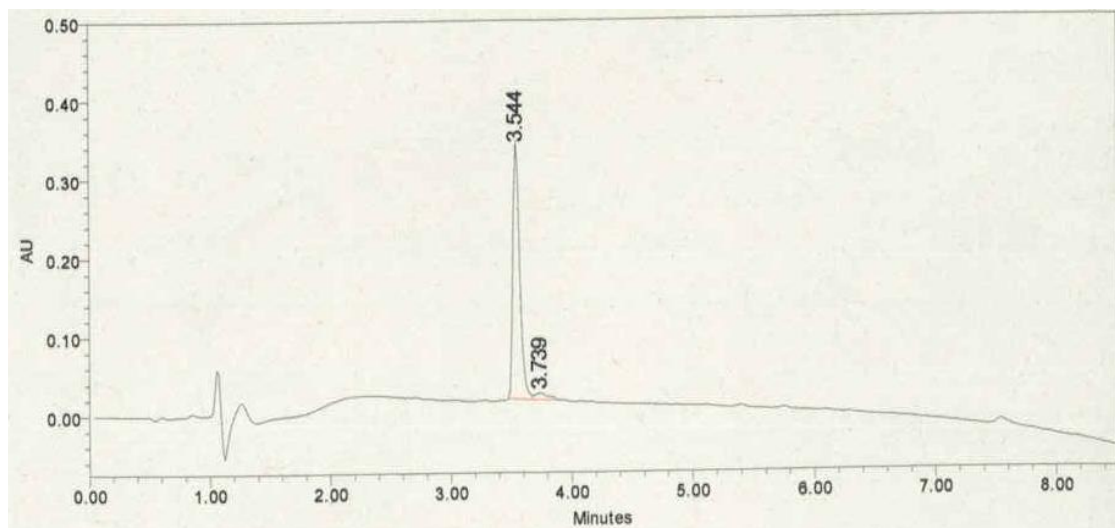


Figure A1.3 Auto-Scaled Chromatogram from c-myc peptide (C_2). The % area at the real time 3.544 min was 94.84% (peptide) and at real time 3.739 the area was 5.16% (impurities).

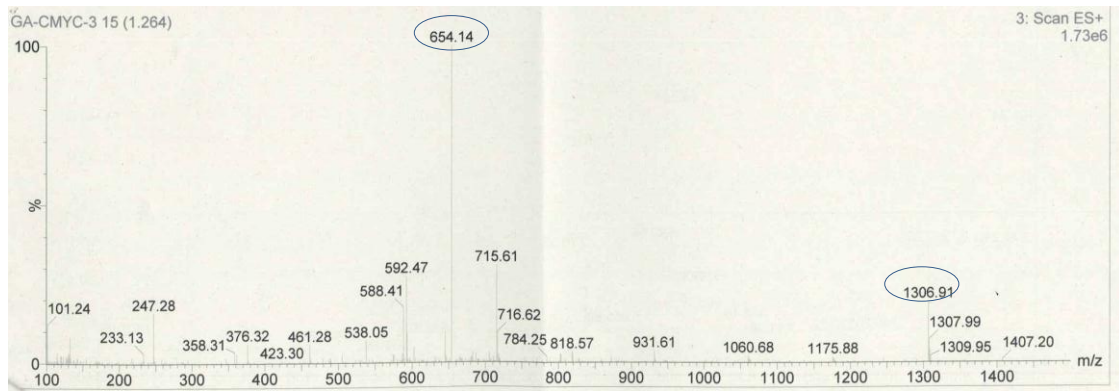
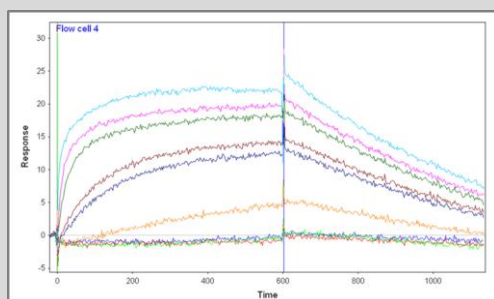


Figure A1.4 HPLC-MS chromatogram from C₂ peptide. In blue are highlighted the characteristic peaks of the peptide. Considering the molecular weight of the C₂ peptide as 1306.44 Da we can observe the peaks corresponding to $M^+ + 1 = 1306.91$ and $M^+ + 2/2 = 654.14$.

Appendix 2. Characterization of c-myc/anti-c-myc interactions using Biacore T100.



A Biacore T100 technology has been used in conjunction with a van't Hoff analysis to characterize the kinetics and the thermodynamic binding of two anti-c-myc antibodies, a commercial one (Ab9E10) and another one produce in our lab (Ab894D12_{f7f9}) directed against the c-myc peptide when they are immobilized onto a surface. The characterization of these two complexes shows the differences that exist between the two mAb and their possible optimal applications.

A2.1 Background

Biacore T100 is a surface plasmon resonance (SPR)-based biosensor technology widely used in the study of the antigen/antibody interactions because the studies are performed in real-time and without the use of labels. These studies require multiple sequential injections of analyte at different concentrations and sometimes at different temperatures and are time-consuming. Thus, an automatic procedure simplifies the analysis¹. In addition, the key component in this instrument is the flow cell. Pairs of flow cells in the T100 are connected within the same plane and form U-shaped flow paths². The most important point is that this design shortens the distance between a reaction and the reference surface providing better referencing (Figure A2.1, for more theoretical details please see *Chapter 4*). The determination of biomolecular interaction kinetics is perhaps the most characteristic application for Biacore systems.

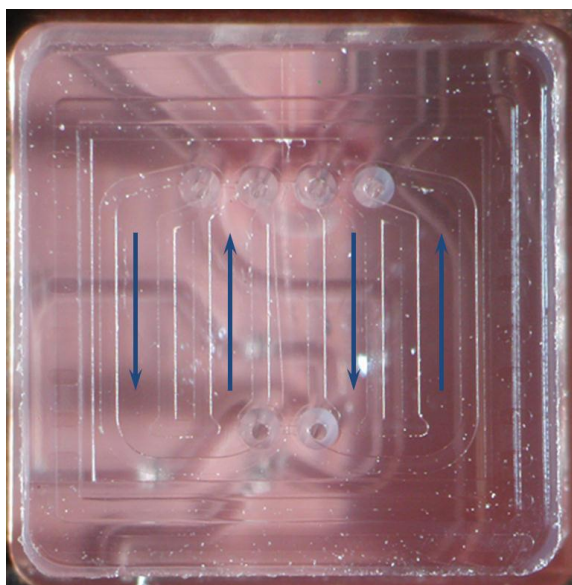


Figure A2.1 Biacore T100 flow cell. Four flow cells (dark blue arrows) are connected in pairs creating two U-shaped flow paths.

Interaction kinetics describes the relation between species defined by non-covalent bindings and/or conformational changes of the molecules involved. In our case, we will study the interaction kinetics between antigens and antibodies. The binding of antigen/antibody takes place by the formation of multiple noncovalent bonds between the antigen and the amino acids of the binding site. It is produced by

summation of the attractive and repulsive forces (van der Waals interactions, hydrogen bonds, salt bridges and hydrophobic force)³.

The simplest interaction is defined as Eq.1:



where A is the analyte (antigen) and B is the ligand immobilized on the sensor surface^{4,5,6}. The analyte in solution will pass over the ligand-surface via the integrated microfluidic system presented above.

Basically, interaction kinetics can be defined by three distinct phases. The association (k_a), when antigen-antibody bind to each other; the steady state, when the amount of antigen that is binding is equal to the amount of bonds that are breaking; and the dissociation (k_d), when the breaking bonds between antigen-antibody take place⁷ (Figure A2.2).

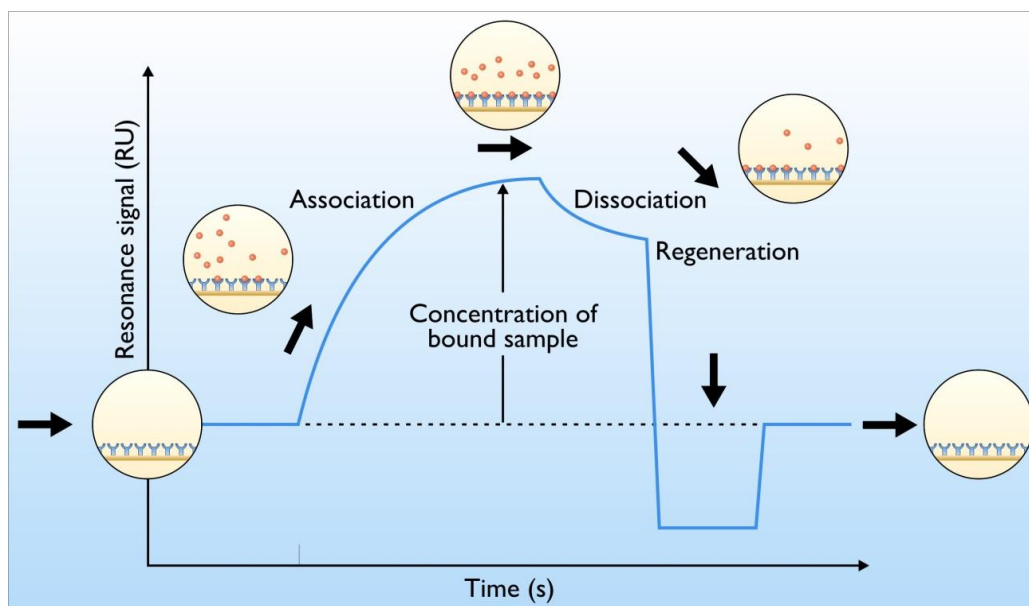


Figure A2.2 Representation of an SPR measurement (sensorgram) showing the steps of an analysis cycle. First, the buffer is in contact with the sensor surface (baseline); then the sample solution is injected (association); after, the buffer is injected (dissociation) and finally, the bounded antigen is remove from the surface during injection of regeneration solutions (regeneration) followed by a new analysis cycle.⁸

Although and IgG antibody has two binding sites, when the antibody density immobilized onto the sensor surface is low, the IgGs are considered to have one

effective site (Figure A2.3). If in addition to this, we analyse the interaction with monovalent analytes, it is possible to work with the simplest model presented above. The kinetic rate constants were determined by fitting the SPR responses to a simple 1:1 (Langmuir) binding model, model equivalent to the Langmuir isotherm for adsorption to a surface. In 1916, Irving Langmuir developed the Langmuir isotherm, a model that describes the dependence of the surface coverage of an adsorbed gas on the pressure of the gas above the surface at a fixed temperature^{9,10}. The equilibrium that exists between gas adsorbed on a surface and molecules in the gas phase is a dynamic state. The equilibrium represents a state in which the rate of adsorption of molecules onto the surface is exactly the rate of desorption of molecules back into the gas phase. It should therefore be possible to derive an isotherm for the adsorption process simply by considering and equating the rates for these two processes.

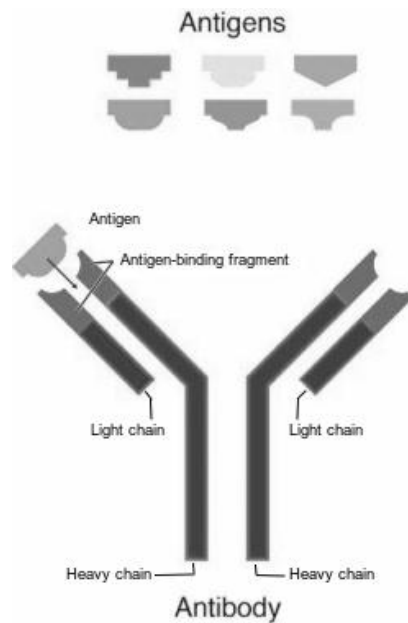


Figure A2.3 An antibody or immunoglobulin (Ig) is a Y-shaped molecule. The antigen-binding site is the area of the antibody that recognizes and binds to the antigen. *Image adapted from: Darryl Leja, NHGRI.*

Furthermore, for antigen/antibody complexes equilibrium is reached when the rates of the association and dissociation reactions are equal. Thus, the equilibrium association and dissociation constants (K_A and K_D) represents the affinity of an interaction and in the simplest example presented above are defined as Eq. 2:

$$K_D = \frac{[A][B]}{[AB]} = \frac{k_d}{k_a} = \frac{1}{K_A} \quad (\text{Eq. 2})$$

where [A], [B] and [AB] denote the molar concentrations of antigen, ligand (antibody) and complex.

The rate constants and equilibrium constants of biomolecular interactions provide information on the strength of association and the tendency of dissociation. For example, the dissociation rate constant (k_d , also called “off rate”) determines how fast the antigen dissociates from the antigen/antibody complex. Another value to describe this phenomenon is the antigen/antibody complex half-life ($t_{1/2}$). A high $t_{1/2}$ indicates an antibody as binder with high antigen complex stability. In addition, stability of AB is defined also by K_D , high K_D , low stability of the complex, lower affinity to associate (low K_A).

Furthermore, equilibrium constants can be directly correlated with thermodynamic values due to the Gibbs’ equation¹¹ (Eq.3). The ΔG° represents a balance between enthalpic (ΔH°) and entropic (ΔS°) forces. The binding of a ligand to a target protein is normally driven by the decrease in the free energy of the protein-ligand complex compared to the free energy of both the ligand and the protein existing independently¹².

$$\Delta G^\circ = \Delta H^\circ - T\Delta S^\circ \quad (\text{Eq. 3})$$

The energy of formation (ΔG°) and an antigen-antibody complex is given by Eq. 4,

$$\Delta G^\circ = -RT \ln K_A \quad (\text{Eq. 4})$$

where R is the gas constant and T the temperature.

ΔG° is defined as ΔH° originates from changes in bond energy during binding whereas ΔS° describes the change in order of the system, both of which, in addition to the water/solvent of the surrounding environment. Considerable number of antigen/antibody interactions are enthalpy-driven, i.e. they make favourable enthalpy changes with some opposition from the negative entropy contribution to association³. In addition, both ΔH° and ΔS° per complex association reactions have a temperature

dependence determined by the change in heat capacity (ΔC_p). Favourable entropy changes in protein-protein interactions commonly arise from desolvation, i.e. the hydrophobic effect. Expulsion of ordered water from the apolar surface upon ligand binding increases the total entropy of the system¹³. To investigate the importance of desolvation, we also determined the heat capacity change (ΔC_p) from the temperature dependence of ΔH for our system (Eq. 5).

$$\Delta C_p = \frac{\Delta H_{T_1} - \Delta H_{T_2}}{T_2 \cdot T_1} = \frac{\Delta S_{T_1} - \Delta S_{T_2}}{\ln\left(\frac{T_2}{T_1}\right)} \quad (\text{Eq. 5})$$

The ability to determine association and dissociations kinetics as well as thermodynamic binding characteristics for antigen/antibody interactions provides detailed insight into the mechanism of complex formation. This information is essential to select the best monoclonal antibody depending on their future application. The specificity and affinity of antibody-antigen interactions can be summarized by the following rate constants, k_d , k_a , K_A , K_D and the thermodynamic parameters ΔG , ΔH , ΔS and ΔC_p .

But to measure rate constants accurately, the experimental design is critical. It is important to consider the following issues:

1. Mass transport limitations have to be considered. This limitation is considered when analyte transported from the bulk analyte solution to the surface is much slower than analyte-ligand association. It can be minimized using low surface binding capacity (maximum analyte binding response no greater than 50 to 150 RU) and high flow rates ($\geq 30 \mu\text{L min}^{-1}$)^{14,15}.
2. Kinetic analysis requires at least data from four to six analyte concentrations.
3. Analytes should be in the same buffer as the running buffer to minimize bulk refractive index differences to avoid the bulk effect.
4. The assay should include series of start-up cycles using running buffer to equilibrate the sensor surface to perform an accurate double-referencing data analysis¹⁶.
5. Analyte should be injected over both a reference surface and an active ligand surface. Reference surfaces are necessary to subtract bulk refractive index

responses from the specific binding signal as well as ensure that there is no nonspecific interaction with the sensor chip surface¹⁶.

The main goal of this *Appendix* is to present the preliminary analysis performed on the characterization of the binding properties of two c-myc antibodies, a commercial one (Ab9E10) and the other produce in our lab (Ab894D12_{FT9}, see *Chapter 2*) against the c-myc peptide. Also, we will compare their binding kinetics (k_a , k_d , K_D and $t_{1/2}$) and their thermodynamic binding (ΔH , ΔS , ΔG and ΔC_p) values. The measurement of the temperature-dependence of antibody binding kinetics generates a unique thermodynamic fingerprint of each antibody/antigen interaction¹⁷. As well, the ionic strength effect of the analysis buffer has been evaluated in both complex bindings.

A2.2 Materials and Experimental Procedures

A2.2.1 Materials

Biochemical reagents such as c-myc peptide (*EQKLISEEDL*), PBS (phosphate buffer saline), thiol solution of SH(CH₂)₁₅COOH (16-MHDA) and SH(CH₂)₁₁OH (11-MUOH), glycine were purchased from Sigma Chemical Co. (St. Louis, MO). The commercial monoclonal anti-c-myc IgG₁ 9E10 antibody was supplied by Roche Diagnostics (Mannheim, Germany). The home-made monoclonal anti-c-myc (Ab894D12₁₇₁₉, 1.44 mg mL⁻¹, *Chapter 2*) was produced and purified by Abyntek Biopharma (Bizcaia, Spain). The monoclonal anti-carcino embryonic antigen CEA antibody (anti-CEA IgG₂) was purchased from Abcam (Cambridge, United Kingdom). The ¹C₁-M(CH₂)₂CO-BSA (BSA protein linked with 1 c-myc peptide) bioconjugate was synthesized in the lab following protocols described in *Chapter 2*. NaOH pellets were obtained from Panreac Química S.A.U. (Barcelona, Spain). The C1 sensor chips and the SIA kit of bare gold chips, the 1-ethyl-3-(3-dimethylaminopropyl)carbodiimide hydrochloride (EDC), the N-hydroxysuccinimide (NHS), and the 1.0 M ethanolamine-HCl pH 8.5 were acquired from GE Healthcare Bio-Sciences AB (Uppsala, Sweden).

A2.2.2 Buffers and Solutions

Buffers used were as follows (always filtered): phosphate-buffered saline (PBS) 10mM at pH 7.5, the PBST buffer contained PBS with 0.05% Tween 20 and the PBT buffer 10 mM of potassium dihydrogen phosphate/disodium hydrogen phosphate at pH 7.5 with 0.05% Tween 20. 10 mM sodium acetate buffer has been adjusted at different pHs: 3.6, 4, 4.41, 5, 5.49 and 6.

A2.2.3 Equipments/Software

The anti-c-myc mAb affinity and thermodynamic experiments were performed on a Biacore T100 instrument, GE Healthcare Bio-Sciences AB.

Concerning the software used: The biosensor data processing and analysis was performed using the software Scrubber2 (BioLogic Software), BIA-evaluation 1.1 (BIAcore software) and the Biacore T200 software for the thermodynamic analysis.

A2.2.4 Thiol self-assembled monolayer (SAM) preparation

Studies were performed at 20°C using Biacore T100 and bare gold Biacore sensor chips (SIA Kit Au chips). Before use, the chips were sonicated for 5 min in UHQ water, then for 5 min in absolute ethanol, then for 5 minutes in piranha solution ($\text{H}_2\text{SO}_4/\text{H}_2\text{O}_2$, 7/3), then for 5 min in UHQ water and finally for 5 min in absolute ethanol. SAMs were prepared by immersion of the SPR sensor chip in the appropriate solution prepared in absolute ethanol: *a*) in 4 mM thiol solution $\text{SH}(\text{CH}_2)_{15}\text{COOH}$ (16-MHDA), *b*) in 4 mM mixed thiol solution $\text{SH}(\text{CH}_2)_{15}\text{COOH}$ (16-MHDA)/ $\text{SH}(\text{CH}_2)_{11}\text{OH}$ (11-MUOH) (3:7) and *c*) in 4 mM mixed thiol solution 16-MHDA/11-MUOH (1:9); for 16-20 hours at 4°C to obtain a uniform SAM surface coverage. Then the substrates were rinsed with absolute ethanol in order to remove physisorbed molecules, dried under a nitrogen stream and immediately used.

A2.2.5 Ligand immobilization

A2.2.5.1 Pre-concentration analysis: determining the ligand (antibody) concentration for optimal immobilization

10 mM sodium acetate buffer has been used to perform the pH study. The pH range is chosen to be below the estimated isoelectric point (pI) of the antibody. In our case, the pre-concentration was done at 6 different pHs in the range between 3.6-6. Then, the two anti-c-myc antibodies (Ab9E10 and Ab894D12_{t7f9}) and the anti-carcinoma embryonic antigen CEA antibody (anti-CEA, used as control) were diluted in the 10 mM buffer solutions prepared at several pH values at the concentration of 30 $\mu\text{g mL}^{-1}$. Then, the solutions were flown through the inactivated $-\text{COOH}$ functionalized gold sensor chip surface. The study was performed in a Biacore T100 instrument. The injection time was 60 s at the flow rate of 10 $\mu\text{L min}^{-1}$. The washing step was done with NaOH 50 mM for 60 s at 10 $\mu\text{L min}^{-1}$.

A2.2.5.2 Antibody immobilization

Immobilization procedures were performed using PBS buffer as running buffer. The buffer was vacuum filtered and degassed immediately prior to use. Antibody surfaces were prepared using amine-coupling chemistry at a flow rate of $15 \mu\text{L min}^{-1}$. EDC/NHS (0.4M/0.1M; 1:1) was injected for 20 min at $15 \mu\text{L min}^{-1}$ to activate the sensor chip surface, $30 \mu\text{g mL}^{-1}$ antibody (dissolved in 10 mM sodium acetate, pH 5.49) was injected for 20 min at $5 \mu\text{L min}^{-1}$, and finally ethanolamine (1M, pH 8.2) was injected for 20 min at $15 \mu\text{L min}^{-1}$ to block residual activated groups. This immobilization procedure yielded at different resonance units (RU) of immobilized antibody depending on the SAM-functionalized surface (see above). For 16-MHDA SAM was between 2000 to 4000 RU, for the mixed SAM 16-MHDA/11-MUOH (3:7) was between 1400 to 1900 RU and finally, for the mixed SAM 16-MHDA/11-MUOH (1:9) was between 200 to 900 RU. Each antibody (Ab9E10, Ab894D12_{F719}, and anti-CEA) was captured on individual flow cell, the fourth flow cell was left free to serve as a reference following activation and blocking on each chip in the absence of mAb immobilization. After immobilization, the instrument was primed extensively with the analysis running buffer, at least with 4 start-ups, in order to stabilize the electrode surface. The analysis running buffer was PBST (PBS pH 7.4 with 0.05% Tween 20).

A2.2.6 Binding measurements

For each Biacore kinetic experiment, a series of six to nine antigen (c-myc peptide or $^1\text{C}_1\text{-M}(\text{CH}_2)_2\text{CO-BSA}$ bioconjugate, see *Chapter 2*) concentrations were prepared in the analysis running buffer (PBST). Then, they were injected two or 4 times from more diluted to more concentrate concentration as in random order for 10 min at $30 \mu\text{L min}^{-1}$ followed by 10 min of dissociation (all data obtained at 20 °C). All covalent surfaces were regenerated with one 120-s pulse of 10 mM glycine-HCl (pH 2.2). Sometimes the binding measurements were performed in the same functionalized sensor chip and other times onto a new one with the same amount (RU) of antibodies immobilized on it.

A2.2.7 Experiments on C1 sensor chip

First, the four-channel sensor chip C1 was primed with running buffer which was previously degassed and vacuum filtered. The surface of the chip was washed with two injections of 0.1 M glycine–NaOH, pH 12, containing 0.3% v/v Triton X-100, at $100 \mu\text{L min}^{-1}$ for 60 s followed by a prime run with running buffer to remove the Triton X-100. The sensor surface was activated by treating with a mixture of EDC/NHS (0.4M/0.1M; 1:1) injected for 7 min at $15 \mu\text{L min}^{-1}$, $30 \mu\text{g mL}^{-1}$ antibody (dissolved in 10 mM acetate buffer, pH 4.5) was injected for 10 min at $5 \mu\text{L min}^{-1}$, and finally ethanolamine (1M, pH 8.2) was injected for 7 min at $15 \mu\text{L min}^{-1}$.

A2.2.7.1 Effect of the ionic strength

For the ionic strength Biacore kinetic experiment, a series of four c-myc peptide concentrations ($0.1, 1, 5, 10 \mu\text{g mL}^{-1}$) were prepared in the analysis running buffer (PBT with 300 mM of NaCl) and injected for 400 s at $30 \mu\text{L min}^{-1}$ followed by 10 min of dissociation (all data obtained at 20 °C). All covalent surfaces were regenerated with one 120-s pulse of 10 mM glycine-HCl (pH 2.2).

A2.2.7.2 Temperature analysis

At each temperature, three buffer blanks were first injected to equilibrate the instrument fully. Using a flow rate of $30 \mu\text{L min}^{-1}$, c-myc peptide was injected for 400 s and dissociation was monitored for 10 min. (The selected injection and dissociation times were determined in the previous ion strength-dependent study). For the bound complexes, a regeneration step was required as has been explained above. The c-myc peptide was studied in a narrow temperature range: 12, 20, 24, 30 °C at four different concentrations: $0.1, 1, 5, 10 \mu\text{g mL}^{-1}$.

A2.2.8 Processing antigen binding data

Changes in the SPR angle, given in response units, are proportional to the amount of material in the immediate vicinity of the sensor chip surface. As solutions of

an analyte are passed over the surface, the affinity and kinetics of the binding event can be calculated from analysis of the resultant binding curve. Biacore sensorgrams were processed using Scrubber software (version 2.0) or BIAevaluation software (1.1). Both buffer and antigen binding responses were first zeroed on the y axis and aligned on the x axis at the beginning of the antigen injection. Data from the reference flow cell (anti-CEA mAb immobilized on it) was subtracted to remove systematic artefacts (bulk refractive index changes and unspecific adsorption) that occurred in all the rest of the flow cells. Each antigen response was then double-referenced (see *Chapter 4*) by subtracting the buffer response collected in the same binding cycle. This means that the average response of all blank injections was subtracted from all antigen and blank sensorgrams.

A2.2.9 Kinetic analysis from antigen binding data

Biosensor data, processed and analysed using Scrubber 2 or BIAevaluation 1.1, was fit to a simple “Langmuir 1:1” model ($A+B=AB$). Where A corresponds to the analyte and B to the ligand. These softwares allow us to estimate the corresponding k_a and k_b from the processed data sets. Affinities (K_D) were then calculated from the quotient of the rate constants (k_d/k_a).

A2.2.10 Thermodynamic analysis from antigen binding data

Biosensor data, processed and analysed by Biacore T200 software, was fit to obtain an automatic generation of Eyring and van't Hoff plots from kinetic data in order to calculate the thermodynamic parameters (ΔH° , ΔS° , ΔC_p and ΔG°).

Two different models were used to fit the temperature dependence of the equilibrium and rate constants for c-myc/anti-c-myc interaction. In the first model, the enthalpy (ΔH°) is assumed to be constant over the temperature interval of the experiment (i.e. $\Delta C_p=0$). This, results in linear van't Hoff and Eyring equations. Van't Hoff plots were fit to Equation 6:

$$\ln K_{eq} = -\frac{\Delta H^\circ}{RT} + \frac{\Delta S^\circ}{R} \quad (Eq. 6)$$

The second model, the enthalpy is not assumed to be temperature-independent (i.e. $\Delta C_p \neq 0$). The resulting non-linear van't Hoff plots were fit to Equation 7 where T_0 is an arbitrary reference temperature (typically 298 K); ΔH° is the standard enthalpy; ΔC_p is the change in heat capacity at constant pressure; and ΔS° is the standard entropy.

$$\Delta G = \Delta H_{T_0} - T\Delta S_{T_0} + \Delta C(T - T_0) - T\Delta C \ln\left(\frac{T}{T_0}\right) \quad (Eq. 7)$$

Standard free energy (ΔG°) values were calculated by one of the two methods. Because the region of the van't Hoff and Eyring curves being fit do not contain the 298 K data point, ΔG° was calculated using Equation 8¹¹.

$$\Delta G^\circ = \Delta H^\circ - T\Delta S^\circ \quad (Eq. 8)$$

A2.3 Results and Discussion

A2.3.1 pH determination for optimal antibody immobilization

Exist different ways to immobilize antibodies to a sensor surface. The most commonly use working with a $-\text{COOH}$ terminated functionalized surface is by the amine coupling chemistry where the antibody is covalently attached to the sensor chip surface. With this method, the sensor chip surface is first activated (with EDC/NHS mixture) giving reactive succinimide esters. Then, the antibody is passed over the surface and the esters groups react with the amino groups to link the antibody covalently to the surface. After, ethanolamine is passed over the sensor surface to deactivate the remaining active esters (Figure A2.4).

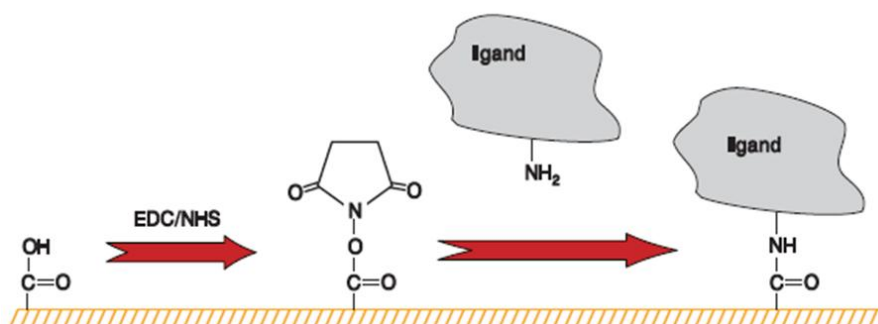


Figure A2.4 Amine coupling of ligands to the sensor chip surface¹⁸.

To determine the optimum buffer pH to perform the appropriate antibody immobilization a pH-scouting analysis was firstly done (also called a pre-concentration analysis). The antibody passed over the inactivated surface at different pH: 3.6, 4, 4.41, 5, 5.49 and 6. The main mechanism for this concentration process is based in the electrostatic attraction of the antibody to the surface. The $-\text{COOH}$ terminated functionalized gold sensor chip carries a net negative charge at pH values above 3.5¹⁹. Then, the pH of the immobilization buffer should be higher than 3.5 and lower than the isoelectric point of the antibody in order to obtain an efficient pre-concentration. It is reported that the isoelectric point (pI) of IgG antibodies is found in the range of 6.4 to 9.0¹⁹ and at pHs below the pI, the antibody will carry a net positive charge.

In our study, where we want to study the affinity of two different anti-c-myc antibodies when are immobilized onto a SAM functionalized surface; three different

antibodies were immobilized, the commercial monoclonal anti-c-myc (9E10), the home-made monoclonal anti-c-myc (Ab894D12_{T779}), and the monoclonal anti-CEA used as control antibody (to remove the unspecific interactions).

First, the three antibodies were diluted in sodium acetate buffer at different pH (mentioned above) to a final concentration of $30 \mu\text{g mL}^{-1}$ and were passed over the inactivated $-\text{COOH}$ sensor chip (16-MHDA SAM). A maximum adsorption level of the antibodies was observed at the optimal buffer pH. Also, reference buffers without antibody were also injected in an independent flow cell to correct the buffer effects because SPR-signal was sensitive to mass adsorption and to buffer changes (refractive index).

As it is shown in Figure A2.5 we observed an optimum antibody adsorption with 10 mM sodium acetate buffer at pH 5.49 for all antibodies. However, they showed different adsorption behaviour. It is important to consider this fact for the antibody immobilization process. The immobilization time must be adjusted for each antibody to obtain the same adsorption level (RU) for all the antibodies. Then, the optimal adsorption buffer was used for the covalent immobilization protocols of the different antibodies.

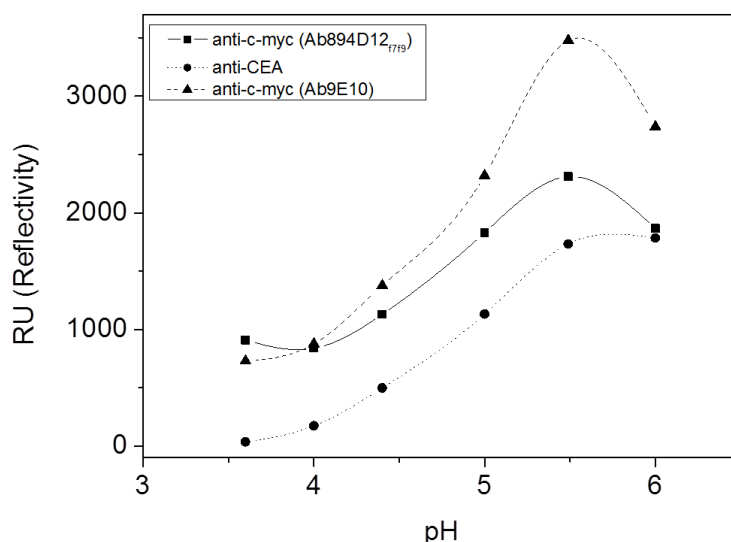


Figure A2.5 Pre-concentration experiments of anti-c-myc antibodies and anti-CEA using SPR. The relative adsorption signals (expressed RU, Reflectivity) for the different antibody are plotted versus the buffer pHs used during electrostatic concentration of the antibody.

A2.3.2 Random covalent antibody immobilization

The antibody immobilization on the different thiol layers: *a)* 100% 16-MHDA, *b)* 70% 11-MUOH and 30% 16-MHDA and *c)* 90% 11-MUOH and 10% 16-MHDA; via the random covalent coupling procedure was monitored using the Biacore instrument (Figure A2.6).

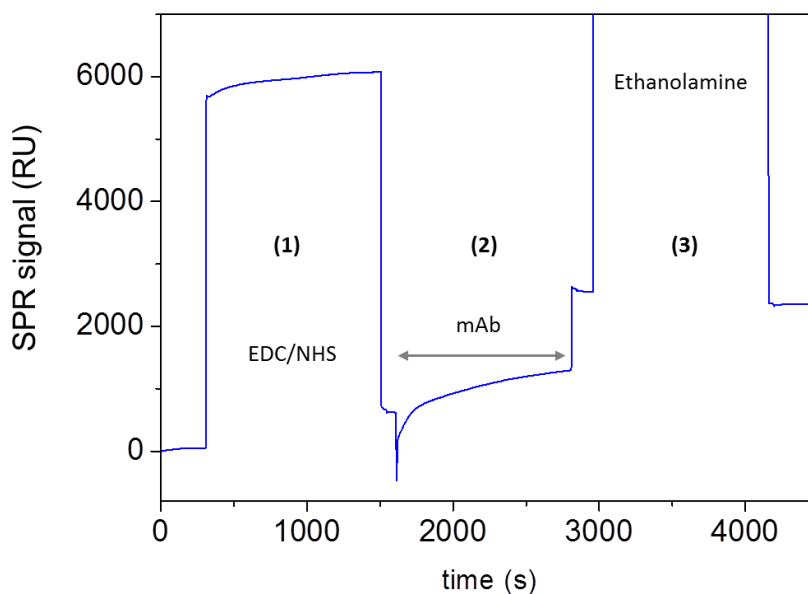


Figure A2.6 SPR sensorgram of a random covalent antibody immobilization on a thiol SAM: (1) activation of the surface using EDC/NHS mixture, (2) injection of the antibody, (3) deactivation of the surface using ethanolamine.

We mention random immobilization because the antibodies attach to the sensor surface via their lysine residues ($-\text{NH}_2$ groups) to the surface activated COOH-groups (NHS-esters, see Figure A2.7). This, results in a random orientation where the antigen binding sites can be towards the surface, resulting in non-accessible bioreceptor molecules, or against the surface.

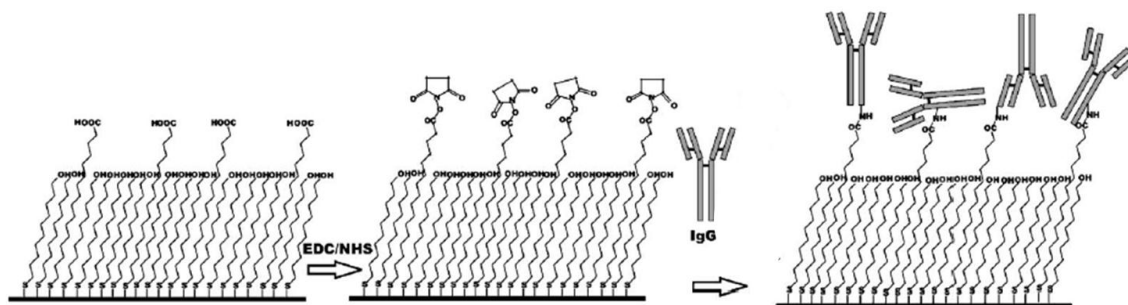


Figure A2.7 Random (via the $-\text{NH}_2$ groups) covalent antibody coupling procedure on an EDC/NHS activated mixed thiol layer (5% 16-MHA and 95% 11-MUOH)²⁰.

Table A2.1 shows the RU immobilization values of the antibodies obtained in the three different self-assembled monolayers. As it was expected, when the number of active sites is lower, the immobilization SPR level decreases.

Table A2.1 Observed SPR immobilization levels (RU) of the antibodies on the different SAMs.

SAM functionalized surface	Immobilization level (RU) ^a
100% 16-MHDA	2945 ± 772
70% 11-MUOH – 30% 16-MHDA	1606 ± 242
90% 11-MUOH – 10% 16-MHDA	563 ± 339

^a Average values of minimum 3 measurements (considering all the three antibodies).

A2.3.3 Evaluation of the c-myc binding on the immobilized antibody

Two antigens have been used to study the anti-c-myc antibody affinities, the c-myc peptide and the $^1\text{C}_1\text{-M}(\text{CH}_2)_2\text{CO-BSA}$ bioconjugate. C-myc peptide has chosen to be the simplest antigen model and the $^1\text{C}_1\text{-M}(\text{CH}_2)_2\text{CO-BSA}$ bioconjugate because mimic better the configuration that the c-myc peptide has when is attached to the olfactory receptors (see *Chapter 2*). In addition, the ratio of c-myc peptides:bioconjugate is 1:1, which also simplify the model.

First, the binding tests were performed with the c-myc peptide as antigen in a random anti-c-myc immobilization 16-MHDA functionalized gold surface. In order to evaluate if the c-myc behaviour had any impact in the antibody affinity the study follows using the $^1\text{C}_1\text{-M}(\text{CH}_2)_2\text{CO-BSA}$ bioconjugate as antigen. Finally, three different SAMs (presents above) have been used to study the effect of the low-density antibody on the surface in the affinity constants between the two anti-c-myc antibodies: the commercial one (Ab9E10) and the home-made (Ab894D12_{17f9}). An example of a binding test is shown in Figure A2.8. It is obtained after a double-reference subtraction (see *Chapter 4*)¹⁶. In this case, the c-myc was injected over the three different antibody surfaces (different flow cells) at nine different concentrations (from 798 pM to 399 μM). Each concentration was tested in duplicate (or depending on the experiment in triplicate).

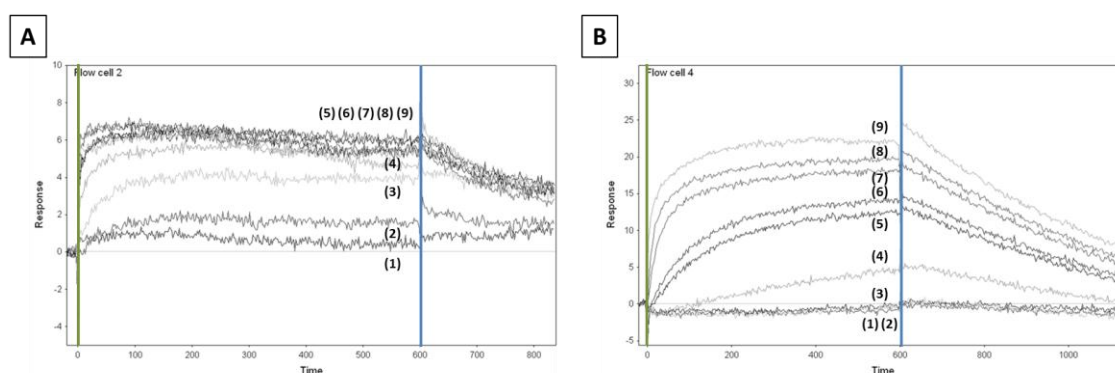


Figure A2.8 c-myc peptide response (RU) test. Antigen binding responses were done at a wide range of c-myc concentrations (in this example: (1) 798 pM, (2) 7.98 nM, (3) 79.8 nM, (4) 798 nM, (5) 3.99 μM , (6) 7.98 μM , (7) 39.9 μM , (8) 79.8 μM , (9) 399 μM). Green line refers to the injection point and the blue line determines the end of the injection point. **(A)** c-myc peptide was injected over the home-made anti-c-myc antibody (Ab894D12_{17f9}). **(B)** c-myc peptide was injected over the commercial anti-c-myc antibody (Ab9E10).

A2.3.4 Interpretation of binding kinetics

The antigen binding data was fit to a simple interaction model ($A + B = AB$)²¹. It is clear from a visual inspection of the antigen binding profiles that the two anti-c-myc antibodies have different binding kinetics (Figure A2.9). This is an example of a simple Langmuir 1:1 fitting from antigen/antibody interaction from our system.

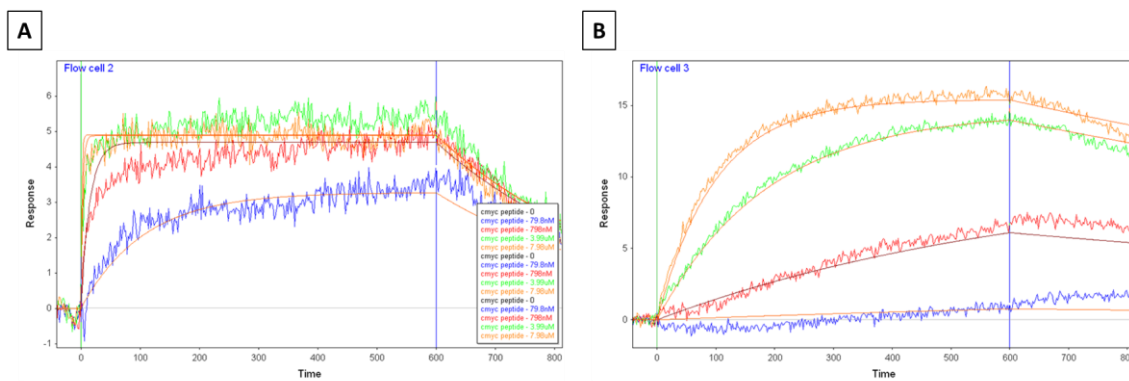


Figure A2.9 Example of biacore data of c-myc antigen binding to mAb amine coupled to a 16-MHDA functionalized gold sensor chip. Straight red lines correspond to a Langmuir 1:1 fitting. **(A)** Double-referenced sensorgram from a serie of four antigen concentrations (79.8 nM – 3.99 μ M) injected for 10 min with a dissociation followed for 10 min flown onto home-made anti-c-myc (Ab894D12_{f7f9}). **(B)** Double-referenced sensorgram from a serie of four antigen concentrations (79.8 nM – 7.98 μ M) injected for 10 min with a dissociation followed for 10 min flown onto a commercial anti-c-myc (Ab9E10).

The preliminary results obtained for the study of the anti-c-myc antibodies affinity when are immobilized randomly onto a –COOH functionalized sensor chip are presented in Table A2.2. The rate constants from the kinetic analysis of all the experiments are reported.

Analysing the association phases, the k_a constant rate of the interaction Ab894D12_{f7f9} to the c-myc peptide is higher than the c-myc/Ab9E10 k_a , independently to the sensor surface. This means that, the c-myc/Ab894D12_{f7f9} system reach the equilibrium faster than the c-myc/Ab9E10 system and as can be observed in Figure A2.9 the antibody Ab894D12_{f7f9} surface reach the saturation faster.

A hypothesis for the faster saturation of the Ab894D12_{f7f9} can be due to the amount of NH₂- groups in the binding site of the antibody. As has been mentioned before, we worked with an amine coupling chemistry which the antibody is covalently attached to the sensor chip surface through their NH₂- groups to the reactive succinimide esters of the surface. Then, if the Ab894D12_{f7f9} has more NH₂- in the binding site than the Ab9E10 their random immobilization could be affected having more binding sites towards the surface resulting in non-accessible bioreceptor molecules than in the Ab9E10 functionalized surface. However, this assumption cannot be verified since the amino acid sequences of the anti-c-myc antibodies used in this study are not available.

Table A2.2 Affinity and Kinetic constants for antigen-antibody interactions determined on different SAM surfaces.

Binding assay (antigen + antibody)	Surface	Fitting model ^a	n ^b	k_a ($M^{-1} \cdot s^{-1}$)	k_d (s^{-1})	K_D (nM)
c-myc + Ab894D12 _{f7f9}	16-MHDA	1:1	4	$(7.2 \pm 1.3) \cdot 10^4$	$(2.9 \pm 0.4) \cdot 10^{-3}$	(41.8 ± 2.2)
c-myc + Ab9E10			2	$(1.5 \pm 0.4) \cdot 10^3$	$(0.9 \pm 0.6) \cdot 10^{-3}$	$(6.4 \pm 2.1) \cdot 10^2$
c-myc + Ab894D12 _{f7f9}	11-MUOH :16-MHDA (7:3)	1:1	2	$(1.2 \pm 0.3) \cdot 10^6$	$(2.2 \pm 2.1) \cdot 10^{-3}$	(2.3 ± 2)
c-myc + Ab9E10			2	$(2.5 \pm 0.4) \cdot 10^3$	$(8.9 \pm 0.6) \cdot 10^{-4}$	$(3.4 \pm 1.7) \cdot 10^2$
¹ C ₁ -M(CH ₂) ₂ CO-BSA + Ab894D12 _{f7f9}	11-MUOH :16-MHDA (7:3)	1:1	2	*	*	*
¹ C ₁ -M(CH ₂) ₂ CO-BSA + Ab9E10			2	$(2.6 \pm 0.1) \cdot 10^4$	$(2.9 \pm 0.2) \cdot 10^{-4}$	(11.4 ± 0.02)
¹ C ₁ -M(CH ₂) ₂ CO-BSA + Ab894D12 _{f7f9}	11-MUOH :16-MHDA (9:1)	1:1	--	--	--	--
¹ C ₁ -M(CH ₂) ₂ CO-BSA + Ab9E10			1	$2.0 \cdot 10^4$	$4.2 \cdot 10^{-4}$	20.8

^a The data was fit with the simple Langmuir model $1:1^{21}$

^b number of experiments done

* Fitting problems

-- Experiment not done

In addition, both systems dissociate with a similar k_d . But, calculating the half-life of the interaction ($t_{1/2}$), ~ 175 s for c-myc/Ab894D12_{f7f9} complex and ~ 530 s for the c-myc/Ab9E10 complex, we can conclude that c-myc/Ab9E10 complex takes longer time to dissociate. However, although the c-myc/Ab9E10 complex is more stable, the affinity ($K_D = k_d/k_a$) of the monoclonal anti-c-myc Ab894D12_{f7f9} to the free c-myc peptide is lower (high affinity) and allow us to detect lower c-myc concentrations.

Then, we studied the interaction of both anti-c-myc mAb against the ¹C₁-M(CH₂)₂CO-BSA bioconjugate as antigen. The affinity of the c-myc/Ab9E10 complex decreases one order of magnitude when the peptide is attached to a macromolecule instead of being free on the solution (see Table A2.2). This affinity decrease is absolutely independent of the antibody density onto the functionalized gold surface. This result suggested us that Ab9E10 is a promising antibody to be used on the

development of platforms to immobilized c-myc-carriers such as nanovesicles carrying c-myc-olfactory receptors.

Same experiments were done with the Ab894D12_{f7f9} antibody. The data fitting did not adjust to a Langmuir 1:1 model properly. These, could be due to a bioconjugate aggregation or due to the model proposed. We expected to have a 1:1 analyte/antibody interaction, but could be possible that some of the bioconjugates had 2 c-myc/bioconjugate instead of 1 (the ratio of c-myc per bioconjugate was characterized with MALDI-TOF). Then, a bivalent interaction should be performed. Thus, the experiment optimization should be necessary to be done.

A2.3.5 Temperature and buffer studies

Temperature- and buffer-dependent studies were performed onto a C1 Biacore sensor chip. C1 sensor chips have as well a negatively charged carboxyl groups on their surface and are activated and blocked with the same procedures as explained before. The difference is that this carboxymethylated prepared surface has a low binding capacity (-COOH groups) to immobilize the antibodies thus simplify the study due to a more controlled immobilization step.

To more clearly demonstrate how the c-myc/anti-c-myc interactions are affected by the assay conditions, we took advantage of the Biacore T100 ability to automatically run experiments at different temperatures and under different buffer conditions. The binding activities of c-myc peptide to the two anti-c-myc antibodies were tested at four different temperatures 12°C, 20°C, 24°C and 30°C. Figure A2.10 shown the association (k_a) and dissociation (k_b) rates plotted in the y and x axis respectively for each anti-c-myc antibody.

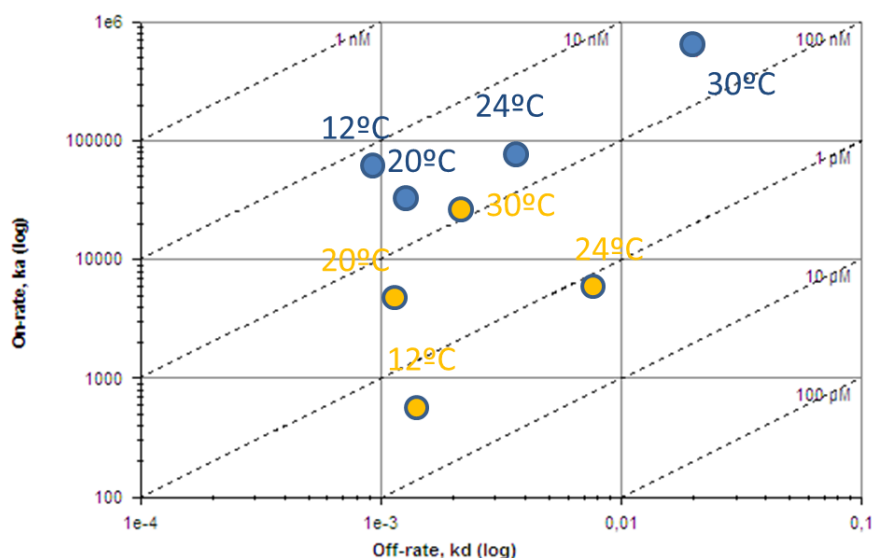


Figure A2.10 Kinetic distribution plot for antibody/antigen interactions with dashed isoaffinity lines. The blue dots correspond to the c-myc/Ab894D12_{f7f9} complex while the yellow dots correspond to the c-myc/Ab9E10 complex. Graph obtained with the Biacore T200 software.

From Figure A2.10 we can conclude that the c-myc/Ab894D12_{f7f9} interaction has almost the same K_D independent of the experiment temperature (~ 40 nM) while the c-myc/Ab9E10 K_D varies significantly depending on the experiment temperature (see Table A2.3). Thus, the temperature chosen to perform the experiment has an important effect onto the c-myc/Ab9E10 interaction.

Table A2.3 Affinity and Kinetic constants for antigen-antibody interactions determined at different assay temperatures.

Binding assay (antigen + antibody)	T (°C)	k_a ($M^{-1} \cdot s^{-1}$)	k_d (s^{-1})	K_D (nM)
c-myc + Ab894D12 _{f7f9}	12	$6.3 \cdot 10^4$	$9.1 \cdot 10^{-4}$	14.4
	20	$3.2 \cdot 10^4$	$13.3 \cdot 10^{-4}$	41.3
	24	$7.0 \cdot 10^4$	$37.2 \cdot 10^{-4}$	53.2
	30	$5.8 \cdot 10^5$	$205.8 \cdot 10^{-4}$	35.3
c-myc + Ab9E10	12	$5.7 \cdot 10^2$	$14.5 \cdot 10^{-4}$	$25.3 \cdot 10^2$
	20	$46.7 \cdot 10^2$	$11.6 \cdot 10^{-4}$	$2.6 \cdot 10^2$
	24	$61.7 \cdot 10^2$	$73.6 \cdot 10^{-4}$	$11.9 \cdot 10^2$
	30	$2.6 \cdot 10^4$	$22.5 \cdot 10^{-4}$	86.1

In addition, and after performed the analysis at this four temperatures, Biacore T100 technology was also used in conjunction with van't Hoff analysis to characterize the thermodynamic binding parameters (ΔH° , ΔS° and ΔG°) of c-myc peptide binding to the two different anti-c-myc monoclonal antibodies. After a non-linear and linear van't Hoff analysis, seems that both interactions (c-myc/anti-c-myc) fit better in a non-linear one. This kind of analysis is often assumed that the enthalpy and entropy of transfer change with temperature. Thus, the thermodynamic parameters were temperature-dependent (see Table A2.4).

Table A2.4 Thermodynamic parameters for the interaction between c-myc and monoclonal anti-c-myc

Binding assay (antigen + antibody)	ΔH° /kJ mol ⁻¹	ΔS° /kJ K ⁻¹ mol ⁻¹	T ΔS° ^{oa} /kJ mol ⁻¹	ΔG° /kJ mol ⁻¹	ΔC_p° /kJ K ⁻¹ mol ⁻¹
c-myc + Ab894D12 _{f7f9}	15	190	57	-42	13
c-myc + Ab9E10	17	180	53	-36	-11

^a Experimental parameter at 25°C obtained by a non-linear van't Hoff analysis of the SPR data.

Both complexes presented endothermic enthalpy ($\Delta H^\circ > 0$ kJ mol⁻¹) and positive entropy (ΔS°). It is important to realize that K_D is a function of both ΔH° and ΔS° (see Eq. 3 above) which becomes clear by the Gibbs equation $\Delta G^\circ = RT \ln K_D$ (see Eq. 4 above). Furthermore, when we study ΔG° , it is known that enthalpic contributions dominate when $\Delta H^\circ + T \Delta S^\circ < 0$, whereas entropic contributions dominate when $\Delta H^\circ + T \Delta S^\circ > 0$ and entropic and enthalpic contributions contribute equally to ΔG° when $\Delta H^\circ + T \Delta S^\circ = 0$. As it can be shown in Table A2.4 for both c-myc/mAb complexes basically the enthalpic contributions dominate the standard free energy (ΔG°). It is reported that large negative values of ΔG° (spontaneous reaction) characterizes a high affinity interaction (smaller K_D) by summing up all its energy contributions in the antibody antigen interface. These agree with our results (see Table A2.3), while the Ab894D12_{f7f9} has more affinity for the c-myc peptide than the Ab9E10 and the free energy in the c-myc/Ab894D12_{f7f9} interface is smaller than the c-myc/Ab9E10 one.

When we talk about binding enthalpy primarily reflects the strength of the interactions of the ligand with the target protein (i.e. van der Waals, hydrogen bonds, etc.) relative to those existing with the solvent. The entropy change, on the other hand,

mainly reflects two contributions: changes in solvation entropy and changes in conformational entropy. Upon binding (desolvation occurs) water is released and a gain in solvent entropy is observed. This gain is particularly important for hydrophobic groups. At the same time, the ligand and certain groups in the protein lose conformational freedom resulting in a negative change in conformational entropy.

The main difference between both complexes is the value of ΔC_p° . C-myc/Ab9E10 show negative values suggesting that the binding interface was more hydrophobic than the c-myc/Ab894D12_{f7f9} one. ΔC_p° is a hydrophobicity and conformational change indicator from the antigen/antibody binding site^{22,23}.

Finally, we performed the c-myc/mAb binding analysis at two different buffer NaCl concentrations in order to study the ionic-strength effect onto the binding affinity (K_D). As analysis buffer we use PBST and PBT with NaCl 300mM at four different c-myc peptide concentrations: 0.1, 1, 5, 10 $\mu\text{g mL}^{-1}$. Table A2.5 shows the results obtained.

Table A2.5 Affinity and Kinetic constants for antigen-antibody interactions determined at different assay temperatures

Binding assay (antigen + antibody)	[NaCl] (mM)	k_a ($\text{M}^{-1} \cdot \text{s}^{-1}$)	k_d (s^{-1})	K_D (nM)	$t_{1/2}$ (s)
c-myc + Ab894D12 _{f7f9}	137*	$2.3 \cdot 10^3$	$1.3 \cdot 10^{-3}$	59.3	244.2
	300	$2.1 \cdot 10^5$	$3.9 \cdot 10^{-3}$	18.9	248.1
c-myc + Ab9E10	137*	$9.1 \cdot 10^3$	$1.5 \cdot 10^{-3}$	166	583
	300	$2.9 \cdot 10^3$	$4.2 \cdot 10^{-3}$	$1.4 \cdot 10^3$	294

*NaCl concentration in the PBST analysis buffer

We can conclude that independent on the ion strength the Ab894D12_{f7f9} has more affinity for the c-myc peptide than the Ab9E10 (K_D Ab894D12_{f7f9} < K_D Ab9E10). However, the c-myc/mAb interaction is more stable with the Ab9E10 ($t_{1/2}$ higher). It is important to focus the attention in the association rate constant. At higher NaCl concentration the association of c-myc/Ab894D12_{f7f9} is faster than at lower NaCl concentration. In addition, at higher NaCl concentration the dissociation in both

complexes was also faster. Thus, the c-myc peptide interaction with the Ab894D12₁₇₁₉ is based basically with electrostatic interactions while the c-myc/Ab9E10 is based with hydrophobic interactions.

A2.4 Conclusions

In this **Appendix** we described a comparative study of the c-myc peptide interaction with two different monoclonal anti-c-myc antibodies (Ab894D12_{f7f9} and Ab9E10) randomly immobilized onto a –COOH functionalized gold surface. We demonstrate with preliminary results that their binding kinetics, their affinity and thermodynamic characteristics, evaluated using SPR (Biacore T100), are significantly different. It was observed that the Ab894D12_{f7f9} had more affinity (smaller K_D) for the c-myc peptide than the Ab9E10 independently to the antibody density in the sensor surface. On the other hand, the c-myc/Ab9E10 complex is more stable than the c-myc/Ab894D12_{f7f9} one because takes more time to dissociate (higher $t_{1/2}$). It is also showed that buffer ion-strength and temperature assay can affect the binding between the c-myc peptide and its specific mAb. These assays allow us to determine that the c-myc peptide interaction with the Ab894D12_{f7f9} is based basically with electrostatic interactions while the c-myc/Ab9E10 is based with hydrophobic interactions.

Thus, Ab9E10 could be used in sensor surfaces to immobilize c-myc-target analytes due to their high complex stability. On the other hand, Ab894D12_{f7f9} could be used in competitive ELISA assays due to their high affinity for the c-myc peptide (low amount of peptide can be detected) and their lower complex stability.

A2.5 References

- (1) Van der Merwe, P.A. *Surface plasmon resonance*, 1-50.
- (2) Biacore T100 Instrument Handbook BR-1006-47 Edition AD
- (3) Kumagai, I., Tsumato, K. *Encyclopedia of Life Sciences* **2001**Antigen-Antibody Binidng. 1-7
- (4) Papalia, G.A., Baer, M., Luehrsen, K., Nordin, H., Flynn, P., Myszka, D. G. *Anal Biochem.* **2006**, 359, 112-119.
- (5) Cooper, M.A., Williams, D.H. *Anal Biochem.* **1999**, 276, 36-47.
- (6) Canziani, G.A., Klakamp, C., Myszka, D.G. *Anal Biochem.* **2004**, 325, 301-307.
- (7) *Handbook of Surface Plasmon Resonance*. Edited by Richard B M Schasfoort and Anna J Tudos. RSC Publishing
- (8) Cooper, M.A. *Nat Rev Drug Discov.* **2002**, 1, 515-528.
- (9) Langmuir, I. *J. Am. Chem. Soc.* **1916**, 38, 2221–229.
- (10) Langmuir, I. *J. Am. Chem. Soc.* **1918**, 40, 1361–1404.
- (11) Papalia, G.A., Giannetti, A.M., Arora. N., Myszka, D.G. *Anal. Bichem.* **2008**, 383, 255-264.
- (12) Nilapwar, S. *Thesis: Characterization and Exploitation of Protein Ligand Interactions for Structure Based Drug Design.* **2009** University College London.
- (13) Bostrom, J., Haber, L., Koenig, P., Kelley, R.F., Fuh, G. *PlosOne*, **2011**, 6, 4, 1-12.
- (14) Myszka, D.G., He, X., Dembo, M., Morton, T.A., Goldstein B. *Biophys. J.* **1998**, 75, 583-594.
- (15) Karlsson, R. *J. Mol. Recognit.* **1999**, 12, 285-292.
- (16) Myszka, D.G. *J. Mol. Recognit.* **1999**, 12, 279-284.
- (17) Schr, M., Von Proff, L. *Chapter 12: Temperature-dependent antibody kinetics as a tool in antibody lead selection.* Book: Antibody methods and protocols, Methods in Molecular Biology. **2012**.
- (18) Biacore X100 Getting Strated. 28-9615-81 Edition AA
- (19) Li, G., Stewart, R., Conlan, B., Gilbert, A., Roeth, P., Nair, H. **2002**, *Vox Sanguinis*, 83, 332-338.
- (20) Bonroy, K., Frederix, F., Reekmans, G., Dewolf, E., De Palma, R. et al. *J. Immunol. Methods* **2006**, 312, 167-181.
- (21) Biaevaluation Software Handbook. Version 3.0 **1997**.

(22) Kauzmann, W. *Adv. Protein Chem* **1959**, *14*, 1.

(23) Tanford, C. *The hydrophobic Effect*, John Wiley & Sons, New York. **1980**

Publications.

Book Chapter

Sanmartí, M., Iavicoli, P., Samitier, J.

Nanomedicine in Diagnostics.

ISBN 978-1-57808-738-9 (2012)

Book edited by: Prof. Noemi Rozlosnik

Ed. CRC Press, Taylor & Francis Group.

Chapter 6: Biosensors for Diagnostic Based on Olfactory Receptors.

Journals

Calò, A.* , Sanmartí-Espinal, M.*, Iavicoli, P., Persuy, M.-A., Pajot-Augy, E., Gomila, G., Samitier, J. *Diffusion-controlled deposition of natural nanovesicles containing G-protein coupled receptors for biosensing platforms.* Soft Matter, (2012), 8, (46), 11632 – 11643.

Sanmartí, M., Iavicoli, P., Pajot-Augy, E., Gomila, G., Samitier, J. *Human olfactory receptors immobilization on a mixed self assembled monolayer for the development of a bioelectronic nose.* Procedia Engineering, (2010), 5, 786 - 789.

Oral presentations

Sanmartí-Espinal, M., Iavicoli, P., Galve, R., Persuy, M.A., Pajot, E., Marco, M.P., Samitier, J. *Accurate c-myc-olfactory receptor quantification on characterized natural nanovesicles for biosensor applications.* International Conference on Nanotechnology in Medicine, NanoMED, NANOSMAT (emerged from the NANOSMAT conference), University College London, 7-9 November 2012 London, UK.

Sanmartí, M., Iavicoli, P., Pajot-Augy, E., Gomila, G., Samitier, J. *Nanosomes immobilization for a bioelectronic olfactory neuron device*. XV Trobada Transfronterera de Sensors i Biosensors, IRTA Recerca i Tecnologia Agroalimentàries. 16-17 September 2010 Sant Carles de la Ràpita, Tarragona, Spain.

Poster presentations

Sanmartí, M., Iavicoli, P., Calò, A., Taulés, M., Pajot-Augy, E., Gomila, G., Samitier, J. *Nanosomes characterization and immobilization for the development of an olfactory biosensor*. Workshop on Nanomedicine for healthy ageing, IBEC/Bioplò'H. Hospital Universitari de Bellvitge. 19 October 2011 L'Hospitalet, Spain.

Sanmartí, M., Iavicoli, P., Calò, A., Taulés, M., Pajot-Augy, E., Gomila, G., Samitier, J. *Nanosomes characterization and immobilization for the development of an olfactory biosensor*. 4th IBEC Symposium on Bioengineering and Nanomedicine, IBEC. Hospital Universitari de Bellvitge. 18 October 2011 L'Hospitalet, Spain.

Sanmartí, M., Iavicoli, P., Calò, A., Taulés, M., Pajot-Augy, E., Gomila, G., Samitier, J. *Nanosomes characterization and immobilization for the development of an olfactory biosensor*. International Symposium on Olfaction and Electronic Nose (ISOEN) 2011, Engineering Conferences International. 2-5 May 2011 New York, EEUU.

Iavicoli, P., Sanmartí, M., Calò, A., Taulés, M., Pajot-Augy, E., Gomila, G., Samitier, J. *Biosensor based on immobilized olfactory receptors for the detection of odorant compounds*. MRS Spring Meeting & Exhibit. 25-29 April 2011 San Francisco, California, EEUU.

Sanmartí, M., Iavicoli, P., Pajot-Augy, E., Samitier, J. *Nanosomes immobilization for a bioelectronic olfactory neuron device*. Workshop on Bioinspired computation for chemical sensing, NeuroChem. 9-11 March 2011 Barcelona, Spain.

Sanmartí, M., Iavicoli, P., Pajot-Augy, E., Samitier, J. *Nanosomes immobilization for a bioelectronic olfactory neuron device*. NanoJASP 2010. Nanomaterials based biosensors and biosystems, Institut Català de Nanotecnologia. 29-30 November 2010 Barcelona, Spain.

Sanmartí, M., Iavicoli, P., Pajot-Augy, E., Samitier, J. *Human Olfactory Receptors immobilization on a mixed Self Assembled Monolayer for the Development of a Bioelectronic Nose*. Eurosensors XXIV, Johannes Kepler University Linz (JKU), Austria y Austrian Center of Competence in Mechatronics (ACCM). 5-8 September 2010 Linz, Austria.

Sanmartí, M., Iavicoli, P., Pajot-Augy, E., Sampietro, M., Ogurtsov, V., Bausells, J., Jaffrezic, N., Reggiani, L., Johnson, G., Gomila, G., Samitier, J. *Bioelectronic Olfactory Neuron Device*. 3rd IBEC Symposium, IBEC. Auditorio AXA, 1-2 June 2010 Barcelona, Spain.

Sanmartí, M., Iavicoli, P., Pajot-Augy, E., Sampietro, M., Ogurtsov, V., Bausells, J., Jaffrezic, N., Reggiani, L., Johnson, G., Gomila, G., Samitier, J. *Bioelectronic Olfactory Neuron Device*. EC Advanced Workshop on Infochemical Communication Technology, iCHEM. Granada, Spain.

Resum en català.

Estudi de la utilització de nanovesícules naturals amb receptors olfactivs pel desenvolupament de biosensors.

L' introducció del nassos electrònics en el mercat ha estat un fet revolucionari a causa dels recents esdeveniments que han demostrat les noves capacitats i possibilitats d'aquests aparells. Es coneix com a **nas electrònic** un dispositiu de detecció capaç de produir una empremta digital, també coneguda com a patró, d'un grup de compostos volàtils químics que caracteritzen una **olor** específica. La comparació dels perfils detectats amb una base de dades de patrons estàndard permet la identificació i quantificació de les substàncies odorants presents en una barreja. Bàsicament, aquests dispositius consten de dos components principals: un sistema de detecció química i un sistema de reconeixement de patrons (Figura R.1).

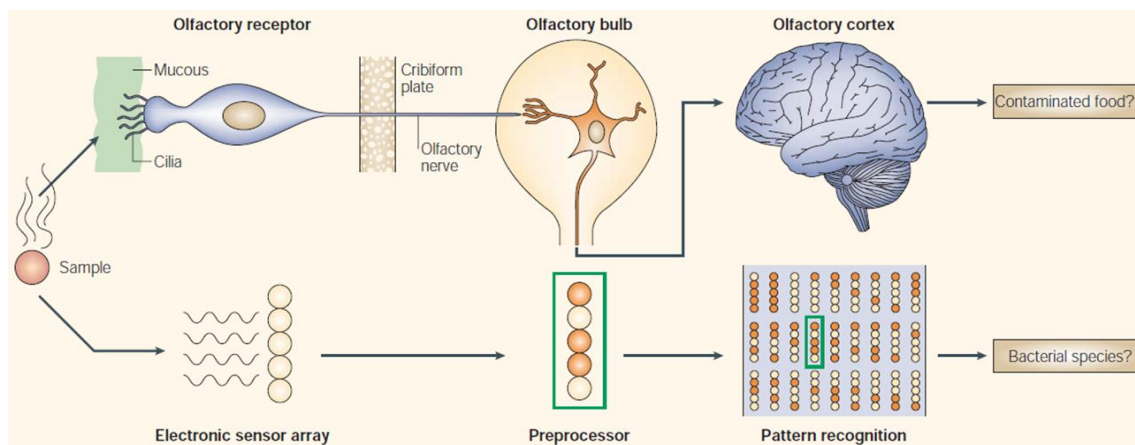


Figura R.1 Els nassos electrònics simulen els diferents estadis del sistema olfatiu humà, bàsicament reconeixent l'odorant volàtil, que pot servir per discriminar entre diferents infeccions bacterials.¹

Les tecnologies utilitzades per a sensors basats en un nas electrònic són les mateixes que s'utilitzen pels transductors utilitzats per obtenir sensors químics genèrics.² Per exemple, podríem parlar de sensors conductors, sensors piezoelèctrics, sensors òptics, sensors electroquímics, etc.

Però el principal inconvenient dels sensors químics genèrics és la poca selectivitat, que requereix d'un complex processament del post-tractament de la senyal, i les limitacions relatives a la sensibilitat i fiabilitat entre d'altres. Per tant, els investigadors han intentat desenvolupar dispositius de detecció artificials basats en el

sistema olfatiu per obtenir una major sensibilitat i selectivitat. Es va proposar utilitzar **receptors olfactius** (OR) com l'element biològic de detecció (transductor primari) i els sensors químics descrits anteriorment com la part de plataforma sensora (transductor secundari), es per tot això que s'anomenen **nassos bioelectrònics**. El nas dels mamífers és el referent per tenir una bona detecció de l'olor degut a la alta sensibilitat que presenta, ja que els mamífers arriben a límits de detecció d'olors des de 0.1 ppb fins a 10^{-6} ppb.³

L'investigació científica i tecnològica dins de l'àmbit dels nassos bioelectrònics és avui en dia un camp de desenvolupament prometedori. Aquests dispositius tenen el potencial de ser utilitzats com a eines eficaces per detectar i discriminar una gran quantitat de substàncies oloroses amb alta sensibilitat i selectivitat. Per tant, aquests dispositius es poden aplicar a la indústria d'aliments i begudes, el diagnòstic de malalties, la seguretat, el medi ambient, etc.

Així doncs, quan es parla de receptors olfactius (OR), es fa referència a una subfamília de proteïnes molt important de la superfamília dels receptors acoblats a proteïnes G (GPCR). Avui en dia, les GPCR han guanyat un gran interès per la seva alta potencialitat en el diagnòstic biomèdic.

Les proteïnes GPCR consten de set segments majoritàriament amb residus d'aminoàcids hidrofòbics que formen una estructura α -hèlix a través de la membrana de bicapa lipídica, alternats amb segments hidrofílics que formen bucles. Aquests, són estables en aigua i que connecten cada una de les hèlices^{4,5,6}. Les GPCRs són un grup de proteïnes que presenten una topologia de set dominis transmembrana. Són proteïnes molt conegudes i tenen dos llocs d'unió importants. Un, el lloc d'unió de l'odorant a la capa de la mucosa, al costat extracel·lular; i l'altre, en el domini citoplasmàtic on té lloc la unió a una proteïna G heterotrimèrica a través de tres subunitats (Figura R.2).

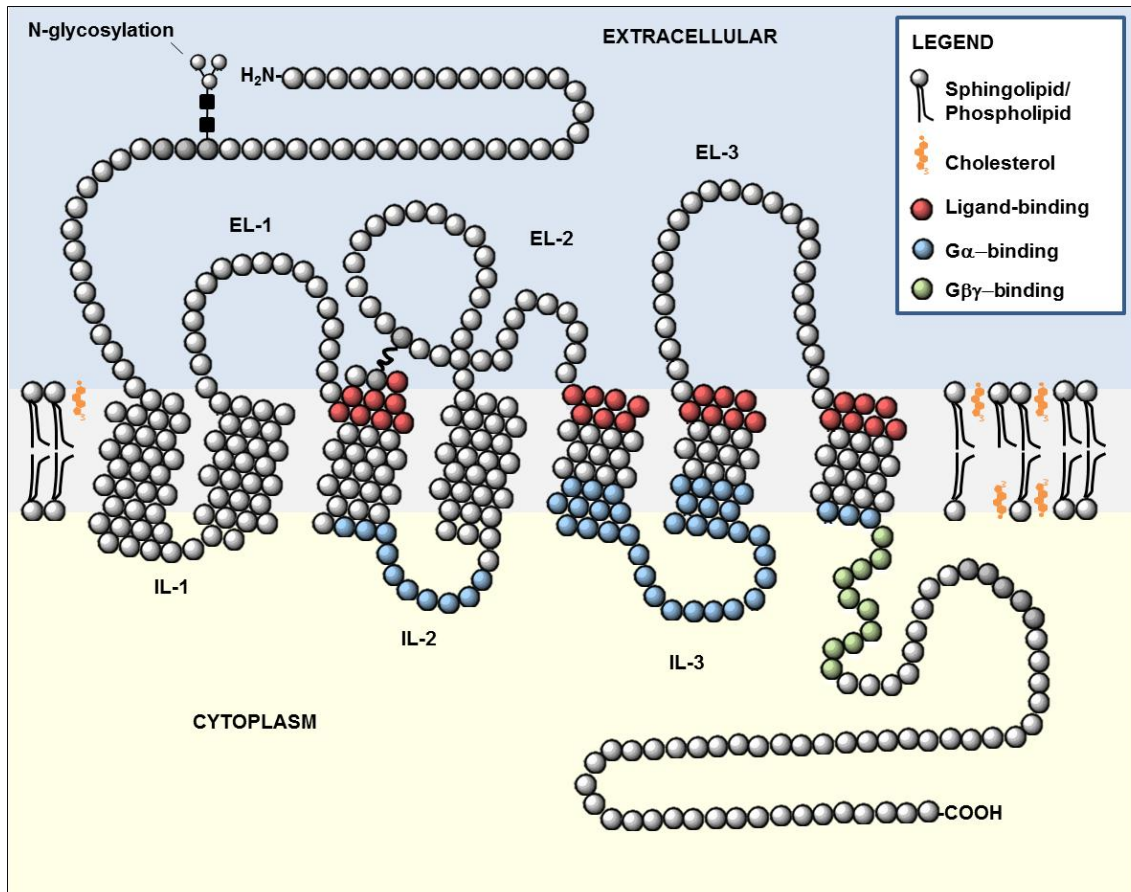


Figura R.2 Representació esquemàtica d'una proteïna GPCR. Les esferes blanques, vermelles, blaves, i verdes representen els aminoàcids. S'observa els tres bucles extracel·lulars (EL-1, EL-2, EL-3) i tres bucles intracel·lulars (IL-1, IL-2, IL-3). Les diferents esferes de colors estan implicats en la unió al lligand i a la proteïna G d'unió com s'indica en la llegenda (*Adaptat de la pàgina web de Bioquímica Mèdica: <http://themedicalbiochemistrypage.org>*).

A més a més, està descrit en la literatura, que les vesícules naturals produïdes a partir de cèl·lules modificades genèticament són prometedors components de sensat per utilitzar com a detectors en biodispositius⁷. Això és particularment cert en el cas de receptors adjuntats a proteïna G (GPCRs) presents en molts processos cel·lulars, on la seva funcionalitat depèn estrictament del seu entorn lipídic⁸ (Figura R.3). Els receptors de membrana estan involucrats en una gran varietat de vies bioquímiques i per tant són objectiu d'estudi per teràpia i desenvolupament de nous fàrmacs. Per tant, plataformes bioanalítiques i assajos de unió receptor-ligand, utilitzant receptors transmembrana, requereixen la construcció de matrius de membranes lipídiques ben caracteritzades, actuant com a suport per evitar la desnaturalització de proteïnes durant el processament del bioxip⁸⁻¹¹.

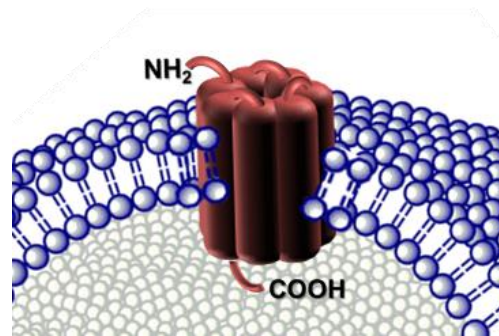
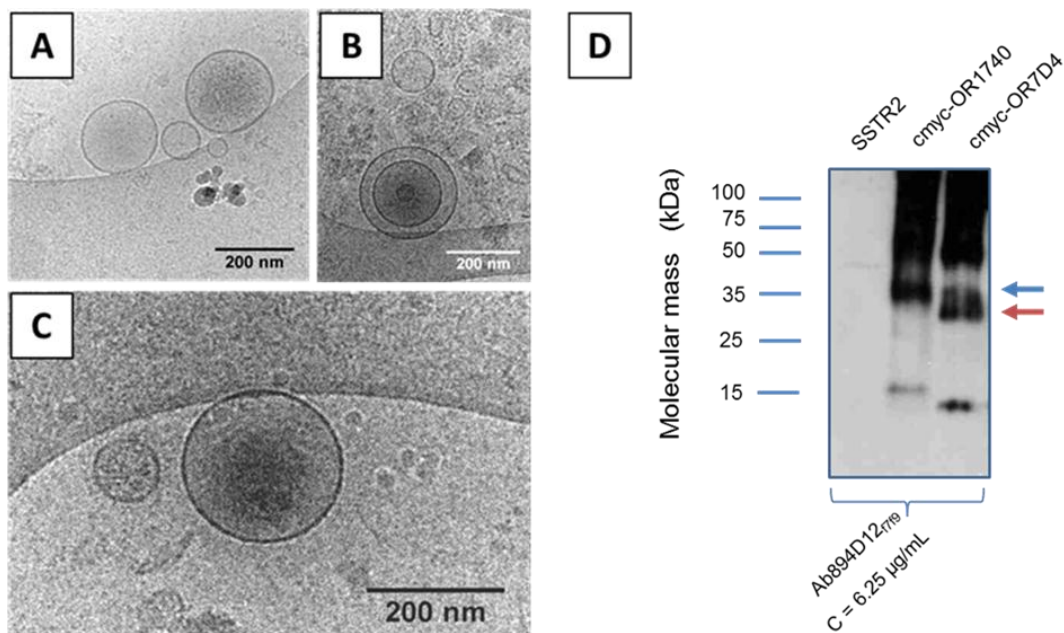


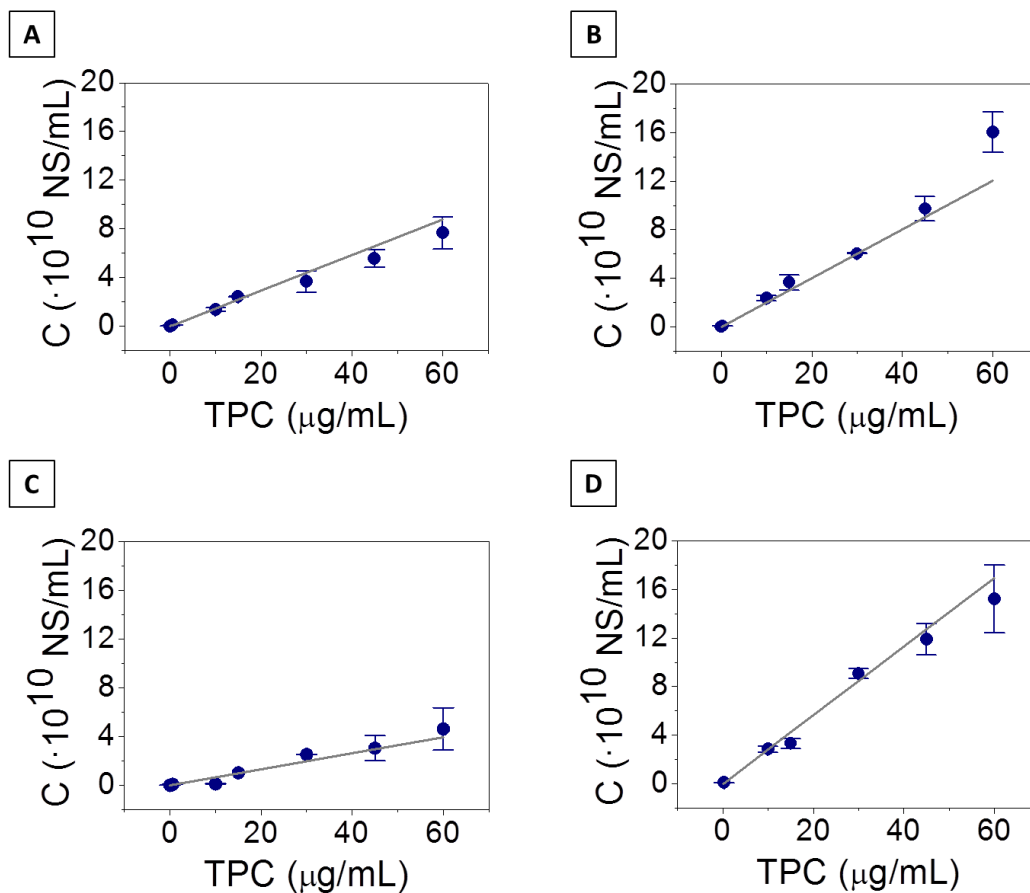
Figura R.3 Esquema d'un receptor olfatiu (proteïna transmembrana de 7 dominis) integrat a la membrana lipídica.

En aquesta **Tesi** es presenta la producció i caracterització de nanovesícules de membrana (NV) provinents de cèl·lules de llevat *Saccharomyces cerevisiae* que contenen receptors olfatius (un membre de la família de GPCRs) heteròlogament expressats a la membrana. Hem demostrat que les fraccions de membrana, a partir de cèl·lules de llevat, en solució formen espontàniament nanovesícules esfèriques tancades (Figura R.4A,B,C). També s'ha demostrat, que després d'un procés d'enginyeria genètica els receptors olfatius van ser expressats correctament a la membrana del llevat (Figura R.4D).



Nanovesícules que contenen receptors SSTR2 van ser utilitzades com a control (-). Nanovesícules que contenen el receptor c-myc-OR1740 o c-myc-OR7D4 van ser utilitzades com a models de mostra d'avaluació (+). El pes molecular del monòmer del receptor olfactiu és d'uns 26 kDa per al OR7D4 (fletxa vermella) i al voltant de 35 kDa per al OR1740 (fletxa blava). L'expressió d'altres receptors utilitzats en la tesi com el ORI7 i SSTR2 està descrit en la literatura per col·laboradors nostres¹².

A més a més, s'ha presentat un mètode simple, basat en la sonicació i filtració de les fraccions de membrana, per homogeneïtzar la mida de les nanovesícules obtenint vesícules de diàmetre ~ 100 nm a la concentració de més de 10^{10} nanovesícules mL^{-1} . La concentració de nanovesícules en solució es va calcular mitjançant la tècnica de Nanoparticle Tracking Analysis (NTA) obtenint rectes de calibració que correlacionaven el contingut proteic total de la solució (paràmetre conegut, TPC) amb la concentració de nanovesícules en solució (paràmetre desconegut fins al moment però molt important per la realització d'aquesta tesi). La Figura R.5 mostra totes les corbes de calibració obtingudes per a les nanovesícules treballades en aquesta tesi.



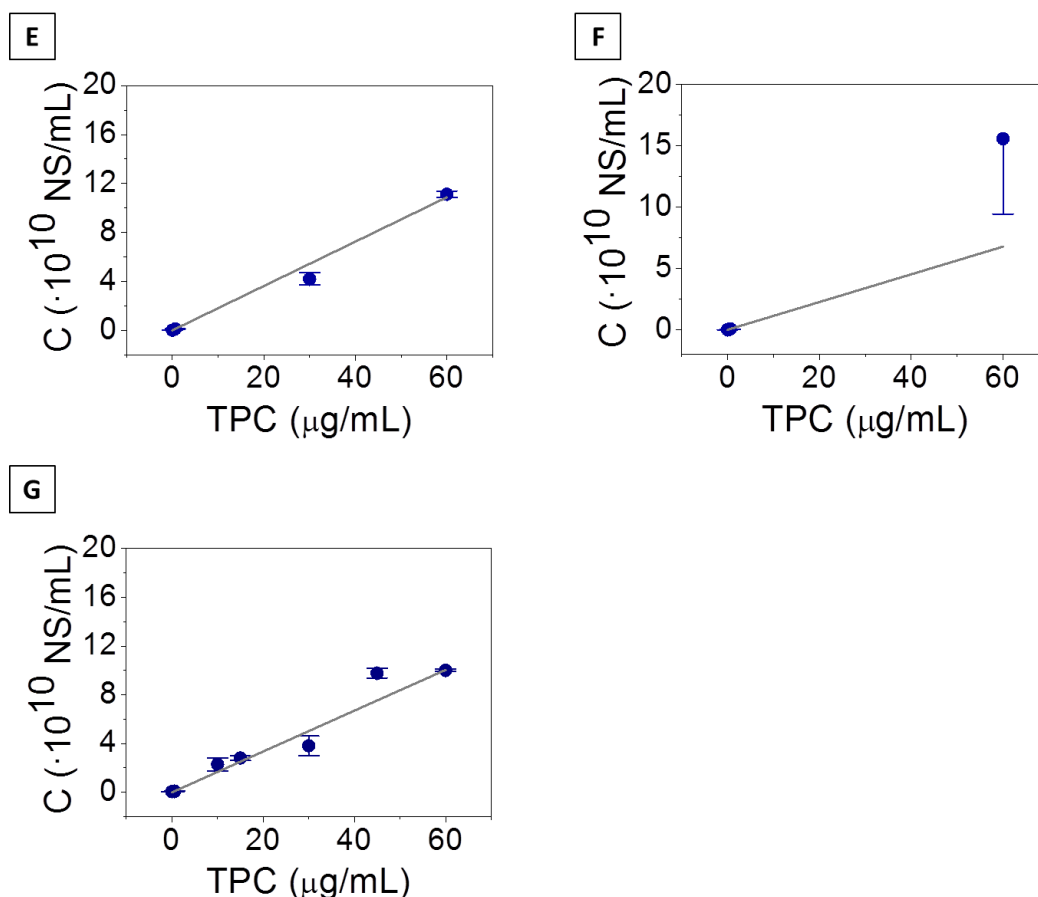


Figura R.5 Rectes de calibració de la concentració de nanovesícules (C), obtinguda a partir de l'àrea total de les distribucions de la mida calculat amb NTA a diferents concentracions de contingut total proteic (TPC). Existeix una tendència lineal amb el TPC (expressat com $\mu\text{g/mL}$) i la concentració de nanovesícules (C, expressada com NS/mL)¹³. S'ha calculat que les dades experimentals segueixen un correcte ajust lineal (les equacions corresponents es troben al *Capítol 1*) per cada una de les solucions de nanovesícules diferents (A) nanovesícules que contenen el receptor SSTR2 (F, #41). (B) nanovesícules que contenen el receptor SSTR2 (G, #43, una preparació d'expressió genètica diferent a la anterior). (C) nanovesícules que contenen el receptor OR1740 (A, #26.1). (D) nanovesícules que contenen el receptor OR1740 (B, #44). (E) nanovesícules que contenen el receptor ORI7 (D, #new). (F) nanovesícules que contenen el receptor ORI7 (C, #old) i (G) nanovesícules que contenen el receptor OR7D4 (E, #58).

Es presenta per primer cop un nou mètode immunoquímic per la quantificació directa de les proteïnes transmembrana (GPCR) en el seu ambient lipídic natural sense necessitat de fer cap etapa prèvia de purificació o extracció de la proteïna d'interès. El mètode permet la detecció directa de receptors marcats amb seqüències peptídiques (com per exemple el pèptid c-myc). S'utilitza anticossos monoclonals contra el pèptid c-myc i l'assaig està basat en un ELISA treballant a alta detectabilitat. El mètode immunoquímic quantifica el pèptid c-myc unit a les proteïnes o bioreceptors que estan incorporats a la membrana lipídica de les nanovesícules amb una detectabilitat en el

rang picomolar. S'utilitzen proteïnes bioconjugades amb el pèptid com a referents estàndards (Figura R.5).

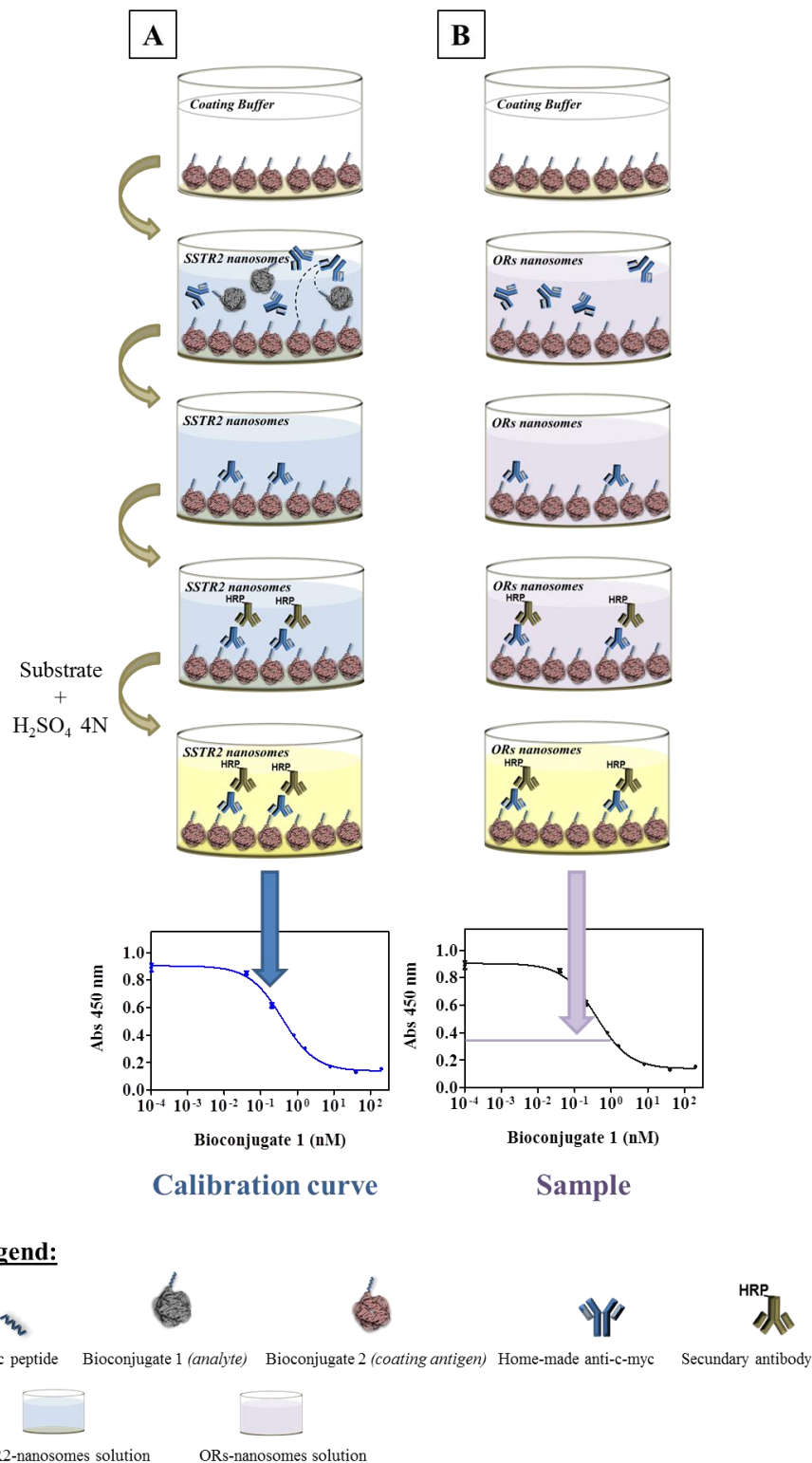


Figura R.6 Esquema de l'assaig ELISA competitiu. (A) Corba de calibració generada utilitzant un c-myc-Bioconjugat en una solució de nanovesícules (també anomenats nanosomes) que contenen el receptor SSTR2. (B) El senyal obtingut de les nanovesícules que contenen el c-myc-OR d'interès és comparat a la corba de calibració obtinguda en (A).

L'aplicació del mètode es demostra a través de la quantificació del receptors olfactius OR1740 i OR7D4 expressats en nanovesícules de membrana plasmàtica obtenint (3 ± 1) OR per nanovesícula i (6 ± 2) OR per nanovesícula respectivament (Figura R.6).

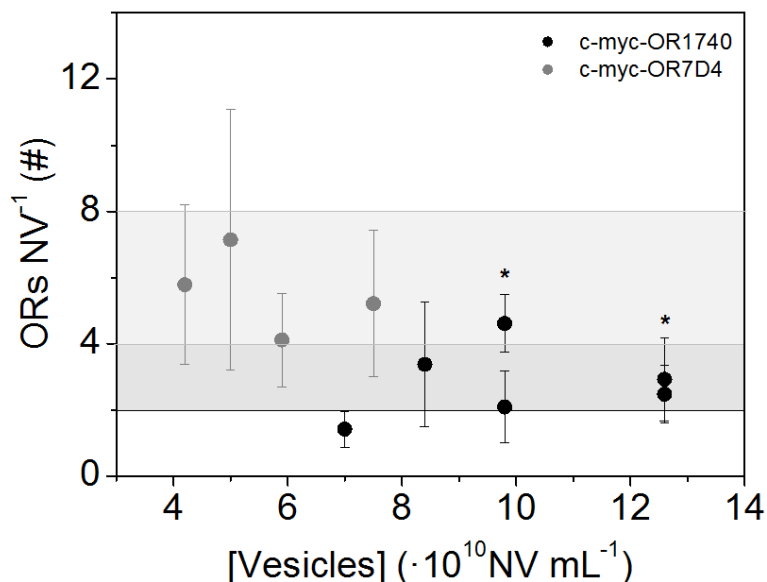


Figura R.7 Número de receptors per NV (ORs NV $^{-1}$) a cada concentració. Les rodones negres corresponen a la quantificació de c-myc-OR1740-NS i les rodones grises corresponen a la quantificació de c-myc-OR7D4-NS. La zona sombrejada gris fosc mostra la quantificació de (3 ± 1) c-myc-OR1740/NS i el gris clar mostra la quantificació de (6 ± 2) c-myc-OR7D4/NS. La reproducibilitat de la quantificació en dos dies diferents (*) també està representada.

També es presenta, mitjançant observació directa amb AFM, com les nanovesícules es depositen i s'aplanen sense trencar-se (Figura R.7) sobre substrats de vidre i or funcionalitzat seguint la llei de difusió¹⁴⁻¹⁷ amb una relació d'aspecte (altura vs. amplada) d'entre 0.1-0.3.

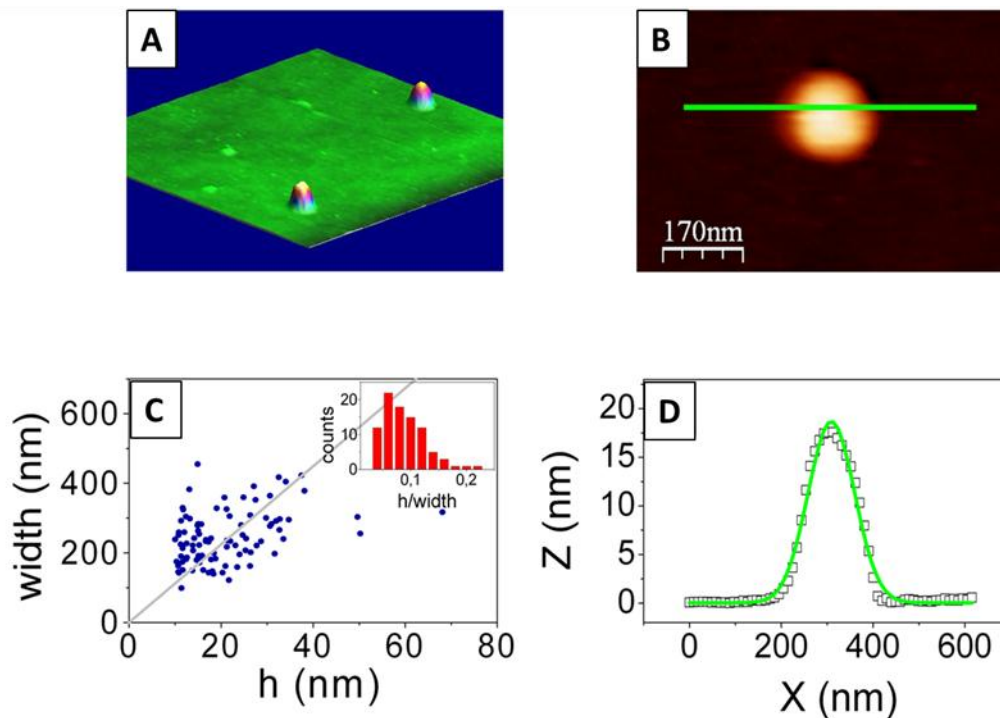


Figura R.8 (A) Imatge de AFM en 3D obtinguda en mode “tapping” en tampó PBS sobre una superfície de vidre mostrant nanovesícules individuals provinents d’una solució de $C = 3.22 \cdot 10^8$ NV mL^{-1} (temps d’incubació = 900 s) (escla $z = 22$ nm). (B) Detall de la Figura R.8A mostrant una nanovesícula individual (B) i el seu perfil topogràfic (D). La línia verda és l’ajust a una Gaussiana d’on s’ha pogut extreure l’altura i l’amplada. (C) Amplada vs. altura extret del perfil topogràfic d’una població de 95 nanovesícules. (C, inserció) La línia gris indica una relació d’aspecte de 0.097. L’histograma de la relació d’aspecte és obtingut dels resultats presentats en (C).

Es demostra com en el cas del vidre els màxims recobriments superficials obtinguts són del 20-25% (Figura R.8) i en el cas del or del 10-15% (Figura R.9), controlant la concentració de nanovesícules, el temps de depòsit, la presència de residus procedents del procés de producció de les nanovesícules, la química de la superfície, la força iònica del medi, etc.

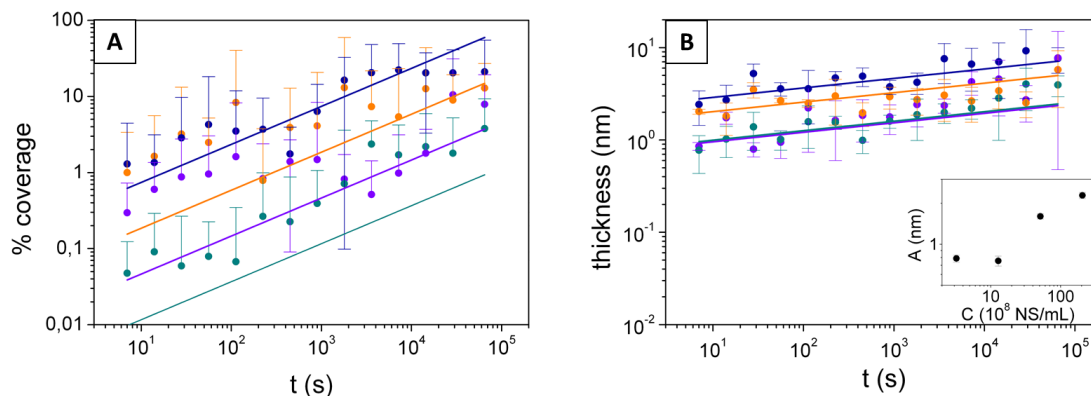


Figura R.9 Recobriment en superfícies de vidre (A) i gruix de la capa adsorbida (B) vs. temps d'incubació a la concentració de nanovesícules de $3.22 \cdot 10^8$ NV mL⁻¹ (dades en cian fosc), $12.83 \cdot 10^8$ NV mL⁻¹ (dades en lila), $51.40 \cdot 10^8$ NV mL⁻¹ (dades en taronja) and $205.66 \cdot 10^8$ NV mL⁻¹ (dades en blau). Les línies rectes en (A) corresponen a un procés d'adsorció purament difusiu sense paràmetres ajustables

segons l'equació: $Coverage \times 100 = 100 \cdot \pi \cdot a^2 \cdot 2 \cdot \sqrt{\frac{D \cdot t}{\pi}} \cdot C$ on a és el radi de les partícules adsorbides, D el coeficient de difusió en la solució, t i C corresponen al temps d'incubació i a la concentració en la solució respectivament. Per altra banda, les línies rectes en (B) corresponen a l'ajust de $y = A \cdot t^b$. (B, insició) Tendència del prefactor A , extret de l'ajust del temps d'evolució vs. gruix de la capa residual adsorbida.

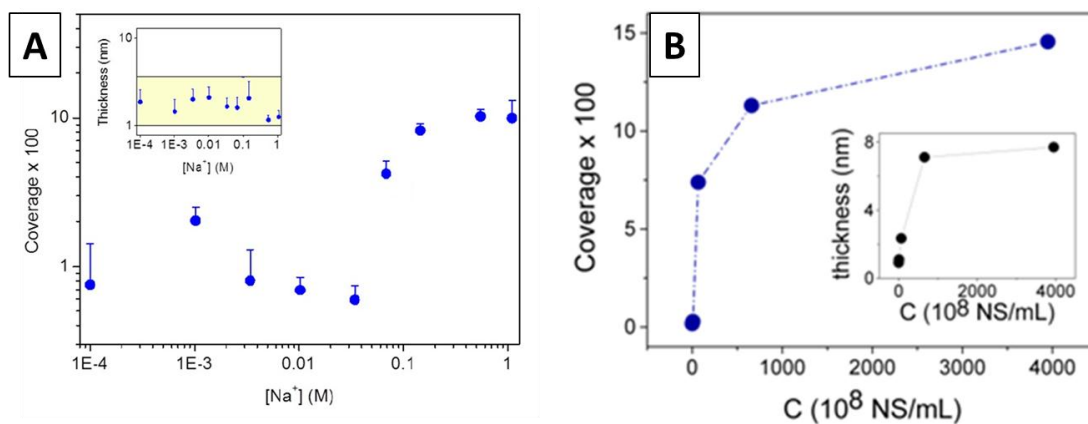


Figura R.10 (A) Recobriment superficial (amb nanovesícules sobre una superfície d'or funcionalitzada amb una SAM amb terminació carboxílica) vs. concentració de NaCl ($[Na^+]$). (Inserció) Gruix de la capa residual adsorbida. Condicions de treball: [nanovesícules] = $1.67 \cdot 10^{11}$ NV mL⁻¹, temps d'incubació = 3600 s, incubació en estàtic afegint una gota de volum conegut de la solució de nanovesícules sobre la superfície de treball. A aquestes condicions el màxim recobriment superficial obtingut va ser ~ 10%. (B) Recobriment superficial vs. concentració de nanovesícules. (Inserció) Evolució del gruix de la capa residual adsorbida obtinguda a través de l'anàlisi d'imatges de AFM obtingudes un cop les nanovesícules han estat adsorbides mitjançant un flux continuu i monitoritzat per SPR. A la concentració de $3.9 \cdot 10^{11}$ NV mL⁻¹ el màxim recobriment obtingut va ser ~ 15 %.

A més a més, s'observa com els substrats que mostren grans potencials-zeta negatius i que permetre la formació d'enllaços d'hidrogen són els millors candidats per donar grans recobriments superficials amb nanovesícules. Un exemple és el que es mostra a continuació a la Figura R.10.

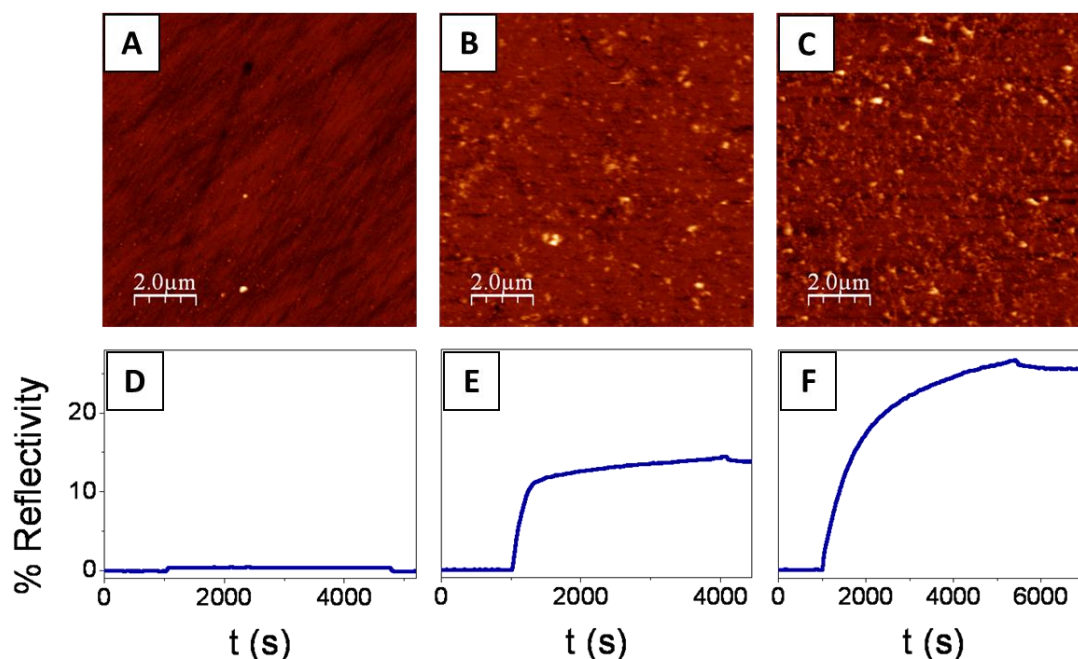


Figura R.11 Imatges realitzades després d'incubar una solució de nanovesícules que contenen el receptor olfatiu OR1740 a la concentració de $C = 394.86 \cdot 10^8 \text{ NV mL}^{-1}$ sobre una superfície d'or funcionalitzada amb una SAM-OH ($t = 3600 \text{ s}$) (A), SAM-NH₂ ($t = 3000 \text{ s}$) (B) and SAM-COOH ($t = 4500 \text{ s}$) (C) mitjanant un flux continu. Els recobriments superficials obtinguts per la deposició de les nanovesícules són al voltant del 0.03 % en el or funcionalitzat amb una SAM-OH, al voltant de un 10 % en el or funcionalitzat amb una SAM-NH₂ o amb una SAM-COOH. També es presenten el corresponents sensogrames de SPR (D-F).

Els resultats presentats constitueixen un pas important en la realització pràctica del dispositius biosensors basats en nanovesícules naturals que integren els receptors de membrana acoblats a proteïna G. Resultats preliminars demostren que la deposició de nanovesícules sobre substrats d'or funcionalitzat (Figura R.12) o vidre (Figura R.13) podrien utilitzar-se per a la generació d'una matriu de múltiples nanovesícules, contenent cadascuna d'elles un tipus de receptor olfatiu diferent a la superfície que podria ser integrat en el mateix xip i utilitzar-se com a suport biosensor.

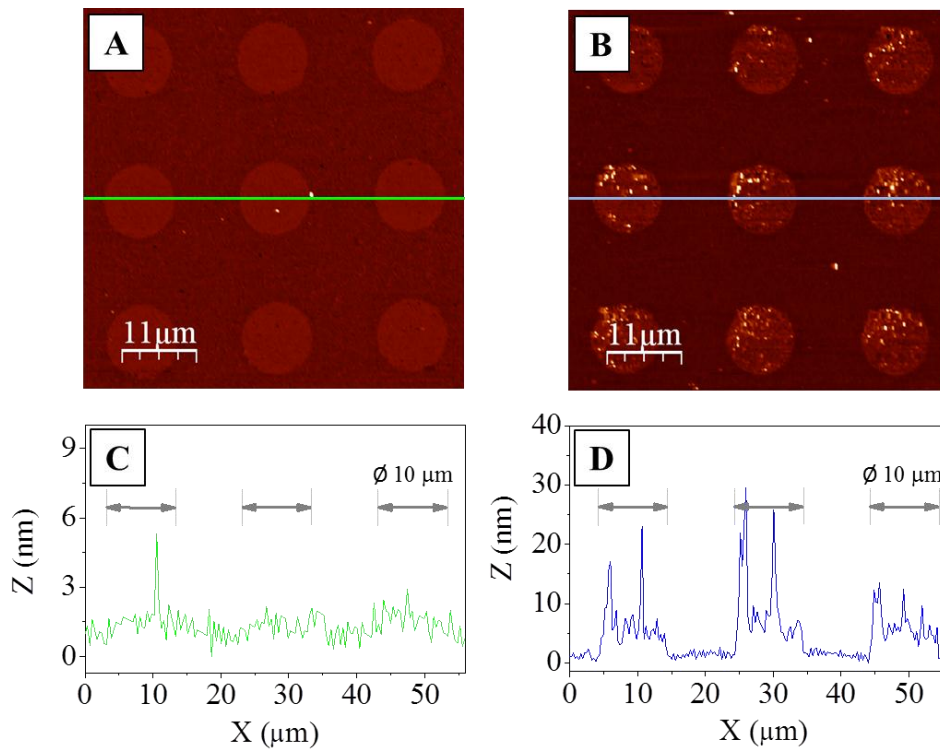


Figura R.12 Imatges d'AFM obtingudes en mode "tapping" d'un patró de discs de 10 µm de diàmetre en or funcionalitzat amb SAM-COOH (disc) i SAM-OH (contorn) abans (A) i després (B) d'incubar una solució de nanovesícules que contenen el receptor olfatiu OR1740 $C = 3.29 \cdot 10^{10}$ NV/mL durant 4200 s. (C), (D) Perfils topogràfics corresponents.

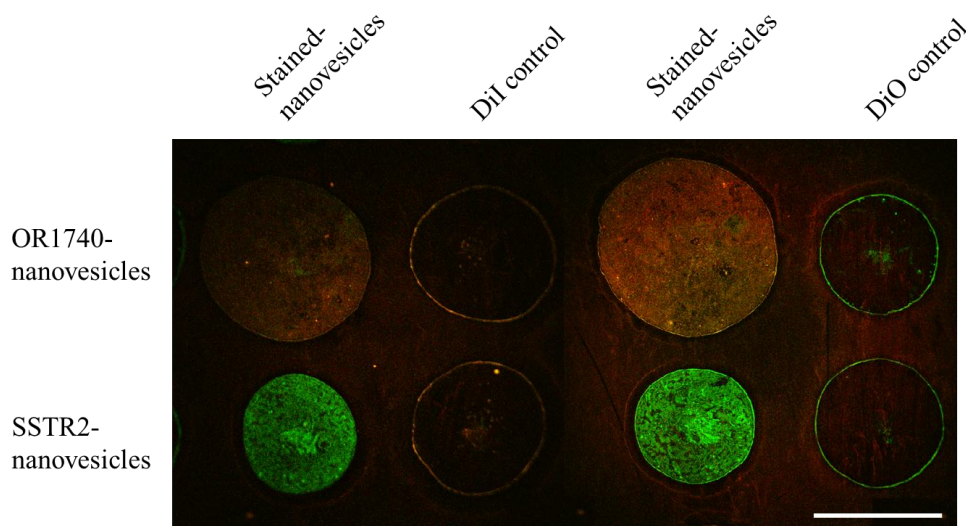


Figura R.13 Nanovesícules ($C = 1.67 \cdot 10^{11}$ NV mL⁻¹) que contenen diferents receptors, tenides prèviament amb DiI (OR1740-nanovesícules, vermell) o DiO (SSTR2-nanovesícules, verd), immobilitzades durant una hora en una superfície de vidre neta i tractada. Els corresponents controls negatius (tints en PBS) també van ser impresos. La matriu obtinguda abans de rentar la superfície de vidre va ser observada mitjançant microscopia confocal. Imatges confocals van ser realitzades amb làsers a 488 nm (per l'excitació del DiO) i a 532 nm (per l'excitació del DiI) al 70% de la potència del làser. Els mateixos paràmetres d'adquisició van ser utilitzats durant la visualització de les diferents matrius per a cada tipus de làser. Escala: 200 µm.

Així doncs, quan s'expressen genèticament els receptors olfactius en vesícules tancades provinents de fraccions de membrana naturals de llevat, la verificació de la seva capacitat per a la captura de molècules odorants de forma específica és crítica per al disseny de nassos artificials.

Per tant, hem demostrat mitjançant la tècnica de ressonància de plasmons superficials (SPR), utilitzant els xips L1 de Biacore per a les mesures, que els receptors eren funcionals. Tot i que l'expressió de receptors olfactius en nanovesícules és baixa, un fet que és coherent amb el nivell d'expressió general de les proteïnes GPCR en les cèl·lules¹⁸, la integració en nanovesícules juntament amb una acurada elecció de les condicions experimentals de SPR i d'un bon tractament analític de dades ens va permetre obtenir una resposta de SPR. Aquesta resposta, era dependent de la concentració d'odorant amb una sensibilitat de 0.5-1.8RU/ μ M (Taula R.1). La selectivitat dels receptors olfactius, integrats en NV, cap al seu odorant específic es va demostrar en experiments amb molècules odorants inespecífiques i receptors control. Aquests resultats són una prova de concepte que els receptors olfactius integrats en nanovesícules naturals responen adequadament als odorants específics. A més a més, es pot considerar la tècnica de ressonància de plasmó superficial com una bona tècnica per a la detecció de petites molècules odorants a una concentració en el rang micromolar.

Taula R.1 Característiques de l'assaig de funcionalitat realitzat per SPR

	OR1740-NV vs. helional		OR7D4-NV vs. androstenone
<i>Control NV</i>	SSTR2-NV	OR7D4-NV	OR1740-NV
<i>L.O.D.</i>	0.3 μ M	0.4 μ M	1.1 μ M
<i>Sensitivity</i>	1.8 RU/ μ M	1.2 RU/ μ M	0.5 RU/ μ M
<i>n</i>	7	4	20
<i>Reproducibility</i>	76%	75%	35%

Així doncs, s'ha demostrat per SPR que els receptors expressats eren funcionals i que aquesta tècnica òptica permet la detecció de petites molècules, com són els odorants, a les concentracions en el rang micromolar.

Els resultats presentats en aquesta tesi contribueixen, donant un pas endavant important, a la realització de dispositius biosensors basats en nanovesícules naturals que integren receptors de membrana adjuntats a proteïna G.

Aquesta **Tesi** s'ha dut a terme en el marc d'un projecte europeu (BOND) coordinat pel Prof. Dr. Josep Samitier. Els estudis realitzats durant els quatre anys de tesi s'han integrat en el consorci del projecte, un grup multidisciplinari de persones amb experiència en diferents àrees científiques. Aquesta tesi es basa en recerca bàsica. És a dir, el seu objectiu era aconseguir resultats i experiències per tal de dissenyar i provar teories, hipòtesis i lleis per obtenir una base àmplia de coneixement orientada a l'aplicació del projecte BOND. Per tant, d'estudi de nanovesícules naturals amb receptors olfactivs ha contribuït directament en el desenvolupament de la plataforma biosensora BOND (per a més informació del projecte llegir l'Epíleg de la tesi).

Referències

- (1) Turner, A.P.F., Magan, N. *Nature Reviews/Microbiology*, **2004**, 2, 161–166.
- (2) Gardner, J.W., Bartlett, P.N. *Electronic Noses: Principles and Application*, Oxford Univ Press, UK. **1999**.
- (3) Angioy, A.M. et al. *Chem Senses*, **2003**, 284, 279.
- (4) Breer, H. *Anal Bioanal Chem*, **2003**, 377, 427–433.
- (5) Zarzo, M. *Biological Reviews*, **2007**, 82, 455–479.
- (6) DeMaria, S., Ngai, J. *The Journal of Cell Biology*, **2010**, 191, 3, 443–452.
- (7) Jin, H.J., Lee, S.H., Kim, T.H., Park, J., Song, H.S., Park, T.H., Hong, S. *Biosens. Bioelectron.* **2012**, 35, 335–341.
- (8) Bally, M., Bailey, K., Sugihara, K., Grieshaber, D., Vörös, J., Städler, B. *Small*. **2010**, 6, 22, 2481-2497.
- (9) Minic, J., Persuy, M.-A., Godel, E., Aioun, J., Connerton, I., Salesse, R., Pajot-Augy, E. *FEBS Journal*. **2005**, 272, 2, 524-537.
- (10) Bieri, C., Ernst, O. P., Heyse, S., Hofmann, K. P., Vogel, H. *Nat. Biotechnol.* **1999**, 17, 11, 1105-1108.
- (11) Wittenberg, N. J., Im, H., Johnson, T. W., Xu, X., Warrington, A. E., Rodriguez, M., Oh, S. H. *ACS Nano*, **2011**, 5, 9, 7555-7564.
- (12) Minic, J., Persuy, M.-A., Godel, E., Aioun, J., Connerton, I., Salesse, R., Pajot-Augy, E. *FEBS Journal*, **2005**, 272, 524.
- (13) Calò, A., Sanmartí-Espinal, M., Iavicoli, P., Persuy, M.-A., Pajot-Augy, E., Gomila, G., Samitier, J. *Soft Matter*, **2012**, 8, 46, 11632 – 11643.
- (14) Johnson, C.A., Lenhoff, A.M. *J. Colloid Interface Sci.*, **1996**, 179, 587.
- (15) Rivetti, C., Guthold, M., Bustamante, C. *J. Mol. Biol.*, **1996**, 264, 919.
- (16) Lang, D., Coates, P. *J. Mol. Biol.*, **1968**, 36, 137
- (17) Hilbert, D.B., Gooding, J.J., Erokhin, P. *Langmuir*, **2002**, 18, 1770
- (18) Sarramegna, V., Talmont, F., Demange, P., Milon, A. *CMLS, Cell. Mol. Life Sci.* **2003**, 60, 1529–1546.

